Behaviour of in Plane and out of Plane Curved Steel Beams Strengthened with Carbon Fiber Reinforced Polymers

Kuda Anthonige Buddhika Weerasinghe

188074 P

Degree of Doctor of Philosophy in Civil Engineering

Department of Civil Engineering

University of Moratuwa

Sri Lanka

April 2022

Behaviour of in Plane and out of Plane Curved Steel Beams Strengthened with Carbon Fiber Reinforced Polymers

Kuda Anthonige Buddhika Weerasinghe

188074 P

A thesis submitted in Partial fulfilment of the Requirements for the Degree of Doctor of Philosophy in Civil Engineering

Department of Civil Engineering

University of Moratuwa

Sri Lanka

April 2023

Declaration

I declare that this is my own work and this thesis does not incorporate without acknowledgement any material previously submitted for a Degree or Diploma in any other University or institute of higher learning and to the best of my knowledge and belief it does not contain any material previously published or written by another person except where the acknowledgement is made in the text.

Also, I hereby grant to University of Moratuwa the non-exclusive right to reproduce and distribute my thesis, in whole or in part in print, electronic or other medium. I retain the right to use this content in whole or part in future works (such as articles or books).

Signature: Date: 22.05.2023

The above candidate has carried out research for the PhD thesis under my supervision.

Name of the supervisor: Prof J C P H Gamage

Signature of the supervisor: Date: 23.05.2023

Abstract

Application of curved steel members in constructions have shown an increasing demand during last few decades not only due to the aesthetic appearance, but also some structural advances. The curved steel beams used in structures may be either curve on a vertical plane or curved in a horizontal plane. A considerable number of steel structures contained vertically curved steel tubular members such as in bridges and curved roofs. Horizontally curved steel members are mostly made with steel I beams which can be seen in bridges and floor beams. These curved steel beams (either tubular or I beams) need retrofitting due to many reasons; errors in design stage, loss of original material properties due to material degradation, exposure to severe environments, or load increments in service stage. Though many methods available to retrofit steel structures, CFRP becoming popular within industry due to many of its favourable properties; comparatively higher durability when considering with other materials, superior fatigue performances, higher strength-to-weight ratio, less labour requirement, and easy applicability for any sectional shape. This study focussed on the behaviour of CFRP strengthened vertically curved circular hollow sectioned beams and the behaviour of I beams curved in a horizontal plane strengthened with CFRP. The study was conducted in several stages as explained below.

In phase one, Coupon tests were conducted in order to obtained the properties of steel tubes, steel I beams, CFRP and adhesives. All the specimens were prepared referring to ASTM standards and the tests were conducted according to same standard. Three samples from steel tubes, three samples from steel I beams, five samples from CFRP and Five samples from adhesive were prepared for testing. Tensile tests were conducted on all the samples and required properties for experimental studies and numerical studies were recorded. Some properties of the considered materials were calculated using empirical relationships found in the literature.

In phase two, experimental and analytical study for vertically curved circular hollow sectioned beams were conducted. Total sixteen samples bent in to four radii 0 mm, 2000 mm, 4000 mm and 6000 mm were prepared. Three specimens from each set of beams were strengthened with 500 mm, 750 mm and 1000 mm long CFRP patches. All the beams were tested under flexure until the failure occurs. It was noted that the curvature of the beams and the CFRP wrapping length have showed a major effect on the maximum load carrying capacity of the strengthened beams compared to control

beams. The proposed analytical method based on the equations found in literature to calculate the load deflection relationship of CFRP strengthened vertically curved steel hollow sectioned beams. The analytical model was verified using experimental results.

In phase three, a numerical analysis was performed to identify the effect of sensitive bond parameters such as number of CFRP layers, elastic modulus of CFRP, aspect ratio of steel sections, CFRP layer orientation. 3D finite element models were created and validated compared experimental results prior to conduct the parametric study. With the parametric study results, it was found that the rise in number of CFRP layers increases the ultimate load and this ultimate strength gain does not proportional to number of CFRP layers (percentage increment in ultimate loads reduced with successive increase in number of CFRP layers). It was also noted that the increase in CFRPs elastic modulus drastically increase the ultimate load of CFRP strengthened vertically curved beams while CFRP wrapping configuration showed a significant effect too. It was also noted that there is no significant effect of aspect ratio of beams on the strength gain, however, for beams having same dimeter the ultimate strength gain reduced with the increased thickness.

In fourth phase of the study, an experimental and analytical study was conducted on the CFRP strengthened horizontally curved steel I beams. The experimental study was conducted on twelve samples, consisted of beams bent in to three radii 0 mm, 4000 mm and 6000 mm. Three beams from each category was strengthened with three CFRP application profiles having 750 mm long CFRP patches while keeping one beam as a control beams. All the beams were tested under flexure until the failure with fixed end conditions at the either ends of the beams. The load-deflection responses and the failure modes were recorded. It was noted that the curvature of beams and CFRP application profile has significant effect on load-deflection behaviour and failure modes of CFRP strengthened horizontally curved steel I beams. An analytical model was developed base on the available literature to analyse the load deflection behaviour of CFRP strengthened horizontally curved steel I beams. The results obtained through experimental study and analytical method showed a good agreement which enable the use of analytical method for practical applications.

On the final stage of this research, a numerical study was performed in order to evaluate the effect of various bond parameters on the ultimate strength gain of the

CFRP strengthened horizontally curved steel I beams. 3D finite element models were developed using commercial available finite element modelling software and the results of numerical models were calibrated prior to conduct the parametric study. Influence of CFRP bond length, elastic modulus of CFRP, number of CFRP layers and elastic modulus of steel were studied. It was found that for both straight and horizontally curved beams strengthened with CFRP, ultimate strength increases until CFRP length increased to 750 mm. But, increase in CFRP length greater than 750 mm reduces the ultimate strength, and hence the optimum economical length of CFRP may be taken when CFRP length to span ratio become 0.75. Increase in elastic modulus of CFRP enhance the ultimate load for straight beams. However, this effect is not significant in beams curved to 4000 mm radius. The increase in CFRP layer count drastically increase the ultimate load for both straight and horizontally curved I beams. It was also noted that the percentage strength gain reduces with the increase in elastic modulus of steel.

Key words: Curved Beams, Circular Hollow Sections, Carbon Fibre Reinforced Polymer, Retrofit, Numerical Modelling, Debonding, Cohesive Zone Modelling

Acknowledgements

My experience as a PhD student at UoM has been more than enjoyable. Though this dissertation has a single author, the work done has involved a great support of many people, without whom I could not have completed it. The author would like to give heartiest gratitude to the people who have contributed and given their supported to this work in various ways.

First, I would like to express my greatest gratitude to my principle supervisor, Prof. (Mrs.) J.C.P.H. Gamage. She is not only the first one to be acknowledged, but also the most important contributor of this project. Prof. Gamage offered invaluable guidance, encouragements, advices and support throughout this study. Her enthusiasm to sacrifice her precious time to monitor and guide the author during the experimental and numerical investigations are greatly appreciated. Working with her over the years, I have learnt a lot and have enjoyed researching and teaching together.

I would like to express my deepest gratitude to Prof. Rangika Halwatura and Dr. Indika De Silva, who were the members of y progress review panel for their continuous guidance and comments throughout this period. Their comments helped me immensely to enhance the output of this research.

The kind support and valuable guidance of my co-supervisors, Professor David P. Thambiratnam and Dr Sabrina Fawzia, is appreciated in to greater extent. Their continuous inspiration, guidance and advice on my research have been invaluable. Their guidance on writing research papers for publications, helped me a lot to improve my scientific writing.

I would like to give special thanks to department of Civil Engineering, University of Moratuwa for providing me with lodging facilities and requirement to conduct experimental studies and providing required facilities for numerical studies. It should be also appreciated the tuition fee waiver offered by the Department of Civil Engineering.

Thanks are also extended to the staff members Mr Lanka, Mr Piyal, Mr Chandana, Mr Lines, Mr Roshan and all the other staff members from the Department of Civil Engineering. I would like to thank my fellow postgraduates for their fabulous ideas and for assisting me in preparing and testing samples in the laboratory. I would also

like to thank the other staff and my fellow postgraduates of the Department of Civil Engineering, UOM, for their friendship, encouragement and support.

I would also like to express my gratitude to all the suppliers and Sales Consultant for providing the research materials at reasonable price.

Most especially, this study could never have been achieved without the patience, constant support and understanding of my loving wife, Shanika Dilahani, Daughter Senadi Binulya and Son Vidas Damyuth.

Finally, I would like to express my gratitude to my family members, especially my eldest brother, for their support and encouragement.

Table of Content

List of Figures

List of Tables

List of Publications

1. Weerasinghe, K.A.B., Gamage, J.C.P.H., Sabrina Fawzia, and Thambirathnam, D.P., (2021), Experimental Investigation on Flexural Behaviour of Vertically-Curved Circular-Hollow Steel Sections Strengthened with Externally Bonded Carbon Fibre Reinforced Polymer, *Eng. Struct.(236)*

2. Weerasinghe, K.A.B., Gamage, J.C.P.H., Thambirathnam, D.P., and Sabrina Fawzia, "Experimental and Numerical Investigation of Carbon Fibre Reinforce Polymer Strengthened In-plane Curved Beams with Circular Hollow Sections Subjected to Flexure", Thin Walled Structures– **Under Review**

3. Weerasinghe, K.A.B., Gamage, J.C.P.H., Thambirathnam, D.P., and Sabrina Fawzia, "Effect of Beam Curvature on the Strength Gain of Carbon Fibre Reinforced Polymer Strengthened Vertically Curved Beams With Circular Hollow Sections", Australian Journal of Civil Engineering – **Under Review**

4. Sajinthan R., Weerasinghe K.A.B, Gamage J.C.P.H., (2020), Experimental investigation on torsional behaviour of carbon fibre reinforced polymer strengthened concrete beams curved in horizontal plane, Annual Sessions, Society of Structural Engineers, Sri Lanka.

5. Weerasinghe, K.A.B., Gamage, J.C.P.H., Thambirathnam, D.P., and Sabrina Fawzia," Experimental and Theoretical Investigation of the Behaviour of Carbon Fibre Reinforced Polymer Strengthened Out of Plane Curved Steel I Beams", **(On Preparation)**

6. Weerasinghe, K.A.B., Gamage, J.C.P.H., Thambirathnam, D.P., and Sabrina Fawzia, "Experimental and Numerical Investigation of Carbon Fibre

Reinforce Polymer Strengthened Out of plane Curved Steel I Beams Subjected to Flexure", **(On Preparation)**

Chapter 1
Introduction

1.1 Background

Steel is one of the major construction materials used in the construction industry to construct both building and bridges all over the world due to many advantages; low self-weight and strength to weight ratio, higher stiffness, quick installation, high ductility, no formwork required, easy to recycle and allows for off-site fabrication and on-site construction. Steel sections used in construction have various section shapes including; I-sections, H-sections, angle sections, channel sections and hollow sections (circular, square, rectangular). Mostly, the steel beams used in steel structures are straight beams, but a large number of curved beams also found. These curved beams either curved in elevation and curved on plane. Some of these steel structures found to be structurally inadequate due to many reasons; errors in design stage, loss of original material properties due to material degradation, exposure to severe environments, or load increments in service stage (Kabir et al. 2016).

There are several methods available to retrofit steel structures and each method has its own pros and cons. Strengthening using steel plates and externally bonded Fibre Reinforced Polymers (FRPs) are two major methods among them. The usage of FRP composites as a retrofitting material gives several advantages when compared to the use of steel plates. FRP composites poses a higher strength to weight ratio (the strength of CFRP found to be 10 times greater than the strength of mild steel), gives excellent corrosion resistance, high durability, superior fatigue endurance, less labour intensive work, and suitable for any sectional shape (Kabir et al. 2016; Teng, Yu, and Fernando 2012a; X. L. Zhao and Zhang 2007).

The applications of FRP in steel structures enhance the ultimate load capacity of structural members. Several researchers have found the influence of FRP composites on ultimate load capacity of straight steel beams with various cross sectional shapes(El Damatty et al 2003; Elchalakani 2014a; Kabir et al. 2016; Madhavan et al. 2015; Teng et al 2015a; Zhou and Young 2007). An attention is required on the behaviour of curved steel beams strengthened with FRP composites.

1.2 Research Significance

A significance number of researches have reported in the literature on the behaviour of CFRP strengthened straight steel beams under various loading conditions such as tension, compression, bending, torsion, and combined effect of them. Even though a considerable number of structures are constructed with curved steel beams (Curved in plane and curved out of plane), only a very few studies were done on the behaviour of these structural elements strengthened with CFRP. Therefore, its timely to conduct a study on the behaviour of curved steel beams strengthened with CFRP which is beneficial to the whole engineering community work of rehabilitation and retrofitting of existing structures. This study primarily focussed on in plane curved circular hollow sectioned beams and out of plane curved steel I beams. These two were selected based on the construction industry applications of curved steel beams. The all experimental, analytical and numerical analysis were conducted in order to access the real behaviour of these beams and to conduct parametric studies to investigate the influence of critical factors on the behaviour of these beams after strengthening with CFRP. The findings of this study are significantly contribute to the construction industry in advancement of retrofitting of steel beams using FRP materials.

1.2 Research Objectives

The key objective of this study is to determine the effectiveness of CFRP in strengthening vertically curved steel circular hollow sectioned beams and horizontally curved steel I beams. To achieve this main objective, firstly, experimental studies were conducted. Then numerical analyses were conducted using a commercially obtainable finite element modelling software package and the results of FEM were validated with experimental results. Then a number of parametric studies have been conducted on both control and strengthened specimens to evaluate the effect of sensitive bond parameters on the maxumum strength gain of CFRP strengthened curved beams. Following specific objects were achieved in order to address the main objectives of the study.

1. To Identify the Current Status of Knowledge on FRP Strengthened Curved Structural Elements
2. To Determine the Bond Performance of CFRP Strengthened CHS Beams Curved in Plane
3. To Determine the Bond Performance of CFRP Strengthened I Beams Curved Out of Plane
4. To Develop a Theoretical Relationship to Determine the Strength Gain of CFRP Strengthened in Plane Curved CHS Beams
5. To Develop a Theoretical Relationship to Determine the Strength Gain of CFRP Strengthened Out of Plane Curved I Beams

These objectives are achieved with contributory conference and journal papers as shown in Figure 1.1.

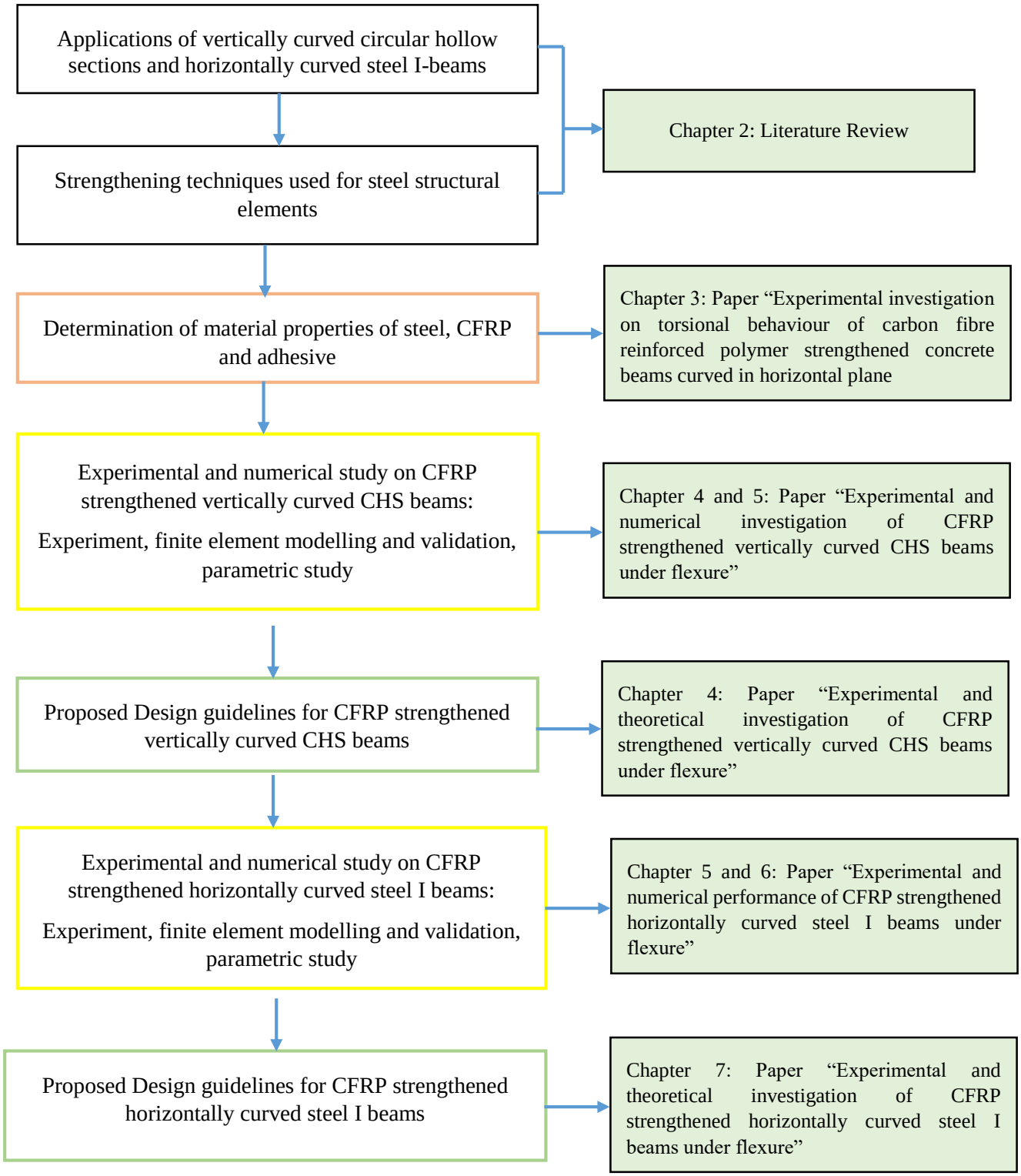

Figure 1.1 Research flow chart

1.3 Thesis Outline

This thesis comprised of seven chapters and their contents are as follows;

Chapter 1 gives an introduction to study, identification of objectives and formation of research activities.

Chapter 2 describes the related literature to the current study. Is provide literature on application of curved steel beams (vertically CHS and horizontally curved I beams) and their applications, need of retrofitting of steel structures, available retrofitting methods and their effectiveness, previous researches on CFRP strengthened steel hollow sections (circular, square and rectangular) under various loading conditions, previous researches on CFRP reinforced steel I beams under different loading conditions, different failure mechanisms in CFRP strengthened beams, analysis of curved steel members and related literature on numerical analysis of CFRP strengthened steel structures.

Chapter 3 describes detailed test programme on finding material properties of steel, CFRP and adhesive. It also includes the results obtained through the material level testing.

Chapter 4 describes the detailed test programme on CFRP strengthened vertically curved steel CHS beams under three-point bending. This is included sample preparation, testing and test results along with the recommendations. This chapter also describes the development of analytical method to analyse the behaviour of CFRP strengthened vertically curved CHS beams under flexure.

Chapter 5 describes the numerical analysis of CFRP strengthened vertically curved CHS beams under flexure. It discusses the model development, model validation and conducting of parametric study on the influence of sensitive bond parameters on the

strength gain of CFRP strengthened vertically curved CHS beams under flexure. The later part of the chapter elaborates on developed bond slip model for these strengthened beams under flexure.

Chapter 6 describes the detailed test programme on CFRP strengthened horizontally curved steel I beams under three-point bending. This is included sample preparation, testing and test results along with the recommendations. This chapter also describes the development of analytical technique to analyse the behaviour of CFRP reinforced horizontally curved steel I beams under flexure.

Chapter 7 describes the numerical analysis of CFRP strengthened horizontally curved steel I beams under flexure. It discusses the model development, model validation and conducting of parametric study the influence of sensitive bond parameters on the strength gain of CFRP strengthened horizontally curved steel I beams under flexure.

Chapter 8 describes the overall conclusions of the conducted study, recommendations for industry and the future work related to the current study.

Chapter 2
Literature Review
2.1 Introduction
This chapter expresses the literature review of existing literature on the performance of CFRP-reinforced steel structural elements with various section shapes under different loading conditions. The literature reviews mainly focus on the effect of various parameters, surface preparation, FRP length, CFRP configuration, adhesive properties, CFRP properties and environmental condition etc., on the performance of structural steel members under axial, flexure, torsion, fatigue, and dynamic loading. The effects of the parameters mentioned above on the failure modes of strengthened beams were also reviewed.

The first part of this chapter briefly discusses the applications of curved steel members since this PhD study mainly focussed on the retrofitting of curved steel beams using CFRP. The curved steel members considered for this study are Circular Hollow Sections (CHS) and universal beam sections. The chapter starts with discussing the pros and cons of steel CHS. Then the applications of curved CHS beams and universal beam sections are discussed. A detailed literature review is then presented on strengthening steel structural elements under various loading conditions, axial forces, flexural loading, torsion, fatigue, and dynamic loading. The effect effects of various CFRP application parameters are discussed concerning ultimate loads, ultimate deflections, stress and strain variations and failure modes.

The later part of the chapter discusses the behaviour of curved universal beam sections under flexural loading. Then the behaviour of CFRP-strengthened straight universal beams was studied and presented. Even though the study mainly focuses on the performance of curved steel beams, the behaviour of curved concrete beams

strengthened with CFRP was reviewed to relate those behaviours to steel beams in various ways.

2.2 Steel Hollow Sections (SHS) in Structural Applications

2.2.1 Advantages of hollow sections

Steel hollow sections have drastically grabbed the structural engineers' attention due to their superior properties to open steel sections. Those properties include the following listed in Table 1.

Table 2.1. Advantages of steel hollow sections compared to open section.

Advantage	Reason for advantage
Compression	Radius of gyration of hollow sections are much higher compared to weaker axis of open sections, and hence decrease the slenderness effect which increases the axial compression capacity
Bending	Hollow sections are favarouble when bending is present about both axis
Torsion	Torsional capacity of hollow sections is greater than the open section having nearly identical mass
Internal pressure	Circular hollow sections can resist higher pressure than other hollow sections
Combined loading	Hollow sections can carry higher combined loadings compared to open sections
Drag coefficient	Hollow sections, especially circular hollow sections have low drag coefficient compared to open sections with sharp edges
Aesthetic appearance	Normally structures constructed with hollow sections provide more aesthetic appearance than the open sections

Corrosion protection	SHS shows excellent resistance to the corrosion compared to open sections. This is due to the smooth transition of the coating in round corners in hollow sections. Further, hollow sections have 20% to 50% lower area to be protected against the corrosion compared to open sections.
Other uses	• Can be used as concrete infilled tubular sections having higher compressive strength. • Voids can be filled with water to increase the fire protection of the structure. • Internal voids can be used to circulate air and water for the ventilation purposes. • Voids can be used to place cables and wires used in building services

2.2.2 Applications of hollow sections in constructions

Applications of SHS in construction have drastically increased in recent years due to their versatile properties. These applications extend from simple building structures to complex structures such as bridges and larger-span roof structures.

SHS is commonly used to construct offshore structures to support the platforms to produce oil and gas. The reasons to use them include the higher resistance to cyclic loading due to currents, waves and winds, higher durability in severe marine environments and easy maintenance. Figure 2.1 shows the offshore structures constructed out of circular hollow sections.

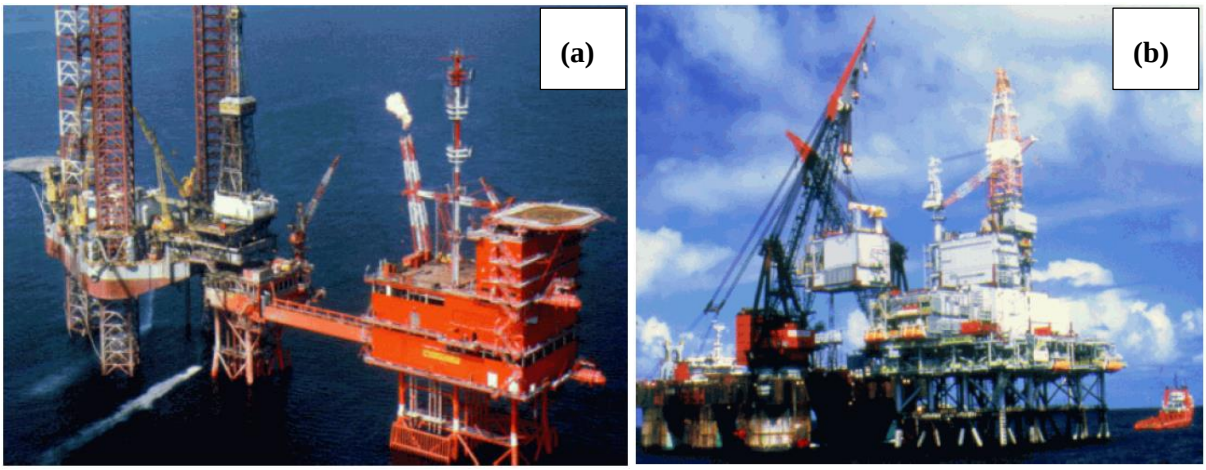

Figure 2.1. (a) Offshore platform with jack up; (b) offshore topside with various applications (Wardnier, 2001)

SHS are mainly used in buildings as structural components such as columns, lattice girders and space frames of roofs. Their application also extended as architectural components that bring aesthetic appearance to buildings. There are several examples to show the excellent use of SHS as components of bridges. In bridges, SHS may use mainly as arches and braces. The circular hollow section is sometimes used as a flange for the plate girders due to its higher compressive strength. Figure 2.2 and Figure 2.3 shows some applications of SHS in buildings and bridges, respectively.

Figure 2.4 shows applications of SHS as barriers in hydraulic structures. SHS function excellently in hydraulic barriers due to their properties, such as a lesser drag coefficient leading to reduce drag forces due to waves and excellent corrosion protection due to the absence of sharp edges, which leads to an increased life span.

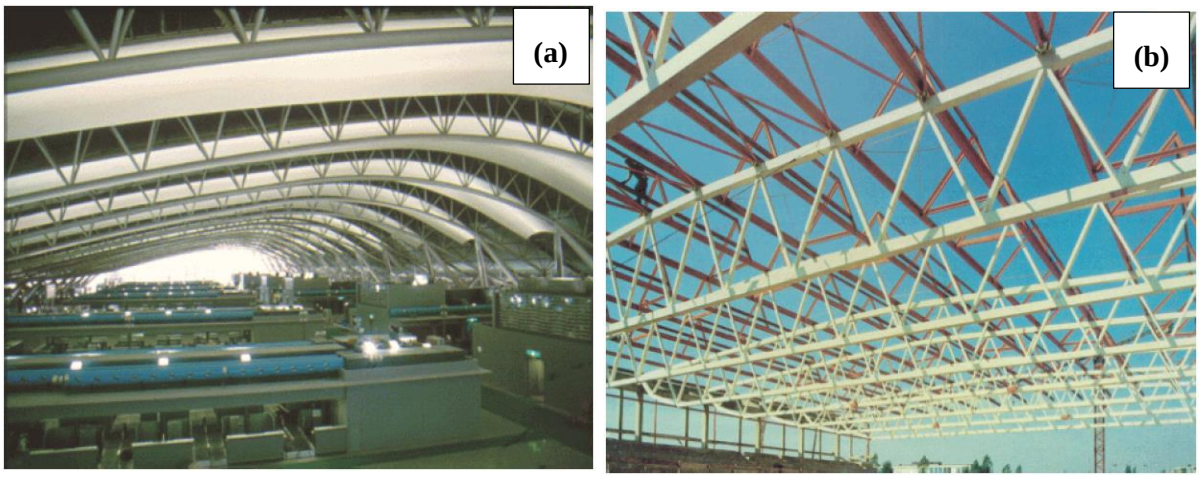

Figure 2.2. (a) Kansai airport roof, Japan (b) A roof with lattice girders (Wardnier, 2001)

Figure 2.3. (a) Railway bridge with CHS arch;(b) Pedestrian bridge in France (Wardenier 2001)

SHS are prepared for masts and towers due to their excellent properties, corrosion protection, wind loading and architectural appearance. Even though most of the

transmission towers are constructed with angle sections, the current trends in aesthetic and environmentally friendly structures led these structures to be designed with SHS. Figure 2.5 shows two applications of SHS in towers and masts. Further applications of SHS sections include gantries, parapets, and guard rails. They have mechanical engineering applications such as jibs and cranes. They also have applications such as radio telescopes and roller coasters (Figure 2.6).

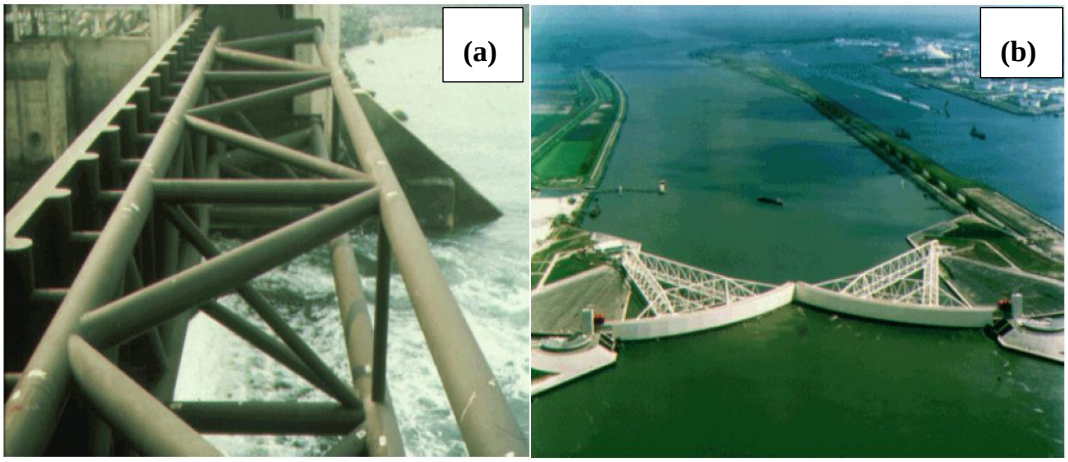

Figure 2.4. (a) Eastern Scheldt barrier, The Netherlands (b) Storm surge barrier near Hook of Holland, The Netherlands(Wardenier 2001)

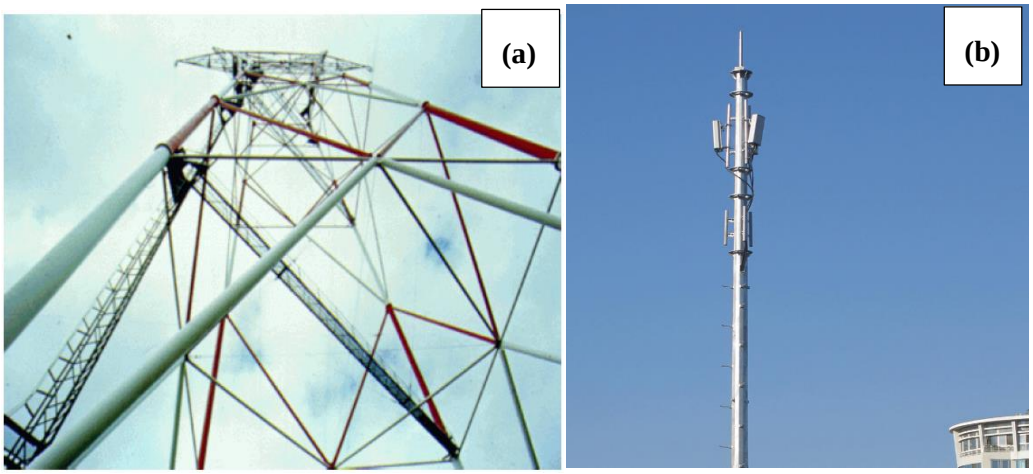

Figure 2.5. (a) Electrical transmission tower(Wardenier 2001) (b) A telephone mast (Wikipedia, 0n 15/07/2020)

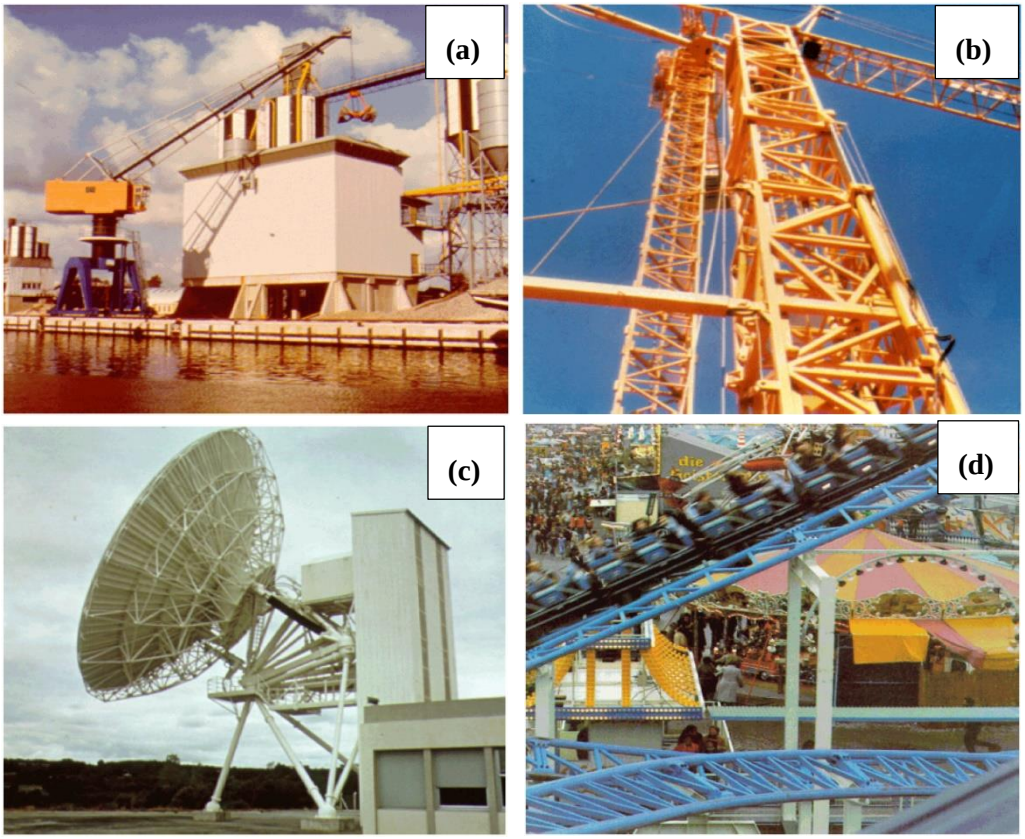

Figure 2.6. (a) Jib (b) Crane (c) Radiotelescope and (d) Roller coaster (Wardenier 2001)

2.3 Use of Curved Steel in Constructions

The use of curved steel for construction has a long history. In earlier days, curved structures were constructed with the iron cast for curved profiles. However, during the 20th century, curved steel was used for construction with the development of the steel industry (D. Brown, 2007). The primary purpose of curved beam elements in structures is to give an aesthetic view. It provides a variety of forms than straight members and makes exposed and elegant solutions. Curved steel elements also provide grandeur and spaciousness for structures like shopping malls, airports, sports facilities, and recreational centres. Figure 2.7 shows some examples of the effective use of curved steel in different structures.

Curved steel may be curved in elevation or on the plane (horizontally curved beams). Steel beams curved in a vertical plane have significant applications in bridges and

roof structures arches. In contrast, the major applications of horizontally curved beams include horizontally curved bridge girders and curved floor beams. Figure 2.8 shows some applications of horizontally and vertically curved beams.

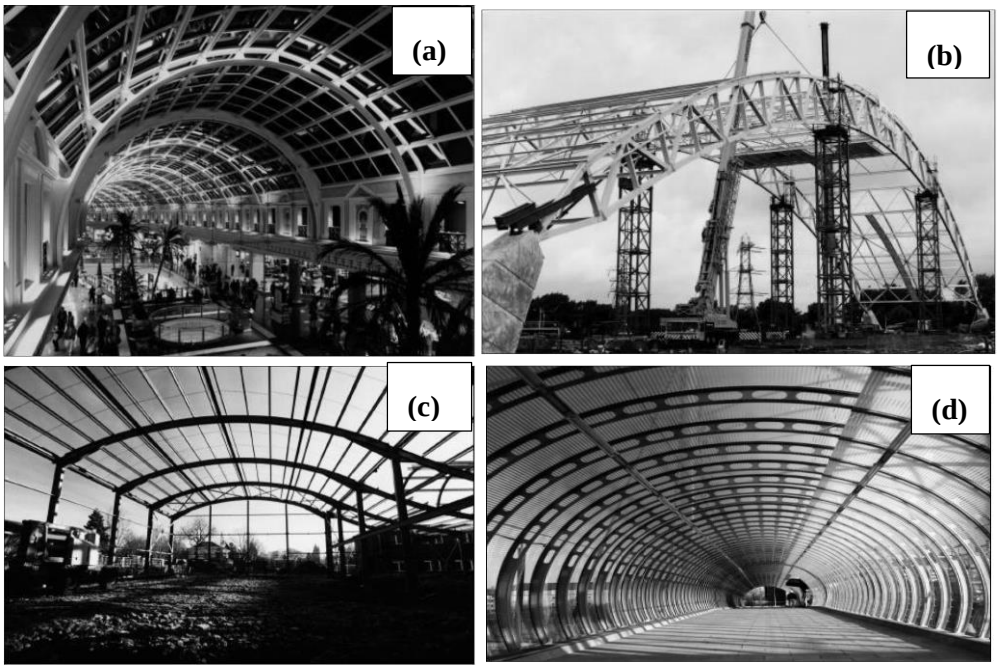

Figure 2.7. Use of curved steel in different steel structures;(a) Roof steel work; (b) Curved truss in a sport facility; (c) curved rafters of a portal frame; (d) Curved steel supports for walkway enclosure(D. Brown 2007)

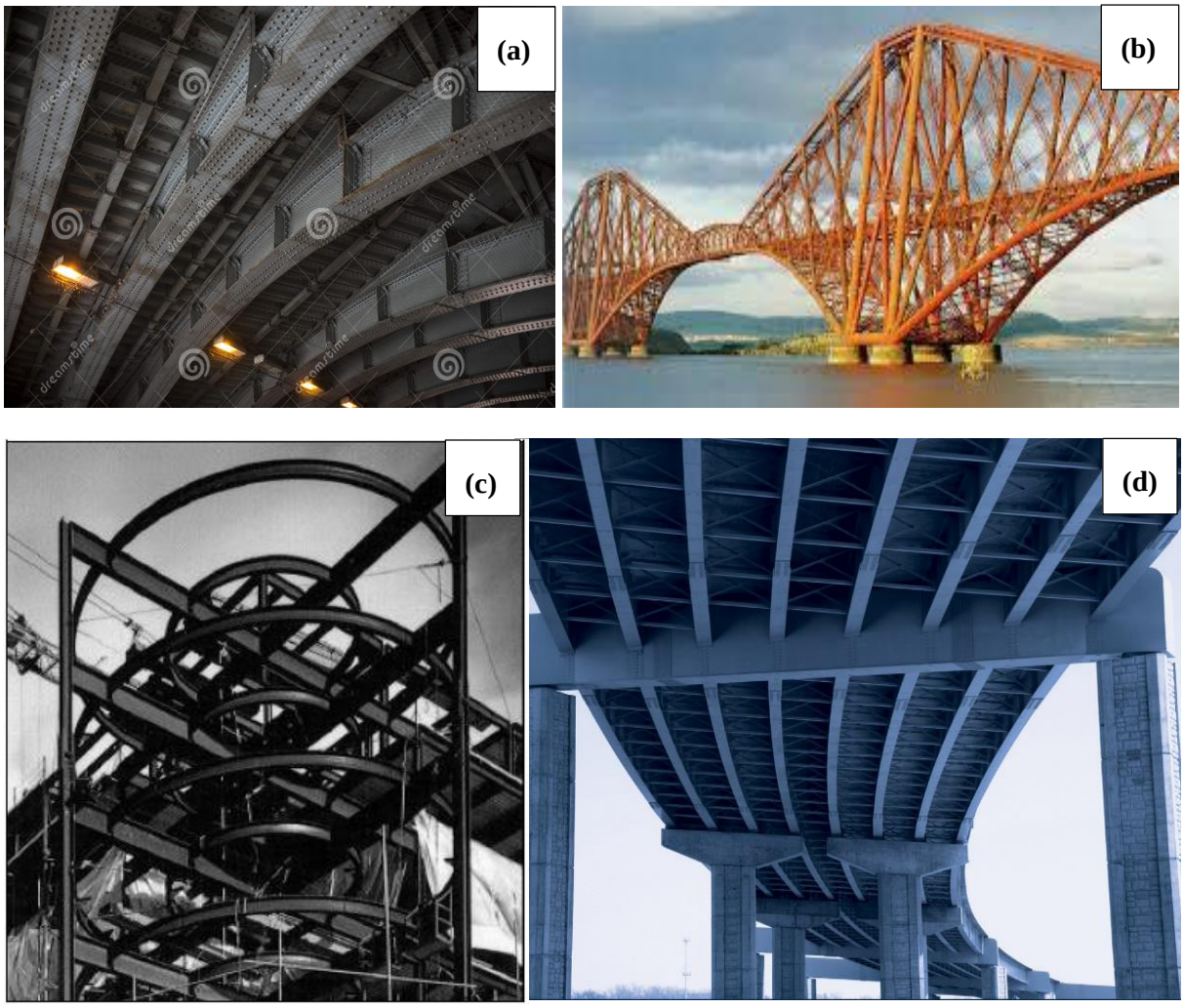

Figure 2.8. Applications of vertically and horizontally curved steel beams, (a) vertically curved roof I-beams; (b) Vertically curved tubular beams in a bridge; (c) horizontally curved floor beams; and (d) horizontally curved I-beams in a highway bridge (Wardnier, 2001).

2.4 Curving Process of Steel

Curving (bending) of steel sections can be done using two principal methods; roller bending and induction bending, of which the latter is more expensive. Nevertheless, the advantages of induction bending include the ability to bend into small radii and the ability to bend lighter sections. Most curved steel required for construction is produced using the roller bending process, considered a cold process. Roller bending is done by passing the steel section through bending rollers progressively. The roller arrangements are different for hollow sections and I-beams. An additional roller is required to prevent buckling the web of I-sections during the bending process. Figure

2.9 shows the bending processes and roller arrangement for bending hollow, and I sections.

In the induction bending process, the section to be curved is passed through an electrical coil under a temperature between 700 ºC and 1050 ºC. The section is heated to the above temperature range within a narrow bend. Air and water are used to cool the section immediately after the heated coil. Induction bending and roller bending are combined for some of the bending processes when large radii or multiple radii are required. Figure 2.10 shows the induction bending process and bending equipment.

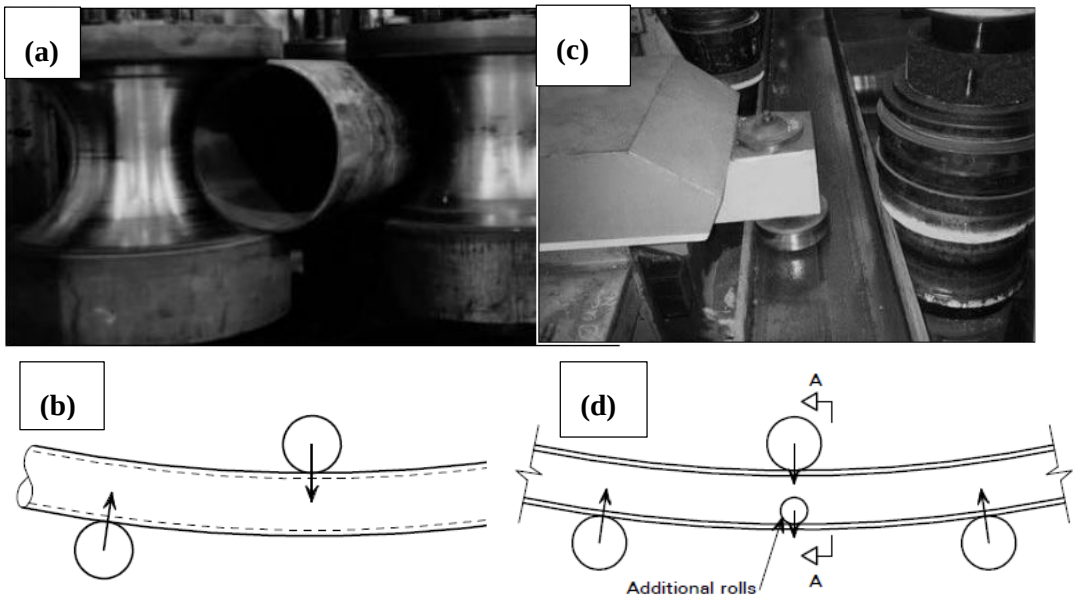

Figure 2.9. (a) Roller bending of a tubular section; (b) roller arrangement for a tubular section; (c) bending of an I section; and (d) position of additional roller to avoid web buckling

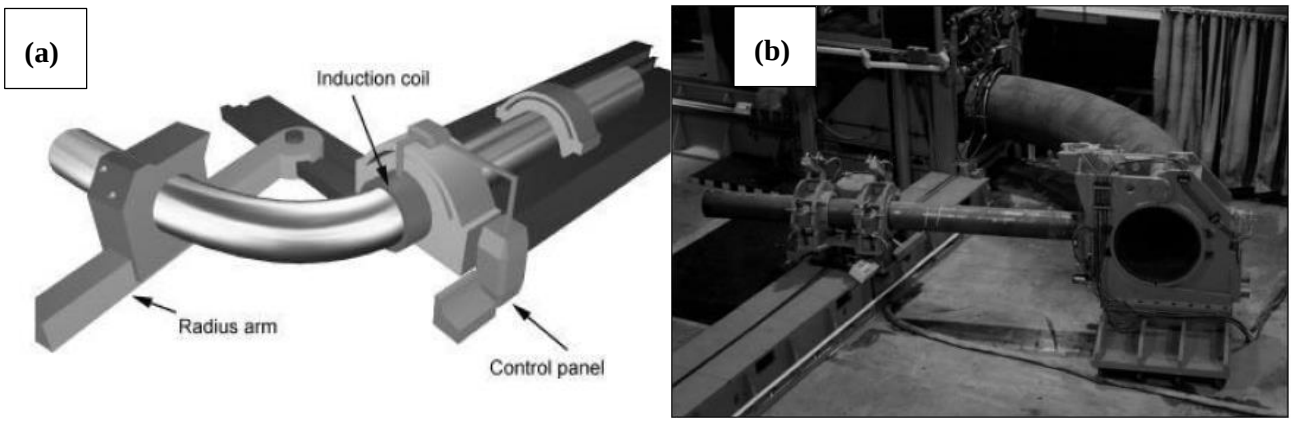

Figure 2.10. (a) Induction bending equipment; and (b) induction bending of a large diameter tube (D. Brown 2007)

2.5 Analysis of Curved Beams

As found in the literature, many researchers worldwide have found different ways to analyse beams curved in elevation and plane. This section of the chapter discusses on few methods available.

2.5.1 Theoretical analysis of horizontally curved steel beams

The analysis and design of horizontally curved beams differ from that of straight beams due to the torsional load induced by vertical loading. Therefore, such members should be designed to restrain the internal bending moment, torsional moment as well as transverse shear. Horizontally curved steel or reinforced concrete beams are continuous or monolithic at the ends. The capability of resisting the torsional moment of curved beams depends on the torsional rigidity of the section. Higher torsional rigidity of the sections provides higher torsional capacity. The cross-sectional shape of the beam influences the magnitude of the torsional rigidity constant.

In 1969 (Wong, 1970) developed a method to analyse horizontally curved beams with fixed ends under concentrated and distributed loads. This method was developed based on Castigliano's theorem to evaluate bending moment, torsional moment, and maximum span moments. Mid-span deflections were calculated using the moment area method, and solutions for the multi-span curved beams were developed based on

the moment distribution method. He has made three basic assumptions during the derivation of the equations:

1. The material is homogeneous and isotropic.
2. The material has a linear stress-strain relationship, so the superposition method is valid.
3. The cross-section shape of the beam is uniform, and the dimensions are smaller when compared to the radius of curvature.

The sign conventions used for bending moment, torsion and vertical force during the derivation are shown in Figure 2.11. According to that sign convention, the bending moment was positive if it produced clockwise rotation about the radial axis when looking outward from the centre of the curvature. Torsional moments were considered positive; looking along the beam's tangent in a counterclockwise direction produces a clockwise rotation. The vertical force was taken as positive when it acted upward.

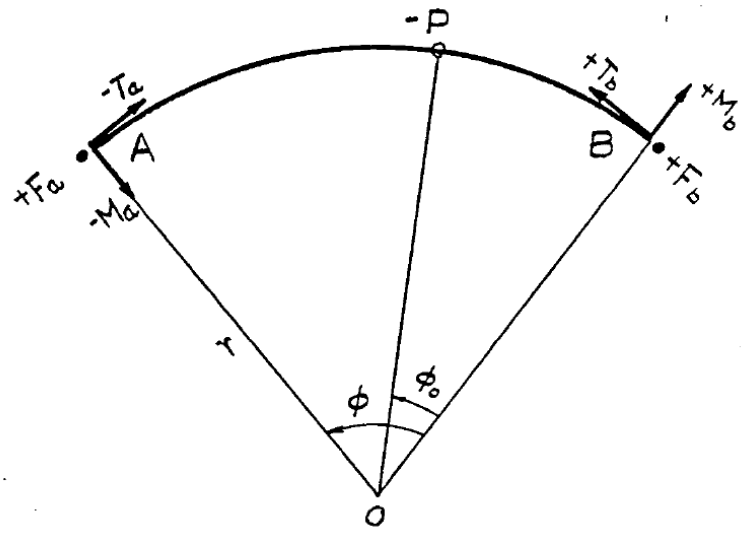

Figure 2.11. Sign convention

A concentrated load P is applied on a horizontally curved beam at the point D with an angular distance Φ_0 from support B as shown in Figure 2.12. The bending moment

and torsional moment at any section cross section C at an angular distance θ from B is given by M_θ and T_θ respectively. Here Φ is the subtended angle at the centre of the curvature of the beam.

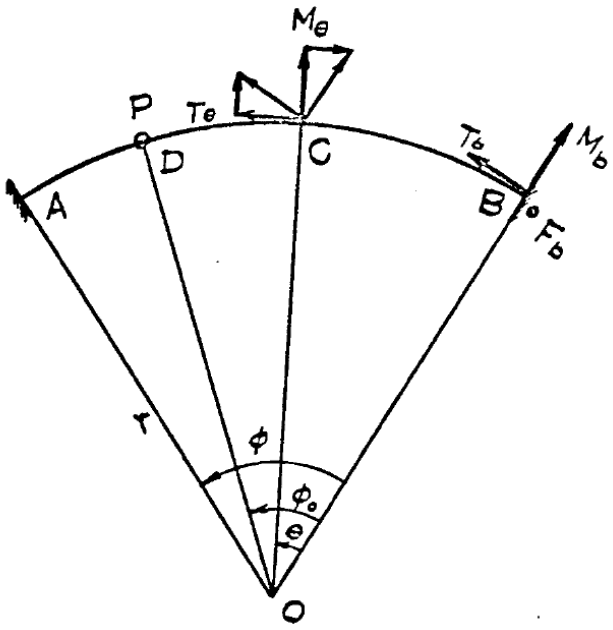

Figure 2.12. Horizontally curved beam loaded with a point load and the developed reactions.

By applying the Castigliano's theorem for the beam.

$$U = \int \frac{M_\theta^2}{2EI} r d\theta + \int \frac{T_\theta^2}{2GJ} r d\theta \quad (1.1)$$

Where; $M_\theta^2 = M_b \cos\theta + T_b \sin\theta - F_b \mathrm{r} \sin\theta$ (1.2)

$$T_\theta^2 = -M_b \sin\theta + T_b \cos\theta + F_b \mathrm{r}(1 - \cos\theta) \quad (1.3)$$

By substituting from equations (2) and (3) to (1) and performing the integration by applying boundary conditions;

$Angle\ of\ rotation\ due\ to\ bending\ moment\ (\omega_{b)} angle\ of\ rotation\ due\ to\ torsinal\ moment(\varphi_b) = vertical\ deflection(\Delta_b) = 0$ will give;

$$M_b = \frac{1}{|A|}\begin{bmatrix} a_0Pr & -b_1 & c_1 \\ b_0Pr & b_2 & c_2 \\ c_0Pr & c_2 & c_3 \end{bmatrix} = PrC_m$$

(1.4)

$$T_b = \frac{1}{|A|}\begin{bmatrix} a_1 & a_0Pr & c_1 \\ -b_1 & b_0Pr & c_2 \\ c_1 & c_0Pr & c_3 \end{bmatrix} = PrC_t \qquad (1.5)$$

$$F_br = \frac{1}{|A|}\begin{bmatrix} a_1 & -b_1 & a_0Pr \\ -b_1 & b_2 & b_0Pr \\ c_1 & c_2 & c_0Pr_0 \end{bmatrix} = PrC_f$$

(1.6)

$F_b = PC_f$ Where, $|A| = \begin{vmatrix} a_1 & -b_1 & c_1 \\ -b_1 & b_2 & c_2 \\ c_1 & c_2 & c_3 \end{vmatrix}$ and the constant in the matrices as follows.

$a_1 = \emptyset(n+1) - \sin\emptyset\cos\emptyset(n-1)$

$b_1 = \sin^2\emptyset(n-1)$

$c_1 = \sin^2\emptyset(n-1) + 2n(\cos\emptyset - 1)$

$a_0 = (n-1)\cos\emptyset_0(\sin^2\emptyset - \sin^2\emptyset_0) + \sin\emptyset_0(\emptyset - \emptyset_0)(n+1)$

$$- \sin\emptyset_0\left(\frac{n-1}{2}\right)(\sin 2\emptyset - \sin 2\emptyset_0) + 2n(\cos\emptyset - \cos\emptyset_0)$$

$a_2 = b_1$

$b_2 = \emptyset(n+1) + \sin\emptyset\cos\emptyset(n-1)$

$c_2 = 2n\sin\emptyset - \emptyset(n+1) - \sin\emptyset\cos\emptyset\,(n-1)$

$$b_0 = -\cos\emptyset_0\,(\emptyset - \emptyset_0)(n+1) - \frac{1}{2}\cos\emptyset_0\,(n-1)(\sin 2\emptyset - \sin 2\emptyset_0)$$

$$- (n-1)\sin\emptyset_0\,(\sin^2\emptyset - \sin^2\emptyset_0) + 2n(\sin\emptyset - \sin\emptyset_0)$$

$$a_3 = c_1$$

$$b_3 = c_2$$

$$c_3 = \emptyset(n+1) + \sin\emptyset\cos\emptyset(n-1) - 4n\sin\emptyset + 2m\emptyset$$

$$c_0 = \frac{(n-1)}{2}\cos\emptyset_0\,(\sin 2\emptyset - \sin 2\emptyset_0) + (\emptyset - \emptyset_0)[\cos\emptyset_0(n+1) + 2n]$$
$$+ (n-1)\sin\emptyset_0(\sin^2\emptyset - \sin^2\emptyset_0)$$
$$- 2n(1+\cos\emptyset_0)(\sin\emptyset - \sin\emptyset_0) + 2n\sin\emptyset_0(\cos\emptyset - \cos\emptyset_0)$$

$$n = \frac{EI}{GJ} = \frac{EI}{\frac{E}{2(1+\gamma)}J} = \frac{2(1+\gamma)I}{J}$$

Here, in these equations M_b, T_b and F_b are vary with $\emptyset, \emptyset_0, n$ and r. These variations are expressed by the coefficients C_m and C_t and relationships between them and the angle $\emptyset$ are given in Figure 2.13 and Figure 2.14 respectively.

Obviously, the maximum bending moment occurs when $\emptyset = \emptyset_0$ and is given by;

$$M_{max} = M_{\emptyset_0} = M_b\cos\emptyset_0 + T_b\sin\emptyset_0 - F_b r\sin\emptyset_0 = PrC_{mm} \quad (1.7)$$

The variation of C_{mm} with respect to $\emptyset$ and m are shown in Figure 2.15.

Deflection

Deflection of horizontally curved beam can be found by the moment area method (neglecting the rotation of the section and the deformation caused by the transverse shear);

$$EI\Delta_\theta = \int_0^\theta M_\theta r sin\left(\frac{\emptyset}{2} - \theta\right) ds + m\int_0^\theta T_\theta r\left[1 - \cos\left(\frac{\emptyset}{2} - \theta\right)\right]\text{ds} \quad (1.8)$$

To solve for the vertical deflection under the load, which is acting at the mid span, substituting from (2) and (3) and let $ds = rd\theta$ and $\theta = \emptyset/2$;

$$\Delta_{\emptyset/2} = \frac{Pr^3}{EI} C_d$$

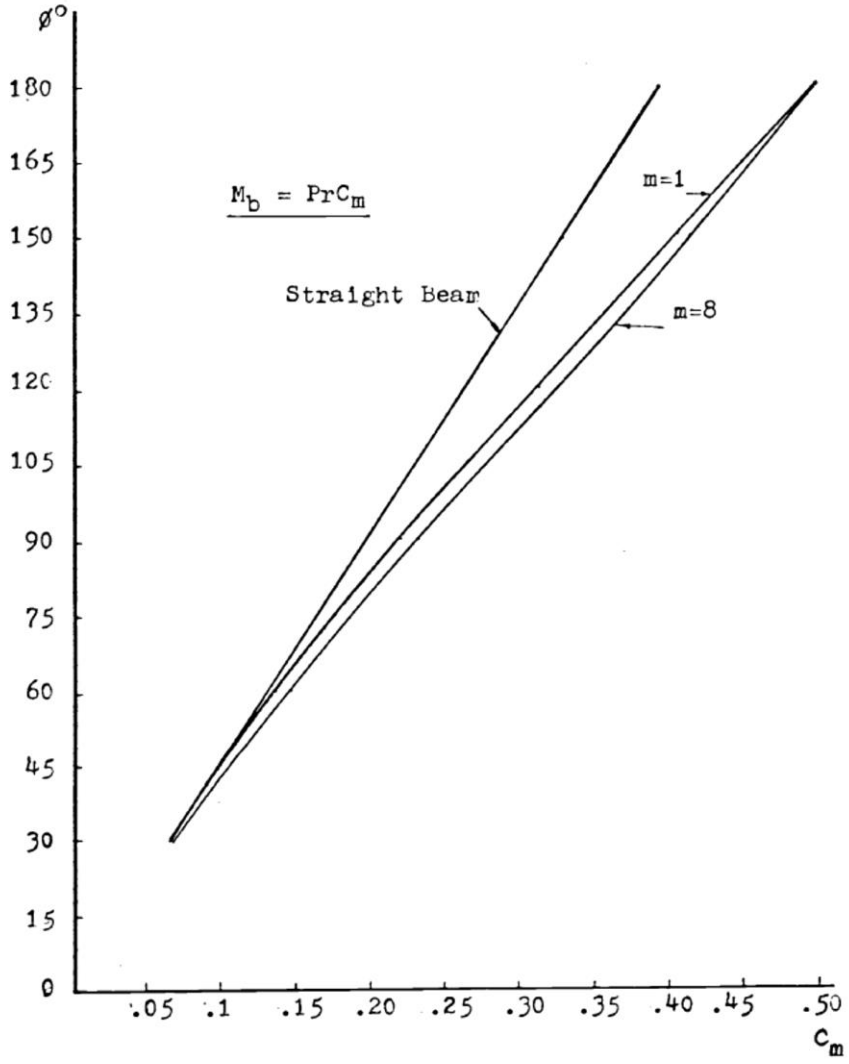

Figure 2.13. Variation of the fixed end bending moment coefficient with span angle for curved beams loaded with concentrated load.

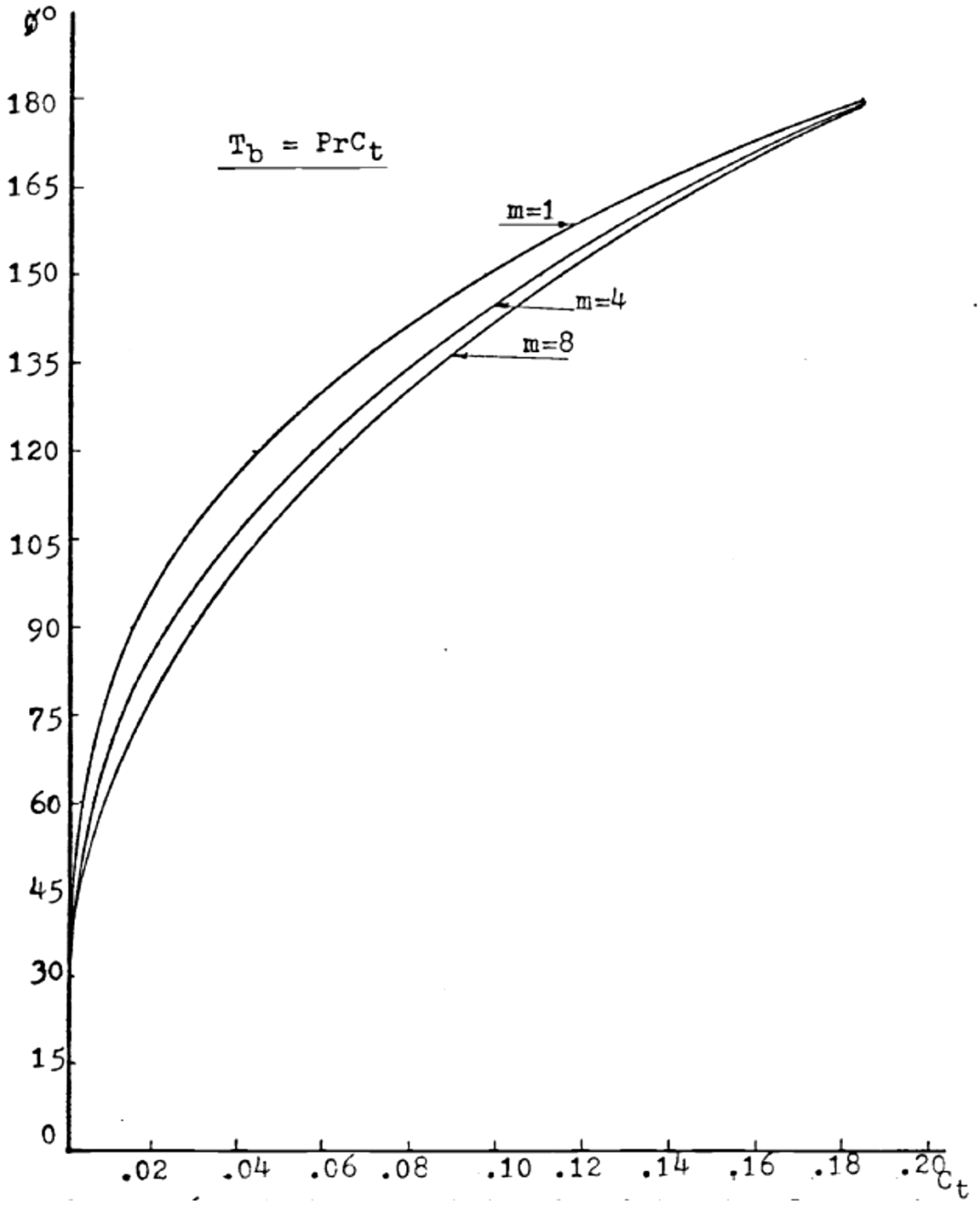

Figure 2.14. Variation of the fixed end torsional moment coefficient with span angle for curved beams loaded with concentrated load.

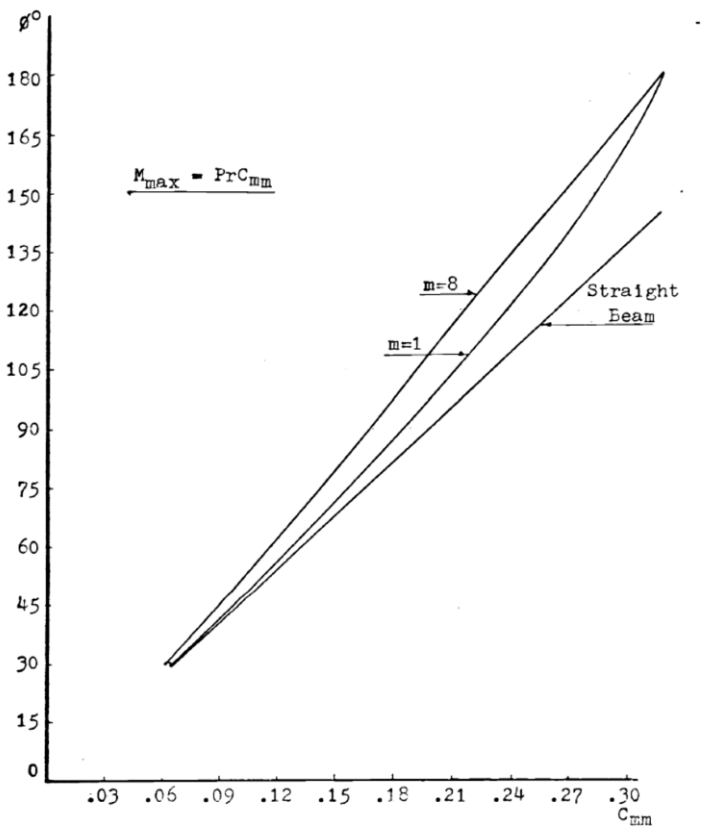

Figure 2.15. Variation of the maximum span moment coefficient with span angle for curved beams loaded with concentrated load.

Horizontally curved beam fixed at both ends with uniformly distributed load.

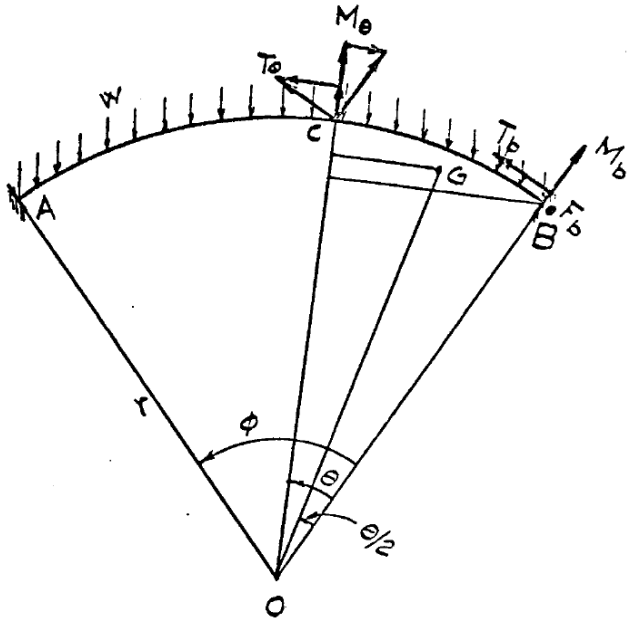

Figure 2.16. Curved fixed end beam with uniformly distributed load.

Because of the symmetry of the beams support reaction at B, F_b can be expressed as;

$$F_b = \frac{Wr\emptyset}{2} \tag{1.10}$$

The distance OG to the centre of gravity of part BC is given by;

$$OG = \frac{r\sin\frac{\theta}{2}}{\theta/_2}$$

At any section C;

$$M_\theta = M_b\cos\theta + T_b\sin\theta - F_b r\sin\theta + wr\theta\left(\frac{r\sin\theta/_2}{\theta/_2}\sin\frac{\theta}{2}\right)$$

$$= M_b\cos\theta + T_b\sin\theta - \frac{wr\theta}{2}r\sin\theta + wr^2(1-\cos\theta) \tag{1.11}$$

$$T_\theta = T_b\cos\theta - M_b\sin\theta + F_b r(1-\cos\theta) - wr\theta\left(r - \frac{r\sin\theta/_2}{\theta/_2}\cos\theta/_2\right)$$

$$= T_b\cos\theta - M_b\sin\theta + \frac{wr^2\theta}{2}(1-\cos\theta) - wr^2(\theta-\sin\theta) \tag{1.12}$$

By applying Castigliano's Theorem,

$$U = \int\frac{M_\theta^2}{2EI}rd\theta + \int\frac{T_\theta^2}{2GJ}rd\theta \tag{1.13}$$

By applying in equation 1.13;

$\frac{\partial U}{\partial M_b} = \omega_b = 0$ and $\frac{\partial U}{\partial T_b} = \varphi_b = 0$

$$M_b(a-c) - T_b b - wr^2 d = 0$$

$$-M_b(b) + T_b(a+c) - wr^2 e = 0$$

Solving for M_b and T_b will give;

$$M_b = -wr^2 \frac{be + d(a+c)}{-a^2 + b^2 + c^2} \tag{1.14}$$

$$T_b = -wr^2 \frac{bd + e(a-c)}{-a^2 + b^2 + c^2} \tag{1.15}$$

Where;

$$a = \emptyset(n+1)$$

$$b = \sin^2 \emptyset(n-1)$$

$$c = \sin \emptyset \cos \emptyset\,(n-1)$$

$$d = \emptyset(n+1) + n\emptyset(1 + \cos \emptyset) - \frac{\emptyset}{2}\sin^2 \emptyset(n-1) - 2\sin \emptyset(n+1) - \sin \emptyset \cos \emptyset(n-1)$$

$$e = \frac{1}{2}\emptyset^2(n+1) + \frac{\emptyset}{2}\sin \emptyset \cos \emptyset\,(n-1) - \sin^2 \emptyset(n-1) + n\emptyset \sin \emptyset - 2(n+1)(1 - \cos \emptyset)$$

After substituting for a, b, c, d and e for the equations P and Q, fixed end bending moment and torsional momenr become;

$$M_b = M_{fb} = -wr^2 \left| \frac{2(n+1)\sin \emptyset - n\emptyset(1 + \cos \emptyset)}{\emptyset(n+1) - \sin \emptyset(n-1)} - 1 \right| = wr^2 C_m \tag{1.16}$$

$$T_b = T_{fb} = -wr^2 \left| \frac{2(n+1)\,(1 - \cos \emptyset) - n\emptyset \sin \emptyset}{\emptyset(n+1)n - \sin \emptyset(n-1)} - \frac{\emptyset}{2} \right| = wr^2 C_t \tag{1.17}$$

Where;

$$n = \frac{EI}{GJ} = \frac{EI}{\frac{E}{2(1+\gamma)}J} = \frac{2(1+\gamma)I}{J}$$

By substituting values for equations for $M_b$and T_b in equations Y and Z; M_θ and T_θ can be expressed as;

$$M_\theta = wr^2 C_{m\theta}$$

$$T_\theta = wr^2 C_{t\theta}$$

The values of C_m and C_t are varying with n and $\emptyset$, are plotted as in Figure 2.17 and Figure 2.18 respectively.

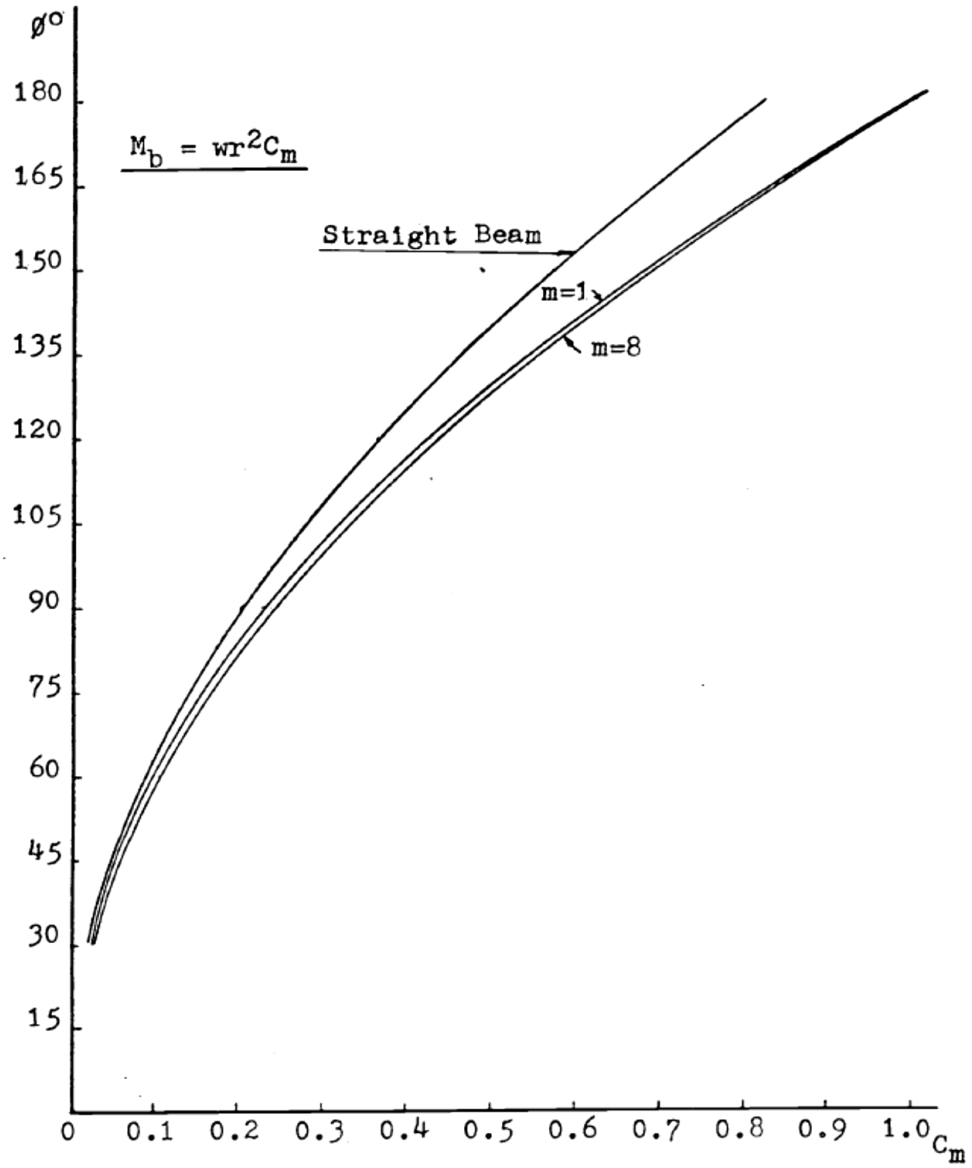

Figure 2.17. Variation of fixed end bending moment coefficient with span angle for uniformly curved beams

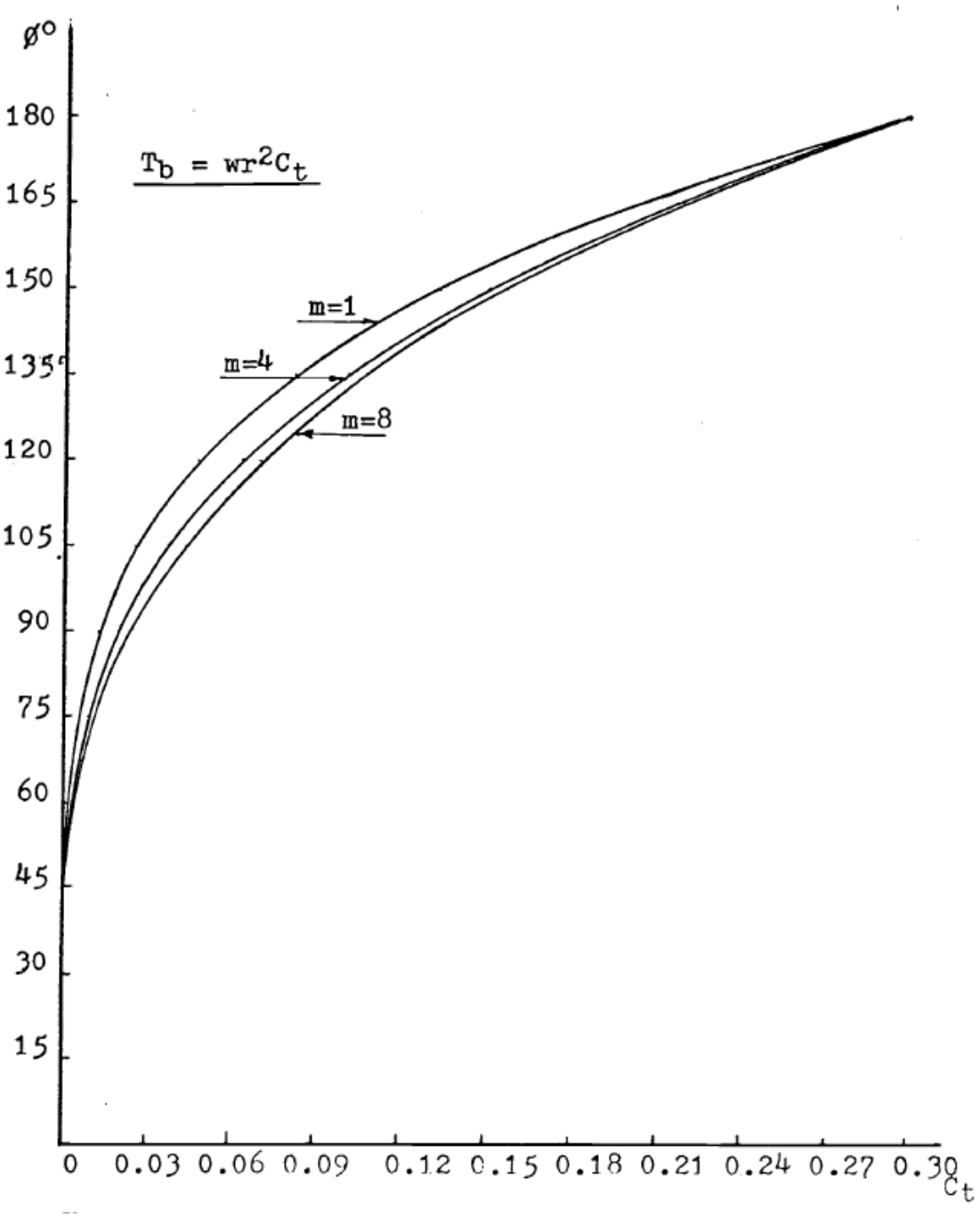

Figure 2.18. Variation of fixed end bending moment coefficient with span angle for uniformly curved beams

The maximum bending moment occurs at the mid span and at that section $\theta = \frac{\emptyset}{2}$;

$$M_{max} = M\left(\emptyset/_2\right) = M_b \cos\frac{\emptyset}{2} + T_b \sin\frac{\emptyset}{2} - \frac{wr^2\emptyset}{2}\sin\frac{\emptyset}{2} + wr^2\left(1 - \cos\frac{\emptyset}{4}\right)$$

$$= wr^2\left[C_m \cos\frac{\emptyset}{2} + C_t \sin\frac{\emptyset}{2} - \frac{\emptyset}{2}\sin\frac{\emptyset}{2} + \left(1 - \cos\frac{\emptyset}{4}\right)\right] =$$

$$wr^2 C_{mm} \tag{1.18}$$

The variation of C_{mm} with respect to ∅ is given in Figure 2.19.

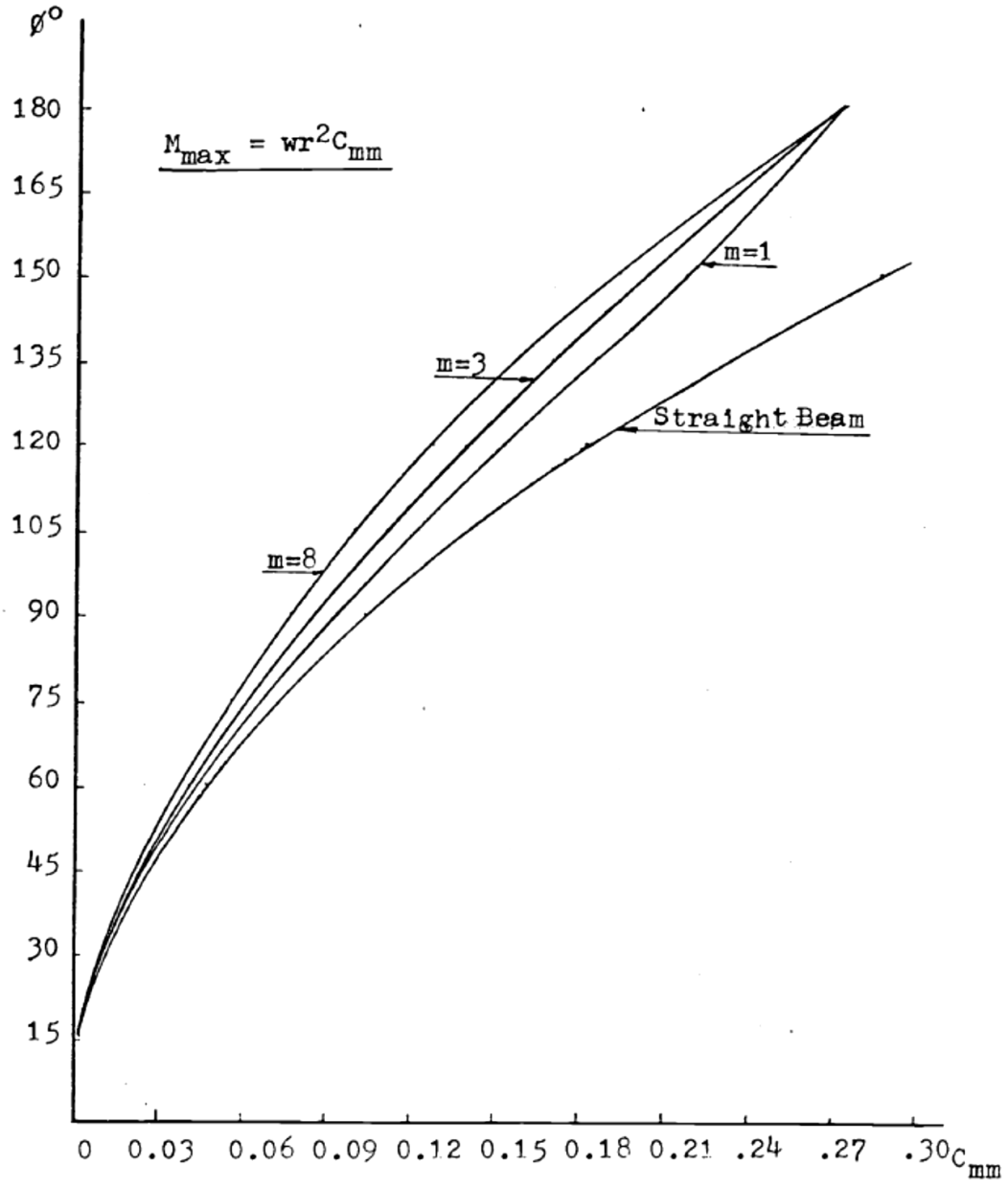

Figure 2.19. Variation of maximum span moment coefficient with span angle for uniformly curved beams

Deflection

The vertical deflection at any point on the beam can be evaluated using the moment area method as follows;

$$\Delta_\theta = \frac{1}{EI}\int_0^\theta M_\theta r sin\left(\frac{\emptyset}{2}-\theta\right) ds + \frac{1}{GJ}\int_0^\theta T_\theta r\left[1-\cos\left(\frac{\emptyset}{2}-\theta\right)\right]\text{ds} \quad (1.19)$$

Maximum deflection occurs at the mid-span when $\theta = {}^{\emptyset}/_{2}$. Substituting to equation 1.19, maximum deflection will be given by;

$$\Delta_\theta = \frac{wr^4}{EI}\left[\sin\frac{\emptyset}{2}\left\{\frac{(\emptyset+\sin\emptyset)(C_m-1)}{4} + \left(C_t-\frac{\emptyset}{2}\right)\left(\frac{1-\cos\emptyset}{4}+n-\frac{n(1-\cos\emptyset)}{4}\right)\right\} - \cos\frac{\emptyset}{2}\left\{\frac{C_m(1-\cos\emptyset)(1+n)}{4} - \frac{(1-\cos\emptyset)(1-n)}{4} + \frac{\left(C_t-\frac{\emptyset}{2}\right)(\emptyset-\sin\emptyset+n\emptyset+n\sin\emptyset)}{4} + \left(1-\cos\frac{\emptyset}{2}\right)(1+n)\right\} + n\left(\left(\cos\frac{\emptyset}{2}-1\right)(C_m-1)+\frac{\emptyset^2}{8}\right) + \sin\frac{\emptyset}{2}\left(\frac{(1-n+n(C_m-1)(\emptyset-\sin\emptyset)}{4}\right)\right]$$

$$\Delta_\theta = \frac{wr^4}{EI}C_d \quad (1.20)$$

The values of C_d are plotted into curves as shown in Figure 2.20;

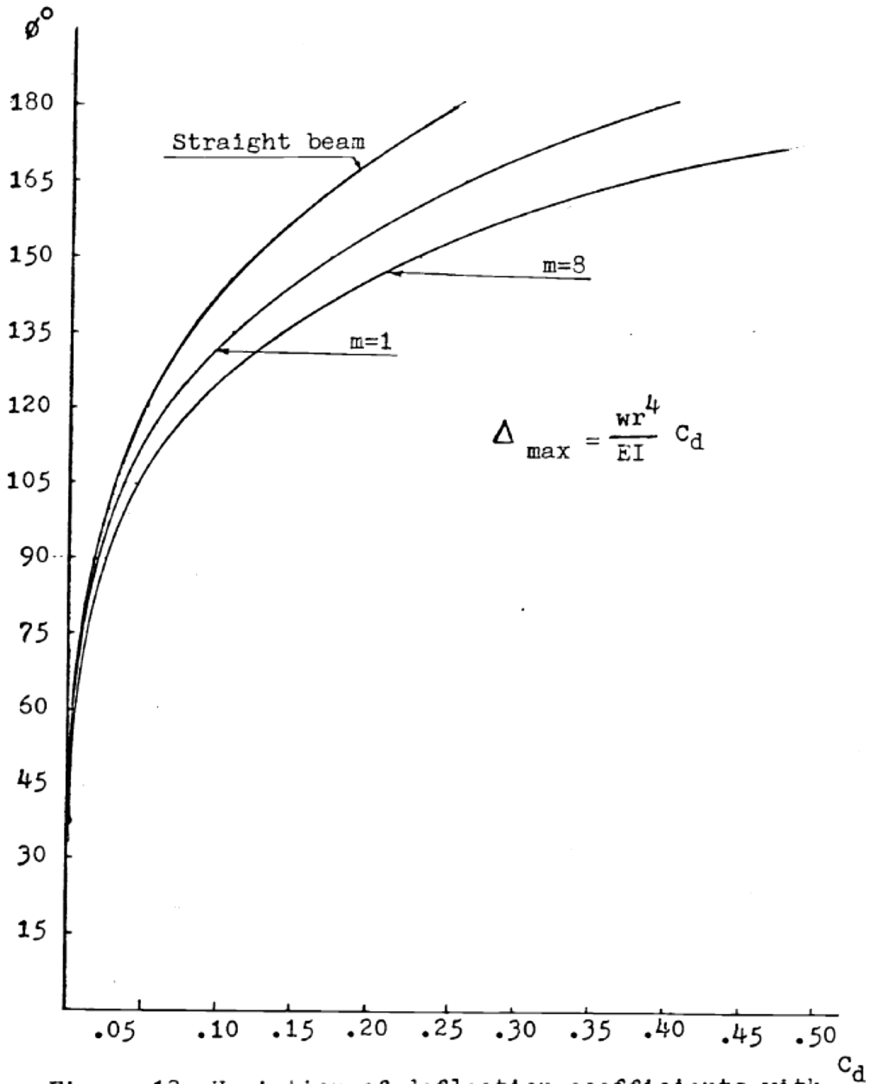

Figure 2.20. Variation of deflection coefficients with span angle for uniformly loaded curved beams with fixed ends.

Many researchers have developed elastic methods to analyse horizontally curved beams. Gendy and Saleeb 1992 (Gendy & Saleeb, 1992) developed governing differential equations for shearing, stretching, bending, twisting and warping modes of deformation of curved beams using three-dimensional, two-field variational formulations. The equations they have developed for the curved beams with general boundary and loading conditions. They have considered a circular curved beam element with radius R and the line of centroids taken as the beam reference axis. The

coordinate system used concerning the reference coordinate axis is shown in Figure

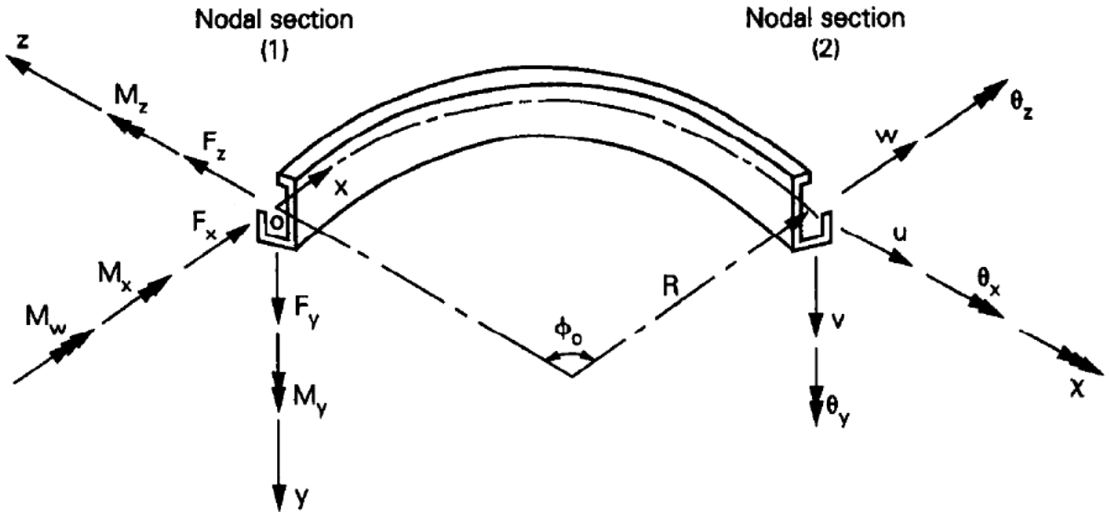

2.21.

Figure 2.21. A typical curved beam element

Several equations were developed, by considering the equilibrium of the system as follows.

$$F'_x + \frac{F_z}{R} + p_x = 0, \qquad (1.21(a))$$

$$F'_y + p_y = 0, \qquad (1.21(b))$$

$$F'_z - \frac{F_x}{R} + p_z = 0, \qquad (1.21(c))$$

$$T'_{s\gamma} = \frac{M_z}{R} + T_w = 0' \qquad (1.21(d))$$

$$M'_y - F_z = 0, \qquad (1.21(e))$$

$$M'_z + F_y - \frac{1}{R}(T_{sv} + T_w) = 0, \qquad (1.21(f))$$

$$M'_w + T_w = 0. \qquad (1.21(g))$$

Displacement forms of the equations 1.21(a) to 1.21(g) were obtained by substituting;

$$F_i = \int \sigma_{xi} dA \ \ (for\ i = x, y, z) \qquad (1.22)$$

$$M = \int \sigma_{xx\,[-\omega, z, -y]^T}\, dA \qquad (1.23)$$

$$M_x = T_{sv} + T_w \qquad (1.24)$$

$$T_{sv} = \int \left[-\sigma_{xy}\left(z + \omega_y\right) + \sigma_{xy}(y - w_z)\right] dA \qquad (1.25)$$

$$T_w = \int \sigma_{xi}\omega_i dA \ \ (sum\ on\ i = y, z) \qquad (1.26)$$

They have proved that these developed formulae are capable in predicting the behaviour of curved beams adequately. Furthermore, they have extended their study to address the numerical simulation with a simple two-node (seven degree of freedom) finite element.

Inelastic Analysis of Horizontally Curved steel I-beams

An in-plane curved I-beam under vertical loading will be under bending and non-uniform torsion action due to the coupling of vertical deflection with the rotation due to twist. Hence, these primary actions induce second-order bending moment about the minor axis and produce early nonlinear behaviour and yielding, which cause the significant reduction of ultimate load-carrying capacity.

A considerable number of researchers have conducted studies to analyse horizontally curved I-beams using various approaches. Pi and Trahair studied the inelastic analysis and performance of horizontally curved steel I-beams. (B. Y. Pi, Bradford, and Trahair 2000b). They have developed a finite element model to analyse the behaviour of steel I-beams curved in the plane. They have compared their model with the existing

models to analyse horizontally curved I-beams and found that the developed model is compatible and economical.

A research team from Singapore (Liew et al., 1995) has investigated the behaviour of curved I beam and proposed a simplified design method to estimate ultimate load-taking capacity. The load Vs deflection and maximum loads obtained through the numerical analysis matched the reported results in the literature. Based on these, an equation (eq. 1.31) was developed to calculate the maximum moment carrying capacity of horizontally curved I-beams for various boundary and loading conditions. The simplified method developed is explained below.

The Cartesian coordinate system of I-beams curved in the plane is given in Figure 2.21. The initial in-plane radius of curvature can be approximated with the sinusoidal function given in equation (1.27):

$$u_0(x) = U_0 \sin\frac{\pi x}{L} \text{ with } U_0 = \frac{L^2}{8R} \qquad (1.27)$$

The function for centroidal cross section rotation $\varphi_0(x)$ is supposed to be given by;

$$\varphi_0(x) = \emptyset_0 \sin\frac{\pi x}{L} \qquad (1.28)$$

$\emptyset_0$=0 for a cross section which is initially undistorted. The u and φ which are the displacement components measured from the beam initial curved configuration, and the total displacement, u_{total}, measured from x-axis is;

$$u_{total} = u_0 + u \qquad (1.29)$$

and the total rotation, φ_{total}, is;

$$\varphi_{total} = \varphi_0 + \varphi \qquad (1.30)$$

The principal differential equations for lateral torsional buckling, twisting, and warping, which are derivatives in the form of Euler-Lagrange equations of the functional, can be written as:

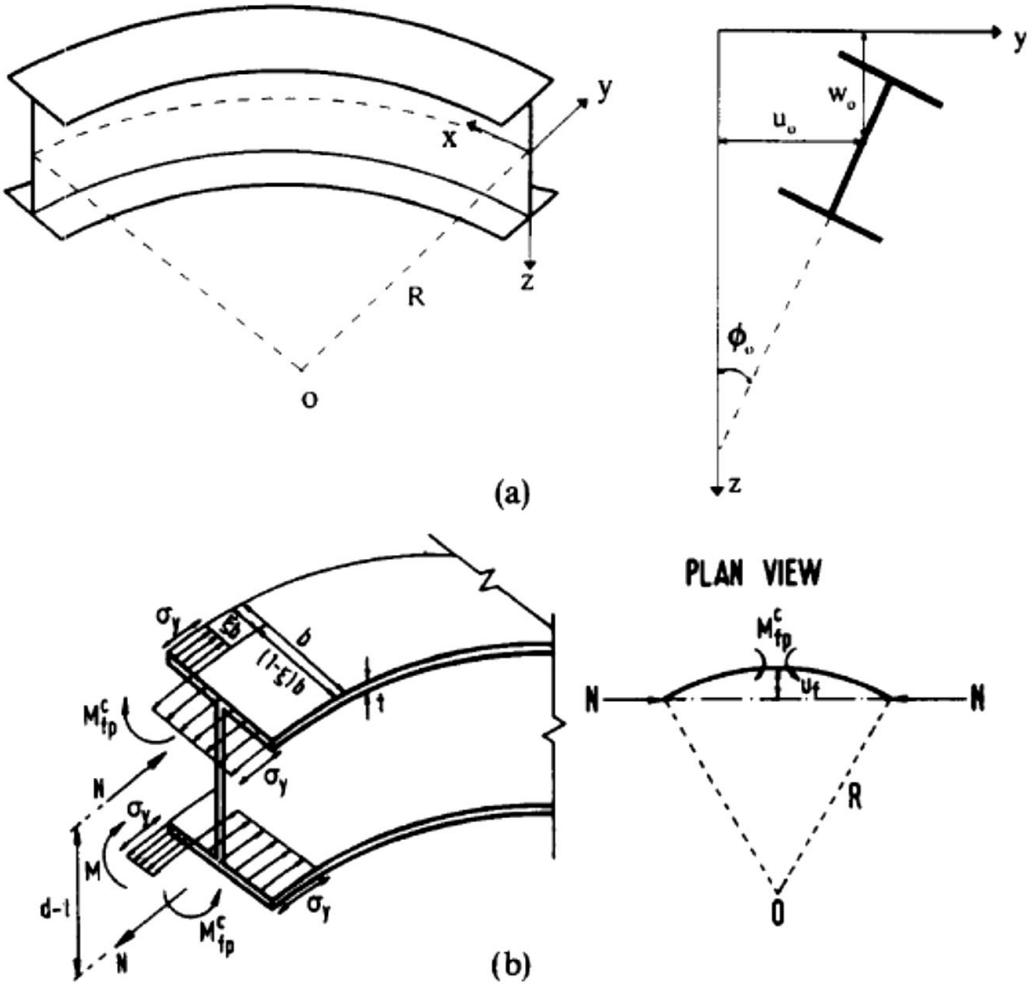

Figure 2.21. (a) The coordinate system and initial displacement of cross-section (b) plastic moment carrying capacity of curved beams section under flexure (source: Liew et al. 1995)

$$EI_z\left[u'''' + 2\frac{u''}{R^2} + \frac{u}{R^4}\right] + \frac{EA}{R}\left[v' + \frac{u}{R}\right] - \left[\left\{F_x + \frac{M_z}{R}\right\}\left\{u' - \frac{v}{R}\right\}\right]' - \frac{1}{2}(T'_{sv}w')'$$

$$+ \left[\left\{M_y + \frac{B}{R}\right\}\left\{\varphi' + \frac{w'}{R}\right\}\right]' - F_z\left\{\varphi' + \frac{w'}{R}\right\} + F_y\left\{v'' + \frac{v}{R^2}\right\}$$

$$+ F'_y\left\{v' + \frac{u}{R}\right\} - \left[M_x\left\{w'' - \frac{\varphi}{R}\right\}\right]' = 0 \qquad (1.31)$$

$$EI_w\left[\varphi'''' + 2\frac{\varphi''}{R^2} + \frac{\varphi}{R^4}\right] - \frac{EI_y}{R}\left[w'' - \frac{\varphi}{R}\right] - GK_T\left[\varphi'' + \frac{w''}{R}\right] + M_z w''$$

$$+ \left[\left\{M_y + \frac{B}{R}\right\}\left\{u' - \frac{v}{R}\right\}\right]' - r^2\left[\left\{F_x + \frac{M_z}{R}\right\}\left\{\varphi' + \frac{w'}{R}\right\}\right]' + F_z\left[u' - \frac{v}{R}\right]$$

$$- \frac{M_x}{R}\left[u' - \frac{v}{R}\right] = 0 \qquad (1.32)$$

Above equilibrium equations are developed as per the deformed shape of the beam that combined curvature and second order effects due to various initial loads F_x, F_y, F_z, M_x, M_z and B.

For horizontally curved beams subjected to end moments $M = M_y$ and equations 1.31 and 1.32 can be simplified by letting $F_x = F_y, =, M_x = M_z = B = 0$ as;

$$EI_z\left[u'''' + 2\frac{u''}{R^2} + \frac{u}{R^4}\right] + \frac{EA}{R}\left[v' + \frac{u}{R}\right] + M\left[\varphi' + \frac{w'}{R}\right]$$

$$= 0 \qquad (1.33)$$

$$EI_w\left[\varphi'''' + 2\frac{\varphi''}{R^2} + \frac{\varphi}{R^4}\right] - \frac{EI_y}{R}\left[w'' - \frac{\varphi}{R}\right] - GK\left[\varphi'' + \frac{w''}{R}\right] + \left[M_y\left\{u' - \frac{v}{R}\right\}\right]'$$

$$= 0 \quad (1.34)$$

If the inextensibility $v' + {}^{u}/_{R} = 0$ and ${}^{1}/_{R^4} = 0$ are imagined, and only terms related to lateral deflection (u) and twisting (φ) are considered;

$$EI_z\left[u'''' + 2\frac{u''}{R^2}\right] + M\varphi'' = 0 \qquad (1.35)$$

$$EI_w\left[\varphi'''' + 2\frac{\varphi''}{R^2}\right] - \frac{EI_y}{R^2}\varphi - GK_T\varphi'' + Mu'' = 0 \qquad (1.36)$$

Where M is the applied end moment; $G$is the shear modulus; $I_w$is the warping constant and K_T =St Venant torsional parameter.

For beams with simply supported boundary condition, u and φ may be approximated by

$u = U \sin\frac{\pi x}{L}$ and $\varphi = \emptyset \sin\frac{\pi x}{L}$

Substituting these equations into the equations 1.35 and 1.36 gives solution for U and $\emptyset$ are obtained:

$$U = \frac{U_0}{\left[\frac{M_E}{M}\right]^2\left[1-\frac{2L^2}{\pi^2R^2}\right]-\frac{2P_E}{R^2M^2}+\frac{P_E EI_y}{R^2M^2}\left[\frac{L}{\pi}\right]^2-1} + \frac{\emptyset_0}{MR^2}[r_0^2 P_{ZE}R^2-2] \qquad (1.35)$$

$$\emptyset = \frac{\frac{U_0\left[P_E-\frac{2EI_z}{R^2}\right]}{M}+\emptyset_0}{\left[\frac{M_E}{M}\right]^2\left[1-\frac{2L^2}{\pi^2R^2}\right]-\frac{2P_E}{R^2M^2}+\frac{P_E EI_y}{R^2M^2}\left[\frac{L}{\pi}\right]^2-1} \qquad (1.36)$$

In which $M_E = \sqrt{P_E r_0^2 P_{ZE}}$, $M_E = {\pi^2 EI_z}/{L^2}$, $r_0^2 P_{ZE} = GK_T + {\pi^2 EI_w}/{L^2}$ and $I_z$is the bending stiffness about the minor axis.

When account the horizontal curvature and it leads to;

$$u_f = U_0 + U + \frac{d-t}{2}[\emptyset_0 + \emptyset] \qquad (1.37)$$

If $\emptyset_0 = 0$, it can be shown that;

$$u_f = \left\{\frac{\left[\frac{M_E}{M}\right]^2\left[1-\frac{2L^2}{\pi^2R^2}\right]-\frac{2P_E}{R^2M^2}+\frac{d-t}{2M}\left[P_E-\frac{2EI_z}{R^2}\right]+\frac{P_E EI_y}{R^2M^2}\left[\frac{L}{\pi}\right]^2}{\left[\frac{M_E}{M}\right]^2\left[1-\frac{2L^2}{\pi^2R^2}\right]-\frac{2P_E}{R^2M^2}+\frac{P_E EI_y}{R^2M^2}\left[\frac{L}{\pi}\right]^2-1}\right\} \qquad (1.38)$$

The equation (1.38) illustrates the second order elastic curve in which the association between the applied end moment M and the beams' top flange lateral displacement u_f can be found.

The plastic strength of the top compression flange of a horizontally curved beam governs the second-order rigid plastic curve. For the compression flange under lateral bending, the axial compression force N induces a plastic moment in the flange M_{fp}^c, which may be written as:

$$M_{fp}^c = \sigma_y A_f (\varepsilon - \varepsilon^2) b \tag{1.39}$$

The resultant axial force can be expressed as;

$$N = 2\sigma_y A_f \varepsilon - \sigma_y A_f \tag{1.40}$$

By rearranging the terms;

$$\varepsilon = \frac{N + \sigma_y A_f}{2\sigma_y A_f} \tag{1.41}$$

Where, ε = a non-dimensional parameter related to the location of neutral axis for in-plane bending for flange (ε = 0 for straight beams)

$A_f = bt$, is the area of the cross section of the flange;

$b =$ flange width;

$t =$ thickness of the flange

$\sigma_y =$ yield strength of steel

From Figure 1.21(b);

$$M_{fp}^c = N u_f \tag{1.42}$$

Substituting in equation X into Equation Y and equating it to equation Z yields the following expression:

$$Nu_f = \frac{b}{2\sigma_y A_f}\left(A_f^2\sigma_y^2 - N^2\right) \qquad (1.43)$$

Letting $M \approx N(d-t)$ and $\delta = M/M_p$, above equation becomes;

$$u_f = \frac{A_f\sigma_y(d-t)}{4\delta M_p} - \frac{\delta M_p}{4A_f\sigma_y(d-t)} \qquad (1.44)$$

Substituting $M_p \approx \sigma_y A_f(d-t)$ yields the following equation:

$$\frac{u_f}{b} = \frac{1-\delta}{4\delta} \qquad (1.45)$$

Where, $u_f =$ total lateral displacement of the compression flange at the beam's mid span.

The maximum load taking capacity of a curved beam $\delta_u (= M_u/M_p)$ can be calculated by the intersection point of the second order elastic curve and the second order rigid plastic curve. The equation (1.46) can be used to evaluate $\delta_u$and is derived from the equations 1.37 and 1.38.

$$\delta_u^4\lambda^4 - \left[\left(1 + \frac{(d-t)P_E L^2}{4M_p Rb} - \frac{(d-t)EI_z L^2}{2M_p R^3 b} - \frac{2P_E}{M_p^2 R^2} + \frac{P_E EI_y}{M_P^2 R^2}\left[\frac{L}{\pi}\right]^2\right)\lambda^4 + 1 - \frac{2L^2}{\pi^2 R^2}\right]\delta_u^2 - \left[\frac{L^2}{2RB} - \frac{P_E L^2\lambda^4}{bM_p^2 R^3} - \frac{L^4}{bR^3\pi^2} + \frac{P_E EI_y}{2M_P^2 R^3}\left[\frac{L^4}{\pi^2 b}\right]\lambda^4\right]\delta_u + 1 - \frac{2L^2}{\pi^2 R^2} - \frac{2P_E\lambda^4}{R^2 M_P^2} + \frac{P_E EI_y}{M_P^2 R^2}\left[\frac{L}{\pi}\right]^2\lambda^4 = 0 \qquad (1.46)$$

This equation is capable of calculating ultimate load carrying ability of horizontally curved beams subjected to equal end moments producing uniform bending. Figure

2.23 shows an example set of curves to represent the relationship between slenderness ratio (λ) and ultimate strength of horizontally curved beams with R/L ratio of 25.

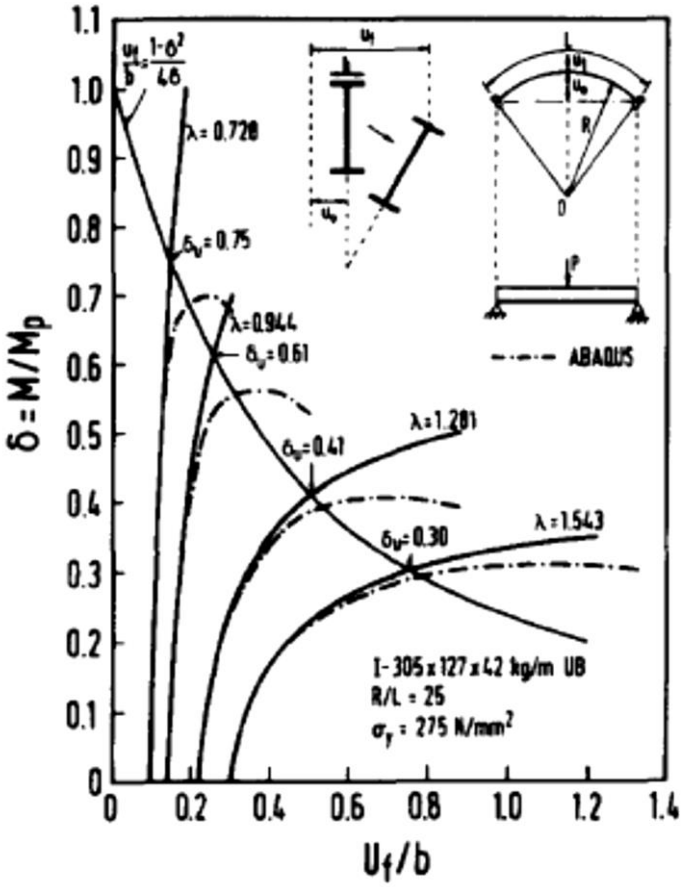

Figure 2.23. The relationship between slenderness ratio (λ) and maximum strength of horizontally curved beam with R/L ratio of 25 (Source: Liew et al.*, 1995)*

Figure 2.24 shows the connection between R/L ratio and the ultimate strength of horizontally curved 305×127×42 kg/m UB sections.

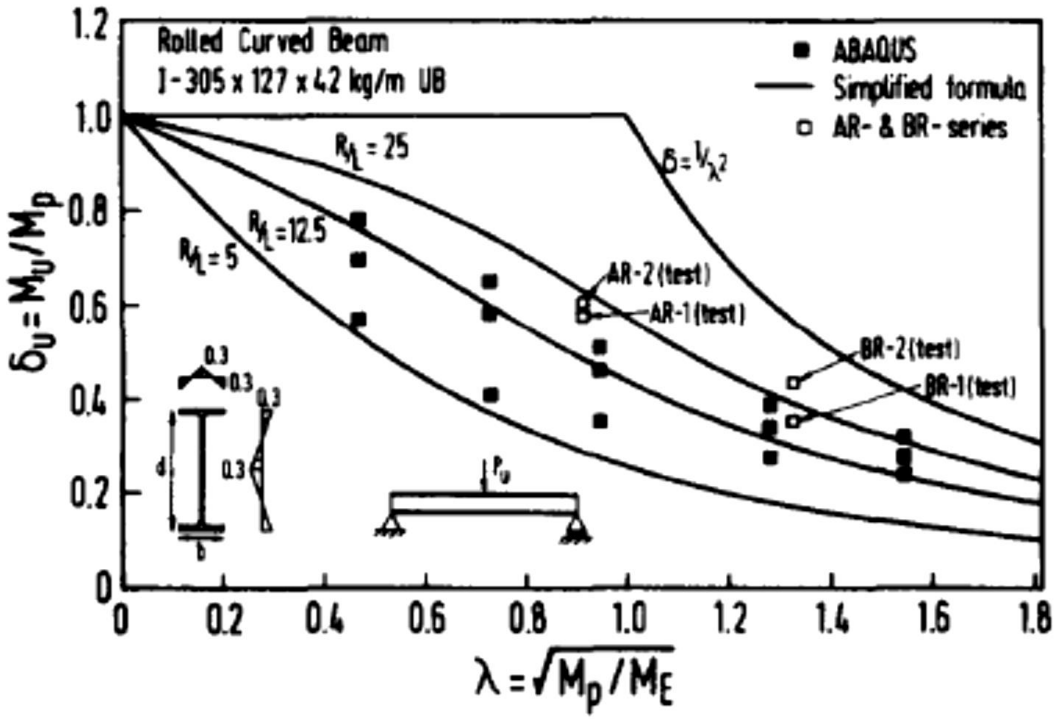

Figure 2.24. The relationship between R/L ratio and the maximum strength of horizontally curved 305×127×42 kg/m UB sections (Source Liew et al. 1995)

Shanmugam et al. (1995) experimentally investigated the behaviour of horizontally curved steel I-beams. They have extended their study to predict ultimate load behaviour of two sets of steel I beams including both rolled sections and built-up sections. The test results obtained through a series of experiments were noted to have a notable agreement with the results of a numerical analysis performed using finite element models. The relationship between radius of curvature and residual stresses to span to length ratio (R/L) on ultimate load carrying capacity was considered. The key findings of the study included; (i) reduction in load carrying capacity when (R/L) ratio decreases; (ii) the influence of residual stresses on the maximum load of horizontally curved I beams is only bordering for curved beams with higher radius of curvature; and (iii) the cold bending process causes a certain amount of strain hardening, which provide rise to a greater material strength. It was also noted that the ABAQUS FEA

is capable of forecasting the ultimate strength with required accuracy (Shanmugam et al. 1995).

In the early stage plastic collapse analysis (Boulton, N. S., and Boonsukha 1959; Jackson 1966; Yoo, C. H., and Heins 1972) and transfer metrix method (Fukumoto, Y., Nishida 1981; Nakai, H., and Yoo 1988; Yoshida and Maegawa 1983) were used to analyse horizontally curved I beams. As per the plastic collapse analysis, fully plastic state of horizontally curved I beams is defined with yield interaction equation;

$$\left(\frac{M_x}{M_p}\right)^2 + \left(\frac{T}{T_p}\right)^2 = 1 \qquad (1.47)$$

Where, M_x = the ultimate major axis BM in the curved beam; T = the ultimate torque in the curved beam; M_p = the major axis full plastic moment of the cross section; and T_p = the full plastic torque of the cross section. However, this equation may not be appropriate to predict the ultimate strength of horizontally curved I-beams due to the unavailability of a rigorous model to evaluate the full plastic torque under non-uniform torsion.

Several researchers (Fukumoto, Y., Nishida 1981; Nakai, H., and Yoo 1988; Yoshida and Maegawa 1983) have used the transfer matrix method successfully to analyse horizontally curved beams. However, for the inelastic analysis, this method uses a trial-and-error procedure to determine the inelastic stiffnesses that are related to the longitudinal normal strains, and uses total strain theory to determine the uniform torsional stiffness. These procedures may introduce errors in the calculation of the inelastic stiffnesses. During the transfer process, these errors are accumulated and may become significant(B. Y. Pi, Bradford, and Trahair 2000a).

Few researchers have conducted studies to understand the lateral torsional buckling of steel I beams curved on plane. Nishida et al.(Nishida S, Yoshida H 1978) proposed equation (1.48) determine the elastic lateral torsional buckling strength of horizontally curved beams.

$$M_{cr(cu)} = \sqrt{1 - \frac{L^2}{\pi^2 R^2}} \sqrt{\left(\frac{\pi^2 E I_y}{L^2}\right)\left(GJ + \frac{\pi^2 E C_w}{L^2}\right)} \qquad (1.48)$$

Where

$M_{cr(cu)}$ is the elastic buckling capacity for LTB of curved I beam with equal end moment

L is the girder length

R is the radius of curvature of the beam

G is the shear modulus

J is the torsional constant

C_w is warping constant

In 1994, Kang and Yoo (Kang and Yoo, 1994) suggested an equation to calculate the ultimate load capacity of a horizontally curved I beam. This equation suggests a strength reduction factor, which is depend the radius of curvature of the beam and which may be applied for both elastic torsional buckling moment and ultimate bending moment of a curved I beam. Yoo C. H and Davidson, (1997) used yield interaction equations when developing this equation.

$$[M_p, M_u, M_{xcr}]_{cu} = (1 - 0.1058\theta^{2.129})^{2.152}[M_p, M_u, M_{xcr}]_{st} \qquad (1.49)$$

Where

$M_{p)cu}$: Plastic bending moment of the section of a curved beam

$M_{u)cu}$: Ultimate bending moment of the section of a curved beam

$M_{xcr)cu}$: Lateral-torsional buckling moment of a curved beam

M_p: Plastic bending moment of the section of a straight beam

M_u: Ultimate bending moment of the section of a straight beam

M_{xcr}: Lateral-torsional buckling moment of a straight beam.

In recent years K. Lee et al.(Keesei Lee et al. 2017) suggested an equation to evaluate the maxumum strength of horizontally curved beams based on both numerical and experimental results. This equation was suggested based on the regression analysis conducted on the results obtained through several horizontally curved I beam samples.

$$\frac{M}{M_p} = (-0.046 \ln x - 0.132)\frac{T(\theta)}{T_p} + 1.0396x^{-0.085} \leq 1 \qquad (1.50)$$

Where

$x = L_b/L_p$

L_b = Unbraced (arc) length

L_p = Compact unbrace length

$T(\theta)$ is the ultimate torsional moment acting on the curved beam. Here, the beam is assumed to be under two equal end moments which can be determined using the free body illustration give in Figure 2.24.

$$T_p = \frac{f_{y0}}{\sqrt{3}}\left[Bt_f^2\left(1 - \frac{t_f}{3B}\right) + \left(D - 2t_f\right)\frac{t_w^2}{2} + \frac{t_w^3}{6}\right] \qquad (1.51)$$

In which

f_{y0} - steel yield strength yield stress

B - flange width

D - depth of section

t_f - thickness of flange

t_w - thickness of web.

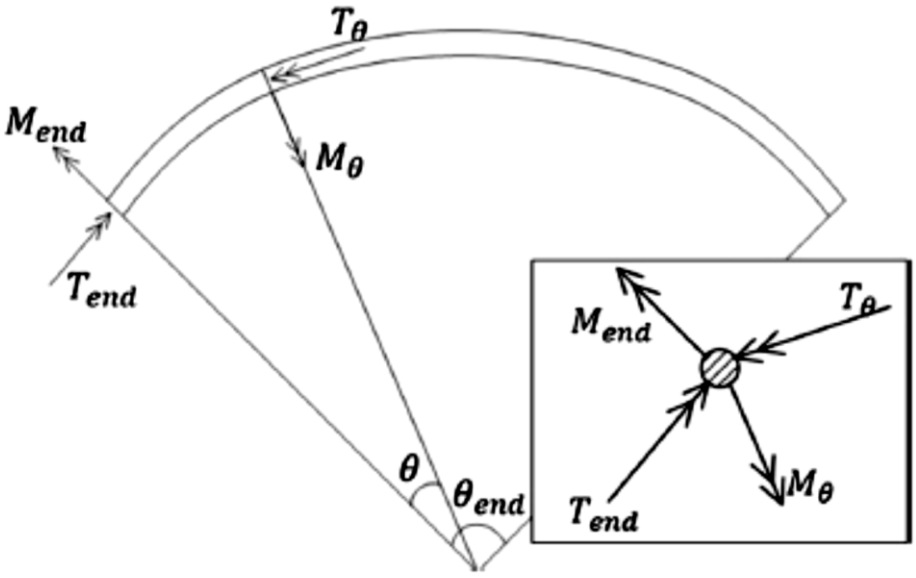

Figure 2.24. Free body diagram of the curvedbeam

2.5.2 Analysis of Vertically curved Beams

Often, vertically curved beams can be considered as arch structures. They may experience various forms of loads under different end conditions(Cazzani, Malagù, and Turco 2014).

Arches (vertically curved beams) resist vertical loading by combining principal axial compression and bending actions. As Pi et al.(Y. L. Pi, Bradford, and Tin-Loi 2008) reported, various loading may appear on vertically curved beams, as shown in Figure 2.26.

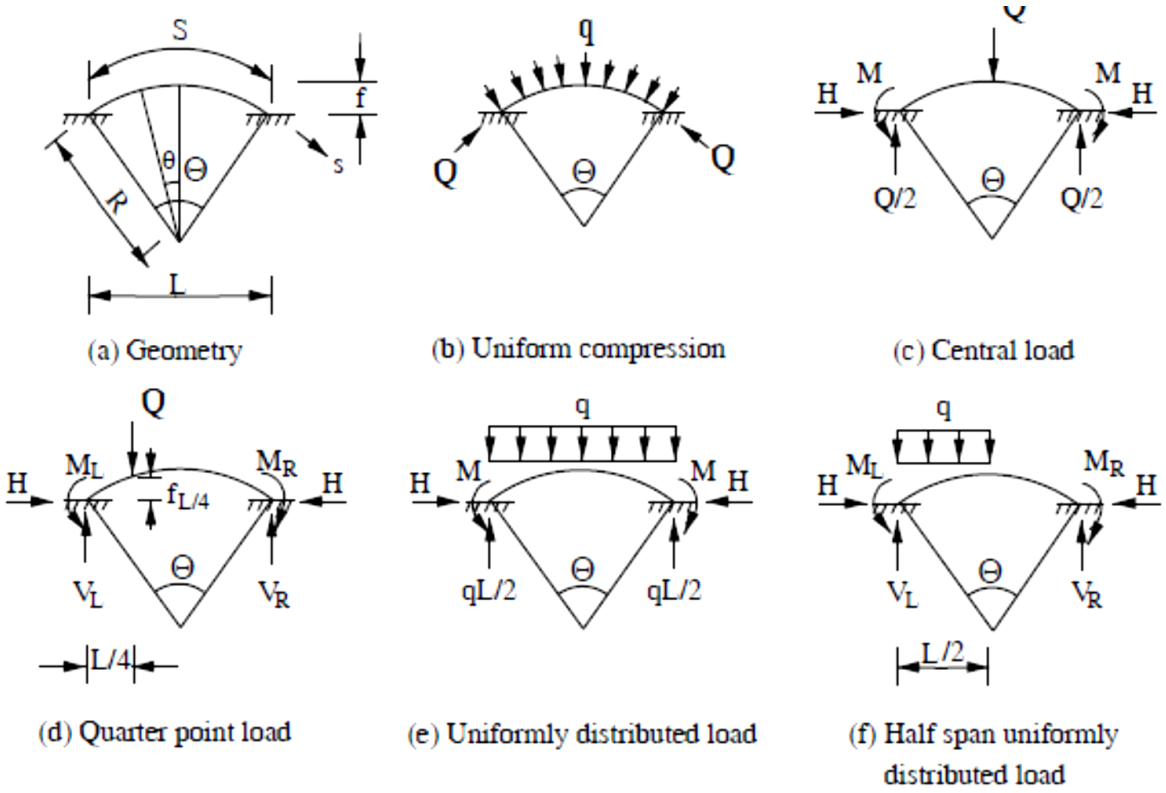

Figure 2.26. Vertical curved beams, support conditions and loadings

Many researchers have studied on in-plane elastic buckling of arches which is a main reference in the evaluation of the stability of steel arches against their in-plane loading (Austin, W.J. and Ross 1976; Chini, S.A. and Wolde-Tinsae 1988; DaDeppo, D.A. and Schmidt 1969; Mirmiran, A. and Wolde-Tinsae 1993). In 1967 Lo and Conway (Lo, C.F. and Conway 1967) used an analytical method to study the instability of circular curved beams subjected to equal but opposite moments. They extended their study (Conway, H.D. and Lo 1967) to a circular curved beam under concentrated load on mid-span. They validated the obtained results through the experimental results found by Gjelsvik and Bodner in 1962 (Gjelsvik, A. and Bodner, 1962). Approximate solutions for the buckling load of fixed shallow arches with rectangular cross sections were obtained by Gjelsvik and Bodner (Gjelsvik, A. and Bodner 1962), while Schreyer and Masur (Schreyer, H.L. and Masur 1966) derived analytical solution for fixed ended shallow arches constructed with rectangular cross sections. Pi et al.

(2002). (Pi et al. 2002) investigated the in-plane buckling of shallow arches with a non-uniform cross-section. They found that the critical buckling load of shallow arches given by this method are much lesser than that given by the classical theory. The elastic-plastic behaviour of pin-ended circular steel aches was studied by Pi and Trahair (Pi, Y.L. and Trahair 1996, 1999), while that of fixed circular steel arches was done by Pi, Y.L. and Bradford (2004).

Kim and Kim (1998) successfully developed beam elements with nodeless degrees of freedom, which is highly accurate and locking-free. They extended their study for the finite element formation and numerically proved the developed equation for circular cantilever arches, pinched rings and arches with moment discontinuity. In recent years, Cazzani et al. (Cazzani, Malagù, and Turco 2014) conducted an isogeometric analysis to analyse plane-curved beams and arches and obtained promising results. Tsiatas and Babouskos (George C. Tsiatas 2017) have presented an integral equation solution to the linear and geometrically non-linear analysis of non-uniform vertically curved shallow arches under a concentrated central force at the mid-span. They have shown that the results obtained through this integral equation are compatible with those obtained through finite element modelling.

In 1989, Rajasekaran and Padmanabhan (Rajasekaran and Padmanabhan, 1989) developed equations to analyse thin-walled vertically curved beams using the principal of virtual work. They have made several assumptions during their study; which includes (a) the length of the beam is much greater than the depth and the lateral dimensions and are larger than the thickness; (b) the displacements are large and the strains are very small (c) cross sections remain plane after deformation (d) the shear strains due to shear stress in equilibrium with the changes of normal stress is small

and can be neglected (Euler Bernoulli's hypothesis) and (e) The shear strains in the planes normal to the middle surface of the thin wall are small and can be neglected. As per their study in plane buckling load for a radially loaded arches and rings is given by;

$$-P_{cr} = EI_x \left[\frac{\left(\frac{n^2\pi^2}{l^2} - \frac{2}{R^2} + \frac{l^2}{n^2\pi^2R^4} \right)}{\left(1 - \frac{l^2}{n^2\pi^2R^2} + \frac{l^4}{n^4\pi^4R^4} \right)} \right] \qquad (1.52)$$

Where

P_{cr} = Critical buckling load

E = Modulus of elasticity

I_x= Second moment of area about x-axis

n = number of buckled half sine waves

l = Arc length of the arch

R = Radius of arch centerline

They also developed an equation to evaluate out-of-plane critical buckling moment of vertically curved beams under uniform bending.

$$M_{cr} = -\frac{\left(EI_y + P_\emptyset r^2 \right)}{2R} \pm \left[\frac{\left(EI_y + P_\emptyset r^2 \right)^2}{4R^2} + \frac{3EI_yP_\emptyset r^2}{l^2} \right]^{\frac{1}{2}} \qquad (1.53)$$

Where

M_{cr} = out-of-plane critical buckling moment

E = Modulus of elasticity

R = initial radius of arch center line

l = Arc length of the arch

I_y= Second moment of area about y-axis

$P_\emptyset$ = Torsional buckling load

$r =$ Radial coordinates

As sited by Karnovsky (I.A. Karnovsky 2012) the method of Maxwell-Mohr integral can be effectively use to evaluate elastic deflection of curved beams. The method of application of this theorem for curved beams as follow;

A common expression for displacement of any deformable structure can be expressed as $\Delta_{kp} = \sum \int_0^S \frac{M_p \overline{M_k}}{EI} ds + \sum \int_0^S \frac{N_p \overline{N_k}}{EA} ds + \sum \int_0^S \mu \frac{Q_p \overline{Q_k}}{GA} ds$ (1.54)

Where

$\Delta_{kp} =$ Displacement of a structure in kth direction

$M_p =$ Applied bending moment

$N_p =$ Applied axial force

$Q_p =$ Applied shear force

$\overline{M_k}, \overline{N_k},$ and $\overline{Q_k} =$ Internal forces due to the applied unit load (M_p, N_p and Q_p)

$A =$ Beam cross sectional area

$I =$ Second moment of the area

$E =$ Elastic modulus

$G =$ Shear modulus

$\mu =$ Non dimensional parameter depends upon the cross section shape ($\mu = 1.2$ for circular cross sections and $\mu = 10/9$ for rectangular cross sections.

But above equation is strictly applied only for straight beams and slight modification should be done to analyse curvilinear rods.

Figure 1.27 shows two inclined parts of a beam with lengths S_n and S_{n+1} are subjected to bending moments and axial forces. By assuming the axial forces $\bar{N}_n$ and $\bar{N}_{n+1}$are constants, axial forces in the unit states are $\bar{N}_n = -sin\beta_n/\lambda_n$and $\bar{N}_{n+1} =$

$-sin\beta_{n+1}/\lambda_{n+1}$ for the left and right portions respectively. Calculation of these forces are shown in Figure 2.27, at joints A and B.

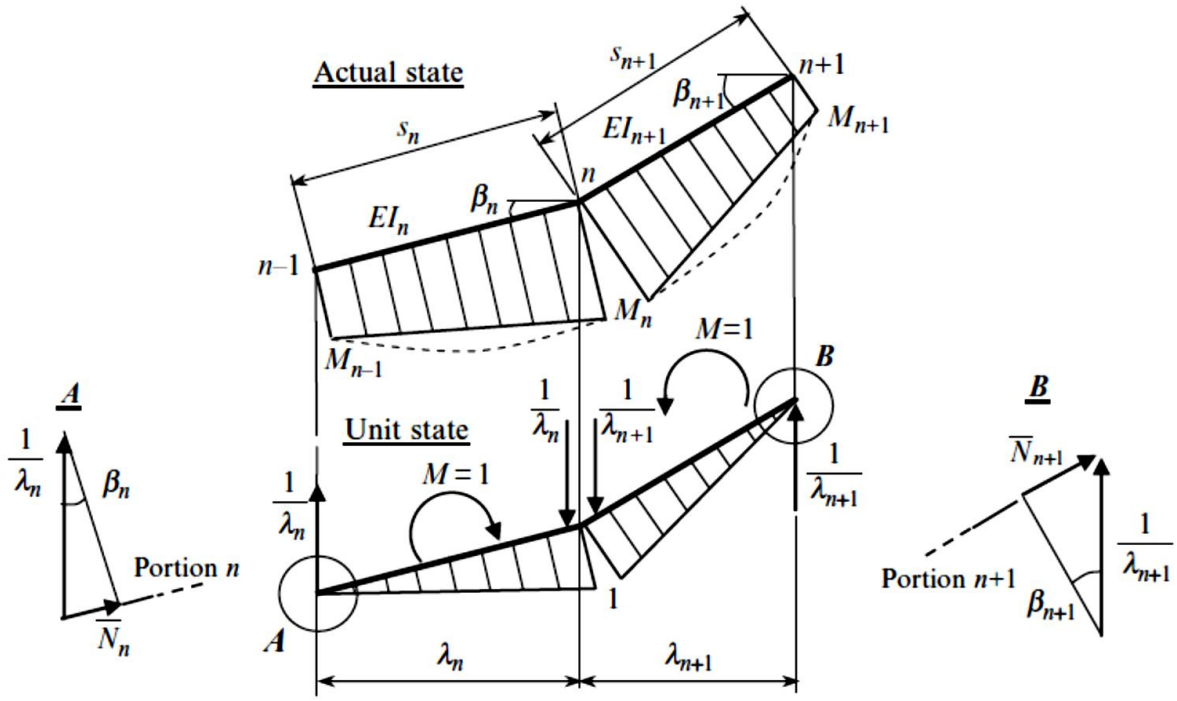

Figure 2.27. Loads acting on left and right portions of curved beams

Where;

S_n - Length of the nth section

M_n - Bending moment at nth node

E - Elastic modulus of beam material

I_n - Moment of inertia for nth section

β_n - Horizontal inclination of nth section

λ_n- Vertical projection of axial force of nth section

For left portion using Maxwell and Mohr integral(Igor A. Karnovsky 2012) for bending moment will give the elastic load on the beam due to bending moment

$$W_n(M) = \sum \int_0^l \bar{M} \frac{M_p}{EI} dx = \frac{s_n}{6EI_n}(2M_{n-1} \times 0 + 2M_n \times 1 + M_{n-1} \times 1 + M_n \times 0)$$

$$= \frac{s_n}{6EI_n}(M_{n-1} + 2M_n) \quad (1.55)$$

where M_p is the bending moment at the n[th] node due to vertical loads and $\bar{M}$ is the bending moment in the unit state. EI_n is the flexural rigidity of the beam portion considered.

By using Maxwell and Mohr integral for axial force will give the elastic load on the beam due to axial force $W_n(N)$;

$$W_n(N) = \sum \int_0^l \bar{N} \frac{N_p}{EA} dx = -\frac{1}{EA_n} \times \frac{\sin \beta_n}{\lambda_n} N_n S_n = -\frac{1}{EA_n} \times \frac{\sin \beta_n}{\lambda_n} N_n \frac{\lambda_n}{\cos \beta_n}$$

$$= \frac{N_n}{EA_n} \times \tan \beta_n \quad (1.56)$$

where N_p is the axial force at the n[th] node due to vertical loads and $\bar{N}$ is the axial force in the unit state. E is the elastic modulus of the beam portion considered and A is the cross-sectional area of the beam.

Then the total elastic load on the beam is given by;

$$W_n = W_n(M) + W_n(N) \quad (1.57)$$

Substituting to (3) from (1) and (2) gives;

$$W_n = \frac{S_n}{6EI_n}(M_{n-1} + 2M_n) + \frac{S_{n+1}}{6EI_{n+1}}(2M_n + M_{n+1}) - \frac{N_n}{EA_n} \tan \beta_n + \frac{N_{n+1}}{EA_{n+1}} \tan \beta_{n+1} \quad (1.58)$$

For un-strengthened beam shown in Figure 2.28;

But;

$$s_n = s_{n+1} = L, I_n = I_{n+1} = I, A_n = A_{n+1} = A, \beta_n = \beta_{n+1} = \beta, M_{n-1} = M_{n+1} = 0, M_n = \frac{WB}{2},$$
$$N_n = N_{n+1} = W/2 \sin\beta \qquad (1.59)$$

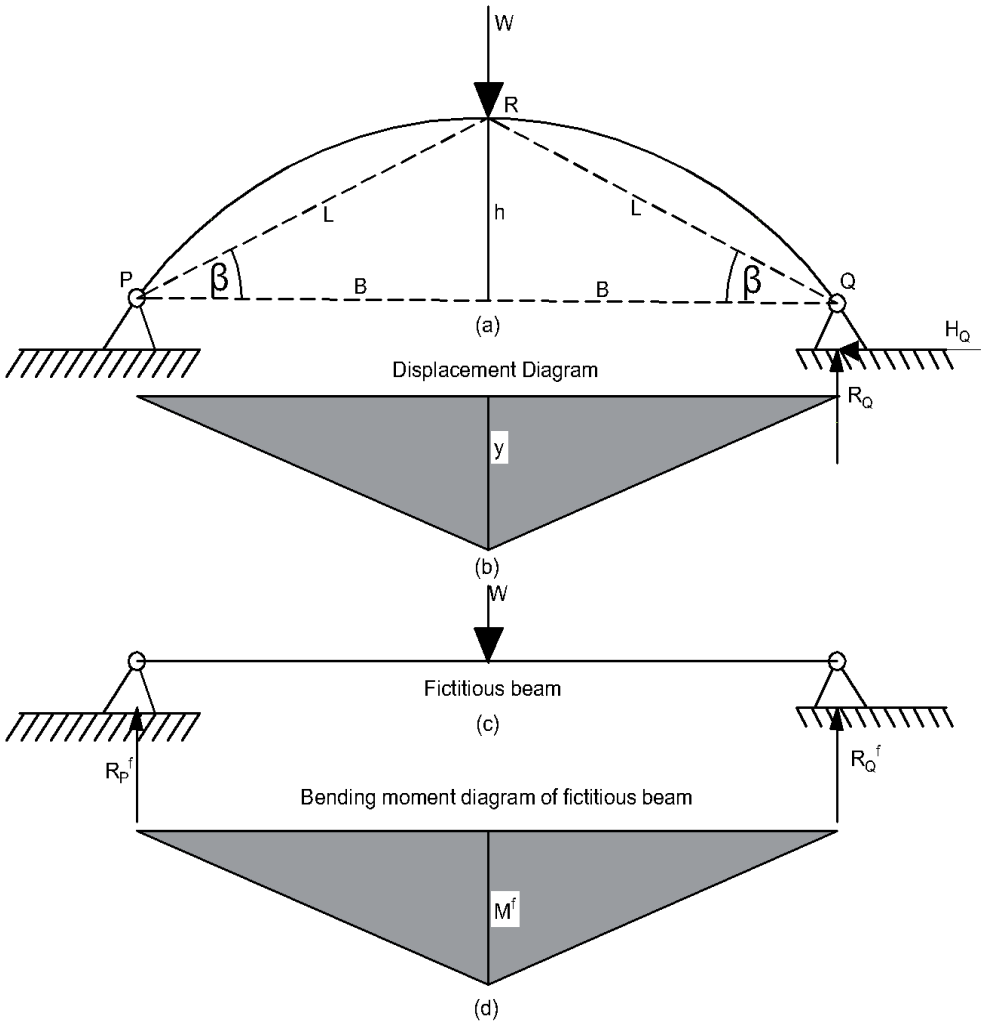

Figure 2.28. Curvilinear simply supported bar; (a) Design diagram; (b) vertical displacements; (c) fictitious beam; (d) corresponding bending moment diagram

Substituting these values in (4) gives;

$$W_n = \frac{L}{6EI}\left(0 + 2\frac{WB}{2}\right) + \frac{L}{6EI}\left(2\frac{WB}{2} + 0\right) - \frac{W}{2EA}\frac{\tan\beta}{\sin\beta} - \frac{W}{2EA}\frac{\tan\beta}{\sin\beta}$$

$$W_n = \frac{WLB}{3EI} - \frac{W}{EA}\frac{1}{\cos\beta} \tag{1.60}$$

$$R_P^f = R_Q^f = \frac{W_n}{2} \tag{1.61}$$

A considerable number of researchers (Belytschko, T. and Glaum 1979; Calhoun, P.R. and DaDeppo 1983; Dawe 1971; Elias, Z. and Chen 1988; Lee, P.-G. and Sin 1994; Noor, A.K., Greene W.H. and Hartley 1977; Noor, A.K. and Peters 1981; Pi, Y.-L. and Trahair 1996; Reddy, B.D. and Volpi 1992; Reddy, J.N. and Sing 1981; Sabir, A.B. and Lock 1973; Stolarski, H. and Belytschko 1982; Surana, K.S. and Sorem 1989; Walker A.C. 1974) have conducted the Finite Element Modelling (FEM) to evaluate the behavior of vertically curved beams. There have been some other methods developed to analyse the vertically curved beams such as finite difference scheme for geometrically nonlinear analysis (Patodi, S.C. and Buragohain 1979), Finite Difference Method (FDM) (Srpčič, S. and Saje 1986), Truss Model (Xenidis, H., Morfidis, K. and Papadopoulos 2013), Integral equation method (Miyake, S., Nonaka, M. and Tosaka 1991), Dynamic relaxation (DR) method, Large deflection method (Horibe T. and Asano 2000), isogeometric analysis frame work for elliptical curved beams (Luu, A.-T. and Lee 2016) and Analog Equation Method(AEM) (George C. Tsiatas 2017).

2.6 Advantages and Disadvantages of CFRP as a Retrofitting Material for Civil Engineering Structures

Application of CFRP is a proven technique for retrofitting and strengthening structures made with steel, concrete and timber due to many favourable physical and mechanical properties. They have a considerable number of advantages compared to other conventional materials used in civil engineering to retrofit existing structural elements. As cited by Kabir (Kabir, H. 2015), several researchers (Abbas, 2010; Deng, 2008; Moy, S. S. J., Hill, P., Moriarty, J., Dier, A. F., Kenchington, A. and Iverson, 2001; D. A. Schnerch 2005a; Shabila, 2005) have listed these advantages.

· High strength and stiffness-to-weight ratios.

· Superb corrosion resistance capacity compared to steel plating.

· Thickness can be increased by using a multilayer to suit design requirements.

· High chemical resistance to acids and bases.

· Excellent confrontation to corrosion, deterioration, and fatigue.

· Negligible increase of dead weight of the structure.

· Aesthetically pleasant.

· It is available in pre-stressed form as required.

· Based on research results, it can be used to resist tensile and bending stress, shear forces and torsion.

- Since the fibres are light and flexible, it is easy and suitable for handling during the application.
- The CFRP sheet or fabric can be shaped into complex shapes to match the structure's existing surface configuration.
- Little interruption of the structures during application.

- Cost savings due to labour savings and reduced machine requirements for stacking and lifting material.
- Though the material costs of CFRP material are very high, overall project costs may be reduced.

Even though CFRP has a considerable number of advantages, it has some disadvantages, as follows;

- Needs to be more adequate codes of practice and design standards.
- Shortage of personnel skilled in polymer industries.
- Fire and ultraviolet (UV) radiation protection is required (Kabir, H., 2015).

2.7 Application of CFRP in Civil Engineering Structures

Many real-world examples can be found on application of CFRP to strengthen and retrofit civil engineering structures constructed with concrete, steel, timber and masonry. Figure 2.29 (a) shows the oldest operational cast iron bridge in the world, Tickford bridge in UK has been strengthened by using CFRP to increase its load carrying capacity (Lane IR & Ward JA. 2000). Moreover, there are several examples reported on the strengthening of steel bridge beams using CFRP all over the world such as King Street railway bridge (Farmer N & Smith I. 2001), I-704 bridge in Delware, USA, Slattocks canal bridge in Rochdale, Uk, Bid bridge in Kent, UK, Bowroad bridge in East London, UK, Hythe bridge in Oxfordshire, UK (L C Hollaway and J Cadei 2002) etc.

Figure 2.29. (a) Tickford bridge, Buckinhamshire, UK; (b) Installation of CFRP plates at Slattocks canal bridge, UK (L C Hollaway and J Cadei 2002).

Moy et al. (2001) discussed the method of strengthening and life extension of tunnel supported by carbon fibre composites (Moy et al. 2001). Figure 2.30 shows how the strengthening of the tunnel structure was done by applying carbon fibre sheets to the tension flange of cast iron girders and supporting jack arch is provided with carbon fibre beams.

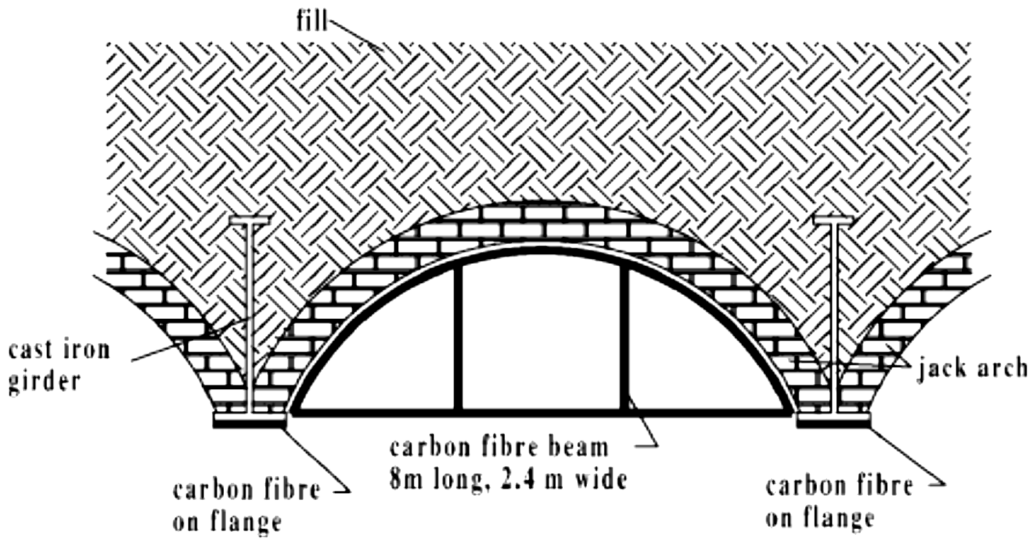

Figure 2.30. Strengthening scheme of arch structure (Source: Moy et al. 2001)

A considerable number of concrete structures have been strengthened using CFRP in different parts of the world. The strengthening schemes include concrete buildings as well as concrete bridges. As reported by Hii and Al-Mahaidi (2006), West Gate bridge

in Melbourne, Australia (Figure 2.31) is one of the largest CFRP strengthening project in the world (Hii, Adrian K. Y. and Al-Mahaidi 2006).

Figure 2.31. CFRP strengthening of West Gate bridge, Melbourne, Australia (Gamage 2009)

Figures 2.32 to Figure 2.33 shows some applications of CFRP in strengthening of various structures.

Figure 2.32. Strengthening of bridge pier beams(https://strongtie.com.au/products/frp-carbon-fibre-reinforcing-systems, 2022 January)

Figure 2.33. Application of CFRP in buildings ;(a) slab strengthening; (b) beam strengthening; (c) strengthening of slab beam connections (https://ctech-llc.com/en/wikitech/beam-strengthening-and-repair-with-frp-composite-system, 2022 January)

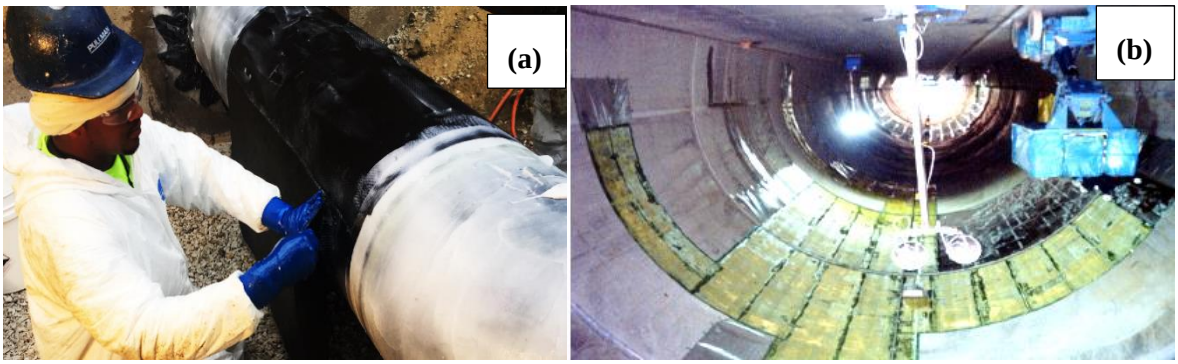

Figure 1.34. CFRP strengthening of (a) steel pipe line; (b) Tunnel lining

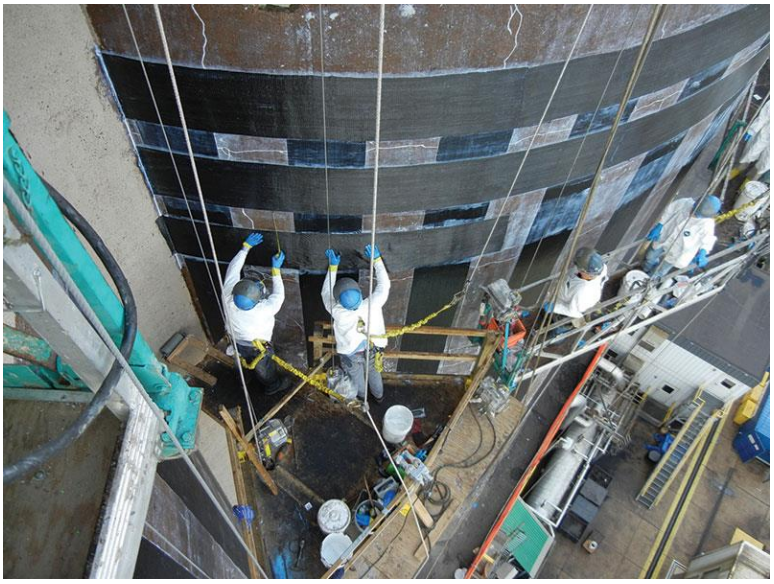

Figure 2.35. Application of CFRP to strengthen a steel cylindrical tank

2.8 Types of Fibre Reinforce Polymers (FRP) and Their Properties

Glass, aramid, basalt and carbon are the most common fibres used in structural applications. They are known as advanced fibre composite materials due to their superior properties (i) high specific stiffness (stiffness divided by density) and (ii) high specific strength (strength divided by density). Table 2 indicates a summary of the indicative fibre properties and a comparison of them. These fibres follow linear stress-strain curves without showing plastic range when loaded axially, as shown in Figure 2.36.

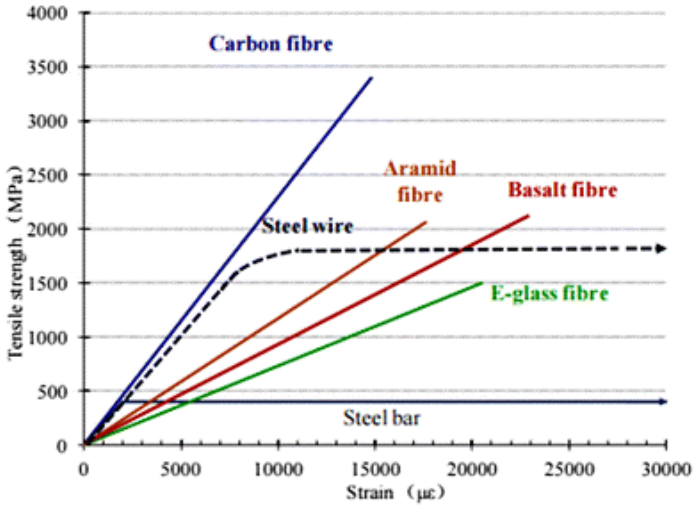

Figure 2.36. Stress-strain curves for steel and advanced composite fibres

2.8.1 Glass Fibre Reinforced Polymers

Glass fibres are made with molten glass drawn in to continuous fibres that are bundled into roving. Fibre surface are then coated to enhance wetting and adhesion properties and to provide better bond between the composite components. Second coating is provided with coupling agent to improve strength and reduce voids. Two common glass fibre types can be found commercially: the “E” type, and the “S” type with first type used for normal applications while the later one used for alkali resistant. Tensile strength of glass fibres are reduced when subjected to chemical corrosive agents, elevated temperatures and under sustained loads for a longer period (Md Humayun Kabir 2015).

2.8.2 Aramid Fibre Reinforced Polymers

Aramid fibres has the best strength-to-weight ratio among the currently available reinforcing fibres. They are manufactured by extruding a crystalline solution of the polymer with partially oriented molecules. Tensile strength of Kelvar is 20% greater than its compressive strength. It behaves as a brittle material and under compression it behaves as a ductile material. Kelvar is suitable in conditions tension fatigue, law creep and it can withstand elevated temperatures. It absorbs certain amount of water. and is sensitive to UV light, alkalis and acids (Md Humayun Kabir 2015).

2.8.3 Basalt Fibre Reinforced Polymers

Basalt Fiber Reinforced Polymers (BFRPs) are produced by extracting fibers from molten basalt rocks under hydrostatic pressure and then cooling them to obtain hardened filaments. These filaments are collected and wound onto a take-up device. Basalt rovings can also be twisted to produce basalt yarn, and continuous basalt filaments can be cut into specific fiber lengths through a dry cutting process to obtain staple fibers (Singha K, 2012). In recent years, basalt fibers have found applications in structural engineering and have been shown to possess properties that are competitive with other high modulus fibers such as glass and carbon. Basalt fiber production is more environmentally friendly and less expensive compared to the manufacturing of carbon and glass fibers. Basalt fiber is recommended over glass and carbon fiber for applications that require ductile mode failure, as it has a high energy absorption capacity (Smriti Raj et al., 2016).

2.8.4. Carbon Fibre Reinforced Polymers

Carbon Fiber Reinforced Polymers (CFRPs) are manufactured through the thermal decomposition of Polyacrylonitrile. The manufacturing process involves three stages: oxidation at 1000-1500 °C, carbonization at 1000-2000 °C, and graphitization at 2500-3000 °C. High modulus carbon fibers are produced through graphitization because graphite possesses a higher tensile modulus compared to carbon fibers. High modulus carbon fibers exhibit high specific strength and stiffness, but their ductility and strength usually decrease as the modulus increases. Carbon fibers have structural properties that remain stable at elevated temperatures and are highly resistant to aggressive environments. They exhibit a brittle failure mode after behaving elastically. When compared to glass and aramid fibers, carbon fibers demonstrate

improved resistance to aggressive environments and greater toughness against fatigue loading (Bank, L.C. and Gentry, 1995; Byars, E.A. et al., 2003). Irrespective, of disadvantages of higher cost of carbon fibres, superior structural properties such as high strength and modulus value, combined with excellent fatigue and chemical resistance make carbon fibres as most feasible material for retrofitting works. Figure 2.37 shows different types of fibres used in structural applications.

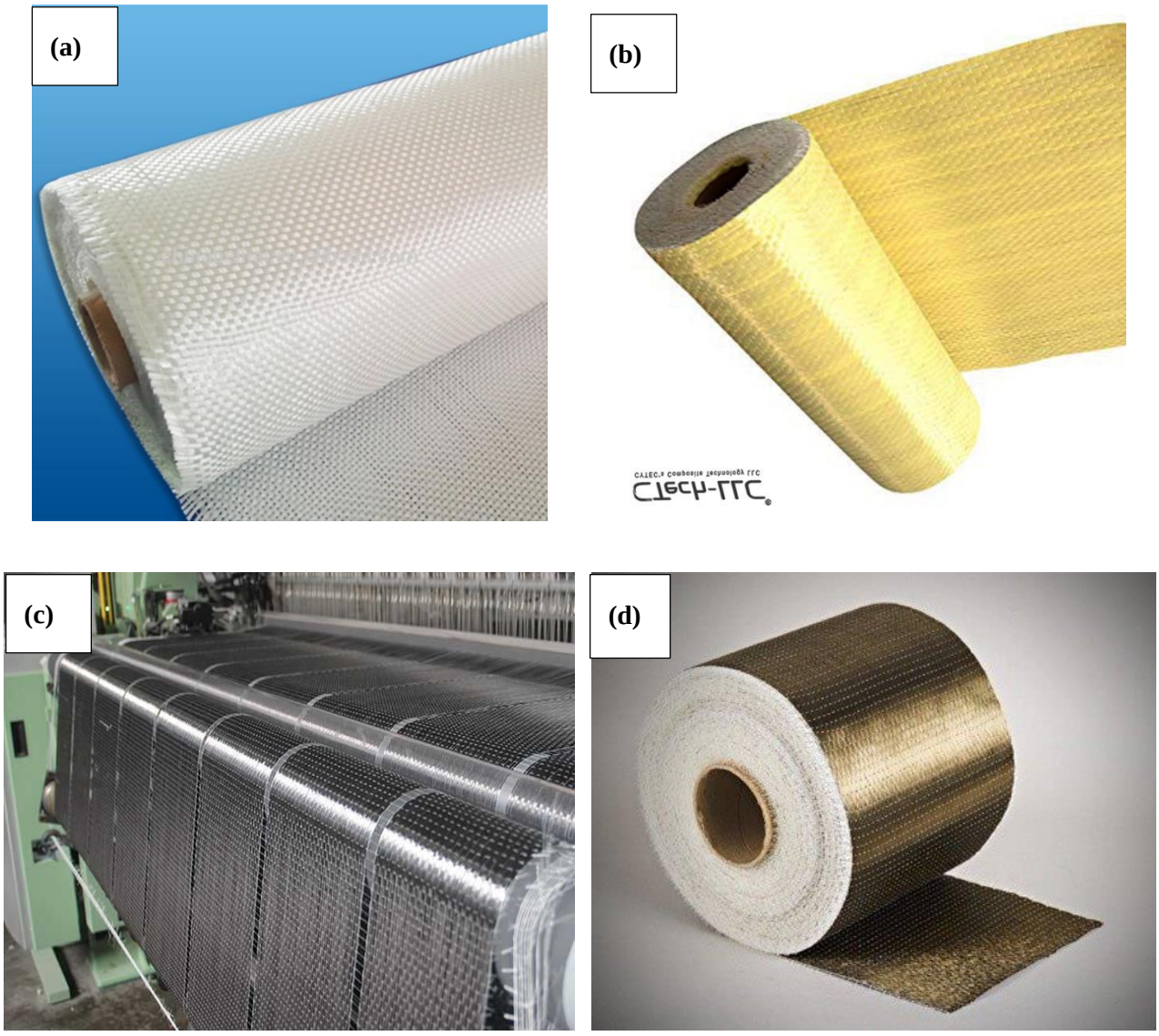

Figure 2.37. Different types of Advanced Polymer Composites; (a) glass fibre; (b) aramid fibre; (c) carbon fibre; and (d) Basalt fibre

Table 1.2. Indicative fibre properties of advanced composite fibres and their comparison

Properties	Glass fibre	Carbon fibre	Basalt fibre	Aramid fibre
Fibre Manufacturing	For making glass fibre, mainly 50% silica in combination with oxides of boron, alumina and/or several other minerals are independently mixed in the metring system before introducing into the furnace	The raw materials of carbon fibres are polyacrylonitrile (PAN), cellulose (rayon) and pitch. Fibres are made from these materials in three steps: stabilization at 400ºC, carbonization at 1200ºC and graphitization at 1000–3000ºC	For making basalt fibre, quarried basalt rock is put into the furnace in crushed form. No secondary materials are mixed before introducing into the furnace. This process requires only a single feed line to carry crushed basalt rock into the furnace	The aramid fibres, are produced by extruding a liquid crystalline solution of the polymer with partially oriented molecules.
Density (gcm^{-3})	2.6	1.4-1.6	2.5-2.9	1.4-1.5
Tensile strength (MPa)	E-type: 3450 S-type: 4580	High modulus: 2500-4000 High strength: 3500	3100-4840	High modulus: 125-175 Low modulus: 60-70
Stiffness (GPa)	E-type: 72.4 S-type: 85.5	High modulus: 350-650 High strength: 240	76	High modulus: 3000-4200 Low modulus: 2750-300
Thermal conductivity (W/(m K))	0.031-0.038	80-270	0.034-0.04	0.04
Coefficient of thermal expansion (1/K)	5.4×10^{-6}	8×10^{-7}	8×10^{-6}	6×10^{-6} to -2×10^{-6}
Ultimate Tensile Strain (%)	E-type: 2.4 S-type: 3.3	High modulus: 0.5 High strength: 1.1	3.15	High modulus: 1.4-3.5 Low modulus: 4.4

Brittleness	less brittle compared to basalt fibre	more brittle compared to basalt fibre	Strengthening and toughening significant than those of carbon fibre for OPC concrete	Tougher and flexible than the carbon fibres

2.9 Adhesives for Bond between Steel and Advance Polymer Composites

There are wide varieties of adhesives which may be used to bond advanced polymer composites to metallic substrate. They include epoxies, polyurethanes, acrylics, cyanoacrylate, but one that is generally used for polymer composite plate bonding to these substrate is the epoxy (L C Hollaway and J Cadei 2002). Polymeric matrices or epoxy adhesives used in CFRP composites can be broadly categorise into two categories; (i) Thermosetting and (2) thermoplastic resins. Thermoplastics soften under heating and can be reshaped with heat and pressure. But, during the fabrication thermoset materials become cross linked and cannot be reshaped with the eating and hence, they are the most commonly used adhesive in civil engineering applications. In comparison to other thermosetting polymers such as polyester or vinyl ester resins, epoxy resins are known to exhibit better mechanical properties and higher resistance to aggressive environments, moisture absorption, and corrosive liquids and environments (Md Humayun Kabir, 2015). Although epoxy resins are generally more expensive than other thermosetting polymers, their superior physical properties and durability in service contribute to a favorable cost-performance ratio when compared to other thermoset plastics. However, epoxy resins also have some drawbacks. They tend to have poor resistance to crack growth, can exhibit brittleness, and have low resistance to UV radiation (Jana S and Zhong WH, 2007; Kotnarowska D, 1999; Liu F, Zhang Z, 2012). Additionally, to achieve their ultimate mechanical properties, epoxy resins often require a certain level of curing or post-curing process of two to four hours at elevated temperature (up to 120°C), making them more difficult to use

(Kelly P 1999). Some important properties of thermosetting adhesives are listed in Table 2.3.

Table 2.3. Important properties of thermosetting epoxies (Source: Kabir 2015)

Property	Matrix		
	Polyester	Epoxy	Vinyl ester
Density (kg/m^3)	1200 - 1400	1200 - 1400	1150 - 1350
Tensile strength (MPa)	34.5 - 104	55 - 130	73 -81
Longitudinal modulus(GPa)	2.1 - 3.45	2.75 - 4.10	3.0 - 3.5
Poisson's coefficient	0.35 - 0.39	0.38 - 0.40	0.36 - 0.39
Thermal expansion coefficient (10^{-6}/°C)	55 - 100	45 - 65	50 - 75
Moisture content (%)	0.15 - 0.60	0.08 - 0.15	0.14 - 0.30

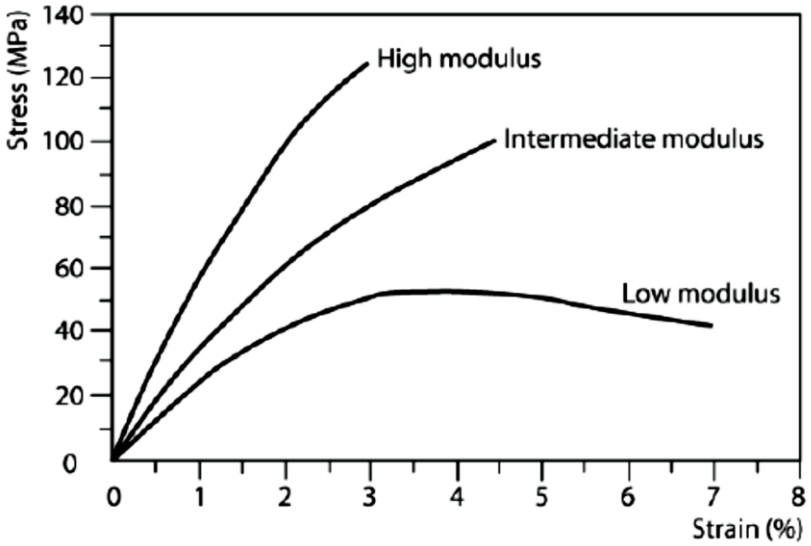

Figure 2.38. Stress strain relationship for epoxy matrix resins of different elastic modulus

2.10 FRP Bonding Systems and Surface Preparation

2.10.1 Bonding systems

As sited (Kabir, 2015) there three main method to apply the FRP to the steel substrate.

1) **Wet lay-up system:** Fibre sheets or impregnated fabrics are used and cured on-site with saturating resin. Any suitable number of fibre layers can be added to meet the design requirements. This method provides maximum flexibility when retrofitting or strengthening of structures due to the possibility of use for any complex shape.
2) **Pre-impregnated FRP:** In this system is consisted of uncured unidirectional/multidirectional fibre sheets or fabrics that are pre-impregnated with a saturating resin in the manufacturer's facility. The saturation process is done off-site and like wet layup systems, cured in place. Additional heating is usually required for curing.
3) **Pre-cured fibre plates:** This system is consisted with pre-impregnated fibres with saturating resin and cured during the manufacturing process. Additional resin required to bond fibre plates to the concrete/steel surface. The main advantages of this system include excellent quality control and easer implantation on site.

As discussed (Dilum Fernando 2010), three main adhesion mechanisms can be found in literature: (a) physical bonding, (b) chemical bonding, and (c) mechanical bonding. The **physical bonding** has two mechanisms: absorption and electrostatic attraction. The absorption considers that the adhesive and the substrate are in closed molecular contact and weak secondary forces operate between them. It also stated that for the successful bonding the adhesive must wet the surface of adherend (Flinn, R.A. and

Trojan 1995). On the other hand, the electronic attraction theory claims that the adhesion between adhesive and adherend surfaces is arise due to the electrons transfer between them, causing in formation of a double layer electrical charge at the interface (Dilum Fernando 2010). But, these attractions are unlikely to make a noteworthy Chemical bonding refers to ionic or covalent bonds formed across the interface between the adhesive and the adherend. These bonds are strong primary forces and have important influence to the final bond strength (Baldan 2004a). Different surface treatment methods form surfaces with various chemical compositions and oxide stoichiometries. These variations in morphology of the surfaces influence the strength of chemical bonds.

When the surface of the adherend is rough thus contains crevices and pores, liquid adhesives will penetrate into these crevices and pores. When the adhesive gets hardened with the time and make mechanical interlocking with the surface layer providing a mechanical bond. Better mechanical interlocking requires substrate surface to have irregularities, which is the reason for roughening of adherend surface former to apply FRPs. A significant degree of bonding may ensure with the mechanical bonding between two surfaces. The strength of mechanical bonding is lower when comparing to the bond strength obtained with chemical bonding (Chawla 1998).

2.10.2 Surface Preparation for Steel and CFRP Bonding

Proper surface preparation is utmost important to obtain a successful CFRP/Steel strengthened system to get the proper bonding between two adherends. Majority of surface preparation methods involve cleaning, removal of weak layers and re-cleaning (Hollaway, L. C., Teng, J. G. 2008; Mays et al. 1992). Degreasing is of the surface is utmost important in preparing adherend surface and is typically done with an organic

solvent such as acetone or ethanol. Moreover, for metallic substrates detergent solutions or alkaline cleaners may be used after solvent treatment to inorganic solids and dirt (Hollaway, L. C., Teng, J. G. 2008; Mays et al. 1992; D. A. Schnerch 2005a). There are several surface preparation method available and solvent cleaning, grit blasting, sand blasting and surface grinding (Fawzia, S. et al. 2007; Hollaway and Cadei 2002; Jiao and Zhao 2004; Teng et al. 2013). As per the previous studies the sand or grit blasting methods seems to be the most effective among those to get a uniform high energy surface (Hollaway and Teng, 2008; Hollaway and Cadei 2002; Schnerch 2005b; Teng et al. 2013). Unlike the wire brushing, grit blasting is capable of cutting the metal surface to expose a clean surface. It also capable of removing inactive oxide and hydroxide layers by cutting distortions of the base material which enables increases the high-energy steel surface. The fibre-reinforced composite joints which were grit blasted shown higher strength than those which were hand- ground (Dilum Fernando 2010). Some researchers suggested to use vacuum or dry wiping to remove fine dust particles other than cleaning with a solvent which will not remove all the dust, but redistribute the remaining dust particles on the entire surface (Hollaway, LC and Cadei 2002).

2.11 Durability of CFRP Strengthened Steel Structures

CFRP materials exhibit excellent resistance to various environmental effects such as corrosion, moisture, and chemical attacks. However, joint strength may be reduced due to the degradation of adhesive properties when exposed to moisture, chemical solutions and high temperature. Environmental degradation of CFRP strengthened system can arise due to three leading causes: (i) Interfacial attack, (ii) adhesive degradation, and (iii) galvanic corrosion (M. M. R. Dawood 2008). The proper surface

preparation is essential to obtain a long-term, environmentally durable bonded interface.

Some researchers claim that **interfacial attack** is the most effective degradation mechanism for reducing strength in steel/FRP joints in damp environments (Hashim, 1999; Hutchinson, 1987). It was found that the moisture diffusion through the adhesive layer is attracted to the high-energy substrate, which results in the absorption of water particles to the joint and causes displacement of the secondary bond between the adhesive and steel substrate (Kabir, 2015). A considerable number of researches have been conducted to investigate possible methods to enhance the durability of CFRP/steel bonded joints in a wet environment and found that the use of adhesion promoters such as silanes, hydrocarbons (monomeric silicon-based chemicals) can enhance the durability of these steel-epoxy bonded joints (M. Dawood, 2008; D. A. Schnerch 2005a).

Adhesive degradation can be defined as the degradation of the overall joint of the strengthened system. Adhesive properties significantly change with water absorption to the joint with various mechanisms such as diffusion. Several researchers (Crasto & Kim, 1996; Hand et al., 1991; Horton et al., 1992; De Nève & Shanahan, 1992) have found that moisture absorption properties of adhesives have a significant effect on adhesive degradation. Some of the key findings of those studies included the consequences of moisture on the glass transition temperature, which reduces the bond strength, the effect of the deterioration of the bonding interface on the durability of the joint and the plasticisation of adhesives.

Corrosion may be expressed as the “degradation of a metal by electrochemical reactions with its environment” (Trethewey et al., 1988). **Galvanic corrosion** occurs when two metals with a sufficient potential difference are coupled and submerged in

an electrolyte. When CFRP-strengthened steel structures are under a wet environment or are in submerged condition, the electro-potential difference between CFRP and steel is adequate to occur galvanic corrosion (Francis, 2000). When a structure undergoes continuous wetting and drying cycles, sufficient dissolved oxygen will start a cathodic reaction on the CFRP surface, facilitating galvanic corrosion (A. Brown, 1974; M. Dawood, 2008). Therefore, it is mandatory to prevent corrosion between CFRP and steel substrate to achieve the long-term durability of any CFRP-strengthened steel structure. Researchers have conducted several studies to identify possible measures to prevent galvanic corrosion, and possible measures identified include applying water-resistant sealant between the two coatings, using of non-conductive material layer between carbon and steel (CFRP/polyester drape veil), an isolating epoxy film on the steel surface, and use of moisture barrier (M. Dawood, 2008; Tavakkolizadeh, and Saadatmanesh 2001; West, 2001).

2.12 Bond Behaviour between FRP and Steel

Application of FRP composites in steel structures can be categorised into two categories: (i) applications where the bond is critical in order to transfer interfacial shear stress through the adhesive layer and FRP layer; (ii) applications where contact is critical in order to transfer normal interfacial stress (contact between steel and FRP need to remain). There are ample examples for both categories: flexural retrofitting of steel beams with externally bonded FRP falls into the first category. In contrast, concrete-filled steel tube confinement with FRP jacketing comes under the second category. The interfacial behaviour between steel and FRP is of utmost importance in determining how effectively the FRP is utilised in bond-critical applications. The interfacial failure can occur only within the adhesive layer or at the steel/FRP joint

due to the higher tensile strength in steel and FRP. For FRP-strengthened steel structures, interfacial failure may occur in four mechanisms;

(a) Cohesion failure – failure within the adhesive layer

(b) Adhesion failure - failure at the material interfaces

(c) Steel/adhesive interface – failure between the steel and adhesive

(d) FRP/adhesive interface – failure between the adhesive and FRP

The failure of FRP-strengthened concrete structures always occurs within a few millimetres below the concrete substrate from the adhesive/concrete interface. Since FRP-strengthened steel structures show more failure mechanisms, theories applied to adhesive/concrete interface cannot be directly used for FRP-strengthened steel structures (Dilum Fernando, 2010). Various failure methods found in steel structures strengthened with FRP are shown in Figure 2.39. The strength of the steel structures strengthened with FRP depends on the adhesion failure, and hence the preparation of steel and CFRP surface, as well as the bond capacity of adhesive, have a direct impact on bond strength.

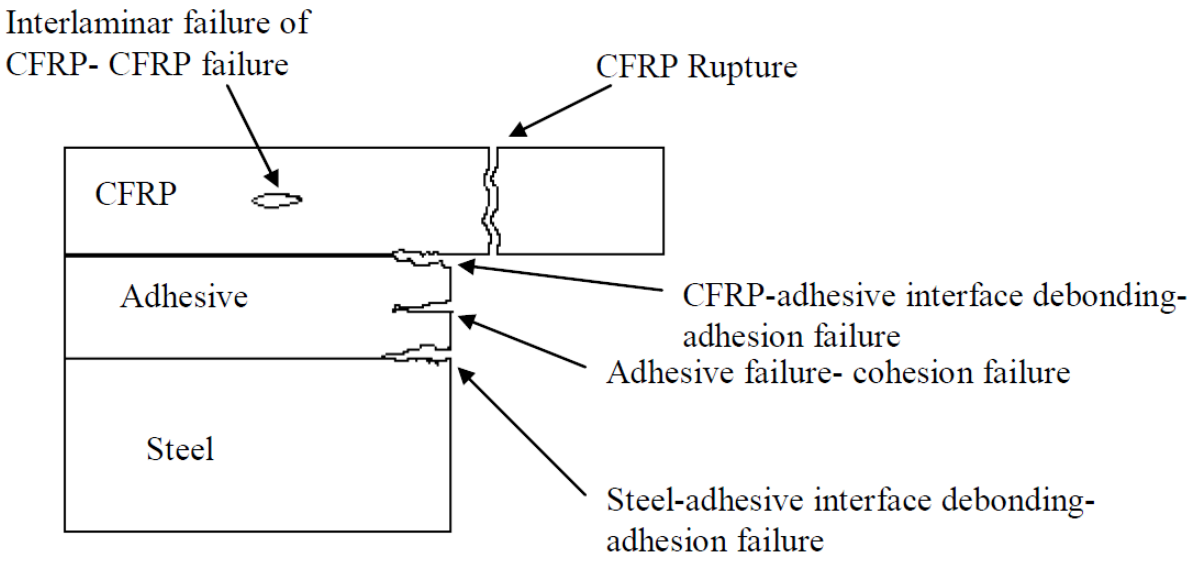

Figure 2.39. Different failure mechanisms in a CFRP - steel bonded joint

1.12.1 Adhesion Failure

Adhesion failure in FRP - steel bonded joints may occur in two ways; (a) Failure in the steel/adhesive interface and (2) Failure at CFRP/adhesive interface. In the wet-layup process of FRP on steel on site, FPR/adhesive failure is seldom observed. When pultruded FRP plates/strips are utilised, a peel need to be removed in order to obtain a proper bonding; If a peel does not exist, the FRP surface should be roughened and cleaned appropriately prior to bonding, and such surface preparation methods drastically minimise the risk of adhesion failure in FRP/steel bonded joints (Hollaway, LC and Cadei 2002). The more frequent adhesion failure in FRP/steel bonded joints found to be the failure between steel/adhesive interface and improving the surface preparation method for FRP/steel bonded joints has attracted significant attention (Mays & Hacinson, 1992; Schenerch et al., 2007). Besides following a suitable surface preparation method, it is advised to characterise the surface to assess whether it is capable of proper strong bonding. Two methods to evaluate surface characteristics were suggested (Fernado, 2010), and suitable recommendations were provided to ensure proper steel/FRP bonding.

(i) The measured surface energy (with a video contact angle) of steel should exceed 50 mJ/m2

(ii) The fractal dimension of the grit blasted surface topography measured with a surface profilometer should lie between the values 1.47 and 1.49.

1.12.2 Bond Behaviour

Two interfacial failures (debonding) can be observed in CFRP strengthened steel structures, similar to CFRP strengthened concrete structures; (i) end debonding (debonding initiates from a FRP plate end); and (ii) intermediate debonding (debonding initiates away from a CFRP plate end). Figure 2.40 shows these two debonding failures found in steel structures reinforced with CFRP. The end debonding is induced by higher interfacial peeling stress and interfacial shear stress near the ends of CFP patches (Sallam et al. 2006; Silvestre et al. 2008), while intermediate debonding is occurred due to higher interfacial shear stress due to a existence of a defect or yielding of the steel substrate (Deng et al. 2009; Fernando et al. 2006). The researchers have found that the intermediate debonding is critical when steel beams and steel sections strengthened for Local buckling (Sallam et al. 2006; Silvestre et al. 2008) and end debonding is critical in flexurally reinforced steel beams (Deng, J. and Lee 2010) and steel rectangular sectioned beams strengthened against end bearing load (Fernando et al. 2006) or local buckling induced by other loads (Harries et al. 2009).

Prior to comprehension and to model the debonding failure modes of FRP strengthened steel structures, behaviour of simple bonded jointed need to be understood (Dilum Fernando 2010). The understanding on the simple single-lap, FRP-steel joint will give an important insight on the performance of the FRP - steel bonded interface, since action of interfacial shear stress is dominant in these joints. In FRP - steel bonded joints, steel substrate failure is impossible, and hence failure of FRP to steel bonded joints initiates within the adhesive, ensure that adhesion failure at the steel/adhesive interface or FRP-adhesive interface is avoided. Several researchers (Colombi, P. and Poggi 2006; EI Damatty, A.A., and Abushagur 2003; S. Fawzia et

al. 2007; Miller et al. 2001) have done studies on FRP - steel bonded joints by using different test methods including double-lap shear test (Colombi, P. and Poggi 2006; Miller, et al. 2001), beam tests (Nozaka et al. 2005), single-lap shear test (EI Damatty, A.A., and Abushagur 2003) and single-lap pull off tests (Xia, S.H., and Teng 2005). Most of these investigations have been focussed on bond strength and bond-slip relationship.

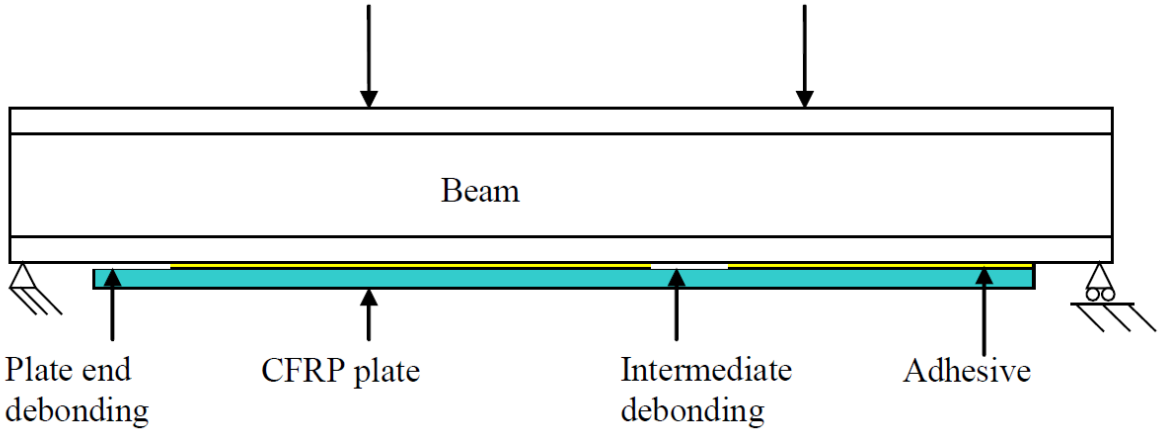

Figure 2.40. Failure modes due to debonding in CFRP-plated steel beams

Several experimental studies have been conducted to investigate the ultimate strength (the ultimate tensile force that the joint can take) of FRP-steel bonded joints and found that the bond strength does not always increase with the bond length (Fawzia et al., 2007; Nozaka et al., 2005; Xia, S.H., and Teng 2005). There is an ultimate bond length value, and a further increase in bond length does not increase the bond strength, and this length is commonly referred to as effective bond length (Chen, J.F., Teng 2001). Calculation of bond strength is a vital task in designing FRP - steel-bonded joints, and two main approaches are used to find this.

- Strength-based approach – assume bond strength is reached when the maximum stress/strain developed in the adhesive reaches its corresponding strength (M. Bocciarelli, 2009; Nozaka et al., 2005; Schenerch et al., 2007). For the use of the

strength-based method, it is essential to predict interfacial stress and/or strain distribution (Rabinovitch, O. and Frostig, 2000; Shenet al., 2001; Smith, S.T. and Teng, 2001; Yang, j. and Ye, 2010; Zhang, L. and Teng 2010).

- Fracture-mechanics based approach (Bocciarelli, M., Colombi, P., Fava, G., and Poggi 2007, 2009) – which are similar to those for the bond strength of Concrete-FRP bonded joints where the bond strength is related to the interfacial fracture energy (Chen, J.F., Teng 2001; Yuan, H. and Wu 1999). Some researchers have verified the applicability of the fracture-based approach to predict bond strength. However, the type of adhesive and the thickness were not considered, which avoids considering interfacial fracture energy (Xia, S.H., and Teng 2005).

1.12.3 Bond-slip Relationship

A bond slip relationship may be defined as the connection between the interfacial shear stress and the relative slip between the two adherends. An accurate bond slip relationship is of paramount important to comprehend and model of the performance of FRP reinforced steel structure (Fernado 2010). Bond slip model explains the behaviour of the bonded interface under shear loading. Single shear pull-off test proposed as the most suitable test method to study about bond slip beahaviour of concrete to FRP bonded joints (Yao et al. 2005). Xia and Teng (2005) studied full range behaviour of bond slip model of FRP to steel bonded joints. It was shown that bi-linear bond slip relationship may also be utilised for FRP to steel bonded joints, with the bond slip parameters which defined with adhesive properties.

Luet al. (2005) conducted a comprehensive study to investigate the bond slip behaviour for FRP concrete joints and suggested three two branched bond slip models. Each of this bond- slip model consists an ascending region and a descending region

which are vary from each other in the shape of the bond slip relationship. The simplest form of this bond slip relationship is considered as bilinear bond slip relationship with adequate accuracy and is shown in Figure 2.41. Several main parameters of bilinear bond slip relationship can be defined as follows;

τ_{max} = maximum local bond stress

δ_1 = corresponding slip at ultimate bond stress

δ_f = the slip when the local bond shear stress decreases to zero

G_f = interfacial fracture energy that may be found by the area under the bond slip model curve and horizontal slip axis

These parameters for FRP to concrete bonded joints depends on the ultimate tensile strength of the concrete since concrete is the weakest in the joint and hence these equations cannot be directly used for FRP to steel bonded joints in which the adhesive film is the weakest. However, bi linear bond slip relationship can be utilised for FRP steel bonded joints in which bond slip parameters are defined using properties of adhesive (Xia, S.H., and Teng 2005).

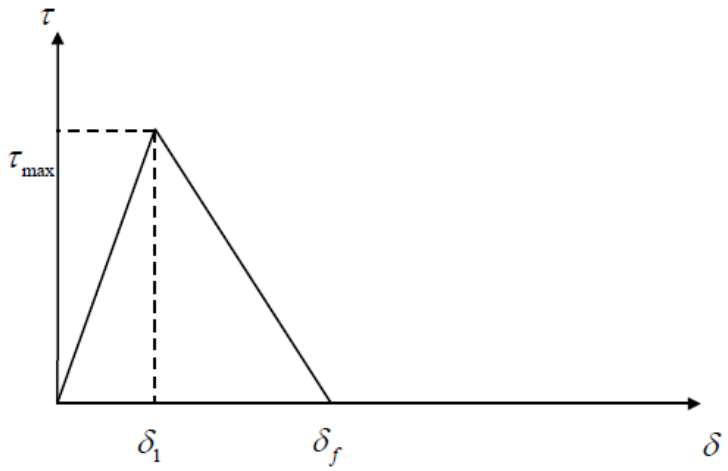

Figure 2.41. Bi-linear bond-slip model

2.13 CFRP Strengthened Steel Structures

Several researchers have conducted extensive numbers of studies to show that CFRP is a compatible material for strengthening concrete structures. Recently, there has been an immense interest in the performance of the CFRP retrofitted steel structural elements under various loading and environmental conditions. The application of CFRP on metallic structures improves the stiffness, strength, structural performance, and ductility of strengthened structural elements. The reported studies on CFRP strengthened steel structures which are open and closed sections. At the same time, the loading conditions include axial, bending, torsional, blast loads and impact loads under various environmental conditions such as underwater applications, aggressive environments etc.

2.13.1 CFRP strengthened open steel sections

A considerable number of research can be found in the literature which was studied on the strengthening of open steel sections using CFRP. Sen et al. (Sen et al., 2001) have studied the feasibility of applying CFRP as a strengthened material for repairing steel bridge girders. Six specimens with spans of 6.1 m and W 8 × 24 flange width were used with concrete slabs. First, beams were loaded until they reached to yield of the tension flange to simulate the severe service distress. Then the damaged specimens were strengthened with various CFRP plates having thicknesses between 2 to 5 mm and lengths of 3.65 m. The first two samples were strengthened with 2 mm thick CFRP, and no adhesive failure was observed at the ultimate load. The third beam, which was strengthened with a 5 mm thick CFRP plate, showed debonding failure, and hence last three beams were strengthened with CFRP having 5 mm thickness with end anchorages to avoid end debonding. The results of the study indicated significant strength gain for the strengthened beams (21% and 52% for 2 and 5 mm thick CFRP,

respectively). It was suggested that the end anchorage effectively prevents premature end debonding, hence the ultimate load capacity. The results of the finite element modelling showed an agreement with the experimental results, and hence the application of CFRP to strengthened steel beams is considered as a feasible option. A similar study regarding the rehabilitation of steel bridge girders using adhesively bonded CFRP has been conducted by Miller et al. (2001). Only a single girder with a span of 7.5 m was used for the study, and the 24 cm wide flange was strengthened with six CFRP plates, each with a 40 cm width. The results of the tested beam confirmed that CFRP plates could be used to restore a considerable portion of loosed strength and stiffness in deteriorated bridge beams. The observed increased stiffness was between 10 – 37% for corroded bridge girders. It was also observed that the placement of the glass fabric layer could be done between CFRP and steel substrate to increase durability in terms of corrosion resistance. A field test conducted on the retrofitted beam showed an 11.6% increase in flexural stiffness.

An experimental study on three large scale steel concrete composite beam specimens made with W 310 × 45 sections having lengths 6.55 m strengthened with high strength CFRP was conducted by (David Schnerch and Rizkalla 2008). Various CFRP strengthening patterns were followed for each specimen with three different parameters, first one being modulus of CFRP fibre being used (High modulus and intermediate modulus), second parameter being the CFRP reinforcement ratio, and third parameter was to check the effectiveness requirement of pre-stressing of CFRP prior to adhesively bonding before bending. The particulars of the test samples are elaborated in Figure 1.41. The results of the study indicated a stiffness increase in strengthened beams were between 10 to 34%, while the ultimate strength increased up to 46%. A noteworthy increase in stiffness of the beam was observed when

strengthened with pre-stressed CFRP strips, which ensure the economical use of CFRP material. A related study to above was conducted by (Soudki and Schumacher 2009) to examine the significance of prestressed CFRP strips on the ultimate strength gain of the steel beams. The have tested five HEA 120 beams of span 1500 mm, including two control beams and three beams reinforced with pre-stressed CFRP strips (prestressed levels of 27%, 40% and 60%) with steel grades of 235 and 355 MPa. It was found that the prestressing system of CFRP was efficient in strengthening steel beams by showing increased yield strength by 7 to 13% while the enhancement in ultimate load ranged 18-28% depending on the steel grade. The observed failure mode of the reinforced beams was local buckling of compression flange followed by debonding of the CFRP strips.

A study performed by (Lenwari et al. 2005) revealed that the percentage strength gain and failure modes obtained by CFRP strengthened steel I beams various CFRP partial lengths have significant differences. Their study was constructed on an experimental study conducted on seven steel beams (W 100 × 17.5) having clear span of 1.8 m. These beams were strengthened using CFRP with three different CFRP lengths with span to CFRP lengths being 5/18, 1/3 and 2/3. The tension flange was strengthened with two CFRP strips. Beams were tested until the failure occurs and observed two main failure modes which were depended on the bonded CFRP length. When CFRP length to span ratios were 5/18 and 1/3, the observed failure mechanisms of the beams were plate debonding while CFRP rupture was dominant for the beams with CFRP length to span ration is 2/3. This observation led to the conclusion that the failure load at the first failure mode improved as plate length increased until the failure mode shifted to second failure mechanism. Further, they have developed analytical methods to calculate the ultimate load of the strengthened beams considering section analysis,

shear lag analysis and the principle of virtual work. It was noted that the shear lag analysis is capable to calculate the bonded plate length to achieve the flexural performance, sections analysis capable of calculating failure load when the failure mode is plate rapture and the principle of virtual work capable of prediction the load deflection behaviour of the retrofitted beams. Later the same researchers (Lenwari et al. 2006) conducted an study to examine the influence of stress intensity on the debonding strength of CFRP strengthened beams. They have conducted a comprehensive parametric study the effect of some key parameters (CFRP plate thickness, CFRP plate modulus, thickness of adhesive, adhesive elastic modulus, and spew-fillet angle of adhesive) on the stress intensity. The results of the parametric study expressed that the debonding strength is significantly subjected to the adhesive modulus, the plate modulus, and the plate thickness. It was also found that the spew-fillet condition angle reduces the singularity and stresses close to the steel adhesive corner, but debonding occurs at other positions with higher stresses.

D. Schnerch et al. 2005, have conducted an study to investigate the bond behaviour of CFRP strengthened steel bridges and structures. The effects of surface preparation methods and the galvanic corrosion prevention methods were discussed. An experimental study was conducted on SLB 100 × 4.8 wide flange steel members strengthened with 36 mm wide 1.45 mm thick CFRP strips. The beams having 813 mm span were tested under flexure using four points bending after strengthening with different types of adhesives with CFRP strip lengths varies from 51 mm to 254 mm. The observed failure modes included debonding for shorter CFRP lengths (51 mm and 76 mm) and CFRP rupture for longer CFRP lengths (102 mm to 254 mm). It was also noted that the failure modes were depended upon the surface preparation method.

Colombi and Poggi (2006), Conducted experimental, numerical, and analytical studies on the load-deflection performance of steel beams strengthened by pultruded CFRP strips. The experimental study was conducted on four steel beams (identical to each other) strengthened with CFRP strips (single or double layers) with two epoxy adhesive types. For all the specimens used in this study showed increments in load carrying capacity and CFRP strips contribute to enhance both elastic and plastic stiffness. Moreover, (Narmashiri et al. 2011) studied the strengthening of steel I-beams under bending, using CFRP patches. Their findings highlight that the failure mode, load capacities, and strain distribution of CFRP sheets are depends on different types and thicknesses of CFRP. Their study was based on eight steel beams (flange width =100 m, flange thickness = 10 mm, Web height = 130 mm, and web thickness = 6.6. mm) of span 2000 mm test under the four-point bending test. One of the key finding of this research include that the thicker layer of CFRP plates caused significant increase in load bearing capacity, but premature end debonding is suspect due to the brittle behaviour.

Some researchers have performed studies on strengthening of deteriorated steel beams due to corrosion, strengthened with CFRP plates. (Zong-xing Zhang et al. 2020) have performed this type of study using five corroded steel beams which were tested under flexural test. The observed failure modes included the fracture of the CFRP plates after the interfacial shear failure at the mid span. It was also noted that the rough surface of corroded steel beams enhances the efficiency of interfacial stress transfer. Ultimate bending moment capacity of the corroded beams retrofitted with CFRP plates with 15% prestressing have shown a 21% increment. It was also noted that the prestressing of CFRP plates play an important role in strengthening of steel structures, by improving the flexural capacity, reducing the burden of the structure, and making

complete use of material performance. More recently, (Siwowski and Siwowska 2018) have conducted an experimental study to evaluate the flexural behaviour of steel I beams reinforced with CFRP. Two strengthened schemes were considered in the study; (i) adhesive-bonded passive plates and (ii) adhesive-bonded prestressed or active plates. During the testing program ten, medium scale HEB 280 I beam of span 4800 mm were tested under four-point bending. Figure 2.42 shows the beams with different strengthening schemes. Results of the study revealed that, irrespective of the strengthening system, both yield and ultimate flexural capacity increased and, it was noted that the prestress level of CFRP does not influence the either yield or ultimate flexure capacity.

Figure 2.42. Strengthened configurations of steel beams (source: Siwowski and Siwowska 2018)

A study was conducted by (Narmashiri, Jumaat, and Sulong 2010) to examine the effect anchorage on the ultimate strength of CFRP strengthened I beams. Four samples including control beam, strengthned beam without end anchorage, two strengthened

beams with end anchorages but anchor lengths are different, were tested under this study. The results of the study indicated that anchored beams had higher load capacities upto 24% compared to non strengthened beams. It was highlighted that the end achorage with closer bolt spacing is more effecive for the anchoring systems.

Various researchers allover the world have conducted reseaches to identify failure mechanisms of CFRP strengthened steel open sections. Lenwari et al. (2006) have condcted a study to investigate the debonding failure mechanism of steel I beams strengthened with adhesively bonded CFRP strips (part of the beams) under fatigue and static loading (Lenwari et al. 2006). Findings of their research revealed that the steel I beams retrofitted with CFRP tend to fail in debonding of CFRP under both fatigue and static loading due to the higher stress concentration at the CFRP plate end. The also found that the lucas of debonding initiation as the steel adhesive corner and hence the preparation of steel surface is prime important on the strength of the bonded joint. Unlike welded steel plates, bonded CFRP strips did not show fatigue cracks under fatigue loading. The factors infuencing the debonding strength were included; adhesive elastic modulus, the plate elastic modulus, and the thickness of the plate.

Narmashiri et al. 2012. Conducted an eperimental and finite element investigation on flexural strengthened beams using CFRP with the main focus on structural beahviour and failure analysis (Narmashiri et al. 2012). Altogether thirteen beams (one control beam and twelve beams stengthned with CFRP) were tested with various types and different dimentions of CFRP strips were tested under gradually increasing load using four point bending test (Figure 2.43). The identified failure mechanisms included; splitting below the point load, debonding below the point load, end debonding, and end delamination (Figure 2.44). The high stress/strain concentration at the tip of the CFRP layer caused the debonding. Below the steel yield point CFRP strips are critical,

but high stress developed under the concentrated force after yielding and cause for the below point load debonding and which is common in CFRP retrofitted steel structures due to the larger deflections. End delamination of the CFRP strengthened beams is due to the discontinuity from the abrupt termination of the CFRP plates while below point load splitting is due to the weaker properties of CFRP in the lateral direction and asymmetrical stress concentration below the loading point. Other important findings of this research were included non-effectiveness of using CFRP lengths greater than effective CFRP length and effect of CFRP thickness/modulus of elasticity of CFRP on the developed stresses, strains, and deflections. They also done finite element modelling using ANSYS to simulate the numerical results which were tally with experimental results.

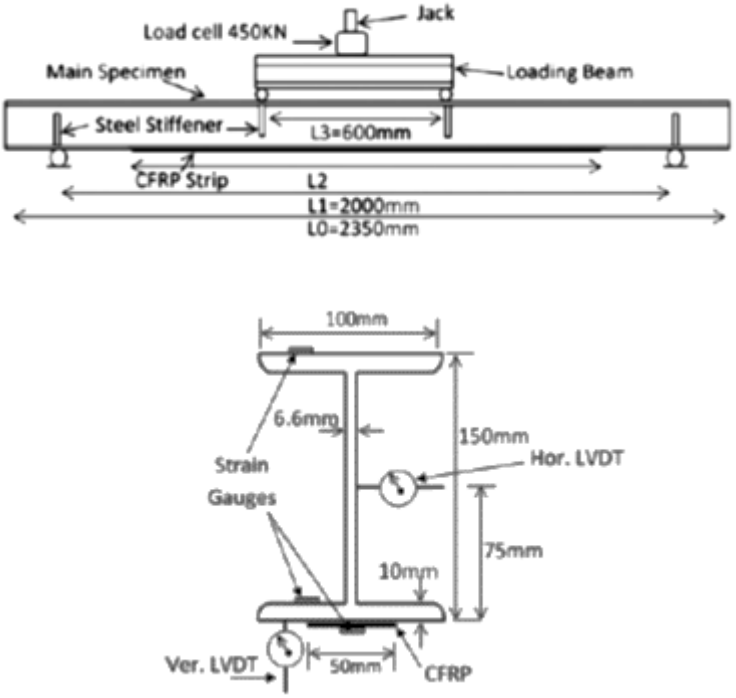

Figure 2.43. Dimensions of tested beams and poisions of strain gauges (source: Narmashiri et al. 2012)

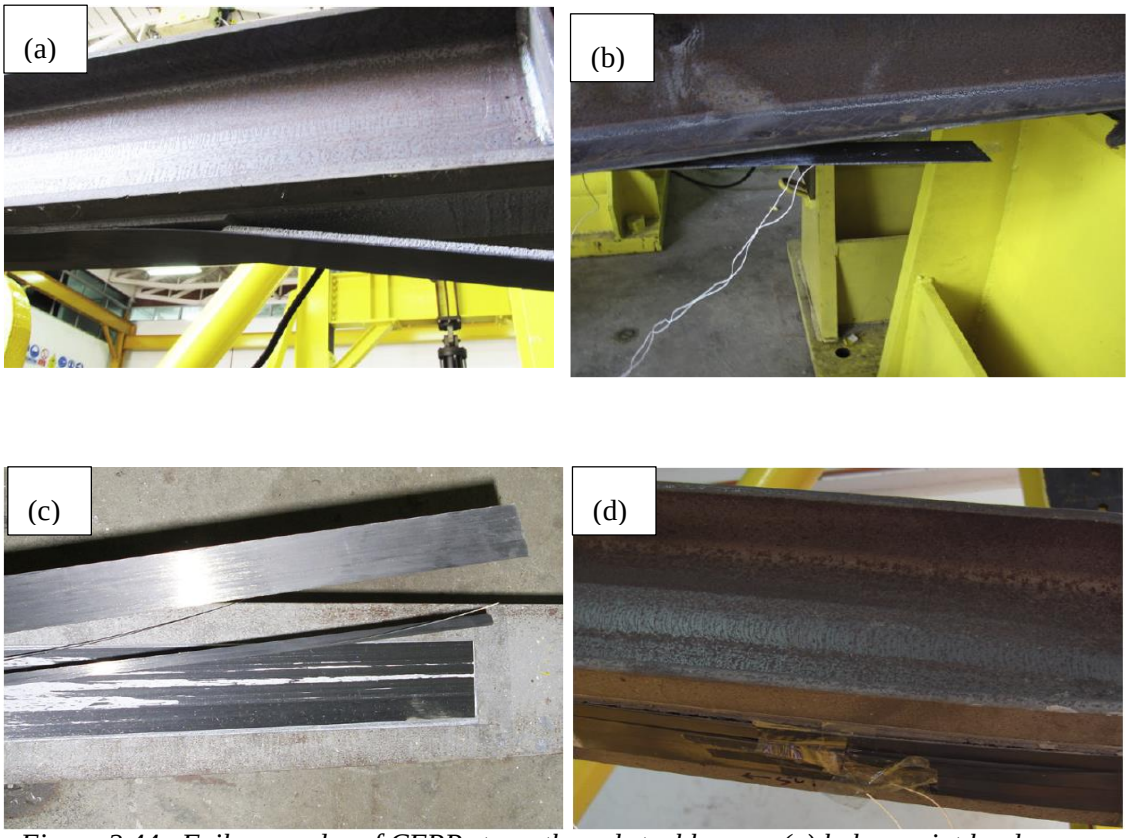

Figure 2.44. Failure modes of CFRP strengthened steel beams; (a) below point load debonding, (b) end debonding, (c) end delamination and (d) below point load splitting.

Chiew and Lee, performed a study to examine the types of bond failures mechanisms of FRP bonded steel structures (Yu et al. 2011). Three types of FRP to steel bonded joints; (i) double lap shear joint, (ii) single lap shear joint, and (iii) Tee peel joint were used for the study (Figure 2.45) were tested and was found that the most critical fact that effect the final bond failure is the stress concentration at the tip of the bond line. All three types of joints were failed due to the adhesive failure and is because, the weakest link in the joint is the connection between adhesive and steel. Based on the results a bond failure model was suggested to overcome some limitations of existing models.

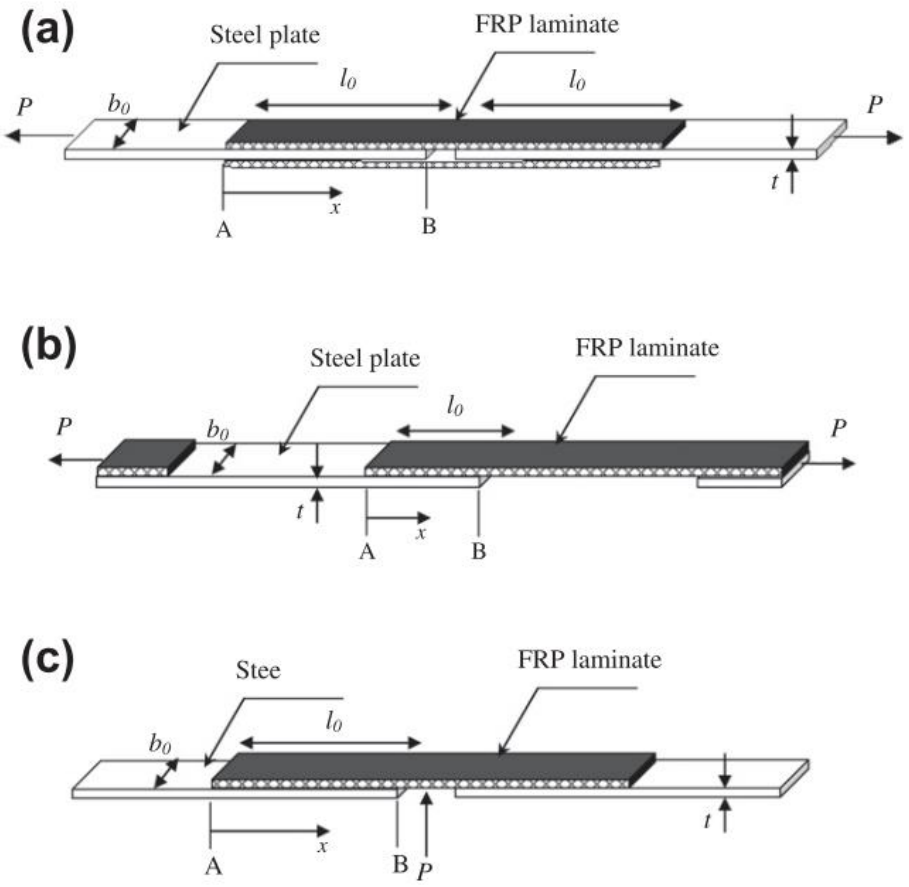

Figure 2.45. Formations of (a) double-lap shear joint, (b) single-lap shear joint and (c) T-peel shear joint (Source: Chew and Lee 2011).

The influence of mechanical properties of CFRP and adhesive on the bond performance of steel structures reinforced with CFRP was studied by (Li et al., 2018). The parameters used in the study included types of CFRP and epoxy adhesive on the bond-slip relationship, bond strength parameters and failure modes. It was noted that the use of various materials caused by the failure of some specimens was due to interfacial debonding characterized by a brittle failure. In contrast, other specimens failed because of the CFRP's cohesive failure or delamination failure characterized by ductile failure. The bond-slip relationship for most of the failures of specimens might be simplified and represented by linear models. However, the trilinear bond-slip model should be adopted for the beams that failed in tearing and delamination of

CFRP. As per the developed finite element models, the parameters, such as maximum shear stresses and interfacial debonding/ CFRP superficial delamination, are linearly correlated with the elastic moduli of adhesive.

In 2011 Chiew and Lee extended their study (Yu, Chiew, and Lee 2011) to verify their findings using real applications on steel I-beams. A full-scale experimental investigation was conducted on steel beams strengthened with CFRP under four-point bending (Figure 2.46) to check the influence of various parameters such as CFRP laminate thickness, CFRP bond length and the thickness of the adhesive. The experimental test setup used for the study is shown in Figure 2.47.

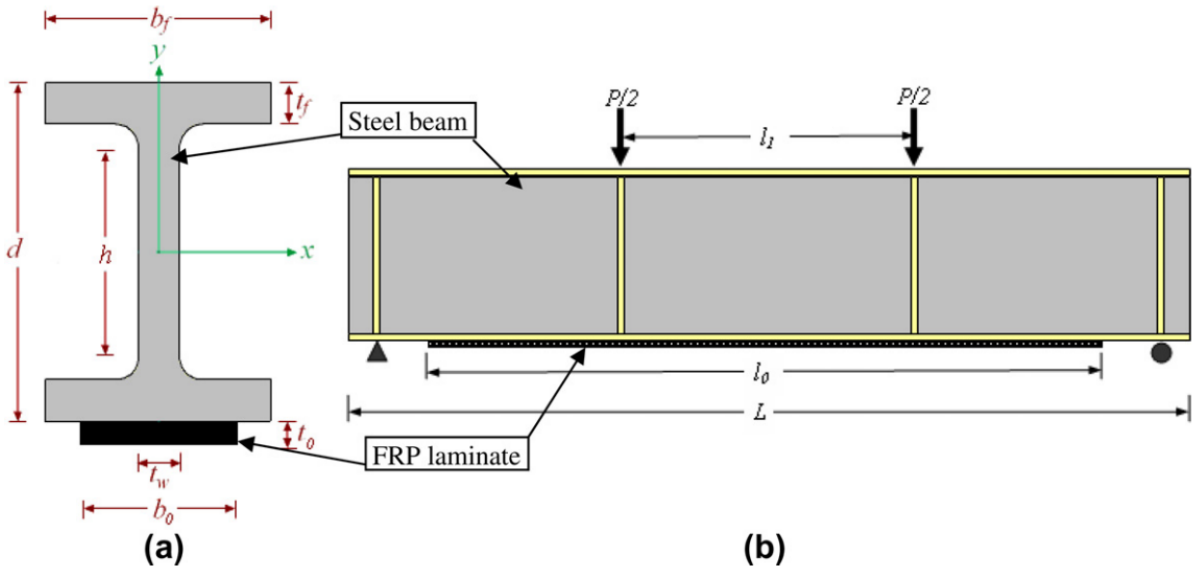

Figure 2.46. Schematic diagram of typical CFRP retrofitted beam specimen: (a) cross section, and (b) side elevation.

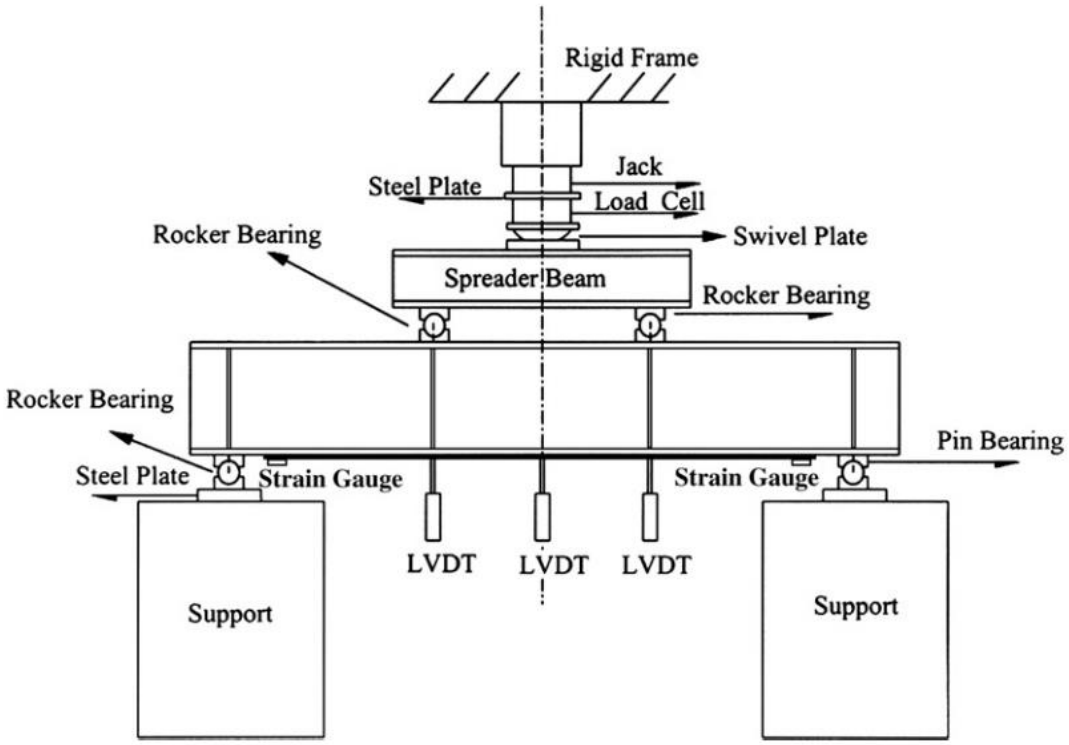

Figure 2.47. Experimental setup.

The bond failure model developed under part 1 of the study (Chiew, Yu, and Lee 2011) was verified using the results experimental study. The parametric study results revealed that the bond strength could be effectively enhanced by using lower laminate thicknesses, lower laminate elastic modulus and lesser adhesive layer thickness or by increasing the CFRP bond length. The developed bond model has shown significant advantages compared to the existing models to analyse the FRP/steel joints, such as the ability to apply without the hypothesis of linear geometry or elastic material and the possibility of predicting the association between adhesive layer thickness and FRP bond strength of FRP strengthened steel beams without using maximum value-based models.

Teng et al. (2012) critically reviewed CFRP-reinforced steel structures and reported several failure mechanisms of CFRP-strengthened I-beam in its tension face. These failure modes include; (a) bending failure, (b) lateral torsional buckling; (c) end

debonding; and (d) intermediate debonding of CFRP due to cracking or yielding away from the plate end. In addition to the above failures, two more failures are possible, (e) compression flange local buckling; and (f) web local buckling. They have highlighted that beams in which the buckling modes are not critical before FRP strengthening may become perilous after strengthening, especially for beams strengthened only applying CFRP on tension flange. The reason for this is the higher load sustained by the flange and web prior to the failure of the beam due to other modes. However, their local buckling resistance does not improve from the bonded FRP laminates (Teng, Yu, and Fernando 2012b). These failure modes are summarised as elaborated in Figure 2.48.

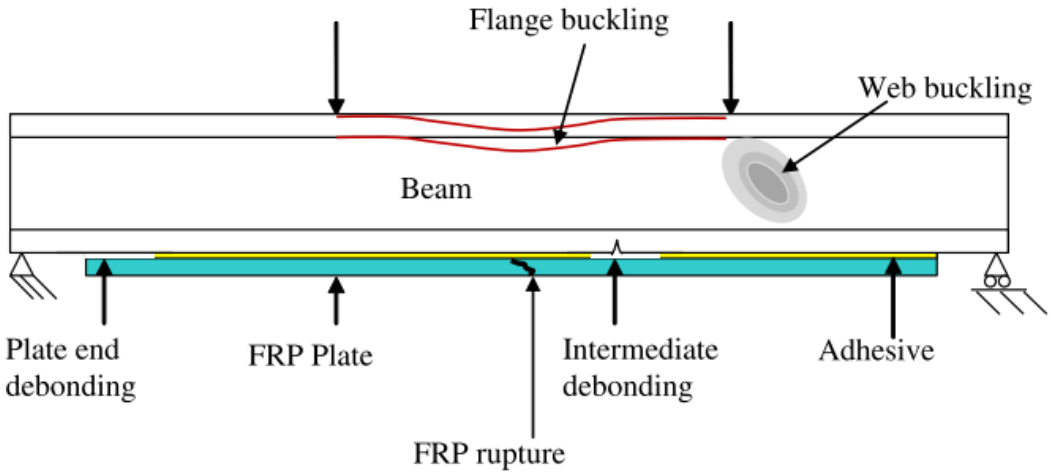

Figure 2.48. Some failure modes of steel beams strengthened with CFRP (Source: Teng et al, 2011)

The feasibility of using low modulus CFRP to strengthened was studied by (Selvaraj et al. 2019). Eighteen low modulus CFRP strengthened laterally restrained beams with various CFRP application configurations (Figure 2.49) were tested under four-point bending. The test setup for the four-point bending which is given in Figure 2.50 with all the dimensions.

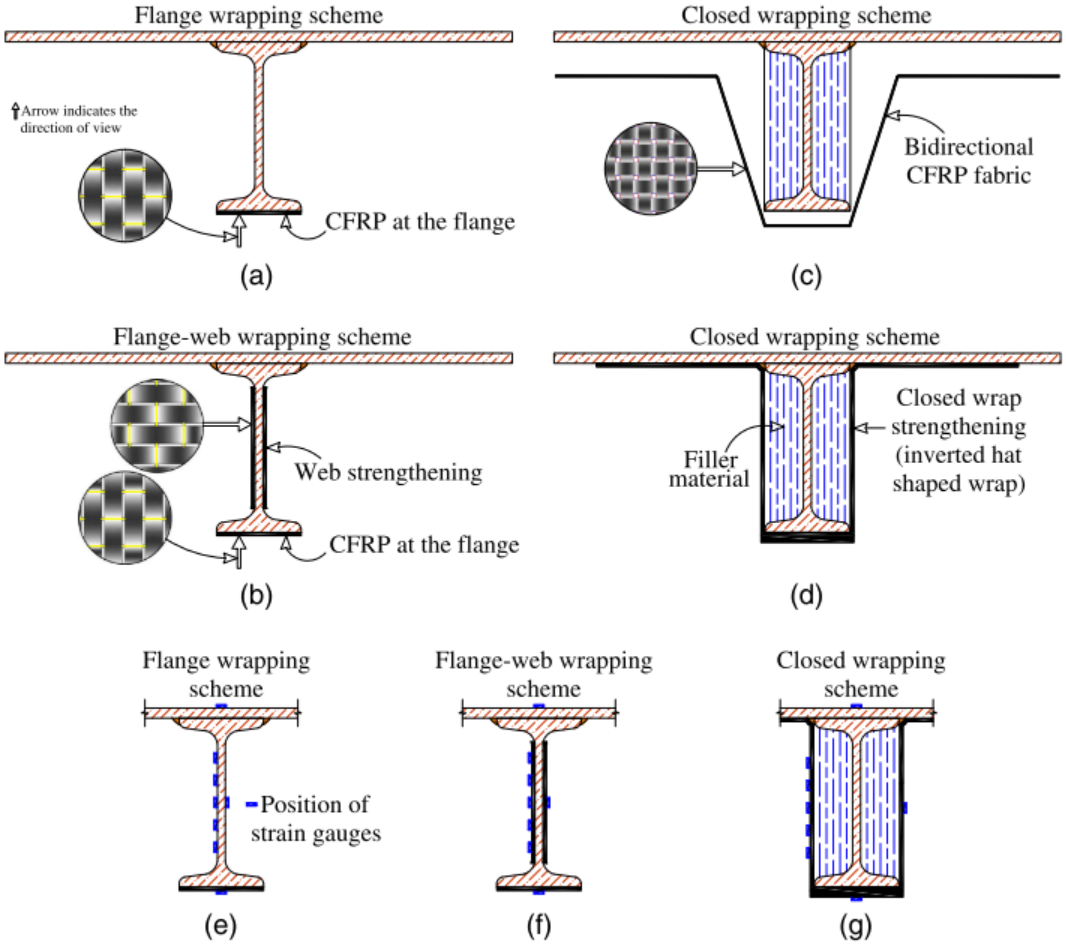

Figure 2.49. Strengthening schemes: (a) flange wrapping; (b) flange-web wrapping; (c) closed wrapping prior to wrapping; (d) closed wrapping scheme after wrapping; and (e, f, and g) location of strain gauges in different strengthening schemes.

It was noted that the flanged-wrapped beam showed a percentage increase of 28.2% in ultimate load capacity but failed in premature debonding of CFRP from the steel surface. A flange web wrapping scheme was introduced to avoid this, and a significant change in ultimate load was observed (49.5%) compared to the control beam. In closed wrapping schemes, the percentage increment of the ultimate load was observed as 42%, but wrinkling of CFRP occurred. However, with the developed closed wrapping scheme (inverted hat shape) ultimate load was observed to be increased by 50% compared to the control specimen. Although the strengthening schemes used low

modulus CFRP, a significant improvement in ultimate load could be obtained. However, some undesirable failure mechanisms were observed within the strengthened beams.

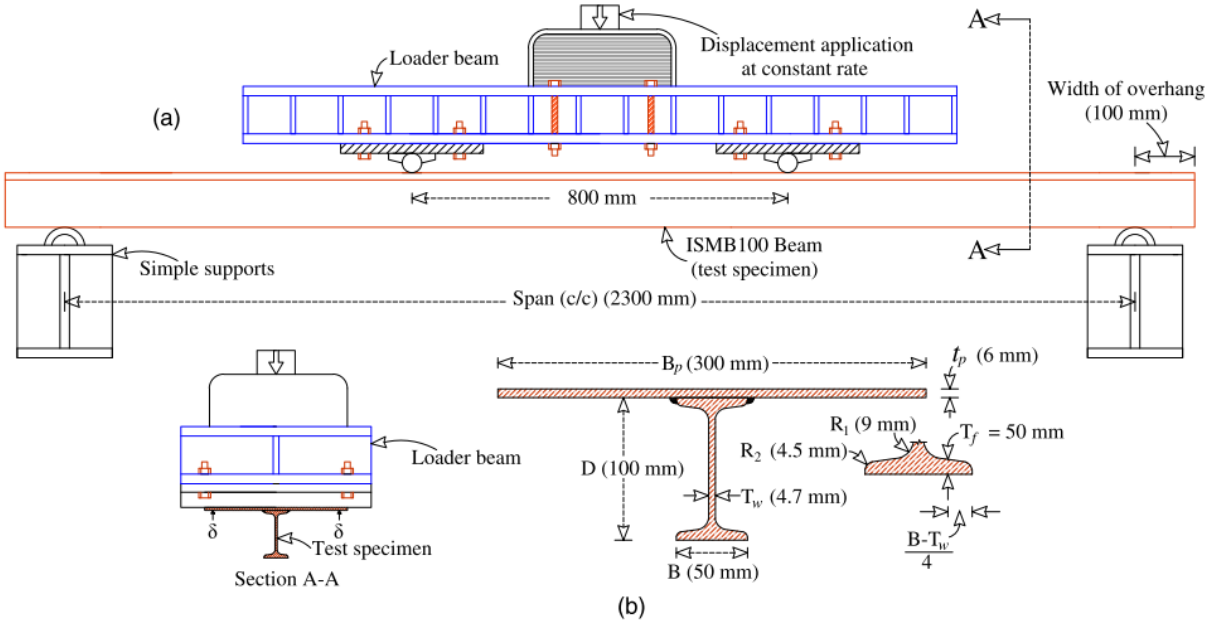

Figure 2.50. Experimental setup for four point bending: (a) view of the arrangements for testing; and (b) dimensions of the test specimen (Source: Selvaraj et al. 2019).

The end debonding of steel beams strengthened with CFRP under flexure is dominated by normal and shear stress intensity. This phenomenon may be delayed by using mechanically fastened CFRP when strengthening steel beams under flexure using CFRP. Katrizadeh and Narmashiri 2019, conducted a study to understand various details of mechanical fasteners and their contribution to the structural behaviour of strengthened beams. They have tested six laterally unbraced I-beams strengthened with CFRP with four different mechanical fastener types as end anchoring made with steel plates and bolts, as indicated in Figure 2.51. The study's findings revealed that the proposed end anchoring enhances the structural behaviour of I-beams by reducing the strain on CFRP. The observed strain reductions were 60% within the elastic region and 30% in the plastic region when compared to control specimens. It was also observed that the use of mechanical fasteners has a significant

influence on the initiation and sequence of CFRP failure modes.

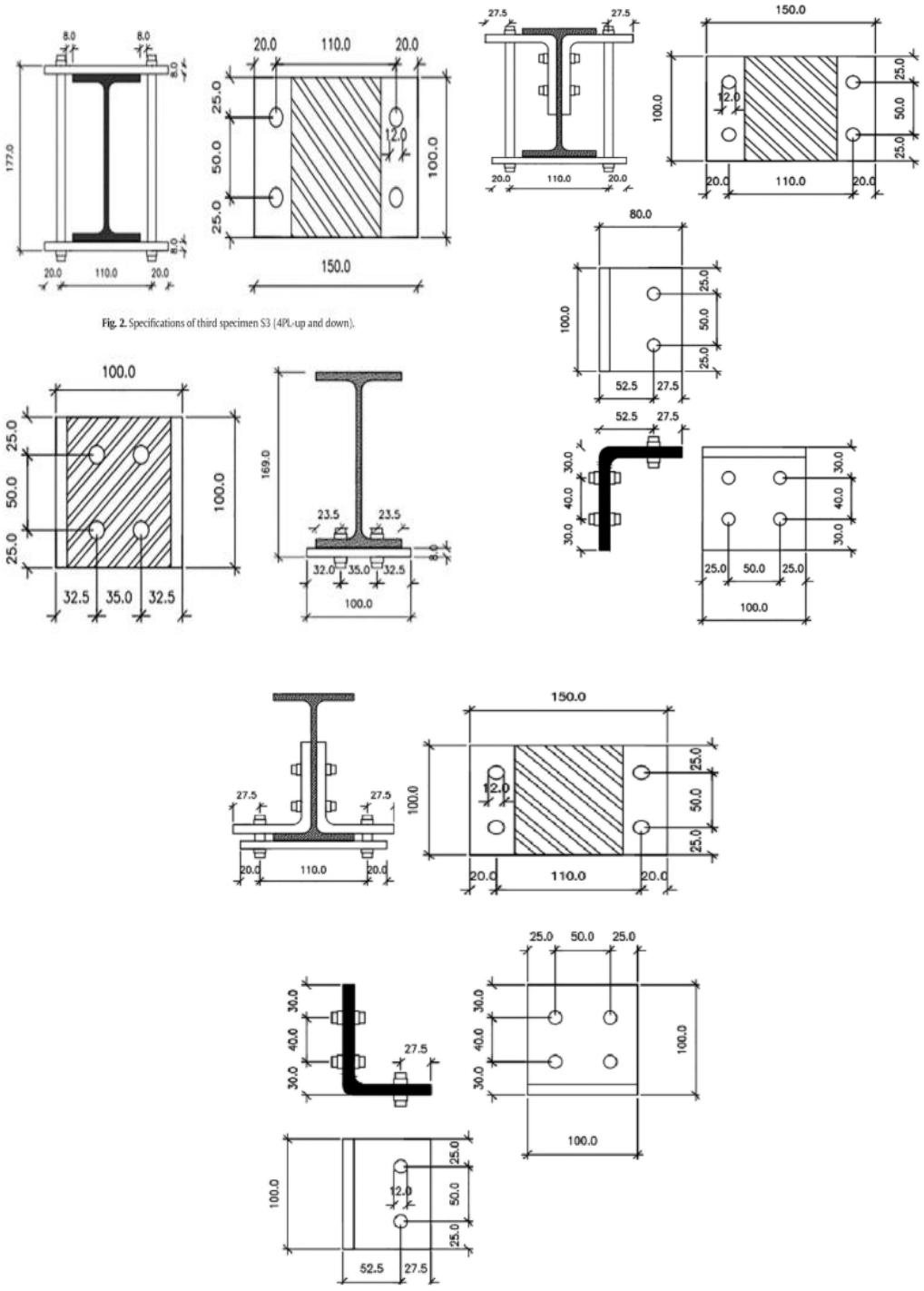

Figure 2.51. Different end anchorage systems (Source: Katrizadeh and Narmashiri 2019)

A study (M. J. Altaee et al. 2017) was conducted to investigate the efficiency of the use of CFRP to strengthened steel I beams with web openings. This study involved both experimental and finite element studies to understand the load behaviour of these

strengthened beams. The six-point bending tests were carried out on four full scale universal beams with web openings at different locations shown in Figure 2.52.

Figure 2.52. Testing arrangement used for strengthened beams with web openings (Source:

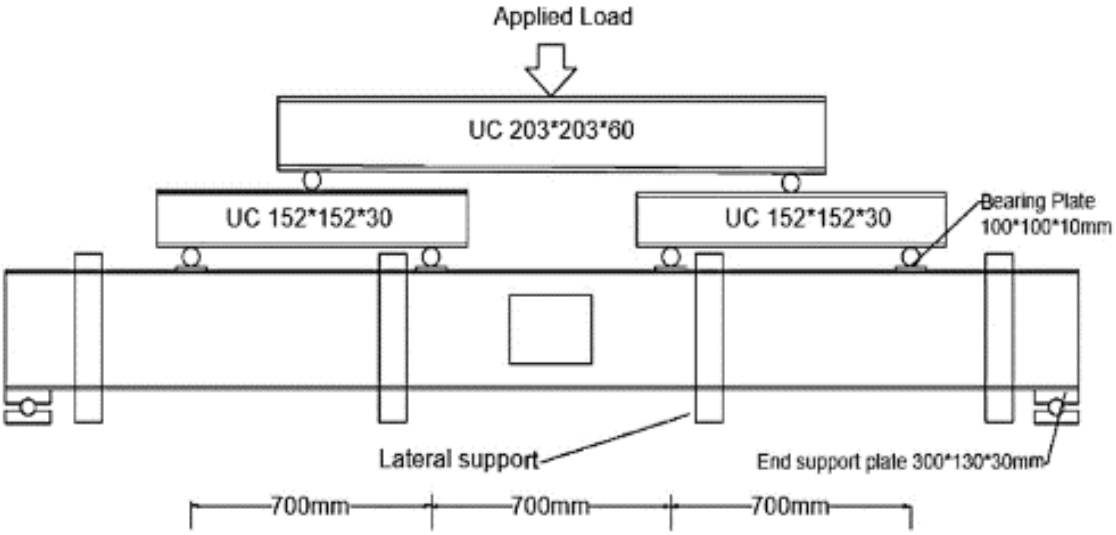

(M. J. Altaee, Cunningham, and Gillie 2017)

The most important observations of this study were:

(1) A stiffer response was observed up to ultimate load in all strengthened beams than in un-strengthened beams. Irrespective of the presence of web openings, strengthened beams have showed greater load capacity compared to control beams with no openings or strengthening.

(2) CFRP strengthening is capable of enhancing both stiffness and strength of steel beams with web openings

(3) Strengthening method used using CFRP can be considered as a useful approach in practice to enhance both serviceability and ultimate limit state

(4) A great attention should pay during the design of CFRP scheme, since the different CFRP configurations shows different failure modes.

In 2019 same research team (M. Altaee, Cunningham, and Gillie 2019) conducted numerical simulations on strengthening of steel floor beams with web openings using CFRP. Finding of numerical study was confirmed the experimental results.

In 2019, the same research team (M. Altaee, Cunningham, and Gillie 2019) conducted numerical simulations on the strengthening of steel floor beams with web

openings using CFRP. The finding of the numerical study confirmed the experimental results.

The failure due to debonding of CFRP-strengthened steel I beam under flexure was successfully modelled using FEM software by (Teng et al., 2015b). The results obtained through the numerical analysis were confirmed after comparing with those obtained through experimental studies conducted by (Deng, J. 2007) on CFRP-strengthened beams, as shown in Figure 2.53. The key findings of the study consisted of; (1) the application of CFRP plates with greater elastic modulus or higher thickness may result in lower ultimate load if the major failure mode is plate end debonding due to earlier debonding of plates (2) end debonding of the plate is more porn to arise when a short length CFRP plate is used, as is generally expected; and (3) when longer CFRP plates used, the failure modes may deviate into intermediate debonding or remaining failure mechanisms such as buckling of compression flange.

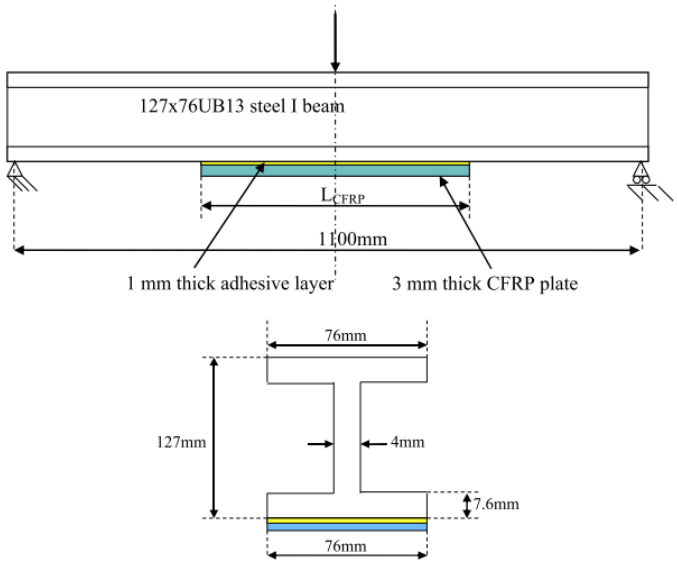

Figure 2.53. CFRP strengthened steel beam used for the experimental study (Source: Deng, J. 2007)

The studies conducted by Selvaraj and Madhavan in 2019 and Selvaraj et al. in 2013 focused on investigating the behavior of CFRP (Carbon Fiber Reinforced Polymer)

strengthened channel sections. These studies aimed to determine the effectiveness of CFRP wrapping mechanisms in increasing the strength and stiffness of flexural members. In the study by Selvaraj and Madhavan in 2019, the researchers found that CFRP-strengthened channel sections exhibited an increase in ultimate strength of up to 46% compared to control beams. This indicates that the application of CFRP can significantly enhance the load-carrying capacity of the channel sections. The study conducted by Selvaraj et al. in 2013 explored six different CFRP wrapping mechanisms for channel sections. These mechanisms involved the use of unidirectional and bidirectional CFRP wrappings. Unidirectional fibers were employed to improve stiffness and strength, while bidirectional layers aimed to prevent lateral torsional buckling in channel sections. The experimental setup for this study included twenty-one specimens, which were subjected to four-point bending tests. The dimensions of the specimens were outlined in Figure 2.55, as described in the research. The results of the study indicated that closed channel sections wrapped with bidirectional fabrics were effective in enhancing the stiffness and strength of CFRP skin-reinforced sections. Furthermore, the application of unidirectional CFRP layers before the final bidirectional wrapping layer further improved the stiffness and strength. The studies also identified various failure modes associated with different CFRP-strengthened configurations. These findings provide valuable insights into the behavior and performance of CFRP-strengthened channel sections, offering potential solutions for enhancing the structural properties of such members.

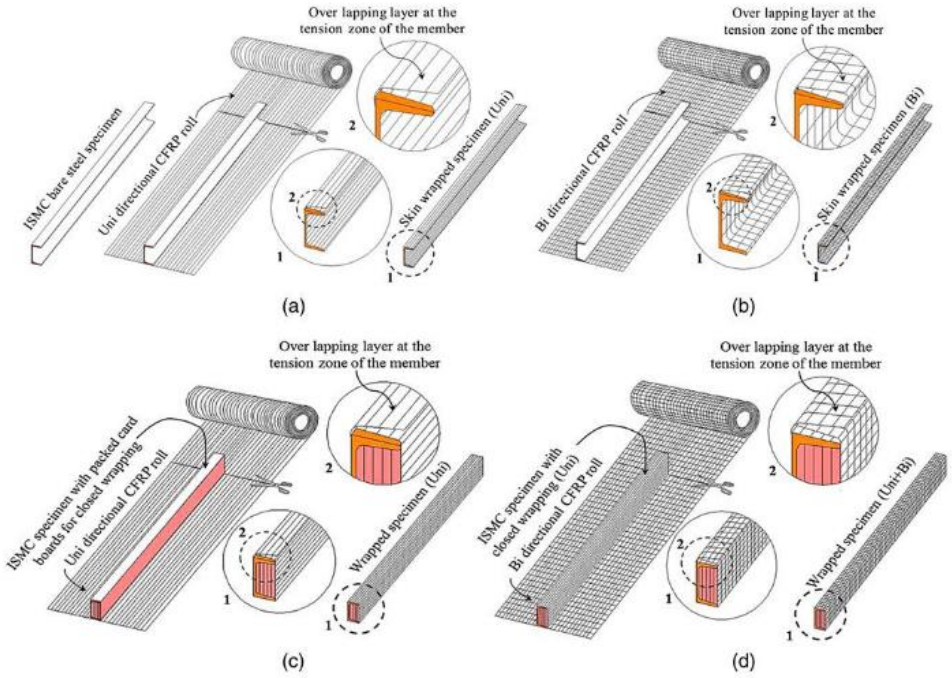

Figure 2.54. CFRP wrapping configurations: (a) skin wrapping unidirectional CFRP layer; (b) skin wrapping bidirectional CFRP layer; (c) closed wrapping I layer; (d) closed wrapping II and III layers (Source: Selvaraj et al. 2013)

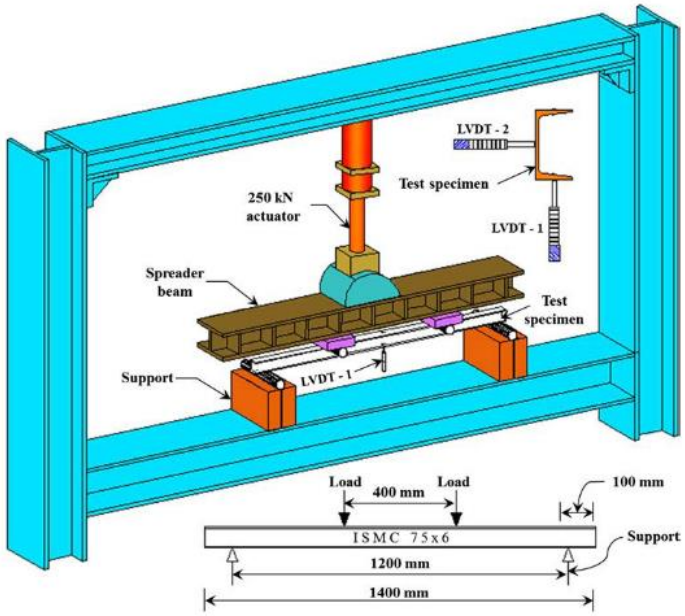

Figure 2.55. Experimental test setup and specimen dimensions (Source: Selvaraj et al. 2013)

The study conducted by Bagale et al. in 2020 focused on the effectiveness of CFRP (Carbon Fiber Reinforced Polymer) in strengthening steel beams subjected to fatigue and impact loading. The researchers investigated the performance of steel beams reinforced with FRP under static and fatigue loading conditions and analyzed the flexural behavior and failure mechanisms. In terms of static loading, the researchers applied CFRP to both failed and intact beams to evaluate the impact of CFRP length and transverse anchorage on flexural behavior. The results demonstrated that CFRP laminates increased the flexural capacity by approximately 1.7 times for damaged beams and 3 times for undamaged beams compared to the control beams. This indicates a significant enhancement in the load-carrying capacity of the steel beams when reinforced with CFRP. The study also determined the optimal bond length for steel beams strengthened with CFRP under static loading to be 2/5 of the span length. This finding provides guidance on the appropriate length of CFRP laminates required to achieve optimal strengthening results. Regarding fatigue behavior, damaged control beams were reinforced with basalt FRP (BFRP) and aramid FRP. The researchers observed a 1.5 times improvement in the bending capacity of the beams under fatigue loading when strengthened with CFRP. Furthermore, by using transverse wraps at the laminate tips, the bending capacity was further increased by 43%. This modification resulted in a shift in the failure mechanism from CFRP end debonding to FRP rupture. Additionally, the study compared the fatigue life of beams reinforced with BFRP and CFRP. It was found that beams reinforced with BFRP exhibited a higher fatigue life compared to those reinforced with CFRP.

The study conducted by Kadhim et al. focused on evaluating the behavior of steel I beams reinforced with CFRP (Carbon Fiber Reinforced Polymer) under impact loading. The researchers specifically examined the effects of CFRP thickness and

length on the performance of the beams during impact tests. In their experimental setup, the researchers subjected the reinforced steel beams to impact tests using a 91 kg impactor with a velocity of 4.43 m/s. This allowed them to simulate and analyze the behavior of the beams under impact loading conditions. The results of the study indicated that the utilization of CFRP layers with different thicknesses had a noticeable impact on the beam's performance during impact tests. When CFRP layers with a thickness of 1.2 mm were applied, the maximum lateral displacement of the beam was reduced by approximately 10% compared to the unreinforced beam. Similarly, when CFRP layers with a thickness of 2.4 mm were used, the reduction in maximum lateral displacement increased to around 14%. This indicates that thicker CFRP layers provided greater resistance to lateral displacement during impact loading.Additionally, the study found that the magnitude of the impact load plateau was affected by the thickness and length of the CFRP layers. Thicker CFRP layers resulted in an increase in the magnitude of the impact load plateau, indicating improved load-carrying capacity. On the other hand, shorter CFRP lengths contributed to a decrease in the magnitude of the impact load plateau.

In addition to the experimental investigation, numerical simulations were also conducted. The researchers found that the numerical results demonstrated better agreement with the experimental results in terms of impact load history, transverse movement, failure modes, and strain development. Furthermore, it was emphasized that the distribution of CFRP quantity significantly affected the effective strength, and the internal energy absorbed by the CFRP patch increased with changes in the impact energy. The study presented the experimental test setup in Figure 2.56 and the corresponding numerical model in Figure 2.57 (Kadhim et al., 2019).

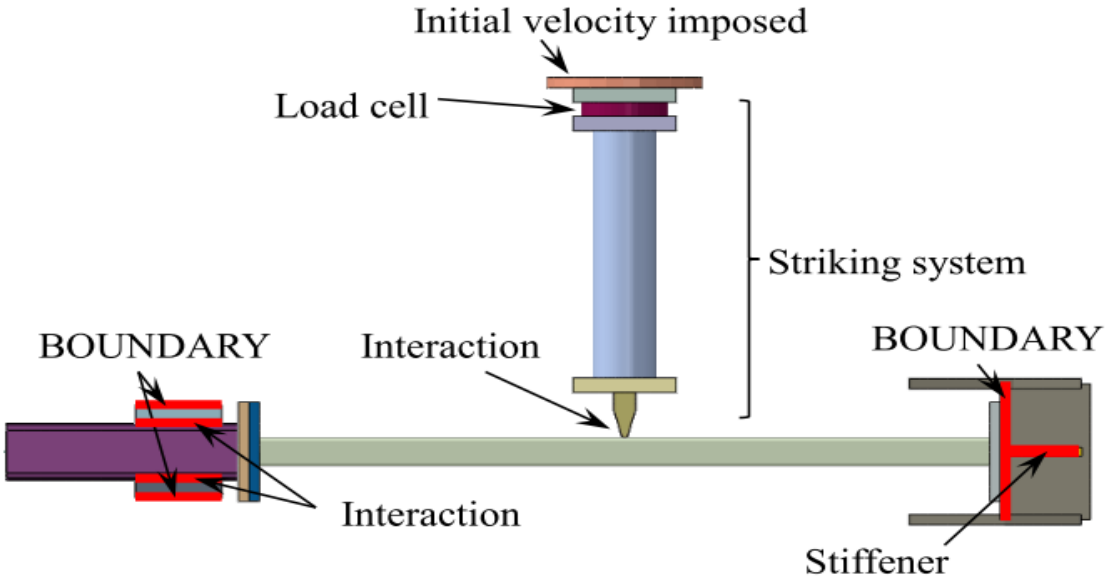

Figure 2.56. Schematic numerical model diagram

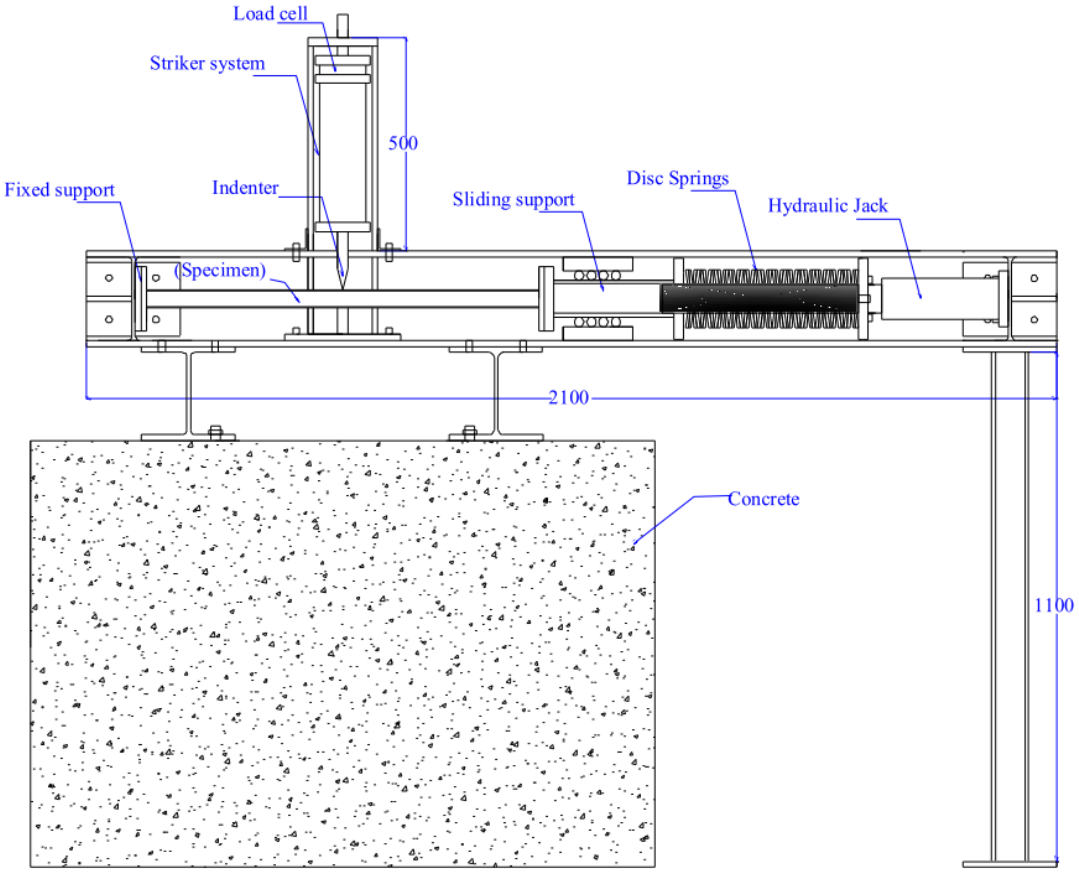

Figure 2.57. Schematic diagram of experimental test setup

The study conducted by Massimiliano Bocciarelli et al. in 2016 aimed to propose design guidelines and analysis models specifically for steel beams strengthened with CFRP (Carbon Fiber Reinforced Polymer), with a particular focus on analyzing debonding failures. To evaluate the edge bond strength of steel beams reinforced with CFRP patches, the researchers presented two methods that employed different approaches: a stress-based criteria method and an energy-based method. The stress-based criteria method utilized stress-based parameters to assess the bond strength of the CFRP-strengthened steel beams. It involved determining the maximum load that the beams could sustain before debonding occurs. This method relied on stress-based indicators to predict the onset of debonding failure. On the other hand, the energy-based method relied on the concept of energy release rate to evaluate the bond strength of CFRP-strengthened steel beams. This approach considered the maximum value of the strain energy release rate as the critical threshold for debonding initiation. By analyzing the energy release rate, the method provided insights into the energy absorption capacity of the CFRP strengthening system and its effectiveness in preventing debonding failure. Both methods shared the fundamental concept that fracture initiation occurs when the rate of strain energy release reaches its maximum value. However, they differed in terms of the parameters used (stress-based or energy-based) to assess the bond strength and predict debonding failure. These two approaches proposed by the researchers offer alternative methods for evaluating the edge bond strength of CFRP-strengthened steel beams. By considering both stress-based and energy-based criteria, engineers and researchers can analyze and design such structures more effectively, taking into account the critical aspect of debonding failure. These design guidelines and analysis models contribute to improving the

understanding and performance of CFRP-strengthened steel beams in practical applications.

Edge debonding – Energy based failure criterion

Consider the simply supported beam strengthened with CFRP as shown in Figure 2.58. It is reinforced using CFRP attached to the tension flange bottom. Since the fracture initiated when SERR, G, is reached to its maximum value G_c. The release rate of strain energy is given by the equation;

$$G = \frac{\partial U^*}{\partial A} = \frac{1}{b_f}\frac{\partial U^*}{\partial B} \qquad (1.62)$$

Where U^* = complementary strain energy, b_f= CFRP width and b = crack length. It is then required to perform two steps for applying the energy failure criterions; (i) calculating complementary strain energy after calculating stress concentrations in the steel and the epoxy adhesive; and (ii) computation of SERR. In CFRP strengthened steel members, the interface physically represented by the adhesive layer and the failure mechanism does not comprise the steel substrate.. Among various bond slip models between the interfacial shear stress (τ) and relative displacement (δ) exists and the most common relations ships are bilinear bond-slip relationship and exponential bond slip relationships which are expressed as follows.

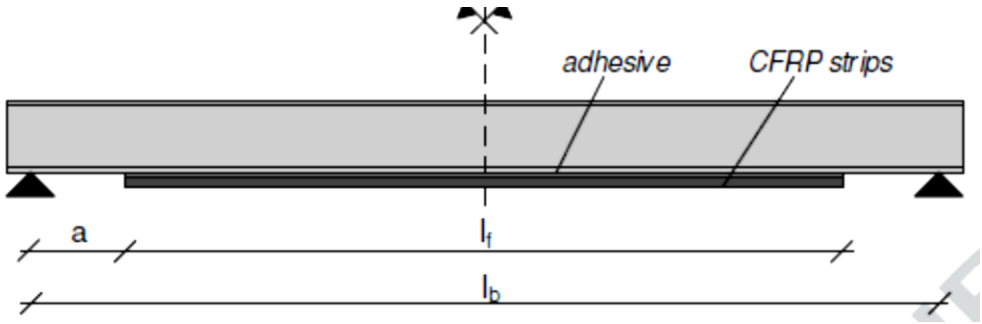

Figure 2.58. Simply supported beam strengthened with CFRP

Bilinear bond-slip model

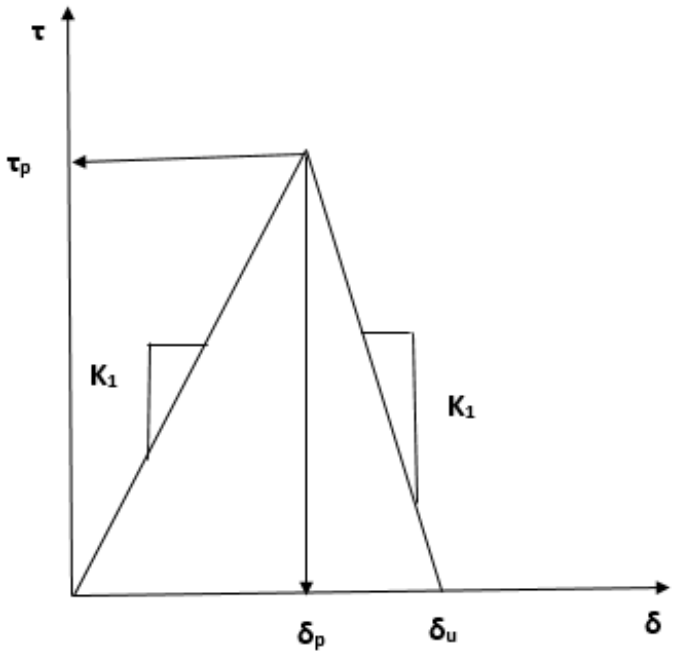

$$\tau = \begin{cases} k_1 \delta & \text{for} \quad \delta \le \delta_p \\ -k_2 \delta + \tau_p \left(\dfrac{k_1 + k_2}{k_1} \right) & \text{for} \quad \delta_p \le \delta \le \delta_u \\ 0 & \text{for} \quad \delta \ge \delta_u \end{cases}$$

Figure 2.59. The bilinear bond-slip model

Exponential bond-slip model

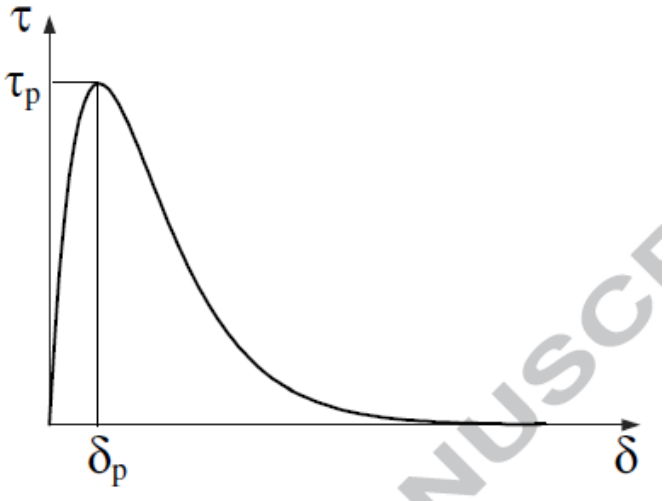

$$\tau = \delta \frac{\tau_p}{\delta_p}\left[exp\left(1 - \frac{\delta}{\delta_p}\right)\right]$$

Figure 2.60. Exponential bilinear model

In both models,

τ_p = ultimate shear stress,

δ_p = relative displacement at τ_p,

δ_u = ultimate relative displacement, and

k_1 and k_2 = slopes of the elastic and the softening branch, respectively.

The area under the bond-slip model represents the energy required to separate the adherents and to form the interface crack and hence;

$$G_c = \int_0^{\infty} \tau d\delta \qquad (1.63)$$

Where G_c is the critical fracture energy at the interface. When apply the bond-slip models to the above integration yields, for bilinear bond-slip relationship;

$$G_c = \mu \frac{\tau_p^2}{2k_1} \qquad (1.64)$$

Where $= {}^{\delta_u}\!/_{\delta_p}$, while for exponential bond slip relationship:

$$G_c = e\delta_p\tau_p \qquad (1.65)$$

When the interface is linear brittle $\mu = 1$ and then the connection between the ultimate shear stress at the common face and the SERR is provided by;

$$G_c = \frac{\tau_p^2}{2k_1} \qquad (1.66)$$

For a simple plated beam under the three point bending, the maximum load at the center of the span is calculated as:

$$P_{max} = \frac{2b_f f_2 E_s I_s}{y_s} . \frac{\tau_p \sqrt{\mu}}{\lambda a + \sqrt{\mu}} \qquad (1.67)$$

Where;

$f_2 = {}^{1}/_{E_f b_f t_f}$,

$\lambda^2 = \frac{k_1}{E_f t_f}$, ,

$\mu = {}^{\delta_u}/_{\delta_p}$,

$E_s \; and \; E_f$ = are elastic modulus of steel and reinforcement respectively

b_f = Reinforcing width

y_s = distance to the centroid of the steel beam from lower flange

τ_p = maximum shear stress

But, from equations (1.66) and (1.67);

$$\lambda^2 = \frac{\tau_p^2 \mu}{2 G_c E_f t_f} \tag{1.68}$$

Hence,

$$P_{max} = \frac{2 b_f f_2 E_s I_s}{y_s} . \frac{\tau_p}{1 + \frac{\tau_p a}{\sqrt{2 G_c E_f t_f}}} \tag{1.69}$$

and is independent of the shape of the bond slip model and implies that the ultimate load depend only of fracture energy G_c and respective ultimate shear stress τ_p.

Edge debonding - Simple energy based method (Massimiliano Bocciarelli et al. 2016)

During the derivation of the simplified analysis method, several assumptions were made. These assumptions include:

1. Elastic Limit: It is assumed that both the steel and CFRP materials operate within their elastic limits, meaning they do not experience plastic deformation.

2. Linear Elastic and Brittle Adhesive: The adhesive used in the CFRP strengthening is assumed to behave as a linear elastic and brittle material. This assumption simplifies the analysis by neglecting any plastic behavior or energy dissipation within the adhesive layer.
3. Constant Cross-Sections: The assumption is made that the plane sections of the beam remain unchanged even after the application of loads, implying that the beam does not undergo significant geometric deformation.
4. Negligible Bending Action on Composite Strips: The influence of bending action on the composite strips is considered negligible, simplifying the analysis by focusing primarily on the effects of shear.
5. Simplified Interface Modeling: The epoxy adhesive layer and its interface are treated as a single common interface, neglecting any complexities in the interfacial behavior.
6. Shear Lag: It is assumed that no normal stresses are present in the adhesive layer, and only the shear stress component is considered. This assumption treats the adhesive layer as a shear lag element.

These assumptions allow for a simplified analysis approach, but it is important to note that they may introduce some limitations in capturing the complete behavior of the CFRP-strengthened steel beams.

The sign convention and notation used in formulation are shown in Figure 2.61.

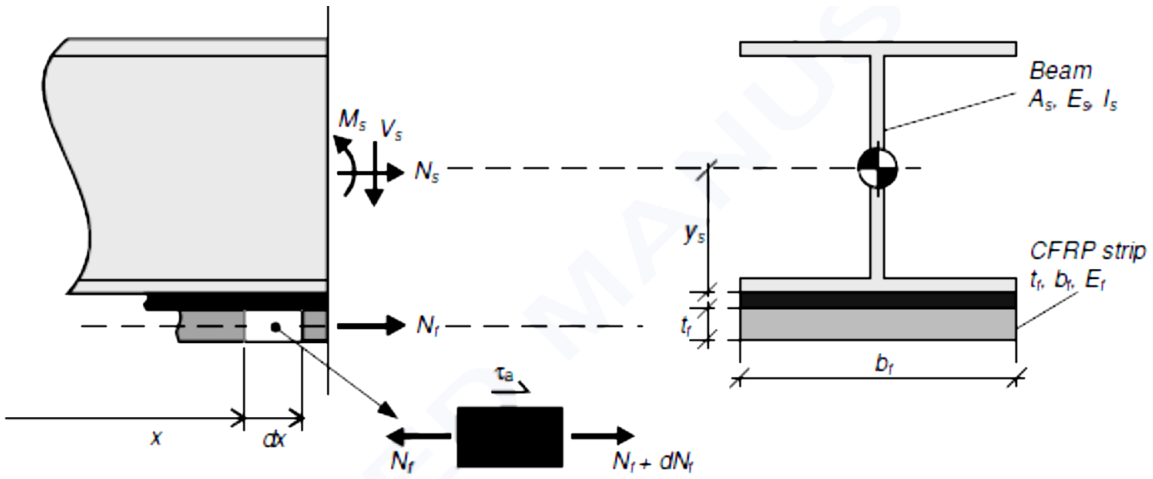

Figure 2.61. Sign conventions and notations

The relative displacement in longitudinal direction at the adhesive layer (δ) is defined as;

$$\delta = u_{sa} - u_f$$

Where; u_{sa} = longitudinal displacement of the beam at the interface; and u_f = longitudinal displacement of FRP layer at the interface.

There for the axial relative displacement at the interface may be expressed as;

$$\delta = u_s + \psi_s y_s - u_f$$

Where $\psi_s$is the section rotation of steel beams u_s is the axial movement of the centroid of the beam section and y_s is explained as in Figure 1.62. The bond-slip relation adopted can be written as;

$$\tau = k_1 \delta$$

Since the debonding take place when $|\tau_{max}| = \tau_p$ and hence the following relationship can be obtained;

$$\tau_p = \frac{M_0 y_s}{b_f f_2 E_s I_s}\left[\lambda + \frac{V_0}{M_0}\right] \qquad (1.70)$$

By considering the CFRP strengthened steel I beams under three-point bending (Figure 2.62), the shear force V_0 and the BM, M_0 at the CFRP edge is given by;

$$V_0 = \alpha V_0' \text{ and } M_0 = \alpha M_0'$$

Where $V_0' = {}^{1}/_{2}$ and $M_0' = {}^{a}/_{2}$ and hence;

$$\tau_p = \frac{\alpha_{max} y_s}{2 b_f f_2 E_s I_s} [\lambda a + 1] \qquad (1.71)$$

Where α_{max} is the debonding load which is given by;

$$\alpha_{max} = \frac{2 b_f f_2 E_s I_s}{y_s} . \frac{\tau_p}{\lambda a + 1}$$

Therefore, the debonding load α_{max} is given by;

$$\alpha_{max} = \frac{2 b_f f_2 E_s I_s}{y_s} . \frac{\tau_p}{1 + \frac{\tau_p a}{\sqrt{2 G_c E_f t_f}}} \qquad (1.72)$$

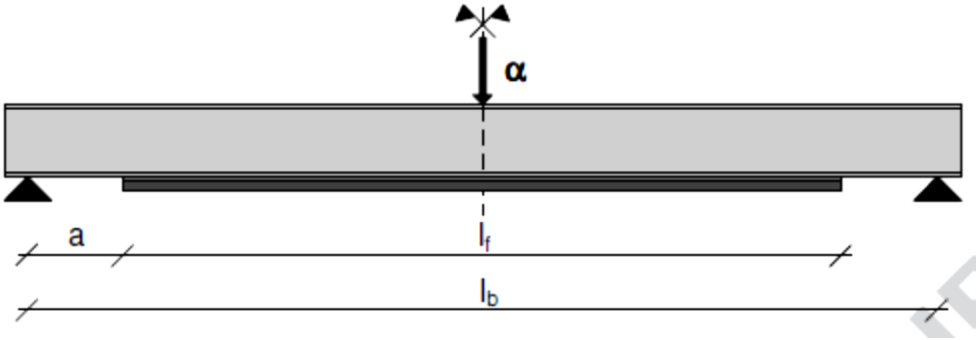

Figure 2.62. Simply supported beam strengthened with CFRP patches

It is also possible to calculate the axial force ($N_{f,max}$) at which the composite strips debonding as follows.

From equation (z), taking into account that $f_2 = {}^{1}/_{E_f A_f}$ and that:

$$\sigma_f = m . \sigma_s = m . \frac{M_0 y_s}{I_s}$$

Where, $m = {}^{E_f}/_{E_s}$ is the modular ratio and hence;

$$\tau_p = \frac{N_{f,max}}{b_f}\left[\lambda + \frac{V_0'}{M_0'}\right]$$

And hence $N_{f,max}$:

$$N_{f,max} = \frac{1}{\frac{1}{\overline{N_{f,max}}} + \frac{1}{b_f \tau_p}\frac{V_0'}{M_0'}} \qquad (1.73)$$

Where:

$$\overline{N}_{f,max} = b_f\sqrt{2G_c E_f t_f}$$

The ultimate tensile stress $\sigma_{s,max}$, in the bottom tensile flange of the steel beams is then given by;

$$\sigma_{s,max} = \frac{N_{f,max}}{m.A_f}$$

Then, by using simple material strength cocepts, the ultimate bending moment, $M_{0,max,}$at the CFRP tip is expressed by:

$$M_{0,max,} = \left[\sigma_{s,max} + \frac{N_{f,max}}{A_s}\right].\frac{I_s}{y_s} \qquad (1.74)$$

And the load factor at the initial debonding is given by equation (1.75),

$$\alpha_{max} = \frac{M_{0,max}}{M_0'} \qquad (1.75)$$

In 2006, Colombi and Poggi conducted an investigation on steel beams strengthened with CFRP, which involved both experimental and theoretical analyses. During the derivation of the theoretical equations used to analyze the strengthened beams, they made several assumptions. These assumptions include:

1. Elastic Materials: All materials involved, including steel, CFRP, and epoxy adhesive, were assumed to behave elastically. This assumption simplifies the analysis by neglecting any plastic behavior or material nonlinearity.

2. Perfect Composite Section: It was assumed that there is no slipping or relative displacement between the layers of the composite section. This assumption considers the composite section as a perfectly bonded unit without any interfacial debonding.
3. Constant Stresses in Adhesive: The adhesive layer was assumed to be thin, resulting in constant stresses throughout its section. This simplifies the analysis by assuming uniform stress distribution within the adhesive layer.
4. Thin Adhesive Layer: The adhesive layer was considered very thin compared to the dimensions of the steel beam and CFRP strip. This assumption allows for a simplified analysis, as the behavior of the adhesive layer is assumed to have a negligible effect on the overall response.

The beam configuration shown in Figure 2.63 was considered for the derivation of the theoretical equations.

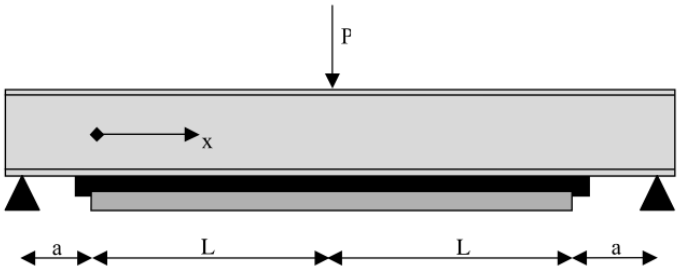

Figure 2.63. CFRP strengthened beam with a point load at the mid-span (Source: (Colombi and Poggi 2006)

The shear stress within the adhesive is expressed by;

$$\tau(x) = \frac{G_a P}{2sE_sW_s}\frac{a\lambda e^{-\lambda x} + 1}{\lambda^2} \qquad (1.76)$$

Where G_a is the elastic shear modulus, s is the thickness of the adhesive, E_s = steel elastic modulus, W_s = section modulus of steel and a is the length from the support to the reinforcement end.

Here, $$\lambda = \frac{G_a b_c}{s}\left(\frac{1}{E_c A_c} + \frac{1}{E_s A_s} + \frac{h}{2E_s A_s}\right) \quad (1.77)$$

Where E_c, A_c and b_c are elastic modulus, area of the cross section and the width of the CFRP layer respectively. h denoted the full height of steel section and area of steel is given by A_s.

The ultimate shear stress is obtained when x = 0;

$$\tau_{max} = \frac{G_a P}{2sE_s W_s}\frac{a\lambda + 1}{\lambda^2} \quad (1.78)$$

Then the tensile stress within the CFRP layer can be evaluated by;

$$\sigma_c(x) = \frac{b_c G_a P}{2A_c sE_s W_s}.\frac{x + a(1 - e^{-\lambda x})}{\lambda^2} \quad (1.79)$$

The calculation of the stress for peeling is simple but end up with a multifaceted long expression.

The method of transform section can also be adopted to calculate the stress in CFRP patch as follows. Figure 2.64 shows the transformed section of a CFRP strengthened steel I beam and is used to explain the method.

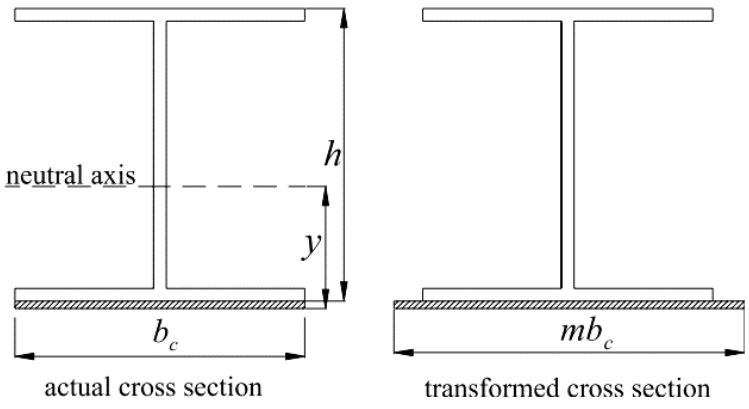

Figure 2.64. Transformed section of CFRP strengthened beam

When applying the transformed section method to evaluate stresses in the CFRP patch, several assumptions need to be made. These assumptions include: (i) Linear Elastic Correlation: It is assumed that there is a linear elastic correlation between stress and strain for all materials involved, including the steel, adhesive, and CFRP. (ii) Plane Sections Remain Plane: The assumption is made that the plane sections of the beam remain plane even after bending. (iii) Perfect Composite Action: It is assumed that perfect composite action exists between the layers of the beam, including the steel and CFRP. To evaluate the position of the neutral axis and the moment of inertia of the area, the CFRP thickness is neglected. Equations (1.80) and (1.81) are used to calculate these values.

$$y = \frac{A_s . \frac{h}{2}}{A_s + mA_c} \tag{1.80}$$

$$I = I_s + A_s \left(\frac{h}{2} - y\right)^2 + mA_c y^2 \tag{1.81}$$

Where I_s = moment of inertia of steel section and then the tensile stress, σ_s, in the strengthened section is calculated as:

$$\sigma_c(x) = m \frac{P(x+a)}{2I} y \tag{1.82}$$

(Selvaraj et al. 2020) have suggested a design technique for CFRP strengthened steel beams with low modulus CFRP. The calculation procedure they have developed include several steps which can be expressed using Figure 2.65.

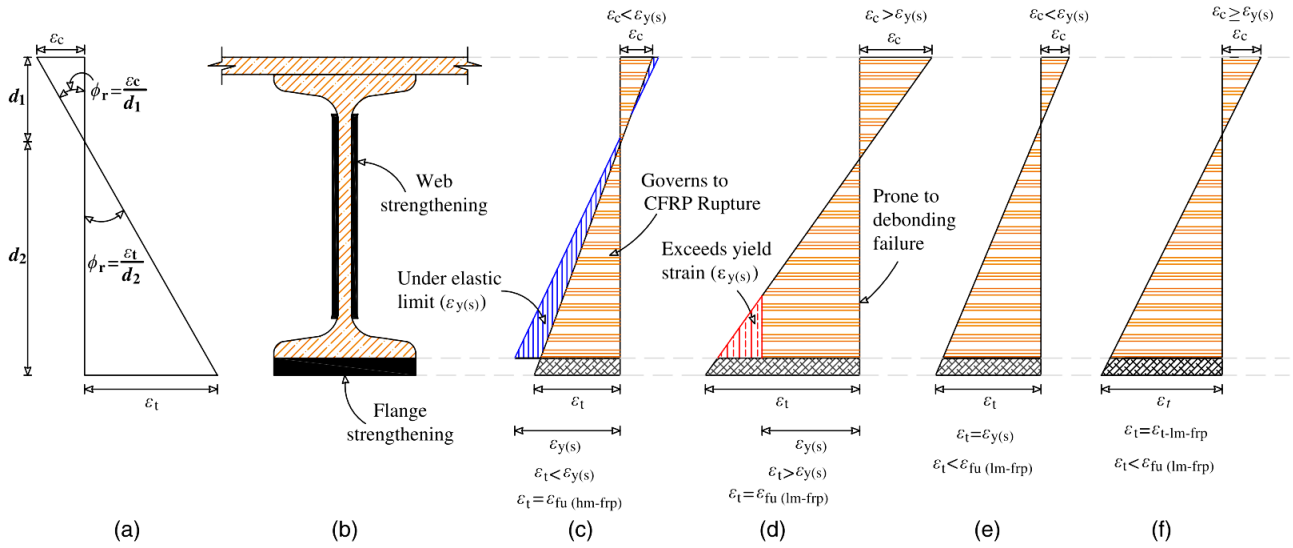

Figure 2.65. (a) strain profile due to bending; (b) steel beam strengthened with CFRP; (c) ultimate limit strain variation with HM CFRP; (d) ultimate limit strain variation with LM CFRP; (e) elastic limit strain variation with LM CFRP; and (f) transition limit strain variation with LM CFRP

The calculation procedure for determining the design moment follows the steps outlined below:

Step 1: Identify the initial strain at the extreme fibers of either the top compression flange (ε_c) or the bottom tension flange (ε_t) of the composite section (as shown in Figure 1.66(a)).

Step 2: Calculate the curvature (ϕ_r) of the cross-section by assuming a length to the neutral axis (NA) from either the top (d_1) or the bottom (d_2) of the composite cross-section, using Equation (1.83).

Step 3: Perform a back-calculation of strains at each portion of the composite section, considering the presumed depth to the neutral axis.

Step 4: Calculate the stresses in each portion using the strain values determined in step 3. For the steel portion, use Equation (1.84) with the yield stress as the maximum stress. For the CFRP portion, use Equations (1.85) or (1.86) with a modified Ramberg-Osgood function considering a bilinear stress-strain response.

Step 5: Determine the resultant force of the section using force equilibrium (Equation (1.87)). An iterative process is employed to determine the position of the neutral axis, ensuring that the resultant force becomes zero.

Step 6: Determine the moment capacity by summing the multiplication of each resultant force (R) by its respective distance from the neutral axis (X) (Equation (1.88)). The moment-curvature response can be obtained by increasing the assumed strain values from Step 1 to a desired level.

By following these steps, the design moment of the composite section can be calculated, taking into account the contributions of both the steel and CFRP components.

$$\emptyset_r = \frac{\epsilon_c}{d_1} \; or \; \frac{\epsilon_t}{d_2} \tag{1.83}$$

$$F_s(x) = E_s \epsilon_{s(x)} \left[A + \frac{1 - A}{\left[1 + \left(B \epsilon_{s(x)} \right)^C \right]^{1/C}} \right] \tag{1.84}$$

$$F_{CFRP}(x) = E_{I-CFRP} \varepsilon_{CFRP(x)} \text{ when } \varepsilon_{CFRP} < \varepsilon_t \tag{1.85}$$

$$F_{CFRP}(x) = E_{II-CFRP} \varepsilon_{CFRP(x)} \text{ when } \varepsilon_{CFRP} > \varepsilon_t \tag{1.86}$$

$$R = \int_a^b F(x)\, b(x) dx \tag{1.87}$$

$$M = \sum R\bar{\bar{X}} \tag{1.88}$$

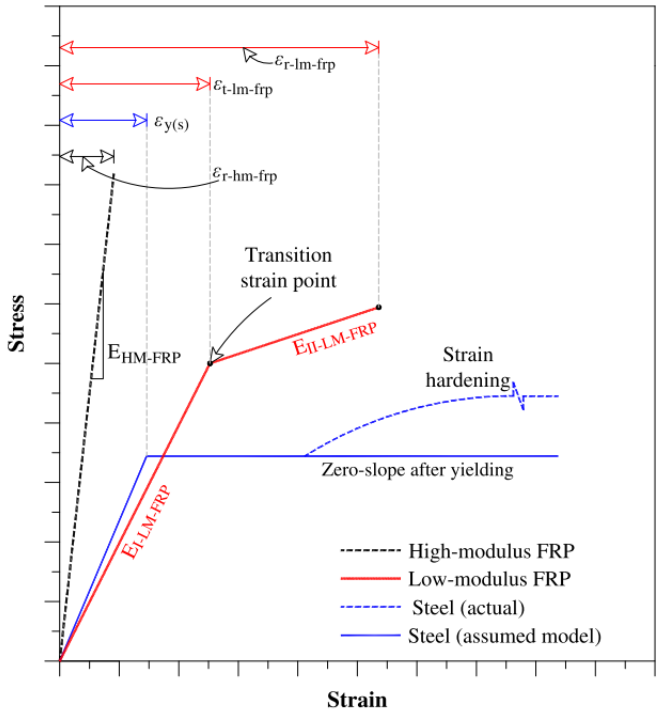

Figure 2.66. Typical stress–strain curves of steel and FRP materials and their strain limits.

where ϕ_r = curvature of cross section; ε_c and ε_t = strains in compression and tension flanges, respectively [Figure 1.66(a)]; d_1 and d_2 = length from neutral axis to compression and tension flanges respectively; E_s = Elastic modulus of steel; ε_s = strain in steel beam section [Figure 1.66(a)]; $F_s(x)$ = stress in steel beam section; and A, B,and C =Ramberg–Osgood parameters, that may be evaluated from the stress and strain relationship of the steel beam specimens according to steel material model (Figure 2.66) in which elastic–perfectly plastic region preents (no sloping line after yielding), and A is the stiffness after the yielding occure, and B is the ratio between elastic stiffness (E,) to yield strength (f). Since, the material model assumed to have null slope region after yielding, the parameter A is equal to 0, and hence parameter C may not show a major role. Es-CFRP and E-CFRP are the initial elastic modulus and the elastic modulus after the transition strain. ECFRP and & are the strain and

transition strain of the CFRP. (Figure. 2.66); b(x) is the width of the section; Mis the moment of resistance.

(D Schnerch et al. 2007) et al. proposed a design method for high modulus CFRP (HM CFRP) to enhance the bending capacity of typical steel-concrete composite bridge beams. The developed bond model is capable of calculating the shear stress and peel stress within the adhesive layer. To exclude the premature debonding failure of the strengthening steel beams, by introducing a criterion, which specify the ultimate principle, stress attainable in the adhesive layer, which cannot be surpassed for a given specific strength of an adhesive. The proposed design method in this study based on three conditions to be satisfied which are shown in Figure 2.67.

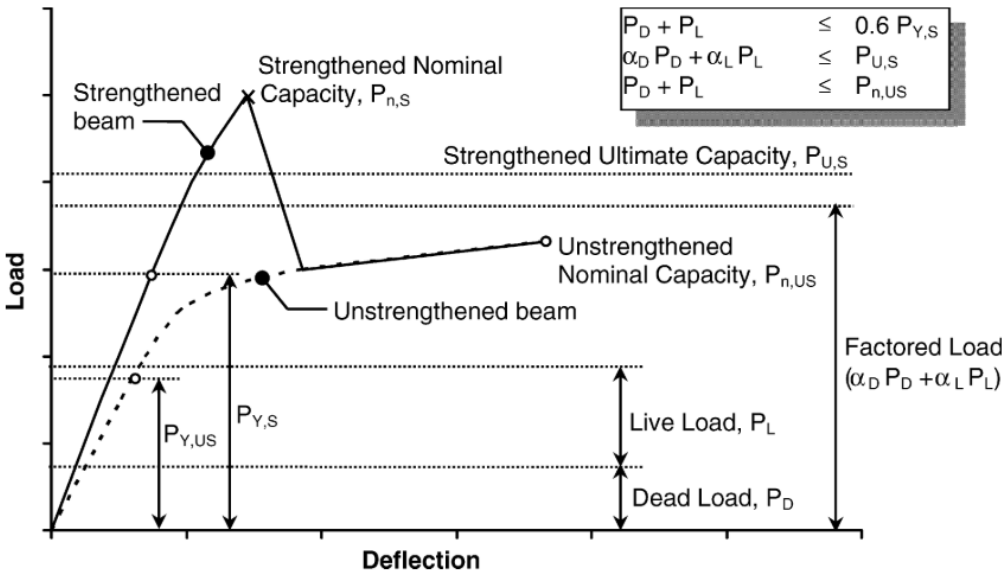

Figure 2.67. Design criteria proposed for steel beams strengthened with high modulus CFRP (Source: D Schnerch et al. 2007) .

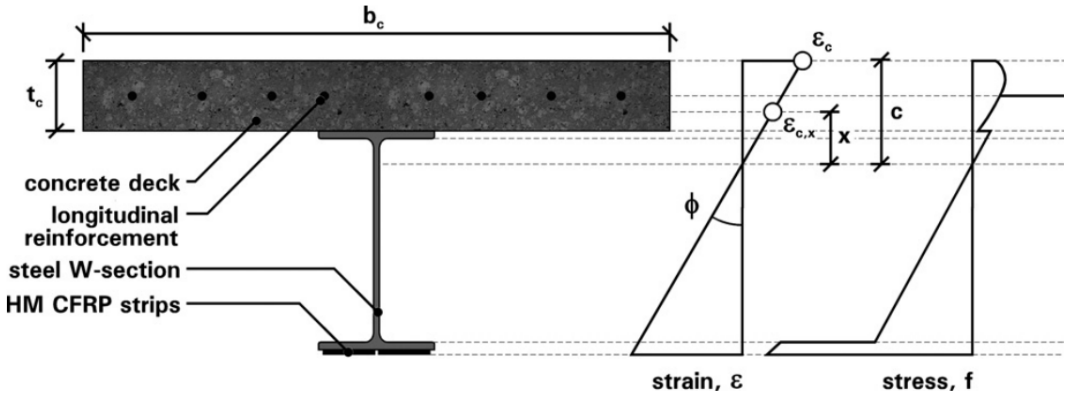

Figure 2.68. Strain and stress variations for steel to concrete composite beam section reinforced with HM CFRP layers

As per the proposed design criteria it should make sure that the reinforced beam behaves elastically under the influence of the improved live load, and the total load at the serviceability limit of the reinforced beam, which include the dead load, PD, and the additional live load, PL, should not greater 60% of the intended bigger yield capacity of the CFRP reinforced beams. It should be highlighted that the increase in the load at the yield of the beam is due to the existence of the HM CFRP is heavily rely on the magnitude of the dead load acting on the un-strengthened beam before applying of the CFRP strengthening system. To fulfil the maximum required strength, the total factorized load calculated based on the suitable dead load and live load factors, u_p and a_z, respectively, should not go beyond the maximum load capacity of the reinforced beam, Pus after the factorized by a suitable strength reduction factor. Also, to guarantee that the structure behaves safe in case of possible loss of the strengthening system, the total load, including the dead load and the increased live load should not exceed the residual capacity of the unstrengthened beam, P_{us}.

The design procedure suggested by (D Schnerch et al. 2007) was developed rely on the moment curvature examination using a non-linear constitutive model for concrete. The cross section considered for the elaboration of design procedure is shown in

Figure 2.68. The moment-curvature behaviour of the beam section is evaluated based on concrete strain, &, at the compression flange (extreme fibre) along with an imagined neutral axis depth, c

The resultant force on the section can be found using integration of the variation in stress profile of different portions of the cross section. As an example, for a concrete deck, the strain, stress and force can be calculated as:

$$\epsilon_{c,x} = \emptyset x \qquad (1.89)$$

$$f_c = \frac{f_c' n\left(\varepsilon_{c,x}/\varepsilon_c'\right)}{n - 1 + \left(\varepsilon_{c,x}/\epsilon_c'\right)^{nk}} \qquad (1.90)$$

$$F_c = b_c \int_{c-t_c}^{c} f_c(x)\, dx \qquad (1.91)$$

where: $\epsilon_{c,x}$ is the strain in the concrete deck (at a distance x from the neutral axis); $\emptyset$ the beam curvature; f_c is the stress component related to $\epsilon_{c,x}$; f_c' is the maximum concrete stress measured from cylinder tests; ε_c' is the concrete strain at the maximum stress; n is the curve fitting factor; k is the post-peak decay factor; F_c is the resultant force in the concrete deck; b_c is the concrete deck width ; c is the neutral axis depth; and t_c is the concrete deck thickness. ACI is suggested that the strength of the FRP strengthened system may be lower by an environmental degradation reduction factor (0.85 for CFRP), to count for some possible environmental deterioration of composite materials. Therefore, the design maximum strength of the CFRP,$f_{FRP,u}$, is given by:

$$f_{FRP,u} = 0.85\left(\bar{f}_{FRP,u} - 3\sigma\right) \qquad (1.92)$$

They also suggested a way to evaluate bond strength of the adhesive joint based on peeling stresses and shear stresses. The characteristic strength, σ_{c} , at the adhesive layer can be determined as;

$$\sigma_c = \frac{\sigma}{2}\sqrt{\left(\frac{\sigma}{2}\right)^2 + \tau^2} \qquad (1.93)$$

where σ is the ultimate stress at the peeling of the joint and τ is the equivalent peak shear stress.

The shear stress distribution for any FRP strengthened steel concrete composite beam with simply supported ends and loaded as per the four-point bending (Figure 2.69), shear stress variation is given by;

$$\tau(x) = \begin{cases} B_1\cosh(\lambda x) + B_2\sinh(\lambda x) + m_1 P & 0 \leqslant x \leqslant (b-a) \\ B_3\cosh(\lambda x) + B_4\sinh(\lambda x) & (b-a) \leqslant x \leqslant L_{\text{frp}}/2 \end{cases} \qquad (6)$$

where

$$\lambda^2 = \frac{G_a b_{\text{frp}}}{t_a}\left[\frac{(y_s + y_{\text{frp}})(y_s + y_{\text{frp}} + t_a)}{E_s I_s + E_{\text{frp}} I_{\text{frp}}} + \frac{1}{E_s A_s} + \frac{1}{E_{\text{frp}} A_{\text{frp}}}\right]$$

$$m_1 = \frac{G_a}{t_a \lambda^2}\left(\frac{y_s + y_{\text{frp}}}{E_s I_s + E_{\text{frp}} I_{\text{frp}}}\right)$$

$$B_1 = \frac{-G_a}{t_a \lambda}\left[(\alpha_{\text{frp}} - \alpha_s)\Delta T - \frac{y_s}{E_s I_s} Pa\right] - m_1 P e^{-k}$$

$$B_2 = \frac{G_a}{t_a \lambda}\left[(\alpha_{\text{frp}} - \alpha_s)\Delta T - \frac{y_s}{E_s I_s} Pa\right]$$

$$B_3 = \frac{-G_a}{t_a \lambda}\left[(\alpha_{\text{frp}} - \alpha_s)\Delta T - \frac{y_s}{E_s I_s} Pa\right] + m_1 P \sinh(k)$$

$$B_4 = \frac{G_a}{t_a \lambda}\left[(\alpha_{\text{frp}} - \alpha_s)\Delta T - \frac{y_s}{E_s I_s} Pa\right] - m_1 P \sinh(k)$$

$$k = \lambda(b-a)$$

$A_{s,FRP}$ denoted the beam cross sectional area; $E_{s,FRP}$ is denoted the elastic modulus of beam material; $I_{s,FRP}$ is denoted the moment of inertia of the section; $y_{s,FRP}$is the distance to the centroidal axis from the bottom extreme fibre of the steel section; $\alpha_{s,FRP}$is the thermal expansion coefficient of CFRP; b_{FRP} the FRP strip width; $G_a$is the adhesive's shear modulus; t_a the thickness of the adhesive; ΔT = temperature variation; x = measured distance to CFRP tip from the point, where stresses need be

calculated and the terms *a*, *b*, *L*, L_{FRP} and *P* are as shown in Figure 2.69.

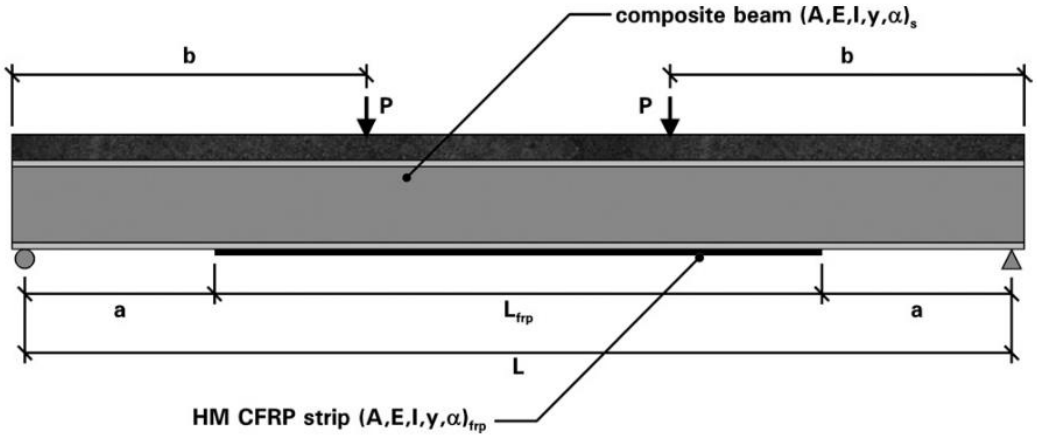

Figure 2.69. Beam formation for bond stress equations.

2.13.2 CFRP strengthened closed sections

Researchers have conducted numerous studies over the past few decades to investigate the structural behaviour of steel closed sections reinforced with CFRP (Carbon Fiber Reinforced Polymer). These studies have primarily focused on improving the axial load capacity, torsional capacity, and bending capacity of the reinforced sections. However, comparatively fewer studies have been carried out to evaluate the fatigue performance, resistance to impact loading, and environmental durability of steel tubular sections strengthened with CFRP.

Axial load capacity of CFRP strengthened tubular sections

In a study conducted by Sundarraja, Sriram, and Ganesh Prabhu (2014), an experimental and numerical investigation was performed on tubular columns subjected to axial loading and reinforced with CFRP strips. The researchers examined two different types of spacing between the CFRP strips. The results showed a significant increase in load-carrying capacity and a reduction in axial deformation due to the application of CFRP strips. The CFRP reinforcement also effectively delayed the occurrence of local buckling in the steel tubes, and the buckling mode changed

from outward buckling to inward buckling as the number of CFRP layers increased. No debonding failures were observed in the strengthened beams, indicating a strong bond between the steel substrate and the CFRP material. The numerical study results showed good agreement with the experimental findings. Similarly, Keykha et al. (2015) conducted a similar study on nine specimens, including both short and slender columns, wrapped with CFRP strips. They investigated the effect of different coverage percentages and layers of CFRP on the critical load of hollow steel columns. The study revealed several important findings, including the increase in critical load of the columns reinforced with CFRP, the influence of the coverage percentage of CFRP on the critical load, the effect of the number of CFRP layers on the maximum critical load, and the direct impact of the CFRP position on the maximum critical load. The study also found that for short columns, a coverage rate of 100% was most effective, while for slender columns, a percentage of CFRP coverage less than 100% yielded the best results.

In their study, Shaat and Fam (2006) investigated the performance of axially loaded short and long square hollow sectioned columns reinforced with CFRP patches. They conducted tests on twenty-seven short column specimens and five long column specimens. The influence of CFRP wrapping direction, whether longitudinal or transverse, was evaluated for short columns (as depicted in Figure 2.70). For long columns, CFRP sheets were only laid in the longitudinal direction. The results showed that the peak strength gains for short columns were 18% when two layers of CFRP were used for reinforcement. For long columns, a peak strength increase of 23% was achieved when three CFRP layers were attached in the longitudinal direction on all four sides of the column. All strengthened beams exhibited reduced lateral deflection compared to the un-strengthened beams.

Although there was no clear correlation found between the strength enhancement and the number of CFRP layers applied, the strength obtained for long columns was highly dependent on the imperfections present in the columns. The failure modes observed in the strengthened short columns included local buckling, delamination, and rupture of CFRP. In contrast, the major failure mode for CFRP-strengthened long columns was excessive global buckling, leading to crushing and delamination of CFRP patches due to local buckling in the compression side of the column.

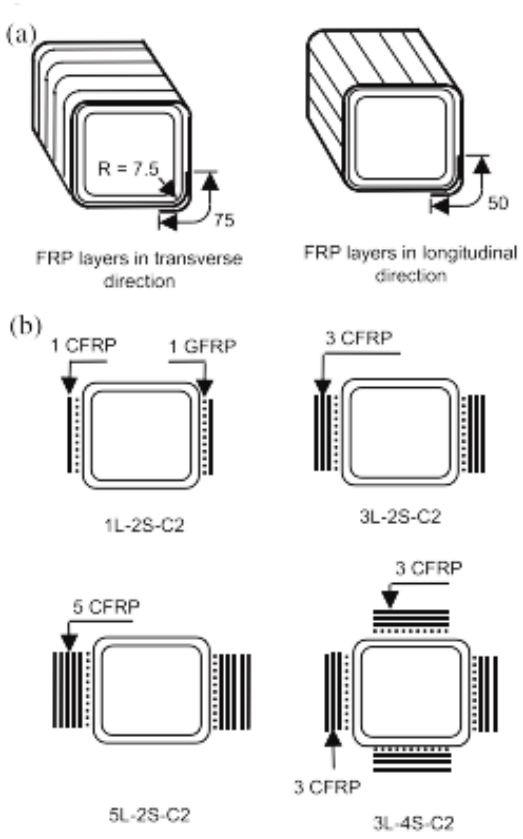

Figure 2.70. Details of FRP strengthening configurations: (a) short and (b) long columns.

In a study conducted by Gao, Balendra, and Koh (2013), the behavior of circular tube braces strengthened using CFRP was investigated. The experimental investigation involved testing seven long hot finished CHS braces with a diameter (D) of 88.9 mm and a thickness (t) of 4 mm. The braces were made from steel with a nominal yield

stress of 355 MPa and tensile strength of 490 MPa. The length of the braces was set at 2.4 m, and the slenderness ratio was kept at 80 to ensure that the principle failure mode would be buckling.

The test arrangement and instrumentation used in the study are described in detail in Figure 2.71. The major failure mechanism observed in the tested samples was excessive overall buckling under compression near the mid-height of the braces. This failure was attributed to delamination and crushing of the CFRP sheets. Depending on the number of CFRP layers applied, the ultimate critical load and stiffness of the braces ranged from 28% to 124% and 25% to 105%, respectively. It was also observed that imperfections such as out-of-straightness affected the strengthening effectiveness of the CFRP.

The results of a numerical study conducted in parallel with the experimental investigation showed good agreement with the experimental outcomes, indicating proper compatibility between the two.

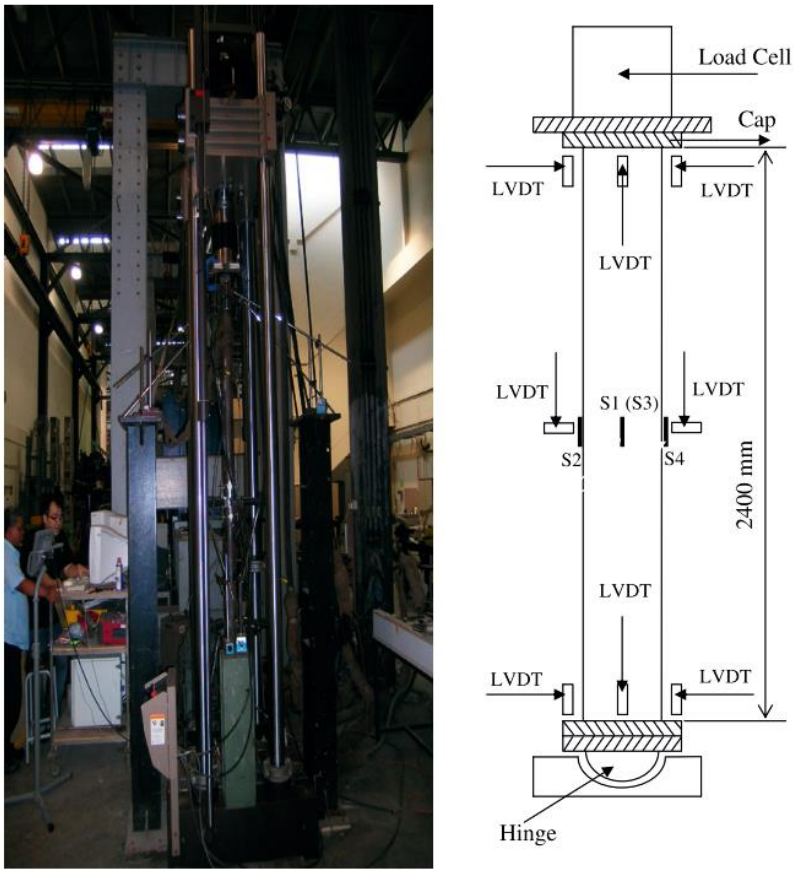

Figure 2.71. Experimental test setup and instrumentation (source: Gao, Balendra, and Koh 2013).

In a comprehensive study conducted by Jimmy Haedir and Zhao (2011), the behavior of CFRP reinforced steel columns was investigated. This study encompassed both experimental research and theoretical development of equations for designing CFRP strengthened steel tubular columns. The experimental results revealed that the application of a combination of longitudinal and hoop CFRP layers in slender steel tubes can effectively increase the yield strength of the unstrengthened tube. It was observed that the enhancement of the yield stress of circular hollow sections (CHS) reduces the slenderness capacity, resulting in a fully efficient section. Additionally, the study examined the effect of the percentage of fiber reinforcement and found that the respective strengths of CHS columns improved with a higher percentage of CFRP reinforcement.

The theoretical development of equations in this study aimed to provide a design approach for CFRP strengthened steel tubular columns, taking into account the experimental findings and the behavior of the reinforced columns. Overall, the study contributed valuable insights into the performance and design considerations of CFRP reinforced steel columns, highlighting the benefits of specific reinforcement strategies and the impact of reinforcement percentage on column strength.

In a study conducted by Teng and Hu (2007), the performance of FRP-wrapped circular hollow sections (CHS) and cylindrical shape shells under direct compression was investigated. The study incorporated both experimental tests and numerical modeling to assess the behavior of these structures. The results of both experimental and numerical studies indicated that the ductility of steel tubes can be significantly enhanced by providing a thin layer of CFRP wrapping. However, it was observed that further increasing the thickness of the jacket did not yield substantial benefits once the jacket thickness reached an optimal value. Beyond this point, the dominant failure mode shifted to inward buckling deformations. The study also revealed that FRP wrapping of CHS led to a noteworthy improvement in ductility. Although the maximum load capacity showed only a limited increase, the retrofitting with FRP jackets proved to be advantageous in seismic applications. The retrofitted tubes demonstrated the ability to resist significant loads, which is particularly important in scenarios where adjacent structural members may collapse. Overall, the study emphasized the effectiveness of CFRP wrapping in enhancing the ductility of steel tubes and its suitability for seismic retrofitting purposes. The findings highlighted the importance of optimizing the thickness of the jacket and recognized the significant role of FRP in improving the overall performance and resilience of CHS and cylindrical shape shells subjected to direct compression.

Some researchers (Huang, Chen, and Wang 2017; Karimian et al. 2017) have studied on the effect of CFRP retrofitting of deficient steel tubes based on both experimental and numerical studies. It was noted that with the outcomes of control samples, deficiency led to reduce bearing capacity of steel columns and the impact of horizontal deficiency was more critical than the vertical deficiency. It was observed that the application of CFRP yielded expected impact on enhancing bearing capacity, stress reductions at the damaged location, and avoiding local buckling around the deficiency (Karimian et al. 2017). The study of (Huang, Chen, and Wang 2017) was based on 22 specimens including both control samples and strengthened samples. The parameters studied included the amount of loss in wall thickness, extent of damage along tube height, and the damage angle around the circumference. This study also revealed that the ultimate load capacity enhancement and the more ductile compressive behavior could be obtained through CFRP retrofitting of CHS due to the lateral confinement against outward buckling.

Several studies (Che, Wang, and Shao 2012; Ren et al. 2017; Sundarraja and Prabhu 2012; Tao and Han 2007; Tao, Han, and Wang 2007; Tao, Han, and Zhuang 2007; Z. Bin Wang, Yu, and Tao 2015) found on literature on the compressive behavior of CFST strengthened with CFRP. Through this researches, it was found that load taking capacity in the axial direction of the columns, larger axial deformations at the ultimate load can be obtained with the CFRP confinement of steel columns. It was also highlighted that the deformation in the axial direction of the CFRP wrapped columns rises as the amount of CFRP layers increases, however, axial deformation enhancement not proportional. IT was also noted that the CFRP strips with smaller spacing delayed the buckling of CFST columns and enhance ultimate load capacity and also the enhancement in axial load carrying capacity which are depend on

properly designed CFRP strips spacing (Sundarraja and Prabhu 2012). (Tao, Han, and Zhuang 2007) noted that sectional shape of CFST column has a considerable effect on the confining effect of CFRP wrappings. They also highlighted that CFRP wrapping can improve the load taking capacity of the circular CFST columns efficiently. However, this enhancement is not noteworthy for rectangular CFST columns. They also noted that the axial load capacity rises with the increase of amount of CFRP layers for CFST columns with circular sections, but not evident for rectangular columns. Furthermore, they have noted that the ductility of CFRP strengthened specimens with circular sections decreases with the increased number of layers, but for retrofitted specimens with rectangular sectio is to the contrary. A study on the strengthening of fire-exposed CFST columns using CFRP was done by (Tao and Han 2007). Their study also confirmed the enhancement in load taking capacity and stiffness. It was also highlighted that the strength gain from CFRP strengthening reduced with the increasing of slenderness ratio or eccentricity. In their recommendation they have suggested that when repairing fire-exposed severely deteriorated CFST members, slender members/members subjected to large bending moments, strengthening with CFRP is not effective. The failure modes of this CFRP strengthened CFST columns included fibre rupture at the top side of the column, fibre delamination occurred due to outward buckling of CHS, rupture of the CFRP wrapping at the bottom of the specimen, rupture of the fibre at the mid height of the specimen and CHS local buckling. These failure modes observed were depended on the magnitude of the applied load on the specimens, number of CFRP layers and aspect ratio of steel tube (Sundarraja and Prabhu 2012).

(S. Fawzia et al. 2007) conducted a study to examine the performance of CFRP strengthened steel tubes under tensile loads. The parameters included in the study

were bond length and amount of CFRP layers. The strain variation over the thickness of CFRP layers and along the CFRP bond length was studied. It was found that there exists a lowering in strain along the CFRP bond length away from the joint. It was also noted that the strain is reducing from the bottom to top layer. The optimum CFRP bond length for CHS bonded with HM CFRP wrapping was noted as around 50 mm (this was about 75 mm for NM CFRP).

The study conducted by Z. Bin Wang, Yu, and Tao in 2015 focused on investigating the behavior of CFST (Concrete-Filled Steel Tube) members reinforced with externally bonded eccentrically applied tensile force. The researchers considered various parameters in their experimental study, including the number of CFRP layers and their orientations, the magnitude of load eccentricity, the count of CFRP layers, and the end anchorage system used for the CFRP sheets. The study highlighted that the most effective layer orientation for enhancing the strength of CFST members under combined bending and tension is in the longitudinal direction. This indicates that applying CFRP layers parallel to the axis of the CFST member provides the greatest strengthening effect. Furthermore, the study observed that specimens strengthened with CFRP layer orientations at ±45° angle to the axis exhibited the largest deformation capacity. This suggests that CFRP layers oriented at this angle provided the highest ductility and ability to withstand deformation. The researchers noted that within the elastic-plastic range of the specimen, a significant interaction was observed between the concrete and steel due to the ability of the concrete core to resist ovelling. This indicates that the presence of the concrete core contributed to the overall response and behavior of the CFST member. However, the study found that the effect of the CFRP wrap on the interaction between the CHS (Circular Hollow Section) and concrete was relatively moderate. This implies that while the CFRP

reinforcement had a positive impact on the overall performance of the CFST member, its influence on the interaction between the steel tube and concrete was not significantly pronounced. These findings provide valuable insights into the behavior and performance of CFST members reinforced with externally bonded CFRP under eccentric tensile loading. They highlight the importance of CFRP layer orientation and the role of the concrete core in enhancing the strength and deformation capacity of CFST members. Additionally, the study sheds light on the moderate effect of CFRP wraps on the interaction between the CHS and concrete in CFST members.

The researchers mentioned, including Sundarraja et al. (2013), Haedir and Zhao (2011), Viveka et al. (2014), Gao, Balendra, and Koh (2013), and Babu and Sundarraja (2017), have proposed various design methods and models for CFRP (Carbon Fiber Reinforced Polymer) reinforced steel CHS (Circular Hollow Section) under axial loads. These methods and models aim to predict the behavior and strength of CFRP-reinforced CHS structures. Many of these analytical methods are based on the equivalent section method, which simplifies the complex behavior of the CFRP-reinforced CHS structure into an equivalent section with uniform properties. This allows for simpler analysis and design calculations. Gao, Balendra, and Koh (2013) developed a numerical model capable of predicting the axial load carrying capacity, lateral and axial displacements of CFRP-strengthened tubular steel braces. This model takes into account initial shape, material, and geometric nonlinearities. The developed equations were validated using experimental results. Haedir and Zhao (2011) developed a set of design curves for steel-CFRP composite CHS short columns. These curves were developed based on the design guidelines provided in AS/NZS 4600, AS 4100, and Eurocode 3. The study investigated the effect of CFRP thickness and found that greater percentages of CFRP reinforcement enhance the strength of the tubes. The

design curves provided by Eurocode 3 were found to be lower than those provided by AS/NZS 4600 and AS 4100 for slender members. The study also highlighted that the strengthening effect of the reinforced columns increases with the percentage of reinforcement. Babu and Sundarraja (2017) developed an analytical model to predict the lateral confinement strength provided by CFRP patches when used to reinforce SSHS (Square and Rectangular Hollow Sections). The model considered factors such as the number of CFRP layers, the influence of buckling mode, and confinement effectiveness. Based on this model, the load capacity of wrapped HSS sections can be estimated.

Bending Capacity of CFRP strengthened tubular members

In the research conducted by Elchalakani (2014a, 2014b), J. Haedir et al. (2009), Kabir et al. (2016), and Mitsui et al. (2017) on the behavior and design of CFRP (Carbon Fiber Reinforced Polymer) strengthened steel tubes under bending, several findings were reported in the literature.

J. Haedir et al. (2009) conducted an experimental investigation on circular hollow section (CHS) beams strengthened with CFRP fabrics under pure bending. The study involved eighteen beam samples, including control beams and strengthened beams, categorized into three series based on their aspect ratios. The research highlighted the significant potential of CFRP in strengthening steel tubes under pure bending. The amount and orientation of CFRP sheets and the layout of the fiber significantly influenced the characteristics of the strengthened beams. The use of hoop fibers induced confining action in the steel face of the CHS, while longitudinally oriented fiber elements provided enhanced resistance to buckling. The researchers developed design strength curves for CFRP strengthened steel CHS beams to assist designers.

The proposed analytical approach suggested the use of the modular ratio concept to calculate an equivalent steel area instead of fibers and to consider the slenderness limits as per the guidelines provided in AS 4100.

The influence of CFRP layer orientation on the ultimate bending capacity of CFRP strengthened CHS was studied by Sabrina Fawzia et al. (2015). The study found that by using three CFRP layers in various configurations and orientations, the maximum service and ultimate load capacities could be increased by up to 43% and 33%, respectively. The best arrangements of three CFRP layers were identified as LHL and LLH (Longitudinal-L and Hoop-H) layer orientations. The stiffness of both retrofitted and control beams was similar for lower loads, but at higher loads, a significant increase in stiffness was observed for all strengthened beams. The failure mechanisms of the beams depended on the different layer orientations. Beams with LHL and LLH layer orientations exhibited local buckling of the CHS wall and crushing of CFRP layers in the compression area near the loading point. Beams with HHL layer orientation failed due to complete CFRP rupture and steel yielding at the tension face.

These studies contribute to the understanding of CFRP strengthening in steel tubes under bending, providing insights into the effects of CFRP layer orientation, fiber layout, and the potential for enhancing load capacity and stiffness. The developed design curves and analytical approaches aid designers in utilizing CFRP reinforcement effectively in CHS beams.

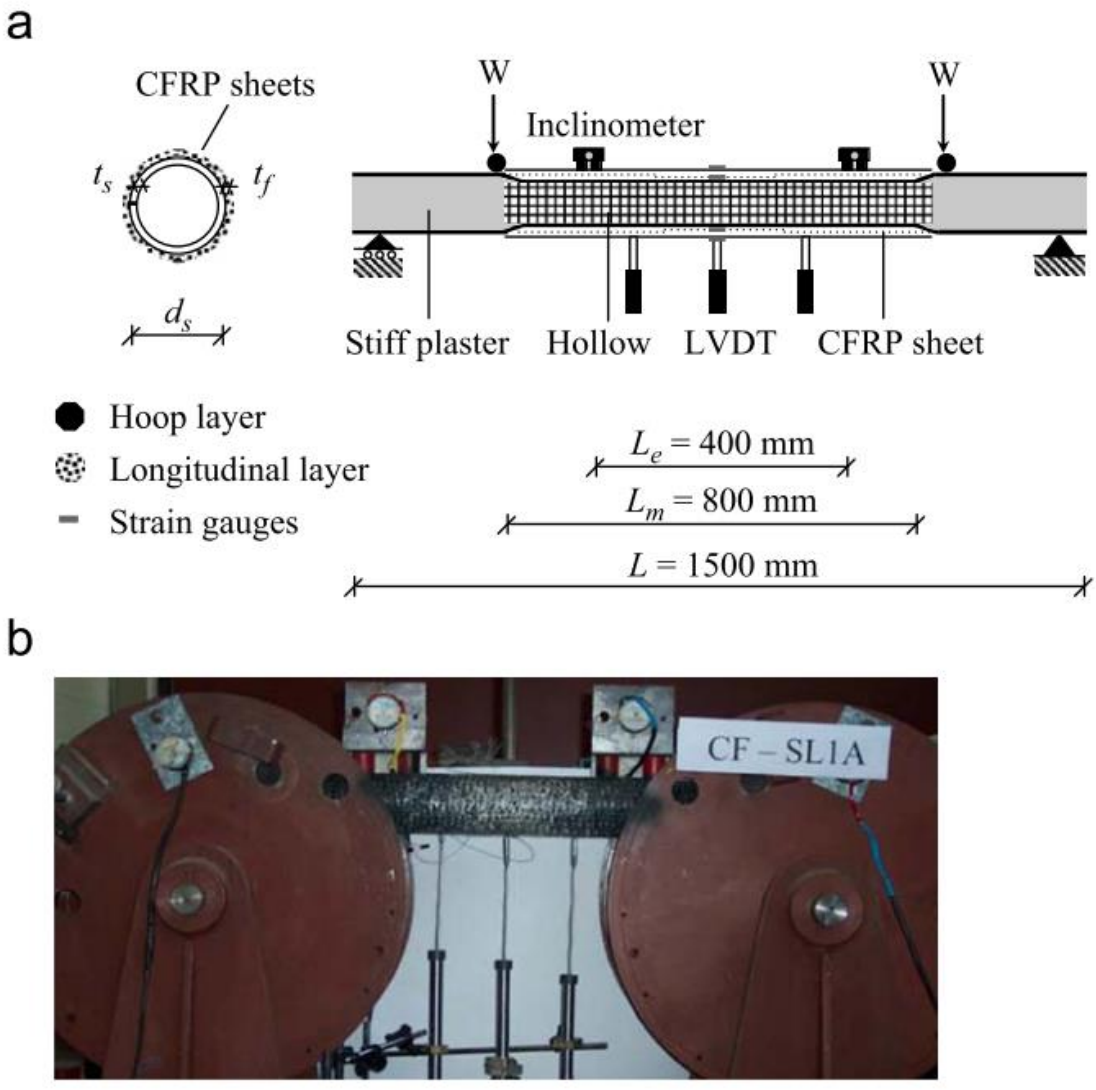

Figure 2.72. Test set-up and apparatus for bending test (Source: J. Haedir et al. 2009)

In the study conducted by Elchalakani (2014a), the focus was on reinforcing and rehabilitating steel box girders using CFRP sheets under combined bending and bearing. The study consisted of two test series: one involving un-degraded rectangular hollow sections strengthened with CFRP sheets, and the other involving artificially degraded samples reinforced with externally wrapped CFRP sheets or plates. All tests were conducted under three-point bending. In the first test series, it was found that the average strength gains were 47% and 83% when using a single wrap and two wraps of CFRP, respectively. It was also observed that retrofitting with two CFRP wrapping

layers was most suitable for slender sections, as premature weld fractures were observed in very thin bare steel sections. For the rehabilitated degraded beams, the average strength increase was found to be 19.9%. The study highlighted that greater strength gains could be achieved by using CFRP plates instead of CFRP sheets, and reinforcing with CFRP sheets in both the web and flange was more effective. The most effective repair mechanism was identified as applying CFRP to the web and enhancing its load carrying capacity by applying at least two layers of CFRP around the section. An equation for the plastic moment and web bearing of the composite hollow section was derived using an equivalent thickness approach. This equation, along with the revised web yielding equation in BS 5950, provided a good approximation for the bearing strength based on the composite properties. Overall, the study provided valuable insights into the reinforcement and rehabilitation of steel box girders using CFRP sheets. The findings demonstrated the effectiveness of CFRP strengthening in improving the strength of both un-degraded and degraded beams.

Flexural performance of CFRP strengthened concrete filled steel hollow sections was investigated by (Q.L. Wang et al. 2015). As per the results of the study, it was found that the application of transverse/ longitudinal CFRP provide transverse confinement and longitudinal reinforcement to concrete filled square hollow sections which increase the flexural load capacity and stiffness. The moment curvature curve for concrete filled CFRP strengthened square hollow sections may be divided in to three stages elastic stage, elasto-plastic stage and softening stage. It was also found that the impact of adhesive strength on the flexural load capacity of tested specimens is negligible and with the increase of the adhesive force, the interaction force between the outer tube and the core concrete reduces drastically.

Torsional strengthening of steel tubes using CFRP

The torsional performance of CFRP strengthened CHS (Circular Hollow Section) members has been the subject of several research studies, including those conducted by Abdollahi Chahkand et al. (2013), Amir Hamzeh Keykha (2018), Keykha (2017, 2018), and Wu et al. (2018). Abdollahi Chahkand et al. (2013) conducted an experimental and analytical study on CFRP retrofitted SSHS (Square and Rectangular Hollow Sections) under torsion. They tested six steel beams that were reinforced with different wrapping configurations, as illustrated in Figure 2.73. The study found that the ultimate torque of all reinforced steel tubes was greater than that of the control beam specimens, and the increase in torsional capacity depended on the percentage of CFRP reinforcement and the strengthening method. The specimens wrapped with spiral and reverse-spiral configurations exhibited higher ultimate torque compared to the specimens with vertical CFRP orientation. This can be attributed to the fact that the direction of the fibers aligns with the principal tensile stresses. The study concluded that the best CFRP orientation for resisting cyclic torque is a combination of spiral and reverse spiral layers. Additionally, the study highlighted that for reinforced samples with the same percentage of CFRP wrappings, the torsional resistance increases as the reinforcing method transitions from reverse spiral wrap to spiral wrap. An analytical model based on the equivalent thickness method was proposed in the study and showed promising results compared to the experimental findings. This analytical model provides a means to estimate the torsional behavior of CFRP strengthened CHS members. Overall, the research conducted by Abdollahi Chahkand et al. (2013) contributes to understanding the torsional performance of CFRP reinforced CHS members and provides insights into the effectiveness of different CFRP wrapping configurations in enhancing torsional capacity.

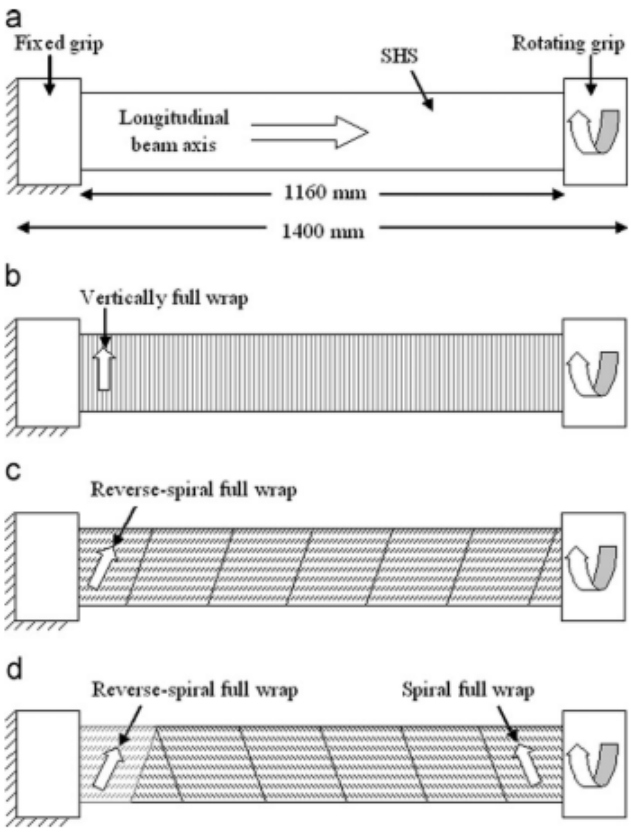

Figure 2.73. Types of CFRP strengthening configuration (Source: (Abdollahi Chahkand et al. 2013)

(Wu et al. 2018) conducted a study to investigate the performance of CFRP strengthened circular hollow sections under torsional loads. The studied parameters were included the diameter of the hollow section, wall thickness and the CFRP wrapping configuration such as spiral (S), reverse spiral (R) and different mix of S and R as given in Figure 2.74. The failure mechanisms of observed in strengthened specimens included CFRP crushing, CFRP rupture, and cracking of adhesive (no fiber failure). It was noted that the application of CFRP is more effective CHS with higher diameter and higher thickness. It was found that to obtain the maximum torsion capacity the spiral wrapping is most effective and to obtain the best reinforcing behaviour of the scheme for a mixed S/R CFRP strengthening method, it was suggested to use the S wrapping as inside layers.

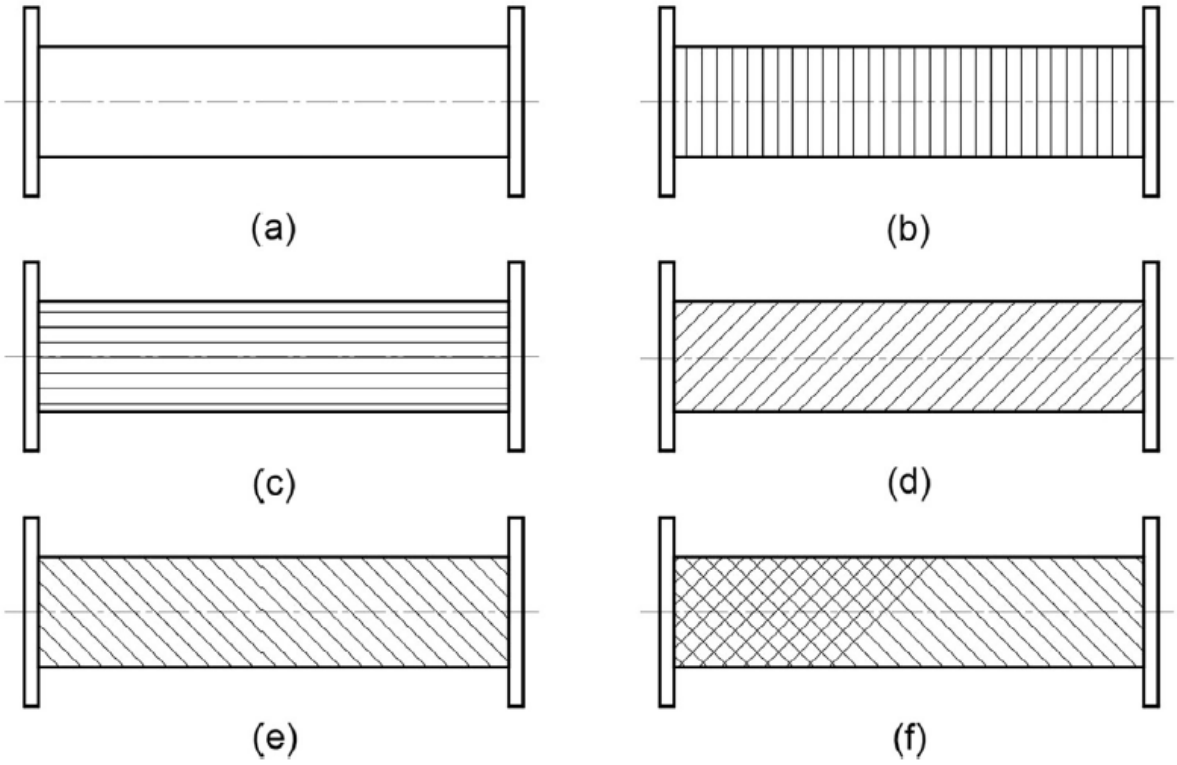

Figure 2.74. CFRP strengthening mechanisms (a) control without strengthening; (b) type 1 of VVVV; (c) type 2 of HHHH; (d) type 3 of SS or SSSS; (e) type 4 of RRRR and (f) type 5 of SRRR, SSRR, SSSR, RSSS, RRSS, RRRS.

Keykha (2018) conducted a study focusing on the performance of damaged steel beams retrofitted using CFRP under combined compression and torsion. The study found that the use of CFRP for reinforcing deteriorated hollow steel elements under combined compression and torsion could restore the lost capacity caused by the deficiencies. In a related study, Keykha (2017) performed a 3D finite element analysis on the torsional behavior of CFRP retrofitted deficient steel hollow beams. The results obtained from the finite element analysis were validated by comparing them with experimental results from a series of tests conducted on twelve samples, including both control and strengthened specimens. The deficiencies in the beams were categorized as vertical and horizontal deficiencies based on their direction. The study demonstrated that the use of CFRP sheets for strengthening deficient hollow steel

elements could restore the strength lost due to the deficiencies. Additionally, the failure mechanisms of the CFRP retrofitted steel tubes were identified. These studies by Keykha (2018) and Keykha (2017) contribute to the understanding of the behavior of damaged steel beams retrofitted with CFRP under combined compression and torsion. They highlight the effectiveness of CFRP strengthening in restoring the lost capacity and provide insights into the failure mechanisms associated with the retrofitting process.

Fatigue, cyclic, and dynamic performances of CFRP strengthened hollow sections

(Hu, Feng, and Zhao 2017) have proposed design guidelines of fatigue design of CFRP strengthened hollow CHS beams. The results of their study highlighted that CFRP is revealed to be efficient for strengthening steel tubular structures under fatigue. CFRP can enhance the fatigue life under a definite loading condition or rise the allowable stress variety when a certain fatigue life is expected. They have further elaborated the design concepts using a clear worked example. Performance of CFRP retrofitted cracked rectangular hollow sections under fatigue loads was investigated by (Chen et al. 2018). The aim of this study was to evaluate the influence of the magnitude of pre-stressing force in CFRP plates, repairing material modulus and initial depth of the crack on the fatigue performance of RHS beams. The experimental results revealed that a higher material modulus or a greater pre-stressing force could enhance the fatigue performance. Retrofitted beams with pre-stressed CFRP plates displayed a slight stiffness reduction, whereas retrofitted beams with non-prestressed CFRP plates showed noteworthy stiffness deprivation during the fatigue loading. Various failure mechanisms were witnessed for retrofitted specimens. For samples repaired by CFRP with an elastic modulus of 190 MPa, the flexural fracture was

observed at the middle cross section along with CFRP failure around the anchorage system. The beams retrofitted with CFRP having ultra-high modulus plates initiated fractured at the central location. It was suggested that the magnitude of pre- stressing force may be evaluated based on a stress analysis of a reduced cross section.

The performance of CFRP strengthened steel CHS under lateral impact was studied by few researchers (Alam et al. 2014; Alam et al. 2015; Alam et al. 2017; Kadhim et al. 2018a, 2018b). Finite element modelling of steel square hollow sections columns strengthened with CFRP under dynamic impact load was done by (Alam et al. 2014). The outcomes of the study revealed that the initial impact forces of strengthened tubular columns increase considerably. The behavior of CFRP strengthened tubular columns under lateral impact loading is substantial due to the significant reduction in axial and lateral deformations (by 58% and 72%) for column retrofitted with four sided CFRP. The CFRP wrapping configuration seemed have a great impact on performance enhancement of strengthened beams under lateral impact, because columns with four-sided CFRP have shown higher improvement compared to columns with two sided CFRP. (Alam et al. 2015) have conducted a similar kind of study on behavior of CFRP retrofitted tubular beams under lateral impact loading and effect of impact velocity of the impact load, impact mass, end conditions, magnitude of axial loading and Thickness of CFRP were studied. The results of the study show that CFRP wrapping significantly increases the impact resistance by reducing the lateral displacement of retrofitted columns up to 58%. Boundary condition of columns is a crucial factor in enhancement of impact strength and was deduced by comparing three types of columns with different boundary conditions. Columns with fixed end condition have shown comparatively higher strength gain compared to fixed-pinned and pinned-pinned conditions. Applied axial load on the column found

to have a huge impact on strength gain, since the lateral displacement increases with the increased axial force. Four sided CFRP configuration was observed to be the most efficient strengthening scheme, which yielded a 70% reduction in lateral displacement. A gradual decrease in axial and lateral displacements were observed with the rise of thickness of the CFRP.

(Kadhim et al. 2018a) studied the effect of the loading rate on the CFRP reinforced SSHS under lateral impact. The loading was applied using two methods; (a) quasi static (0.05 mm/s) and (b) impact (4.43 m/s) with the aid of testing arrangement shown in Figure 2.75. Effect of some parameters such as different CFRP layer arrangement with fibres layup in the longitudinal, transverse directions and mixture of both directions was investigated too. It was observed that the efficiency of CFRP strengthening was enhanced when loading rate is higher to diverse degrees depending on various CFRP configurations. It was also noted that the used of mixture of CFRP fibres (both transverse and longitudinal directions) showed the highest efficiency compared to other strengthening patterns. This is because of the its ability to enhance both shear and flexural resistance which is govern by the local and global buckling. The efficiency of the strengthening of SHS with enhanced with the higher loading rate. But, the noted enhancement in the retrofitting efficiency was relatively low since the conducted impact test was used a relatively lower impact velocity. This may because of the application of a comparatively greater ductile, strain rate dependent adhesive in the this experimental programme. The specimens tested under impact loading were with the local damage happened in the vicinity of the impact region that include local deflections of steel section, CFRP debonding and CFRP rupture. The tested beams showed a combination of failure modes under quasi static loading,

including local deformation, plastic hinge forming, and local failure at the loading point.

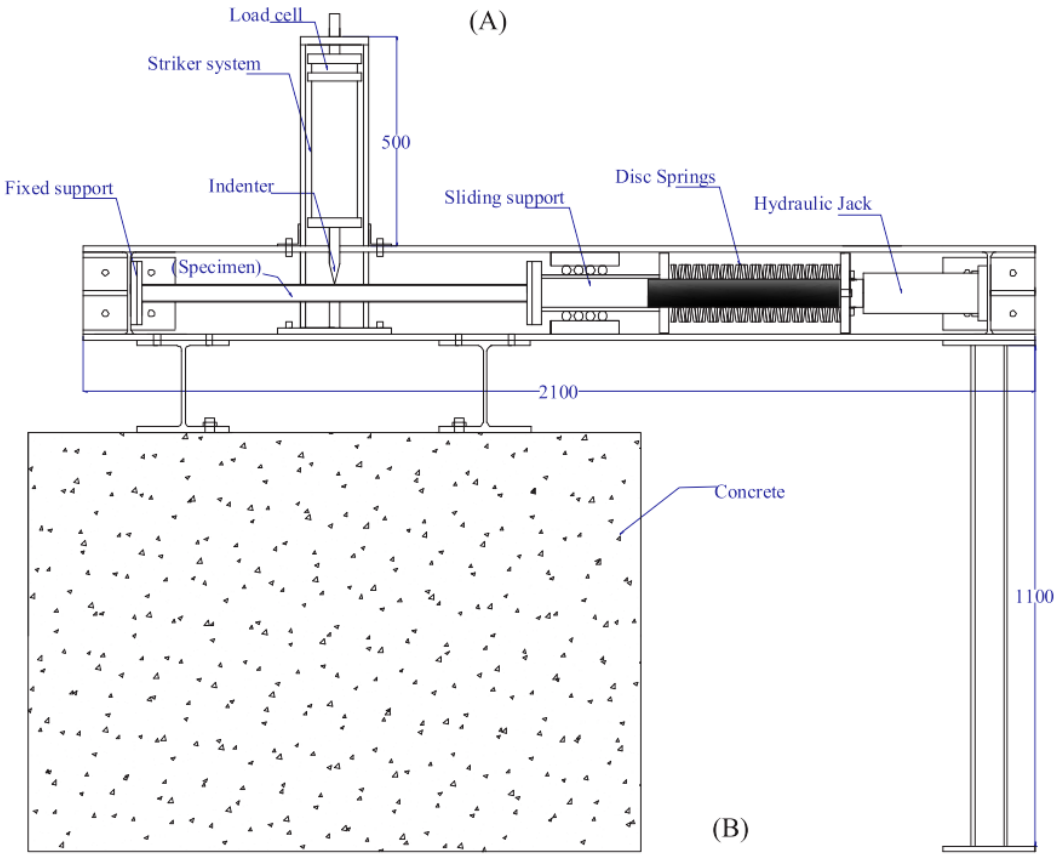

Figure 2.75. Schematic diagram of testing arrangement (source: Kadhim, Wu, and Cunningham 2018a)

An investigation on cyclic performance of bonded sleeve connection was conducted by (Zhujing Zhang et al. 2018). The examined parameters were included different end plate thickness and number of bolts. It was noted that an excellent ductility and energy dissipation capacity can be achieved through yielding of the end plate prior to the final connection failure. Results from the parametric study suggested that the model with

the thinnest end plate achieved the highest ductility, because the thinner steel endplate was associated with more comprehensive development of yielding.

Environmental durability of CFRP strengthened steel hollow sections

The literature review highlights the importance of considering environmental factors in assessing the potential durability of adhesively bonded FRP steel joints. Several researchers have investigated the effects of exposure on adhesively bonded steel-CFRP joints, with a focus on moisture as a primary environmental condition. Studies such as A. Brown (1974), Crasto and Kim (1996), M. Dawood (2008), Hand et al. (1991), Hashim (1999), Horton et al. (1992), De Nève and Shanahan (1992), Tavakkolizadeh and Saadatmanesh (2001), and West (2001) have examined various aspects of the behavior of adhesively bonded joints under extreme environmental conditions. Hand et al. (1991) investigated the effect of moisture ingress on the bond capacity of adhesively bonded joints using stress relaxation and fracture analysis methods. Their findings indicated that some adhesives can retain about half of their "dry" strengths at equilibrium moisture strain, while the study on fracture toughness showed a reduction in ductility with increased exposure duration. De Nève and Shanahan (1992) conducted a study on the aging effect of structural epoxy adhesive due to exposure to high temperature and humidity. They observed changes in the complex modulus with water uptake and a decrease in the glass transition temperature. Torsional shear tests on the adhesive properties suggested that water ingress occurs homogeneously through the joint geometry. Failure of the joint after aging was closely related to plasticization of the polymer by water and weakening of the steel substrate adhesive interfacial zone. Figure 2.77 depicts the failure mechanisms associated with water absorption in epoxy adhesive.

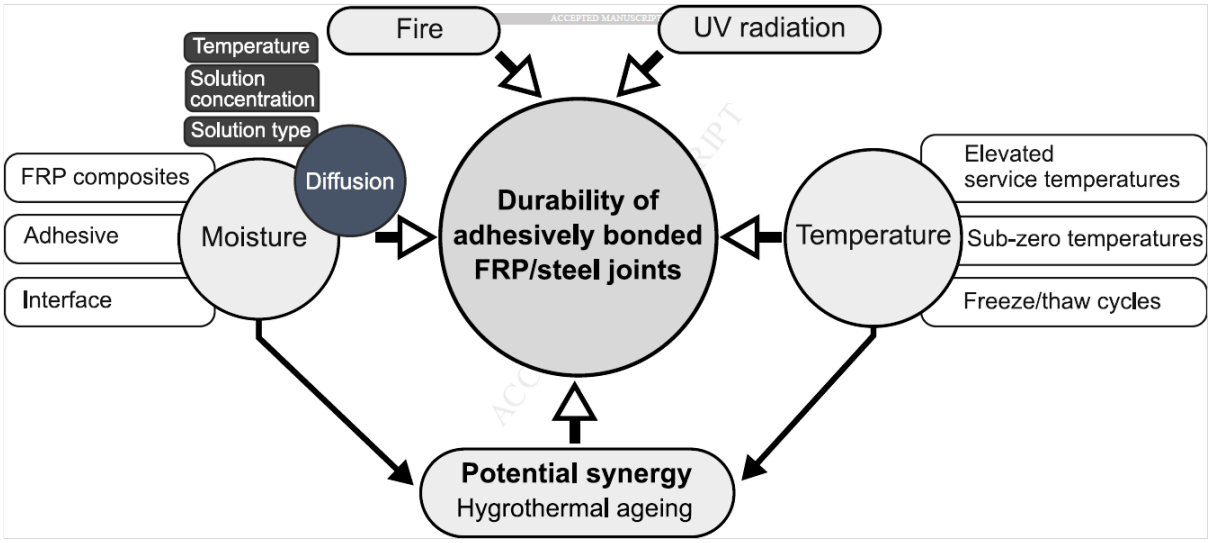

Figure 2.76. Factors influencing the environmental durability of adhesively bonded FRP/steel joints. (source: Heshmati, Haghani, and Al-emrani 2015).

The behavior of adhesively bonded steel/FRP joints in marine environments is indeed a crucial factor to consider. Researchers have conducted studies to assess the durability of such joints under marine conditions. Horton, Spinks, and Isles (1992) conducted a study comparing the bond durability of acrylic adhesives and epoxy resins in a marine environment. They found that acrylic adhesives exhibited higher bond durability compared to epoxy resins. Furthermore, they highlighted that the combination of stress and environmental exposure had a more detrimental effect on bond durability than environmental exposure alone. The combination of stress and exposure to dilute sodium solution was particularly unfavorable, likely due to adherend corrosion and interface instability. Tavakkolizadeh and Saadatmanesh (2001) investigated the possibility of galvanic corrosion between CFRP and steel adherends. Their findings indicated that direct contact between a CFRP laminate and steel substrate could lead to galvanic corrosion, and the severity of corrosion depended on the thickness of the epoxy coating. They suggested that applying a thin film of epoxy coating could significantly reduce galvanic corrosion. In a study conducted by Hashim (1999), loaded small lap shear joints were exposed to a severe wet

environment over the long term. The study found that this exposure caused a reduction in joint strength of approximately 10% per year. These studies underscore the importance of considering the marine environment when evaluating the behavior and durability of adhesively bonded steel/FRP joints. Factors such as the choice of adhesive, combination of stress and environmental exposure, and the potential for galvanic corrosion should be taken into account to ensure the long-term performance of such joints in marine applications.

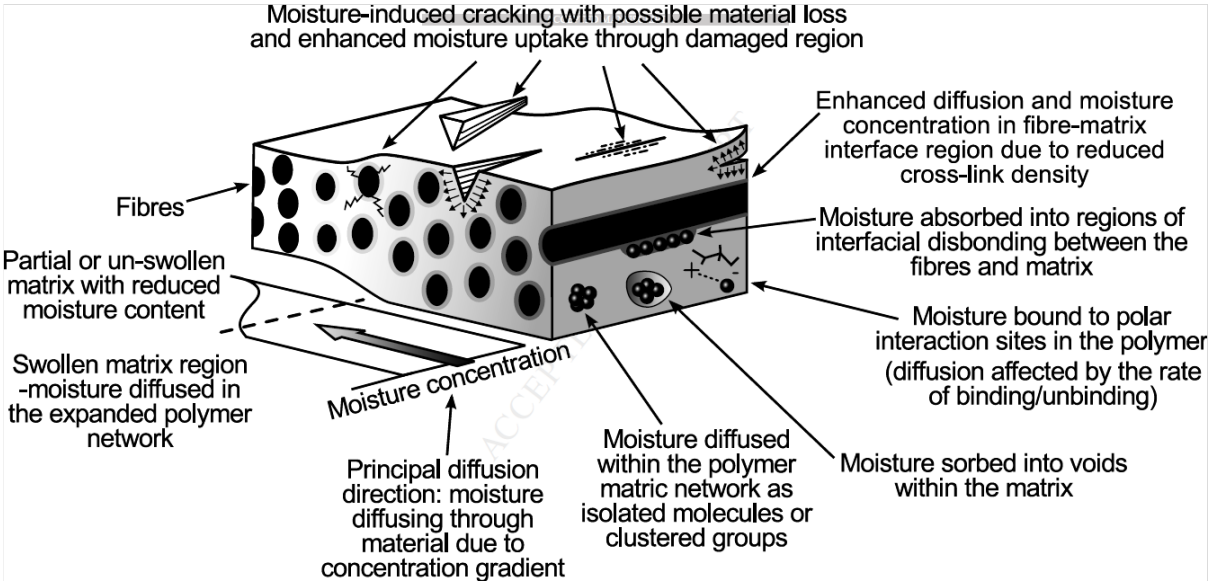

Figure 2.77. Locations and mechanisms of moisture sorption in fibre reinforced polymer composites (source: Heshmati et al. 2015).

The durability of CFRP reinforced steel tubular specimens has been the subject of study by various researchers. Kabir (2015), Kabir et al. (2016b, 2016a), Chan (2016), Kabir et al. (2014), and Seica and Packer (2007) have conducted investigations in this area. Seica and Packer (2007) specifically focused on the utilization of CFRP for retrofitting steel structures with tubular sections for underwater applications. Their study involved seven samples, including one control sample and six samples with

CFRP wrapping. The samples were tested under four-point bending, and the parameters studied included the type of fiber/epoxy and the curing condition of the matrix. The results of the experimental program showed that the maximum bending strength, rotation capacity, and flexural stiffness of the strengthened beams were enhanced compared to the control beam. However, it was observed that the steel tubes strengthened and cured underwater could not achieve the same flexural capability as those cured in air. Despite this, no significant debonding was observed in the tested samples. Thus, the feasibility of retrofitting steel tubular structures using CFRP was demonstrated.

The effect of the type of adhesive on the durability of CFRP strengthened hollow sections was investigated by Kabir et al. (2015). The study involved the use of two types of adhesives, and twelve samples including control beams and beams strengthened with each type of adhesive were tested under four-point bending until failure. The results indicated that all CFRP strengthened beams conditioned under cold weather exhibited lower strength compared to the control beams. This suggests that cold weather has an unfavorable effect on the ultimate strength of CFRP strengthened CHS. For design purposes, load reduction factors of 0.95 and 1.20 for service deflection were suggested, which are consistent with Australian and Italian guidelines. However, these factors are valid only for short-term exposures. The durability design factors are influenced by parameters such as the thickness and diameter of the CHS, while keeping other parameters constant. The study also found that CFRP with higher elastic modulus and higher adhesive thickness showed improved durability under flexure, resulting in increased ultimate load and stiffness. Similarly, increasing the number of CFRP layers enhanced durability by increasing stiffness and strength under flexure (M. H. Kabir, 2016). Furthermore, an exposure

period of 12 months was found to reduce the ultimate strength of strengthened beams by approximately 8% (M. H. Kabir et al., 2016). Additionally, the use of an epoxy-based adhesion promoter was shown to enhance the durability of CFRP strengthened circular hollow sections under cold weather conditions (Kabir et al., 2014).

The durability of CFRP strengthened Steel Circular Hollow Sections (SCHS) when exposed to sea water was investigated by M. H. Kabir et al. (2016a). To simulate the conditions, an accelerated corrosive environment was used. Control beams and strengthened beams subjected to the accelerated corrosive environment were tested under 3-point bending until failure. The major observation from the failure modes was the rupture of CFRP and yielding of steel due to local buckling near the loading point, which resulted from the accelerated corrosion effects on the beams at ambient and 50 °C temperatures. A significant drop in strength was noted for beams without or with embedded Glass Fiber Reinforced Polymer (GFRP) with a 10% mass reduction at both nominal and 50 °C temperatures. The inclusion of a layer of GFRP enhanced the durability of CFRP strengthened SCHS exposed to the marine environment. The study also revealed that the influence of elevated temperature compared to normal temperature was not significant. Durability factors were applied in calculating the maximum design load for CFRP reinforced CHS under saline environments, and the most conservative value was taken as 0.7. Numerical models were developed to simulate and conduct parametric studies. The durability design factors were dependent on parameters such as section thickness and diameter while keeping other parameters constant. It is important to note that a durability design factor defined for a particular section in a severe environment should not be applied to another section size unless it is conservative (M. H. Kabir et al., 2016b).

2.14 Finite Element Modelling (FEM)

The term Finite Element Method (FEM) was first introduced by Clough, and the earliest widely used FE program was developed by Wilson in the early 1960s, as mentioned by Ashcroft I.A. (2011). Since then, FEM has evolved from being an expert technique for stress analysis in aerospace engineering to a commonly used tool for advanced engineering analysis. Finite Element Analysis (FEA) has been developed and extensively utilized as a computer-based method capable of solving various boundary problems in engineering. It can address structural analysis, heat transfer mechanisms, material transport models, fluid flow mechanisms, dynamics analysis, free/forced vibrations, and electrical/magnetic fields. FEA has the advantage of being able to model damage and failure, which is only possible through non-linear analysis. Damage modeling is achieved by discretizing a domain and solving a set of equations to determine the response of the continuum. Continuum damage models can predict both damage and failure. However, despite the remarkable capabilities of FEM, it has yet to fully incorporate the environmental degradation of materials caused by factors such as moisture and temperature. The interaction between materials and their environment remains a challenging aspect for FEM. Several powerful and widely used general-purpose finite element software packages, such as ABAQUS, STRAND7, ANSYS, ATENA, and others, are available in the market. These software packages offer a wide range of capabilities and can handle various engineering problems effectively.

2.14.1 Finite element analysis of adhesively bonded FRP/steel structures

Finite Element Analysis (FEA) has been widely used in the study of adhesively bonded FRP/steel structures, and there are several research papers and reviews available in the literature on this topic. (He, 2011) conducted a review specifically on

FEA of adhesively bonded joints. The focus of this review was to explore the use of FEA in analyzing the behavior and performance of adhesively bonded joints in various applications. (Baldan, 2004b) conducted a review on joints bonded with adhesives in steel alloys, with a specific emphasis on surface pre-treatment for adhesively bonded joints. The review aimed to understand the effects of different surface treatments on the bond strength and performance of adhesive joints in steel structures. (Banea, M. D. and Silva, 2009) conducted a comprehensive review on adhesive bonded joints in composite materials. This review aimed to provide an overview of the current state of the art in adhesive bonding of composite materials, including the use of FEA in analyzing the performance of such joints. While there are numerous studies available on FEA of adhesively bonded FRP/steel structures, there is limited information specifically on FEM of FRP strengthened curved beams. However, there is a growing demand for finite element analysis to study the environmental degradation of adhesively bonded steel-FRP joints in steel structures. Recent works on the structural performance of such joints using FEM methods can provide valuable insights and help expand the research scope in other fields where similar structures are subjected to bending.

The study conducted by Teng and Hu (2007) focused on the finite element analysis of CFRP strengthened steel tubes and shells under axial loading, using the ABAQUS software package. The analysis considered both material nonlinearities and geometric effects. In the finite element models, the steel tubes were represented using S4R elements, which are 4-noded doubly curved general-purpose shell elements. These elements were chosen to account for the influence of transverse shear deformation. The mesh size used in the analysis was 5 mm × 10 mm, which was found to provide accurate results. The CFRP wrapping was modeled using beam elements oriented in

the hoop direction. The beam sections were modeled as rectangular cross-sections, with the width representing the normal thickness of the CFRP wrapping and the height representing the mid-height of the shell element. The element type used in ABAQUS for these conditions was B33, a two-noded cubic beam element with six degrees of freedom per node (three translations and three rotations). The CFRP material was assumed to have linear elasticity. For the overlapping zone between the CFRP wrapping and the steel tube, two alternative modeling approaches were considered. In the first approach, the additional thickness of the overlapping zone (150 mm) was directly included in the finite element model. In the second approach, the additional thickness of the overlapping zone was smeared around the tube. The results obtained from the finite element models showed good agreement with experimental results, indicating the accuracy and validity of the modeling approach used in the study.

The study conducted by Karimian et al. (2017) focused on the effective finite element modeling of CFRP strengthened deficient short steel columns using ABAQUS 6.13 software. In their analysis, the steel columns, CFRP patches, and adhesive layer were modeled using 3-dimensional twenty node hexahedral elements. To observe the failure modes and post-buckling behavior, risk analysis was adopted. Risk analysis is a technique used to predict unstable geometrically nonlinear failures of structures, taking into account nonlinear boundary conditions and materials. A mesh size of 5mm was used in the analysis, and the selected elements were 3-dimensional twenty node elements with reduced integration. The tie constraint method was employed to ensure the connection between the tube-adhesive and adhesive-CFRP, generating surface-to-surface interactions. The CFRP patch was modeled with isotropic and linear properties, while the steel was modeled using nonlinear properties. This allowed for capturing the nonlinear behavior of the steel material. Before conducting the

parametric study, the results obtained from the finite element analysis were validated using experimental results. The simulations were capable of predicting the failure modes of both strengthened and non-strengthened columns, providing confidence in the accuracy and reliability of the modeling approach.

The study conducted by Sundarraja et al. (2014) involved a three-dimensional finite element analysis of CFRP strengthened square hollow sections using ANSYS 12.0 software. The analysis aimed to investigate the failure modes and load-deformation behavior of the strengthened sections, and the results were validated using experimental data. In their analysis, an 8-node solid element (SOLID45) was used to model both the steel tube and the CFRP patch. The SOLID45 element is defined by eight nodes, with three degrees of freedom for each node (translation in the x, y, and z directions). This element type is suitable for capturing the behavior of solid structures. A comprehensive bond was assumed between the CFRP and steel sheets, ensuring effective interaction between the two materials. This modeling approach aimed to accurately represent the bonding and load transfer mechanism between the CFRP patch and the steel tube. The numerical model was compared with the deformed shapes obtained from the corresponding experimental results for tubular columns. By validating the results with experimental data, the accuracy and reliability of the finite element model were assessed, providing confidence in its ability to predict the behavior of CFRP strengthened square hollow sections.

The study conducted by Devi and Amanat (2015) focused on the performance of steel columns with square hollow sections (SHSS) reinforced with CFRP. In their analysis, both the steel tubes and CFRP were modeled using general shell elements, allowing for the consideration of geometric and material nonlinearities. To validate the

numerical models, the results obtained were compared with data available in the literature. This validation step ensured the accuracy and reliability of the finite element models before proceeding with a parametric study. The parametric study aimed to investigate the influence of various factors on the strength enhancement of non-compact SHSS columns. These factors included the number of CFRP layers, the geometry of the cross section, and the slenderness ratio of the columns. The results of the parametric study indicated that CFRP reinforcement can significantly improve the axial load carrying capacity of the SHSS columns. The axial strength of the column samples was found to be enhanced up to twice that of the non-strengthened specimens, regardless of the slenderness ratio and the number of CFRP layers. It was observed that the axial load carrying capacity of the SHSS columns increased with an increasing number of CFRP layers. This enhancement can be attributed to the reduction in slenderness values and the increase in effective thickness, which leads to an increase in the buckling strength of the square hollow sections. Additionally, the study noted that CFRP retrofitting tends to be more effective for beams with higher slenderness ratios. For smaller sections with lower slenderness ratios, the retrofitting technique can still provide efficient strengthening.

The study conducted by Keykha et al. (2015) focused on the finite element analysis (FEA) of CFRP-reinforced steel short and slender square columns using the ANSYS software. The numerical results obtained from the FEA were validated against experimental data, ensuring the accuracy and reliability of the models. In the FEA models, SOLID elements were utilized to develop 3D models of the columns. For cases with irregular mesh, SOLID187 elements were employed to capture the geometry and behavior of the structures effectively. Through a parametric study, the researchers examined the influence of various factors on the enhanced axial load

capacity of the CFRP-reinforced columns. The factors investigated included the coverage percentage of CFRP, the number of CFRP layers used, and the position of CFRP within the column. The results of the parametric study indicated that these factors directly affect the axial load capacity enhancement of the columns. By varying the coverage percentage, number of CFRP layers, and position of CFRP, the researchers were able to determine the most appropriate values for enhancing the axial load capacity of both slender and short columns.

The study conducted by Kabir et al. (2016) aimed to examine the performance of circular hollow sections (CHS) strengthened with CFRP beams under bending. Both experimental and numerical investigations were carried out to gain insights into the behavior of the strengthened CHS beams. Finite element models (FEMs) were developed using ABAQUS 6.12-2 software, ensuring that the models accurately represented the configurations of the experimentally tested beams. The numerical models were validated by comparing the results with those obtained from the experimental study. Parametric studies were then conducted using the validated models to assess the effects of various parameters on the behavior of the strengthened CHS beams. These parameters included the CFRP bond length, aspect ratio of the section, modulus of elasticity of CFRP, thickness of the adhesive layer, and types of adhesive. In the FEMs, the steel tube was modeled using eight-node 3D solid elements (C3D8H), while the adhesive layers between the CFRP layers were modeled using 3D cohesive elements (COHD8) with eight nodes. The CFRP and GFRP patches were modeled using 8-node quadrilateral in-plane general-purpose continuum shell elements with reduced integration and hourglass control (SCSR). These elements were capable of predicting CFRP failure and allowed for a full 3D model. They were also more efficient in calculations compared to standard brick elements as they could

capture through-the-thickness shear stress without requiring one element per layer. Mesh densities were selected to ensure accurate results, with 10 mm elements used for the steel tubes, 4 mm elements for the adhesive layer, and 10 mm elements for the GFRP and CFRP patches. Tie constraints were employed to establish proper connections between the steel adherent and adhesive surface, as well as between the adhesive surface and CFRP surface. The steel and CFRP surfaces were considered as master surfaces, while the adhesive surface was treated as a slave surface. By comparing the results of the experimental and numerical studies, the researchers made several observations regarding the behavior of the CFRP-strengthened CHS beams under bending.

- Two failure mechanisms were detected for reinforced beams which are depend on layer orientation; (a) near loading point tube local buckling, and (b) Total rupture of CFRP layers and steel yielding at tension face
- The beams strengthened with three CFRP layers including two layers in hoop direction and one longitudinal direction layer (HHL) indicated more ductility compared with the beams with two longitudinal layers and a hoop layer (LLH).
- Ultimate load capacity at service limit and failure stages were observed were 53.0% and 37.0% respectively and the influence of the orientation of layers on ultimate load was not considerable.
- It was noted that 200 mm length CFRP layer is reasonable when considered the cost and strength.
- CFRP having higher elastic modulus and higher adhesive thickness, behave superior under bending by enhancing ultimate load and stiffness. Further, the use of adhesives with higher elastic modulus and higher stiffness parameter

(K) behaved improved manner when consider the maximum load and stiffness.

(M I Alam and Fawzia 2017) have successfully developed finite element models to evaluate the beahaviour of steel circular hollow sections strengthened with CFRP under lateral impact loads. The results of FEMs were confirmed using results of the experimental study. It was observed that the finite element results could simulate the debonding failure at the impact location of the specimen with reasonable accuracy. (Alam et al. 2014) have performed a study on the impact load performance of CFRP reinforced steel square columns. This study was mainly attentive on the FEM and analysis of CFRP reinforced steel tubular column under crosswise impact loading on its structural presentation. The numerical model was developed using four part instances; CHS steel tube, the transverse spring and the drop mass, and longitudinal spring. Various element types were used to model these parts including, conventional shell elements (S4R) and CHS and the drop mass was modelled using 8-node solid element (C3D8R) respectively. Both of these element types can adopt reduced integration as well as hourglass control in numerical modelling problems. In FEMs the steel tube, solid end plate and CFRP composite layers modelled with S4R. The tie constraints is adopted to ensure proper connection between the steel surface and composite layer of reinforced columns. No adhesive layer was modelled since each lamina is arranged by wet lay up of dry fabric with resin. The steel material model adopted the bilinear stress strain relationship and “Hashin” damage criterion was adopted for damage modelling of steel and CFRP material. The FEMs were validated successfully by matching the results obtained through the experimental study. The impact forces carrying capacity of strengthened columns remarkably enhanced.

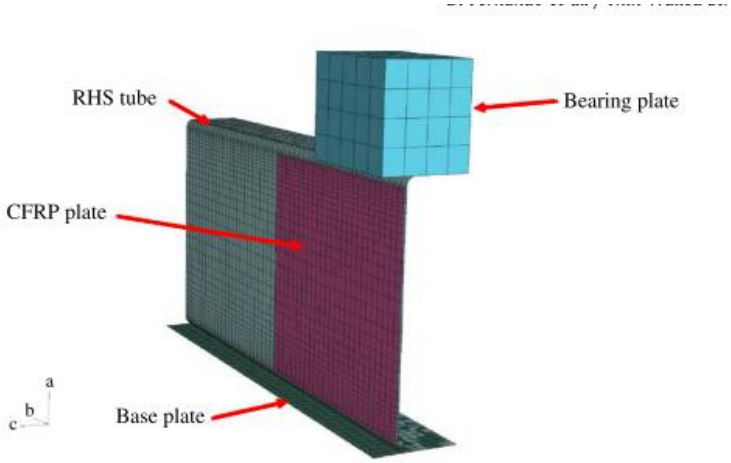

Figure 2.78. Finite element model (source: D Fernando et al. 2009)

(Colombi and Poggi 2006) have used commercially available ABAQUS software package to model and evaluated the stresses in the reinforced beam and in the adhesives. The element types used for beams were standard two nodes beam elements for beams while using standard eight nodes plane stress elements for the adhesive layers and the reinforcement strips. Multi-point constraints were enforced between the beam nodes and the corresponding adhesive nodes. They provide a link between the beam and adhesive nodes to constraint the displacements in such a way to ensure the compatibility of the strip and beam deformations. The finite element mesh was refined in correspondence of the reinforcement ends in order to capture the relevant stress concentration (Figure 2.79). A bilinear elasto-plastic constitutive model was used for the steel beams while a linear elastic stress–strain relationship was adopted for both the CFRP strips and the adhesive layers.

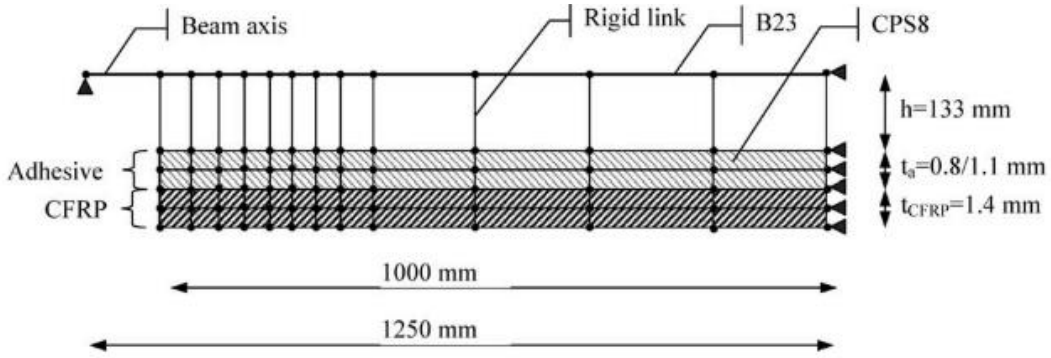

Figure 2.79. Modeling of the bonded reinforcement and necessary constraints to the steel beam (Source: Colombi and Poggi 2006)

(D Fernando et al. 2009) have developed finite element models to investigate the behavior of square hollow sections when loaded with end bearing loads. General purpose shell element (S4R) with reduced integration was used to model the steel tube. Base plate was modelled using fixed rigid body (Figure 2.78). The "Surface to Surface contact" option provided in ABAQUS was employed for the interaction between the base plate and the steel tube. The ''small sliding'' option was adopted so that the nodes on the slave surface (defined as the bottom corner region of the tube in the present study) interacted appropriately with the same local area of the master surface (defined as the top surface of the base plate), even when the surfaces underwent large rotations. The ''hard contact'' option was used for the normal direction while a friction coefficient of 0.45 was adopted to define the interaction in the tangential directions. The bearing plate (Figure 1.79) was modelled using the 8-node continuum shell element. The interaction between the bearing plate and the steel tube was modelled in the same manner as that for the base plate and the steel tube. The bottom surface of the bearing plate was defined as the master surface and the top corner region of the steel tube was defined as the slave surface. In the FE model, loading was applied at the top four corners of the bearing plate by prescribing vertical displacements. The CFRP plates were modelled as orthotropic material. These models developed were capable of predicting the observed failures in the experimental study; (1) adhesion failure; (2) cohesion failure; (3) combined adhesion and cohesion failure; (4) inter laminar failure of CFRP plates. The FE results also explained the effect of adhesive properties on the interfacial stresses developed between the CFRP plate and the steel tube, and hence the test results.

Bond failure of steel beams strengthened with FRP laminates were successfully modelled by (Yu, Chiew, and Lee 2011) using ABAQUS. To create the models isoparametric, three nodes and four nodes first order plain strain elements were employed. Large displacement formulation was used to realize the geometrically nonlinear behavior of the structure. A multistep procedure was adapted in analysisng in which the nodal displacements obtained in a given predecessor step will be applied as the external geometric boundary conditions when performing the corresponding successor step. Figure 2.80 shows the meshes of global model and sub model used in the analysis. Only a small zone around the end of the bond line was extracted from the global model and then meshed with highly refined elements. The mesh had the maximum density at the end of the bond line, where stress concentration was most serious. Compared to other existing bond failure models, there are some obvious advantages of the proposed model. The application of this bond failure model is no longer limited to the hypothesis of elastic material or geometry linearity. The influence of mesh density and local geometry detail on results predicted using this model is much less than that by using the maximum value based models. Further- more, unlike the misleading results predicted by using maximum value based models, the relationship between adhesive thickness and the bond strength of FRP strengthened beams can be predicted correctly.

The researchers Serror, Soliman, and Hassan (2017) conducted a finite element analysis (FEA) on the rotation capacity of CFRP reinforced cold-formed steel beams using the ANSYS software package. The beams were modeled as C-sections, and a web bolted moment resistant type of connection with a through plate was adopted at the connection details. Different element types were used for modeling the steel, CFRP, and adhesives. The steel was modeled using 4-node shell elements (SHELL181), the CFRP using 8-node solid elements (SOLID185), and the adhesives using 8-node solid elements (SOLID185). A mesh sensitivity analysis was performed, and a mesh density of 12.5 mm × 12.5 mm was used for all elements. For steel, a bi-

linear material model was adopted with variations in profile thickness, web height, and flange width. The CFRP model utilized an orthotropic stress-strain behavior, while the adhesive model employed an isotropic stress-strain behavior. The numerical parameters used in the study, including the element types, mesh size, and material models, were verified against numerical and experimental models found in the literature. Based on the results of the experimental and numerical studies, several conclusions were drawn. These included:

(a) CFRP strengthened beams can achieve a strength ranging from 0.2 Mp to 1.0 Mp. (b) Strengthening with CFRP can delay premature buckling. (c) Doubling the number of CFRP layers significantly increased the rotation capacity. (d) Strengthening the beam flanges in addition to the webs did not provide a significant increase in terms of strength, initial stiffness, and rotation capacity. (e) Enhancing the mechanical properties of the CFRP sheet/plate requires a relevant enhancement in the mechanical properties of the associated adhesive material for effective contribution.

These findings highlight the potential benefits and considerations for CFRP reinforcement in cold-formed steel beams and provide insights for structural design and optimization.

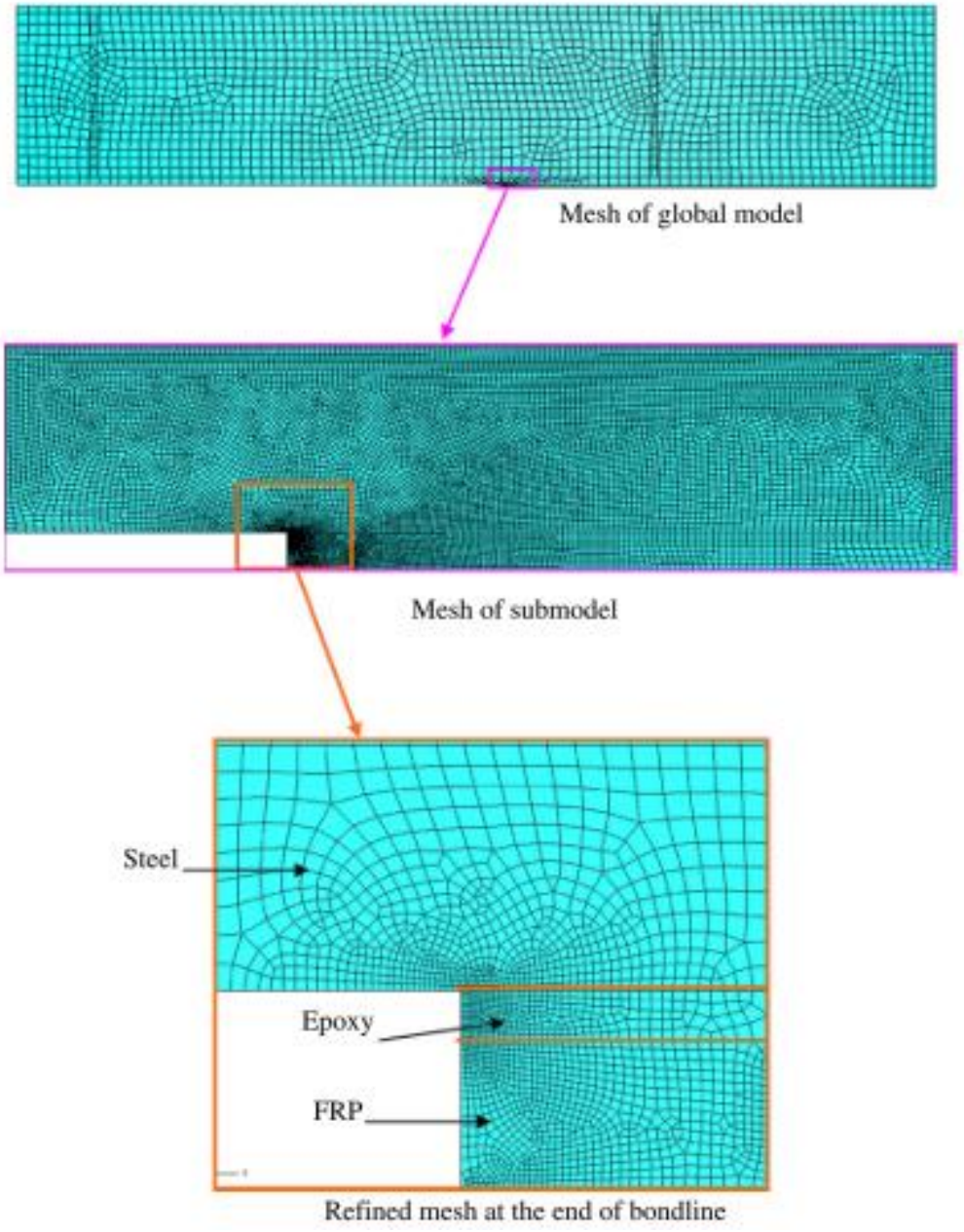

Figure 2.80. Meshes sizes of global model and sub-model of FRP reinforced steel beam (Source: Yu, Chiew, and Lee 2011).

In their study, M. Altaee, Cunningham, and Gillie (2019) conducted a numerical analysis on CFRP strengthened steel floor beams with openings in the web using ABAQUS finite element modeling software. The element types used for modeling the steel beams and CFRP were four-node shell elements (S4R), while the adhesive layer was modeled using an eight-node, three-dimensional cohesive element (COH3D8)

that incorporates traction-separation behavior. To account for potential debonding between the CFRP plate and the steel substrate, a bilinear traction-separation law was employed. This law allows for softening after damage initiation, with the softening behavior being linear. By using this approach, the researchers aimed to capture any debonding that may occur during the analysis. The results of the numerical analysis indicated that the CFRP strengthening method was able to restore the stiffness and strength of the beams with web openings to levels comparable to those of beams without openings. Importantly, debonding did not occur in any of the CFRP-strengthened cases. Typically, debonding can occur when the bond length between the CFRP plate and the substrate is insufficient for effective mobilization of the plate, or when high shear stresses concentrate at the plate ends. The absence of debonding observed in this study suggests that the adopted plate length and thickness were adequate for the examined configurations. This finding indicates the effectiveness of the CFRP strengthening method in mitigating debonding issues and highlights the importance of proper plate dimensions to ensure structural integrity and performance.

In their study, Li et al. (2018) investigated the influence of the mechanical properties of the adhesive and CFRP on the bond behavior of CFRP strengthened steel structures. They conducted an experimental study involving seventeen single-lap adhesively bonded joints between CFRP and steel, which were tested under tension. To analyze the bond behavior between CFRP and steel, a simplified method was adopted, where the nodes of the CFRP were coupled with the nodes of the steel near the interface. This coupling approach takes into account the strong nonlinearity and complex failure process of the bond. In their numerical analysis, Li et al. used cohesive elements, which are capable of representing the nonlinear traction-separation relationship across the interface and simulating the deterioration behavior of the bond. The cohesive zone

modeling (CZM) technique was employed using ABAQUS software. Two-dimensional elements were used to reduce the computational scale, with the adhesive layer modeled by a four-node cohesive element (COH2D4). The CFRP and steel plates were modeled using plane stress reduction integral elements (CPS4R), and the cohesive elements were coupled with the CFRP and steel elements near the interface by sharing nodes. The results of the numerical models showed good agreement with the experimental study, indicating the effectiveness of the cohesive zone modeling approach in capturing the bond behavior between CFRP and steel. This study contributes to the understanding of the influence of mechanical properties on the bond performance and provides insights for optimizing the design and selection of adhesive and CFRP materials in CFRP strengthened steel structures.

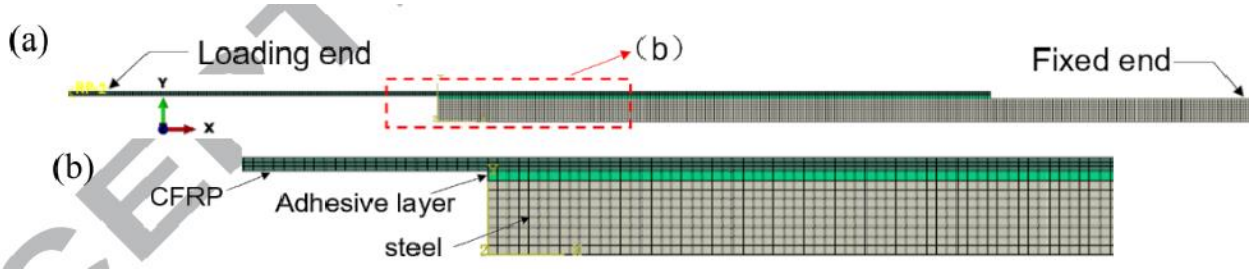

Figure 2.81. 2D – FEM for CFRP–steel single lap specimens (Source. Li et al. 2018)

FEM can utilize in predicting failure mechanisms of CFRP strengthened steel structures accurately. (Narmashiri, Sulong, and Zamin 2012) have conducted a failure analysis of CFRP strengthened steel I beams using ANSYS. The steel I-sections, steel stiffeners, CFRP plates, and adhesive were simulated by using the 3D solid triangle elements (ten-nodes 187). The interface of common surfaces was defined between the steel I-beam, adhesive, and CFRP plates. Debonding, delamination, and splitting occurred when the plastic strains exceeds the ultimate strain. Non-linear static analysis was carried out to achieve the failures. In this case, the load was applied incrementally until the plastic strain in an element reached to its ultimate strain (element is killed).

Linear and non-linear properties of materials were defined. The CFRP plate material properties were de- fined as linear and orthotropic because CFRP materials have linear properties and they were unidirectional. The steel beams and adhesive were defined as the materials having non-linear properties. For meshing, combination of the auto meshing and map meshing were used. The failure modes captured through the finite element models were done using stress concentrations. Four types of failure modes were identified in the CFRP strengthened I beams which were verified by both experimental and numerical analysis; (a) debonding below the point loads (BD), (b) debonding at the CFRP tips (ED), (c) delaminating at the CFRP tips (EDL), and (d) splitting below the point loads (BS).

In their study, Hamood et al. (2020) conducted a finite element analysis (FEA) on the behavior of CFRP strengthened steel channel sections using ANSYS 18.20 software. The steel channel section was simulated using SOLID185 elements, while the CFRP material was simulated using SOLSH190 elements. To model the interaction between the steel and CFRP, the nodes of the steel at the interface with CFRP were assigned the same nodes as the CFRP. This assumption implies that there is no slip between the contact surfaces, and the adhesive used is assumed to provide sufficient bonding to ensure full interaction and work as a unit. The FEM models developed by Hamood et al. showed reasonable agreement with the available test results, including the load-deflection response and mode of failure. The simulation results indicated a significant improvement in the buckling behavior of steel members reinforced with CFRP compared to the bare steel sections.

In their study, Teng, Fernando, and Yu (2015b) successfully used the cohesive zone model (CZM) in conjunction with ABAQUS to model CFRP strengthened steel beams. They employed the in-built CZM capability in ABAQUS to simulate the

behavior of the adhesive layer between the steel section and the CFRP plate. The general-purpose shell element S4R with reduced integration was used to model both the steel section and the CFRP plate. For meshing, the researchers conducted a mesh convergence study and selected element sizes of 2.5 mm × 2.5 mm for the steel beam and the CFRP plate, while the adhesive layer was meshed with 2.5 mm × 2.5 mm × 1 mm elements (with 1 mm being in the thickness direction). The CFRP plate was considered as an orthotropic material in the FE models, taking into account its different material properties in different directions. The coupled cohesive zone model was adopted to capture the constitutive behavior of the adhesive layer, allowing for the simulation of debonding between the CFRP plate and the steel section. The FEM results obtained using this modeling approach were found to be in good agreement with the experimental results. The failure modes observed in the experiments, including plate-end debonding of the CFRP plate and compression flange buckling of the steel section, were accurately captured by the FEM. Based on the FEM results, the study concluded that a higher elastic modulus or larger thickness of the CFRP plate leads to a lower ultimate load at which plate-end debonding occurs. It was also found that plate-end debonding is more likely to occur with shorter CFRP plates, while the failure mode may change to intermediate debonding or compression flange buckling when longer CFRP plates are used.

The interfacial shear and peeling stresses that appear in the bond line between the steel and CFRP laminate are studied in both the elastic and plastic phase of the steel beam using ABAQUS by (Linghoff, D., Al-Emrani 2010). The performance of CFRP reinforced beams were compared with the experimental results prior to perform the detailed FEM. The elements of the FEMs were developed using 20-node (C3D2OR) solid elements. These parts merged together by sharing common nodes at the contact

surface. Therefore, total interaction between various elements was guaranteed. With the results of the FEA, it was found that the value for ultimate interfacial shear stress at the tip of the CFRP layer is not affected by the yielding of the steel beam. It is only after excessive yielding and the formation of a plastic hinge that the theoretical interfacial shear stress expected by analytical solutions changes from that calculated through the FE model.

2.14.2 FEA of Curved Steel Beams Strengthened with CFRP

In the study conducted by Keykha (2019), the influence of CFRP reinforcement on the structural performance of vertically curved SHS (Square Hollow Section) steel beams under concentrated and uniformly distributed loads was investigated using finite element (FE) analysis. The behavior of vertically curved beams differs from straight beams when subjected to vertical loads, especially when axial forces are present. However, there are limited studies available in the literature on the strengthening of curved steel sections, both hollow and open, using CFRP. To evaluate the behavior of vertically curved beams, three-dimensional FE models and non-linear static analysis were employed. Non-linear FE models were developed to examine the structural performance of vertically curved steel beams with pinned ends, retrofitted using CFRP sheets. The CFRP reinforcement used in the models had a constant length of 400 mm, while the width of the CFRP varied (100, 300, and 400 mm). ANSYS version 14.5 software was used to create 3D FE models with different CFRP strengthening configurations. The models included the vertically curved beams, CFRP sheets, and adhesive layers. The boundary conditions, reinforced section, length and width of CFRP, and loading mechanisms were defined as shown in Figure 3. Both concentrated and uniformly distributed loads were applied to the beams, gradually increasing until the vertically curved beam reached its maximum

capacity, as illustrated in Figure 2.83. The FE models utilized 3D solid triangle elements (10-nodes, 187) to represent the vertically curved beams, CFRP sheets, and adhesive layers. The analysis was performed until the failure of the beam, considering both linear and non-linear material properties. CFRP sheets were considered as linear and orthotropic materials since CFRP materials have linear properties. The adhesive was also considered as a linear material since the used adhesive had linear properties as indicated by the manufacturer. The steel in vertically curved beam was defined with nonlinear properties. Mesh size of 25 mm was used for all three parts as adopted from literature. Results obtained from the FEM were validated with the experimental results.

According to the study by Keykha (2019), increasing the width of CFRP sheets from 100 mm to 400 mm led to an increase in the ultimate capacity of the vertically curved steel beams. The maximum ultimate capacity and increased percentage in the ultimate capacity were achieved when the CFRP width was 400 mm. In most of the specimens subjected to concentrated load P, the maximum Von Mises stress was observed near the mid-span on the vertical sides of the beams. This indicates that the CFRP strengthening on the vertical sides of the curved steel beams, specifically at mid-span, played a significant role in delaying the onset of local buckling. By reinforcing the vertical sides, the initiation of local buckling was postponed, resulting in an increase in the ultimate capacity of the beams. It can be inferred that the CFRP reinforcement on the vertical sides of the curved steel beams effectively contributed to enhancing their structural performance by delaying the occurrence of local buckling. This finding suggests that the CFRP strengthening technique can effectively improve the load-carrying capacity and overall structural behavior of vertically curved steel beams, especially under concentrated loads.

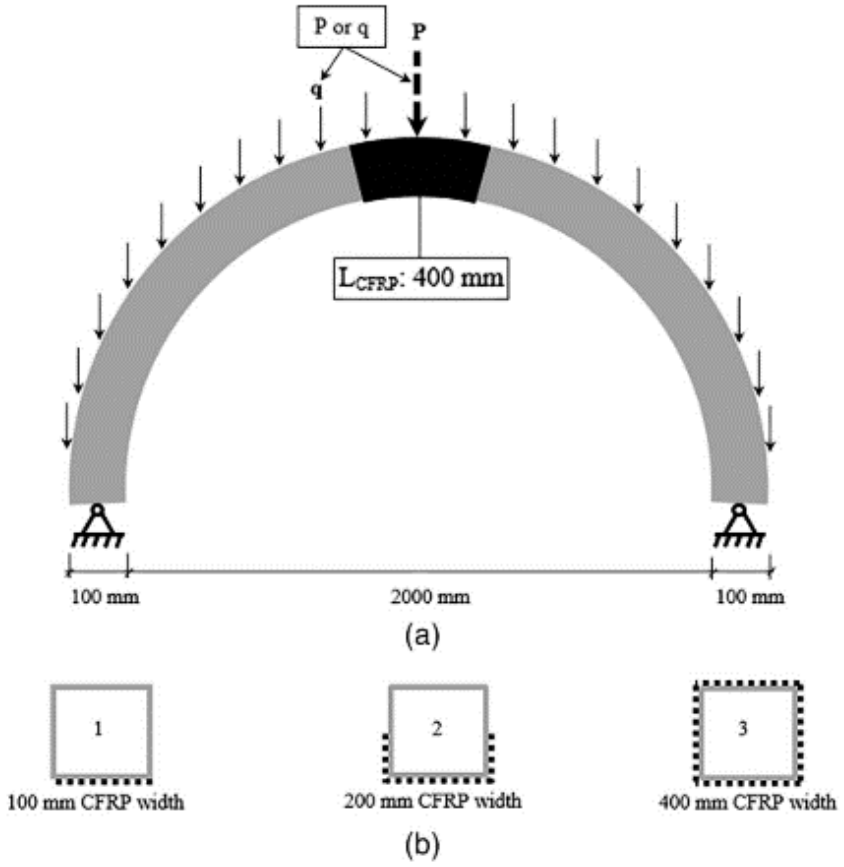

Figure 2.82. (a) Vertically curved steel beams reinforced using CFRP (not to scale); and (b) reinforced cross- section of vertically curved beam

In beams with uniformly distributed loads, maximum Von Mises stress was experience near the supports beams. Moreover, in these local buckling of beams local were experienced near the supports. It was observed that the increase in ultimate load capacity is more significant in beams with concentrated load compared to the beams with uniformly distributed load when strengthened with CFRP. This is because of the failure of beams with uniformly distributed loads occur in the region where no CFRP presents. With the findings of the study, it was final concluded that CFRP strengthening for vertically curved beams is a is a fast, low cost, and practical method with a significant increase in ultimate load capacity.

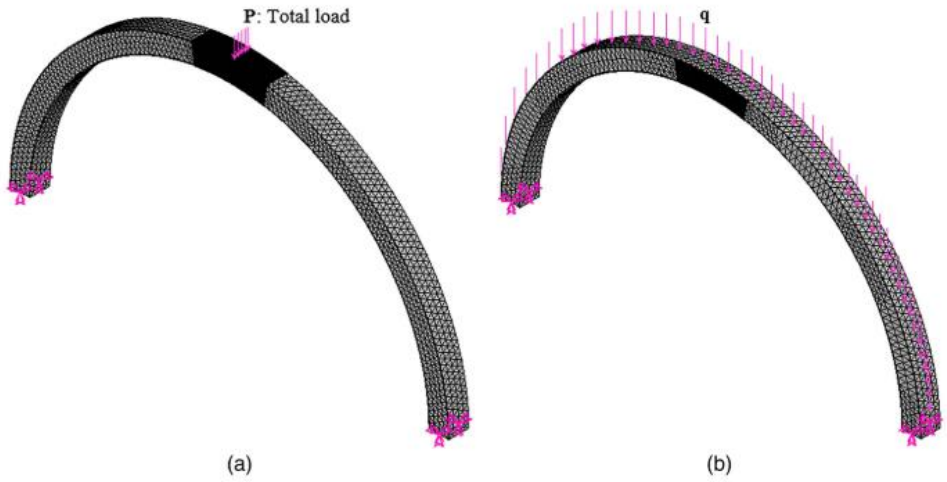

Figure 2.83. FE modeling of CFRP-strengthened specimens under (a) concentrated load; and (b) uniform distributed load

In the extended study by Keykha (2019), the focus was on investigating the effect of CFRP strengthening on the behavior of defective vertical curved beams with a square hollow section. The methodology involved 3D modeling and nonlinear static analysis using ANSYS software. CFRP sheets with a length of 400 mm and three different widths (100 mm, 300 mm, and 400 mm) were used for strengthening the beams. The defect in the beams had dimensions of 100 x 50 x 9 mm and was located at the mid-span. The 3D finite element model was developed in ANSYS, and a concentrated load was applied to the top surface of the beam at the mid-span. The load was incrementally increased until the beam reached its ultimate load capacity. The results obtained from the finite element analysis were then compared and validated with experimental results. The findings of the study showed that the use of CFRP sheets for strengthening defective curved beams led to a significant recovery in the strength lost due to the presence of a defect. The width of the CFRP sheets (100 mm, 300 mm, and 400 mm) had an influence on the ultimate load capacity of the specimens. In all the specimens,

whether non-strengthened or strengthened, the maximum von Mises stress was observed at the mid-span. Due to the hollow cross-section of the curved steel beams, a series of local buckling occurred around the concentrated load. This local buckling resulted in tensile stresses. However, the high tensile strength of CFRP played a beneficial role in increasing the ultimate load capacity of these beams significantly. Overall, the study demonstrated that the use of CFRP strengthening effectively recovered the strength of defective curved beams and increased their ultimate load capacity. The width of the CFRP sheets and their tensile strength played crucial roles in improving the structural behavior of the beams.

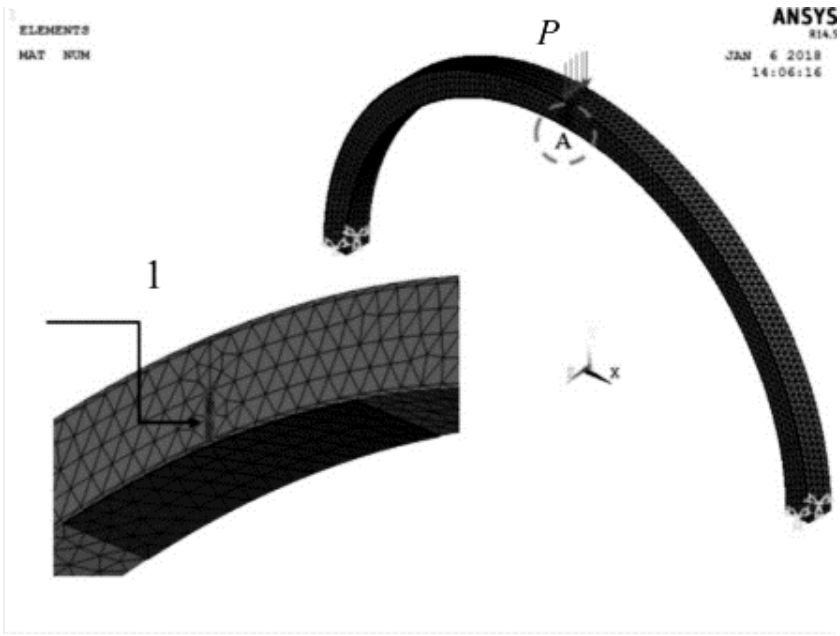

Figure 2.84. FE modeling of a defective curved steel beam retrofitted by CFRP

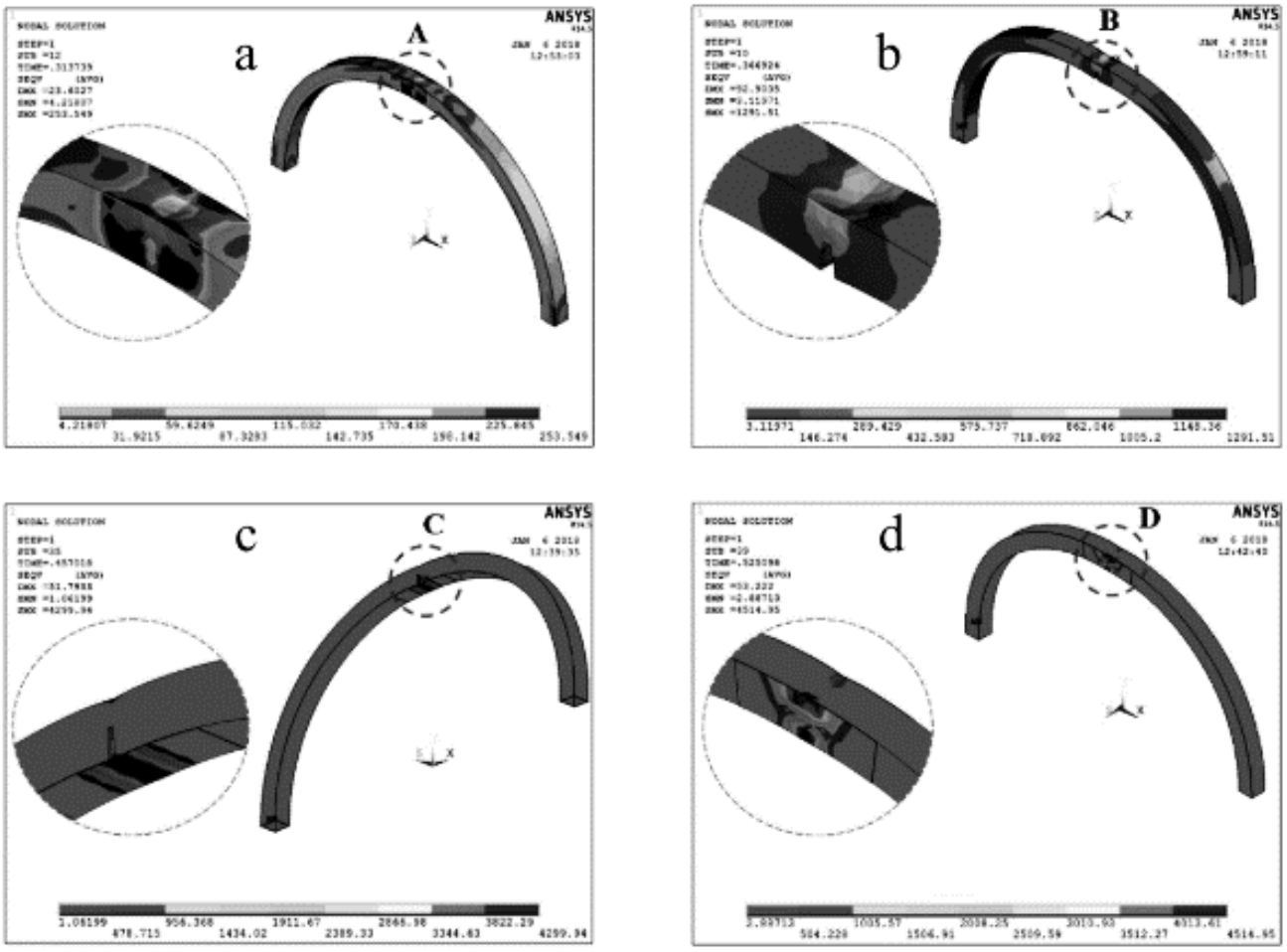

Figure 2.85. Comparison of the von Mises stress in specimens

2.15 Cohesive Zone Modelling (CZM)

To summarize, there are two broad approaches to the mechanics of fracture. The first approach considers an infinitely sharp crack tip and uses stress and strain fields to determine crack equilibrium and stability. The second approach introduces a traction-separation model, which replaces the sharp crack tip with a cohesive zone where stresses remain bounded. The cohesive zone is characterized by two cohesive surfaces held together by a cohesive traction, and material failure occurs when the cohesive surfaces completely separate. The cohesive zone model offers advantages such as intrinsic fracture energy dissipation, unlike classical continuum-based fracture

mechanics. Various cohesive zone concepts have been developed by different researchers. Barenblatt proposed a cohesive zone concept for brittle materials, aiming to describe the actual separation of materials and eliminate crack tip stress singularity. His theory is based on three basic hypotheses. Overall, the cohesive zone model provides a useful framework for studying fracture behavior and capturing the process of crack propagation, offering insights into the mechanics of fracture in different materials. There exists a cohesive zone near the crack tip where the upper and lower crack faces are held by the so-called cohesive traction, which has a magnitude on the order of up to the theoretical strength of the solid. The size of the cohesive zone is much smaller than the crack length. The size of the cohesive zone, and the distribution and magnitude of the cohesive traction at the onset of crack growth are independent of crack geometries and external loads. Stresses are finite everywhere including the crack tip, that is, no stress singularity exists at the crack tip.

As per the Figure 2.86, the size of the cohesive zone, d, is much smaller than the crack length, that is, $d/a \ll 1$. Then, the distribution of the cohesive traction is given by;

$\sigma = g(x), a - d \leq |x| \leq a$

Where σ is the cohesive traction.

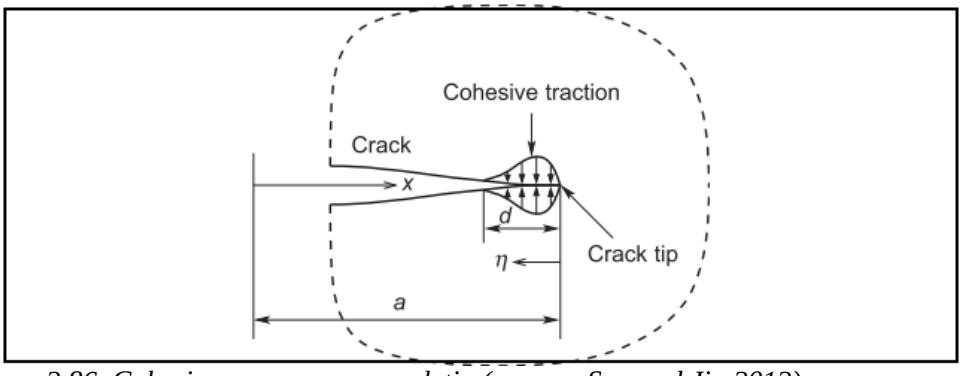

Figure 2.86. Cohesive zone near a crack tip (source: Sun and Jin 2012)

Moreover, there are some cohesive laws developed based on the cohesive zone perception in continuum mechanics. In cohesive zone approach there exists a cohesive A cohesive law describes the relationship between the cohesive traction and the separation displacement as follows:

$$\sigma = \sigma_c f(\delta/\delta_c)$$

Where σ_c is the peak cohesive traction, δ_c a characteristic separation and f a dimensionless function describing the "shape" of the cohesive traction-separation curve. The function f depends on the failure mechanism operative either at the microscopic or macroscopic level. Some of the commonly used cohesive laws as follows. Besides the cohesive parameters σ_c and δ_c, we often use the cohesive energy density Γc, or the work of separation per unit area of cohesive surface, defined by;

$$\Gamma_c = \int_0^{\delta_c} \sigma(\delta) d\delta$$

The cohesive energy density is just the area under the cohesive curve. Once the shape of the cohesive curve is given, only two of the parameters σ_c, v, and Γ_c are independent. Some of the commonly used cohesive laws as follows.

zone, ahead of the physical crack tip, which consists of cohesive surfaces (upper/lower surfaces) held by the cohesive traction. The cohesive traction is linked to the separation movement between the cohesive surfaces by a "cohesive law".

2.15.1. The Dugdale Model

This model used for ductile metals may be considered as a cohesive zone model. The strip plastic zone is now the cohesive zone and the yield stress is the cohesive traction. The cohesive law is thus given by (Figure 2.88(a));

$$\sigma = \sigma_c$$

If the cohesive traction is constant, the critical displacement, or a cohesive energy density need to be specified and the relationship between them is;

$$\Gamma_c = \sigma_c \delta_c$$

Complete separation of materials occurs when

$$\delta = \delta_c$$

2.15.2. Linear Softening Model

This method is regularly used to elaborate the continuum failure in some quasibrittle materials like concrete and ceramic. This cohesive law is elaborated in the form (Figure 2.88(b));

$$\sigma = \sigma_c(1 - \delta/\delta_c)$$

The cohesive energy density is given by;

$$\Gamma_c = \frac{1}{2}\sigma_c \delta_c$$

2.15.3 A Trapezoidal Model

This is a derivation of the Dugdale model and the linear softening model with the traction-separation relationship as given below (Figure 2.88(c);

$$\sigma = \begin{cases} \sigma_{c(\delta/\delta_1)} & 0 \le \delta \le \delta_1 \\ \sigma_c & \delta_1 \le \delta \le \delta_2 \\ \sigma_c\,(\delta_c - \delta)/(\delta_c - \delta_2) & \delta_1 \le \delta \le \delta_2 \end{cases}$$

Where δ_1 and δ_2 are two parameters. This model satisfies Dugdale model when $\delta_1 = 0$ and $\delta_2 = \delta_c$ and linear softening model when both $\delta_1 = \delta_2 = 0$. The cohesive energy Γ_c is given by;

$$\Gamma_c = \frac{1}{2}\sigma_c(\delta_c + \delta_2 - \delta_1)$$

2.15.4 An exponential model

This model has found as having most regular usage in modelling crack growth in ductile metals and is derived from the universal binding energy curve from the atomistic considerations (Figure 2. 87(d)).

$$\sigma = \sigma_c \left(\frac{\delta}{\delta_0}\right) exp\left(1 - \frac{\delta}{\delta_0}\right)$$

Where δ_0 is the separation displacement at which $\sigma = \sigma_c$, the ultimate cohesive traction. The cohesive energy density of the model is;

$$\Gamma_c = \int_0^\infty \sigma d\delta = e\,\sigma_c \delta_0$$

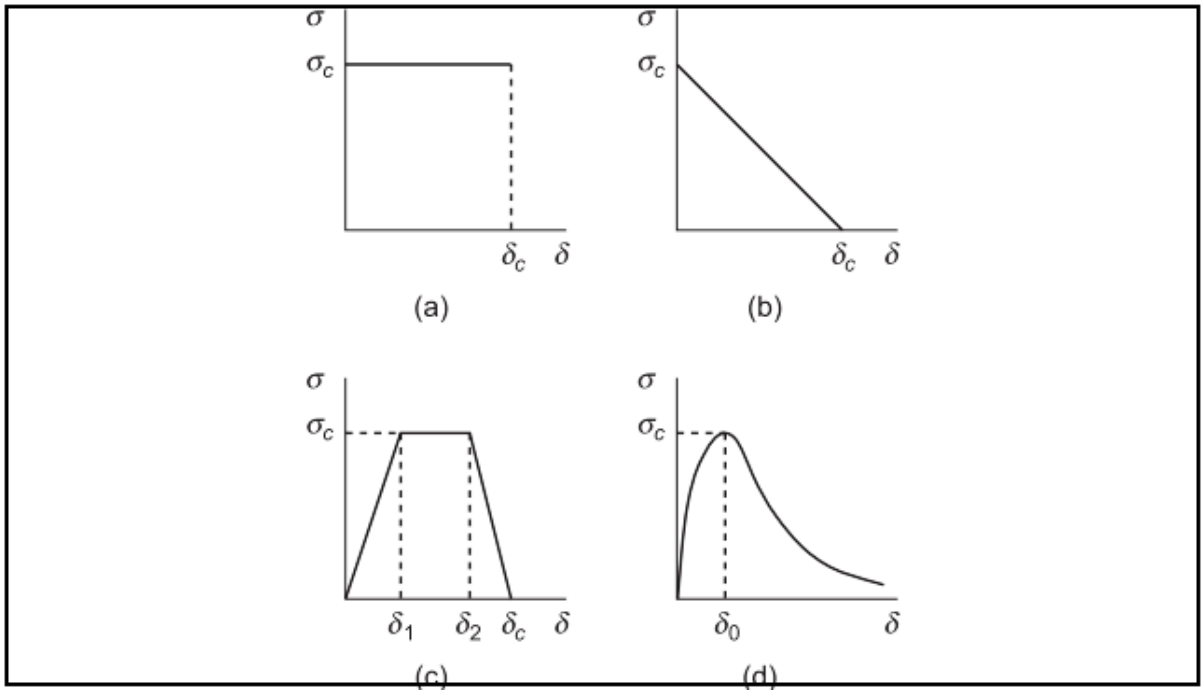

Figure 2.87. Cohesive zone models: (a) the Dugdale model, (b) a linear softening model, (c) a trapezoidal model, and (d) an exponential model.

A considerable number of researchers have used cohesive zone modelling to predict the bond behaviour between concrete/FRP joints or steel/ FRP joints. (Park et al. 2015) have studied interfacial debonding between concrete and fibre reinforced polymer. They have used cohesive zone modelling to evaluate the fracture parameters

such as the fracture energy and bonding strength. A traction separation relation for FRP debonding is proposed with a shape index while providing various initial descending slopes. The traction separation relationship with the shape factor (α) they have developed is expressed as;

$$T_n(\Delta_n) = \begin{cases} \sigma_{max}\left(\dfrac{\Delta_n}{\lambda\delta_n}\right) & for \quad 0 \le \Delta_n \le \delta_{nc} \\ \dfrac{\sigma_{max}}{1-\lambda^{\alpha}}\left[1-\left(\dfrac{\Delta_n}{\delta_n}\right)^{\alpha}\right] & for \quad \delta_{nc} \le \Delta_n \le \delta_n \\ 0 & for \ \Delta_n > \delta_n \end{cases}$$

Where T_n = cohesive traction and Δ_n = separation and λ is defined as the ratio between critical separation to a complete separation ($\lambda = \delta_{nc}/\delta_n$). In this model, the total separation can be evaluated using;

$$\delta_n = \frac{2G_F(1-\lambda^{\alpha})}{\sigma_{max}}\left[1-\lambda+\frac{\alpha-1}{\alpha+1}(1-\lambda^{\alpha+1})\right]^{-1}$$

Where G_F is the total fracture energy. When the cohesive separation (Δn) increases from zero to the critical separation, the proposed model demonstrates a simple linear traction-separation relationship. These researchers conduted three point bending test to check the accuracy of the above model and found that they are well agreed to each other.

In another study (Heshmati et al. 2018) have used cohesive zone modelling to predict various failure modes of steel FRP joints. Their study investigated a number of issues related to CZM analyses of FRP/steel adhesive joints using various test configurations and a comprehensive numerical study. Parameters such as the effect of shape and type of cohesive law, crack path location, length of damage process zone, variations of adhesive and FRP properties, and different failure modes including cohesive, interfacial debonding and FRP failure on the strength of joints are investigated. The critical fracture energy of the interface was calculated based on linear elastic fracture mechanics method, and the elastic energy releasing rate (G_1) was calculated using;

$$G_1 = \frac{1}{4b_f} \frac{F^2}{E_s A_s(\delta + 1)}$$

Where $\delta = \frac{E_S A_S}{2E_f A_f}$

δ is the stiffness balance parameter, E, A and b are E-modulus, cross-sectional area and transverse width, and the subscripts s and f are used for steel and CFRP, respectively. The results of the study revealed that when the variation of the failure modes taken into account, the behaviour of steel/FRP joints can be accurately predct by CZM. It was also noted that the damage process zone in adhesive layer is directly proportional to the shape of cohesive laws which is very important in the design face to ensure a sufficient overlap length to account for important in-service parameters such as temperature and moisture.

The study conducted by Dimitri et al. (2015) aimed to assess the consistency of widely used cohesive zone models (CZMs), specifically the exponential and bi-linear mixed-mode models. The researchers employed a parametric analysis to examine the influence of various parameters, including cohesive stress-interface relative displacement behavior, energy dissipation, and mixed-mode failure domains under different loading conditions. Numerical models were developed using finite element analysis to investigate the behavior of the CZMs. The findings revealed that certain numerical models exhibited local inconsistencies, which could lead to undesired characteristics in the global behavior. These undesirable features included unrealistic hardening branches, oscillations, difficulties in achieving iterative convergence, and failure to reach the expected asymptotic branches during complete failure of the interface. The study emphasized the significance of model consistency for accurately predicting interface phenomena in critical scenarios. In order to ensure reliable and accurate simulations of interface behavior, it is crucial to carefully assess and validate

the chosen CZMs to avoid potential drawbacks and limitations associated with their local inconsistencies.

The effect of various epoxy types adhesives and CFRP properties on the failure mechanisms, bond–slip models, and bond parameters in steel CFRP joints were studied by (Li et al. 2019). They have used bilinear bond slip model for the study with various parameters. The interfacial fracture enegy, G_f id the area underneath the curve and is approximately evaluated using the equation;

$$G_f = \frac{\tau_f \delta_f}{2}$$

Where $\tau_f \; and \; \delta_f$ are the maximum (peak) shear stress and limit slip respectively. A bond strength relationship for CFRP and steel joints developed by Xia and Teng (2005) was utilized The efficient bond length L_{eff} and bond strength $P_{ult}$of CFRP-steel interfaces were given by:

$$L_{eff} = \frac{\pi}{2\sqrt{\tau_f / E_p t_p \delta_f}}$$

and $$P_{ult} = b_p \sqrt{2 E_f E_p t_p}$$

where b_p is the CFRP width. E_p and t_p are the modulus of elasticity and CFRP hickness respectively. The maximum shear strength is take as 80% of the tensile capacity of the adhesive and is written as;

$$\tau_f = 0.8.f_a$$

Based on the experimental results interfacial fracture energy may be written as;

$$G_f = 31.\left[\frac{f_a}{G_a}\right]^{0.56} t_a^{0.27}$$

where G_a and f_a are the shear modulus and adhesive thickness, respectively.

The interfacial damage and failure was simulated using bilinear traction separation law in which the separation is evaluated rely on the relative movement between the bottom and top surfaces of the cohesive layer. The connection between nominal stress and strain of the cohesive elements can be explained as;

$$\bar{t} = \begin{Bmatrix} t_n \\ t_s \\ t_t \end{Bmatrix} = \begin{bmatrix} K_{nn} & 0 & 0 \\ 0 & K_{ss} & 0 \\ 0 & 0 & K_{tt} \end{bmatrix} \begin{Bmatrix} \varepsilon_n \\ \varepsilon_s \\ \varepsilon_t \end{Bmatrix} = K\bar{\varepsilon}$$

where $\bar{t}$ and $\bar{\varepsilon}$ are the nominal stress and strain vectors, respectively. K is the elastic stiffness matrix t_n, t_s and t_t , ε_n , ε_s , and ε_t are the stresses and strains in the normal direction and two shear directions, respectively. K_{nn} , K_{ss} , and K_{tt} are the elastic stiffnesses in three directions.

The quadratic nominal stress criterion has used in this analysis which represents the initial damage criterion based on the critical condition of material degradation and the criterion was expressed as follows;

$$\left\{\frac{\langle t_n \rangle}{t_n^o}\right\}^2 + \left\{\frac{t_s}{t_s^o}\right\}^2 + \left\{\frac{t_t}{t_t^o}\right\}^2 = 1$$

Where t_n, t_s and t_s are the nominal stress strengths in the three directions.

Once damage starts to initiate, an irreversible damage variable D is introduced, which progresses from 0, the undamaged state, to 1, the fully interface failure.

$$D = \frac{\delta - \delta_1}{\delta_f - \delta}$$

Where is the slip for a given load increment, δ_1 and δ_f are the slips at damage initiation and interface failure, respectively.

When the bond is fully failed D = 1 and this failure is governed by the interfacial fracture energy which can be denoted in the form of power law as follows;

$$\left\{\frac{G_n}{G_n^C}\right\}^{\alpha} + \left\{\frac{G_s}{G_s^C}\right\}^{\alpha} + \left\{\frac{G_t}{G_t^C}\right\}^{\alpha} = 1$$

Where G_n, G_s and G_t represent the mode Ⅰ, mode Ⅱ, and mode Ⅲ fracture energy at a given load increment, in normal, first and second shear directions respectively. The quantities G_n^C, G_s^C and G_t^C are the mode Ⅰ, mode Ⅱ, and mode Ⅲ fracture energy in the normal, the first and the second shear directions at interface failure, respectively. The value of α was chosen to be equal to 1. The results of the study reveal that he cohesive zone model can well simulate the nonlinear bond behaviour of bonding interface. The simulated CFRP strain distributions and ultimate bearing capacities of all the specimens were consistent with the test results. It was also noted that bond linear model for most of the adhesive joint can be simplified to bilinear bond-slip model, but for the situations where delamination and tearing of CFRP occur, a tri-linear model should use.

(Teng, Fernando, and Yu 2015b) have conducted an experimental study and a numerical investigation on debonding failures of steel I beams reinforced with. They have suggested two characteristics of finite element model should possess for the successful prediction of debonding failure; (1) it correctly forecasts the performance of the common face under pure Mode-I loading and pure Mode-II loading, and (2) it

appropriately accounts for the effect of connection between Mode-I and Mode-II on damage initiation and spread along the common face. They also mentioned that for (1) an correct bond slip model and an accurate bond separation model required while for (2) mixed mode cohesive law to be used. As they stated among the currently available modelling methods, a coupled cohesive zone technique appears to be the most accurate because of its capability in simulating the fracture of ductile and brittle performance of adhesively bonded joints. The proposed bilinear bond-slip model for this study as follows;

$$\tau = \begin{cases} \tau_{max}\dfrac{\delta}{\delta_1} & if \quad \delta \le \delta_1 \\ \tau_{max}\left(\delta_f - \delta\right)/\left(\delta_f - \delta_1\right) & if \quad \delta_1 \le \delta \le \delta_f \\ 0 & if \quad \delta > \delta_f \end{cases}$$

where τ is the bond shear stress, τ_{max} is the peak bond shear stress, δ is the slip, δ_1 is the slip at peak bond shear stress, and δ_f is the slip at complete failure. They have also derived and proposed some equations for the above bond-slip parameters based on experimental results.

$$\tau_{max} = 0.9\sigma_{max}$$

$$\delta_1 = 0.3\left(\frac{t_a}{G_a}\right)^{0.65}\sigma_{max}$$

$$\delta_f = \frac{2G_f}{\tau_{max}}$$

Here both δ_1 and δ_f are measured in mm. The tensile strength of the adhesive is given by σ_{max} while t_a and G_a are the adhesive thickness and shear modulus of adhesive layer respectively. The parameter G_f is the interfacial fracture energy and is given by;

$$G_f = 628t_a^{0.5}R^2$$

Where R is denoted the tensile strain energy for unit volume of the adhesive, which can be calculated using the area under the uni-axial tensile stress-strain curve. Moreover in this study (Teng, Fernando, and Yu 2015b) a bilinear bond-separation model (mixed mode cohesive law) is used. This model is appropriate for this to account for the interaction between mode-I loading and mode-II loading and the fracture energy for mode-II loading is often much larger than that for mode-I loading. This mixed-mode cohesive law adopted in the present study considered tractions and separations in all three dimensions. If the original thickness ofsolids, the delamination of composites, and the adhesive layer (T_0) as the thickness of the cohesive element, the strain in three directions, ε_n, $\gamma_s$and γ_t in normal and two shear directions respectively are given by;

$$\varepsilon_n = \frac{\delta_n}{T_0}, \gamma_s = \frac{\delta_s}{T_0} \; and \; \gamma_t = \frac{\delta_t}{T_0}$$

It is also assumed that the interfacial behaviour is elastic until the initiation of damage and hence interfacial behaviour prior to damage initiation may be denoted by;

$$\begin{Bmatrix} t_n \\ t_s \\ t_t \end{Bmatrix} = \begin{bmatrix} K_{nn} & 0 & 0 \\ 0 & K_{ss} & 0 \\ 0 & 0 & K_{tt} \end{bmatrix} \begin{Bmatrix} \varepsilon_n \\ \varepsilon_s \\ \varepsilon_t \end{Bmatrix}$$

K_{nn} , K_{ss} , and K_{tt} are the elastic stiffnesses in three directions, normal and the two shear directions and K_{nn} is the initial slope of the bond-separation relationship for mode-I loading and is given by;

$K_{nn} = \frac{E_a}{T_0}$ where E_a is the Young's modulus of adhesive.

K_{ss} , and K_{tt} may be taken as same and should equal to the initial slope of bond-slip model for mode-II loading and are given by;

$K_{nn} = K_{nn} = 3\left(\frac{G_a}{T_0}\right)^{0.65}$ where G_a is the adhesives' shear modulus. For the damage initiation the existing quadratic strength criterion is adopted considering the interaction between mode-I and mode-II loading.

$$\left\{\frac{\langle t_n \rangle}{t_n^0}\right\}^2 + \left\{\frac{t_s}{t_s^0}\right\}^2 + \left\{\frac{t_t}{t_t^0}\right\}^2 = 1$$

Here ⟨ ⟩ is the Macaulay bracket which disappear when the compressive stresses do not lead to damage. After damage initiation, a scaler damage variable D is introduced to modify the elastic equation a follows;

$$\begin{Bmatrix} t_n \\ t_s \\ t_t \end{Bmatrix} = \begin{bmatrix} (1-D^*)K_{nn} & 0 & 0 \\ 0 & (1-D)K_{ss} & 0 \\ 0 & 0 & (1-D)K_{tt} \end{bmatrix} \begin{Bmatrix} \varepsilon_n \\ \varepsilon_s \\ \varepsilon_t \end{Bmatrix}$$

Where * means that if t_n is compressive, D^* is equal to zero. The complete failure of the adhesive is defined when D is equal to one. There are few criteria to define complete adhesive of the effective displacement attained in the loading process as shown in Figure 2.88(b).

failure such as quadratic criterion or BK criterion; this study was adopted the linear criterior which is expressed as below:

$$\frac{G_n^*}{G_1} + \frac{G_s}{G_{11}} + \frac{G_t}{G_{11}} = 1$$

Where G_n, G_s, G_t are the works done by the tractions and their con- jugate displacements in the normal and the two shear directions respectively. G_1 and G_{11} (Figure 2.88(a)) represent the interfacial fracture energies required to cause failure when subjected to pure mode-I loading and pure mode-II loading respectively. The effective displacement is introduced to describe the evolution of damage as follows;

$$\delta_m = \sqrt{\langle \delta_n \rangle^2 + \delta_s^2 + \delta_t^2}$$

The dam- age variable D is then defined by the following equation assuming linear softening of the interface;

$$D = \frac{\delta_m^f (\delta_m^{max} - \delta_m^0)}{\delta_m^{max} (\delta_m^f - \delta_m^0)}$$

where δ_m^0 is the effective displacement at the initiation of damage and δ_m^{max} is the maximum value of the effective displacement attained in the loading process as shown in Figure 2.88(b).

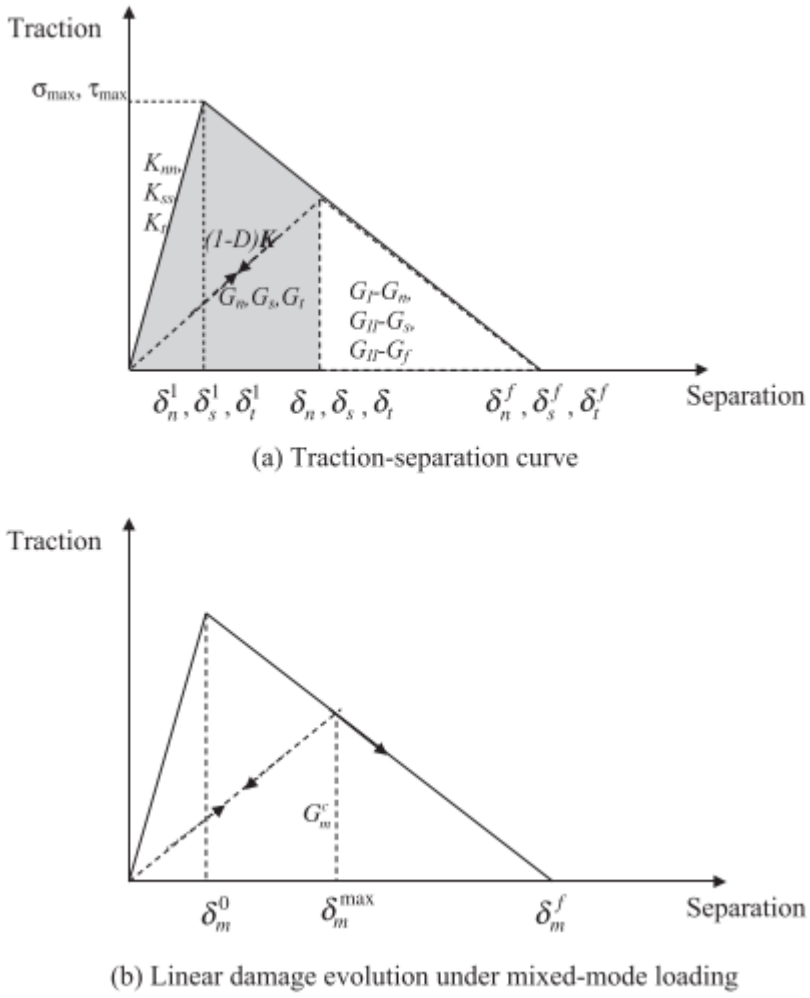

Figure 2.88. Traction–separation curves and linear damage evolution under mixed-mode loading. (a) Traction–separation curve. (b) Linear damage evolution under mixed- mode loading.

The study conducted by M.H. Kabir, Fawzia, Chan, Gamage, et al. (2016) focused on the finite element analysis of circular hollow sections reinforced with CFRP using ABAQUS CAE software. In their analysis, they employed the cohesive zone modeling (CZM) approach to simulate the interface between the CFRP and steel components. The researchers followed the same equations and procedures suggested by Teng, Fernando, and Yu (2015b) in their study. They utilized the quadratic traction damage criterion (QUADS) as the proposed damage criterion, assuming that the nominal stress in the normal and shear directions are similar. Based on the results

obtained from their analysis, the study concluded that CZM is capable and accurate in modeling the interface between CFRP strengthened circular hollow tubes. This finding suggests that CZM can be an effective approach for simulating and predicting the behavior of CFRP-strengthened circular hollow sections, providing valuable insights into the performance and structural response of such systems.

2.15 Summary of Literature

A considerable number of structures are constructed with curved steel structural members which are either closed or open sections. These curved steel beams may be either curved in horizontal plane (horizontally curved beams) or curved in elevation (vertically curved beams). The literature presented here discussed on numerous applications of curved steel members with some examples as well as processes of manufacturing curved steel members. There are various methods of analysing these members and few of them are presented in the literature review. Several structures made with curved steel members need strengthening due to many reasons such as inadequate capacities due to design errors, loss of material properties, exposure to severe environments, or increase in service loads. Fixing of steel plates and retrofit structural elements using FRP materials are two most common methods available to strengthen steel structures and later found to be more advantageous due to many reasons; higher strength-to-weight ratio, high durability and cost saving through labour savings. The most common fibres used for structural applications are glass, aramid, carbon and basalt and their properties are also different. To attach fibres with substrate materials, two basic classes of polymeric matrices or adhesives are used; thermosetting and thermoplastic adhesives. Three common types of FRP bonding systems are used in structural strengthening systems, which are wet lay-up system, pre-

impregnated FRP and pre-cured fibre plates.

The literature clearly explains effective applications of CFRP in strengthening of steel beams (Closed or open sections) for various loading conditions (axial loads, bending, torsion, fatigue and impact loads) and environmental conditions (cold, under water and marine). Moreover, different failure mechanisms of CFRP bonded steel members under these different loading conditions and environmental conditions are extensively discussed in literature. Experimental, theoretical and FEM methods have been used to elaborate the effectiveness of application of CFRP in retrofitting purposes. FEM can be mainly done with commercially available finite element modelling software such as ABAQUS, ANSYS and STRAND 7. It was found that this FEM software are capable of capturing loads, deflections, stresses and strain, and failure mechanisms with an acceptable accuracy. However, they are still to be developed to capture environmental degradation of FRP steel joints under various environmental conditions.

Even though a considerable number of researches found on structural retrofitting of steel structures with CFRP, most of the were focussed only on straight members and a very little studies were focussed on the reinforcing of curved steel members (either closed or open sections) using CFRP. Therefore, this study presented here is mainly focussed on the performance of CFRP reinforced vertically curved hollow section and horizontally curved I beams under pure bending using experimental, theoretical and FEM methods. Moreover, vibration analysis of CFRP reinforced steel beams were conducted to observe the effectiveness of vibration analysis to capture the failure points of CFRP strengthened steel members.

Finally, the effective use of Cohesive Zone Modelling to simulate FRP/ steel joints were discussed. The more focus was given on various bond-slip models and bond-separation models developed by various researchers. Even though some minor drawbacks available CZM is capable of predicting debonding failures of adhesively bonded FRP/steel joints.

Chapter 3

Material Properties

3.1 Introduction

Properties of materials used in the study have a significant impact and uses when conducting various stages of experimental, theoretical and finite element modelling. This chapter is focussed on the experimental process used to obtained material properties required for the study. All the experiments used to obtain material properties were conducted according to ASTM standards testing methods.

Three main materials used in this study were; steel (tubular sections and I beam), CFRP sheets and adhesives. Some of the physical properties of these materials were obtained using experiments conducted at the laboratory level and few properties were extracted from manufacturers guidelines. The main testing method adopted here is the tensile test material to obtain stress-strain relationships.

3.2 Testing of Steel Samples

3.2.1 Coupon Test for Steel Tubes

Steel tubular sections with a diameter of 101.6 mm and the thickness of 3 mm were used to investigate the behaviour of CFRP strengthened vertically curved beams. Prior to experimental, numerical and FEM studies, it was required to evaluate few material properties such as modulus of elasticity, tensile strength, yield strength, tensile strain, and Poisson's ratio of this steel. Three steel samples were prepared according to the dimensions provided in ASTM: A370(ASTM A370 / ASME SA-370, 2016), standard testing methods for steel material products. The standard dimensions of prepared samples are shown in Figure 2.1 in line with the method of extraction of sample from the steel tube.

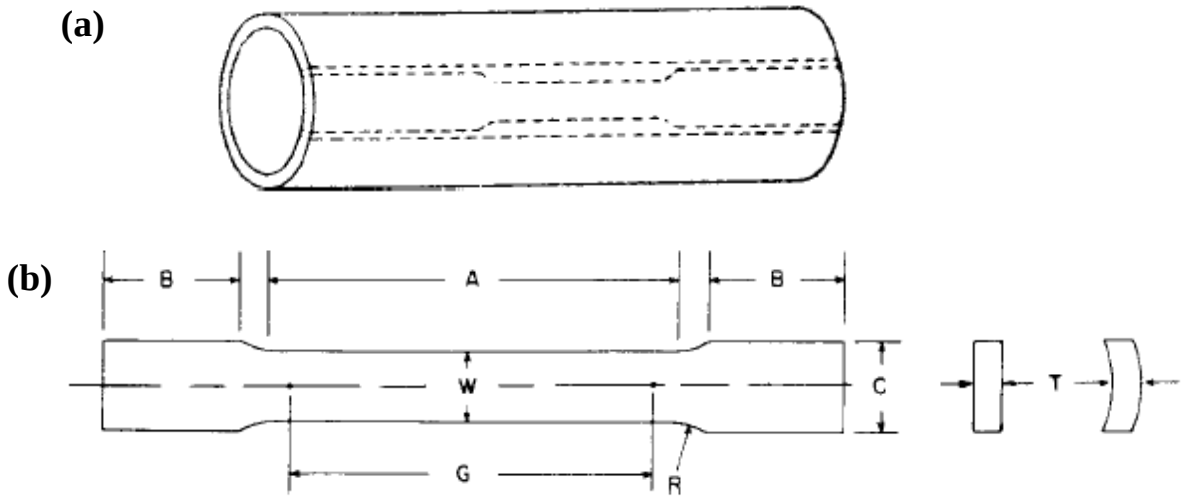

A – 120 mm B – 75 mm C – 25 mm
G – 100 mm R – 25 mm W – 20 mm
T - Thickness of the Tube (3 mm)

Figure 3.1. (a) Positions of sample extraction, (b) standard dimensions of the coupon

Two coupons were extracted from selected random samples. The extracted coupons were fitted with two strain gauges, one in the axial direction and one in the lateral direction (Figure 3.1) to capture the longitudinal and lateral strains. Then the coupons were tested using tensile testing machine by applying a strain rate of 0.025mm/second. The testing arrangement is shown in Figure 3.2. Load was applied until coupons fail in applied tensile load. Load and deformation were recorded using a data logger and later converted them to stress and strain.

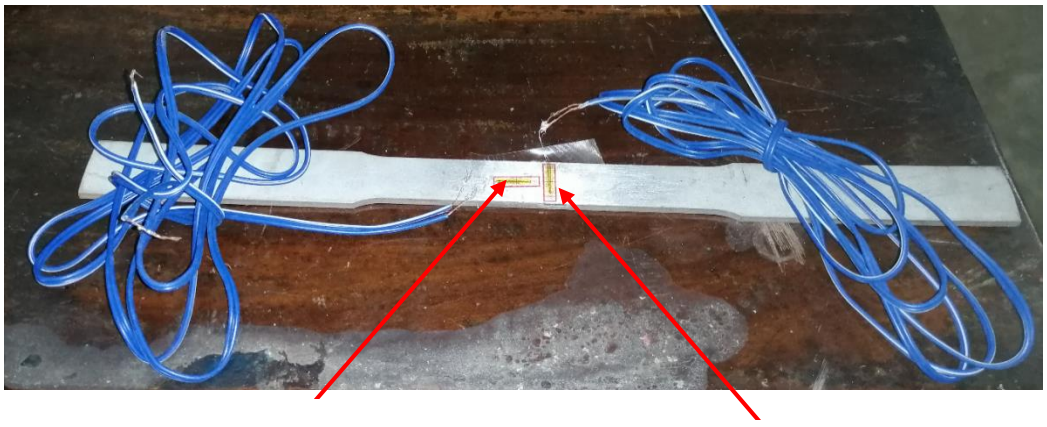

Figure 3.2. Steel coupon fitted with strain gauges

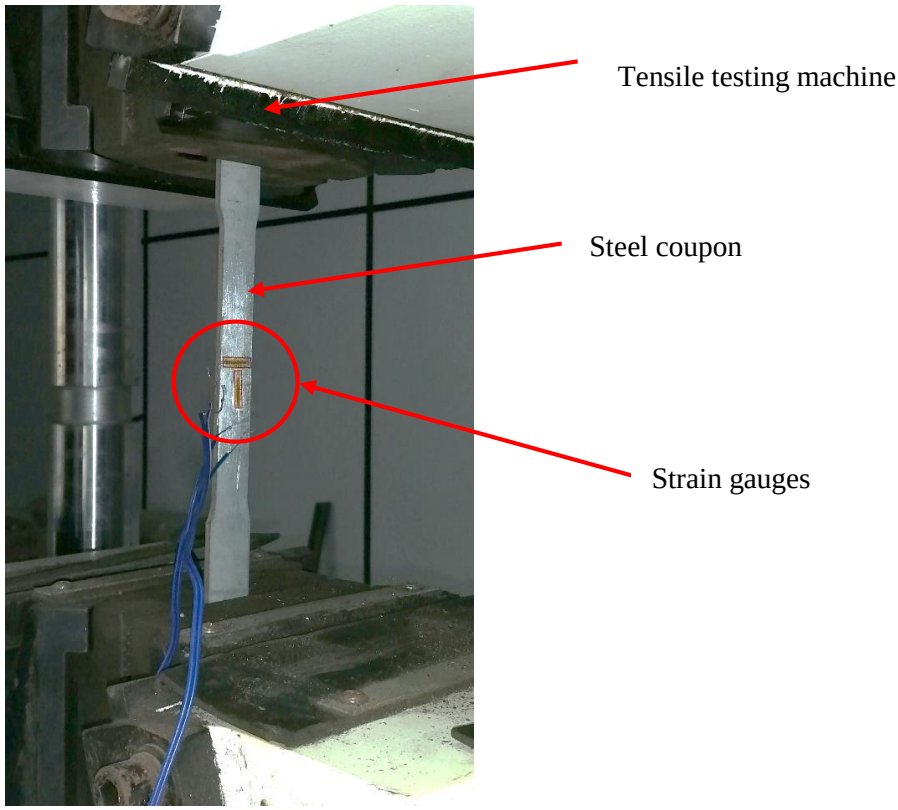

Figure 3.3. Steel coupon test

The steel samples were failed due to necking at close to the mid-point of the sample as indicated in Figure 3.4. The obtained load and deflections were converted to stress and strain and plotted as shown in Figure 3.5. As per the stress strain curve the yield strength of steel is 385N/mm^2, ultimate tensile strength is 535N/mm^2, and tensile strain is 0.025.

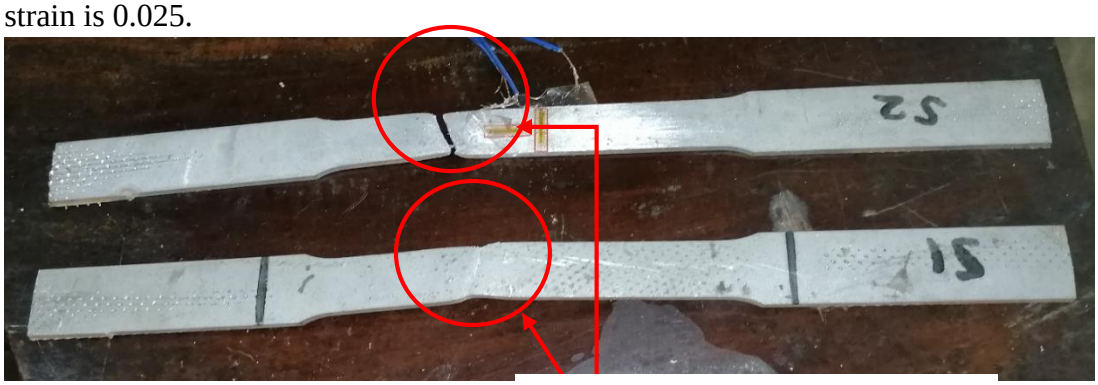

Figure 3.4. Failure mechanisms of steel coupons

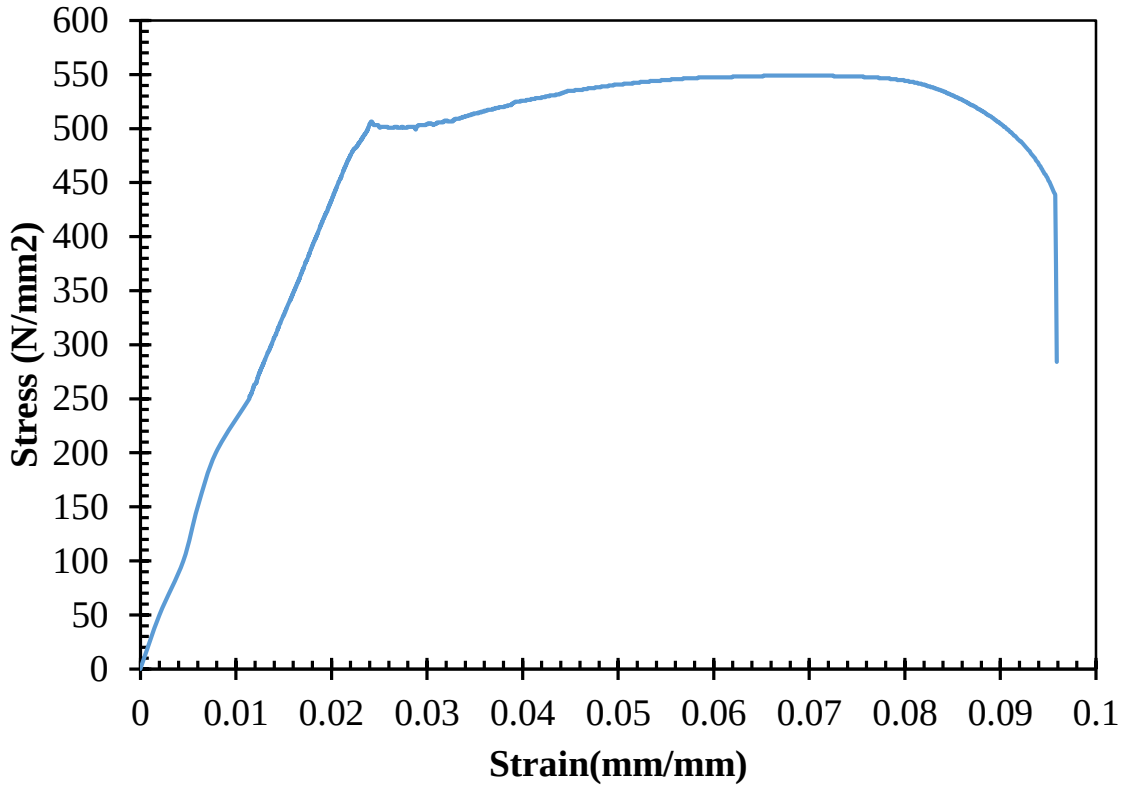

Figure 3.5. Stress-strain relationship for steel

3.2.2 Coupon Test for Steel I Beams

Steel I beams of overall depth of 100 mm and width of 51.50 mm having web and flange thicknesses of 6.4 mm and 6.7 mm respectively were used to examine the performance of CFRP reinforced horizontally curved beams. In order to obtain elastic and plastic properties of this steel coupon tests were performed on three samples taken from three randomly selected beams. The location and the dimensions of extracted samples as shown in Figure 3.6 below. Samples were tested using universal testing machine with the Quisi-static loading with a strain rate of 0.03 mm/sec. Prior to the testing of specimens, two strain gauges were fitted at the mid-point of the sample, in order to measure longitudinal and lateral strains. Observed data involved load, and strains in the axial and lateral directions which are later converted to stress and strains. A prepared sample and testing of a sample is shown in Figure 3.6. The developed

stress-strain curve for this steel is shown in Figure 3.7. A summary of obtained properties for steel of tubular sections and I beam are summarised in Table 3.1.

Table 3.1 Properties of steel coupons from tubes and I beams

Property	Steel tube sample
Thickness (mm)	3
Elastic modulus (GPa)	206
Tensile strength (MPa)	473
Yield strength (MPa)	508
Tensile strain (mm/mm)	0.25

3.3 Testing of CFRP Samples

The Carbon Fibre Reinforced Polymer (CFRP) used for the testing programme is the type of unidirectional normal modulus carbon fibre sheets with nominal thickness of 0.167 mm. The evaluation of tensile properties of CFRP sheets were determined by using tensile test carried out on a thin patch of carbon/epoxy samples. Hence, the tensile properties of pure CFRP are determined by considering two CFRP layers ignoring the thickness of the adhesive. The tensile samples were prepared in accordance with ASTM: D3039/D3039M-08 (ASTM D3030/D3039M, 2002). Figure 3.8 shows the typical dimensions and configuration of tested samples. Two dry fibre sheets were cut according to a prescribed size and then pressed onto a flat release sheet wetted with adhesive Araldite 420 saturant to produce a large panel of carbon/epoxy laminate. After the adhesive attained sufficient working strength, the large panel was cut into required number of coupons in the fibre direction according the dimensions given in ASTM: D3039/D3039M-08 (2008). Steel tabs were bonded using high strength two-

part epoxy resin Araldite 420 at both sides of two ends of the coupon specimens for gripping purposes, apply uniform pressure to the specimen during testing and also steel tabs prevent damage of CFRP laminate and reduce shock wave stress effects. This small tabs were sand blasted and pre-stamped to create small dents in order to improve the mechanical interlocking between CFRP strips and steel tabs to prevent pre-mature slipping or sliding. These specimens were cure for at least seven days prior to testing at ambient temperature as per the instruction provided by the manufacturer. Two strain gauges were fixed on each tested specimens to record axial strain and lateral strain. Specimens were tested using the universal testing until the failure observed. Figure 3.9 and Figure 3.10 show the prepared samples with strain gauges and the testing arrangement respectively.

The observed failure modes of the samples included edge delamination of the gauge at the middle (DGM) and explosion of the gauge at the middle (XGM) of CFRP as shown in Figure 3.11.

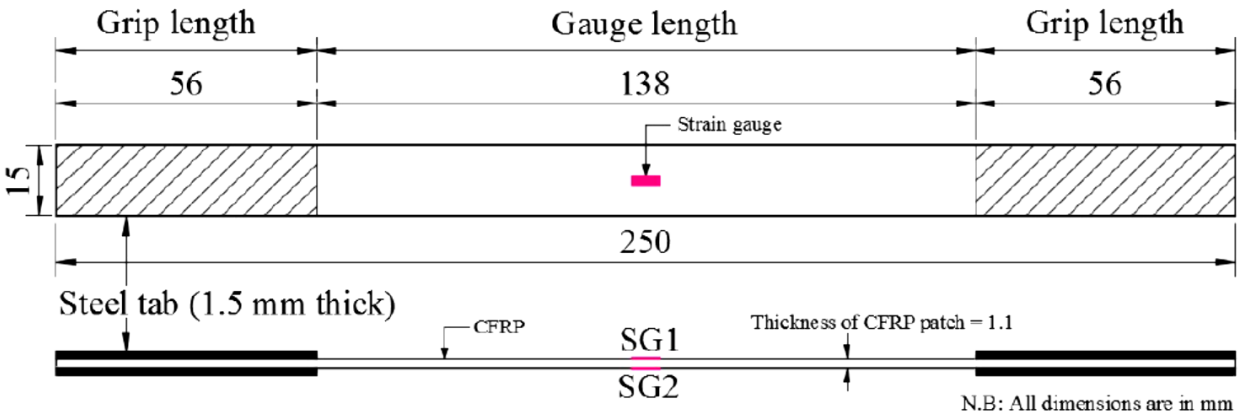

Figure 3.8. Dimensions of the specimens and positions of strain gauges

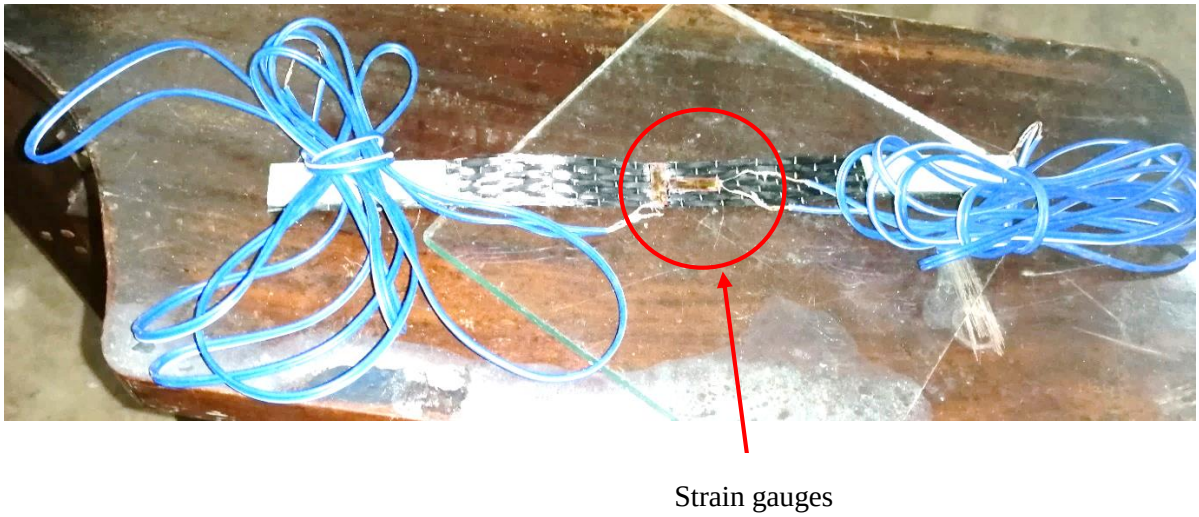

Figure 3.9. A coupon sample with strain gauges

The stress-strain curves plotted for all five sample are shown in Figure 3.12 and for the purpose of FEM purposes, average values of ultimate tensile strength, Poisson's ratio, elastic moduli were used. A summary of material properties obtained are given in Table 3.2.

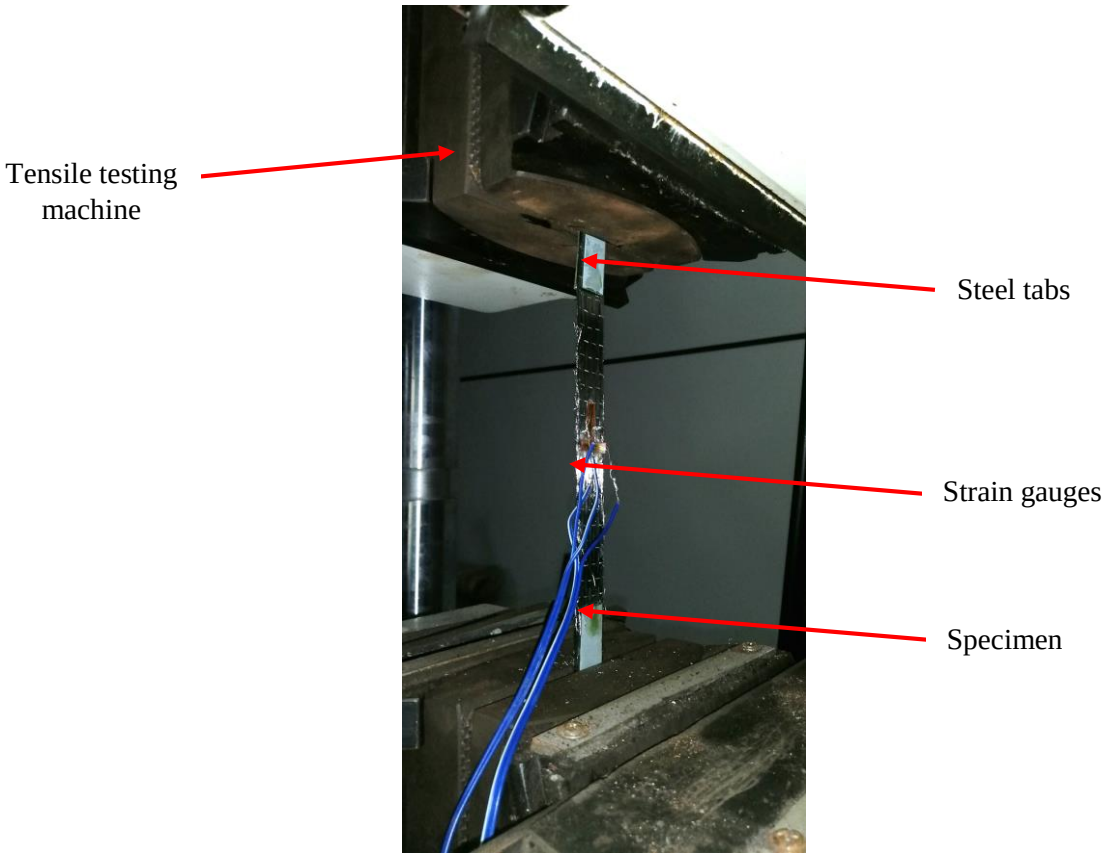

Figure 3.10. Coupon test arrangement for CFRP strips

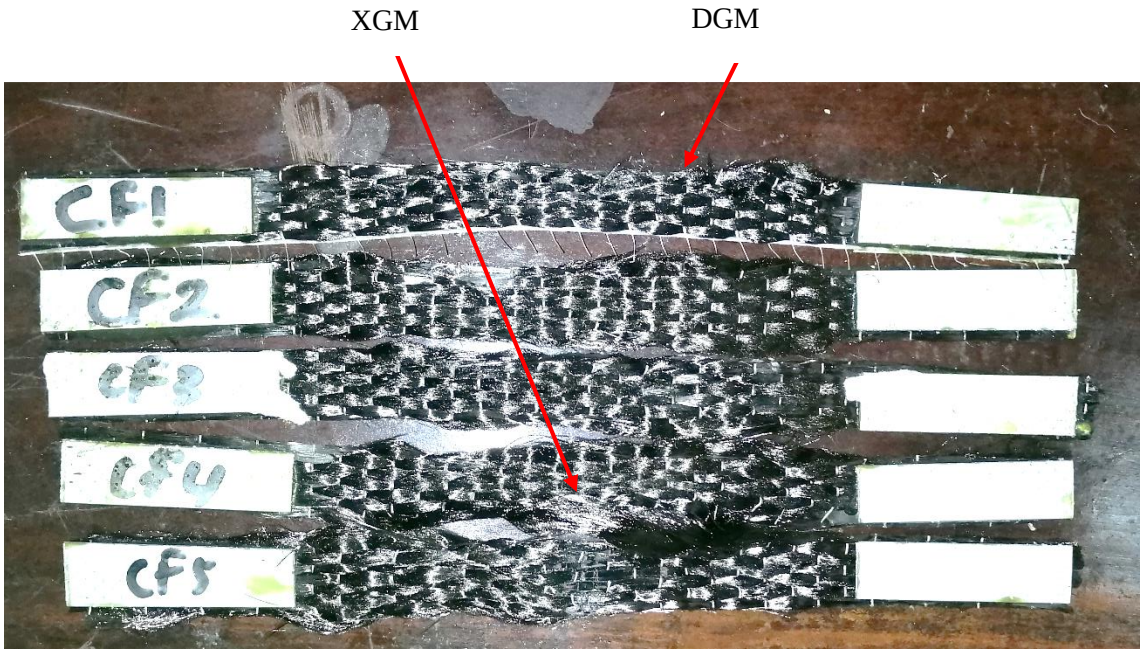

Figure 3.11. Failure modes of coupons

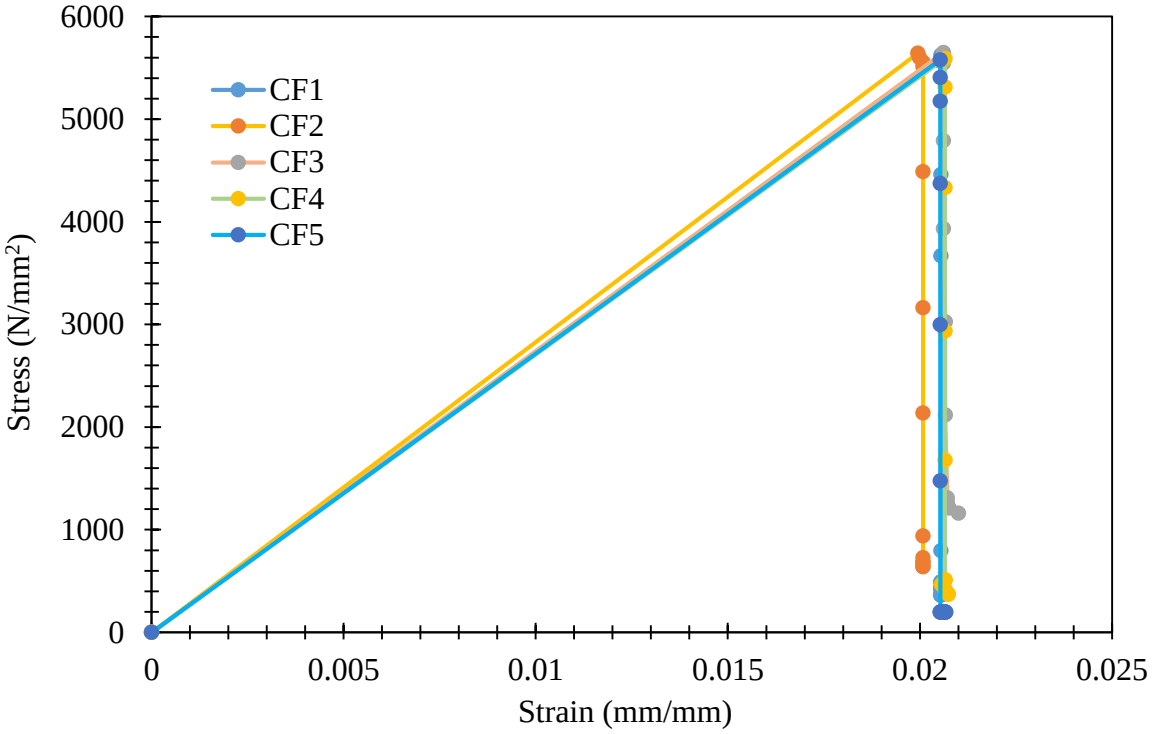

Figure 3.12. Stress Strain curves for CFRP coupons

Table 3.2 Properties of CFRP

Property	Magnitude
Thickness (mm)	0.116
Elastic modulus (GPa)	230
Tensile strength (MPa)	4983
Yield strength (MPa)	-
Tensile strain (mm/mm)	0.021

3.4 Testing of Adhesive Coupons

Since the properties of adhesive used is very much important, tensile test was conducted on it. Araldite 420, two parts epoxy adhesive was tested after preparing the coupons using a fabricated mould. Preparing coupons and testing was done according to ASTM D-638 (ASTM D638, 2015). The shape and the dimensions of the tested standard samples is shown in Figure 3.13. The parts A and B of each adhesive were mixed to the appropriate ratios and poured into the mould. The specimens were kept in the mould for 1-2 days prior to removing them from the mould. The specimens were 250 x 250 mm large panel with 6 mm thickness. These were then cut using a milling machine with an end mill cutter into coupon size according to the coupon dimension. To measure the true strain during testing, two strain gauges were attached in the central area within the gauge length of the specimens on both sides as shown in Figure 3.13. The testing was conducted using tensile testing machine and the applied strain rate was 0.03 mm/s. All the tests were conducted using a quasi-static manner. The readings from the strain gauges, the failure load and head displacement were recorded by a computer programmed software connected to data logger. A pictorial illustration of adhesive coupon testing is shown in Figure 3.14 and some of the

properties obtained are listed in Table 3.3. The average stress strain relationship obtained for adhesive is shown in Figure 3.15.

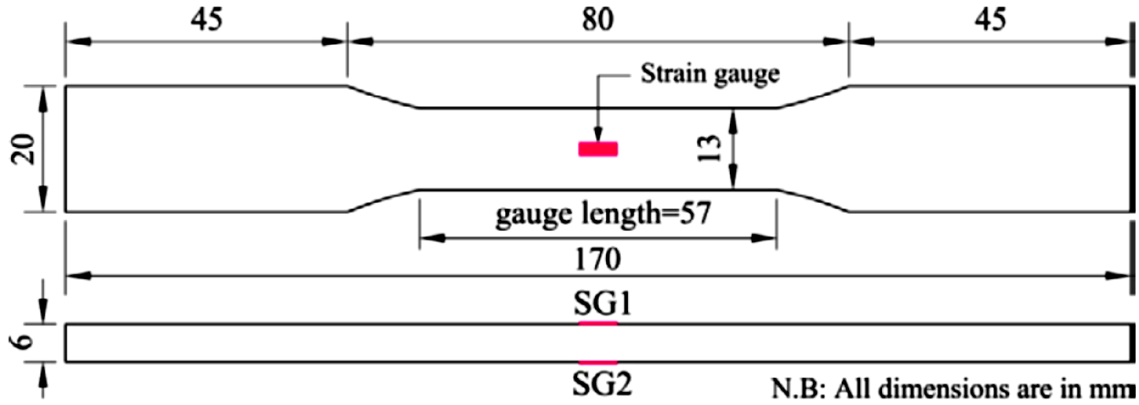

Figure 3.13. The geometry and dimension of adhesive coupons

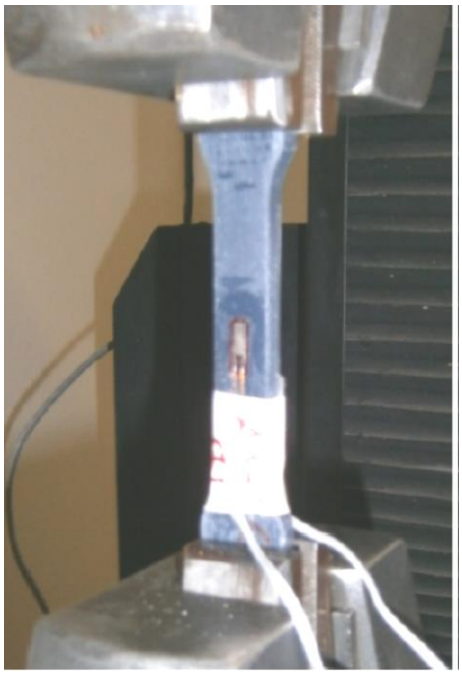

Figure 3.14. Tensile test on adhesive coupons

Table 3.3. Properties of Adhesive

Property	Magnitude
Thickness (mm)	0.05
Elastic modulus (GPa)	2.4
Tensile strength (MPa)	40
Yield strength (MPa)	-
Tensile strain (mm/mm)	-

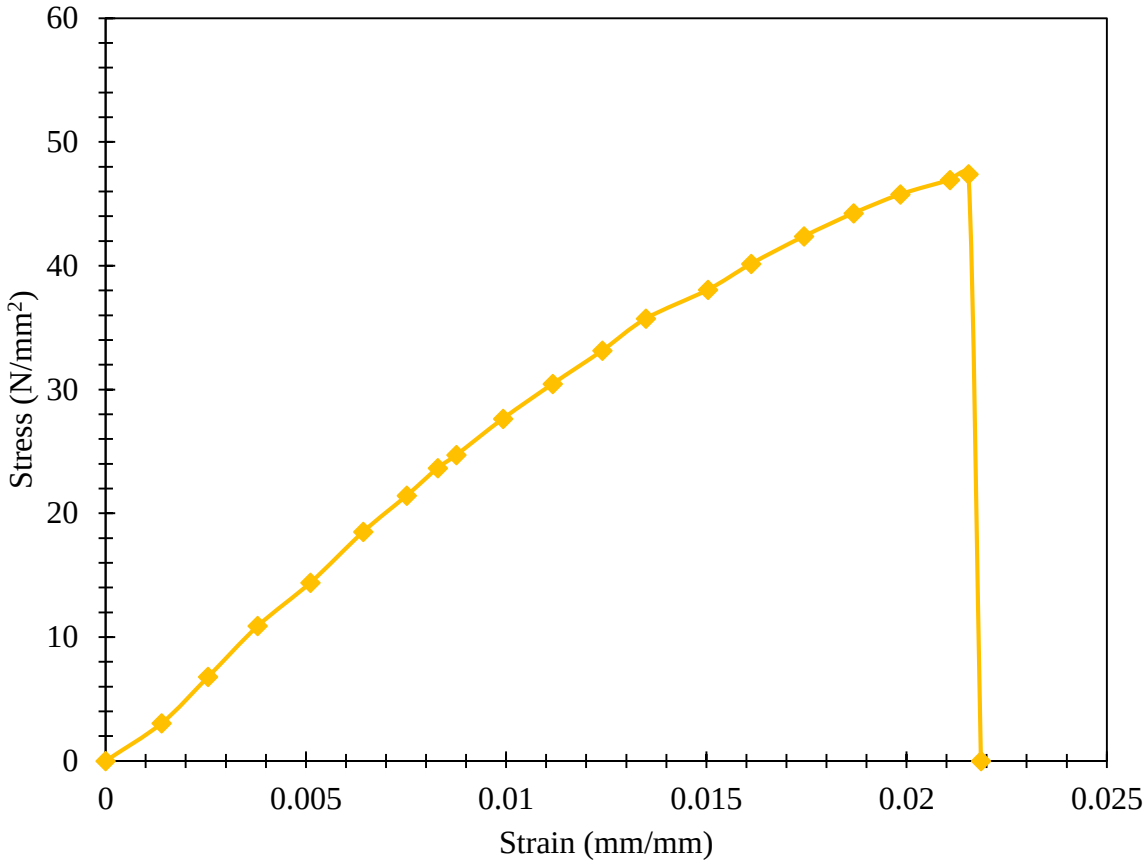

Figure 3.15. Stress – Strain curve for adhesive (Araldite 420)

3.5 Chapter Summary

This chapter was discussed about the methods of evaluation of material properties required for experimental investigation, analytical investigations, and finite element modelling of CFRP strengthened structural elements. The tested materials samples were included samples from steel tube, steel I beams, CFRP and adhesive. All samples were prepared and experiments were conducted according to ASTM standards. The obtained results included stress strain relationships, ultimate loads and failure modes of the coupons. Most of the values obtained for the properties are matched with manufacturer provided data.

Chapter 4

Experimental and Theoretical Investigation of Vertically Curved Circular Hollow Sections Strengthened with CFRP

4.1 Introduction

The use of steel tubular sections for civil engineering applications has become popular due to their excellent structural performance and prolonged life spans. Steel hollow sections have high compression, tensile and bending strengths in all directions and have a small drag coefficient in fluid flows. The life span of steel hollow section is longer than other forms of steel sections because of the closed-shape section without sharp corners which reduce the area exposed to outside environment and thus protects the section from corrosion. Moreover, the section void can be filled with concrete to enhance fire protection. The aesthetical appearance and the space provided by the void for installing electric conduits, network cables and other services are advantages of using steel hollow beams in building construction(Wardenier 2001). Beams with Steel Circular Hollow Sections (SCHS) used in construction can be categorized as straight and curved. Hollow section straight members have numerous applications such as in jackets, towers, cranes, bridges, support structures of helicopter decks and further in various secondary structures, such as staircases and ladders. Curved beams can be either bent in the horizontal or vertical plane depending on the application. Beams curved in elevation have structural applications mainly in steel bridges and portals of curved steel roofs. Figure 1 shows two applications of curved SCHS in a bridge(Wardenier 2001) and a roof(Hamburg airport roof n.d.). During their service lives, structural elements constructed with curved SCHS may become structurally inadequate due to design errors, loss of material properties, exposure to severe

environments, or increase in service loads(M. H. Kabir, Fawzia, Chan, Gamage, et al. 2016). The present study is limited to SCHS curved in elevation.

Use of Carbon Fibre Reinforced Polymer (CFRP) is a proven retrofitting technique for engineered structures because of CFRP's high durability, superior fatigue endurance, high strength-to-weight ratio, less labour intensive work, and suitability for any sectional shape(D. Fernando et al. 2008; M. H. Kabir, Fawzia, Chan, Gamage, et al. 2016). Many studies have been conducted on the behaviour of CFRP strengthened tubular structures under axial(Devi and Amanat 2015; Gao, Balendra, and Koh 2013; Keykha et al. 2015; Shaat and Fam 2006; Sundarraja, Sriram, and Ganesh Prabhu 2014; Teng and Hu 2007), bending(Babu and Sundarraja n.d.; Badawy et al. 2019; Elchalakani 2014a; S. Fawzia et al. 2007; J. Haedir et al. 2009; M. H. Kabir, Fawzia, Chan, Gamage, et al. 2016; Teng, Fernando, and Yu 2015a; O. Zhao et al. 2015) and torsional(Abdollahi Chahkand et al. 2013; Wu et al. 2018) loadings. Furthermore, CFRP strengthening of SCHS can enhance durability against transient loadings such as fatigue(Hu, Feng, and Zhao 2017)and impact loadings (Md Iftekharul Alam et al. 2017; Kadhim, Wu, and Cunningham 2018a) as well as in severe environmental conditions(Kabir, M H. 2015; M. H. Kabir, Fawzia, Chan, and Badawi 2016a, 2016b; M. H. Kabir, Fawzia, and Chan 2016; Mohammad Humayun Kabir et al. 2014; Seica and Packer 2007). However, only a few studies(Keykha 2019) have investigated the flexural behaviour of hollow steel beams curved in elevation and strengthened with CFRP, and they focussed on square hollow sections. A comprehensive study on the flexural behaviour of CFRP strengthened SCHS beams curved in elevation is therefore required to ensure structural safety, minimize maintenance costs and extend their service lives.

With this in mind, an experimental study was conducted to investigate the flexural behaviour of both CFRP strengthened SCHS beams curved in elevation and straight beams. The effect of curvature of beams and CFRP wrapping lengths on ultimate load carrying capacity, mid span deflection and failure modes were studied. An analytical model was also developed and validated to predict the performance of CFRP retrofitted SCHS beams curved in the vertical plane. The results of the study provide referral guidelines to structural engineers on the practical applications of CFRP to retrofit SCHS curved in elevation.

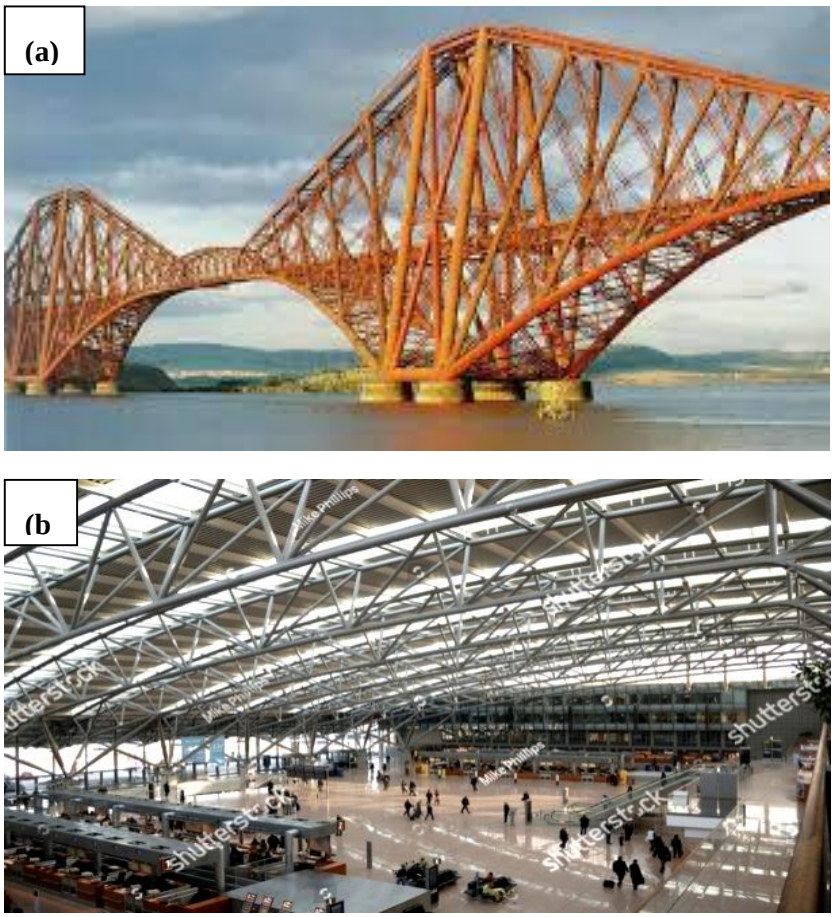

Figure 4.1. Structures constructed using SCHS curved in elevation (a) Firth of forth bridge (b) Hamburg airport roof

4.2. Experimental Programme

2.1 Material Properties

Coupon tests were conducted according to American Standard Testing Methods to obtain the required material properties for steel (ASTM A:370)(ASTM A 370-19ei 2019) and CFRP (ASTM D:3039)(D3039/D3039M-17 2017). Three steel coupons and five CFRP coupons were tested. The stress-strain curves obtained for CFRP sheets and circular hollow steel tubes are shown in Figure 4. 2. Figure 4.3 shows the images taken during the coupon tests for steel and CFRP. Elastic modules in fibre direction (E_1), matrix direction (E_2), and Poisson's ratios in fibre (N_{u12}) and matrix (N_{u13}) directions were obtained during the coupon tests for CFRP. The elastic modulus and Poisson's ratio in third direction were assumed to be equal to those of matrix direction for CFRP. Shear modulus for the CFRP in all three directions were obtained using manufacturer provided data. Both elastic and plastic properties for steel and CFRP obtained during the coupon test are listed in Table 4.1.

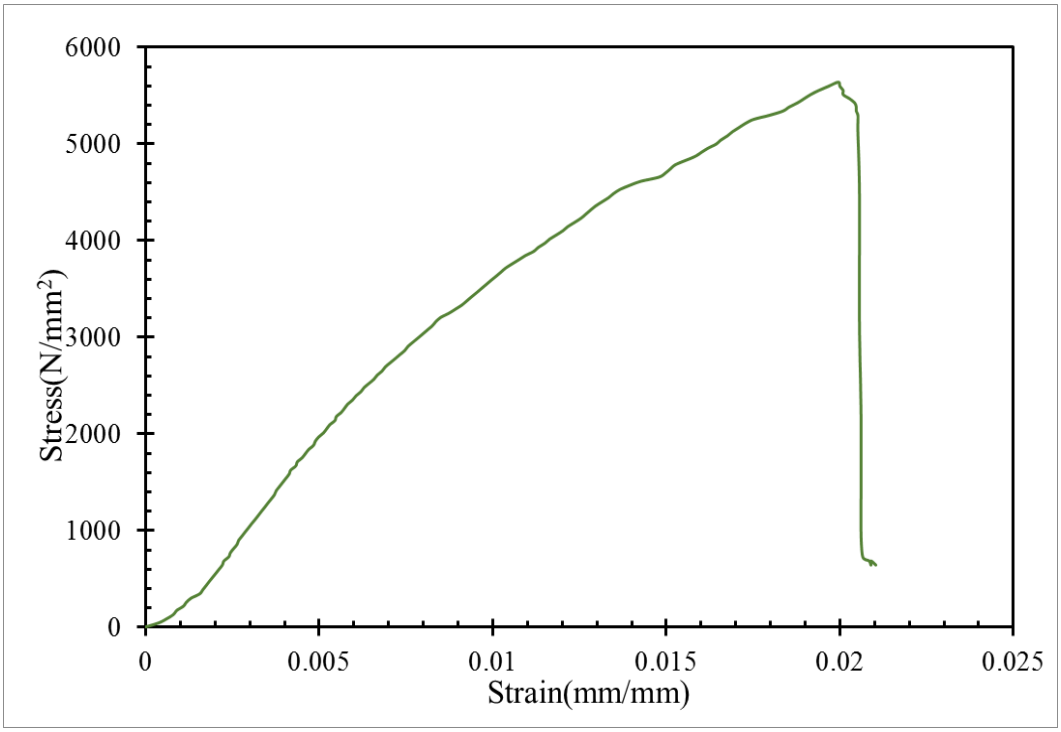

(b)

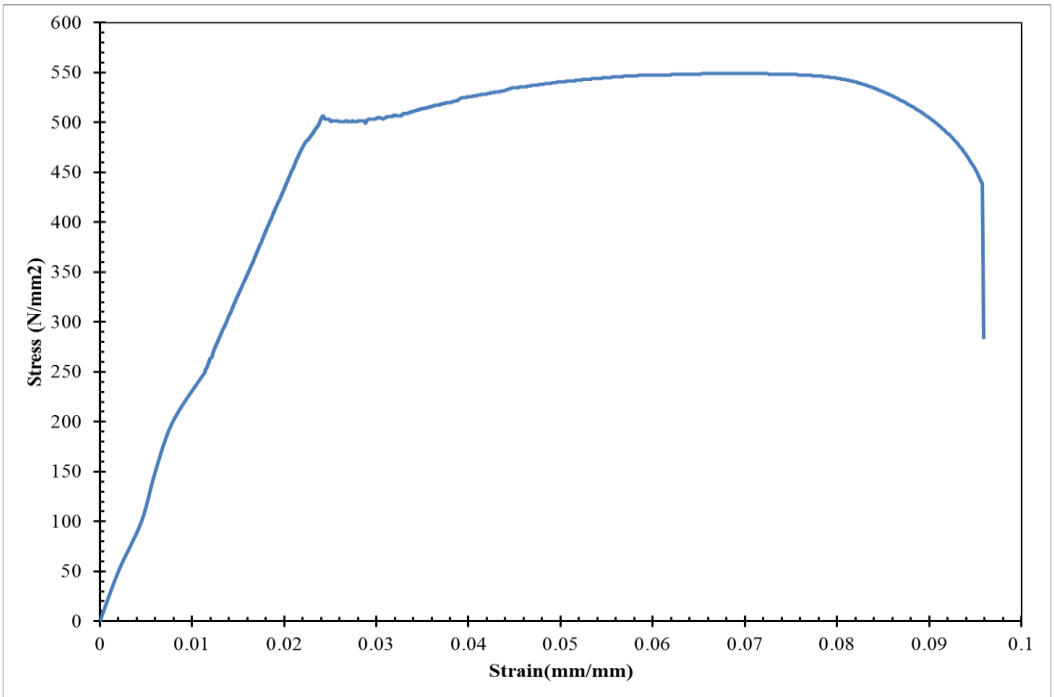

Figure 4.2. Stress strain curve for; (a) CFRP, and (b) steel

Table 4.1. Measured properties of steel, CFRP and Epoxy adhesive

	Steel	CFRP	Epoxy
Thickness (mm)	3	0.116	0.05
Elastic modulus (GPa)	206	230	2.4
Tensile strength (MPa)	473	4983	40
Yield strength (MPa)	508	-	-
Tensile strain (mm/mm)	0.25	0.021	-

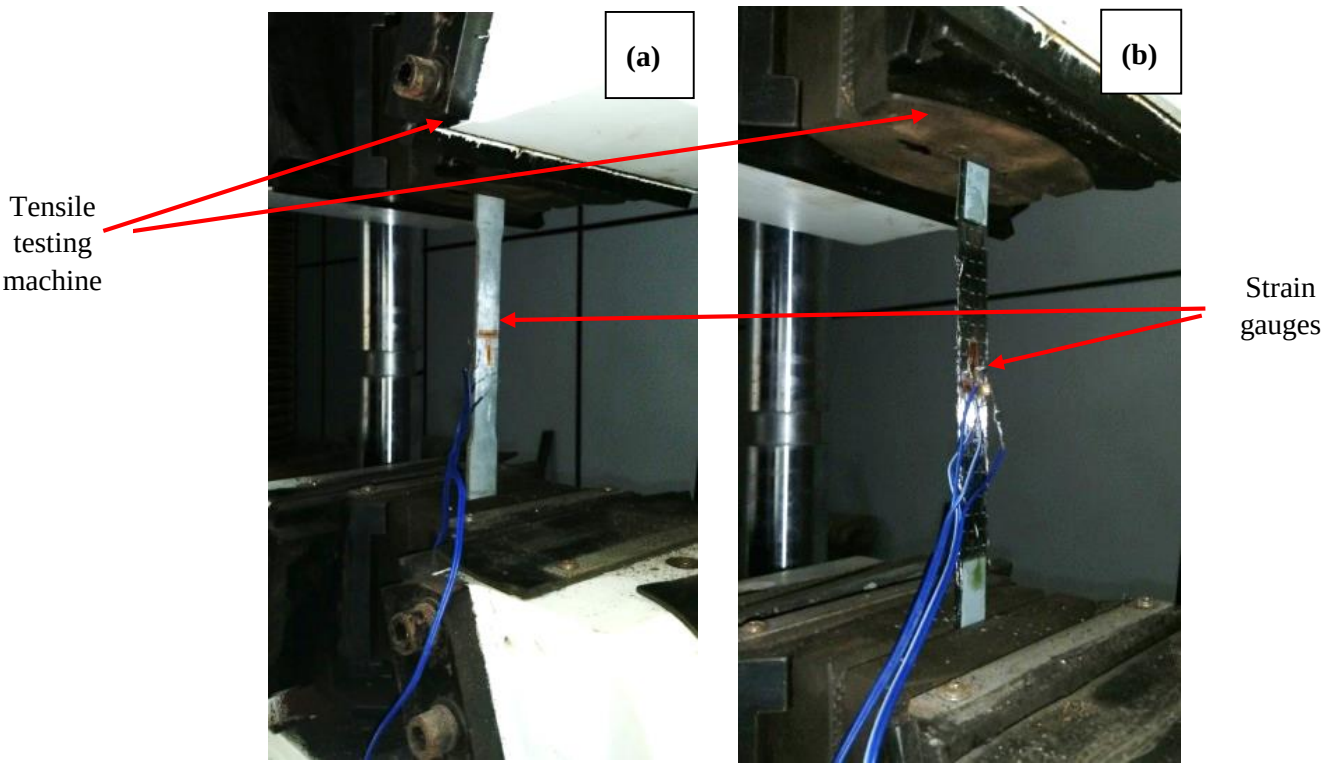

Figure 4.3. Coupon Tests on; (a) steel, and (b) CFRP

4.2.2 Specimens preparation

A total of 16 samples were prepared using 3 mm thick steel hollow tubes with 101.6 mm outer diameter. The horizontal span of the specimens was kept at a constant value of 1200 mm. Four of these beams were kept as straight beams while the remaining 12 beams were bent (Figure 4.4) to have three different radii of 2000 mm, 4000 mm and 6000 mm. Three beams from each radius were strengthened with CFRP and one sample from each category was tested as a control sample.

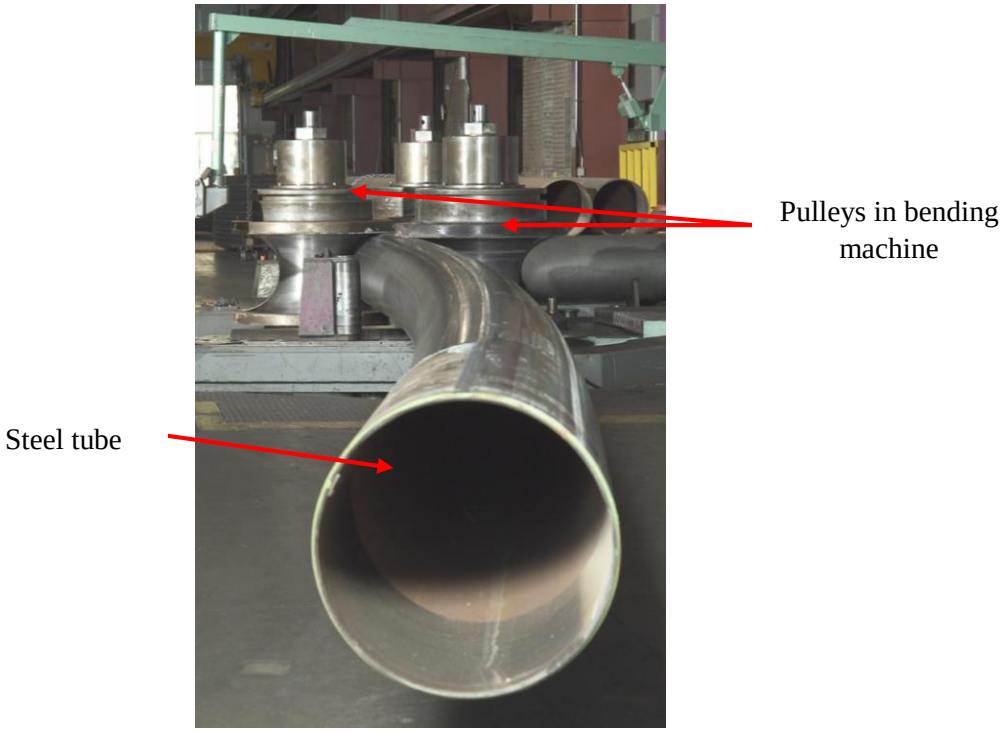

Figure 4.4. Bending of steel tubes

The surface preparation is of utmost importance to obtain a perfect bond between steel substrate and CFRP patch (M. H. Kabir, Fawzia, Chan, Gamage, et al. 2016). As reported in the literature, there are few common methods available to prepare the steel substrate; sand blasting, grit blasting, solvent cleaning and surface grinding(Baldan 2004c; D. Fernando et al. 2008). Past studies revealed that, grit or sand blasting as the most effective surface preparation method among these(Baldan 2004c; Mahmoud and El-Salakawy 2012). Since the current study involves a large surface area to be prepared, a relatively cheap and locally available surface preparation method was required. Sand blasting using garnet abrasive technique was one of the reliable methods and was adopted. The sand blasted surfaces were then cleaned using acetone to remove the loose particles from the surface (El Damatty, Abushagur, and Youssef 2003) prior to applying three strain gauges on the bottom surface of the beam one at the mid span and other two at the end positions of the CFRP layer as shown in Figure 4.5.

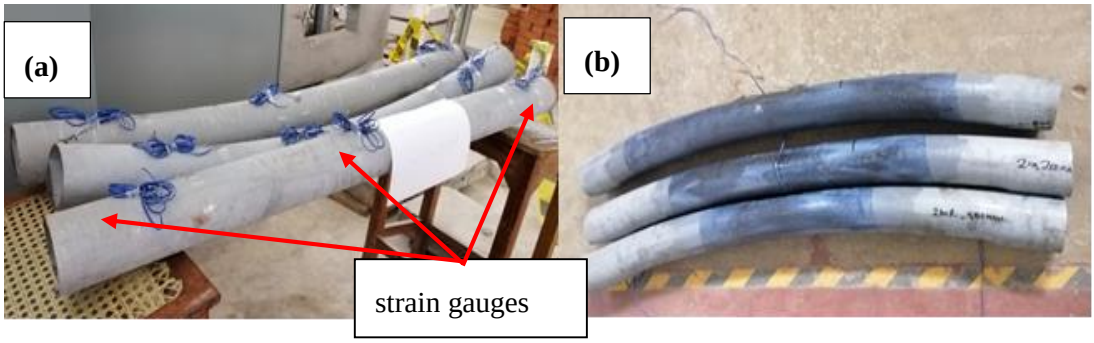

Figure 4.5. (a) Un-strengthened (b) strengthened beams

An adhesion promoter was applied on to the prepared surfaces for bonding and kept approximately for one hour for drying before applying the adhesive layer. CFRP sheets were cut into different lengths of 500 mm, 750 mm and 1000 mm with a suitable width such that an overlap of 30 mm exists once they are wrapped on the steel tube. Two parts epoxy adhesive were selected to stick CFRP to the steel (Sika adhesive group 2009) and a single layer of CFRP sheet was applied on the adhesive following the wet layup method and immediately a rib roller was run in the longitudinal fibre direction on the CFRP until adhesive and entrapped air bled out. This rib rolling also facilitates to obtain a uniform adhesive layer thickness to avoid stress concentrations. After rolling another layer of adhesive was applied at either end of the CFRP and also along the overlap to ensure the avoidance of pre-mature debonding failure of CFRP. Figure 5 shows the specimens prepared before and after applying CFRP. A descriptive diagram of the curved beam is given in Figure 4.6.

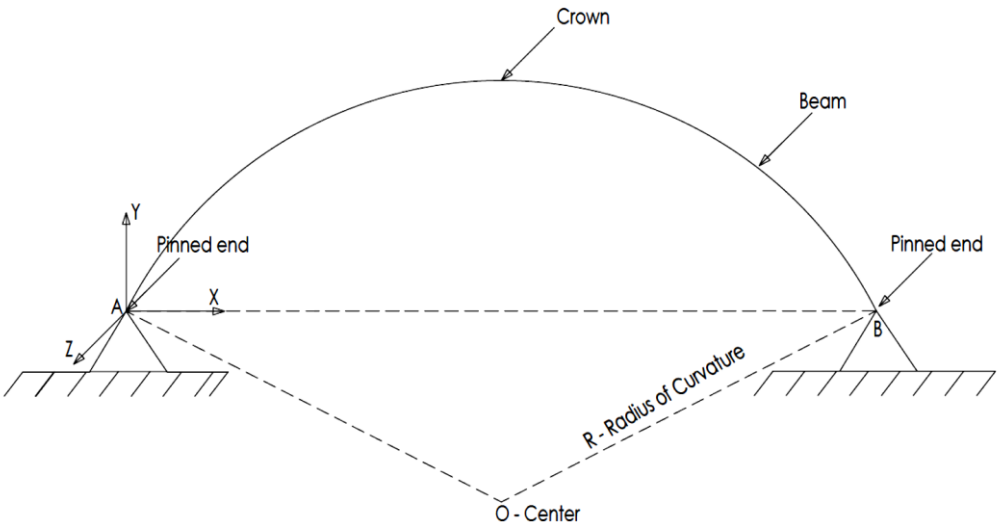

Figure 4.6. Description diagram of vertically curved beam

All the beams were tested under simply supported conditions using three point bending tests in according to the method adopted by previous researchers (Mamalis et al. 2006; Rathnaweera et al. 2012). Tests were conducted using the loading frame available in the structural testing laboratory of University of Moratuwa. A 250 kN capacity load cell was used to transfer the load to the beams at a constant rate of 0.5 mm/min until failure. Two LVDTs were set at 150 mm on either side of the mid span to measure the deflection. Figure 4.7 shows the test set up and instrumentation.

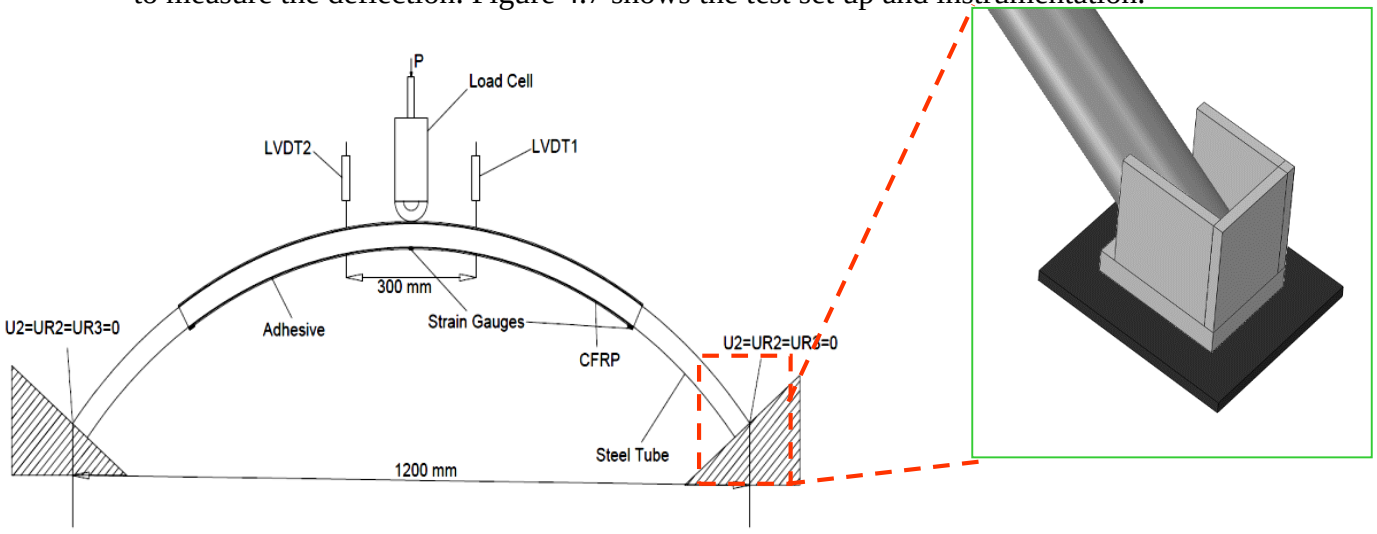

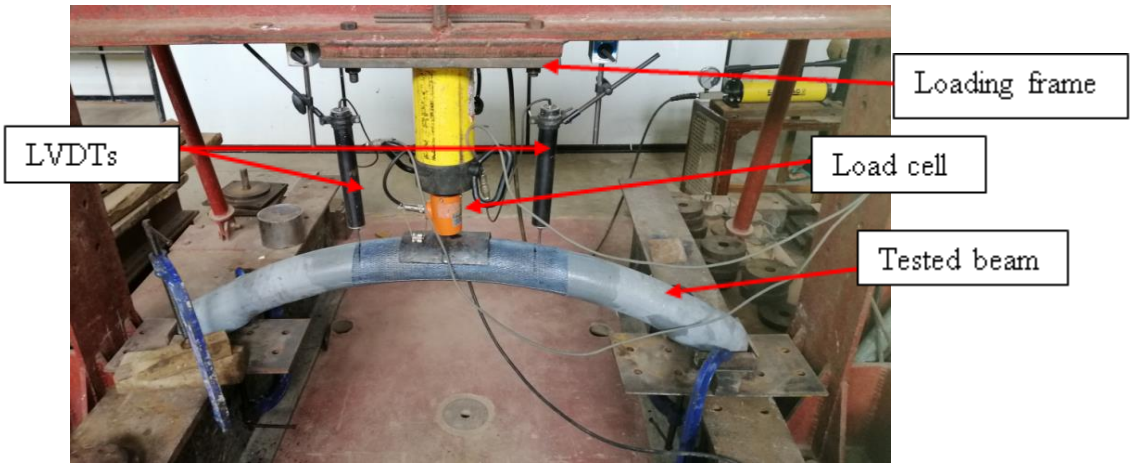

Figure 4.7. Test setup and instrumentation

4. 3. Experimental Results

All un-strengthened and strengthened beams (straight and curved) with various CFRP lengths (0 mm, 500 m, 750 mm and 1000 mm) were tested until failure of CFRP or bearing failure of SCHS. The transient loads and the corresponding deflections and strain variations were noted. The ultimate load of each strengthened beam was compared with that of the corresponding un-strengthened beam. Failure initiation and propagation were also monitored. Furthermore, these failure patterns were used to validate the theoretical predictions.

4.3.1. Failure mechanisms

The four major failure modes observed in both un-strengthened and strengthened beams with different curvatures and different CFRP lengths are shown in Figure 4.8 and are discussed as follows. All un-strengthened beams exhibited the failure mode of local buckling (Mode E) near the loading point at the compression zone, irrespective of curvature. Beams with 500 mm long CFRP failed due to end debonding following the rupture in the fibre direction irrespective of the radius of curvature. This failure can be due to the high stress concentration developed at the ends of CFRP

layers which could not be withstood by the adhesive. For beams with CFRP length 750 mm, a slight debonding at the ends of the CFRP was observed. Then local buckling started in the SCHS near the loading point at the compression zone following the CFRP fibre rapture near the same area. No end debonding failure was observed for the beams with 1000 mm long CFRP sheets. Those beams failed due to local buckling of SCHS near the loading point which led to the CFRP fibre rupture. It can therefore be deduced that the failure modes of strengthened beams were governed by the length of the CFRP which had an effect on the different strain levels within the adhesive. Figure 8 shows the variation of strain within the adhesive at the edges of CFRP layer for various CFRP lengths for beams with 2000 mm radius of curvature. It clearly indicates that strain levels of the adhesive exceed its ultimate strain value before failure in beams with 500 mm long CFRP. Therefore, CFRP debonding has occurred in these beams. However, for the beams with 750 mm and 1000 mm CFRP lengths the strain in the adhesive does not exceed its ultimate value before local buckling of steel tube occurs and hence no debonding could be observed.

It was observed that the failure modes of both un-strengthened and strengthened beams were not influenced by the curvature of the beam. Failure modes for all beams with the different curvatures depended only on the length of CFRP wrapping.

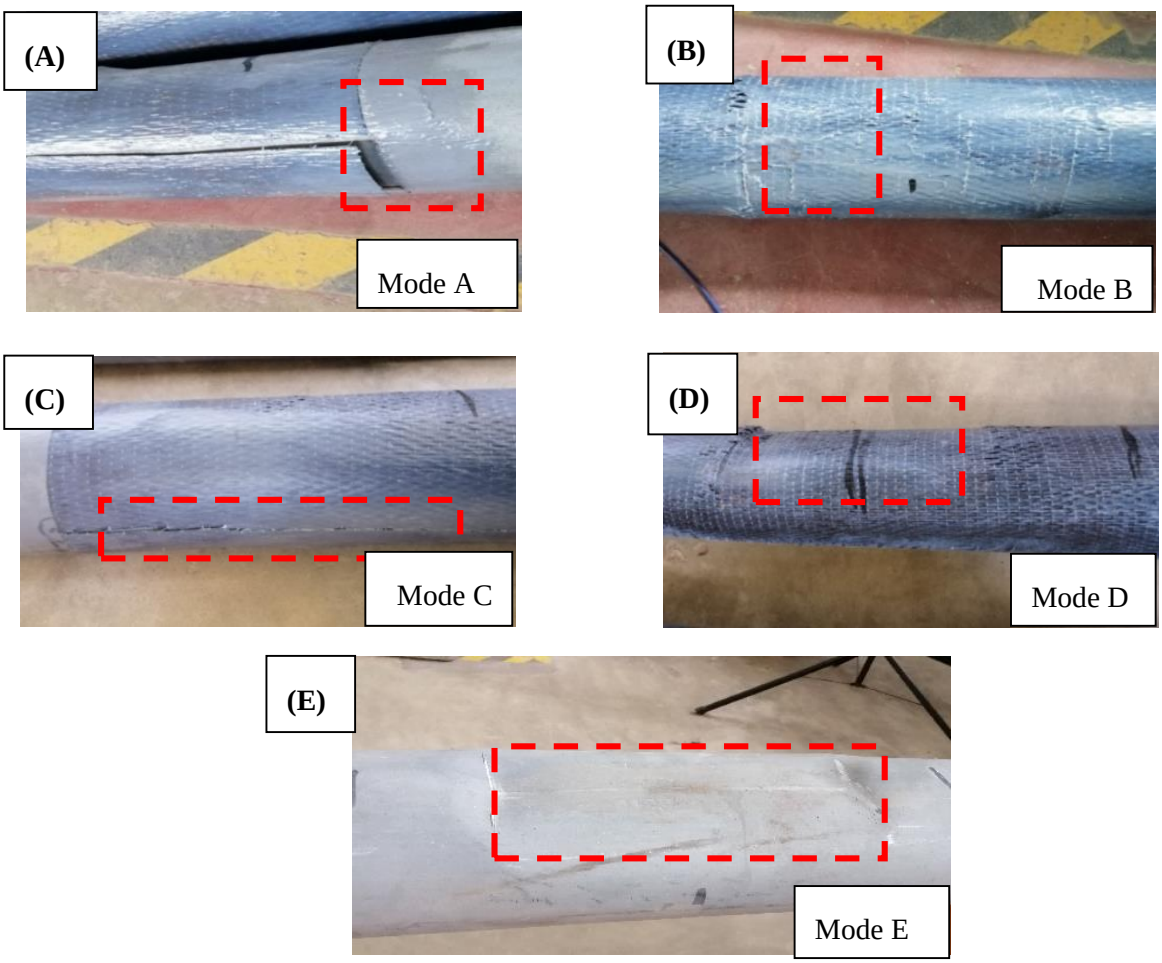

Figure 4.8. Major failure modes of tested beams; (A) end debonding (B) CFRP crushing close to the loading point (C) fracture of CFRP at the tensile face opposite side to the load (D) local bucking of steel tube near the loading point (E) Ductile failure of steel tube near the loading point

4.3.2. Strain variations

Figure 9 shows the strain variations in the adhesive at the edge of CFRP layer, for CFRP strengthened curved beams with different curvatures and CFRP lengths. It clearly indicates that the strains in the beams with 500 mm CFRP lengths exceed the ultimate strain in adhesive. This causes the debonding of CFRP sheet. For the beam with 750 mm CFRP, strain in adhesive attained close to the ultimate value and hence slight debonding is observed. However, for beam with 1000 mm CFRP length adhesive strain was well below the adhesive ultimate strain and hence no debonding

is observed in that beam. The strain variations in Figure 12(b) and Figure 12(c) for beams with 4000 mm curvature and 6000 mm curvature respectively, show identical variations of strain compared to beams with 2000 mm curvature. Ultimate strain in adhesive is shown in each diagram.

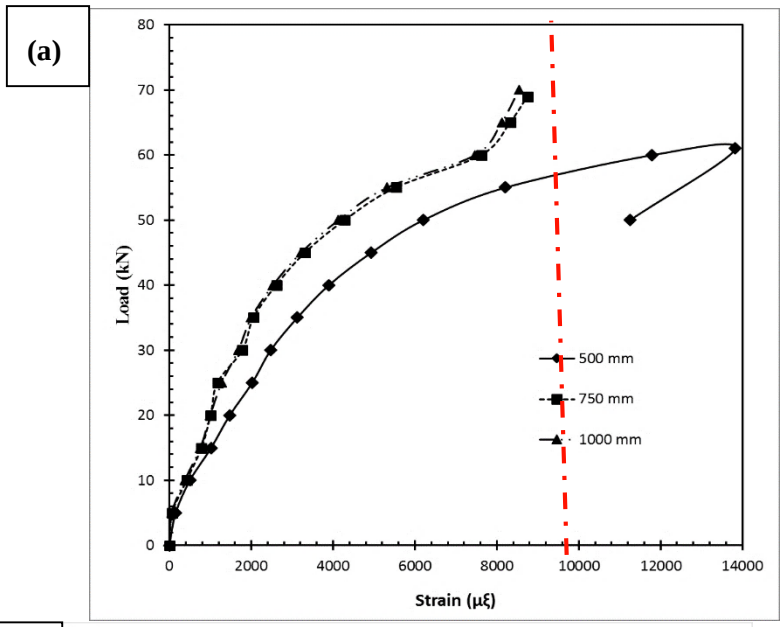

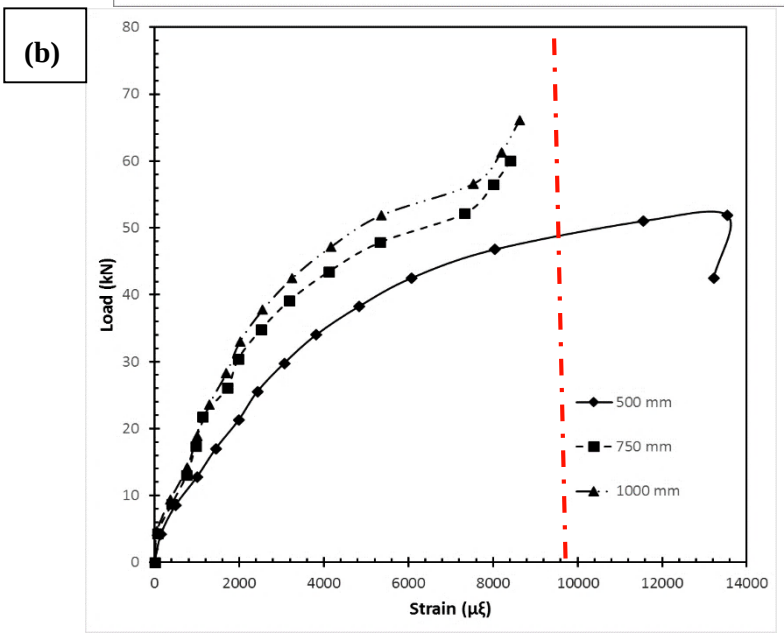

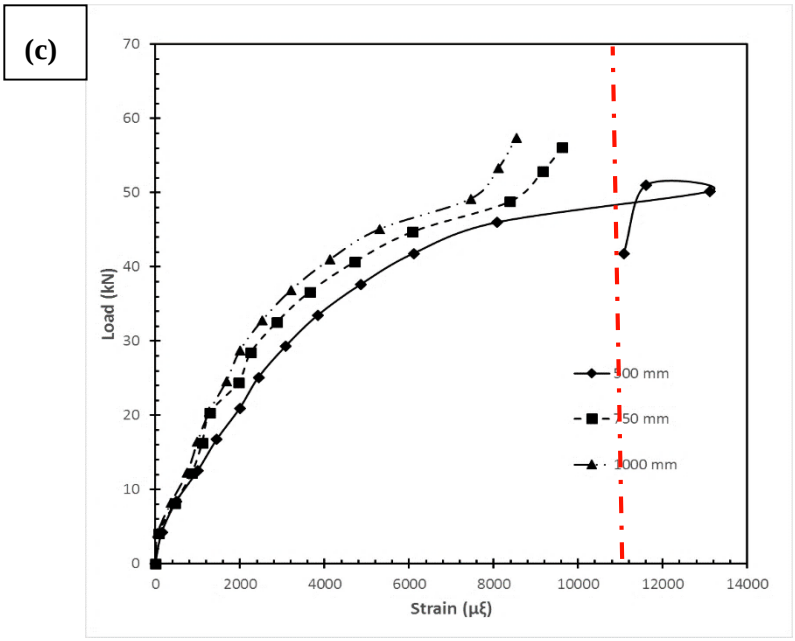

Figure 4.7. Variations of strains in adhesive layer for various CFRP lengths for beam with: (a) 2000 mm curvature, (b) 4000 mm curvature' and (c) 6000 mm curvature

4.3.3 Failure Loads

Table 2 shows the ultimate loads, strength gain and failure mechanisms of both strengthened and un-strengthened beams. It is clearly observed that the ultimate load increases when CFRP length increases in straight beams while the ultimate load increases up to 750 mm CFRP length and a slight reduction was appeared when the length is 1000 mm. This may due to the inefficient load transfer to CFRP due to the relatively larger distance from the loading point.

The highest load carrying capacities of un-strengthened beams were observed in curved beams with radius of 2000mm. When the radius of curvature increases the ultimate loads were observed to be reduced. Compared to straight un-strengthened beams the percentage increments of ultimate loads for beams with 2000 mm, 4000 mm and 6000 mm radii were 40%, 32% and 21%, respectively.

The highest load increment was observed in straight beams with 1000 mm long CFRP. The highest load at 52.7kN is an increase of 31% compared to that in the un-

strengthened beam. For straight beams with 500 mm and 750 mm CFRP lengths the percentage load increments compared to the bare (un-strengthened) beam were 3% and 28%, respectively. Figure 4.8 shows the failure (ultimate) loads observed in the tested beams. The highest load increment for 750 mm CFRP was observed in beams with 2000 mm radius and is 24% which is 5% greater than that in beams with 4000 mm radius of curvature and 10% greater than beams with 6000 mm radius of curvature. The highest percentage increases of 9%, 24% and 23% in the ultimate loads occurred in the beams of 2000mm radius with 500 mm, 750 mm and 1000 mm CFRP lengths respectively. Of the curved beams, the lowest tensile stress developed within the tensile face of the beam with the highest radius and this value is slightly lesser than that in the straight beams. This variation might be due to the reduction in residual stress caused by beam bending(D. Brown 2007). The strengthened curved beams showed similar trends of strength gain irrespective of the beam curvature.

Table 4.2. Details of test specimens, ultimate loads and failure modes

Beam ID	Radius of Curvature (mm)	CFRP Length (mm)	P_u(kN)	(P_u/P_s)%	δ_u(mm)	δ_u/δ_s	Failure Mode	
ST_0	0	0	40.2	-	19.2	1.0	C	
ST_500		500	41.5	3	23.0	1.2	A/B	
ST_750		750	51.6	28	35.1	1.8	A/C/D	
ST_1000		1000	52.7	31	31.6	1.6	C/D	
2R_0	2000	0	56.2	-	29.7	1.0	C	
2R_500		500	61.2	9	24.3	0.8	A/B	
2R_750		750	70.0	24	41.2	1.4	A/C/D	
2R_1000		1000	68.9	23	40.4	1.4	C/D	
4R_0	4000	0	52.9	-	25.8	1.0	C	
4R_500		500	55.6	5	24.5	0.9	A/B	
4R_750		750	63.3	20	33.1	1.3	A/C/D	

4R_1000		1000	60.9	15	36.1	1.4	C/D	
6R_0	6000	0	48.8	-	28.3	1.0	C	
6R_500		500	51.6	6	27.6	1.0	A/B	
6R_750		750	55.8	14	35.1	1.2	A/C/D	
6R_1000		1000	55.0	12	31.2	1.1	C/D	

In Table 2, the failure modes are denoted as: A- CFRP end debonding; B- CFRP rupture in tensile face; C- Local buckling of tube near loading point; D- CFRP rupture close to loading point and ultimate loads and mid span deflections at ultimate loads are denoted as; P_u- ultimate load of strengthened beams; P_s- Ultimate load on un-strengthened beam; δ_u- mid span deflection at ultimate for strengthened beams; δ_s- mid span deflection at ultimate for un-strengthened beams.

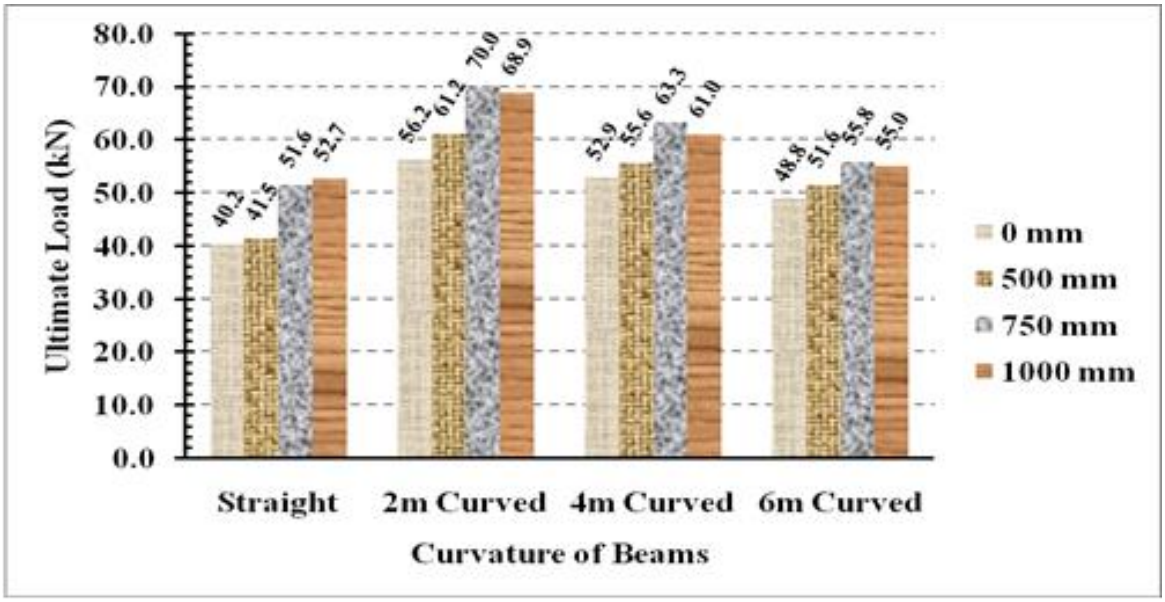

Figure 4.8. Variation of Ultimate Load with CFRP Length for Beams with Different Radii of Curvature

Figure 4.9 shows the final deflected shapes of beams with various curvatures and CFRP lengths. It can be seen that the deflected shapes of all these beams show the same trend. For curved beam with 2000 mm radius, some curvature is evident in the deflected beam even after failure. For the straight beams final deflected shape

indicates negative curvature while beams with 4000 mm and 6000 mm radii seem almost straight.

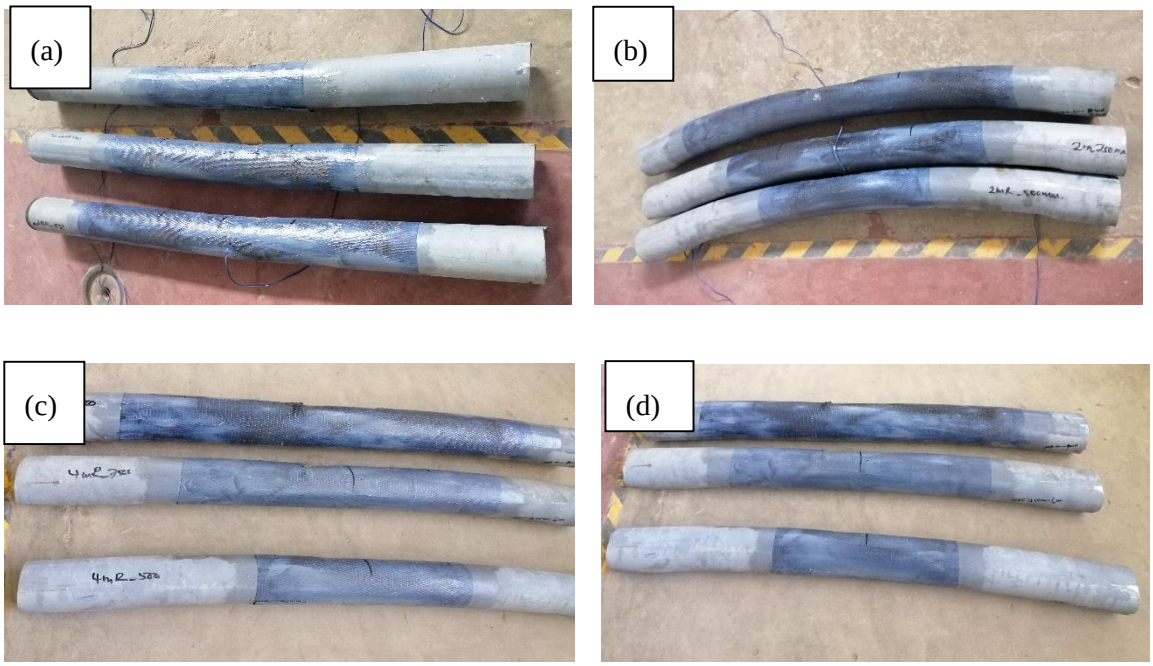

Figure 4.9. Deflected shapes of strengthened beams with different radii R and CFRP lengths (a) straight (b) 2000 mm (c)4000 mm and (d) 6000 mm radii.

3.3 Mid Span Deflection

Load-deflection responses of both un-strengthened and strengthened beams for each radius of curvature and CFRP length are given in Figure 4.10. All the strengthened beams show a higher stiffness than the un-strengthened beams within both elastic and plastic limits. This variation in stiffness was highlighted more within the plastic region. It can be clearly seen that the deflections at failure for strengthened beams with 750 mm and 1000 mm CFRP lengths are greater than those of un-strengthened beams. Beams with 500 mm CFRP lengths show lower deflections at failure compared to un-strengthened beams due to premature deboning of CFRP for all tested beams irrespective from their radii. Until 40 kN load level, deflections of strengthened 2000 mm radius curved beams were almost the same. These curved beams strengthened with 750 mm and 1000 mm CFRP lengths show 39% and 35% increase in deflections

respectively at ultimate load. Strengthened beams with 4000 mm and 6000 mm radii show the same trend, but the deflections were close to each other only up to a load of 30 kN. Highest increments of 20%, 83% and 65% in mid span deflections at ultimate loads were observed in straight beams with 500 mm, 750 mm and 1000 mm CFRP lengths, respectively.

Variation of the experimental ultimate load with CFRP wrapping length for each beam with different curvature is shown in the Figure 4.11(a). It clearly shows that for each CFRP length, the maximum ultimate load was found in 2000 mm radius curved beam. Ultimate loads of beams for each CFRP length gradually decreases when the radius of the beam increases. For each beam ultimate load capacity increases until CFRP length increases to 750 mm and a small reduction was noted when CFRP length greater than 750 mm. Therefore, it can be deduced that the ultimate loads for a strengthened beam attains the highest value when CFRP length is750 mm. At this point the ratio between the CFRP length to total length of beam is 0.625.

(a)

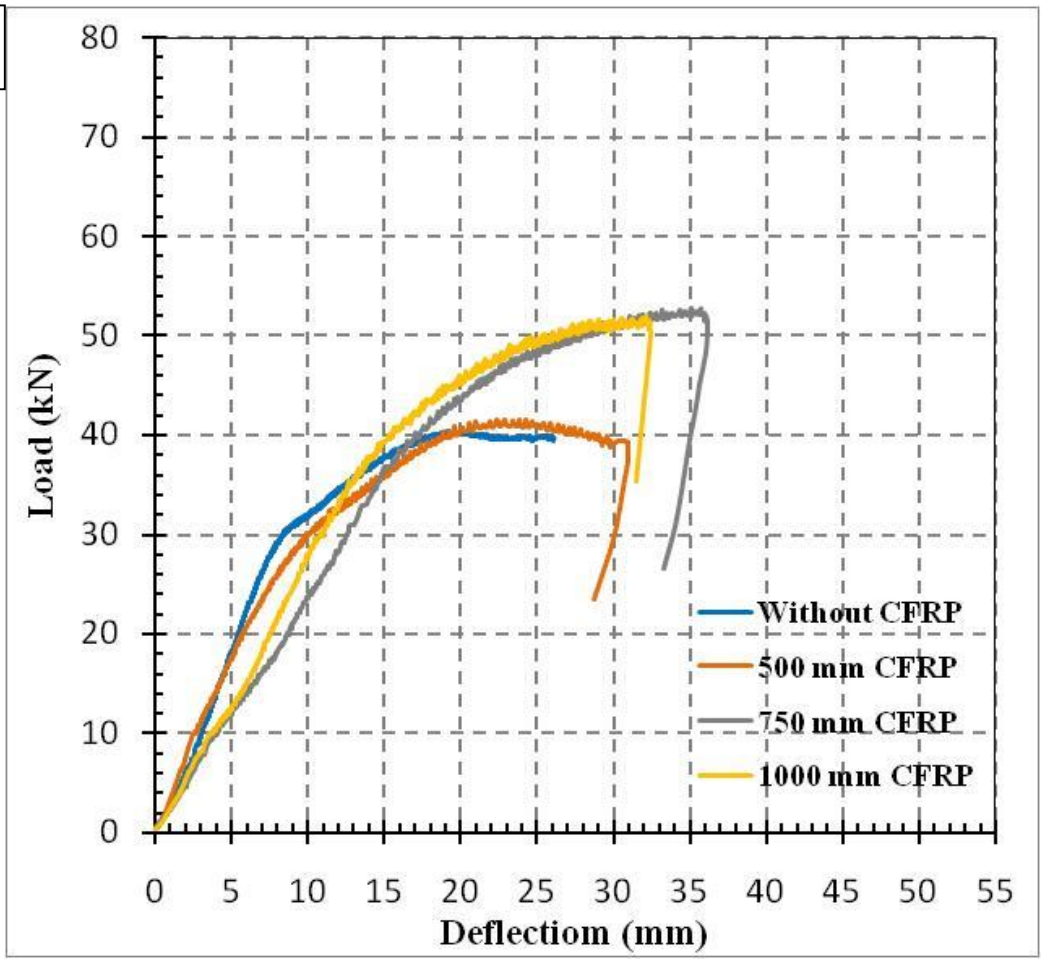
Load (kN)
Deflectiom (mm)
Without CFRP
500 mm CFRP
750 mm CFRP
1000 mm CFRP

(b)

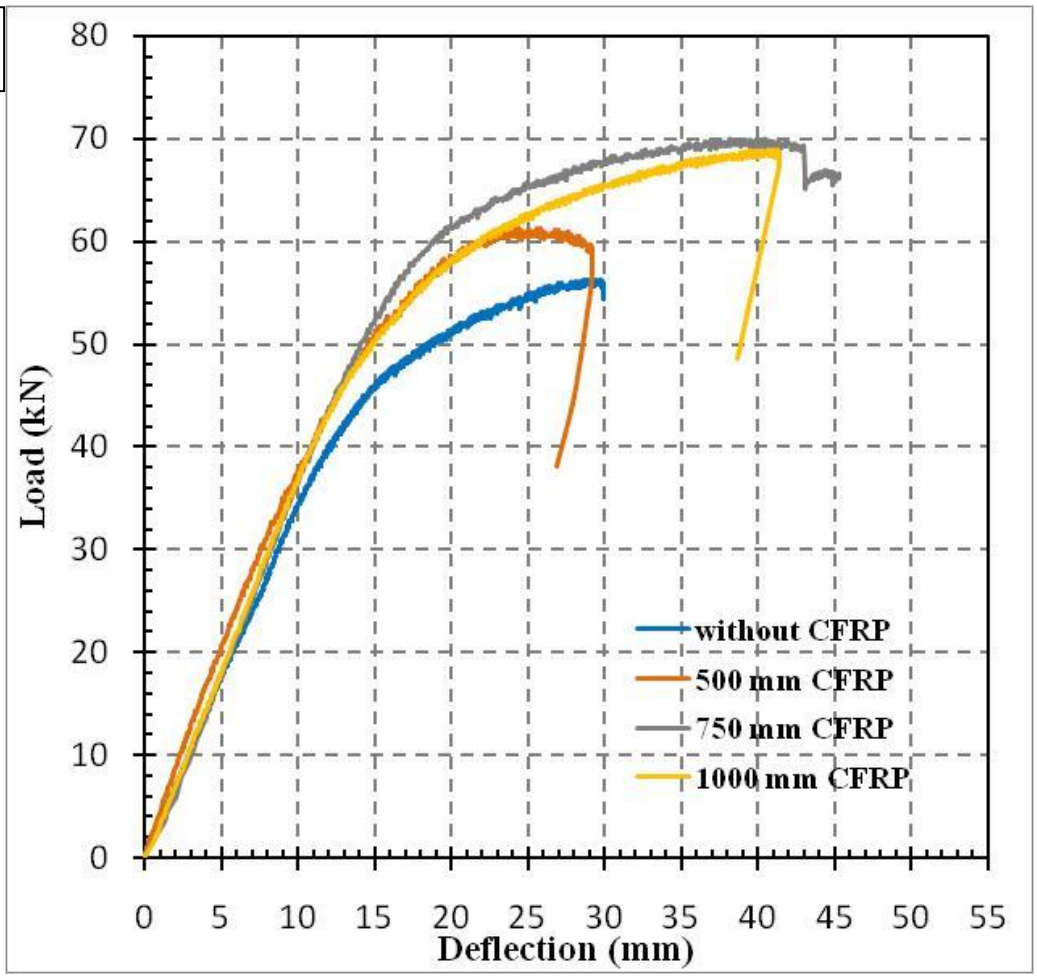
Load (kN)
Deflection (mm)
without CFRP
500 mm CFRP
750 mm CFRP
1000 mm CFRP

(c)

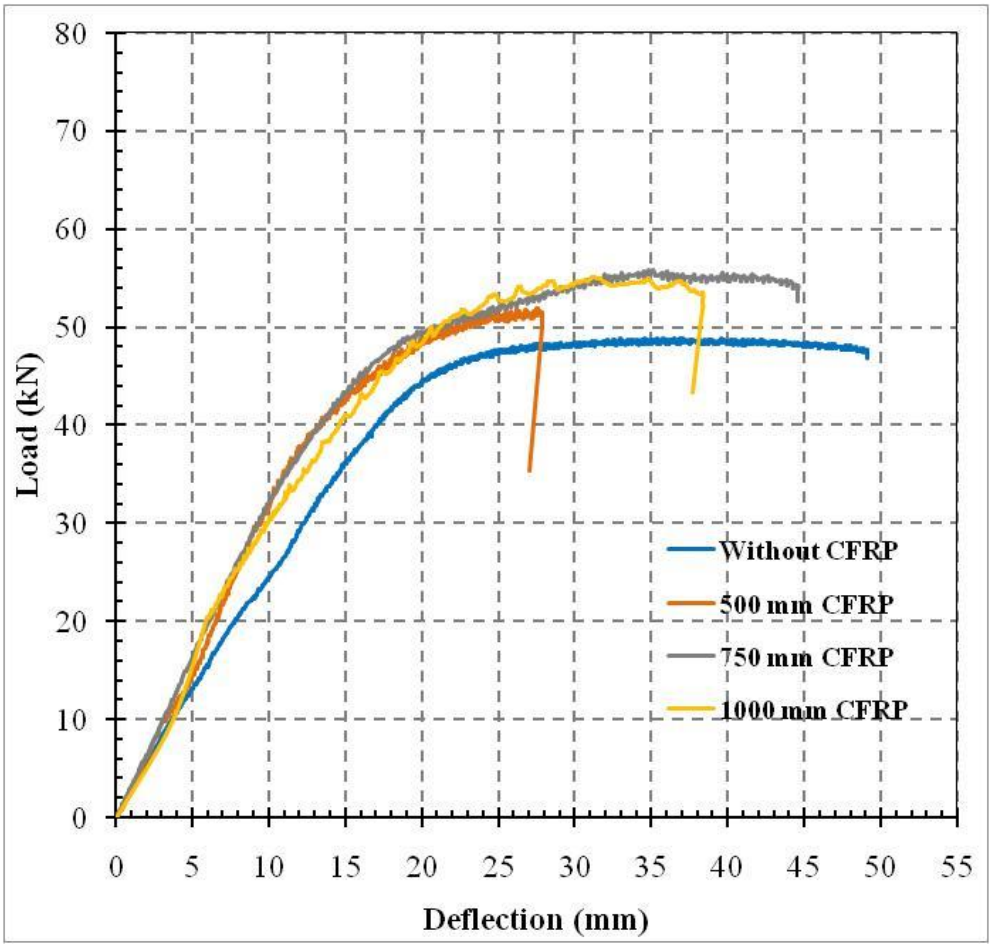
Load (kN)
Deflection (mm)
Without CFRP
500 mm CFRP
750 mm CFRP
1000 mm CFRP

(d)

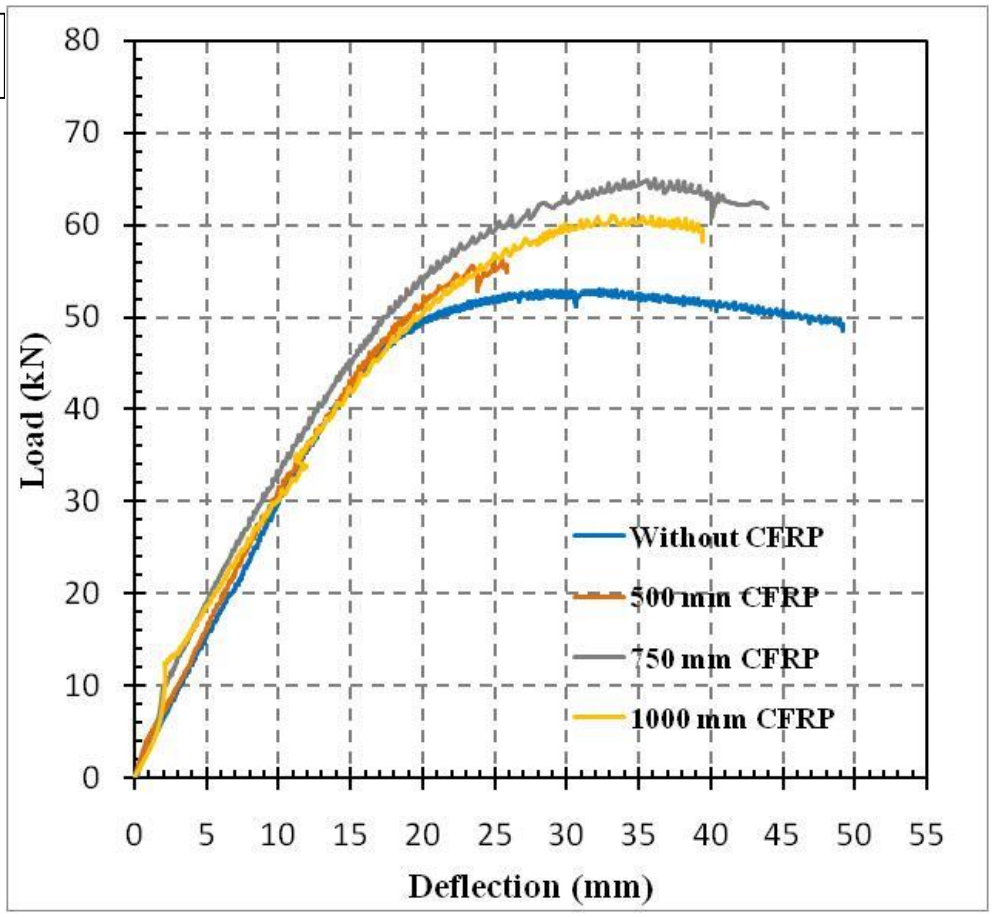
Load (kN)
Deflection (mm)
Without CFRP
500 mm CFRP
750 mm CFRP
1000 mm CFRP

Figure 4.10. Load-deflection curves for curved beams with different radii of curvature and CFRP-bonded lengths: (a) straight beam, (b) 2 m curved beam, (c) 4 m curved beam, and (d) 6 m curved beam

Figure 4.11(b). shows the variation between mid- span deflection with respect to CFRP length for beams with different radii. It can be clearly seen that the highest mid span deflections for 750 mm and 1000 mm CFRP lengths were observed in 2000 mm radius curved beams. For straight beams and 6000mm radius curved beams, deflections for 750 mm and 1000 mm CFRP lengths are almost the same. Except 4000mm radius curved beams, the maximum deflections at ultimate load occurred in the beams with 750 mm CFRP length. All the beams showed the same trends for ultimate loads and mid span deflection for various CFRP lengths.

Mid span deflections at ultimate loads for beams with different radii and CFRP lengths presented in Table 2. For beam with 6000 mm radius and 500 mm CFRP, deflection at ultimate load is smaller compared to the un-strengthened beam. The deflections at the ultimate load for straight beams and 4000 mm radius curved beams have increased irrespective of CFRP length. For the 2000 mm curved beam, the mid span deflection at the ultimate load for 500 mm CFRP length is less compared to un-strengthened beam, but it increases for 750 mm and 1000 mm CFRP lengths.

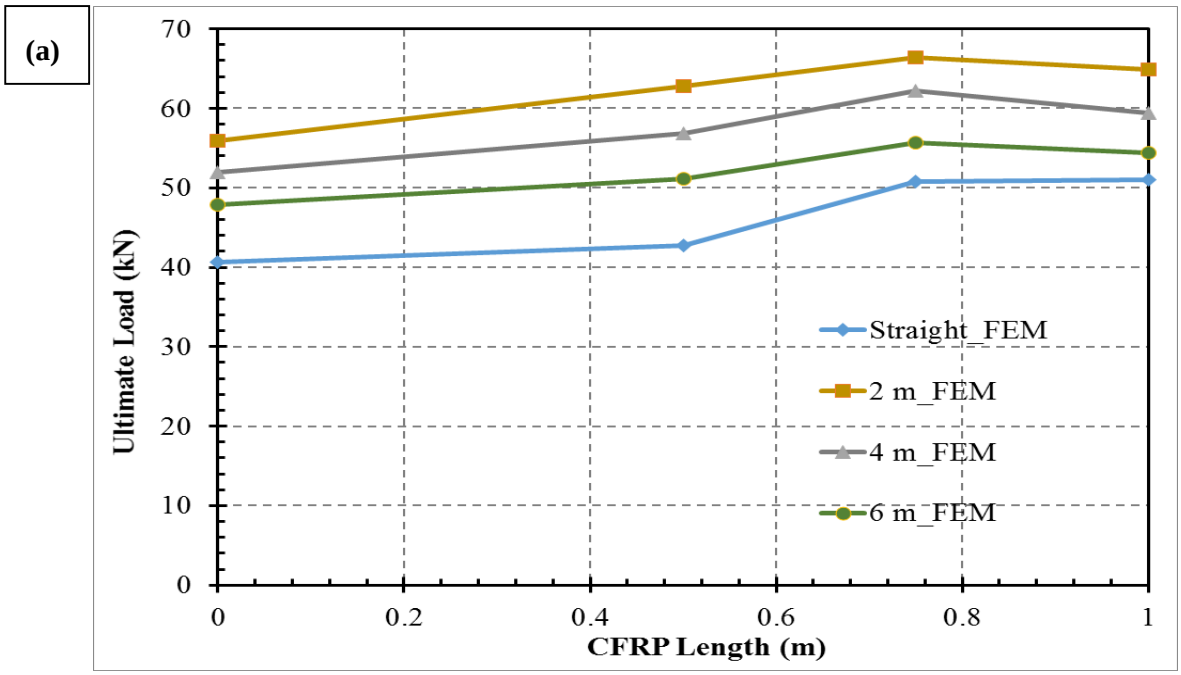

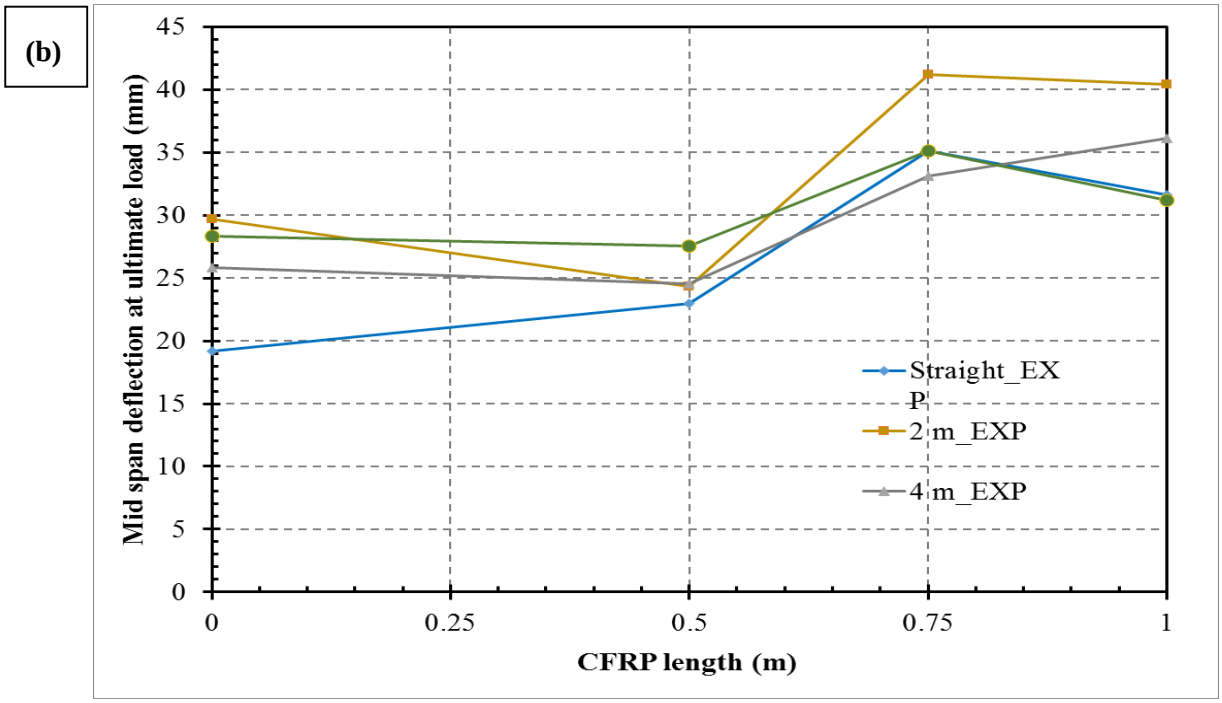

Figure 4.11. Variation of (a) ultimate load (b) mid span deflection at ultimate loads for various CFRP lengths for curved beams

4.4. Analytical Study

In this section an analytical model for curved steel tubular beams strengthened with CFRP is proposed using Maxwell-Mohr integral. Elastic deformations of un-strengthened and strengthened curved beams were evaluated using the conjugate beam method presented in the literature[36]. This method was developed considering not only the bending moment but also the axial force developed in curved beams. Figure 4.12 shows two inclined parts of a beam with lengths S_n and S_{n+1} are subjected to bending moments and axial forces. By assuming the axial forces $\overline{N}_n$ and $\overline{N}_{n+1}$ are constants, axial forces in the unit states are $\overline{N}_n = -sin\beta_n/\lambda_n$ and $\overline{N}_{n+1} = -sin\beta_{n+1}/\lambda_{n+1}$ for the left and right portions respectively. Calculation of these forces are shown in Figure 14, at joints A and B.

S_n - Length of the nth section
M_n - Bending moment at nth node
E - Elastic modulus of beam material
I_n - Moment of inertia for nth section
β_n - Horizontal inclination of nth section
λ_n- Vertical projection of axial force of nth section

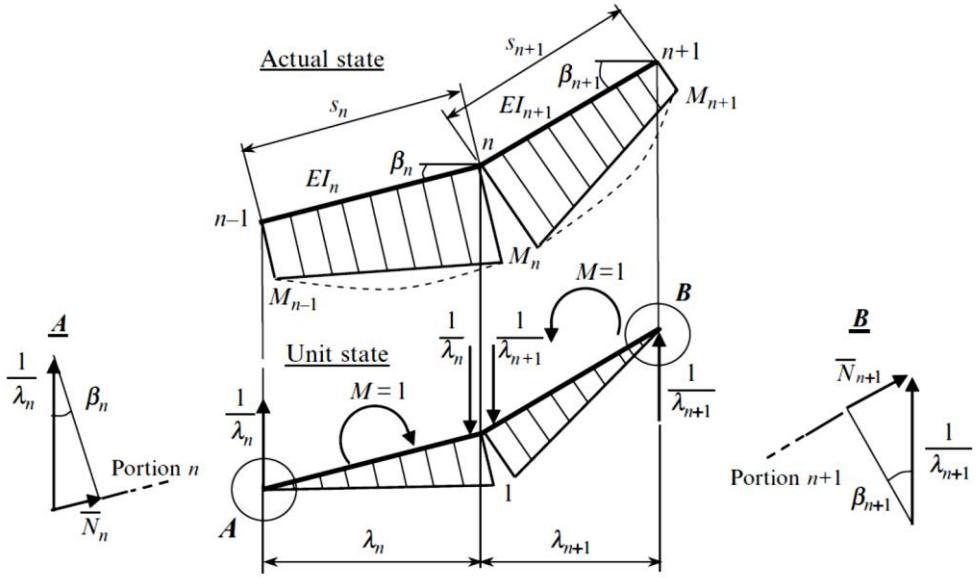

Figure 4.12. Loads acting on left and right portion of curved beams

For left portion using Maxwell and Mohr integral (Igor A. Karnovsky 2012) for bending moment will give the elastic load on the beam due to bending moment

$$W_n(M) = \sum \int_0^l \overline{M} \frac{M_p}{EI} dx = \frac{s_n}{6EI_n}(2M_{n-1} \times 0 + 2M_n \times 1 + M_{n-1} \times 1 + M_n \times 0)$$
$$= \frac{s_n}{6EI_n}(M_{n-1} + 2M_n) \quad (4.1)$$

where M_p is the bending moment at the nth node due to vertical loads and $\overline{M}$ is the bending moment in the unit state. EI_n is the flexural rigidity of the beam portion considered.

By using Maxwell and Mohr integral for axial force will give the elastic load on the beam due to axial force $W_n(N)$;

$$W_n(N) = \sum \int_0^l \overline{N} \frac{N_p}{EA} dx = -\frac{1}{EA_n} \times \frac{\sin\beta_n}{\lambda_n} N_n S_n = -\frac{1}{EA_n} \times \frac{\sin\beta_n}{\lambda_n} N_n \frac{\lambda_n}{\cos\beta_n}$$
$$= \frac{N_n}{EA_n} \times \tan\beta_n \quad (4.2)$$

where N_p is the axial force at the nth node due to vertical loads and $\overline{N}$ is the axial force in the unit state. E is the elastic modulus of the beam portion considered and A is the cross sectional area of the beam.

Then the total elastic load on the beam is given by;

$$W_n = W_n(M) + W_n(N) \quad (4.3)$$

Substituting to (3) from (1) and (2) gives;

$$W_n = \frac{S_n}{6EI_n}(M_{n-1} + 2M_n) + \frac{S_{n+1}}{6EI_{n+1}}(2M_n + M_{n+1}) - \frac{N_n}{EA_n}\tan\beta_n + \frac{N_{n+1}}{EA_{n+1}}\tan\beta_{n+1} \quad (4.4)$$

For un-strengthened beam shown in Figure 4.13(i)

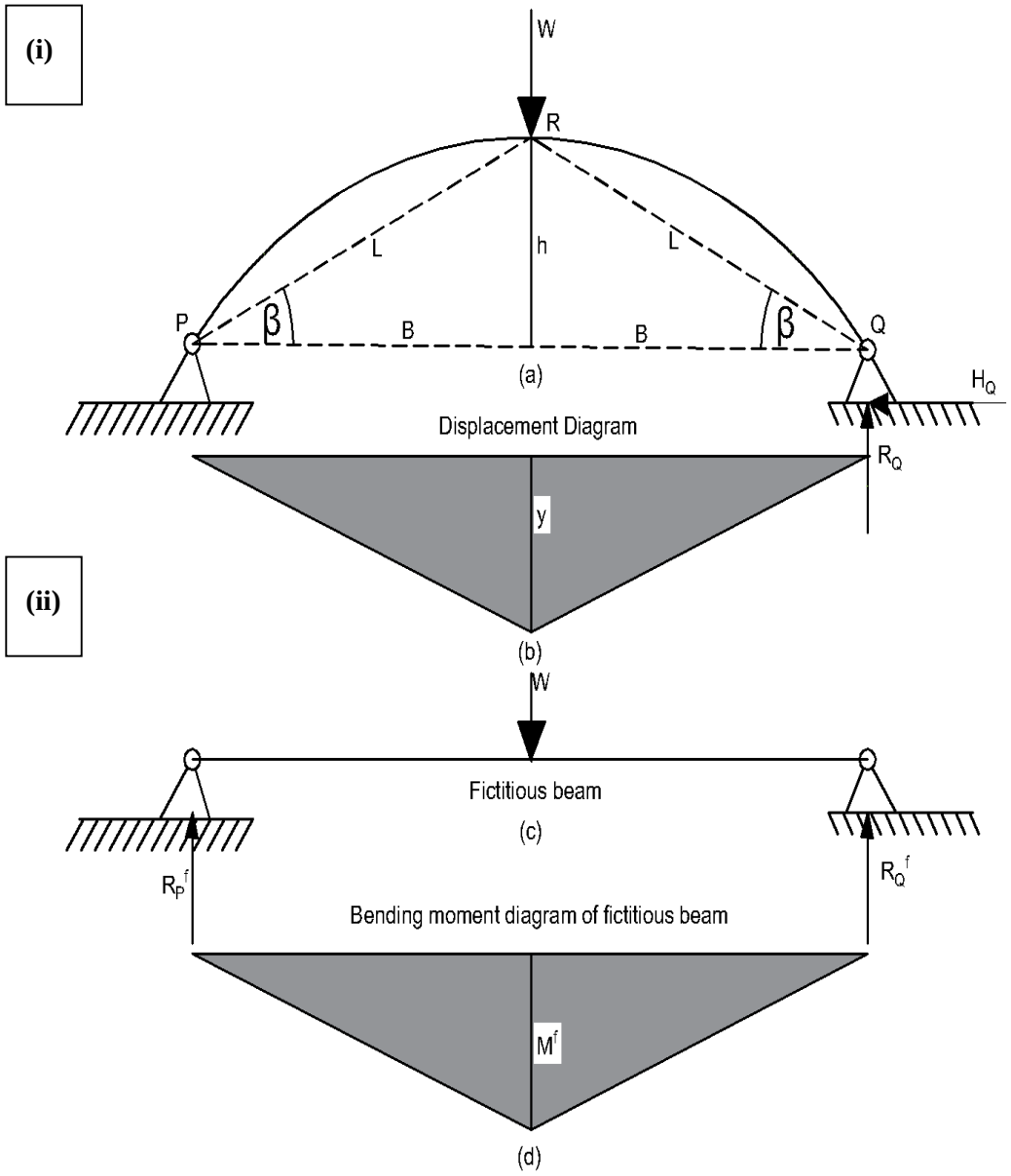

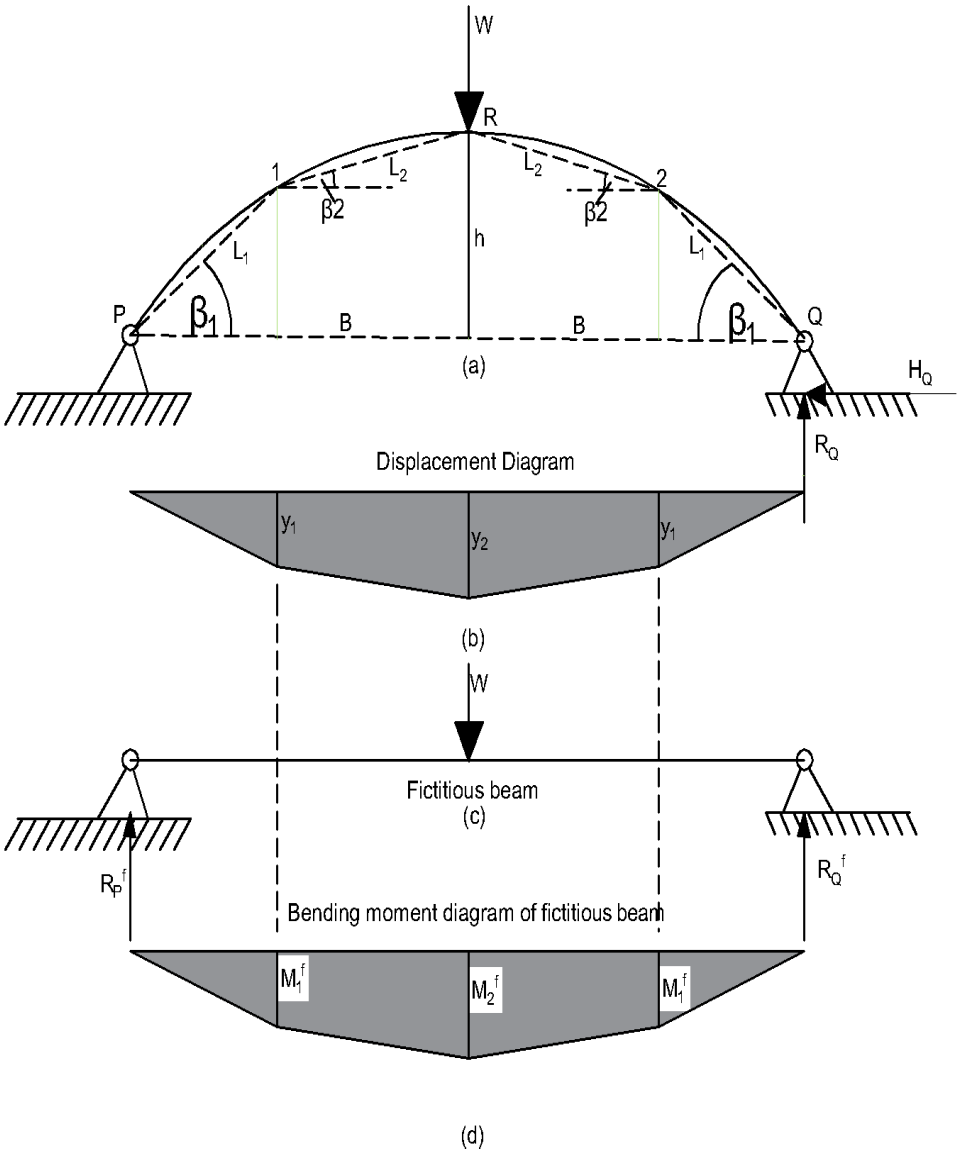

Figure 4.13. Curvilinear simply supported bar. (i) un-strengthened beam (ii) strengthened beam with; (a) Design diagram; (b) vertical displacements; (c) fictitious beam; (d) corresponding bending moment diagram

But,

$$s_n = s_{n+1} = L, I_n = I_{n+1} = I, A_n = A_{n+1} = A, \beta_n = \beta_{n+1} = \beta, M_{n-1} = M_{n+1} = 0, M_n = \frac{WB}{2},$$
$$N_n = N_{n+1} = W/2 \sin\beta$$

Substituting these values in (4) gives;

$$W_n = \frac{L}{6EI}\left(0 + 2\frac{WB}{2}\right) + \frac{L}{6EI}\left(2\frac{WB}{2} + 0\right) - \frac{W}{2EA}\frac{\tan\beta}{\sin\beta} - \frac{W}{2EA}\frac{\tan\beta}{\sin\beta}$$

$$W_n = \frac{WLB}{3EI} - \frac{W}{EA}\frac{1}{\cos\beta} \quad (4.5)$$

$$R_P^f = R_Q^f = \frac{W_n}{2}$$

$$M^f = y = R_P^f \times B = \frac{WB}{3EI}\left(LB - \frac{3I}{A\cos\beta}\right) \quad (4.6)$$

For Strengthened beams;

$$W_n(M) = \frac{s_n}{6EI_n}(M_{n-1} + 2M_n) + \frac{s_{n+1}}{6EI_{n+1}}(M_{n+1} + 2M_n) \quad (4.7)$$

$$W_n(N) = -\frac{N_n}{EA_n}\tan\beta_n + \frac{N_{n+1}}{EA_{n+1}}\tan\beta_{n+1} \quad (4.8)$$

By applying above (4.7) and (4.8) for the strengthened beam shown in Figure 4.13(ii);

For the PR section;

$$W_1(M) = \frac{L_1}{6EI}(0 + 2M_1) + \frac{L_2}{6EI_{eq}}(M_R + 2M_1) \quad (4.9)$$

$$W_1(N) = -\frac{N}{EA}\tan\beta_1 + \frac{N}{EA_{eq}}\tan\beta_2 \quad (4.10)$$

$$W_1 = \frac{L_1}{3EI}(M_1) + \frac{L_2}{6EI_{eq}}(M_R + 2M_1) + -\frac{N}{EA}\tan\beta_1 + \frac{N}{EA_{eq}}\tan\beta_2 \quad (4.11)$$

For the section 1-2 in Figure 4.13(ii);

$$W_2(M) = \frac{L_2}{6EI_{eq}}(M_1 + 2M_R) + \frac{L_2}{6EI_{eq}}(M_2 + 2M_R) \quad (4.12)$$

Since M_1=M_2;

$$W_2(M) = \frac{L_2}{3EI_{eq}}(M_1 + 2M_R) \quad (4.13)$$

$$W_2(N) = -\frac{N}{EA_{eq}}\tan\beta_2 - \frac{N}{EA_{eq}}\tan\beta_2 = -\frac{2N}{EA_{eq}}\tan\beta_2 \quad (4.14)$$

$$W_2 = \frac{L_2}{3EI_{eq}}(M_1 + 2M_R) - \frac{2N}{EA_{eq}}\tan\beta_2 \quad (4.15)$$

It is obvious that $W_1(M) = W_3(M)$ and $W_1(N) = W_3(N)$, where $W_1(M)$ is the $W_n(M)$ for section RQ and $W_3(N)$ is $W_n(N)$ for section RQ.

$$W_n(M) = 2\left[\frac{L_1}{6EI}.(2M_1) + \frac{L_2}{6EI_{eq}}(M_R + 2M_1)\right] + \frac{L_2}{3EI_{eq}}(M_1 + 2M_R) \quad (4.16)$$

$$W_2 = \frac{L_2}{3EI_{eq}}(M_1 + 2M_R) - \frac{2N}{EA_{eq}}\tan\beta_2 \quad (4.17)$$

Total Elastic load on the beam is given by;

$$W_n = \frac{2L_1M_1}{3EI} + \frac{L_2}{EI_{eq}}(M_1 + M_R) - \frac{2N}{EA}\tan\beta_1 \quad (4.18)$$

Elastic reaction at the support R_P^f is given by;

$$R_P^f = R_Q^f = \frac{W_n}{2} \quad (4.19)$$

Therefore, the deflection at the crown due to an elastic load W;

$$M^f = y = R_P^f \times B = \frac{B}{2}\left[\frac{2L_1M_1}{3EI} + \frac{L_2}{EI_{eq}}(M_1 + M_R) - \frac{2N}{EA}\tan\beta_1\right] \quad (4.20)$$

where M_1 is the bending moment at point 1 and M_R is the bending moment at point R due to vertical reaction. y is the vertical displacement at the crown of the beam.

The equivalent second moment of area for the cross section of strengthened part can be calculated as follow (Figure 4.14).

For the un-strengthened beam assuming steel tube as a thin walled section;

$$I = \pi r_0^3 t_s \quad (4.21)$$

where I is the second moment of area, r_0 is the radius of and t_s is the wall thickness of unstrengthened section.

The second moment of area of the equivalent section I_{eq} is given by;

$$I_{eq} = \pi \mathrm{r}_{\mathrm{eq}}^3 \mathrm{t}_{\mathrm{eq}} \quad (4.22)$$

Where r_{eq} and t_{eq} can be found by the equations (4.20) and (4.19) respectively.

$$t_{eq} = t_s + t_{CFRP,eq} \quad (4.23)$$

$$r_{eq} = r_0 + t_{CFRP,eq} \quad (4.24)$$

$$t_{CFRP,eq} = \frac{E_s}{E_{CFRP}} \times t_{CFRP} \quad (4.25)$$

In equation (4.24) $t_{CFRP,eq}$ is found by equation (4.25).

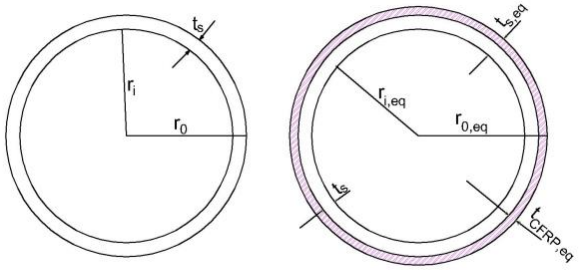

Figure 4.14. Section of steel tube (a) un-strengthened beam; (b) strengthened equivalent section

When evaluating the total deflection at the mid span, the ovalisation of SCHS due to the applied load should be considered. Researchers(Elchalakani, Zhao, and Grzebieta 2004; Ibrahim 2018) have found that the ovalisation depends on the aspect ratio (ratio between diameter and thickness) of the section. According to those researchers, for SCHS having aspect ratio of around 33, the percentage ovalisation was about 5% at the ultimate load. For this study since the elastic limit is considered, it is effective to use a percentage ovalisation of 3%. Since the diameter of the circular hollow sections used in this is 101.6 mm, it is conservative to take amount of ovalisation as 3 mm. Therefore, the total deflection (Δ_T) can be expressed as;

$$\Delta_T = \delta_{al} + \delta_{ol} \tag{4.26}$$

The calculated deflections of the strengthened and unstrengthened beams with different radii of curvature under elastic loads of 40 kN and 30 kN are shown in Table 3. By comparing the analytical model results and experimental results, it was found that the results are in good agreement. Therefore, the developed analytical model based on the Maxwell-Mohr integration can be used effectively to calculate the deflection at a given elastic load or load at a given deflection for CFRP strengthened vertical curved tubular sections.

Table 4.3. Comparison between experimental results and analytical model

Beam ID	Radius of Curvature (mm)	CFRP Length (mm)	Elastic Load Considered (kN)	Experimental deflection (δ_{exp}) (mm)	Analytical deflection (δ_{al}) (mm)	Total analytical deflection including ovalisation ($\Delta_T = \delta_{al}+3$)	Δ_T / δ_{exp}
2R_0	2000	0	40	13.02	11.1	14.1	1.08
2R_500		500	40	10.20	7.02	10.02	0.98
2R_750		750	40	10.20	7.56	10.56	1.04
2R_1000		1000	40	10.18	7.86	10.86	1.07
4R_0	4000	0	30	10.20	8.55	11.55	1.13
4R_500		500	30	9.15	5.41	8.41	0.92
4R_750		750	30	9.00	5.83	8.83	0.98
4R_1000		1000	30	9.54	6.05	9.05	0.95
6R_0	6000	0	30	12.00	8.60	11.60	0.97
6R_500		500	30	9.22	5.58	8.58	0.93
6R_750		750	30	9.15	5.85	8.85	0.97
6R_1000		1000	30	9.65	6.08	9.08	0.94

4.5. Conclusions

An experimental study was conducted to investigate the behaviour of vertically curved tubular steel members strengthened with CFRP. An analytical study was also conducted to evaluate the deflection of both strengthened and un-strengthened beams in the elastic range. Based on the experimental and analytical studies, the following conclusions can be drawn;

- CFRP is an efficient material to strengthened curved steel hollow sections since, it increases the load carrying capacity of the beams and reduces the

deflection of the beam at any given load. Maximum ultimate strengths of the CFRP retrofitted curved SCHS were obtained when the ratio of CFRP length to the total length of beam becomes 0.625. Ultimate strengths were observed to be lower for the values of this ratio less than or greater than 0.625.

- The highest load carrying capacities for all CFRP wrapping lengths were observed for beams with 2000 mm radius of curvature and the lowest values were observed in straight beams. This clearly indicates that the ultimate load carrying capacity of a curved SCHS for a certain CFRP wrapping length decreases when radius of curvature of the beam increases. Strengthening of SCHS using CFRP reduces the amount of mid span deflection at the ultimate load. The highest mid span deflections among all curved beams with different CFRP lengths were observed for those with a radius of 6000 mm. When the radius of curvature decreases the mid span deflection also decreases. The highest deflections at the ultimate load for strengthened beams with various curvatures were observed when the ratio between CFRP length to total length of the beam equals to 0.625.
- Four major failure types were observed in CFRP strengthened curved SCHS beams which include debonding of CFRP due to adhesive failure, bearing of the steel tube near the loading point, crushing of CFRP near the loading point and CFRP rupture on the tension face of the beam. When CFRP wrap length was 500 mm the major failure mechanism of beams was pre- mature debonding of CFRP. Beams strengthened with 500 mm CFRP also showed rupture of CFRP at lower loads. When CFRP length increased to 750 mm and 1000 mm, failure mechanisms of beams were fracture of CFRP and bearing of the steel tube near the loading point.

- A method to analyse CFRP strengthened SCHS under elastic loads was developed according to Maxwell-Mohr integral method (and validated). This method can evaluate the deflection at a given elastic load or the load for a given elastic deflections

4.6 Chapter Summery

The experimental and theoretical investigation of CFRP strengthened vertically curved circular hollow sections are presented under this chapter. The first part of the chapter was targeted on the experimental study and vertically curved beams with radius of curvatures 2000 mm, 4000 mm and 6000 mm were used along with the straight control beams. Span of each specimen kept as a constant value of 1200 mm while change the bonded CFRP length during the experiments. Total sixteen number of samples were tested from which four of the were control beams. The load deflection behavior of the beams was recorded with some strain gauge readings. Ultimate loads of the beams were used to compare the percentage strength gain. Failure modes of the strengthened and unstrengthened beams were observed to identify the relationship between CFRL length, curvature of the beams and failure modes.

A theoretical model was developed to evaluate the elastic deflection of CFRP strengthened beams using Mohr and Maxwell integral for curved beams. The equation was modified replacing the sectional properties for unstrengthened beam with modified equivalent section parameters. An allowance for the ovalisation of the section was considered when evaluating total deflection of beams. The developed theoretical model showed a good agreement with the experimental results. Recommendations were provided to use when strengthening vertically curved beams using CFRP for static loads.

Chapter 5

Numerical Investigation on Flexural Behaviour of Vertically-Curved Circular-Hollow Steel Sections Strengthened with Externally Bonded Carbon Fibre Reinforced Polymer(CFRP)

Nomenclature

COV	coefficient of variance
P_u	ultimate load of the strengthened beams
P_s	ultimate load of the unstrengthened beams
G_n	fracture energy in normal direction
G_s, G_t	fracture energy in shear directions
G_{ij}	shear modulus
$G^T{}_{1C}$ or $G^C{}_{1C}$	mode I Fracture energy in fibre direction
$G^T{}_{2C}$ or $G^C{}_{2C}$	mode II Fracture energy in transverse direction
K_{nn}	elastic stiffness of the adhesive in normal direction
K_{ss}, K_{tt}	elastic stiffness of the adhesive in shear directions
t	thickness
t_n	nominal stress normal mode only
t_s, t_t	nominal stresses in shear directions
t_n^0	peak value of nominal stress in normal direction
t_s^0, t_t^0	peak values of nominal stress in shear directions
X^T or X^C	ultimate in-plane strength in fibre direction
Y^T or Y^C	ultimate in-plane strength in transverse direction

5.1 Introduction

Steel Circular Hollow Sections(CHS) for construction of both onshore and offshore structures has an increasing demand due their favourable properties such as high compression, tensional, and bending strength in all directions and have a small drag coefficient in fluid flows. Moreover, corrosion of steel hollow sections is comparatively less due to the closed shaped sections without sharp edges compares to the other steel section types. Steel hollow sections can be filled with concrete to enhance fire protection as well as to enhance the buckling load capacity. The aesthetical appearance and the voids provide space for installing electric conduit, network cables and other service are some other advantages of steel hollow beams using for building construction(Wardenier 2001). Steel CHS beams used in structural forms may be either straight of curved (in elevation or on plane). Straight CHS beams have numerous applications such as as jackets, towers, cranes, bridges, support structures of helicopter decks and further in various secondary structures, such as staircases, ladders, etc. CHS beams curved in elevation mainly used in structures such as bridges and portals of curved roofs CHS beams curved on plane covers curved slab beams(D. Brown 2007). The present study focused on CHS beams curved in elevation and Figure 1 shows two applications of such beams. It is reported in the literature that structures constructed with CHS need retrofitting due to inadequate due to design errors, loss of material properties, exposure to severe environments, or increase in service loads(M. H. Kabir, Fawzia, Chan, Gamage, et al. 2016).

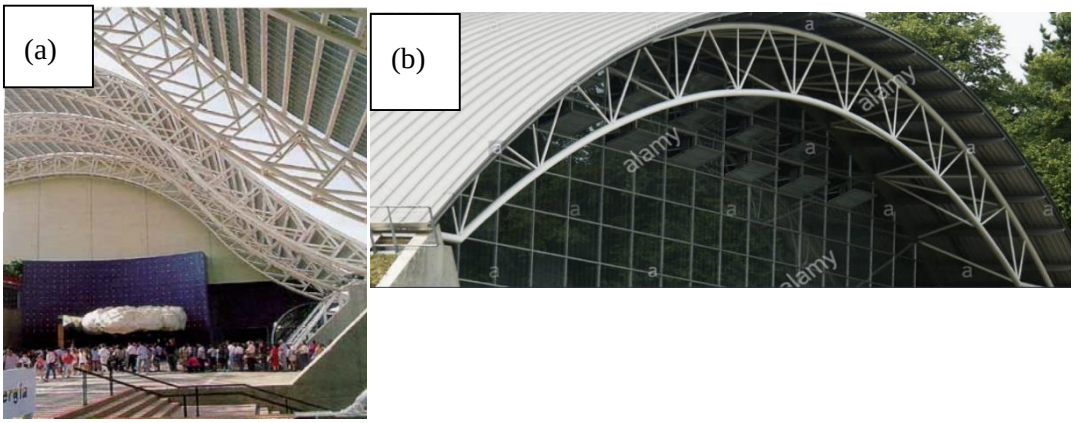

Figure 5.1. Structures constructed using SCHS curved in elevation (a) Firth of forth bridge (b) Hamburg airport roof

Carbon Fiber Reinforced Polymer (CFRP) is widely recognized as an effective retrofitting technique for steel structures due to its numerous advantages. CFRP offers high durability, superior fatigue endurance, a high strength-to-weight ratio, requires less labor-intensive work, and can be applied to various sectional shapes (Harries and El-Tawil, 2008). Previous studies have focused on investigating the behavior of CFRP-strengthened straight members made of Circular Hollow Sections (CHS) under different loading conditions. These studies have evaluated the performance of CFRP-strengthened CHS members subjected to axial force (Gao, Balendra, and Koh, 2013; Jimmy Haedir and Zhao, 2011; Karimian et al., 2017; Keykha et al., 2015; Shaat and Fam, 2006; Sundarraja, Sriram, and Ganesh Prabhu, 2014; Viveka, Shanmugavalli, and Sundarraja, 2014; Z. Bin Wang, Yu, and Tao, 2015), bending (Badawy et al., 2019; S. Fawzia et al., 2007; J. Haedir et al., 2009; M. H. Kabir, Fawzia, Chan, Gamage, et al., 2016), and torsion (Abdollahi Chahkand et al., 2013; Wu et al., 2018). Additionally, CFRP strengthening of steel tubes has shown enhanced capacity against transient loads such as fatigue (Hu, Feng, and Zhao, 2017), impact (Md Iftekharul Alam et al., 2017; Kadhim, Wu, and Cunningham, 2018a), and cyclic loading (Zhujing Zhang et al., 2018). The application of CFRP strengthening to tubular sections provides increased durability against various environmental conditions (M. H. Kabir, Fawzia, Chan, and Badawi, 2016a, 2016b; M. H. Kabir, Fawzia, and Chan, 2016; Mohammad Humayun Kabir et al., 2014). While numerous studies have been conducted on straight CHS strengthened with CFRP, very few studies have been found on the CFRP strengthening of curved beams. Keykha (2019) conducted a study on CFRP-strengthened vertically curved square hollow sections, but no literature was found on vertically curved CHS members. Therefore, it is essential to conduct a comprehensive study on the flexural behavior of CFRP-strengthened steel CHS beams

curved in elevation. Such research is necessary to ensure structural safety, minimize maintenance costs, and extend the service life of these structures.

Finite Element Modelling (FEM) is a valuable tool for conducting parametric studies in the context of CFRP strengthening. FEM enables the accurate prediction of failure loads, deflections, and failure modes in a fast and cost-effective manner. Several researchers, such as S. Fawzia et al. (2007), J. Haedir et al. (2009), and M. H. Kabir, Fawzia, Chan, Gamage, et al. (2016), have successfully developed finite element models to simulate the behavior of CFRP-strengthened straight tubular beams under various loading conditions. These studies have emphasized the importance of proper material modeling and consideration of interactions between layers to obtain reliable results regarding the failure modes of CFRP-strengthened steel tubular beams. In particular, researchers have recommended the use of a continuum shell model for the CFRP and a cohesive model for the adhesive to achieve realistic FEM simulations. Cohesive Zone Modelling (CZM) is a popular and accurate method employed by many researchers to model the interfaces between steel-adhesive and adhesive-CFRP. Prominent studies by Heshmati et al. (2018), Li et al. (2019), Sitnikova et al. (2019), and Teng, Fernando, and Yu (2015a) have utilized CZM to develop interfaces between CFRP and steel. In the FEM developed for this particular study, CZM has been employed to model the interface between CFRP and steel. This approach ensures an accurate representation of the interaction between the materials and enables the analysis of the behavior of CFRP-strengthened curved steel CHS beams under flexural loading.

This study aims to investigate the flexural behaviour of CFRP strengthened steel CHS curved in elevation using both experimental and numerical studies. The results of

experimental study are used to validate the numerical model and then parametric studies were conducted to investigate the effect of various parameters on the capacity of CFRP strengthened CHS beams using numerical modelling. These parameters included CFRP length, CFRP layer orientation, number of CFRP layers, aspect ratio of steel tubes, elastic modulus of CFRP and thickness of the adhesive layers. The results of this study are provide referral guidelines to civil engineers during the practical applications of CFRP to retrofit steel CHS curved in elevation.

5.2. Test Programme

Total sixteen steel circular hollow sections CHS (D=101.6 mm, t=3 mm) beams, including four straight beams were tested. Three different radius of curvatures, 2000 mm, 4000 mm and 6000 mm were considered. The steel surface of specimens to be retrofitted were sand blasted and acetone was applied to remove the loose particles. Immediately after, normal modulus CFRP sheets were bonded to steel tubes in the longitudinal direction using two parts epoxy adhesive (Sikadur 330). Three beams from each curvature were bonded with CFRP sheets having lengths 500 mm, 750 mm and 1000 mm. Remaining four beams, one from each curvature were kept as control specimens. The measured mechanical properties of steel, CFRP and epoxy are listed in Table 5.1. All the specimens were cured at least seven days at room temperature before testing.

Table 5.1. Material Properties

	Steel	CFRP	Adhesive
Thickness (mm)	3	0.116	0.05
Elastic modulus (GPa)	206	230	2.4
Tensile strength (MPa)	473	4983	40
Yield strength (MPa)	508	-	-
Tensile strain (mm/mm)	0.025	0.021	-

All the beams were tested under the simply supported condition using three-point bending test method under a rate of 0.025mm/sec under Quisi static load. A 250 kN capacity load cell was used to transfer load to the beams in a constant rate until they fail. Two linear variable displacement transducers (LVDTs) were set at 150 mm from either side of the mid span. Figure 5.2 shows a schematic diagram of experimental setup with instrumentation.

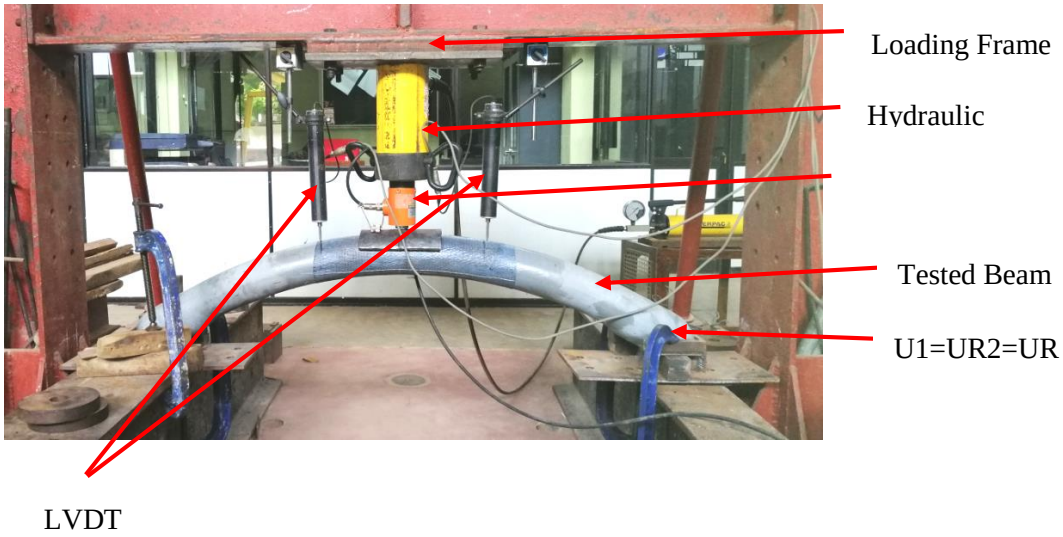

Figure 5.2. Experimental test setup

5.3. Experimental results

Load-deflection responses for both unstrengthened and strengthened beams are shown in Figure 5.3. It can be seen that the mid span deflection for strengthened beams considerably decrease at a given load. This is because, the increased stiffness of beams due CFRP wrapping. Figure 5.4 shows the four major failure mechanisms of CFRP strengthened beams. Beams with 500 mm CFRP wrapping were failed due to edge debonding and CFRP rupture at the tension face. The major failure mechanisms for beams having 750 mm and 1000 mm CFRP lengths were local buckling of steel tube and CFRP crushing near the loading point.

Table 5.2 shows the variation of ultimate load with respect to curvature of beams and CFRP lengths. It can be clearly seen that the increase in ultimate load is depend on the CFRP length and the curvature of beams. The maximum ultimate load for straight beams were observed when CFRP length is 1000 mm and for curved beams the ultimate load was observed when CFRP length was 750 mm.

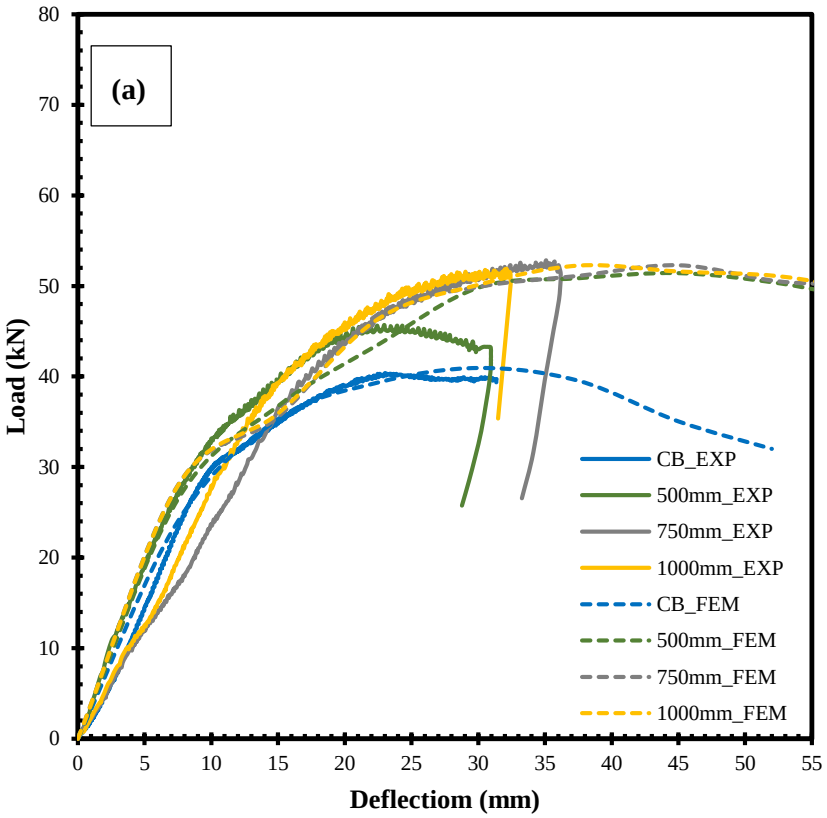

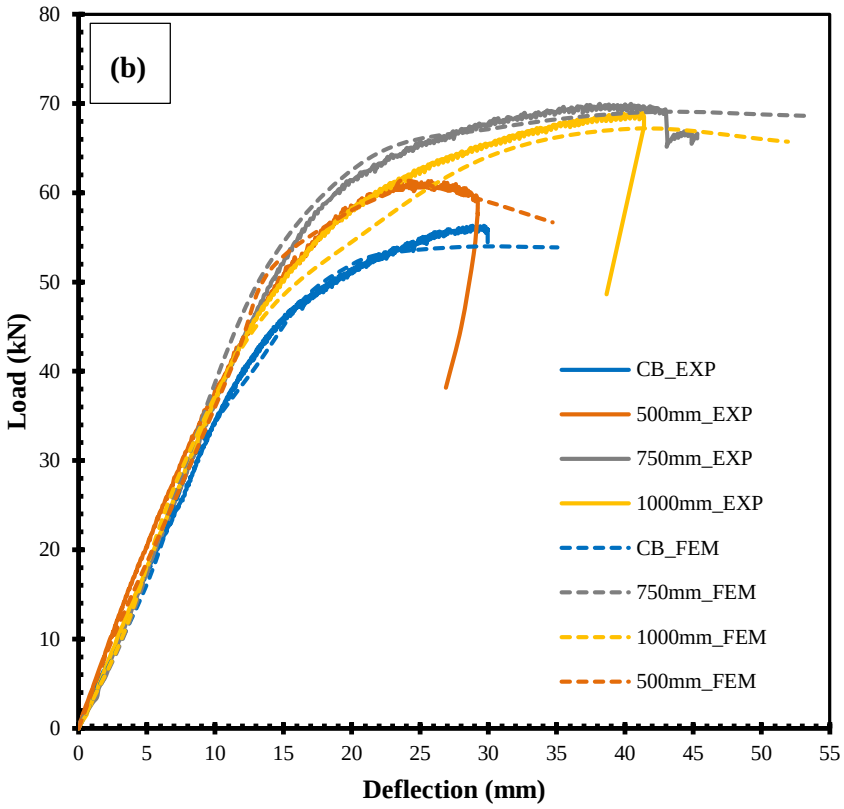
(b)
Load (kN)
Deflection (mm)
0
10
20
30
40
50
60
70
80
0
5
10
15
20
25
30
35
40
45
50
55
CB_EXP
500mm_EXP
750mm_EXP
1000mm_EXP
CB_FEM
750mm_FEM
1000mm_FEM
500mm_FEM

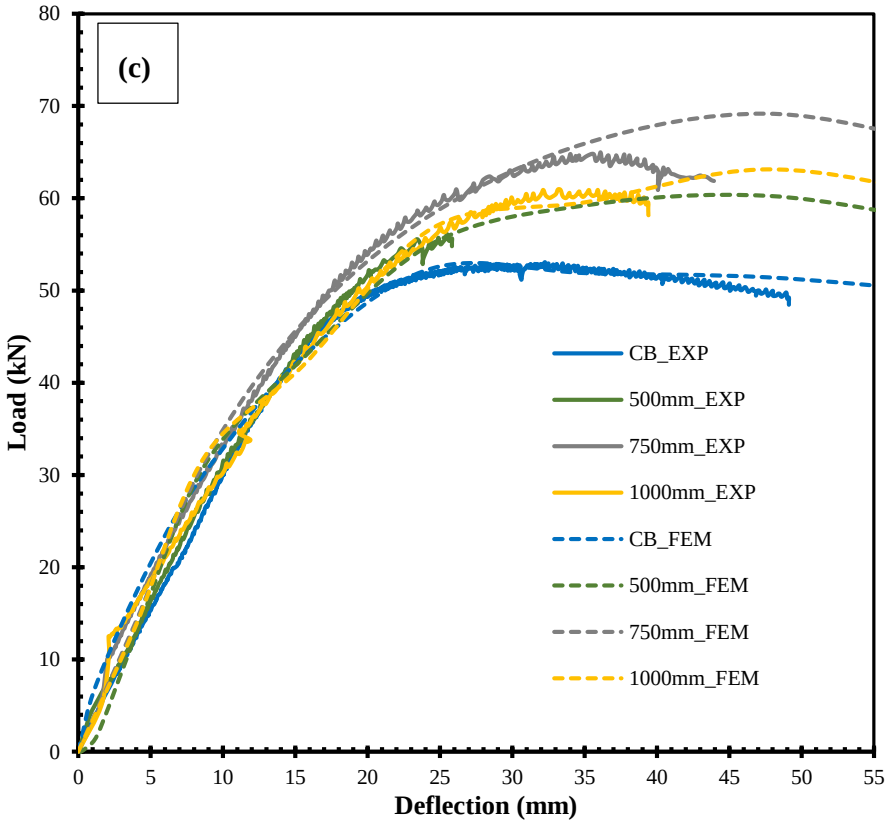
(c)
Load (kN)
Deflection (mm)
0
10
20
30
40
50
60
70
80
0
5
10
15
20
25
30
35
40
45
50
55
CB_EXP
500mm_EXP
750mm_EXP
1000mm_EXP
CB_FEM
500mm_FEM
750mm_FEM
1000mm_FEM

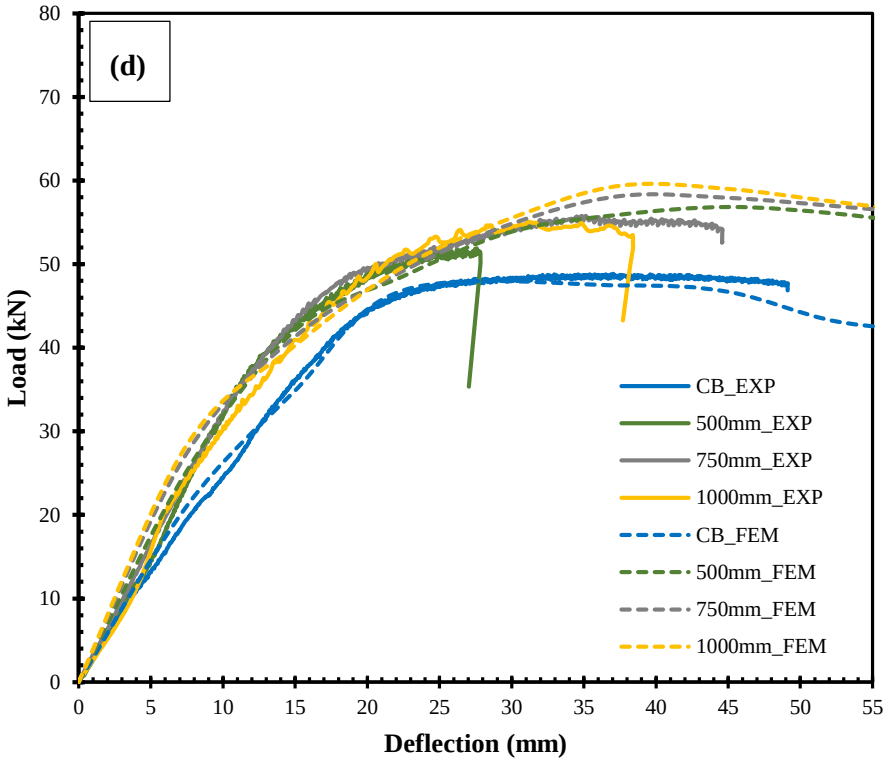

Figure 5.3. Load-deflection curves for curved beams with different curvature and CFRP-bonded lengths: (a) straight beam, (b) 2 m curved beam, (c) 4 m curved beam, and (d) 6 m curved beam

5.4. Finite element modelling

Three dimensional finite element models were developed using a commercially available finite element modelling software[] as given in Figure 5.4. Pinned ends(U2=UR2=UR3=0) was used as boundary conditions of either ends of the beam. Results of the finite element models were validated using experimental results.

Three materials including steel, CFRP and adhesive were modelled using the inbuilt facilities provided in the finite element analysis programme[]. The computational time was managed by defining various mesh densities for different materials. A 10 mm mesh size was used for both steel and CFRP while 5 mm mesh size was used for adhesive. The connection between steel-adhesive and adhesive-CFRP were model

using tie constraints. When defining the tie constraints, steel and CFRP were considered as master surfaces and adhesive surface was considered as slave surface.

The steel tube was modelled as an elastic-plastic metal with isotropic hardening. The element type S4R which is applicable for thin walled sections was used(Zhou and Young 2007). These are four node shell elements with five degrees of freedom with incorporated reduced integration. These S4R elements are the most suitable element type to model the thin walled sections and are accurate than standard shell elements in predicting of the results of contact models(D. Fernando et al. 2008; Zhou and Young 2007)

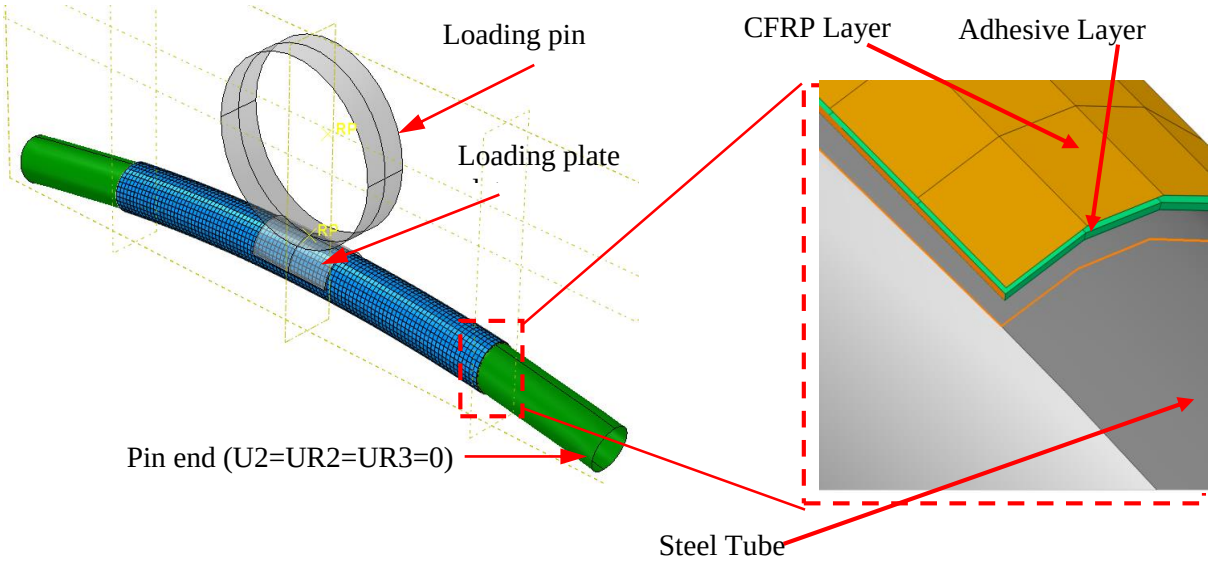

Figure 5.4. 3D finite element model of steel tubular steel beam strengthened with CFRP

The CFRP patch was modelled as continuum shell elements that meshed with an eight-node quadrilateral in-plane general purpose continuum shell with reduced integration and hourglass control(SC8R). This element type allows a full 3-D model which is capable of predicting CFRP failure and also able to compute shear stresses through the thickness than the standard brick elements. Moreover, this element type is more capable of resolving contact problems accurately (Al-Zubaidy, Zhao, and Al-Mahaidi 2013).

Damage of CFRP layers occurs due to four main criteria; fibre rupture in tension, fibre bucking in compression, matrix cracking under transverse tension and shearing, and matrix crushing under transverse compression(Naghipour et al. 2009). Elastic orthotropic material properties of CFRP are shown in Table 5.2. The damages and failures of CFRP were captured by continuum damage mechanism and in-built Hashin damage criteria. Hashin damage criteria is based on the reduction of material stiffness not on the plasticity of CFRP. The damage initiates and propagates when the fracture energy in any afore mentioned criteria exceeds its maximum value. The required damage properties used to facilitate Hashin Damage Criteria are listed in Table 5.3 (M. H. Kabir, Fawzia, Chan, Gamage, et al. 2016).

Table 5.2. Orthotropic elastic material properties of CFRP

Fibre Type	E_1 (Pa)	E_2 (Pa)	G_{12}(Pa)	G_{13}(Pa)	G_{23}(Pa)	N_{12}
Magnitude	230×10^9	230×10^9	1	1	3.0×10^9	0.33

Table 5.3. Orthotropic damage initiation properties and In-plane fracture energies for CFRP

X^T (MPa)	X^C (MPa)	Y^T (Pa)	Y^C (MPa)	S^L (Pa)	S^T (Pa)	G^T_{1C} (N/m)	G^C_{1C} (N/m)	G^T_{2C} (N/m)	G^C_{2C} (N/m)
2760	552	1	50	1	1	91,600	79,000	1	1

The cohesive elements were used for the simulation of adhesive layer. An 8-node three dimensional cohesive element (COH3D8) with reduced integration and element deletion was used as the element type. The triangular cohesive zone degradation was used due to its simplicity and popular use for investigation for brittle adhesives(Avgoulas and Sutcliffe 2016). The damage initiation of adhesive was defined using the mix mode failure criteria which is quadratic nominal stress criterion(QUADS) as given in equation (1).

$$\left\{\frac{t_n}{t_n^0}\right\}^2 + \left\{\frac{t_s}{t_s^0}\right\}^2 + \left\{\frac{t_t}{t_t^0}\right\}^2 = 1 \qquad (1)$$

Where, $t_n$is the nominal stress in normal mode only, t_s and t_t are nominal stresses in first and second shear direction respectively and need as inputs values. t_n^0, t_s^0 and t_t^0 denote the peak values of nominal stresses in normal, first and second shear directions respectively and are generated by the finite element model.

The damage evaluation was defined using an energy power-law, mixed-mode criterion as follows;

$$\left\{\frac{G_n}{G_n^C}\right\}^\alpha + \left\{\frac{G_s}{G_s^C}\right\}^\alpha + \left\{\frac{G_t}{G_t^C}\right\}^\alpha = 1$$

Where G_n, G_s and G_t represent the work done by the traction and their conjugate displacements in the normal, first and second shear directions respectively and required as inputs to ABAQUS. The quantities G_n^C , G_s^C and G_t^C are generated during the execution of finite element model and denote the critical fracture energies in the normal, the first and the second shear directions respectively. The value of α was chosen to be equal to 2 (Avgoulas and Sutcliffe 2016). Table 5.4. shows the elastic and damage properties of adhesive.

5.5. Validation of numerical models

The results obtained through numerical analysis were validated using the experimental results before conducting the parametric study. The load-deflection curves, ultimate load, mid span deflection and failure modes of strengthened and un-strengthened beams were compared.

5.1 Ultimate load

A comprehensive comparison between the ultimate load obtained through the experimental study and those obtained through FEA are shown in Table 5.5. It clearly elaborates that the ratio (P_u/P_F) rages from 0.971 to 1.063 which are close to unity.

The coefficient of variance having values ranges from 0.001 to 0.043 which are almost negligible. Therefore, it can be deduced that the numerical models have been validated reasonably with the experimental results where values obtained from both methods are almost equal.

Table 5.4. Properties of adhesive

E_a (Pa)	t_n (Pa)	t_s (Pa)	t_t (Pa)	K_{nn} (N/mm^3)	K_{ss} (N/mm^3)	K_{tt} (N/mm^3)	G_n (N/m)	G_s (N/m)	G_t (N/m)
4.82×10^9	31.28×10^6	31.28×10^6	31.28×10^6	4.72×10^{13}	2.36×10^{13}	2.36×10^{13}	1000	1250	1250

5.3 Failure modes

Figure 5.5 shows the major failure modes of CFRP strengthened curved beams. These failure modes include yielding of steel tube, bearing failure near the loading point and CFRP debonding and rapture. It can be clearly seen that numerically obtained failure modes have a good agreement with the failure modes obtained through the experimental results (As per the visual observations). Figure 5.6 shows the stress developed on CFRP strengthened 4000 mm curved beams with various CFRP lengths. It clearly shows that the developed stress levels are varies with the CFRP wrapping length.

Figure 5.7 shows the variation of stress within the adhesive layer for various CFRP lengths. It can be seen that for 500 mm CFRP length, stresses are higher at the ends of adhesive layer which cause for the edge debonding.

Table 5.5. Comparison Between Ultimate Load Obtained Through Experimental and Numerical Studies for Beams with Different Curvatures and CFRP Lengths

Beam ID	Ultimate Load (kN)		P_u/P_F	COV	Failure Modes	
	Experimental (P_u)	Numerical (P_F)			Experimental	Numerical
ST_0	40.2	40.68	0.988	0.008	C	C
ST_500	41.49	42.73	0.971	0.021	A/B	A/B/C
ST_750	51.56	50.73	1.016	0.011	A/C/D	A/C
ST_1000	52.69	50.96	1.034	0.024	C/D	C/D
2R_0	56.23	55.87	1.006	0.005	C	C
2R_500	61.16	62.77	0.974	0.018	A/B	A/B/C
2R_750	69.97	66.37	1.054	0.037	A/C/D	C/D
2R_1000	68.9	64.83	1.063	0.043	C/D	C/D
4R_0	52.87	51.95	1.018	0.012	C	C
4R_500	55.56	56.82	0.978	0.016	A/B	A/B/C
4R_750	63.34	62.16	1.019	0.013	A/C/D	C/D
4R_1000	60.95	59.44	1.025	0.018	C/D	C/D
6R_0	48.84	47.91	1.019	0.014	C	C
6R_500	51.56	51.08	1.009	0.007	A/B	A/B/C
6R_750	55.76	55.71	1.001	0.001	A/C/D	C/D
6R_1000	54.96	54.43	1.010	0.007	C/D	C/D

In Table 5.5, the failure modes are denoted as: A- CFRP end debonding; B- CFRP rupture in tensile face; C- Local buckling of tube near loading point; D- CFRP rupture close to loading point and ultimate loads and mid span deflections at ultimate loads are denoted as; P_u- ultimate load of strengthened beams; P_s- Ultimate load on unstrengthened beam; δ_u- mid span deflection at ultimate for strengthened beams; δ_s- mid span deflection at ultimate for unstrengthened beams

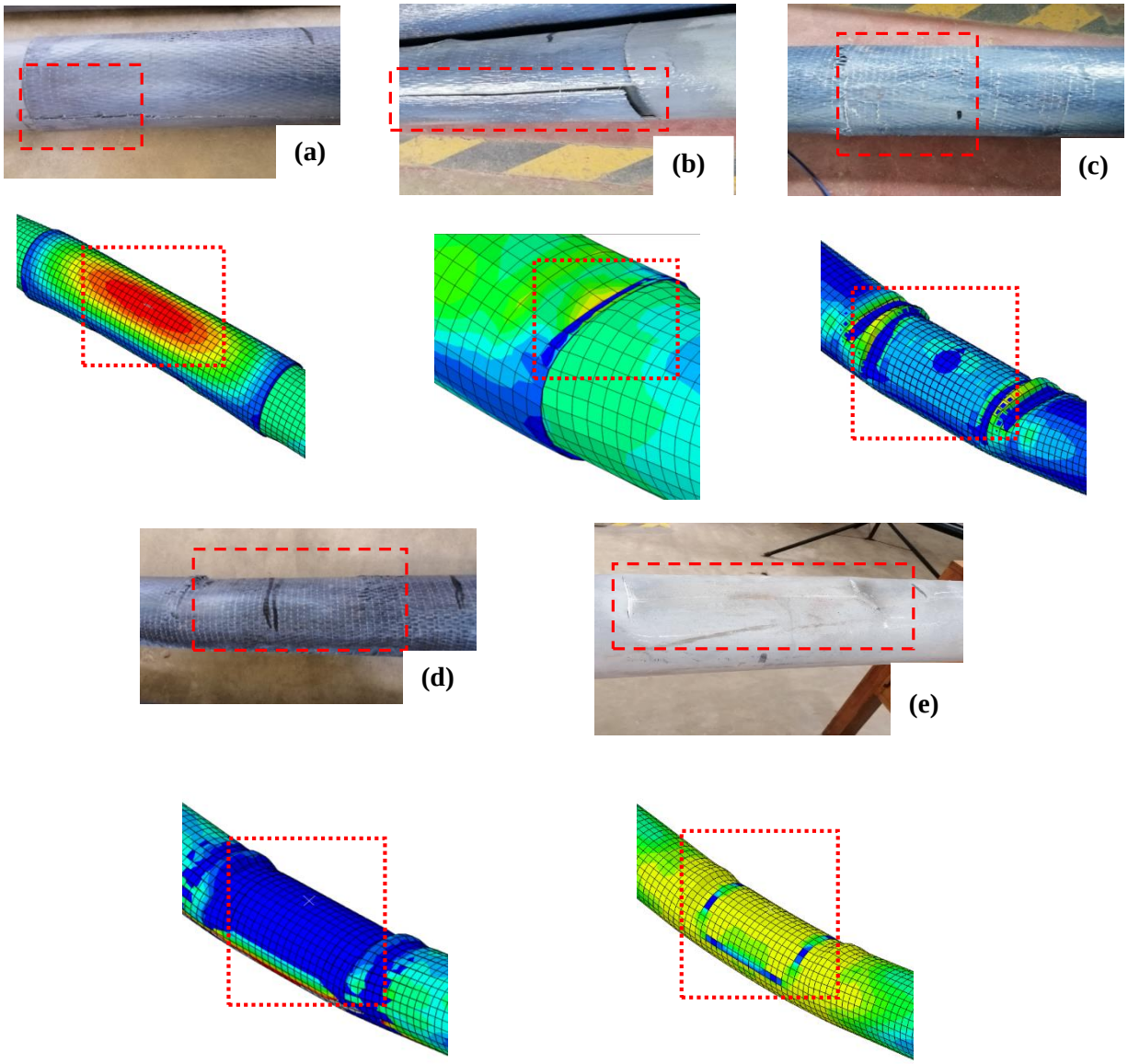

Figure 5.5. Failure modes obtained through numerical modelling (a) CFRP rapture at the bottom side of loading point(b) CFRP crushing at the loading points (c) edge debonding, (d) Bearing of steel beam at the loading point

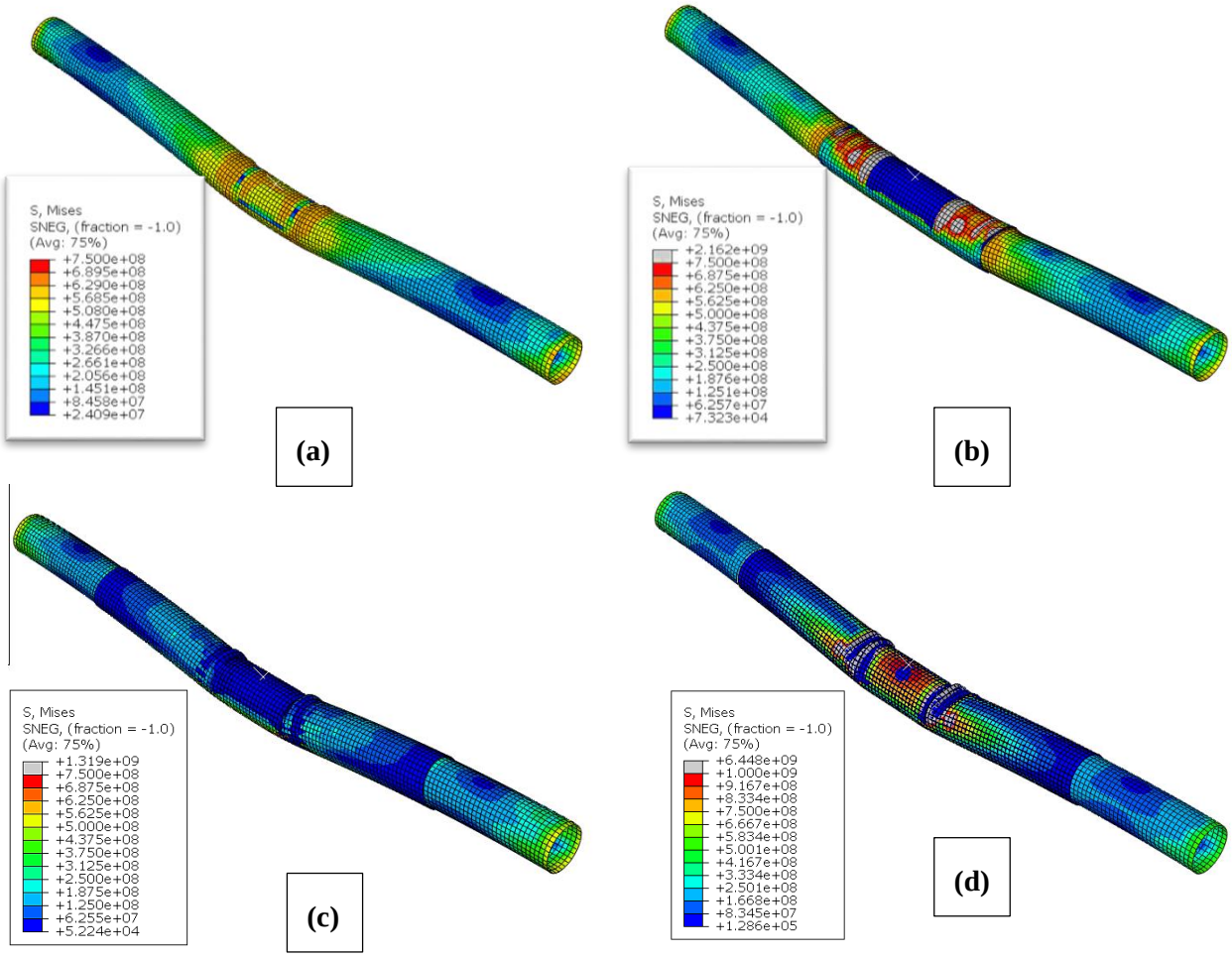

Figure 5.6. Stress variation of CFRP strengthened 4000 mm curved beam with various CFRP lengths; (a) Without CFRP; (b) 500 mm; (c) 750 mm; (d) 1000 mm

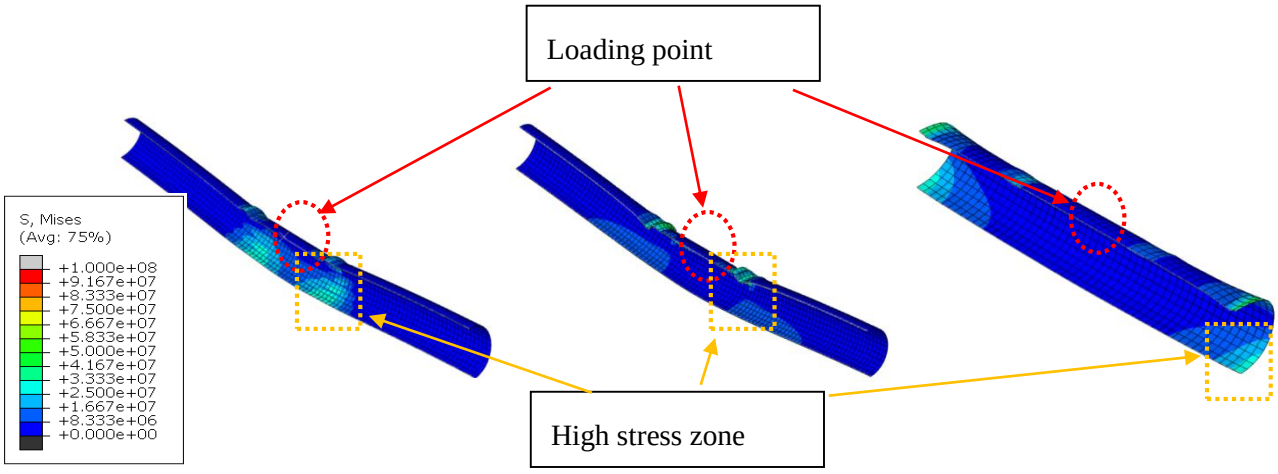

Figure 5.7. Stress variation in the adhesive layer for various adhesive lengths (a) 1000 mm (b) 750 mm and (c) 500 mm

5.6. Parametric study

A parametric study was conducted to identify the sensitive bond parameters and it was conducted on the beams strengthened with 750 mm long CFRP layer with different curvatures since best performance was noted from the specimens with 750 mm long CFRP.

5.6.1 Number of CFRP layers

Number of CFRP layers decides the required strength gain as well as the cost of the retrofitting project. Figure 5.8 shows the load-deflection responses for 4000 mm curved beams with various number of CFRP layers when CFRP bond length is 750 mm. It clearly indicates that the number of CFRP layers drastically enhance the ultimate load carrying capacity of retrofitted vertically curved beams. The stiffness of beams increased within both elastic and plastic regions. The graph also indicates that the rate of increase in ultimate load decreases with the increased number of CFRP layer. These variations are comparatively same compared to the straight beams strengthened with CFRP under bending(M. H. Kabir, Fawzia, Chan, Gamage, et al. 2016). But a designer must select the appropriate number of CFRP layers based on the required strength gain and the cost. As per the Figure 5.8 the effective number of CFRP is 3-4 layers depending on the situation considered.

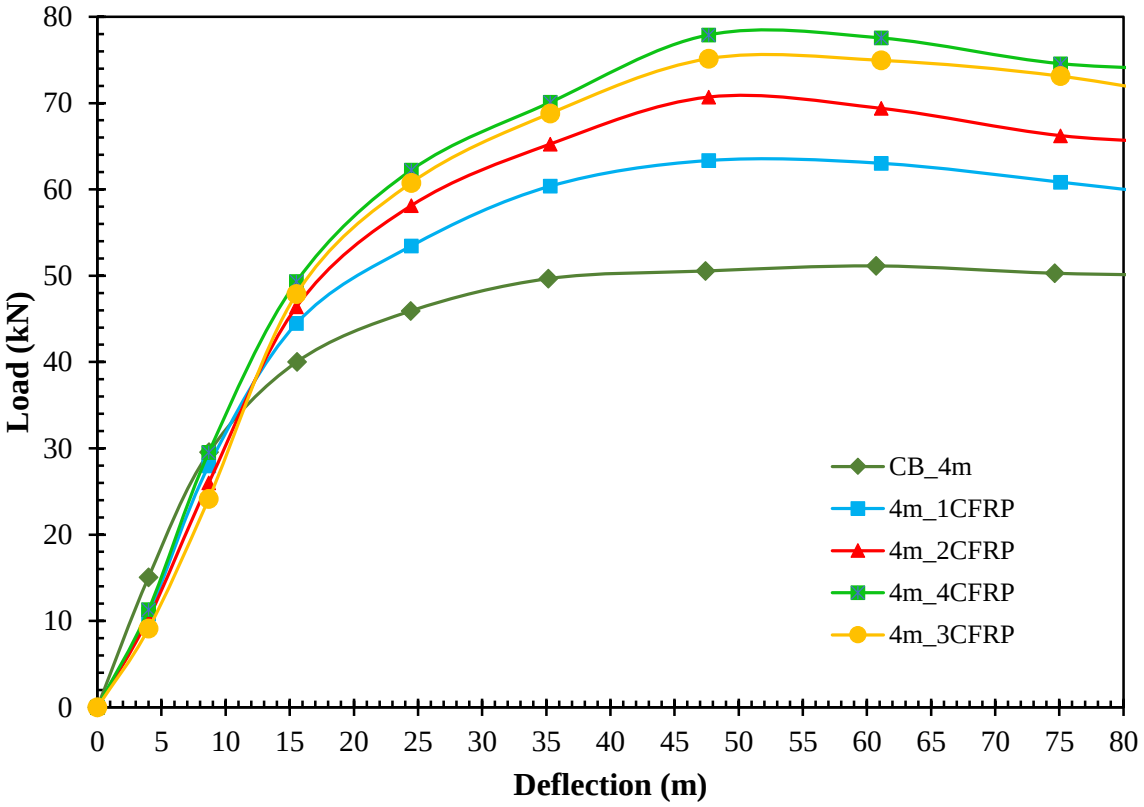

Figure 5.8. Load vs. deflection for 4000 mm retrofitted vertically curved CHS beam with 750 mm long CFRP with various number of CFRP layers

5.6.2 Layer orientation

Unidirectional CFRP can apply on tubular structures in different orientations. Four layer orientations were considered for this parametric study; longitudinal direction (0°), hoop direction (90°), spiral direction (45°) and reverse spiral direction (-45°). Study was conducted for starting from single CFRP layers to four CFRP layers.

Table 5.6. Numerically Obtained Ultimate Loads for 2000 m Curved Beams for Different Number of CFRP Layers with Various Layer Orientations

No. of CFRP Layers	Layer Orientation	Ultimate Load (kN)	Percentage Increase in Ultimate Load (%)
Without_CFRP		53.95	0.00
1	0	64.83	20.17
	90	55.92	3.65
	45	57.01	5.67
2	0-0	70.98	27.04
	0-90	68.40	22.42
	90-0	67.77	21.53
	45-45	62.94	12.65
	90-90	61.01	9.20
3	0-0-0	74.73	33.75
	90-0-90	69.00	23.50
	0-90-0	73.38	31.34
	0-45-90	70.33	25.88
4	0-0-0-0	80.99	44.97
	0-90-0-90	83.59	44.62
	90-0-90-0	80.71	44.46
	0-45-90-45	66.75	19.48
	0-0-90-90	73.85	36.88
	0-45-(-45)-0	75.06	39.13

Table 5.6 shows the numerically obtained ultimate loads for 2000 mm curved beams with different number of CFRP layers for various layer orientations. It can be clearly seen that the highest ultimate loads were obtained when layer orientation is in longitudinal direction. This is due to the effectiveness of fibres in the axial direction to take bending stress developed in the same direction. Spiral and reverse spiral wrapping were effective than the wrapping in the hoop direction. When there is a combination of longitudinal and hoop directions fibres, it shows higher strength gain greater than spiral and reverse spiral wrapping. This may be due to the lateral stability provided by hoop layer to the longitudinal layers.

5.6.3 Aspect ratio of CHS

In this section, ten different commercially available section sizes of steel tubular beams with 4000 mm curvature strengthened with one 750 mm long CFRP layer were studied to understand the effect of aspect ratio (Ds/t) on the increment of ultimate load capacity of curved beams strengthened with CFRP (Table 5.7). As per the values listed in the Table 5.7, there is no significant relationship between the aspect ratio and the percentage increase in ultimate load. CHS with 90 mm diameter and 4 mm thickness shows the highest percentage increase while the beam with 165 mm diameter and 5.4 mm thickness shows the lowest of it. It is interesting to see that for the beams with the same diameter, a highest percentage increase in ultimate loads were obtained for the beam having lower thickness. This is common for all the beams with different section sizes.

Table 5.7. Numerically determined ultimate loads of unstrengthened and strengthened beams with various Aspect Ratios for 4000 mm curved beams

Outer Diameter (D_s) (mm)	Thickness (t) (mm)	Ds/t	Ultimate Load (kN)		Load Increment (%)
			Unstrengthened	Strengthened	
165.0	5.4	30.6	145.92	151.56	3.87
165.0	5.0	33.0	132.56	141.17	6.50
140.0	5.4	25.9	120.03	125.21	4.32
140.0	5.0	28.0	106.06	113.37	6.89
114.0	5.4	21.1	94.46	98.16	3.92
114.0	4.5	25.3	71.13	75.14	5.64
101.6	5.0	20.3	70.78	76.15	7.59
101.6	4.0	25.4	60.57	65.85	8.72
90.0	6.0	15.0	82.33	88.05	6.95
90.0	4.0	22.5	43.62	47.47	8.83

5.6.4 Elastic modulus of CFRP

With the development of technology, people develop new CFRP with higher elastic modulus. The effect of these CFRP with various modulus is an important factor to be considered. Under this section CFRP with three elastic moduli 100 GPa, 210 GPa and 552 GPa were selected and the effect of a single layer of 750 mm length of these on 2000 mm curved beams were studied. The results obtained from the study are given in Figure 5.9. It is clearly observed that when elastic modulus increases both stiffness and the ultimate load capacity for beams also increased.

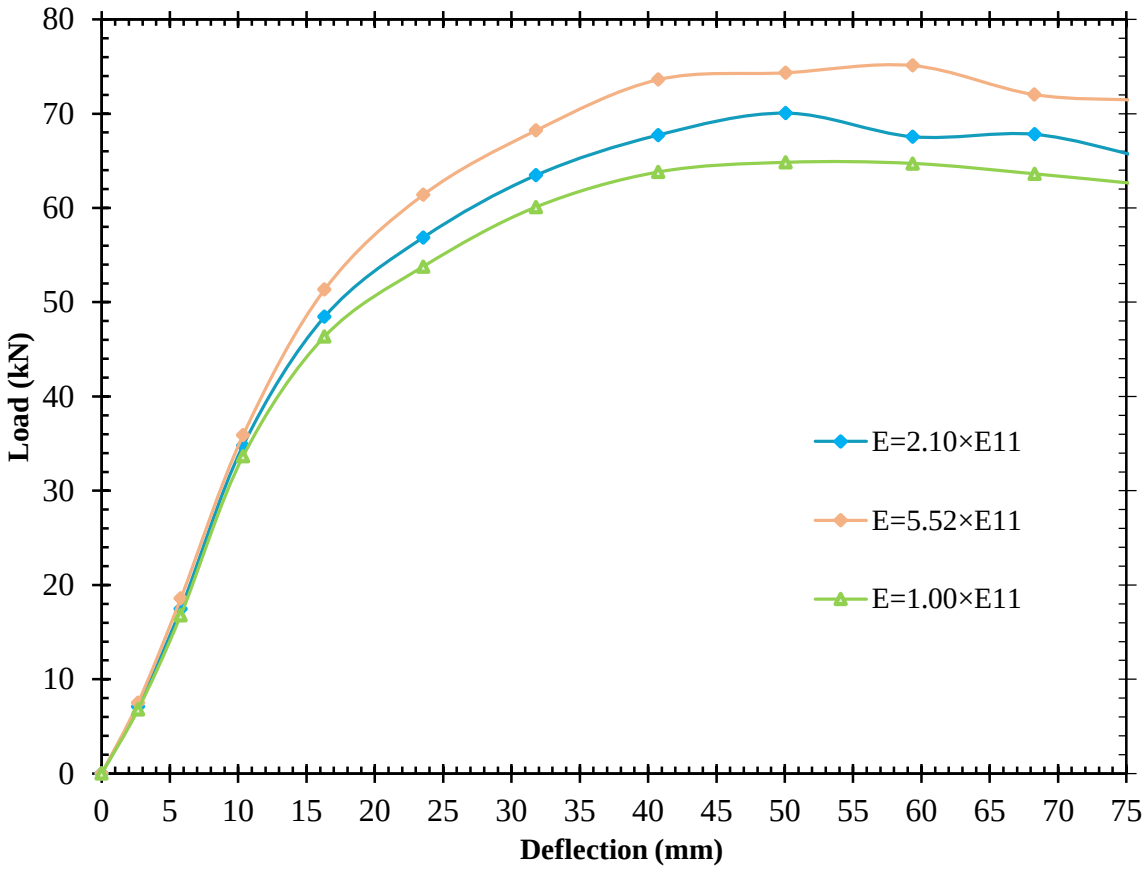

Figure 5.9. Load–displacement Curve of 2000 mm Curved Beam with 750 mm Length CFRP (a) for various modulus of elasticity

5.6.5 Adhesive Thickness

The effect of three adhesive layer thickness 0.15 mm, 0.30 mm, 0.50 mm, 0.8 mm and 1 mm on the ultimate load of CFRP strengthened 2000 mm curved beams were

investigated. Figure 5.10 shows the numerically obtained results under this study. It is noted that, the ultimate load and the stiffness of the beam increase when the adhesive thickness increase. This variation is insignificant and may be achieved due to the additional cross sectional area and moment of inertia due to the adhesive layer.

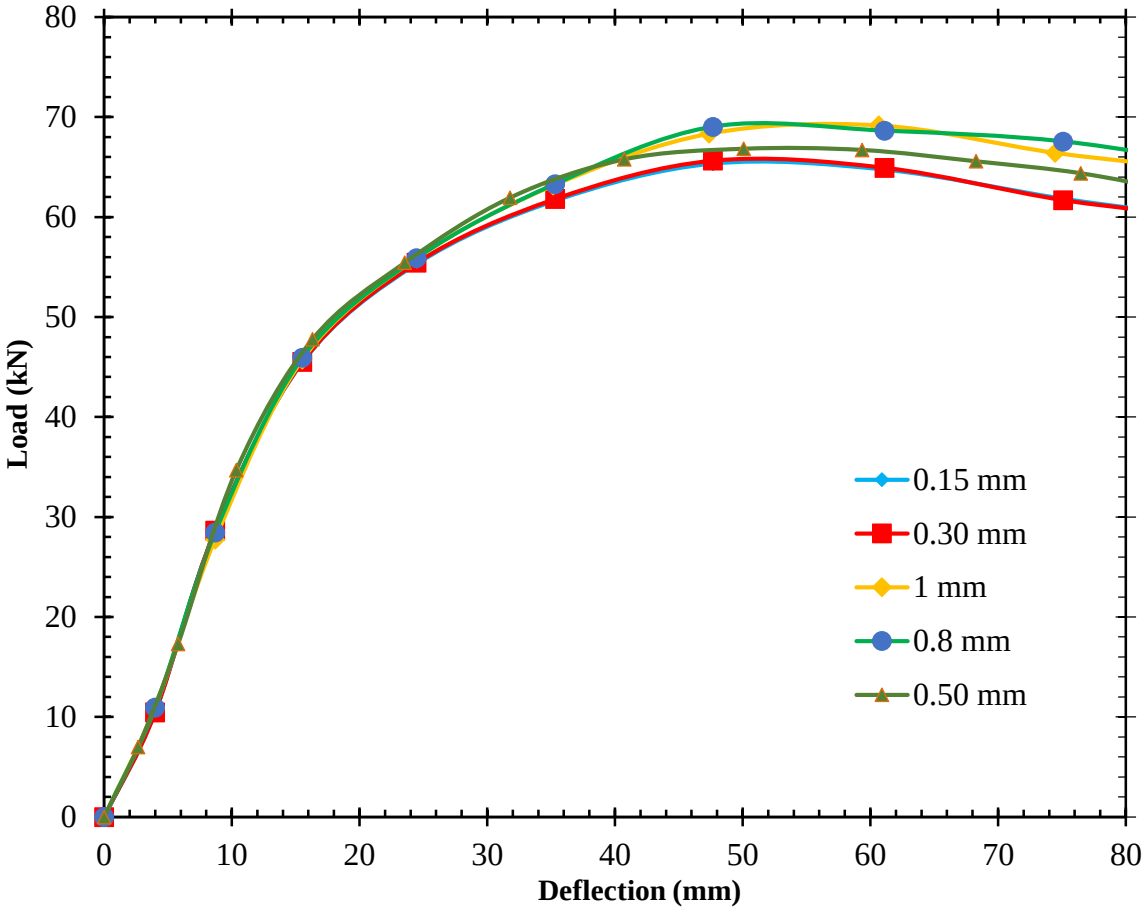

Figure 5.10. Load–displacement Curve of 2000 mm Curved Beam with 750 mm Length CFRP for various adhesive thicknesses

5.7 Recommendation

Figure 5.11 shows the percentage increase in ultimate loads of CFRP strengthened curved beams with respect to number of CFRP layers for various CFRP lengths generated with finite element modelling. These can be used to estimate the number of CFRP layers and the length of CFRP layers to obtain a given increment in ultimate load for CHS beams with various curvatures. It can be seen that the percentage

increment in ultimate loads between successive layers reduced for all the beams. This may be due to the pre mature failures of intermediate adhesive layers due to the weaker bond between CFRP and adhesive. This also gives an insight to the economical use of CFRP for the strengthening of curved CHS beams.

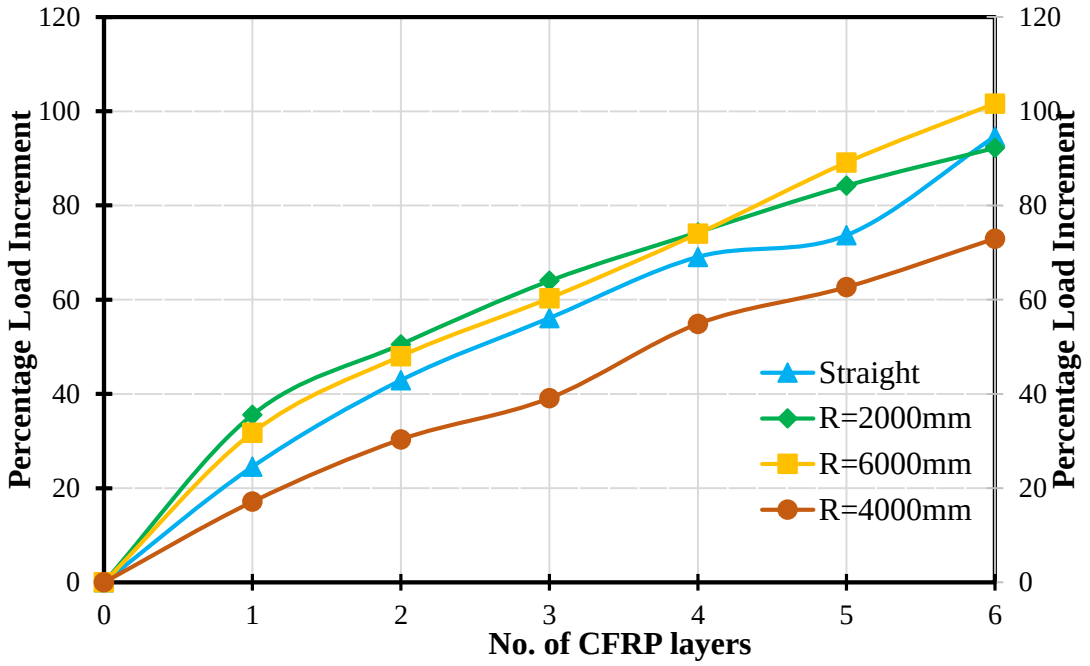

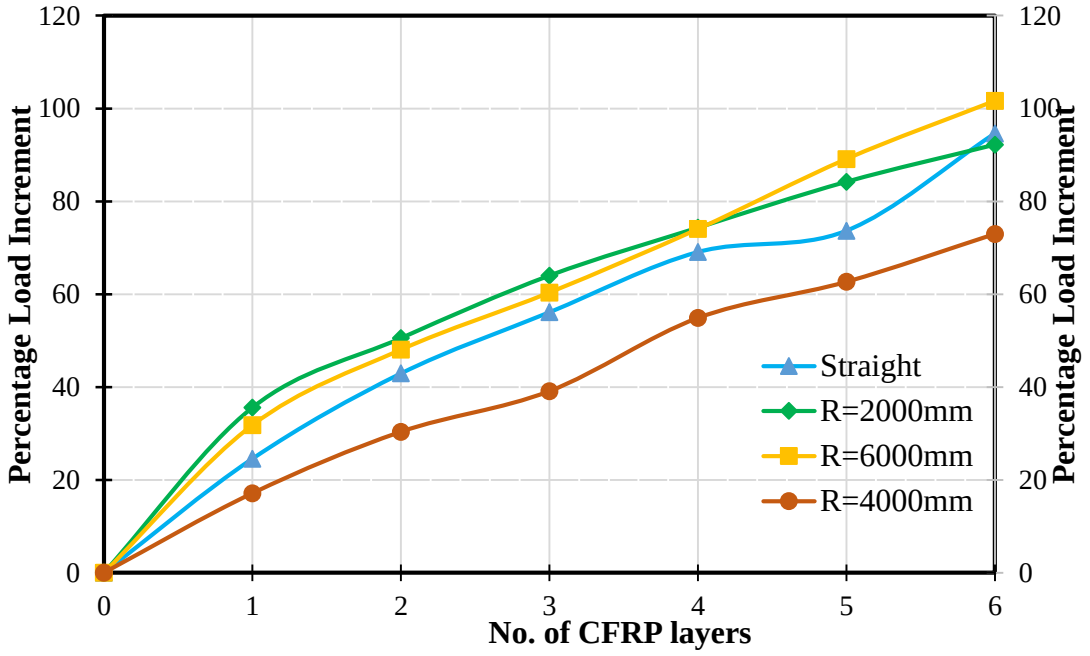

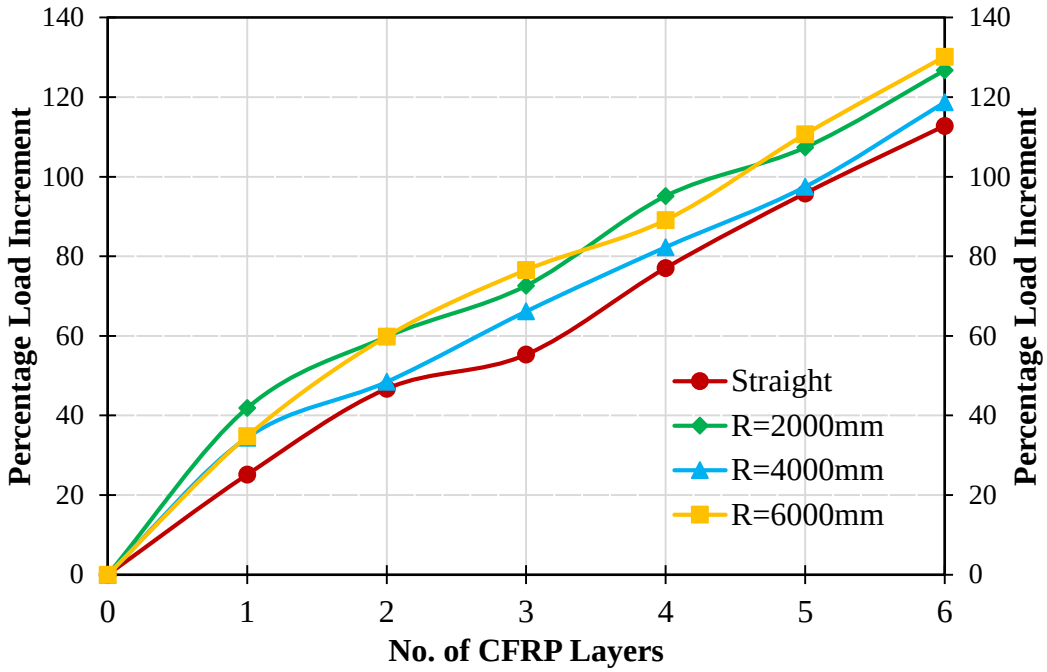

Figure 5.11. Percentage increment in ultimate load with respect to various CFRP lengths; (a) 500 mm; (b) 750 mm; and (c) 1000 mm for beams with different curvatures

5.8. Bond-slip behaviour

Bond behaviour between steel and CFRP is utmost important in predicting the behaviour of CFRP strengthened curved steel hollow sections. Figure 13 shows the bond-slip behaviour of CFRP strengthened tubular beams with different curvatures and with varied CFRP lengths. For all beams, straight and curved, full bond-slip behaviour was obtained in the beams with 500 mm CFRP length, since they show the debonding failure. The downside of bond-slip models for the beams strengthened with 750 mm and 1000 mm long CFRP were not obtainable due to the unavailability of debonding in these beams. A part of bond-slip was developed in other cases due to the local failure of steel substrate.

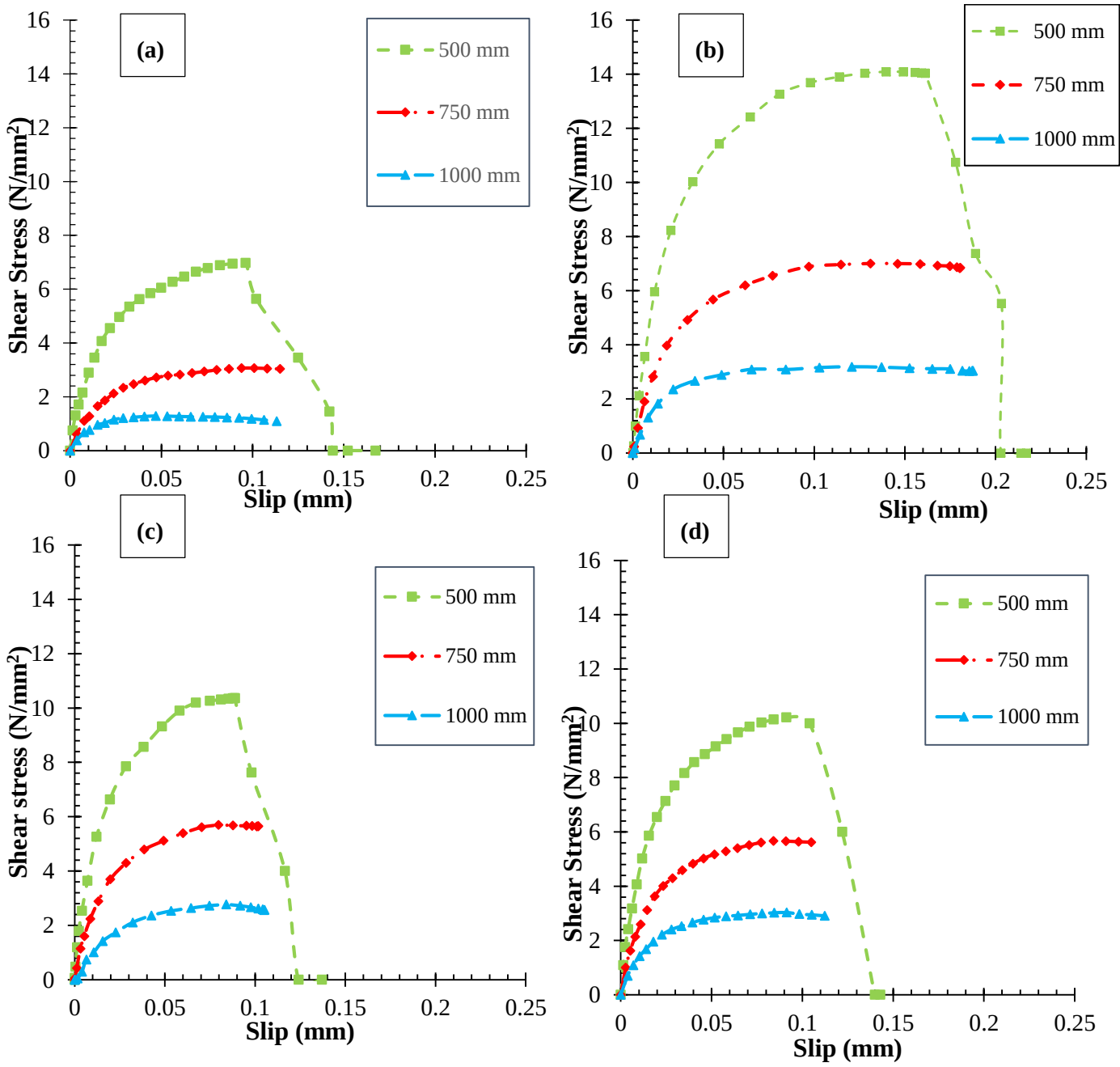

Figure 5.12. Bond-slip models for Beams with various curvatures and CFRP lengths; (a) straight beam, (b) 2000 mm curved beams, (c) 4000 mm curved beams, and (d) 6000 mm curved beam

It can be seen that the highest bond stress between CFRP and steel occurs in the beam with 2000 mm curvature and 500 mm long CFRP which showed the debonding

failure. Similar bond slip behaviour was noted in the beams with radii of 4000 mm and 6000 mm having 500 mm long CFRP, but with lower bond stresses. The lowest bond stress was found in the strengthened straight beams with 500 mm long CFRP. All the beams with 500 mm long CFRP have shown similar bod-slip curves irrespective of their curvatures. These specimens indicated the downward portion of the stress-slip behaviour, because of the observed debonding failure in CFRP laminates. However, specimens with bond lengths of 750 mm or greater did not show the descending parts of the bond-slip curve because the strength gain in flexure due to CFRP application was greater than the section capacity of steel member in result local buckling of steel tube. Hence, the CFRP bond had not reached the optimum level within the tested region.

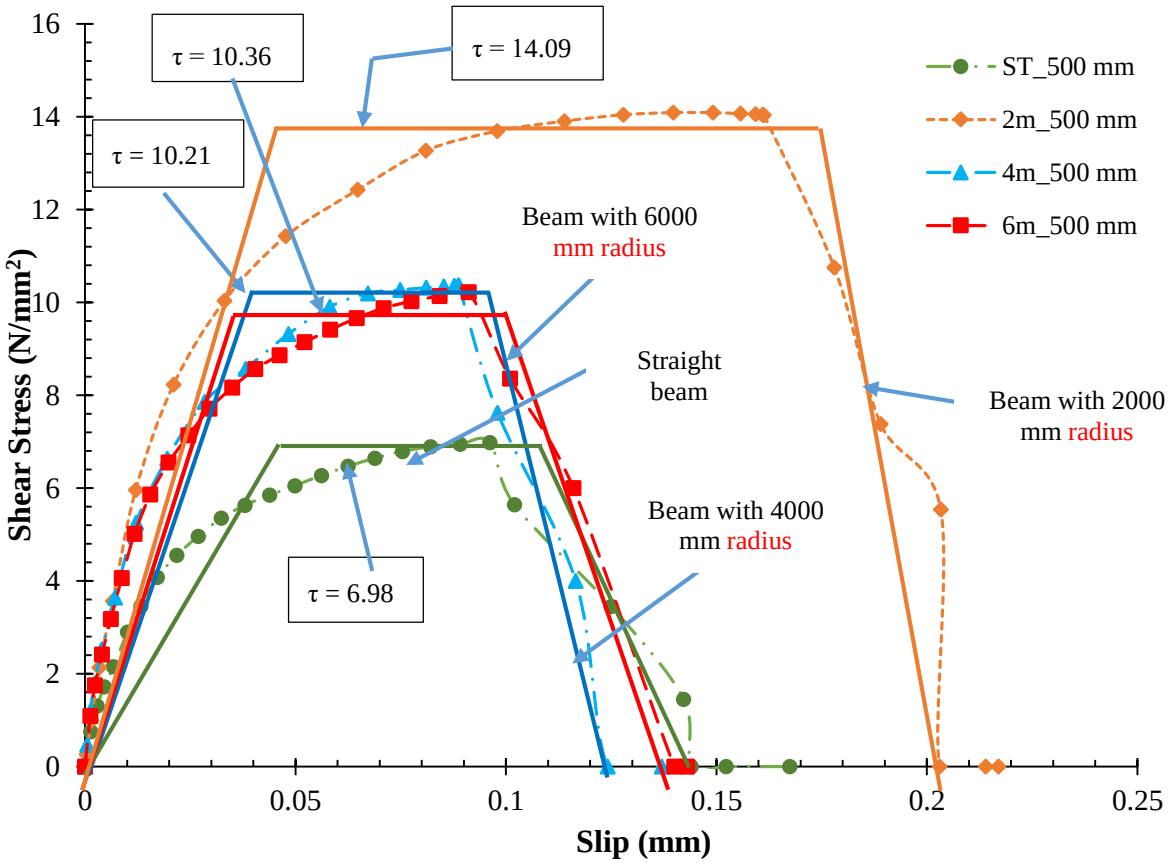

Figure 5.13. Predicted bond-slip models for beams with various curvatures and retrofitted with CFRP (bond length = 42% of the clear span)

Hence, beams which failed due to bond failure are considered for developing the idealized trapezoidal bond-slip models in Figure 14 for beams with various curvatures when CFRP length is 42% of the clear span. It can be clearly seen that these predicted trapezoidal bond-slip models highly depend on beam their curvatures. They can be represented by Eqn. (3) below, where the constants K_1 and K_2 depend on the radius of the beam and the percentage of CFRP along the clear span. Values for K_1 and K_2 for the straight beams and those with radii of curvature of 2000 mm, 4000 mm and 6000 mm are listed in Table 6.

$$\tau = \begin{cases} K_1.\tau_{max}.\dfrac{\delta}{\delta_1}, & \delta \le \delta_1 \\ \tau_{max}, & \delta_1 < \delta \le \delta_2 \\ K_2.\tau_{max}\dfrac{\delta_f - \delta}{\delta_f - \delta_2} & \delta_1 < \delta \le \delta_f \\ 0 & \delta > \delta_f \end{cases} \qquad \text{..... (3)}$$

where; τ_{max}= Adhesive maximum shear stress (MPa), δ = slip (mm), δ_1 = yield slip (mm), δ_2 = Initial slip (mm) and δ_f= Maximum slip (mm).

Table 5.8. Parameters related to the bond-slip models

Curvature (mm)	CFRP length (mm)	τ_{max} (N/mm^2)	δ_1 (mm)	δ_2 (mm)	δ_f (mm)	K_1 (N/mm^3)	K_2 (N/mm^3)
0	500	6.98	0.04	0.12	0.14	174.50	211.51
2000	500	14.09	0.05	0.17	0.20	293.54	503.21
4000	500	10.36	0.04	0.09	0.12	240.93	383.70
6000	500	10.21	0.04	0.11	0.14	268.68	319.06

The fracture energy (G_f) at the debond can be calculated using the area covered by the bond-slip curve as follows:

$$G_f = \frac{\tau_f}{2}\left[\delta_2 + \delta_f - \delta_1\right]$$

As per Figure 15, the straight beam shows the minimum fracture energy at the edge debonding while 2000 mm curved beams show the maximum fracture energy. Since the area under the bond-slip models for beams with 4000 mm and 6000 mm curvatures are almost the same fracture energy at the end debonding of those beams can be considered to be similar for this considered bond length. The fracture energy for debonding of retrofitted beam with 2000 mm radius shows a percentage increment of 360% when compared to the fracture energy for debonding in straight beams. This percentage increment for beams with radii of 4000 mm and 6000 mm are 168% and 131%, respectively.

5.9 Conclusions

This study presents an experimental and numerical investigation on flexural performance of CFRP strengthened CHS curved in elevation. Experimental study clearly shown that CFRP is a promising technique to enhance the flexural performance of CHS beams due to the increased stiffness. Full scale 3D finite element models were developed to conduct parametric study to investigate the effect of various parameter on the performance of CFRP strengthened curved CHS beams. Finite element models were validated using experimental results and following conclusions were drawn with the result of parametric study.

- Four major failure types were observed in CFRP strengthened curved SCHS beams including debonding of CFRP due to adhesive failure, bearing of the steel tube near the loading point, crushing of CFRP near the loading point and CFRP rupture on the tension face of the beam. When

CFRP wrap length was 500 mm, debonding of CFRP and rupture of CFRP were the critical failure modes. Beams tend to fail in other two mechanisms when wrap length was 750 mm and 1000 mm. But, full wrap of the beams did not show the highest ultimate load. It was found that the economical wrapping length of CFRP may obtain when the proportion between CFRP length and the total length of the beams is about 0.625.

- Number of CFRP layers drastically increases the ultimate load capacity of CFRP strengthened curved CHS, but this increment does not proportional to the number of layers. The percentage increment of ultimate loads between successive layers are reducing when the number of layer increases. Therefore, it is not economical to use large number of CFRP layers and the requires optimum number of layers should be evaluated as per the requirement. Layer orientation of CFRP patches is an important factor to be considered and this study focused on four-layer orientation longitudinal, hoop, spiral and reverse spiral. Longitudinal layer orientation was found to be best for the flexural performance. But when layers having mix of longitudinal, hoop ad spiral layer they also provide comparatively higher percentage increments in ultimate load.
- Aspect ratios of steel beams does not have significant effect on percentage increment in ultimate load capacity of CFRP strengthened beams. CFRP with higher tensile modulus and adhesive layer with higher thickness performed comparatively better in ultimate load capacity due to increased stiffness of the beams.
- A bond-slip model was developed for the CFRP strengthened curved steel tubular beams subjected to bending. It was observed that the bod-slip

model has a trapezoidal shape and the fracture energy at the end debonding depends on the beam curvature. Moreover, yield slip, initial slip and final slip for steel-CFRP interface of curved beams depends on the curvature of the beam and the length of CFRP sheet.

5.10 Chapter Summery

This chapter discussed about the numerical investigation of the behaviour of CFRP strengthened vertically curved steel beams under static loads. The first part of the chapter discussed on the experimental investigation part which used to validate finite element models. The section on experimental results discussed on the material selection and properties, sample preparation, testing method and some results obtained. Then the chapter discussed the development of finite element modelling of CFRP strengthened vertically curved steel circular hollow sections based on material models, meshing and element types. Finite element models were validated using respective experimental results; ultimate loads, failure loads and failure modes, prior to conduct parametric study. The parametric study presented here in this chapter is discussed on the effect of various parameters; number CFRP layers, CFRP length, layer orientation, aspect ratio of steel section, elastic modulus of CFRP, and thickness of adhesive layer on the increased in ultimate load of strengthened beams compared to control beams. Later part of the chapter provides some important guidelines for designers to follow when designing CFRP strengthened curved circular hollow sections.

Chapter 6

Experimental and Theoretical Investigation of CFRP Strengthened Horizontally Curved Steel I Beams

6.1. Introduction

Steel I beams are commonly used in structural applications, serving as floor beams in buildings and girders in bridges. These beams can be either straight or curved, either on a horizontal plane or a vertical plane. Vertically curved beams, also known as beams curved in elevation, find applications in bridge arches and curved roof structures. Horizontally curved beams, on the other hand, are used in curved bridge girders and curved floor beams, offering not only structural efficiency but also aesthetic appeal compared to straight beams (Figure 6.1). Curved beams have the advantage of transferring loads through a combination of bending and axial forces (Kostovailis, D.K.S.G., Hussein, M.F.M., and Owen, 2013; Yang et al., 2014).

Analyzing curved beams is more complex compared to straight beams due to the combined action of torsion and axial thrust. Early attempts to analyze horizontally curved beams subjected to concentrated loads and uniformly distributed loads were made by Wong (1970) using Castigliano's theorem and moment area methods. Wong developed equations to calculate bending moments, torsional moments, shearing stresses, and deflections. Gendy and Saleeb (1992) developed a set of governing differential equations for stretching, shearing, bending, twisting, and warping modes of deformation of curved beams using three-dimensional, two-field variational formulations.

A study on the inelastic analysis and behavior of horizontally curved steel I beams curved in-plane was conducted by B. Y. Pi, Bradford, and Trahair (2000a). Liew et al. (1995) investigated the behavior of curved I beams and proposed a simplified design method to estimate the ultimate load carrying capacity. They compared the load-deflection and ultimate loads obtained through numerical analysis with reported results in the literature. They also proposed an equation to evaluate the ultimate moment carrying capacity of horizontally curved I beams under various loading and boundary conditions.

Experimental studies on horizontally curved I beams were conducted by Shanmugam et al. (1995), who extended their study to predict the ultimate load behavior of two types of steel I beams: rolled sections and built-up sections. The test results obtained through a series of experiments showed good agreement with the results of numerical analysis performed using finite element models. In earlier studies, plastic collapse analysis (Boulton, N. S., and Boonsukha, 1959; Jackson, 1966; Yoo, C. H., and Heins, 1972) and the transfer matrix method (Fukumoto, Y., Nishida, 1981; Nakai, H., and Yoo, 1988; Yoshida and Maegawa, 1983) were used to analyze horizontally curved I beams. The effect of lateral-torsional buckling is a significant factor in determining the ultimate load capacity of horizontally curved I beams, and Nishida S, Yoshida H (1978) developed an equation to evaluate the amount of lateral-torsional buckling.

In recent years, Keesei Lee et al. (2017) proposed a set of empirical formulas to calculate the ultimate load capacity of horizontally curved I beams.

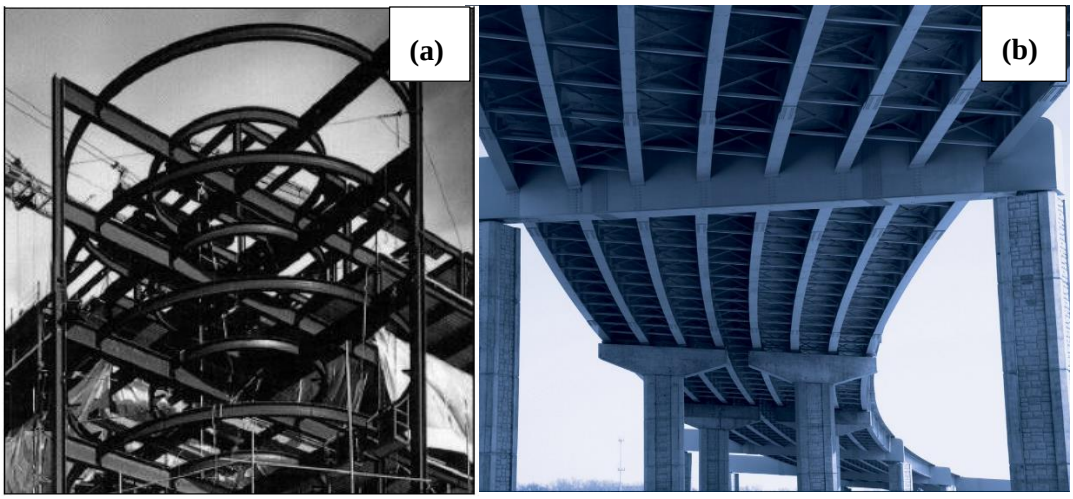

Figure 6.1. Applications of horizontally curved steel beams, (a) horizontally curved floor beams; and (b) horizontally curved I-beams in a highway bridge

Steel structures can deteriorate over time due to factors such as corrosion, lack of maintenance, and fatigue damage. In such cases, it becomes necessary to study rehabilitation methods for these structures, as the cost of replacement is typically higher compared to rehabilitation. Retrofitting and rehabilitation methods offer the advantage of shorter construction time and reduced service interruption. The traditional methods of strengthening steel structures using bolted, welded, or adhesive-bonded steel plates have limitations such as low durability, difficulty in application for complex shapes, increased self-weight of the structure, and susceptibility to fatigue due to stress concentrations caused by welding or drilling (Colombi and Poggi, 2006).

To overcome these limitations, new materials such as fiber-reinforced polymers (FRP), including carbon fiber-reinforced polymer (CFRP), have been introduced for strengthening steel structures. CFRP offers several advantages, including a high strength-to-weight ratio (reducing the increase in self-weight), enhanced durability (resistance to corrosion), applicability to complex shapes, chemical resistance, light

weight, flexibility, and minimal disruption during application. However, there are also some challenges associated with CFRP strengthening, such as inadequate design codes and standards, a shortage of skilled personnel, and the need for fire and UV radiation protection.

Numerous researchers have conducted studies on CFRP strengthening of steel I beams to evaluate various outcomes such as ultimate load capacity, changes in deflection and stiffness, effective bond length, and failure modes. These studies have utilized experimental testing, theoretical analysis, and finite element modeling. It has been found that CFRP strengthening enhances the stiffness of beams, leading to increased ultimate load capacity and reduced deflection at the serviceability limit state (Al-ridha, Abbood, and Atshan, 2020; Miller et al., 2001; David Schnerch and Rizkalla, 2008; Selvaraj and Madhavan, 2017; Sen, Liby, and Mullins, 2001; Soudki and Schumacher, 2009). Bagale, Asce, and Parvin (2020) found that the effective CFRP length under static load conditions for a simply supported beam is 2/5 of the span, and the flexural capacity can be enhanced by 1.5 times under fatigue loading when additional anchorages are used. Proper installation of CFRP materials is crucial to prevent premature failure due to debonding and to achieve the desired level of strength gain (D. Schnerch et al., 2007). The mechanical properties of CFRP and adhesives also affect the bond behavior and ultimate strength gain of CFRP-strengthened beams. Failure modes of CFRP-strengthened I beams include below point splitting, below point load debonding, end delamination, and end debonding, which depend on the strengthening scheme, including CFRP bond length, adhesive and CFRP properties, CFRP thickness, and surface preparation for CFRP bonding (Li et al., 2018; Narmashiri, Sulong, and Zamin, 2012; Selvaraj and Madhavan, 2017).

The use of finite element modeling is a prevalent approach for evaluating the effects of different parameters on the performance and failure modes of CFRP-strengthened steel I beams. Commercially available software like ABAQUS and ANSYS are commonly used for finite element modeling of CFRP-strengthened steel beams. The developed finite element models using these software tools have shown reasonable agreement with experimental results, making them suitable for conducting parametric studies. In many cases, cohesive zone modeling (CZM) is employed to simulate the adhesive layer between the CFRP strip and steel beam. Researchers have found that CZM accurately predicts the behavior of the adhesive layer when modeled using cohesive elements with traction-separation laws (Chiew, Yu, and Lee, 2011; Colombi and Poggi, 2006; Kadhim et al., 2019; Lenwari et al., 2006; Selvaraj and Madhavan, 2017; Teng, Fernando, and Yu, 2015b).

Debonding failures in steel beams flexurally strengthened with CFRP laminates have been successfully modeled by Teng, Fernando, and Yu (2015a). They found that CFRP plates with higher elastic modulus and/or larger thickness may result in lower ultimate loads due to premature debonding of the CFRP plate, particularly if the failure is governed by plate end debonding. Plate end debonding is more likely to occur when shorter CFRP plates are used, while the use of longer CFRP plates may lead to different failure modes such as intermediate debonding or compression flange buckling. Yu, Chiew, and Lee (2011) investigated bond failures in steel beams strengthened with FRP laminate and conducted a parametric study to assess the effects of CFRP thickness, CFRP elastic modulus, adhesive layer thickness, and bond length on bond strength. Narmashiri, Sulong, and Zamin (2012) developed a full 3D model using ANSYS software and employed nonlinear analysis to simulate CFRP-

strengthened steel beams. They observed that the use of longer CFRP plates reduced strain at the CFRP tip compared to shorter CFRP plate lengths.

While there is a considerable body of literature on CFRP strengthening of straight steel I beams, no research has specifically targeted the behavior of CFRP-strengthened horizontally curved steel beams. Therefore, the objective of this study is to investigate the structural behavior of CFRP-strengthened horizontally curved steel beams under vertical loads. Firstly, an experimental study was conducted on horizontally curved steel I beams with varying curvatures and CFRP configurations. Subsequently, theoretical equations were developed, modifying the equations provided by Shanmugam et al. (1995), to evaluate the deflection and rotation of the strengthened beams under vertical loads.

6.2 Experimental Programme

6.2.1 Material Properties

Material properties required for both experimental and theoretical studies were obtained by conducting coupon test on randomly selected material samples. Standard S235 hot rolled IPE 100 section was used to prepare the specimens. The stress strain relationship for steel was obtained using coupon tests conducted as per the ASTM A370/ASME AS-370 for three coupons extracted from both flange and web as per the dimensions given in the same standard (ASTM A370 / ASME SA-370, 2016). Two strain gauges were attached to the sample prior to conduct the test in order to obtain the strains in both axial and lateral directions to calculate the Poisson's ratio. Figure 6.1 (a) and (b) show the coupon dimensions and the stress-strain curve obtained respectively.

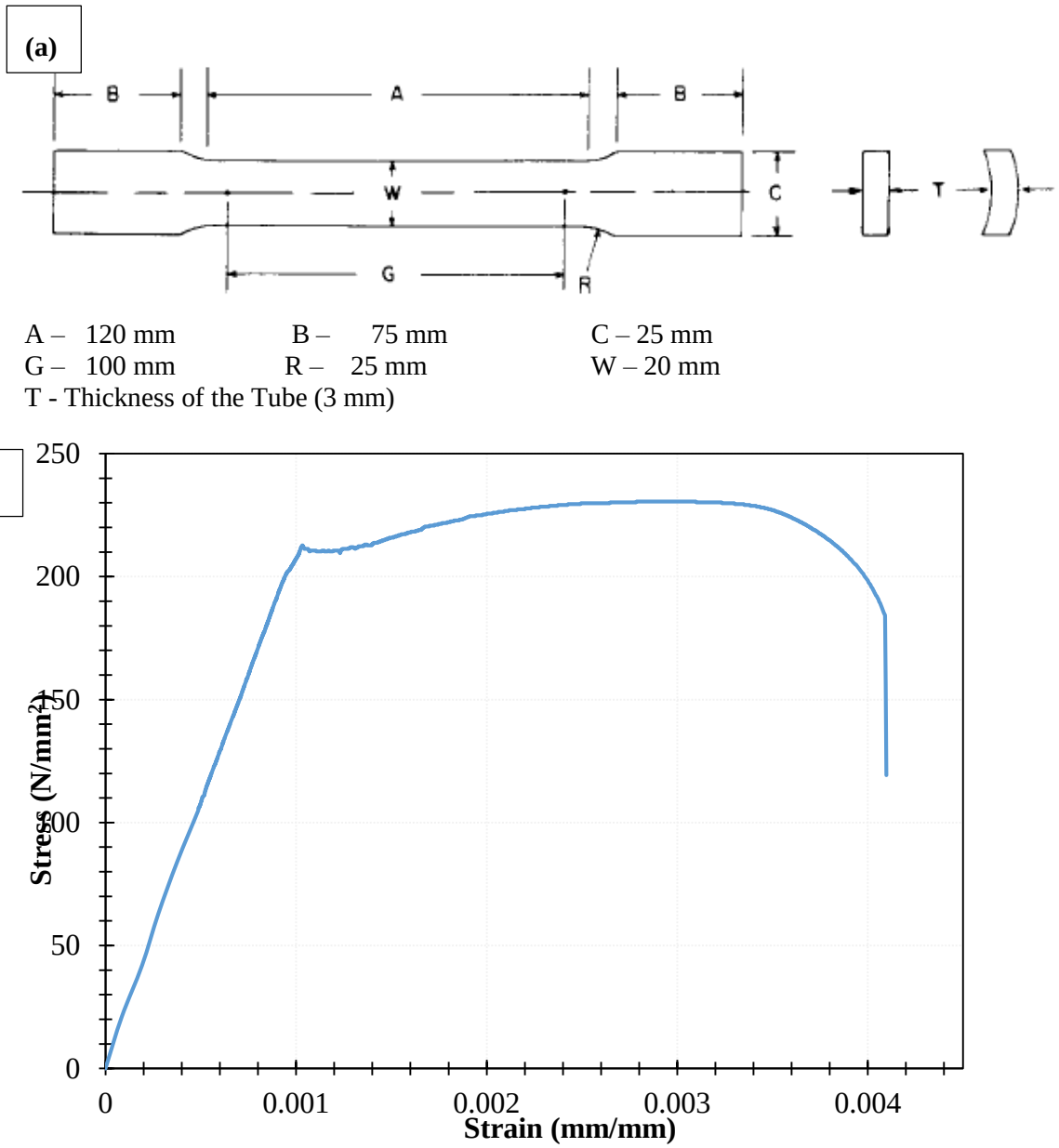

Figure 6.1. (a) Steel coupon test with coupon size; (b) Stress-strain curve

Material properties of CFRP strips were obtained using coupon tests conducted on coupons prepared as per the guidance given in ASTM D-3039/D-3039M. Five coupons were tested under Quisi static loading with a strain rate of 0.025mm/sec. The properties related to the fibre direction of CFRP were obtained. Figure 6.2 (a), (b) and (c) show the coupon dimensions, testing arrangement, and stress-strain curves obtained for five coupons respectively. Average stress and strain were considered when applying values for calculations.

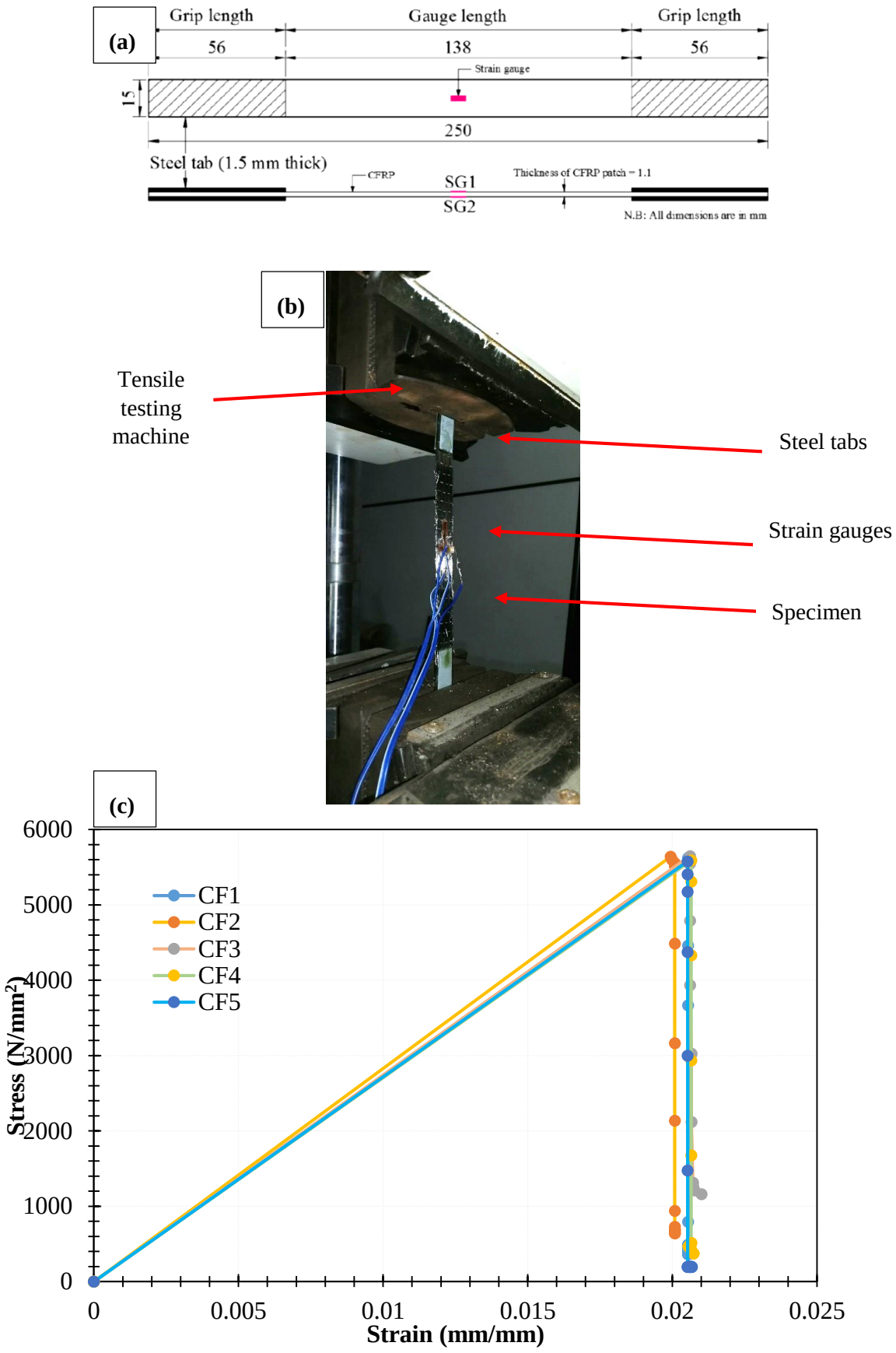

Figure 6.2. (a) Coupon dimensions; (b) testing arrangement; and (c) Stress-strain curves

Two parts epoxy adhesive Araldite 420 was used to bond CFRP strips to the bottom of the tensile flange and the either sides of the web. The mixing ratio of the epoxy was three part of component A (resin) to one part of component B (hardener) by volume/weight. Properties required for the adhesive was obtained through material specifications provided by manufacturer. The related properties for steel, CFRP and adhesives are illustrated in Table 6.1.

Table 6.1. Material properties of steel, CFRP and Adhesive

	Steel	CFRP	Adhesive
Thickness (mm)	5	0.116	0.0005
Elastic modulus (GPa)	206	270	2.4
Tensile strength (MPa)	235	5550	40
Yield strength (MPa)	215	-	-
Tensile strain (mm/mm)	0.011	0.021	0.022

6.2.2 Sample Preparation

Total 12 numbers of sample beams were prepared for testing. 6000 mm long beams were cut into five pieces so that each specimen beam has a total length of 1200 mm. Out of the twelve beams four beams were kept straight while other eight beams curved into two different curvatures 4000 mm and 6000 mm, four from each using roller bending. Three beams from each curvature including straight beams were strengthened with different CFRP configurations while keeping one from each category as control beams. All the beams were sand blasted prior to apply CFRP on to them. The actual section of the beams with dimensions and sand blasted beams prior to apply CFRP are shown in Figure 6.3. CFRP sheets were cut in to appropriate dimensions (750 mm length and 50 mm width for tension flange and 75 mm width for the web). Sand blasted surface of beams then, treated with acetone in order to remove

grease, rust and oil and to obtain a chemically active, clean and rough surface. The adhesive was applied using a spatula on the steel adherent surface and CFRP patches were sticked carefully. Then the CFRP patches were pressed to steel surface using a small roller as shown in Figure 6.4. This force out air bubbles and the excessive epoxy and give a uniform thick epoxy adhesive layer. Three CFRP configurations (PR1, PR2 and PR3) were used to strengthened for the beams with each curvature as shown in Figure 6.5 and the details of specimens are illustrated in Table 6.2.

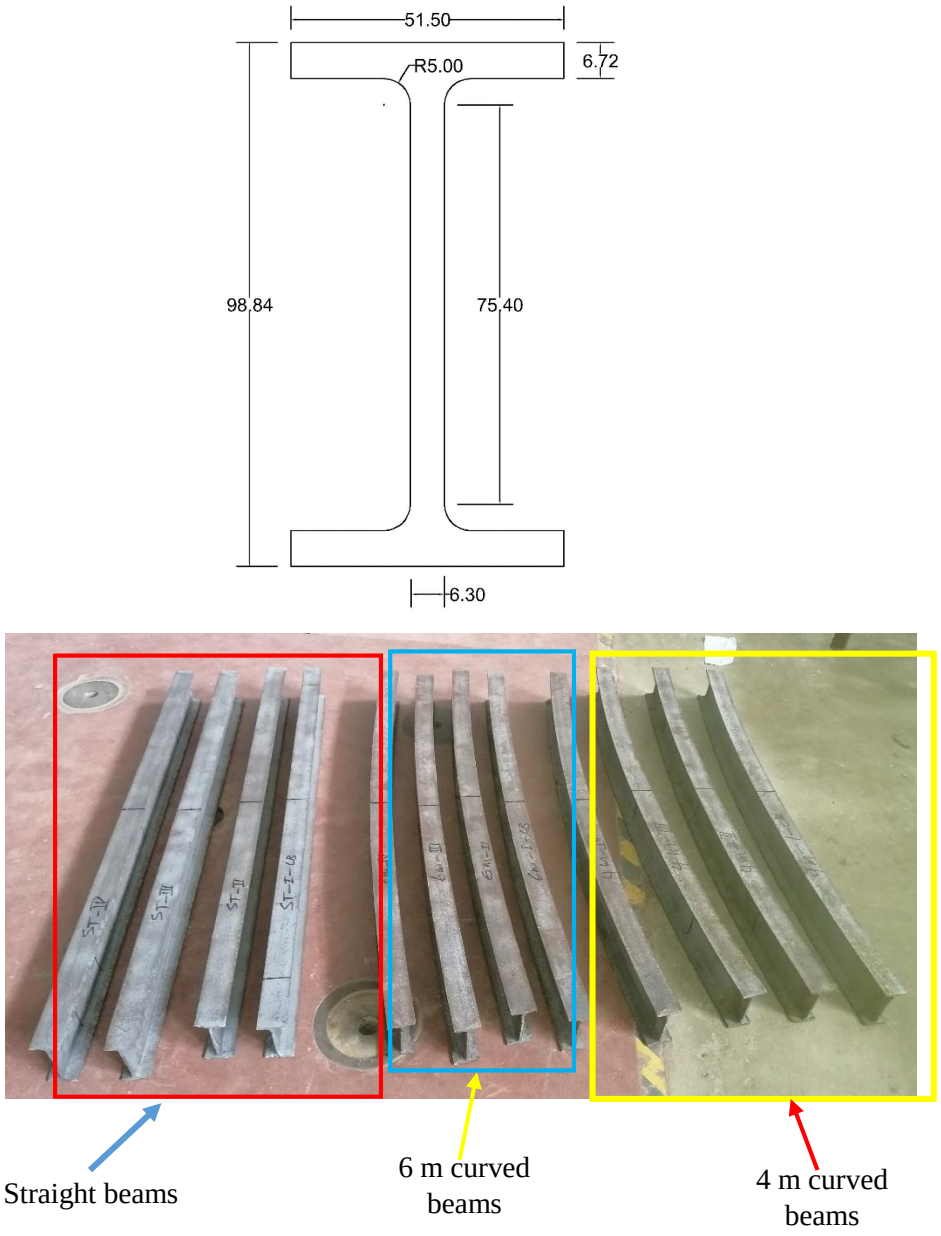

Figure 6.3. (a) Dimensions of the beam section; (b) Sand blasted beams with various curvatures

After application of CFRP, beams were kept for curing for at least seven days under normal environmental conditions prior to testing. Once the beams are cured, three strain gauges were fixed to on CFRP layers and steel beams, one at the mid span of the tension flange, second one at the CFRP tip, and the remaining one at the mid span of the web (Figure 6.6). These strain gauges were fixed to both control and strengthened beams.

Figure 6.4. Pressing of CFRP using a roller

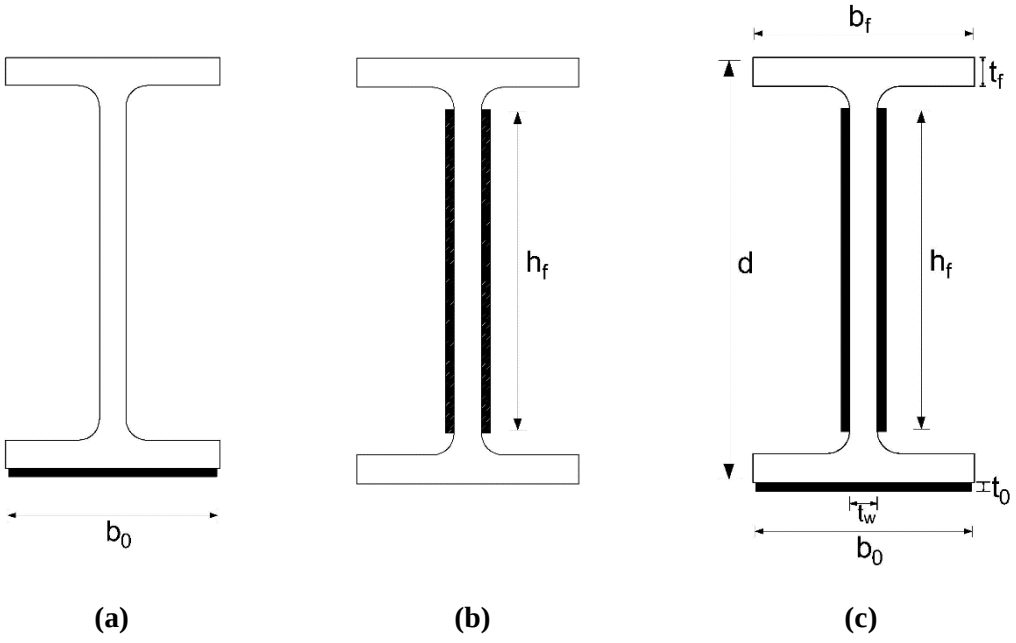

Figure 6.5. CFRP application configurations

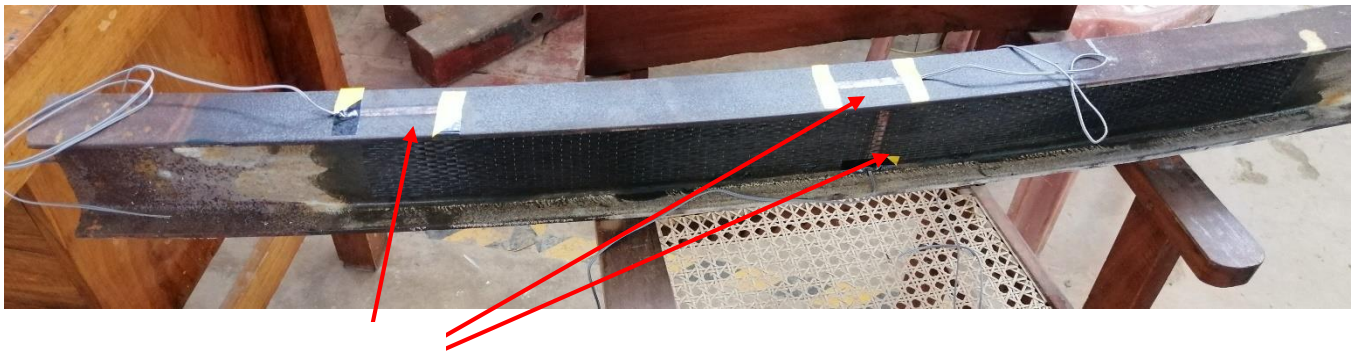

Figure 6.6. Positions of strain gauges

Table 6.2. Details of Specimens

Specimen	$d \times b_f \times t_f \times t_w$	R (mm)	b_0 (mm)	h_f (mm)	L_0 (mm)	L (mm)
ST_CB	98.84 × 51.50 × 6.30 × 6.72	0	-	-	750	1000
ST_PR1	98.84 × 51.50 × 6.30 × 6.72	0	50		750	1000
ST_PR2	98.84 × 51.50 × 6.30 × 6.72	0	-	75	750	1000
ST_PR3	98.84 × 51.50 × 6.30 × 6.72	0	50	75	750	1000
4000_CB	98.84 × 51.50 × 6.30 × 6.72	4000	-	-	750	1000
4000_PR1	98.84 × 51.50 × 6.30 × 6.72	4000	50		750	1000
4000_PR2	98.84 × 51.50 × 6.30 × 6.72	4000	-	75	750	1000
4000_PR3	98.84 × 51.50 × 6.30 × 6.72	4000	50	75	750	1000
6000_CB	98.84 × 51.50 × 6.30 × 6.72	6000	-	-	750	1000
6000_PR1	98.84 × 51.50 × 6.30 × 6.72	6000	50		750	1000
6000_PR2	98.84 × 51.50 × 6.30 × 6.72	6000	-	75	750	1000
6000_PR3	98.84 × 51.50 × 6.30 × 6.72	6000	50	75	750	1000

6.2.3. Experimental Test Setup

All the beams were tested under fixed-fixed condition as shown in Figure 6.7 and loading was applied using a lading frame. A 250 kN capacity load cell was used to measure the applied load. Two LVDTs were fixed at the mid-span in both vertical and horizontal directions, in order to measure both vertical and horizontal deflections. The load, deflections at the mid span and strain reading were recorded using a data logger while applying the load on the beam at a constant rate of 0.5 mm/min. All the beams were tested until the failure.

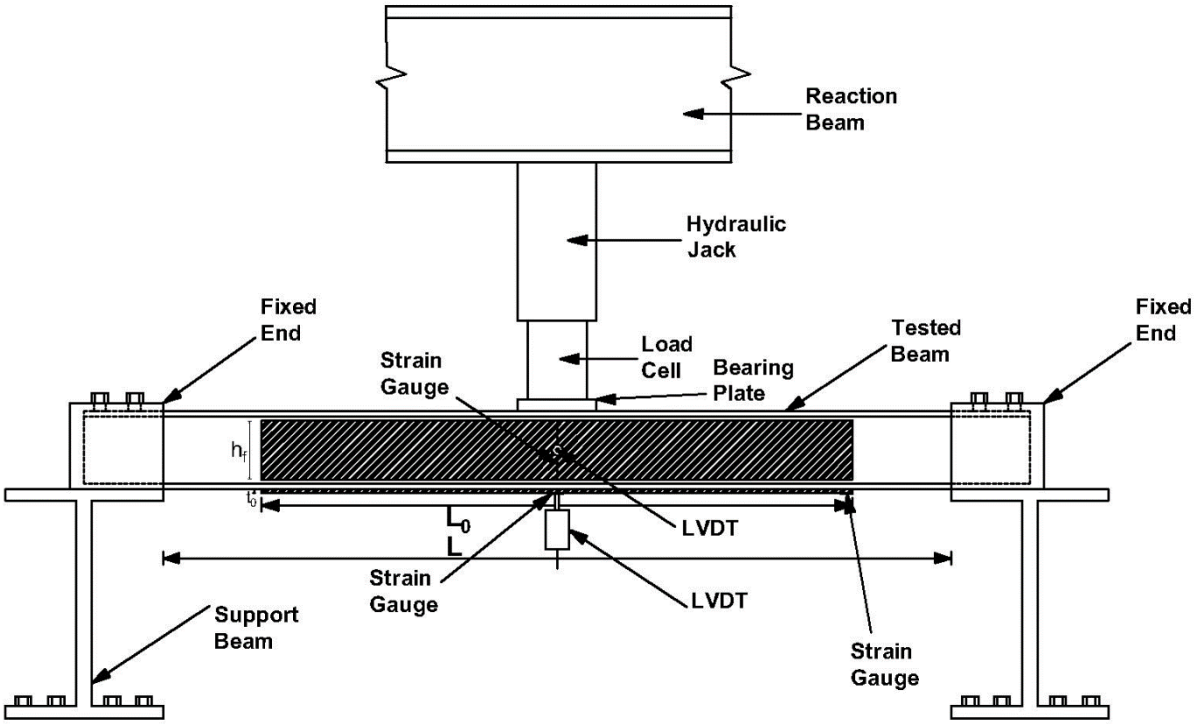

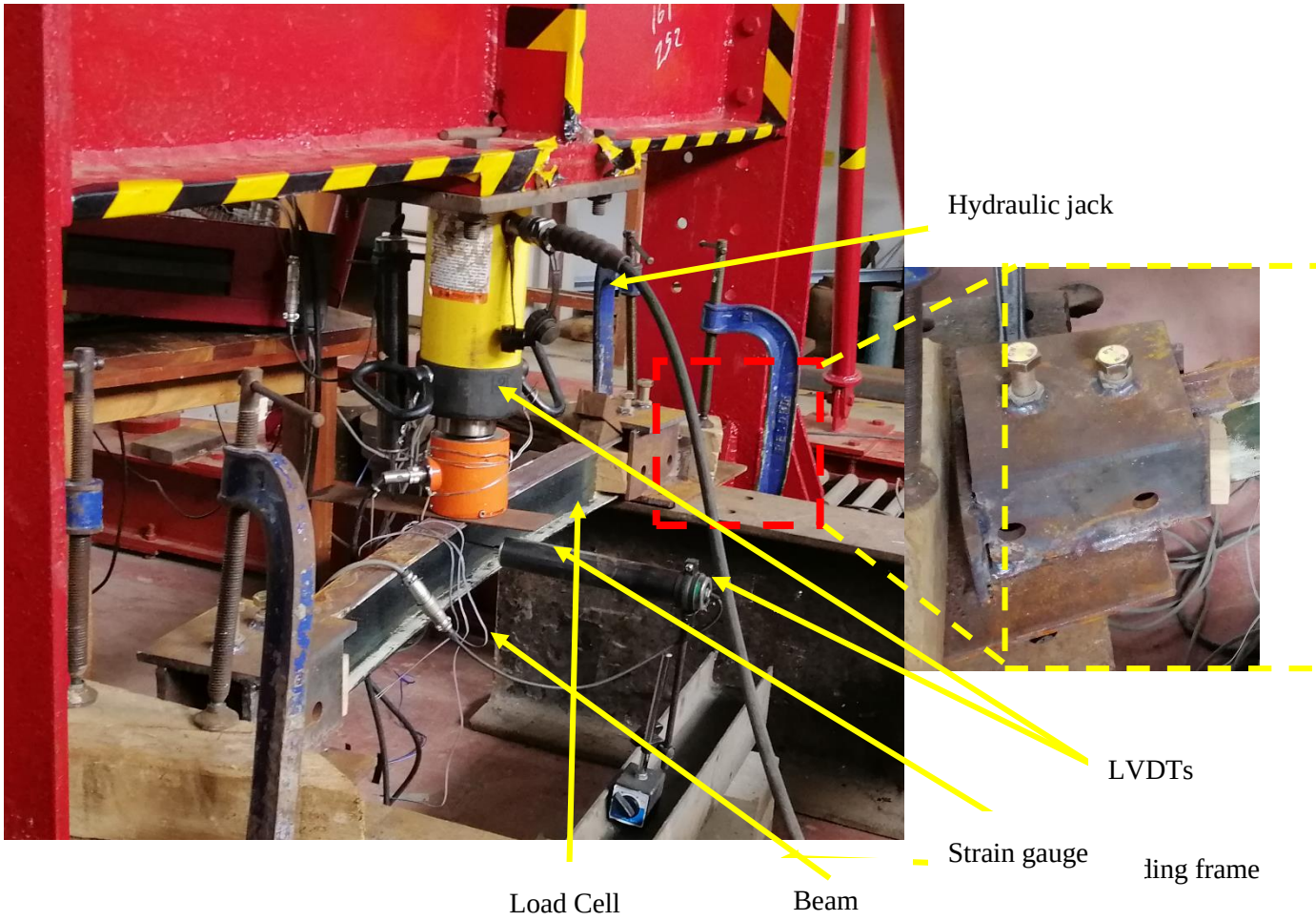

Figure 6.7. (a) Experimental Test Setup and Instrumentation

6.4. Experimental Results

All un-strengthened and strengthened beams (straight and curved) with different CFRP configurations (PR1, PR2, PR3) were tested until failure of CFRP or failure of beams. The transient loads and the corresponding deflections and strain variations were noted. The ultimate load of each strengthened beam was compared with that of the corresponding un-strengthened beam. Failure initiation and propagation were also monitored. Furthermore, these failure patterns were used to validate the theoretical predictions.

6.4.1. Load – deflection behaviour

The load – deflection behaviour of straight, 4000 mm curved and 6000 mm curved beam are shown in Figure 6.8 (a), 6.8(b) and 6.8(c) respectively. It can be observed that all the ultimate load capacity of control beams decreases with the reduction of curvature of beams. The ultimate loads for the control beams with 0 mm, 4000 mm and 6000 mm are, 56.7 kN, 48.1 kN and 55.7 kN respectively. It was also noted that the deflection at ultimate load reduced when the curvature reduced. This is because of the lateral torsional buckling failure of curved beams due to the combined action of bending and torsion. Those deflections are 30 mm, 24 mm and 13.4 mm respectively for beams with curvatures 0 mm, 4000 mm and 6000 mm respectively.

Strengthening of both straight and curved beams using CFRP increases the ultimate load of all the beams irrespective of the curvature. It is clearly visible from Figure 6.8, the strength gains in strengthened beams varies with different CFRP configurations and beams strengthened with profile 3 (CFRP on both web and flange) acquired the highest strength compared to the control beam. In straight beams the percentage strength gains for beams with profile 3 CFRP configuration is 17.2%. This value for straight beams with CFRP profile 1 and profile 2 are 11.1% and 12.5% respectively. It was also noted that the deflection at the ultimate loads for beams with all the CFRP configurations were reduced and the minimum was observed in beam with CFRP profile 3. This was due to the enhanced stiffness of CFRP strengthened beams. It was noted that the strengthened beams shown higher stiffness compared to unstrengthened beam, especially in beams with CFRP applied onto its web (profile 2 and profile 3) which prevent the web buckling.

When considering beams with 4000 mm curvature, highest strength gain was recorded for beams strengthened with PR3 CFRP configuration. This percentage is 13.2%

greater than the ultimate strength of the control beam (CB). Beams strengthened with the CFRP configurations PR1 and PR2 showed strength percentage strength gains of 10% and 4% respectively. Deflections for beams strengthened with CFRP configurations PR2 and PR3 showed similar mid span deflection at the ultimate load. Control beam and the beam strengthened with CFRP configuration PR1 showed lower mid span deflections at the ultimate loads. The deflection at the failure for all the beams with 4000 mm curvature are less than that of straight beams. The stiffnesses of beams with CFRP configurations PR1, PR2 and controlled beam observed to be same until a load of 40 kN and then varied such that the beam with PR2 get a higher stiffness compared to others. The beam strengthened with CFRP configuration showed higher stiffness compared to other beams at any given load.

The deflections at ultimate loads are lower in beams with 6000 mm curvature when comparing to the straight and beams with 4000 mm curvature. Even though ultimate loads are different for CFRP application configurations, deflections at ultimate loads for beams are almost same irrespective of CFRP application configuration for both strengthened and unstrengthened beams with 6000 mm curvature. The beam with CFRP configuration PR3 showed the highest strength gain compared to the unstrengthened control beam of 6000 mm curvature. This percentage was 10.5%, while beams with CFRP configurations PR1 and PR2 showed percentage increment in ultimate loads by 5.1% and 5.8% respectively. For beams with 6000 mm curved beams strengthened with various CFRP configurations showed same stiffness until 50kN load irrespective of CFRP configuration. Overall the highest ultimate load was observed in control beams was observed in in beam with 6000 mm curvature. The lowest ultimate load for control beams was observed in beams with 4000 mm curvature. The highest ultimate for strengthened beams was observed in straight beam

strengthened with PR3 CFRP strengthening configuration while the lowest ultimate for strengthened beams observed in beams with 4000 mm curvature and PR1 CFRP configuration.

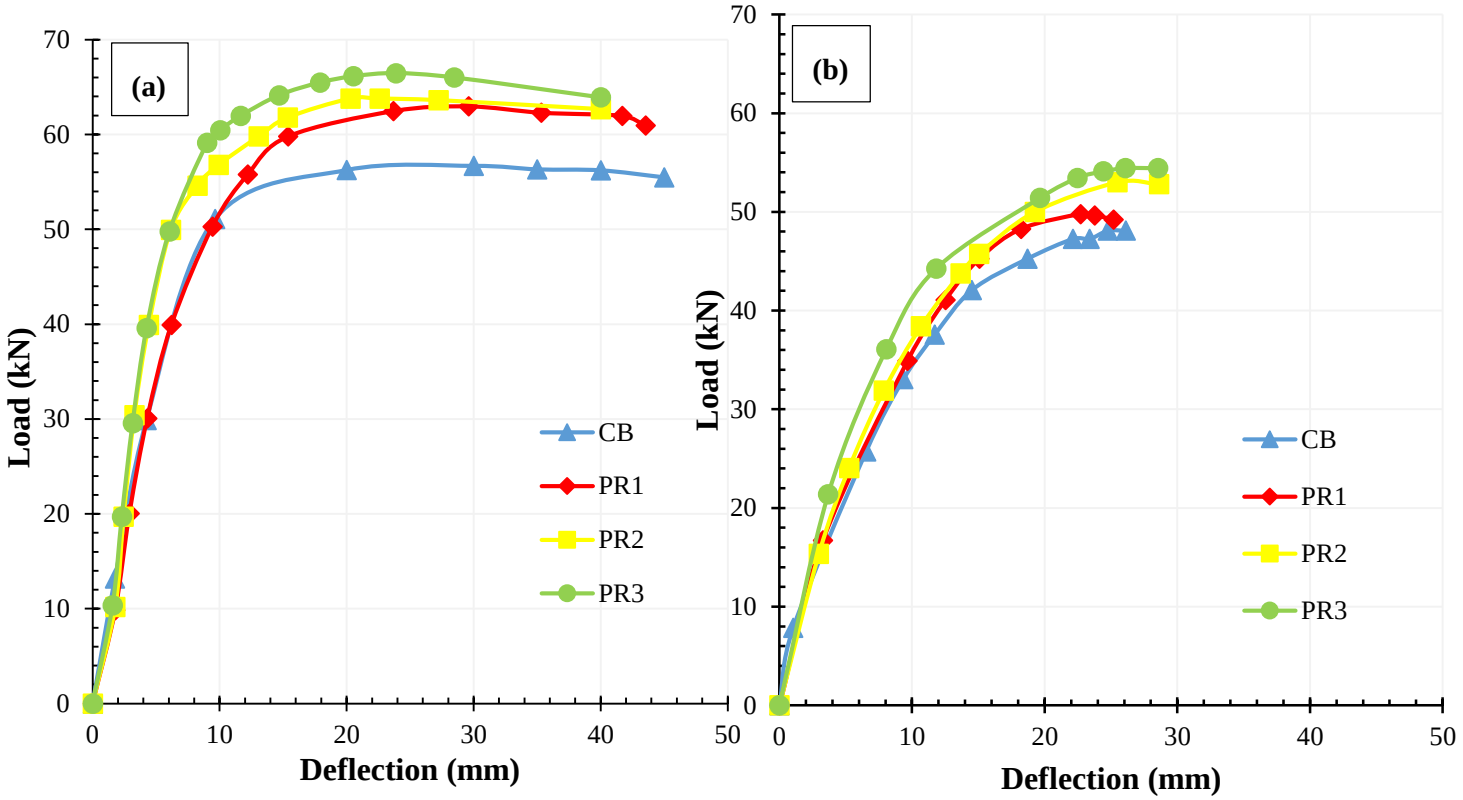

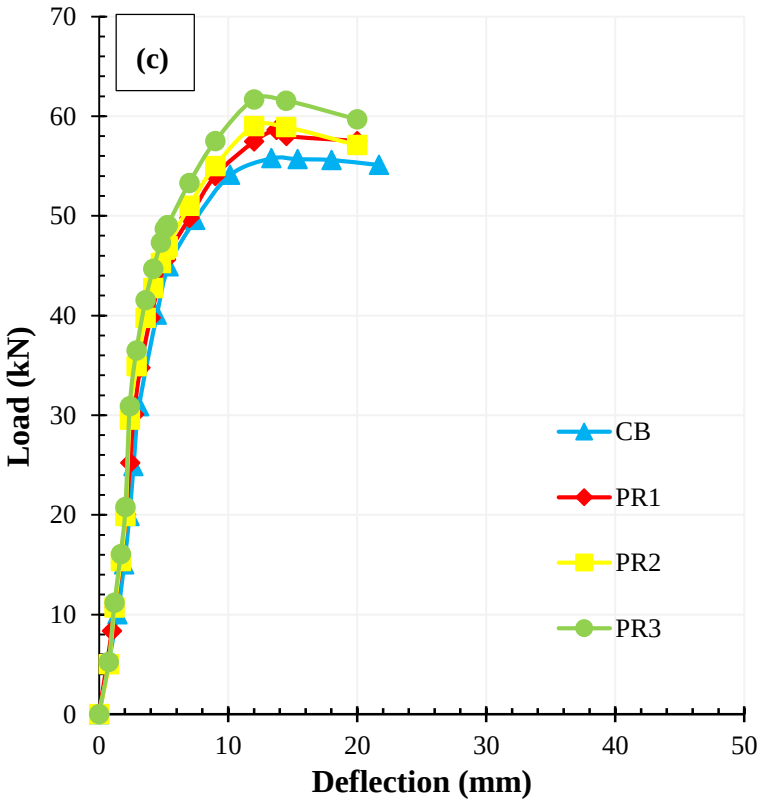

Figure 6.8. Load Vs mid-span deflection curve for (a) straight beams (b) beams with 4000 mm curvature and (c) beams with 6000 mm curvature

6.4.2. Strain variations

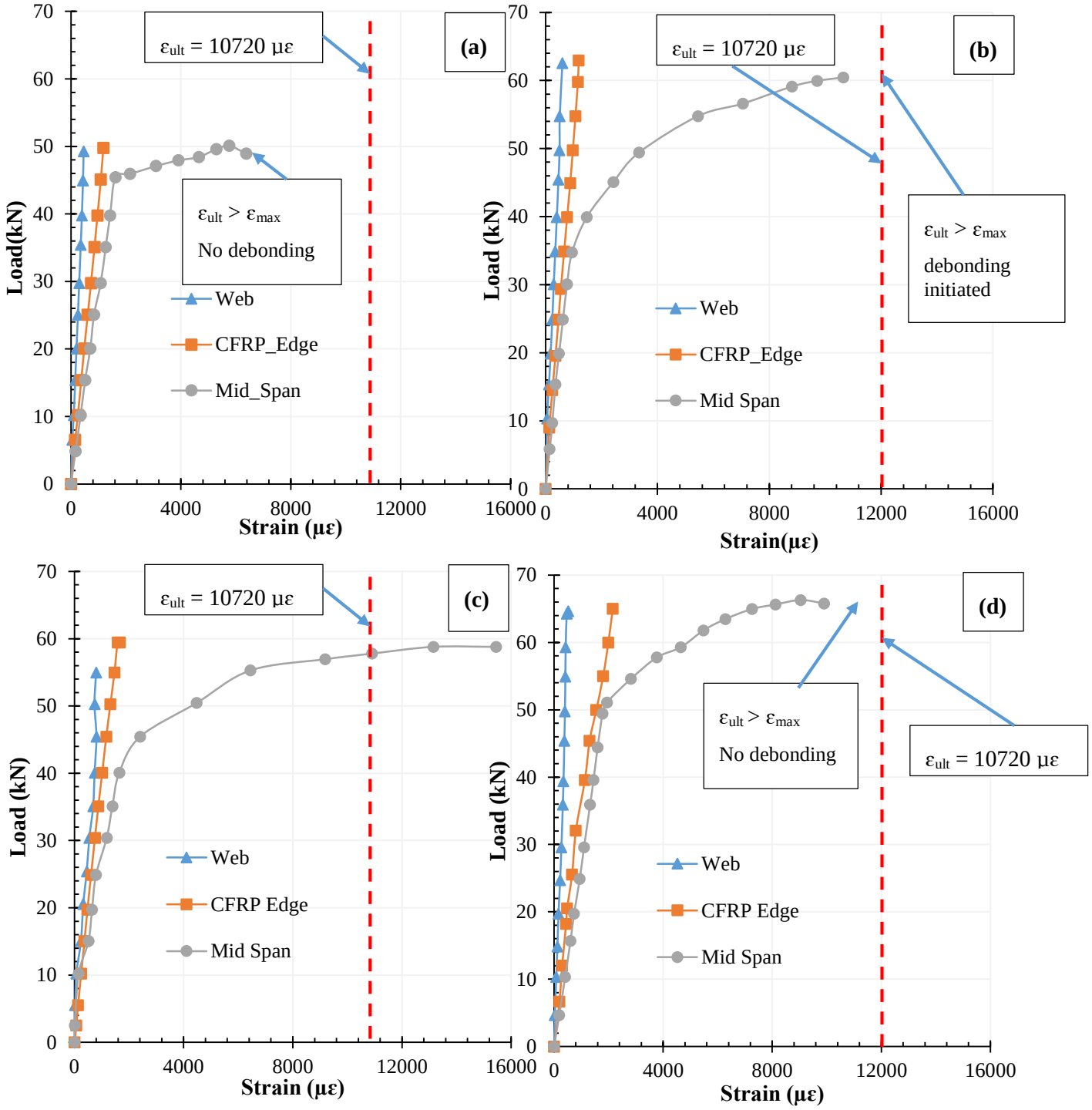

Figure 6.9. Load Vs strain curves for straight (a) control beam (b) beam with PR1 (c) beam with PR2 and (c) beam with PR3

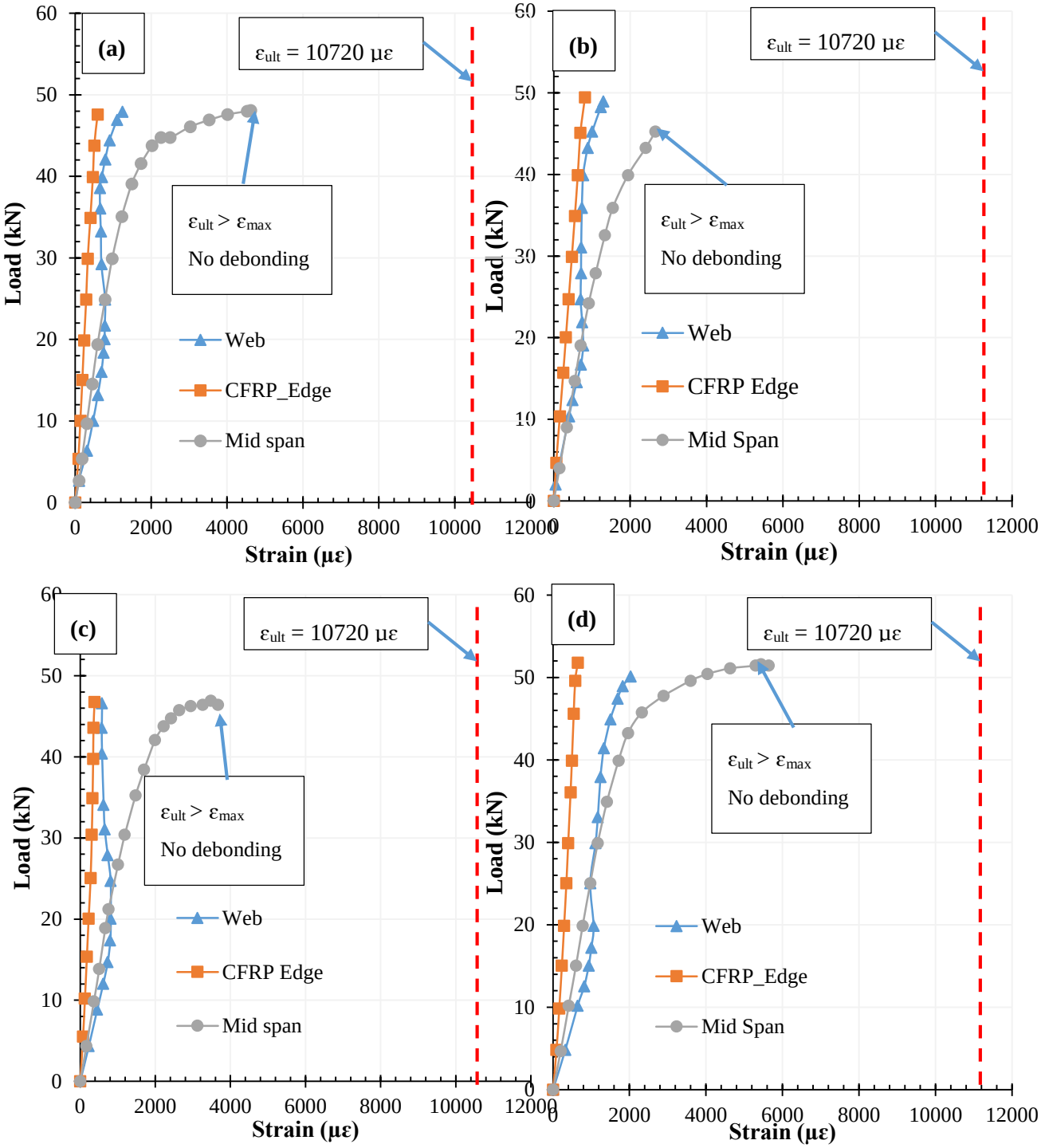

Figure 6.9. Load Vs strain curves for beams with 4000 mm curvature (a) control beam (b) beam with PR1 (c) beam with PR2 and (c) beam with PR3

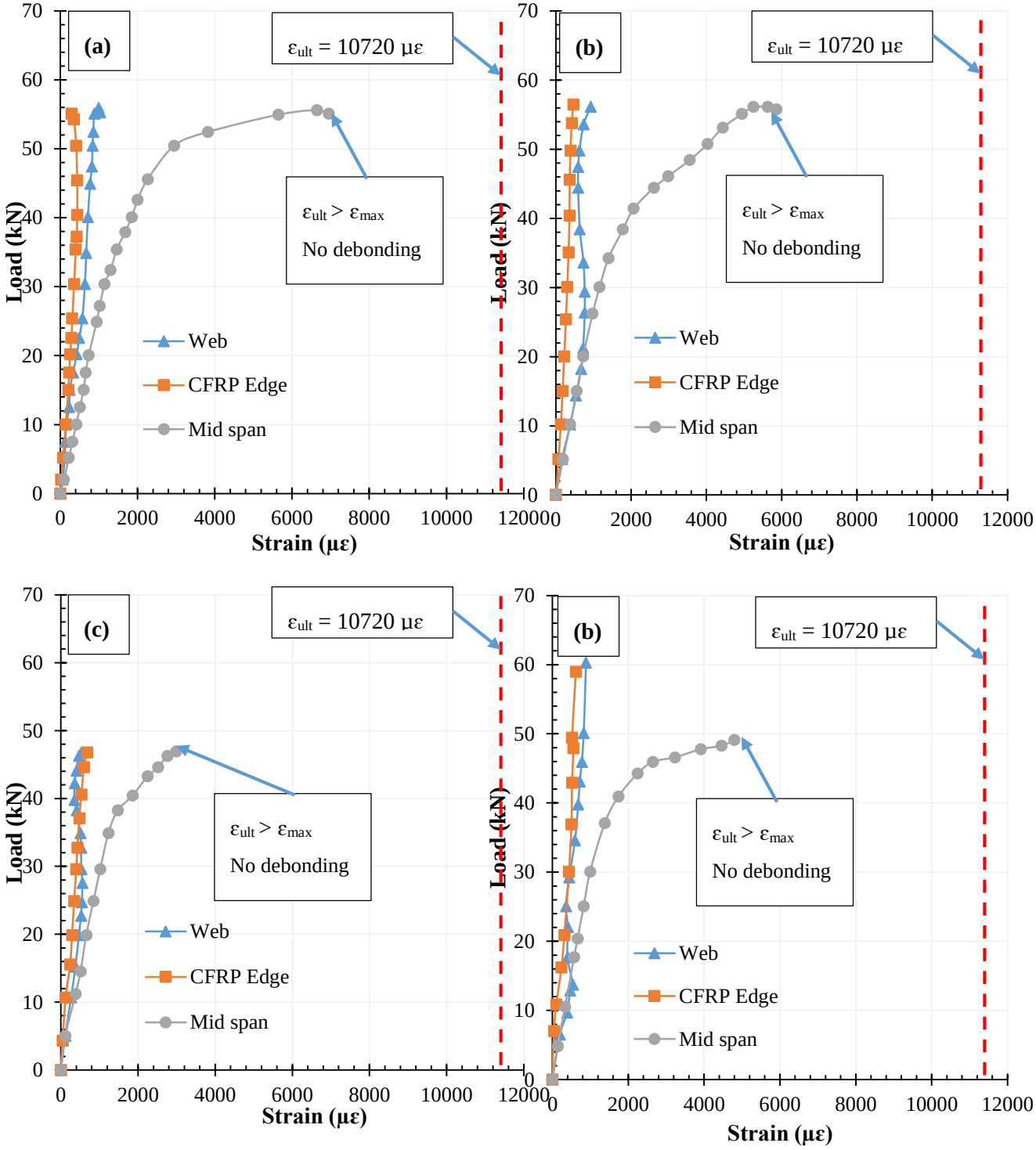

Figure 6.10. Load Vs strain curves for beams with 6000 mm curvature (a) control beam (b) beam with PR1 (c) beam with PR2 and (c) beam with PR3

Figure 6.8, Figure 6.9 and Figure 6.10 show strain Vs load curves for straight beams, beams with 4000 mm curvature and beams with 6000 mm curvature respectively. (a)-

(d) in each Figure indicate strain variations of control beams (unstrengthened), strengthened with profile 1, strengthened with profile 2 and strengthened with profile 3 respectively. The three locations of strain gauges in each sample is shown in Figure 6.11.

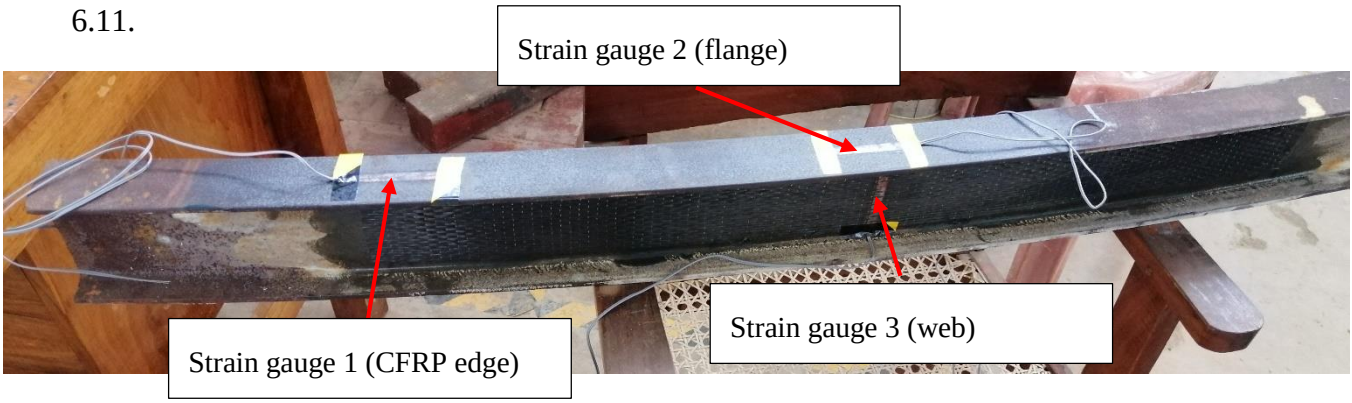

Figure 6.11. Positions of strain gauges and their notations

For all the beams the highest strains were observed in strain gauges placed at the mid span of beams on the tension face irrespective of the curvature and CFRP application profile. In the straight control beam all the strains fall below the ultimate strain of adhesive and hence no debonding observed. In this case lowest strain was observed in the strain gauge positioned at the mid span of the web. In beams with CFRP application profile 1 (PR1), the strain developed in the strain gauge attached to the tension side of the mid span reached to the ultimate strain. Therefore, debonding was observed at that point of the strengthened beam. Other two strain gauges showed lower strains compared to the ultimate strain in adhesive. The strain gauge fixed to the tension face of the strengthened beam with second CFRP profile (PR2) indicated a higher strain than the ultimate strain of adhesive while other two strains were well below the ultimate strain of adhesive. Hence, no debonding was occurred in this beam and failure was due to yielding of steel. In the beam strengthened with third CFRP profile (PR3), strain in tension face at the mid span close to ultimate strain in adhesive

and therefore slight debond was observed. Strains showed in other two strain gauges are below the ultimate strain of adhesive.

In beams with 4000 mm curvature, no strain gauge showed strains greater than the ultimate strain in adhesives. Therefore, no debonding was observed in either controlled or strengthened beams with various CFRP configurations. The strain gauge attached to the web of the mid span shows an increase in strain until 20 kN load and then decrease up 40 kN load ease again with the load irrespective CFRP configuration. All these beams failed in lateral torsional buckling prior to any debonding.

Figure 6.10 clearly shows that the developed maximum strains in adhesives (irrespective of CFRP application profile) do not exceed the ultimate strain in adhesives. Therefore, no debonding was observed in any strengthened beam having 6000 mm curvature. The strain variations observed in beams with 6000 mm curvature were identical to the strain variations of beams having 4000 mm curvature. All the beams having 4000 mm curvature failed in lateral torsional buckling irrespective of CFRP application profile.

6.4.3. Failure modes

The observed failure modes of both strengthened and unstrengthened beams with various curvatures are shown in Figure 6.12. As per the observed failure modes, straight control beam (unstrengthened) showed lateral torsional buckling failure of the beams due to web buckling (Figure 6.12(a)). The beam strengthened with CFRP strengthened profile 1(PR1) showed the lateral torsional buckling but the buckling was delayed due to applied CFRP layer at the bottom (Figure 6.12(b)) A slight debonding of CFRP at the tesion face under the loading point was observed in this beam. The straight beam strengthened with CFRP profile 2 (PR2) failed due to the steel yielding at the tension face of the mid span and the lateral torsional buckling.

This lateral torsional buckling was delayed than in beams with PR1 CFRP profile due to web strengthening. Both an initiated debonding and yielding of steel could observed in beams strengthened with third CFRP strengthening configuration (PR3). The beams with either 4000 mmm curvature or 6000 mm curvature failed due to the lateral torsional buckling irrespective of CFRP application configurations.

Table 6.2 shows the ultimate loads, strength gain and failure mechanisms of both strengthened and un-strengthened beams. It is clearly explained how the ultimate load gain and failure modes are varied with the CFRP application profiles.

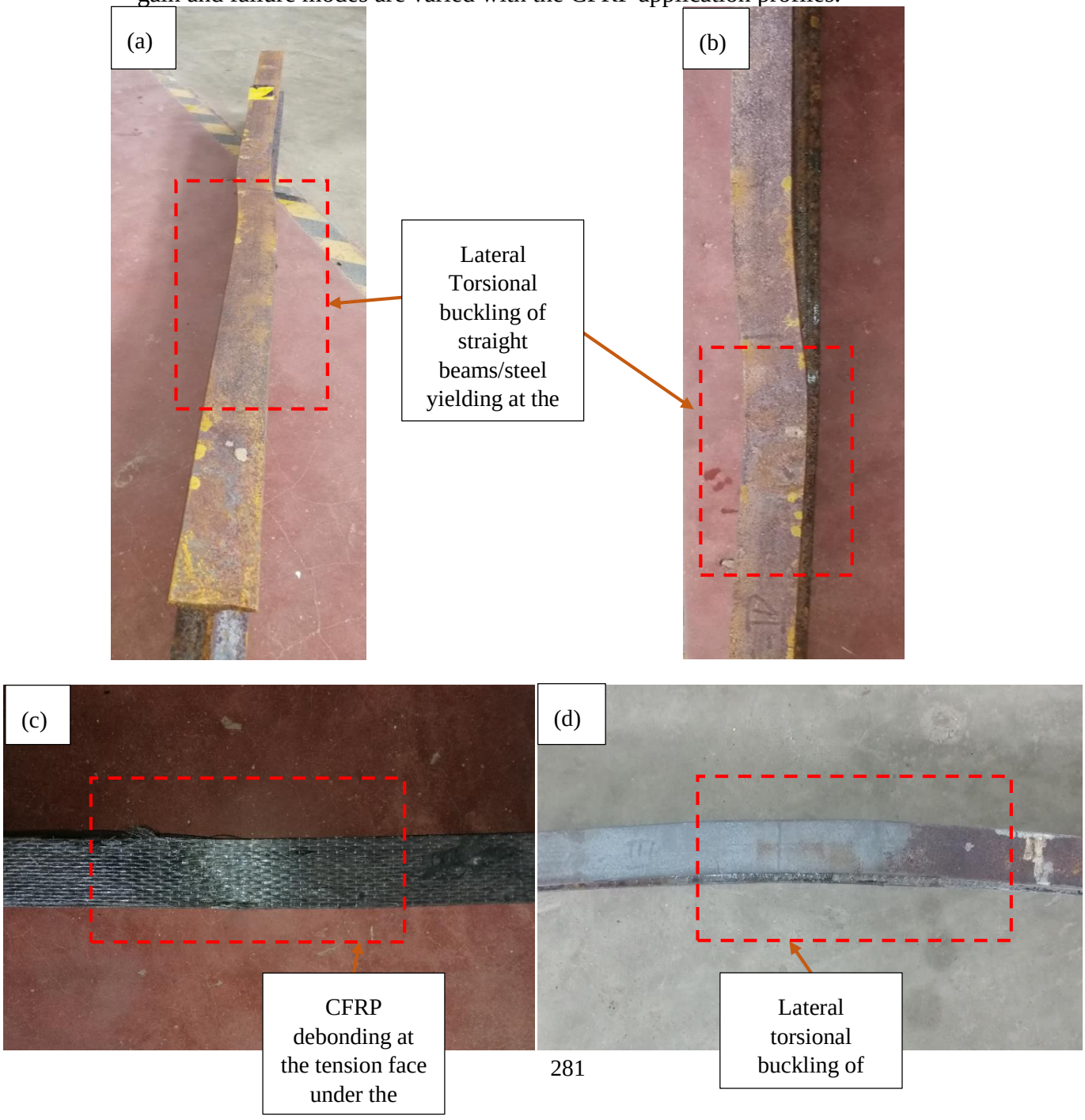

Figure 6.12. Failure modes of straight and curved beams; (a) lateral torsional buckling of unstrengthened straight beam (A) (b) lateral torsional buckling of strengthened straight beam (B) (c) CFRP debonding at the tension face (C) (d) lateral torsional buckling of curved beams (D)

Table 6.3. Details of test specimens, ultimate loads and failure modes

Specimen	Radius of Curvature (mm)	CFRP profile	P_u (kN)	(P_u/P_s)%	δ_u (mm)	δ_u/δ_s	Failure mode
ST_CB	0	-	56.7	-	30.0	-	A
ST_PR1		PR1	63.0	1.11	29.6	0.99	B/C
ST_PR2		PR2	63.8	1.13	22.6	0.75	A/E
ST_PR3		PR3	66.5	1.17	23.9	0.80	B/C
4000_CB	4000	-	48.1	-	26.1	-	D
4000_PR1		PR1	49.8	1.04	22.7	0.87	F
4000_PR2		PR2	53.0	1.10	25.5	0.98	F
4000_PR3		PR3	54.5	1.13	26.1	1	F
6000_CB	6000	-	55.8	-	13.4	-	D
6000_PR1		PR1	58.6	1.05	13.7	1.02	F
6000_PR2		PR2	59.0	1.06	12.0	0.90	F
6000_PR3		PR3	61.7	1.11	12.0	0.90	F

In Table 6.2, the failure modes are denoted as: A – lateral torsional buckling of control straight steel beam; B – lateral torsional buckling of strengthened straight steel beam; C- CFRP debonding on the tension face under the loading point; D – lateral torsional buckling of curved control beams; E- steel yielding on the tension face under the loading point; F- lateral torsional buckling of strengthened curved steel beams and

ultimate loads and mid span deflections at ultimate loads are denoted as; *Pu* – ultimate load of strengthened beams; *Ps* – Ultimate load on un-strengthened beam; δu – mid span deflection at ultimate for strengthened beams; δs – mid span deflection at ultimate for un-strengthened beams.

6.4.4. Lateral deflection

Lateral deflections of the web of the mid span of both strengthened and unstrengthened beams were measured in order to evaluate the effect of CFRP strengthening on lateral deformation of curved beams. Figure 6.13 shows the Load Vs Lateral deformation curves for straight and curved beams. It can be clearly seen that all the curved beams with radius 4000 mm and 6000 mm showed lateral deformation with same trend. The maximum lateral deflection was observed in controlled beam for both beams types with radii 4000 mm and 6000 mm, while the minimum was observed in beams with CFRP applied on both web and the flange (PR3). When comparing beams with CFRP profiles PR1 and PR2, the better performance was observed in beam with CFRP profile PR2. This is due to the reduction in lateral torsional buckling of these beams with the application of CFRP on the web. When comparing beams strengthened with same CFRP profiles, but with different radii, higher deflections were observed in beams having lower radius (4000 mm).

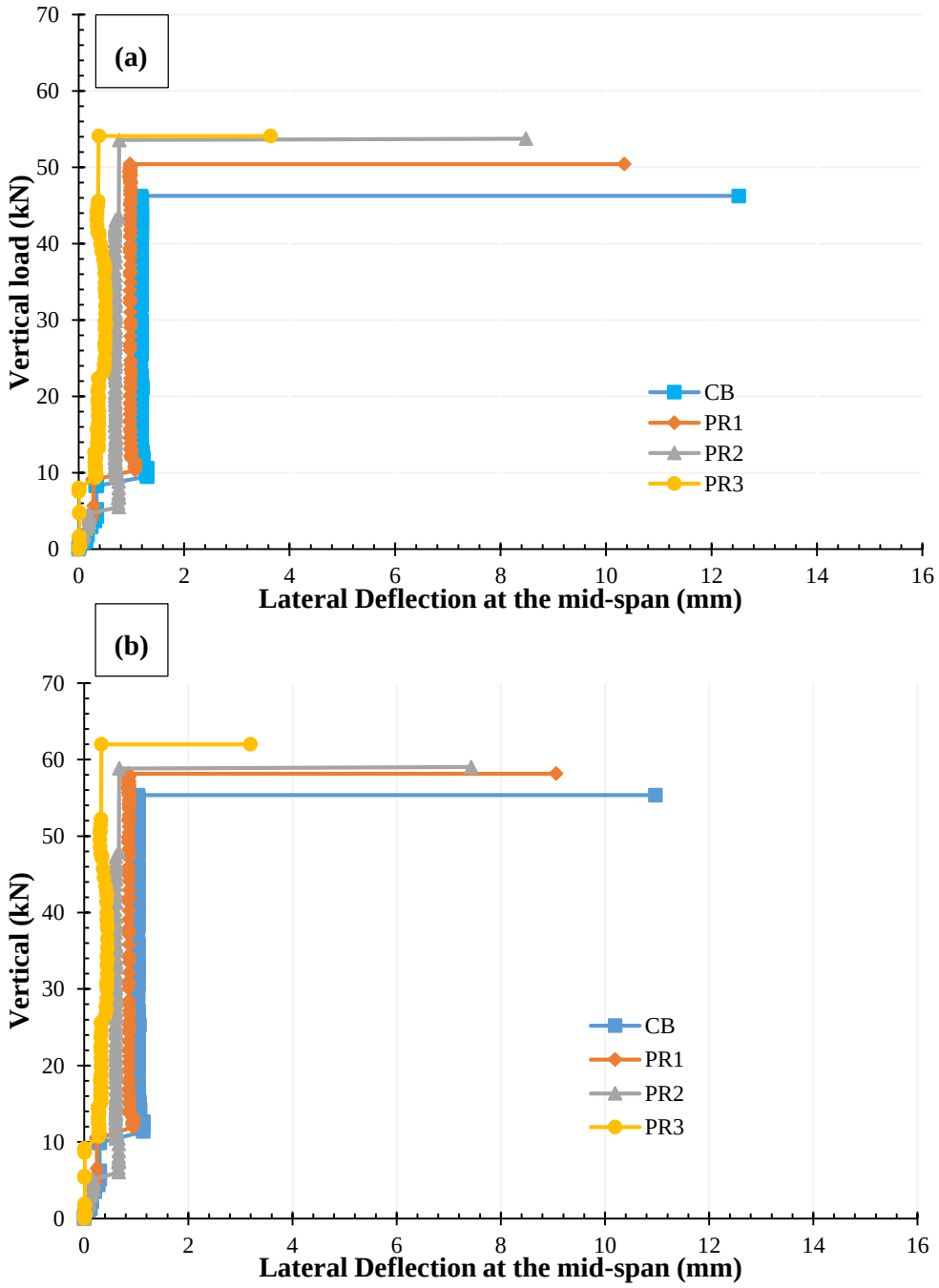

Figure 6.13. Lateral deflection Vs. Vertical loads curves for beams strengthened with various CFRP profiles, (a) beams with 4000 mm radius and, (b) beams with 6000 mm curvature radius.

6.5 Analytical Model and Validation

6.5.1 Analytical Model

Starting from the equations provided by (Liew et al. 1995) in section 2.5;

$$U = \frac{U_0}{\left[\frac{M_E}{M}\right]^2 \left[1-\frac{2L^2}{\pi^2 R^2}\right]-2\frac{P_E}{R^2M^2}+\frac{P_E EI_y}{R^2M^2}\left[\frac{L}{\pi}\right]^2-1} + \frac{\Phi_0}{MR^2}\left[r_0{}^2 P_{ZE} R^2 - T2\right]$$

Let $\Phi_0 = 0$

Then $$U = \frac{U_0}{\left[\frac{M_E}{M}\right]^2 \left[1-\frac{2L^2}{\pi^2 R^2}\right]-2\frac{P_E}{R^2M^2}+\frac{P_E EI_y}{R^2M^2}\left[\frac{L}{\pi}\right]^2-1} \quad \text{----------(6.1)}$$

$$\Phi = \frac{\frac{U_0}{M}\left[P_E-2\frac{EI_Z}{R^2}\right]+\Phi_0}{\left[\frac{M_E}{M}\right]^2 \left[1-\frac{2L^2}{\pi^2 R^2}\right]-2\frac{P_E}{R^2M^2}+\frac{P_E EI_y}{R^2M^2}\left[\frac{L}{\pi}\right]^2-1}$$

But $\Phi_0 = 0$

Then $$\Phi = \frac{\frac{U_0}{M}\left[P_E-2\frac{EI_Z}{R^2}\right]}{\left[\frac{M_E}{M}\right]^2 \left[1-\frac{2L^2}{\pi^2 R^2}\right]-2\frac{P_E}{R^2M^2}+\frac{P_E EI_y}{R^2M^2}\left[\frac{L}{\pi}\right]^2-1} \quad \text{----------(6.2)}$$

Cross – section of composite beam

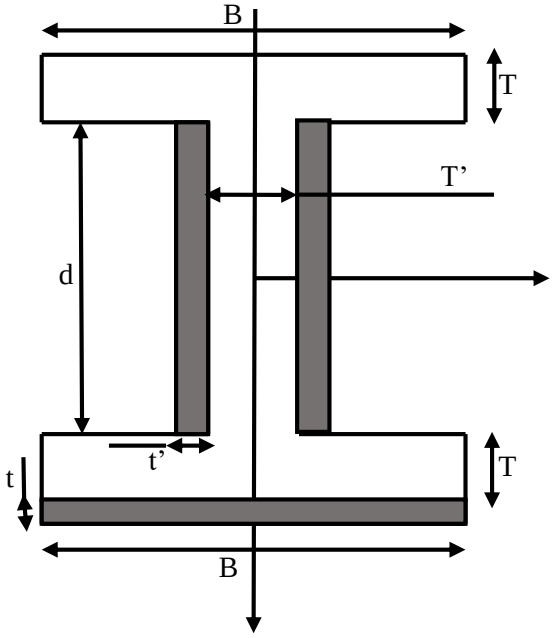

Equivalent Cross – section to composite section

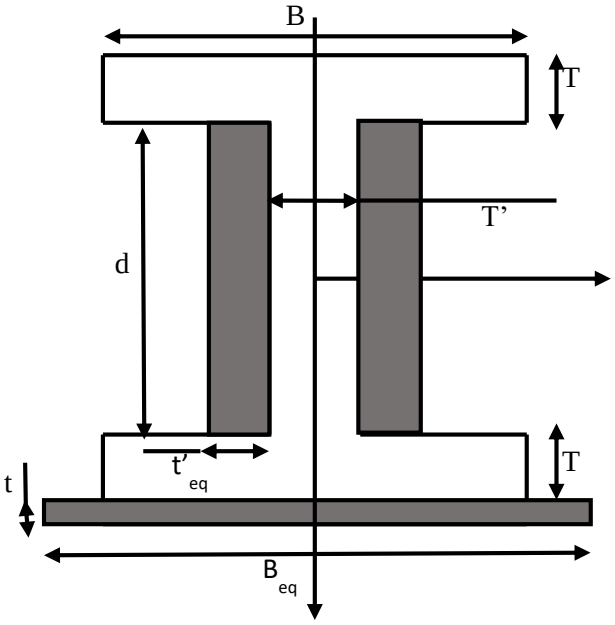

Figure 6.14. (a) Cross section of CFRP strengthened beam (b) equivalent section

Let the horizontal centroidal axis of attached part of the web coincides with y – axis (Figure 6.14).

Breadth of equivalent part attached to the either side of the web $\mathrm{t_{eq}} = \frac{E'}{E}\, t'.$

$\bar{d}$ is the distance from y – axis to the centroid of part attached to the flange.

Here $\bar{d} = \frac{\mathrm{d+T'}}{2} + \mathrm{T}.$

Let the breadth of part attached to the flange is B. So $\mathrm{B_{eq}} = \frac{E'}{E}\,\mathrm{B} = \mathrm{B'}$ (say)

Where E' and E are the modulii of elasticity of CFRP and steel respectively.

By parallel axes theorem, $\mathrm{I_y}$ for the total equivalent section;

$$I'_y = I_y + \left[\frac{1}{12}\mathrm{B'(T')^3} + \mathrm{B'T'}\bar{d}^2 + \frac{2}{12}\,\mathrm{t_{eq}}d^3\right]$$

Substituting $\mathrm{t_{eq}}$ into above and simplifying further;

$$I'_y = I_y + \frac{1}{12}\left[\mathrm{B'(T')^3} + 12\,\mathrm{B'T'}\bar{d}^2 + 2\frac{E'}{E}\,t'd^3\right] \text{----------(6.3)}$$

$\mathrm{I_z}$ for the total equivalent section;

$$I'_z = I_z + \frac{1}{12}\left[2\mathrm{d}(\mathrm{t_{eq}})^3 + 24\mathrm{d}\,\mathrm{t_{eq}}\left(\frac{\mathrm{t_{eq}}+t}{2}\right)^2 + \mathrm{T'B'^3}\right]$$

Simplifying further;

$$I'_z = I_z + \frac{1}{12}\left[2\mathrm{d}\left(\frac{E'}{E}\,t'\right)^3 + 24\,\mathrm{d}\frac{E'}{E}\,t'\left(\frac{\frac{E'}{E}t'+t}{2}\right)^2 + \mathrm{T'B'^3}\right] \text{------(6.4)}$$

P_E for the total equivalent section $P'_E = \frac{\pi^2}{L^2}E\,I'_z$

Substituting I'_z into above;

$$P'_E = \frac{\pi^2}{L^2}E\left\{I_z + \frac{1}{12}\left[2\mathrm{d}\left(\frac{E'}{E}\,t'\right)^3 + 24\,\mathrm{d}\frac{E'}{E}\,t'\left(\frac{\frac{E'}{E}t'+t}{2}\right)^2 + \mathrm{T'B'^3}\right]\right\}$$

(6.5)

Here $M_E = \sqrt{P_E r_0^2 P_{ZE}}$ and $r_0^2 P_{ZE} = \mathrm{G}K_T + \frac{\pi^2 \mathrm{E} I_w}{L^2}$

Substituting $r_0^2 P_{ZE} = \mathrm{G}K_T + \frac{\pi^2 \mathrm{E} I_w}{L^2}$ into $M_E = \sqrt{P_E r_0^2 P_{ZE}}$

$$\therefore M_E = \sqrt{P_E\left[\mathrm{G}K_T + \frac{\pi^2 \mathrm{E} I_w}{L^2}\right]}$$

Warping constant; $I_w = \frac{I_z h_s^2 b_{f1}^3 t_{f1} b_{f2}^3 t_{f2}}{\left(b_{f1}^3 t_{f1} + b_{f2}^3 t_{f2}\right)^2}$; according to code h_s is the distance between shear centres of top & bottom flanges.

Warping constant for equivalent section; $I'_w = \frac{I'_z (h'_s)^2 b_{f1}^3 t_{f1} b_{f2}^3 t_{f2}}{\left(b_{f1}^3 t_{f1} + b_{f2}^3 t_{f2}\right)^2}$ In equivalent section h'_s will be the distance from centroid of top flange to effective centroid of bottom flange.

To find h'_s

Considering first moment of area of bottom flange about centroidal axis of top flange;

$[BT + B'T'] h'_s = BT(d + T) + B'T'(d + \frac{3}{2}T + \frac{1}{2}T')$

$$\therefore \quad h'_s = \frac{BT(d + T) + B'T'(d + \frac{3}{2}T + \frac{1}{2}T')}{[BT + B'T']} \text{ ------(6.6)}$$

$$\therefore \quad I'_w = \frac{I'_z (h'_s)^2 B^3 T\{B^3 T + (B')^3 T'\}}{(2B^3 T + \{B'\}^3 T')^2} \text{ ------(6.7)}$$

St Venant torsional constant; $K_T = \frac{b_{f1} t_{f1}^3 + b_{f2} t_{f2}^3 + h_w t_w^3}{3}$

Where $b_{f1} = B$, $t_{f1} = T$, $b_{f2} = B'$, $t_{f2} = T'$, $h_w = d, t_w = t$ for initial section.

For equivalent section; $K'_T = \frac{BT^3 + \left(BT^3 + B'T'^3\right) + d\,(t + 2t')^3}{3}$

i.e. $K'_T = \frac{2BT^3 + B'T'^3 + d\,(t + 2t')^3}{3}$ ------(6.8)

$$\therefore M'_E = \sqrt{P'_E \left[G K'_T + \frac{\pi^2 E I'_w}{L^2}\right]} \text{ ------(6.9)}$$

Suppose U, U_0, Φ and Φ_0 values for the equivalent section are U^*, U_0^*, Φ^* and Φ_0^* respectively. Then substituting U^*, U_0^*, M'_E, P'_E and I'_y instead of U, U_0, M_E, P_E and I_y into (1) respectively;

$$U^* = \frac{U_0^*}{\left[\frac{M_E'}{M}\right]^2 \left[1-\frac{2L^2}{\pi^2 R^2}\right]+\frac{P_E'}{R^2M^2}\left[E\, I_y'\left[\frac{L}{\pi}\right]^2-2\right]-1} \quad \text{----------(6.9)}$$

We can compute U^* substituting M_E', P_E', and I_y' into above.

substituting Φ^*, U_0^*, P_E', M_E', I_Z' and I_y' instead of Φ, U_0, P_E, M_E, I_Z and I_y into (2) respectively;

Then $$\Phi^* = \frac{\frac{U_0^*}{M}\left[P_E'-2\frac{E\, I_Z'}{R^2}\right]}{\left[\frac{M_E'}{M}\right]^2 \left[1-\frac{2L^2}{\pi^2 R^2}\right]-2\frac{P_E'}{R^2M^2}+\frac{P_E' E\, I_y'}{R^2M^2}\left[\frac{L}{\pi}\right]^2-1}$$

(Initially assuming $\Phi_0^* = 0$)

Simplifying further;

$$\Phi^* = \frac{\frac{U_0^*}{M}\left[P_E'-2\frac{E\, I_Z'}{R^2}\right]}{\left[\frac{M_E'}{M}\right]^2 \left[1-\frac{2L^2}{\pi^2 R^2}\right]+\frac{P_E'}{R^2M^2}\left[E\, I_y'\left[\frac{L}{\pi}\right]^2-2\right]-1}$$

Here $P_E' = \frac{\pi^2}{L^2} E\, I_Z'$

Then $E\, I_Z' = P_E' \frac{L^2}{\pi^2}$ substituting into above;

$$\Phi^* = \frac{\frac{U_0^*}{M}\left[P_E'-2\frac{P_E' L^2}{R^2\pi^2}\right]}{\left[\frac{M_E'}{M}\right]^2 \left[1-\frac{2L^2}{R^2\pi^2}\right]+\frac{P_E'}{R^2M^2}\left[E\, I_y'\left[\frac{L}{\pi}\right]^2-2\right]-1}$$

Simplifying further;

$$\Phi^* = \frac{\frac{U_0^*\, P_E'}{M}\left[1-\frac{2L^2}{\pi^2 R^2}\right]}{\left[\frac{M_E'}{M}\right]^2 \left[1-\frac{2L^2}{\pi^2 R^2}\right]+\frac{P_E'}{R^2M^2}\left[E\, I_y'\left[\frac{L}{\pi}\right]^2-2\right]-1} \quad \text{----------(6.10)}$$

We can compute Φ^* substituting M_E', P_E', and I_y' into above. As per equation 6.10, the lateral torsional buckling of the beam depends of the warping constant and second moment area of the section. The increase in these parameters reduce the risk

of lateral torsional buckling. The application of CFRP improve the stiffness of the beam section which lower the risk of lateral torsional buckling.

6.5.2 Validation of Analytical model

The validation of analytical model was done comparing the analytical model results with the experimental results. Table 6.3 and Figure 6.15 shows the comparison between analytical and experimental results. It can be seen that the results from the analytical model are closed to the experimental results which implies the validation of analytical method. The coefficient of determination between analytical and experimental values is 0.9926, which gives a strong relationship. Hence, the proposed analytical model can be used to calculate vertical deflections and rotations of horizontally curved steel I beams strengthened CFRP.

Table 6.4. Comparison between analytical and experimental results for CFRP strengthened horizontally curved steel I beams

Beam ID	**Experimental Results**	**Analytical Results**
ST_CB	56.7	55.8
ST_PR1	63.0	61.9
ST_PR2	63.8	62.6
ST_PR3	66.5	65.9
4000_CB	48.0	47.2
4000_PR1	49.8	48.4
4000_PR2	53.0	52.2
4000_PR3	54.4	53.8
6000_CB	55.8	55.1
6000_PR1	58.6	56.9
6000_PR2	59.0	58.4
6000_PR3	61.7	61.0

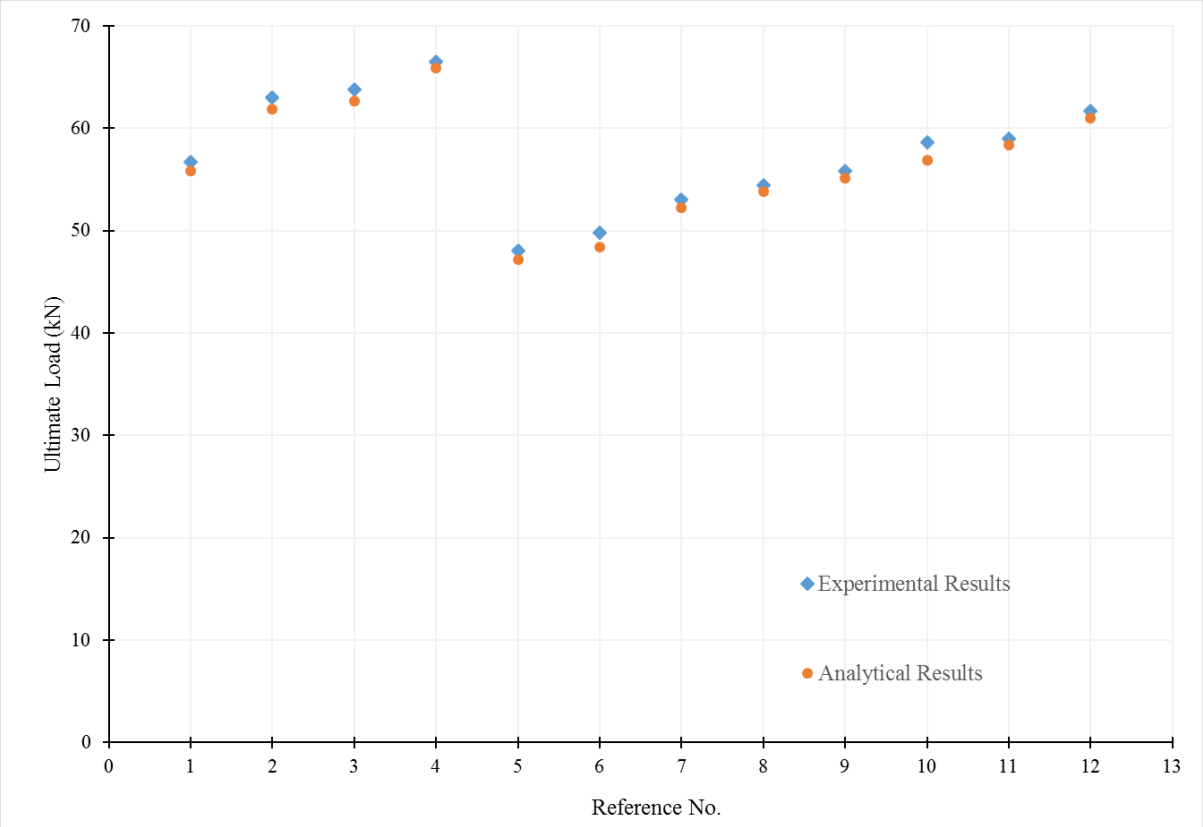

Figure 6.15. Comparison between analytical and experimental results for CFRP strengthened horizontally curved steel I beams

6.6 Conclusions

An experimental study was conducted to evaluate the reliability of CFRP on structural strengthening of horizontally curved steel I beams. A analytical model also developed to predict the vertical deflection and rotation of horizontally curved steel I beams at a given load. Following conclusions can be drawn based on the results of both experimental and analytical studies;

- CFRP is an effective material to retrofit horizontally curved I beams since it enhance the ultimate load carrying capacity and also decrease the deflection at the service load.
- The CFRP application profile drastically effect on the strength gain of CFRP strengthened straight and horizontally curved beams. The most effective

CFRP application profile found under this study was strengthening of beams with CFRP at both web and the tensile face of the beams which delay both lateral torsional buckling and bending failure of the beams.

- Several failure modes were identified in both straight and horizontally curved I beams which include lateral torsional buckling of un-strengthened beams, lateral torsional buckling of strengthened beams, debonding of CFRP either at the web or tensile flange, CFRP tearing etc.
- An analytical model was developed to predict the deflection and rotation of CFRP strengthened horizontally curved I beams based on the simple equations developed to analyse horizontally curved unstrengthened steel I beams by (Liew et al. 1995). The developed analytical model was validated with experimental results successfully.

6.7 Chapter Summery

This chapter discussed the experimental and theoretical analysis of CFRP strengthened straight and horizontally curved I beams with three CFRP application configurations. Total twelve beams including four straight beams, four beams curved to 4000 mm radius and four beams curved to 6000 mm radius were strengthened with three CFRP application configurations. One beam from each category were kept as controlled beams. Length of each CFRP strip was kept as 750 mm while span of the beam kept as 1200 mm. Either ends of the beams were restrained as fixed ends. Load vs. deflection responses were obtained which give ultimate load and the deflection at the ultimate loads. The failure modes of each beams were also recorded. It was noted that the CFRP application configuration has a significant effect on the ultimate loads of strengthened beams.

An analytical model was developed based on the method explained by Liew ela al.(1995) to predict the vertical deflection and rotation of the curved and straight beams at a given vertical load. The analytical method was validated with the experimental results. Further experimental results should be used for the comprehensive validation of the analytical model.

Chapter 7
Numerical Study on CFRP Strengthened Horizontally Curved I-beams

7.1 Introduction

Previous chapter was discussed on experimental study on CFRP strengthened steel I beams strengthened with three CFRP application configurations having three radius of curvatures. This chapter discuss about Finite Element Analysis of CFRP strengthened horizontally curved I beams using commercially available ABAQUS finite element modelling software package. Main objective of the study is to investigate the effects of various parameters on the ultimate strength gain of strengthened beams. These parameters included CFRP length, CFRP application configurations, CFRP thickness, Adhesive thickness and elastic modulus of CFRP. The finite element models were validated using experimental results prior to conduct the parametric study. This chapter further discuss material properties, experimental procedure, and experimental results. Conclusions and recommendations were made using both experimental and numerical study results.

7.2 Test Programme

Total 12 steel I beams including both straight and curved beams with radius 4000 mm and 6000 mm were tested. Three beams from each category were strengthened with three CFRP profiles as shown in Figure 7.1. All the specimens were sand blasted and cleaned with acetone to remove loose particles prior to apply CFRP. CFRP sheets were cut in to strips having two sizes, 75 mm × 750 mm and 50 mm × 750 mm to apply on either side of webs and bottom of the flange respectively. These CFRP strips were applied on beams using two parts adhesive Araldite 420 immediately after cleaning the surfaces with acetone. Few roller passes were applied on the CFRP surface to ensure the uniform thickness of adhesive as well as to remove the air bubble between CFRP layer and steel substrate to ensure proper bonding. All the specimens

were cured under normal environment at least seven days prior to testing. The measured material properties for steel, CFRP and adhesive are shown in Table 7.1.

All the beams were tested using fixed-fixed end conditions using Quasi static loading having a loading rate of 0.025mm/min. A 250 kN capacity load cell was used to transfer load to the beams in a constant rate until they fail. Two linear variable displacement transducers (LVDTs) were set, one at the mid span to record vertical deflection and second one is to record the lateral deflection at the mid span. Figure 7.2 shows a schematic diagram of experimental setup with instrumentation.

Table 7.1. Material properties of steel, CFRP and Adhesive

	Steel	CFRP	Adhesive
Thickness (mm)	5	0.116	0.0005
Elastic modulus (GPa)	206	270	2.4
Tensile strength (MPa)	235	5550	40
Yield strength (MPa)	215	-	-
Tensile strain (mm/mm)	0.011	0.021	0.022

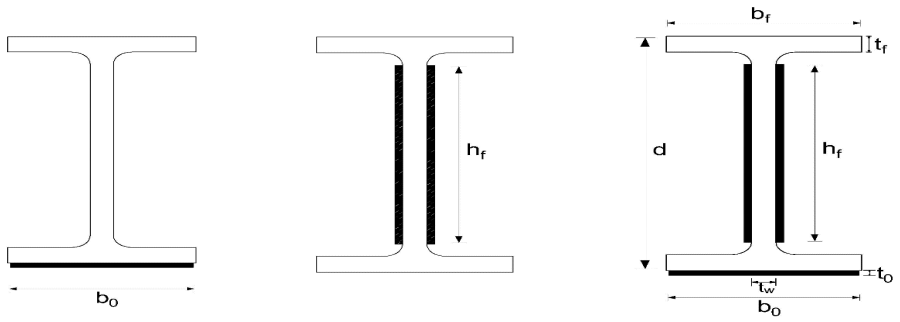

Figure 7.1. CFRP application configurations

Three strain gauges were fixed on each beam to record the strain variations in CFRP at the bottom of the mid-span tension flange, edge of the CFRP patch of bottom tension flange and at the centre of the mid span web. Applied loads, mid-span vertical and horizontal displacements, and strain variations were recorded using a data logger.

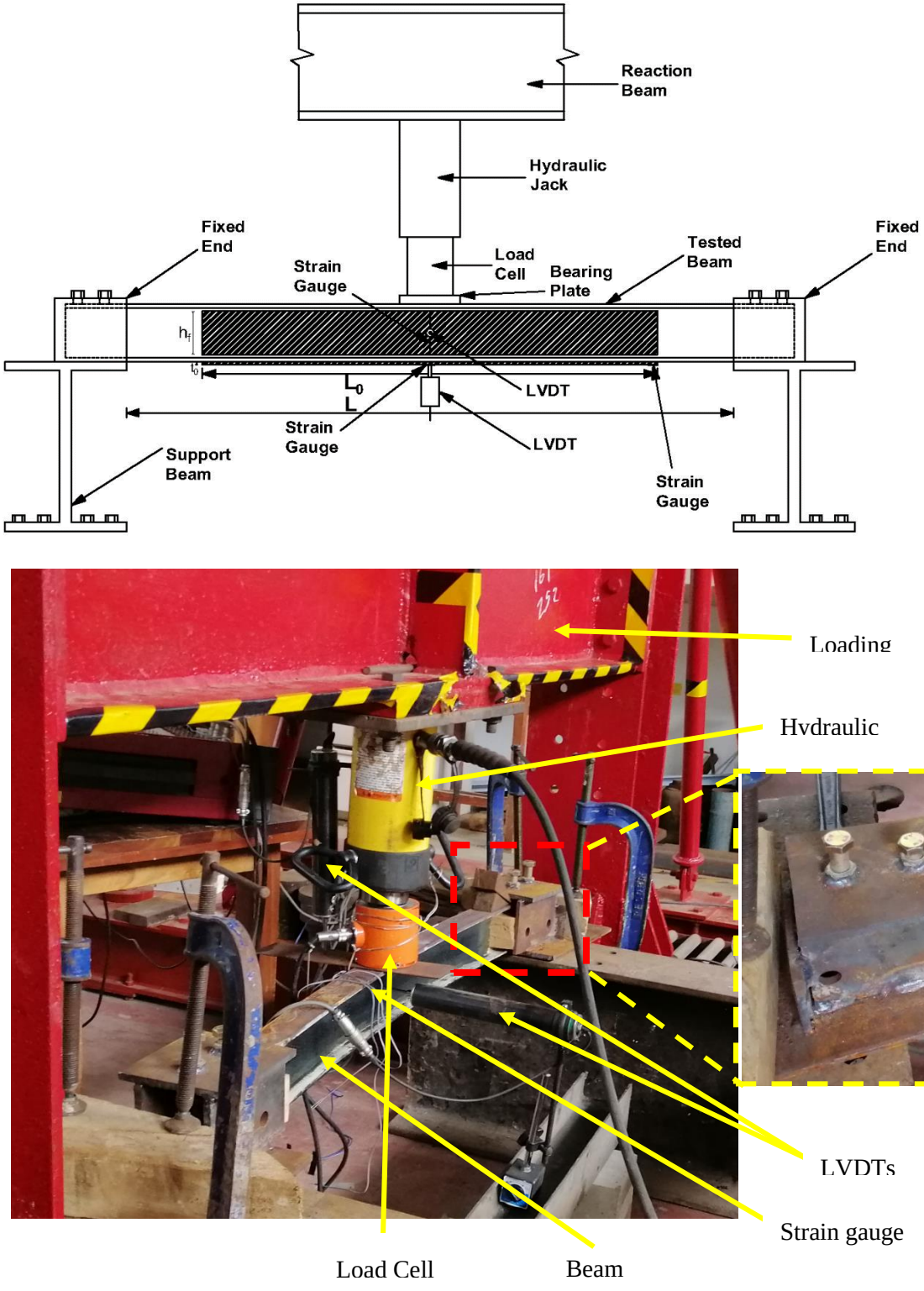

Figure 7.2. Experimental Test Setup

7.3. Finite Element Modelling

Three dimensional (3D) finite element models were developed using commercially available finite element modelling software package to simulate the tested beams. Fixed boundary conditions (U1=U2=U3=UR1=UR2=UR3=0) were assigned to the either ends of beams similar to the test programme (Figure 7.3).

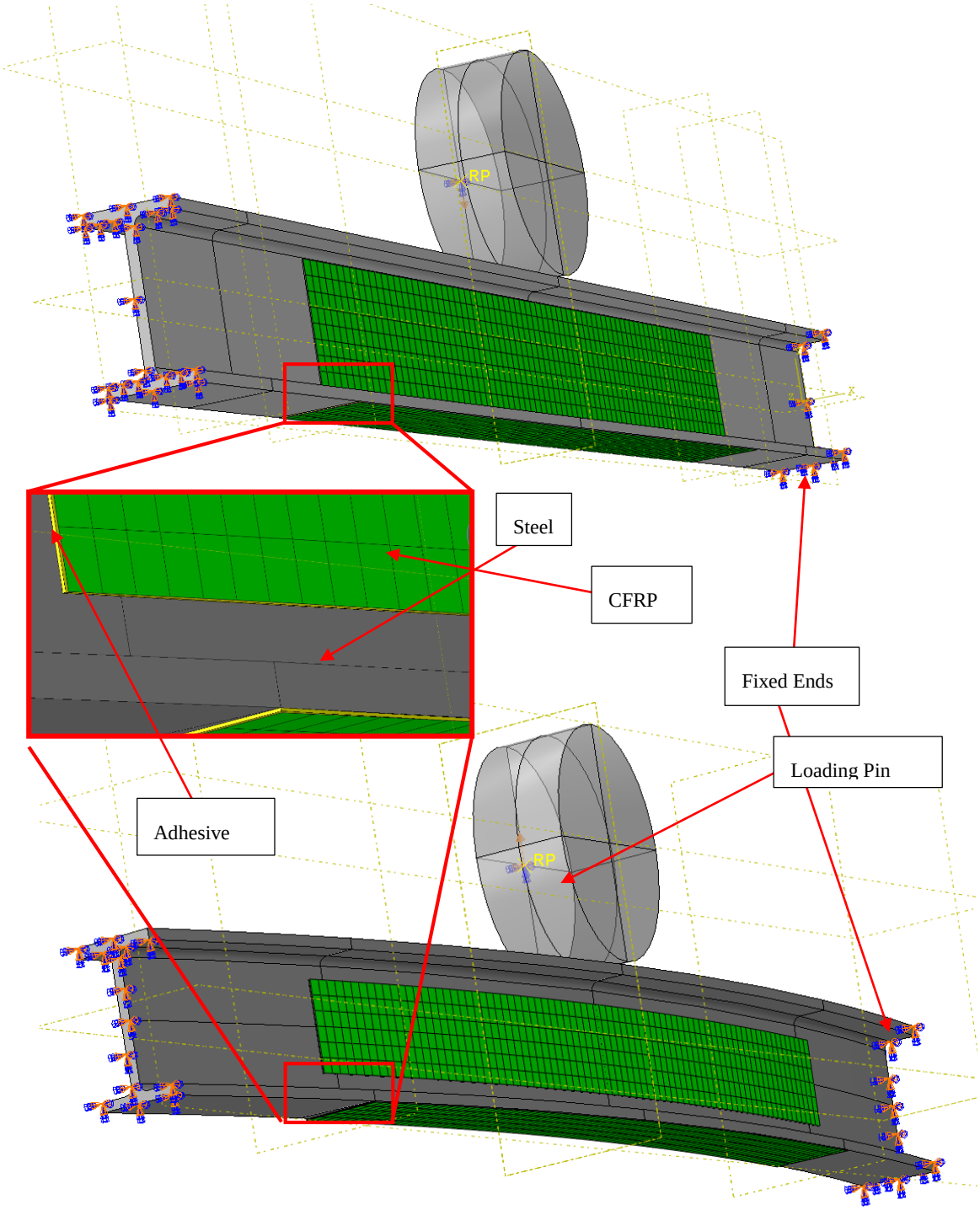

Figure 7.3. 3D finite element model of steel I beam strengthened with CFRP

The aspect ratio of finite element models were kept below two and the connections between steel-adhesive and adhesive-CFRP were defined using tie constraints(Deng J, Lee MMK 2004; Teng, Fernando, and Yu 2015b). The general-purpose shell elements (S4R) with reduced integration was used to model steel beam(Teng, Fernando, and Yu 2015b). These elements have four nodes with five degrees of freedom and suitable to predict the behaviour of contact models. CFRP patches were modelled using continuum shell elements with reduced integrations (SC8R). These elements are eight nodded, quadrilateral in-plane general-purpose continuum shell elements which are capable of predicting CFRP failure. These elements are capable of computing shear stresses through the thickness than the standard brick elements and importantly, they are capable of resolving contact problems more accurately(Al-Zubaidy, Zhao, and Al-Mahaidi 2013).

Four failure mechanism of CFRP are explained in literature; fibre rupture in tension, fibre buckling in compression, matrix cracking under transverse tension and shearing, and matrix crushing under transverse compression(Naghipour et al. 2009). The continuum damage mechanism in built with Hashin damage criteria in ABAQUS captures the damages and failures in CFRP. The damage initiates and propagates when the fracture energy in any afore mentioned criteria exceeds its maximum value. The elastic and orthotropic damage properties of CFRP used in this study are shown in Table 7.2 and Table 7.3 respectively.

Table 7.2. Orthotropic elastic material properties of CFRP

Fibre Type	E_1 (Pa)	E_2 (Pa)	G_{12}(Pa)	G_{13}(Pa)	G_{23}(Pa)	N_{12}
Magnitude	230×10^9	230×10^9	1	1	3.0×10^9	0.33

Table 7.3. Orthotropic damage initiation properties and In-plane fracture energies for CFRP

X^T (MPa)	X^C (MPa)	Y^T (Pa)	Y^C (MPa)	S^L (Pa)	S^T (Pa)	G^T_{1C} (N/m)	G^C_{1C} (N/m)	G^T_{2C} (N/m)	G^C_{2C} (N/m)
2760	552	1	50	1	1	91,600	79,000	1	1

The adhesive layers were modelled using three-dimensional eight-node cohesive elements with reduced integration with element deletion (COH3D8). The coupled cohesive zone modelling was adopted to model the constitutive behaviour of the adhesive layer(Teng, Fernando, and Yu 2015a). The mixed mode cohesive law considers bond stresses (tractions) and interfacial deformations (separations) in three directions, parallel to interface (two shear directions) and perpendicular to interface. t_n, t_s and t_t denote normal and two shear tractions respectively, while δ_n, δ_s and δ_t denote respective separations. The strains in normal (ε_n) and two shear directions (γ_s and γ_t) are given by;

$$\varepsilon_n = \frac{\delta_n}{T_0},\ \gamma_s = \frac{\delta_s}{T_0}, \text{and } \gamma_t = \frac{\delta_t}{T_0}$$

Where T_0 is the original thickness of the adhesive layer.

With the assumption of elastic behaviour of the interface until the damage initiation, it can be represented(Kabir et al. 2016; Teng et al. 2015a);

$$\begin{Bmatrix} t_n \\ t_s \\ t_t \end{Bmatrix} = \begin{bmatrix} K_{nn} & 0 & 0 \\ 0 & K_{ss} & 0 \\ 0 & 0 & K_{tt} \end{bmatrix} \begin{Bmatrix} \delta_n \\ \delta_s \\ \delta_t \end{Bmatrix}$$

Where $K_{nn}, K_{ss}, and\ K_{tt}$ are stifnesses in normal and three shear directions respectively. Since K_{nn} is the initial slope of the bond separation model for mode-I loading and is represented with;

$$K_{nn} = \frac{E_a}{T_0}$$

Where E_a is the elastic modulus of adhesive.

K_{ss} and K_{tt} are assumed to be same and calculated with the slope of the bond-slip model under mode II loading and is given by;

$$K_{ss} = K_{tt} = 3\left(\frac{G_a}{T_0}\right)^{0.65}$$

Where G_a is the shear modulus of the adhesive. Therefore, it can be seen that the stiffness of adhesive in normal and shear directions are inter related with the Poisson's ratio of the adhesive.

The damage initiation of the adhesive occur when either shear stress attain to its ultimate value under pure mode II loading or normal stress reaches to its maximum value under pure mode II loading. The mixed mode criterion used in this study is adopted the following quadratic strength criterion(Camanho et al. 2003);

$$\left(\frac{\langle t_n \rangle}{\sigma_{max}}\right)^2 + \left(\frac{t_s}{\tau_{max}}\right)^2 + \left(\frac{t_t}{\tau_{max}}\right)^2 = 1$$

The t_n is written within the Macaulay's bracket which imply that the compressive stresses do not lead to damage (when t_n is negative $\langle t_n \rangle$ is taken as zero). The damage initiation point is determined using mode-mix ratio (the ratio between the fracture energies of two different modes).

A scalar damage variable D, is introduced once the damage initiation started (D = 0 at the damage initiation and D = 1 at the complete failure of the interface) in order to evaluate the level of damage and hence the Equation(X) can be modified as;

$$\begin{Bmatrix} t_n \\ t_s \\ t_t \end{Bmatrix} = \begin{bmatrix} (1-D^*)K_{nn} & 0 & 0 \\ 0 & (1-D)K_{ss} & 0 \\ 0 & 0 & (1-D)K_{tt} \end{bmatrix} \begin{Bmatrix} \delta_n \\ \delta_s \\ \delta_t \end{Bmatrix}$$

The complete failure of interface, when D = 1 is defined base on the fracture energy principles. Although several other methods (Quadratic method, BK criteria) available to define the complete failure of interface, the present study adopted the linear criterion due to its simplicity and better performance for adhesive joints(Camanho et al. 2003). The linear criterion is explained as below;

$$\frac{G_n^*}{G_I} + \frac{G_s}{G_{II}} + \frac{G_t}{G_{II}} = 1$$

Where $G_{n,}G_s \; and \; G_t$ are the works done by the tractions and their conjugate displacements in normal and shear directions respectively. $G_I$and G_{II} are the interfacial fracture energies required for the complete failure under pure mode I and mode II loading respectively.

The definition for an effective displacement to describe the evolution of damage is introduced as follows;

$$\delta_m = \sqrt{\langle \delta_n \rangle^2 + \delta_s^2 + \delta_t^2}$$

The displacement at complete failure δ_m^f is define using above relationship for a certain mode-mix ratio. Then the damaged variable D is defined by the following expression with the assumption of linear softening of interface;

$$D = \frac{\delta_m^f(\delta_m^{max} - \delta_m^0)}{\delta_m^{max}(\delta_m^f - \delta_m^0)}$$

Where δ_m^{max} is the maximum value of the effective displacement attained during the loading stage and δ_m^0 is the effective displacement at the initiation of damage.

All these equations were derived using the bi-linear bond-slip model proposed in the literature (Fernando ND. 2010). This bi-linear bond-slip model is capable of to provide accurate predictions for the bond behaviour of CFRP-to-steel bonded joints subjected to mode-II loading and defined as follows;

$$\tau = \begin{cases} \tau_{max}\dfrac{\delta}{\delta_1} & if\ \delta \le \delta_1 \\ \tau_{max}\dfrac{\delta_f - \delta}{\delta_f - \delta_1} & if\ \delta_1 \le \delta \le \delta_f \\ 0 & if\ \delta > \delta_f \end{cases}$$

Where τ is the bond shear stress, τ_{max} is the is the peak bond shear stress, δ is the slip, δ_1 is the slip at peak bond shear stress, and δ_f is the slip at complete failure. The bond-slip parameters in the above expression was evaluated based on the experimental results(Fernando ND. 2010) as given in the following equations;

$$\tau_{max} = 0.9\sigma_{max}$$

$$\delta_1 = 0.3\left(\frac{t_a}{G_a}\right)^{0.65}\sigma_{max}\ (mm)$$

$$\delta_f = \frac{2G_f}{\tau_{max}}\ (mm)$$

Where σ_{max} is the tensile strength of adhesive in MPa, t_a and G_a are thickness and shear modulus of the adhesive. G_f is the interfacial fracture energy given by(Teng et al.2015b);

$$G_f = 628t_a^{0.5}R^2\ (\text{N/mm}^2\ \text{mm})$$

R is the tensile strain energy per unit volume of the adhesive which is equal to the area under the uni-axial tensile stress (in MPa)– strain curve.

7.4. Validation of Numerical Models

Results obtained through the numerical modelling were compared with experimental results prior to conduct further analysis. Ultimate loads and deflections, failure modes and strain variations of both un-strengthened and strengthened beams were compared.

7.4.1 Load-deflection responses

Figure 7.4 shows a comparison between load deflection responses obtained for both un-strengthened and strengthened beams with various curvatures and CFRP application profiles. It is clear that the CFRP strengthened beams showed higher ultimate loads compared to un-strengthened beams irrespective of the radius of beams. This ultimate load gains were varied with the different CFRP application profiles. The highest strength gains were observed the beams strengthened with PR3 CFRP profile of CFRP on both web and the tension face of the bottom flange. The percentage strength gains for beams strengthened with this profile were 17%, 13% and 11% respectively for the beams having 0 mm, 4000 mm and 6000 mm radii. The beams strengthened with PR1 CFRP profile showed percentage increments of 11%, 4% and 5% respectively for beams having 0 mm, 4000 mm and 6000 mm radii. It can be also seen that the deflections at ultimate loads were reduced with the increased radius. Higher deflections can be observed in straight beams compared to that of curved beams (irrespective of CFRP profile.

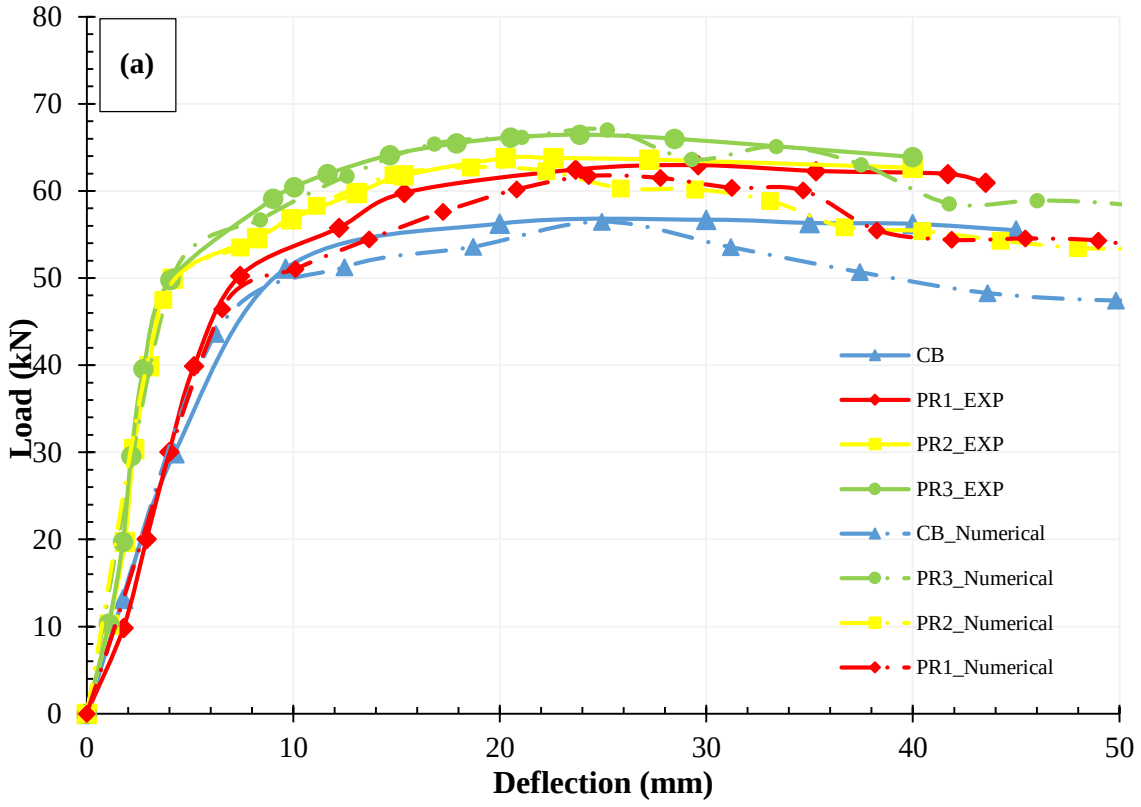
(a)
Load (kN)
Deflection (mm)
0
10
20
30
40
50
60
70
80
CB
PR1_EXP
PR2_EXP
PR3_EXP
CB_Numerical
PR3_Numerical
PR2_Numerical
PR1_Numerical

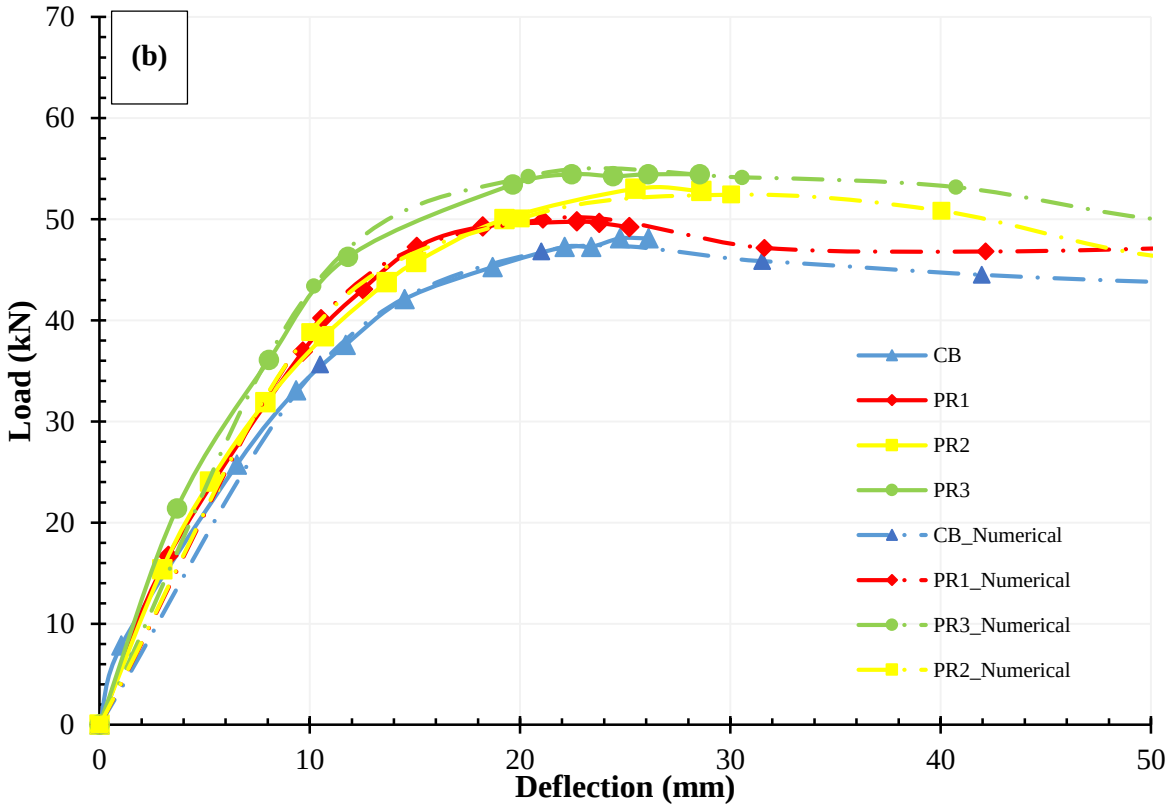
(b)
Load (kN)
Deflection (mm)
0
10
20
30
40
50
60
70
CB
PR1
PR2
PR3
CB_Numerical
PR1_Numerical
PR3_Numerical
PR2_Numerical

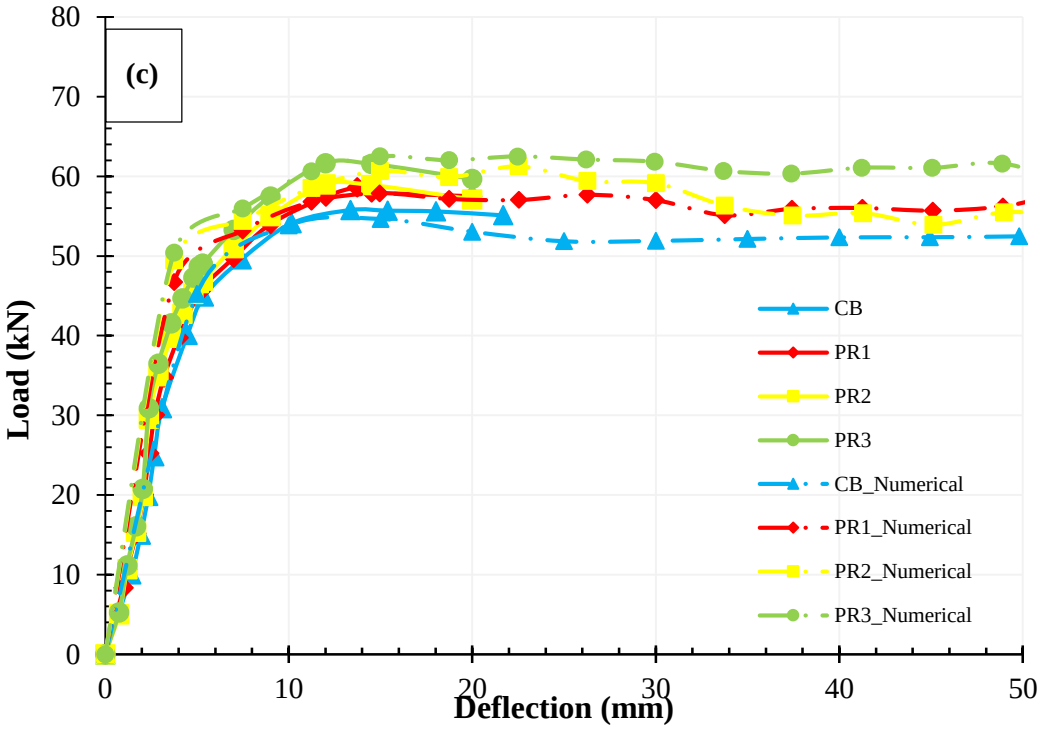

Figure 7.4. Load-deflection responses for beams with different radii and CFRP application profiles; (a) 0 mm radius (b) 4000 mm radius, and (c) 6000 mm radius

Table 7.4 shows the variations of experimentally and numerically predicted ultimate loads and the deflections at the ultimate loads for beams with different radii and CFRP profiles. It can be clearly seen that the increase in ultimate load strongly depends on the CFRP application profile. The mid span deflections at the ultimate loads does not show a significant relationship. But, the lowest value of deflection was observed in the beams strengthened with PR3 CFRP application profile This may be due to the additional stiffness provide by CFRP layers applied on the web.

A comparison between the ultimate loads obtained through experimental and numerical simulations is shown in Table 3. It indicates that the ratio (P_U/P_F) varies within the range 0.97 to 1.03, which is very close to unity. It also found that the coefficient of variation (COV) lies between 0.001 and 0.020, which are almost negligible. Therefore, it can be concluded that the numerical models have been

validated reasonably well with the experimental results where values obtained from both methods are almost equal.

Table 7.4. Comparison between ultimate loads and mid-span deflections at ultimate loads for beams with different curvatures and CFRP profiles

Beam ID	Ultimate Load (kN)		P_U/P_F	COV	Deflection at Ultimate Load (mm)		δ_U/δ_F	COV
	Experimental (P_U)	Numerical (P_F)			Experimental (δ_U)	Numerical (δ_F)		
ST_CB	56.7	56.5	1.00	0.002	29.9	24.9	1.20	0.129
ST_PR1	63.0	61.7	1.02	0.015	29.6	24.3	1.22	0.139
ST_PR2	63.8	62.7	1.02	0.012	22.6	18.6	1.22	0.137
ST_PR3	66.5	67.0	0.99	0.005	23.9	25.2	0.95	0.037
4000_CB	48.0	46.8	1.03	0.018	24.7	21.0	1.18	0.114
4000_PR1	49.8	49.9	1.00	0.001	22.7	21.1	1.08	0.052
4000_PR2	53.0	52.4	1.01	0.008	25.3	30.0	0.84	0.120
4000_PR3	54.4	54.2	1.00	0.003	26.1	20.4	1.28	0.173
6000_CB	55.8	54.7	1.02	0.014	13.4	15.0	0.89	0.080
6000_PR1	58.6	57.8	1.01	0.010	13.7	15.0	0.91	0.064
6000_PR2	59.0	60.7	0.97	0.020	12.0	12.8	0.94	0.046
6000_PR3	61.7	62.5	0.99	0.009	12.89	13.2	0.98	0.017

The comparison between experimental deflections and numerically obtained deflections showed (δ_U/δ_F) ratio between 0.84 and 1.28and the COV varies between 0.017 to 0.173, which are close to unity and zero respectively. Therefore, it can be deduced that the numerical models have been reasonably validated using the experimentally obtained deflections.

7.4.2 Failure modes

The failure modes observed during the experimental programme for unstrengthened and strengthened beams included; lateral torsional buckling of unstrengthened straight beam (A), lateral torsional buckling of strengthened straight beam (B), CFRP debonding at the tension face (C), lateral torsional buckling of curved beams (D), and CFRP debonding at the either side of the web in line with the load for CFRP profiles PR2 and PR3 (Figure 7.5). For straight beams the lateral torsional buckling was observed due to the web buckling with the applied load. This may be due to the slender section of the steel beam (classification gives class III). The curved beams showed lateral torsional buckling due to either slender section or applied torsion due to the vertical force. These curved beams showed lateral torsional buckling earlier than the straight beams because of the induced torsion due to the curvature of beams. The debonding of CFRP on the tension face below the loading point was observed due to the failure of adhesive layer because of the induced tensile stresses.

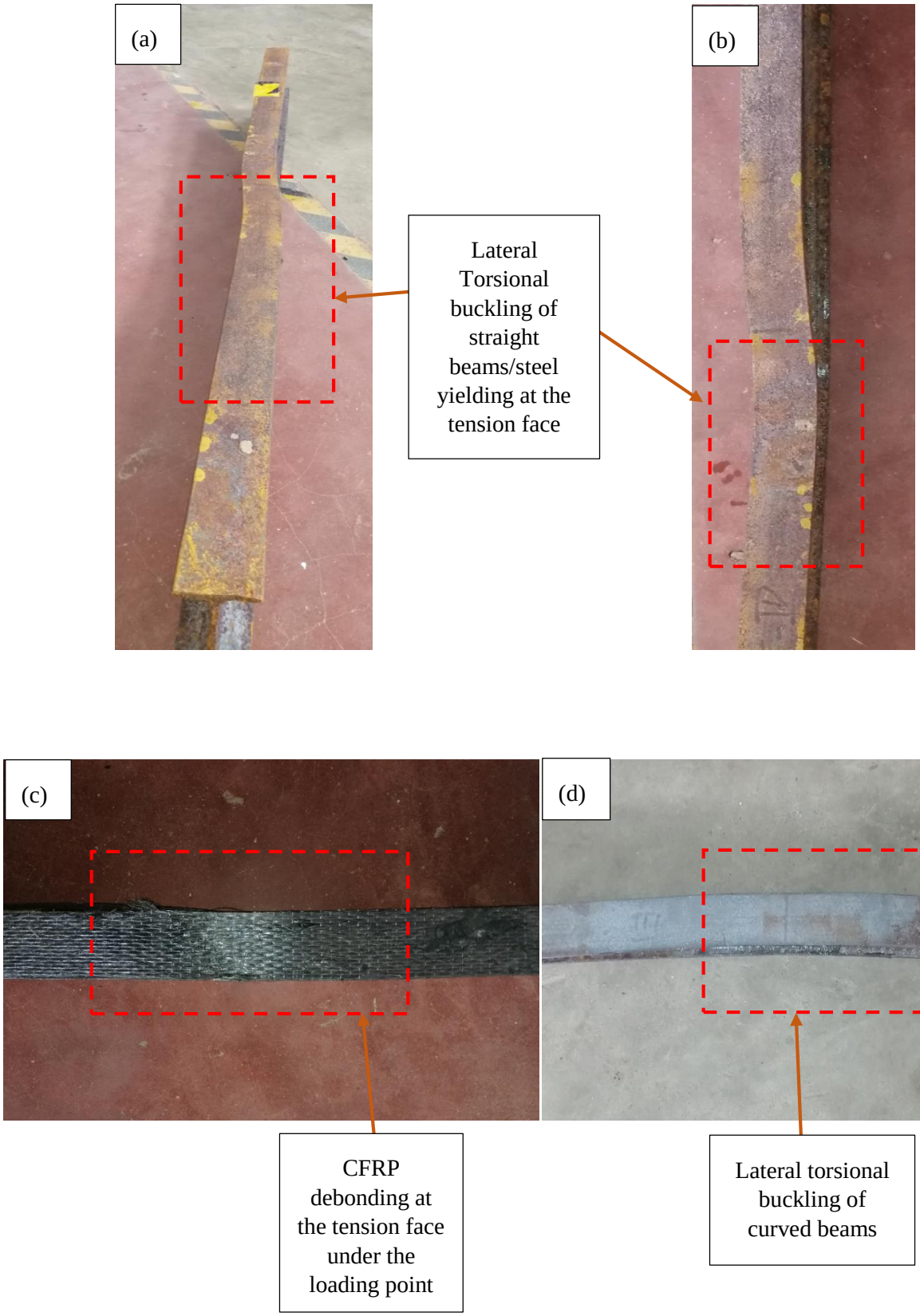
(a)
(b)
Lateral Torsional buckling of straight beams/steel yielding at the tension face
(c)
(d)
CFRP debonding at the tension face under the loading point
Lateral torsional buckling of curved beams

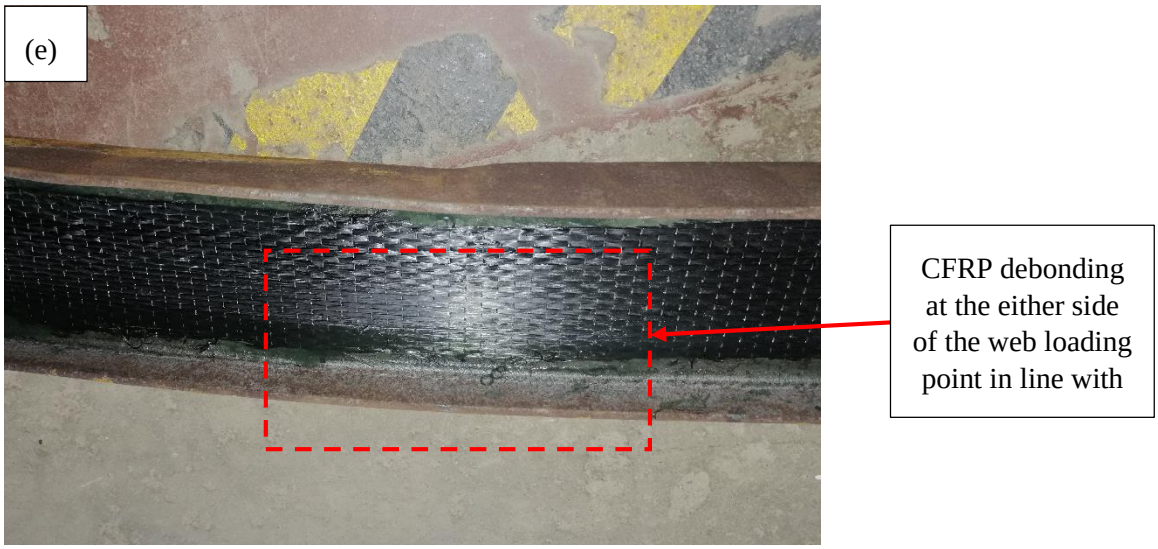

Figure 7.5. Failure modes of straight and curved beams; (a) lateral torsional buckling of unstrengthened straight beam (A) (b) lateral torsional buckling of strengthened straight beam (B) (c) CFRP debonding at the tension face (C) (d) lateral torsional buckling of curved beams (D),and (e) CFRP debonding on the web

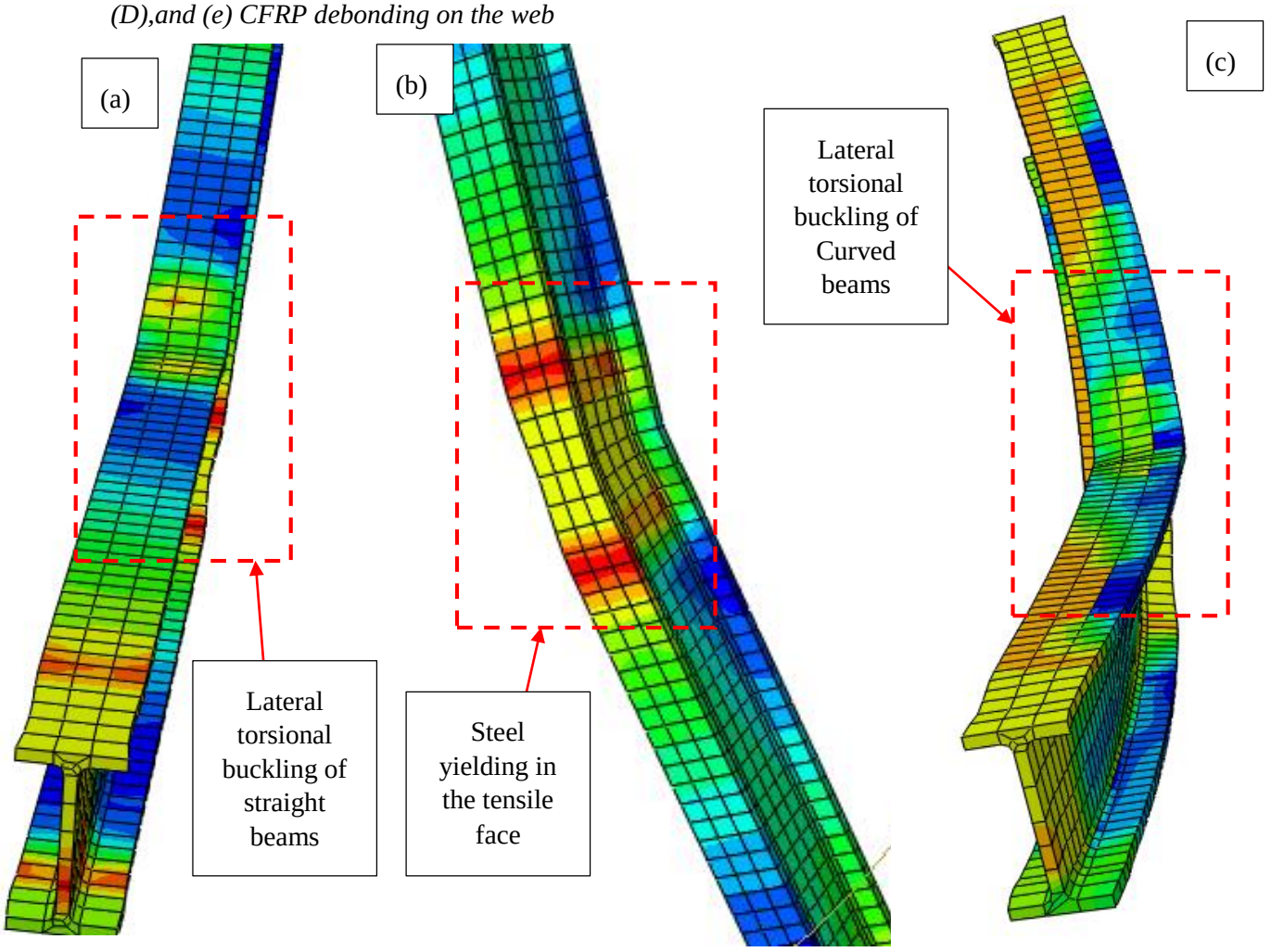

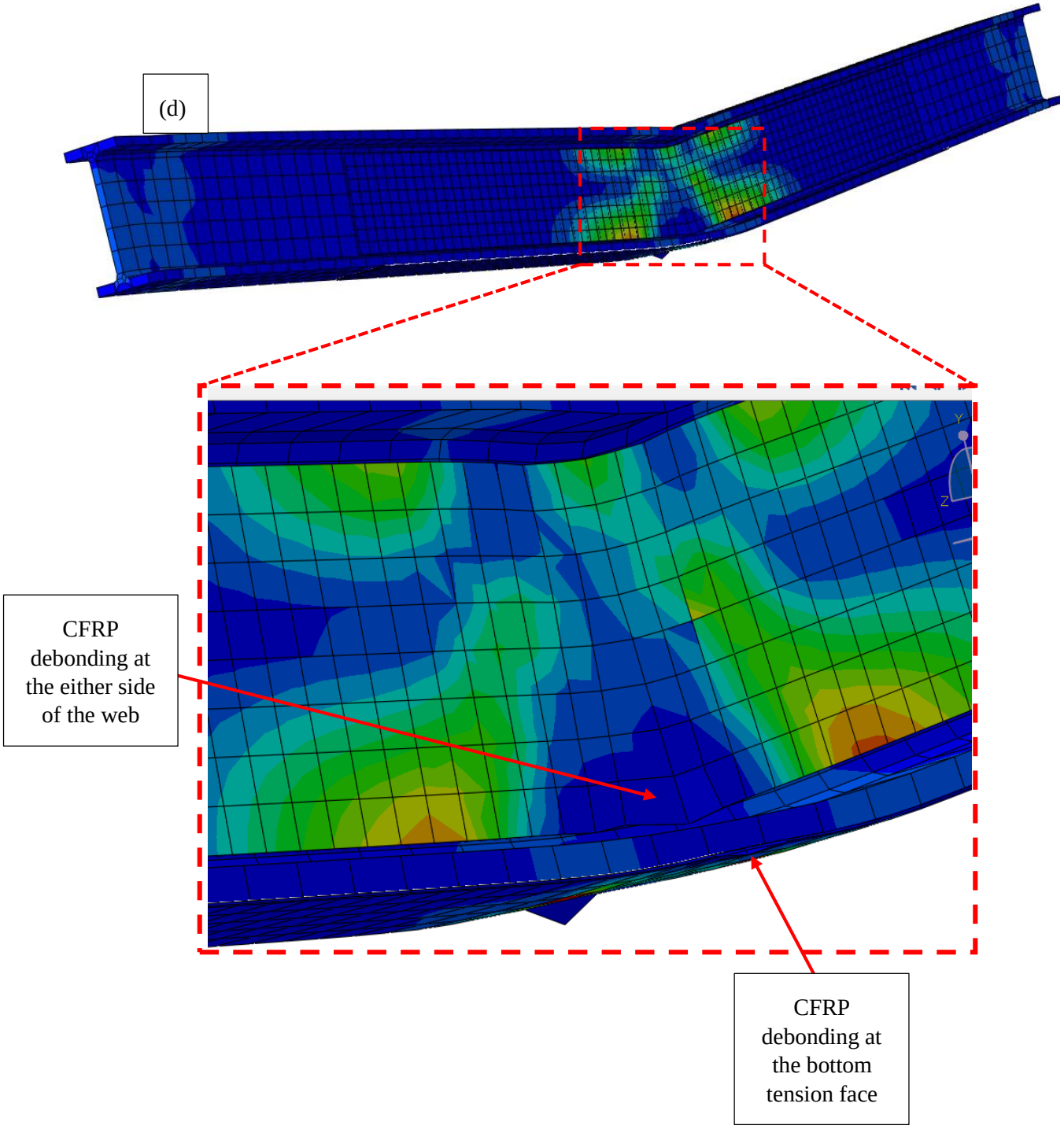

Figure 7.6. Failure modes of un-strengthened and strengthened beams (a) lateral torsional buckling of straight beams, (b) steel yielding in straight beams at the tension face, (c) lateral torsional buckling of curved beams, and (d) CFRP debonding at the either side of the web and tension flange in line with the load

Figure 7.5 and Figure 7.6 show the failure modes observed during the experimental programme and obtained using numerical modelling respectively. When compare these failure modes obtained through both methods, they are having good agreement to each other. The debonding of CFRP on either side of the web and at the tension flange were occurred due to the developed tensile stress concentrations due to bending, at those locations. Figure 7.7 shows the stress contours of un-strengthened and strengthened steel I beams with various radius of curvatures and different CFRP application profiles at a vertical displacement of 100 mm.

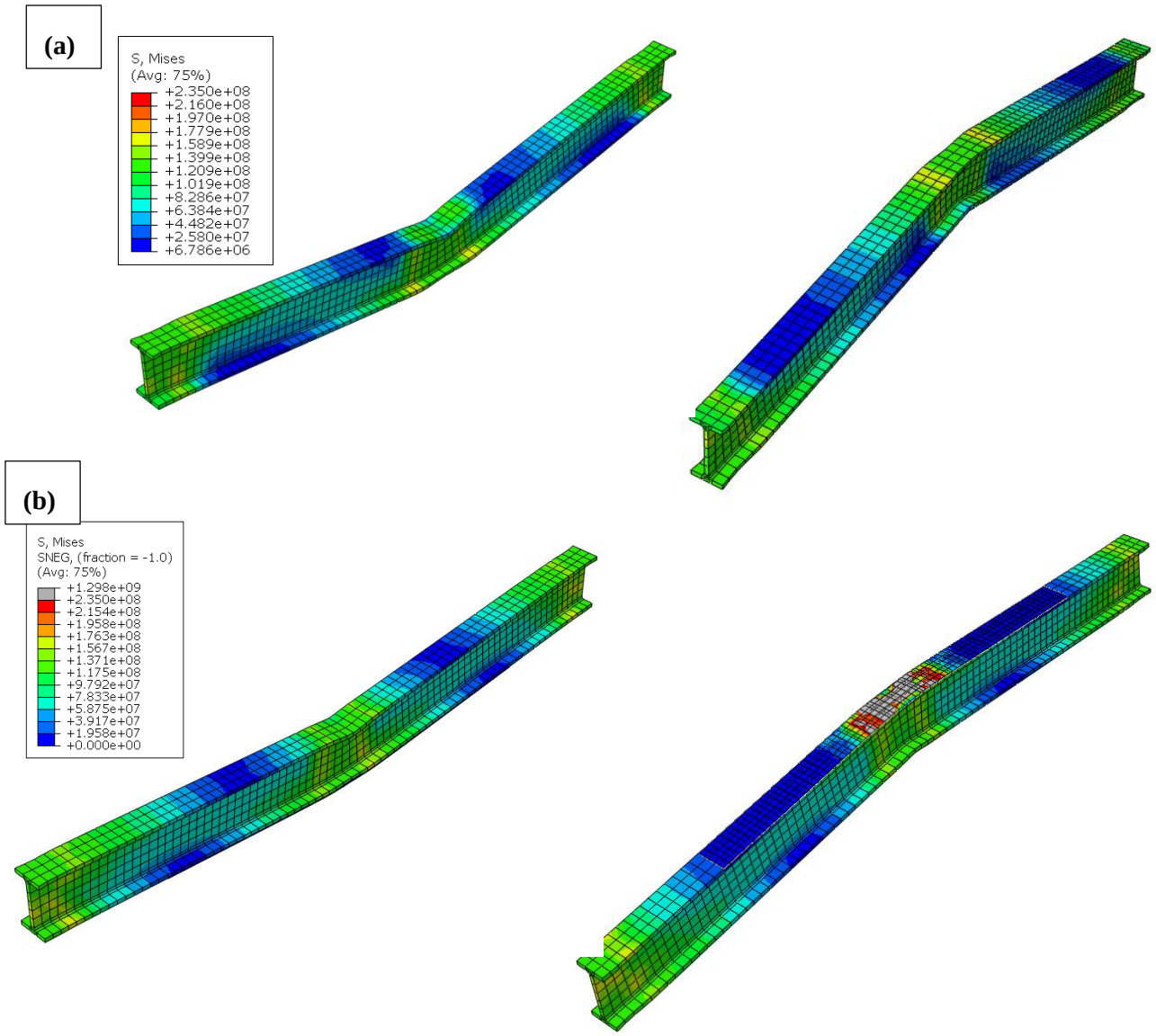

(c)

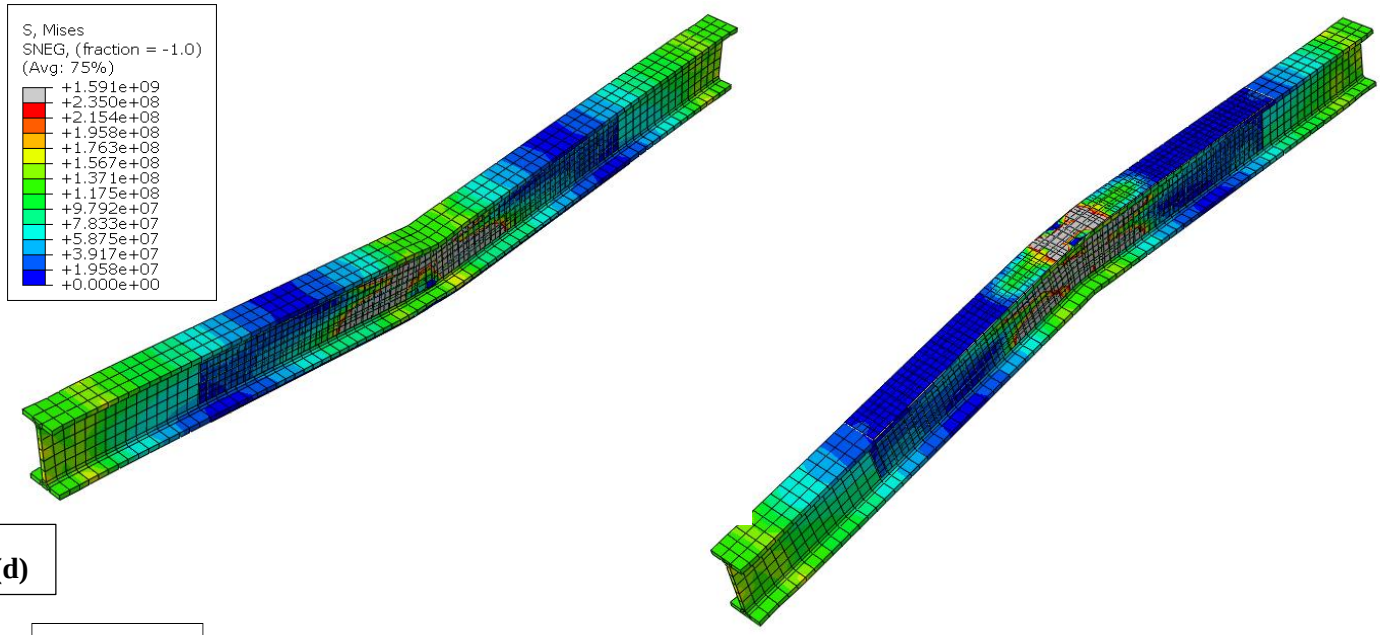
S, Mises
SNEG, (fraction = -1.0)
(Avg: 75%)
+1.591e+09
+2.350e+08
+2.154e+08
+1.958e+08
+1.763e+08
+1.567e+08
+1.371e+08
+1.175e+08
+9.792e+07
+7.833e+07
+5.875e+07
+3.917e+07
+1.958e+07
+0.000e+00

(d)

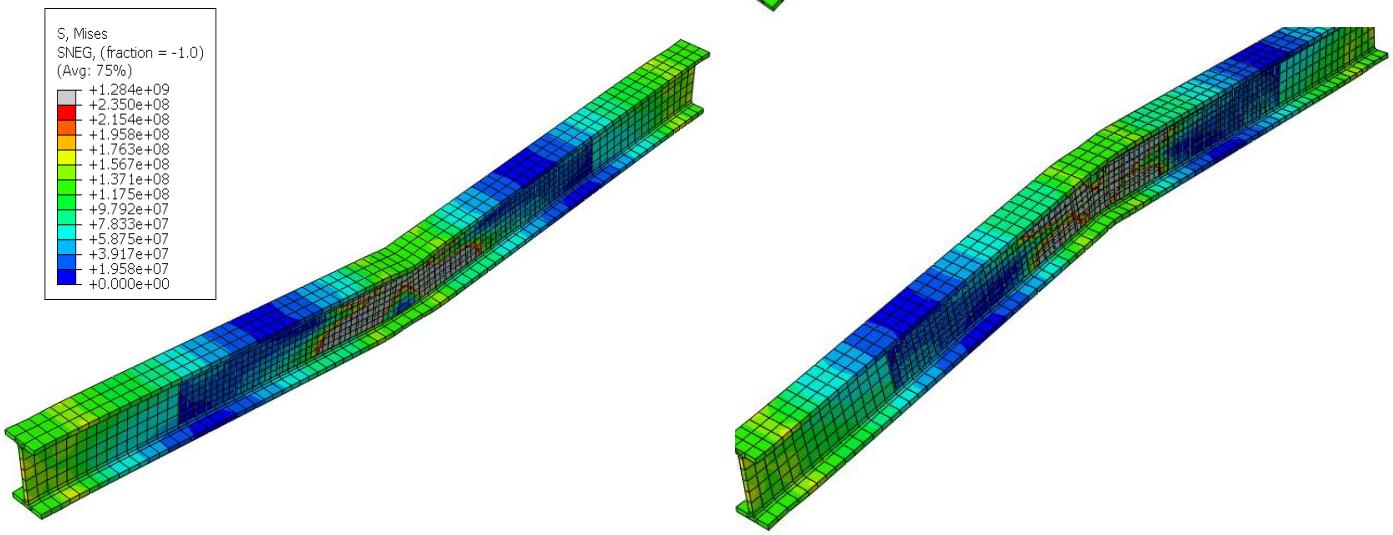
S, Mises
SNEG, (fraction = -1.0)
(Avg: 75%)
+1.284e+09
+2.350e+08
+2.154e+08
+1.958e+08
+1.763e+08
+1.567e+08
+1.371e+08
+1.175e+08
+9.792e+07
+7.833e+07
+5.875e+07
+3.917e+07
+1.958e+07
+0.000e+00

(e)

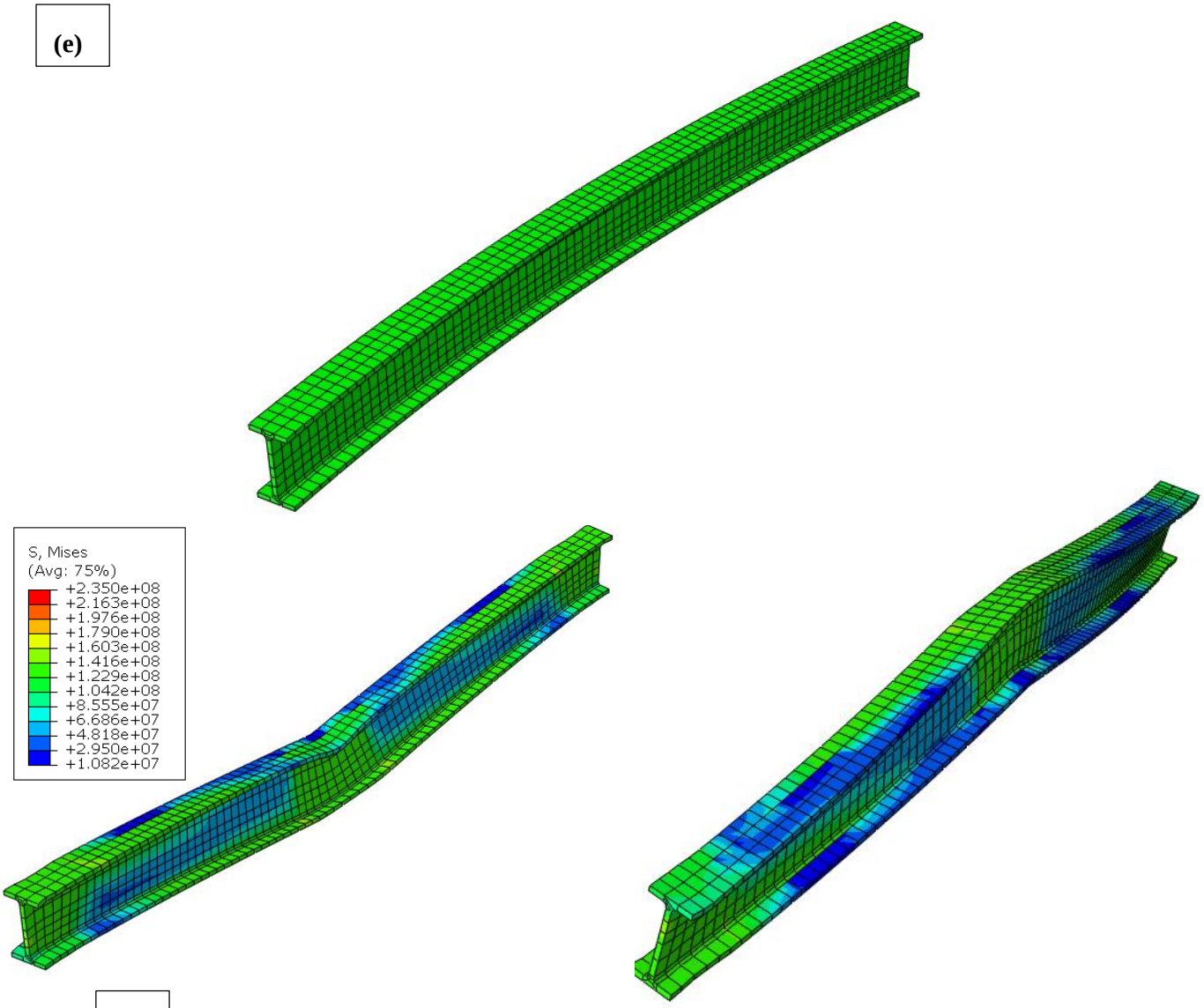
S, Mises
(Avg: 75%)
+2.350e+08
+2.163e+08
+1.976e+08
+1.790e+08
+1.603e+08
+1.416e+08
+1.229e+08
+1.042e+08
+8.555e+07
+6.686e+07
+4.818e+07
+2.950e+07
+1.082e+07

(f)

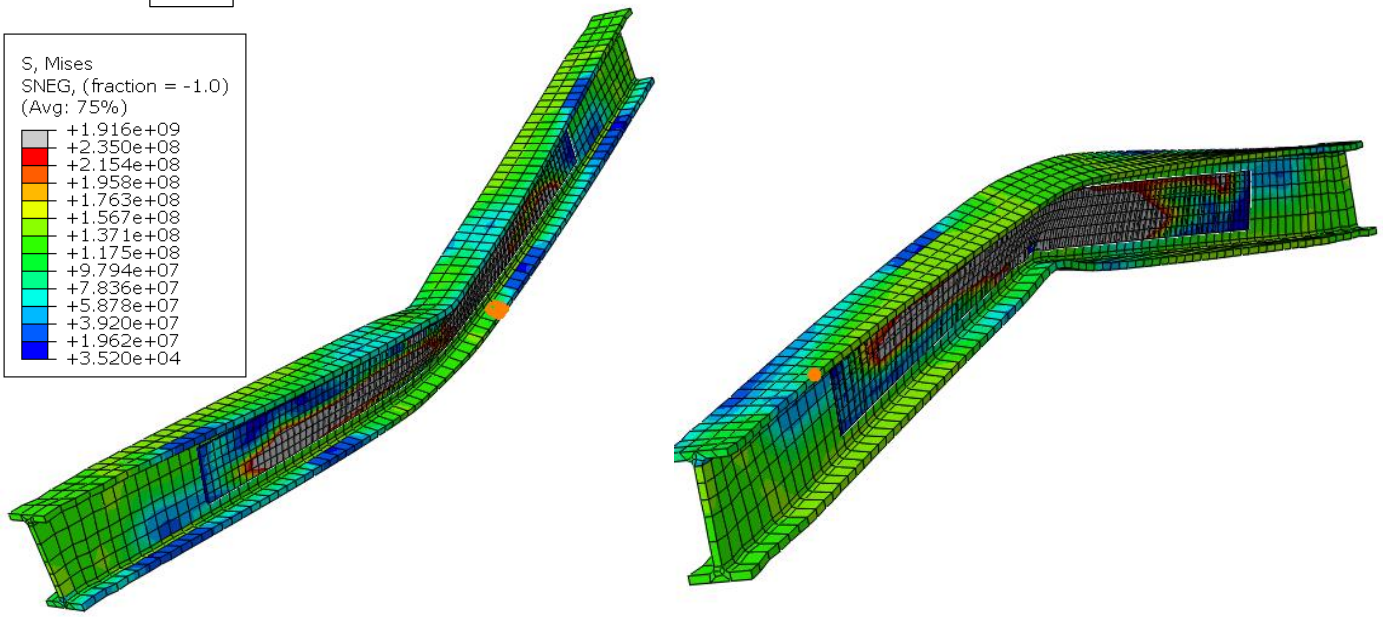
S, Mises
SNEG, (fraction = -1.0)
(Avg: 75%)
+1.916e+09
+2.350e+08
+2.154e+08
+1.958e+08
+1.763e+08
+1.567e+08
+1.371e+08
+1.175e+08
+9.794e+07
+7.836e+07
+5.878e+07
+3.920e+07
+1.962e+07
+3.520e+04

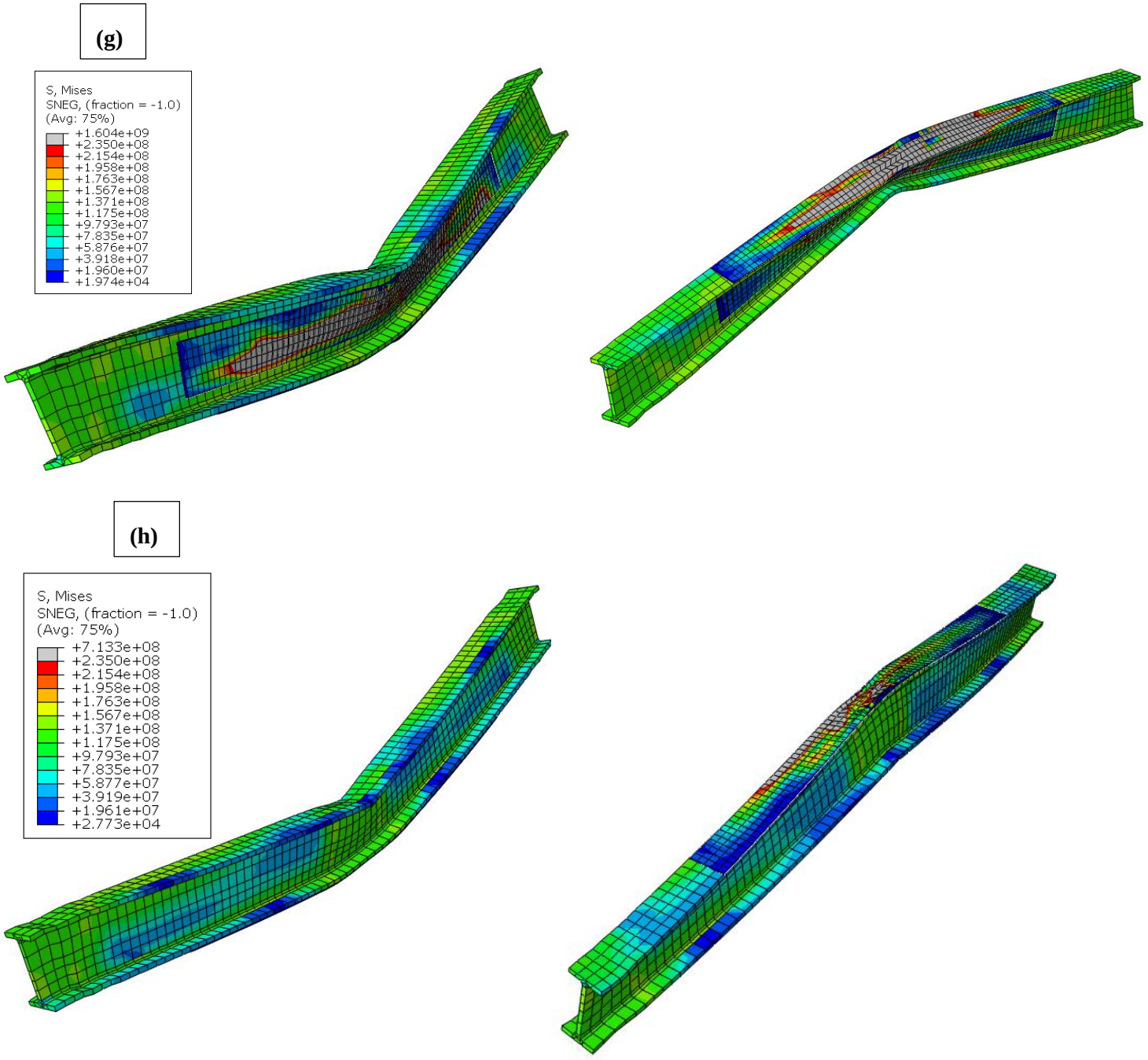

Figure 7.7 Stress variations of Un-strengthened and CFRP strengthened straight and beams with 4000 mm radius; (a) ST_CB, (b) ST_PR1, (c) ST_PR2, (d) ST_PR3, (e) 2000mm_CB, (f) 2000mm_PR1, (g) 2000mm_PR2, and (h) 2000mm_PR3

Figure 7.7 (a) and Figure 7.7 (e) show the stress variation of control steel beam. The maximum stresses found in these beams were 179 N/mm^2 and 154 N/mm^2 respectively. These values are well below the ultimate strength (235 N/mm^2) of steel, though these beams failed in lateral torsional buckling. When the straight beams strengthened with CFRP profile PR1, the stress developed in steel and CFRP were below the ultimate strength of those materials. Therefore, no yielding of steel or fracture of CFRP were observed. But, slight debonding of CFRP was observed due to the failure of the adhesive layer. No steel yielding and CFRP fracture were observed in beams with CFRP profiles PR2 and PR3, but slight debonding of CFRP layers were observed in either side of the web due to the failure of the adhesive layers. The failure mechanisms for the beams with 6000 mm curvature were identical to that of beams with 4000 mm curvature. But these failures were observed at lower loads.

7.5 Parametric Study

A parametric study was conducted to evaluate the effect of few bond parameters on the ultimate strength gain of CFRP strengthened horizontally curved steel I-beams. The parametric study was conducted on the beams having radius of curvatures 4000 mm and 6000 mm strengthened with CFRP application profile of PR3. This configuration of CFRP was selected, since it showed the highest strength gain during the experimental study. The behaviour of the straight I beams with similar conditions was also evaluated and presented for the comparison purpose.

7.5.1 CFRP bond length

Length of the CFRP applied on the beams is a crucial factor on ultimate strength gain and a key parameter which decides the cost of the retrofitting project. Four CFRP lengths 250 mm, 500 mm, 750 mm and 1000 mm were considered with PR3 CFRP application profile to investigate the effect of CFRP length. Figure 7.8 shows the load vs mid span deflection curves

for straight I beams strengthened with various CFRP configuration having different CFRP lengths and various curvatures.

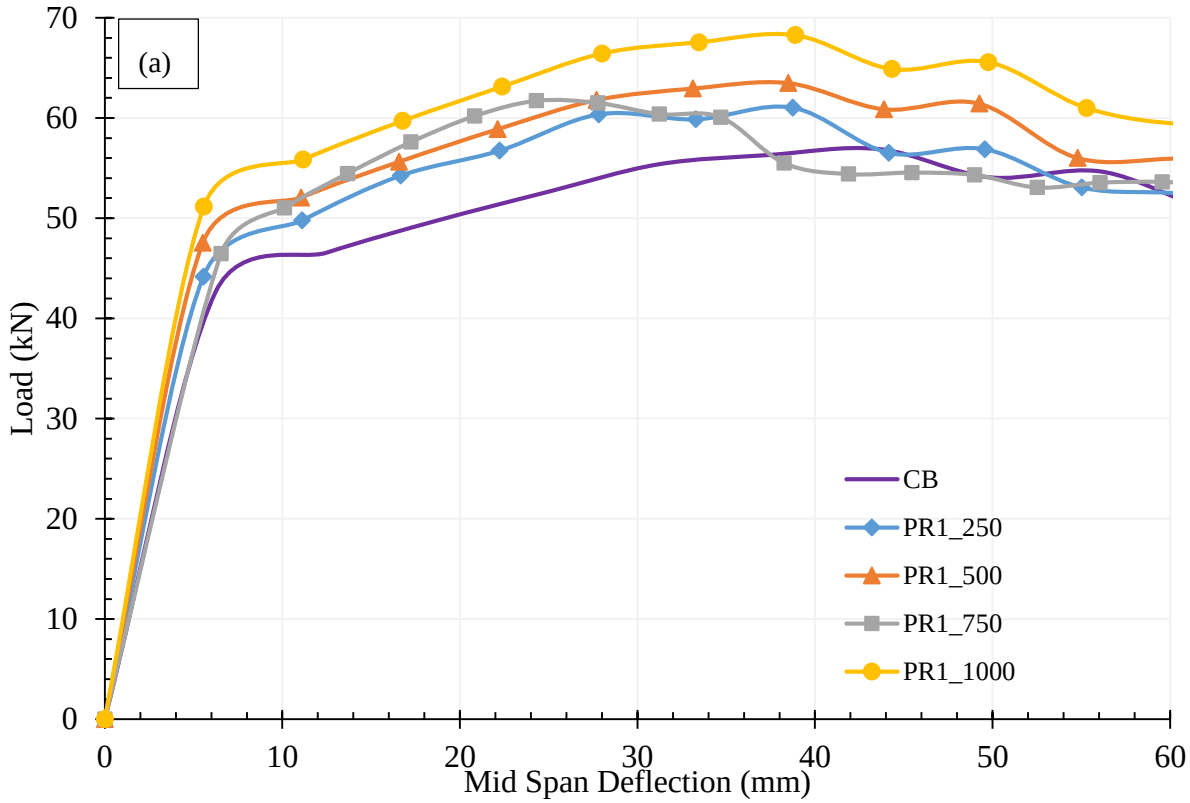

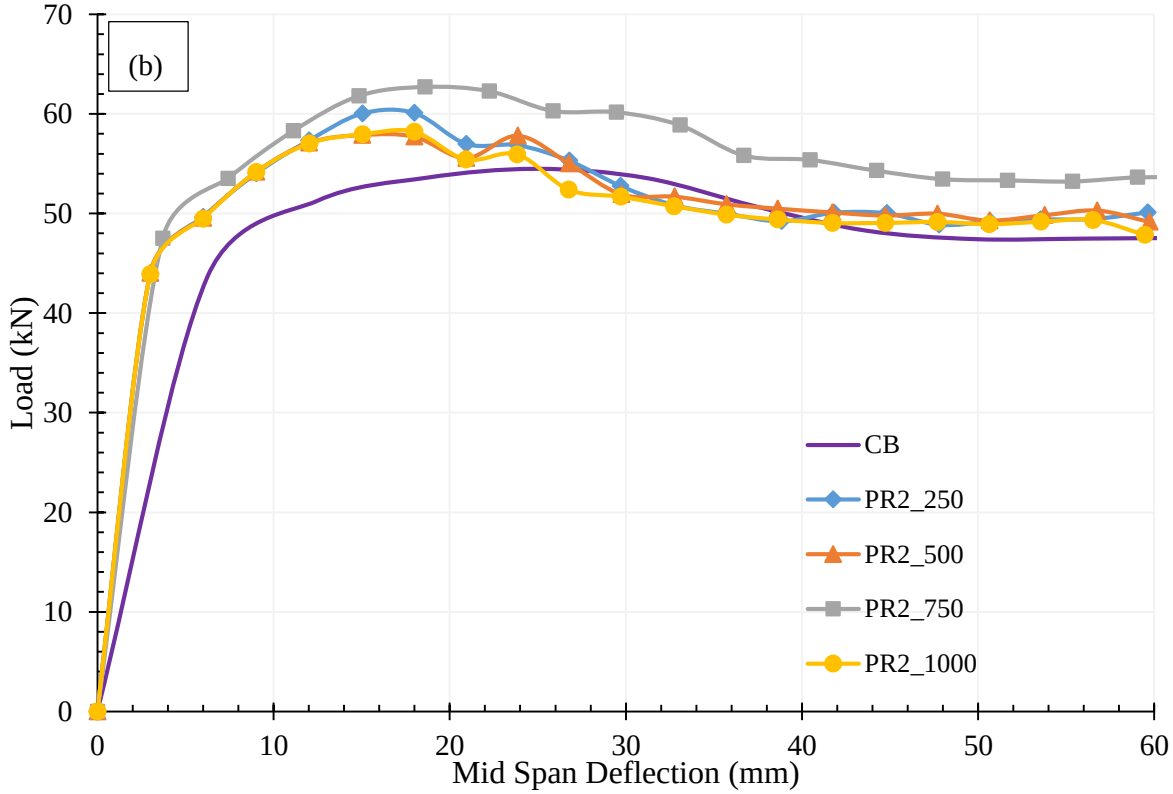

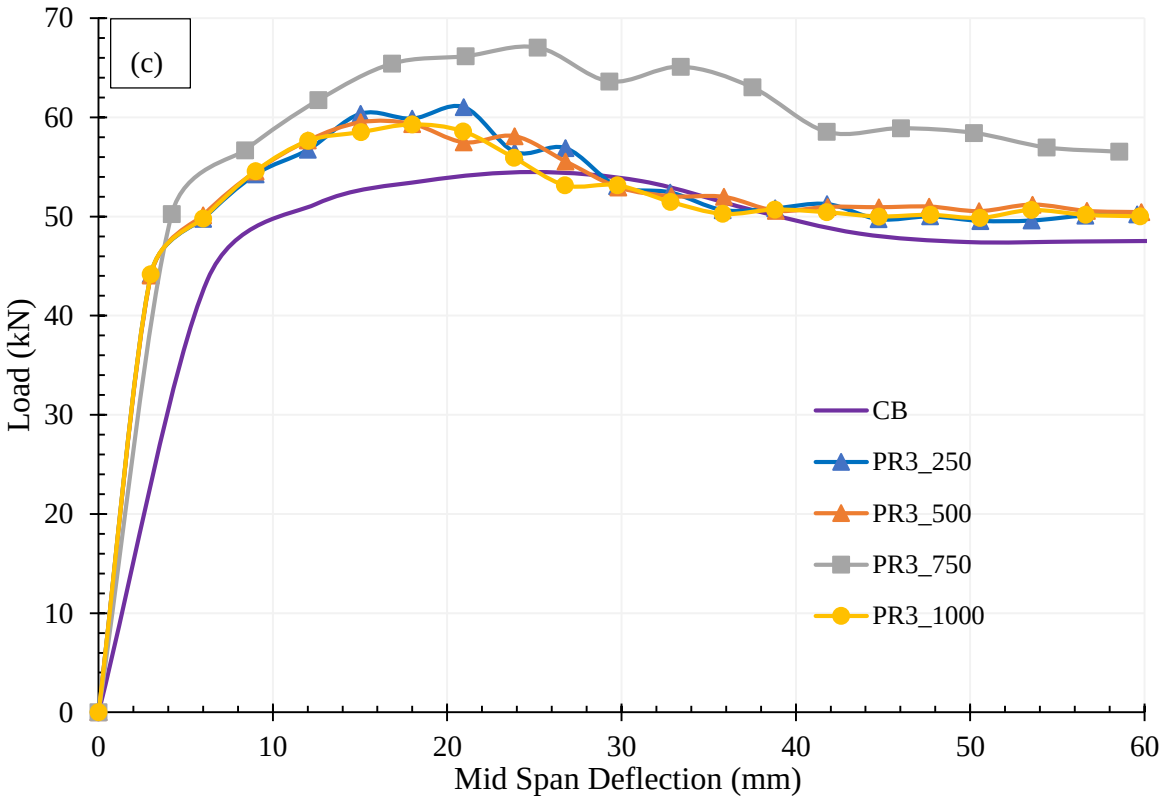

Figure 7.8. Load-deflection responses for straight I beams strengthened with various CFRP configurations and CFRP lengths, (a) PR1, (b) PR2, and (c) PR3

When straight beams strengthened with CFRP application configuration PR1, the highest ultimate load was observed when CFRP length was 1000 mm. This percentage is 25% increment compared to the ultimate load carrying capacity of control specimen. The percentage increment of ultimate load for beams with PR1 CFRP profile having 750 mm long CFRP was observed as 13%. The third and fourth highest strength gains were observed for beams with CFRP lengths 500 mm and 250 mm respectively. The highest strength gains for beams strengthened with CFRP application profiles PR2 and PR3 were observed with an applied CFRP length of 750 mm and the percentage increments were 15% and 23% respectively. The second highest ultimate load for the beams with PR2 and PR3 CFRP profiles were obtained,

when the CFRP length was 1000 mm and these increments were 10% and 12% respectively. The ultimate loads obtained for the beams with 250 mm and 500 mm CFRP lengths were observed to be almost same irrespective of the CFRP application profile.

Deflections at the ultimate load for beams strengthened with 750 mm long and PR2 /PR3 CFRP application profiles are greater than that of control beams, while this quantity is less than that of control beam in beams with other CFRP lengths.

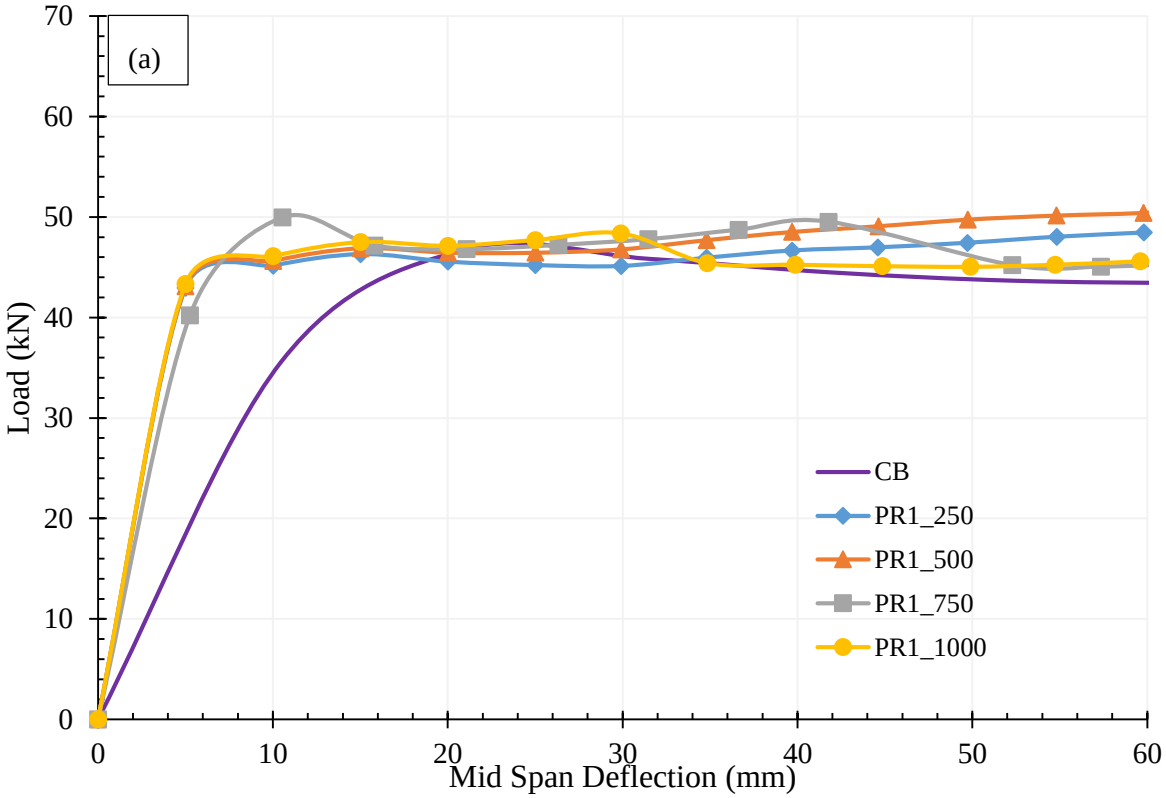

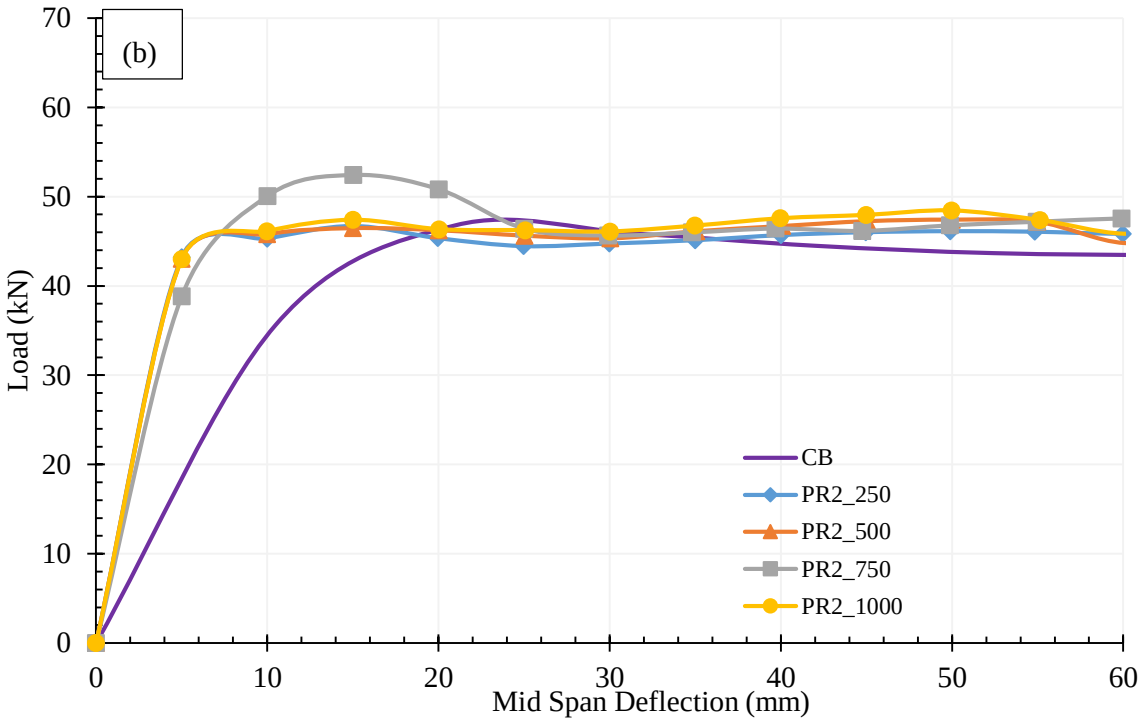

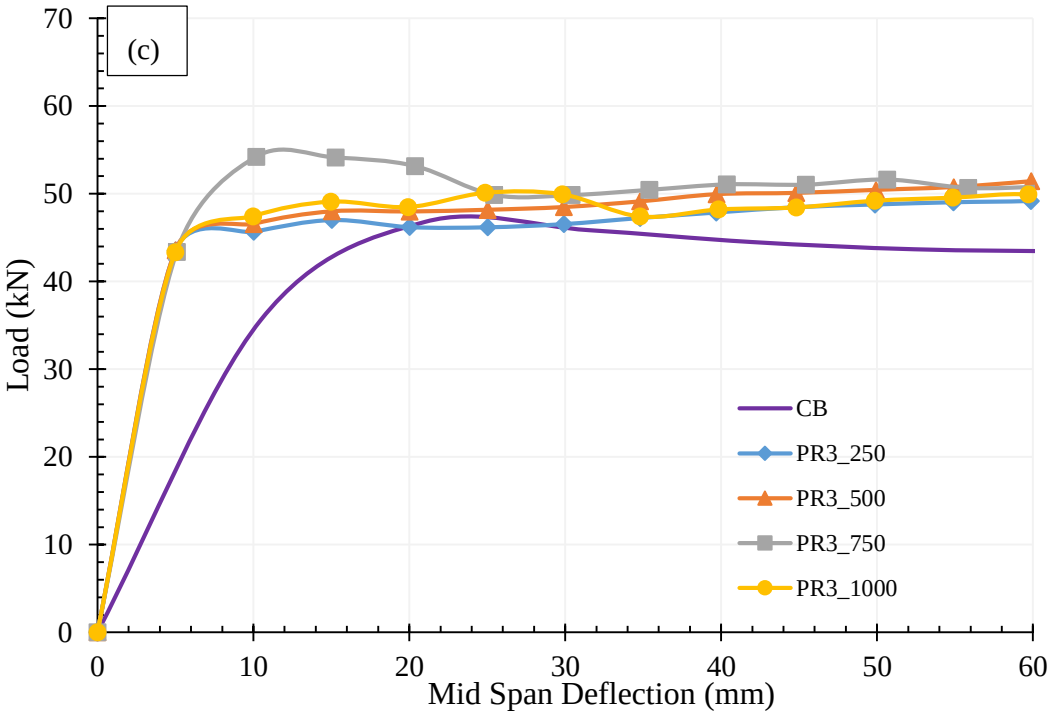

Figure 7.9. Load-deflection responses for I beams with 4000 mm radii strengthened with various CFRP configurations and CFRP lengths, (a) PR1, (b) PR2, and (c) PR3

Figure 7.9 shows the load-mid span deflection of CFRP strengthened horizontally curved steel I beams with 4000 mm radius strengthened with different CFRP lengths. It is clearly see that the stiffness of beams increased drastically when strengthened

with CFRP irrespective of CFRP application profile and CFRP length. When comparing three CFRP application profiles, the highest strength gain was noted in beam strengthened with PR3 CFRP application profile having 750 mm long CFRP. This percentage was 16% greater compared to control beam. This may be due to the prevention of lateral torsional buckling and provided additional stiffness when the beam strengthened with CFRP applied on both web and the tension flange. It was also noted that the highest strength gain for strengthened beams were observed in beams with 750 mm long CFRP irrespective of CFRP application profile. The results also indicated that the increase in CFRP length beyond 750 mm does not increase the ultimate load capacity and this may be due to the weaker load transfer to the CFRP due to increased length. Therefore, the economical length of CFRP may considered, when the proportion between CFRP length to clear span of the beam become 0.75 (750 mm/1000 mm). The beams strengthened with 250 mm, 500 mm and 1000 mm long CFRP patches have shown same range of strength gains irrespective of the CFRP application profile.

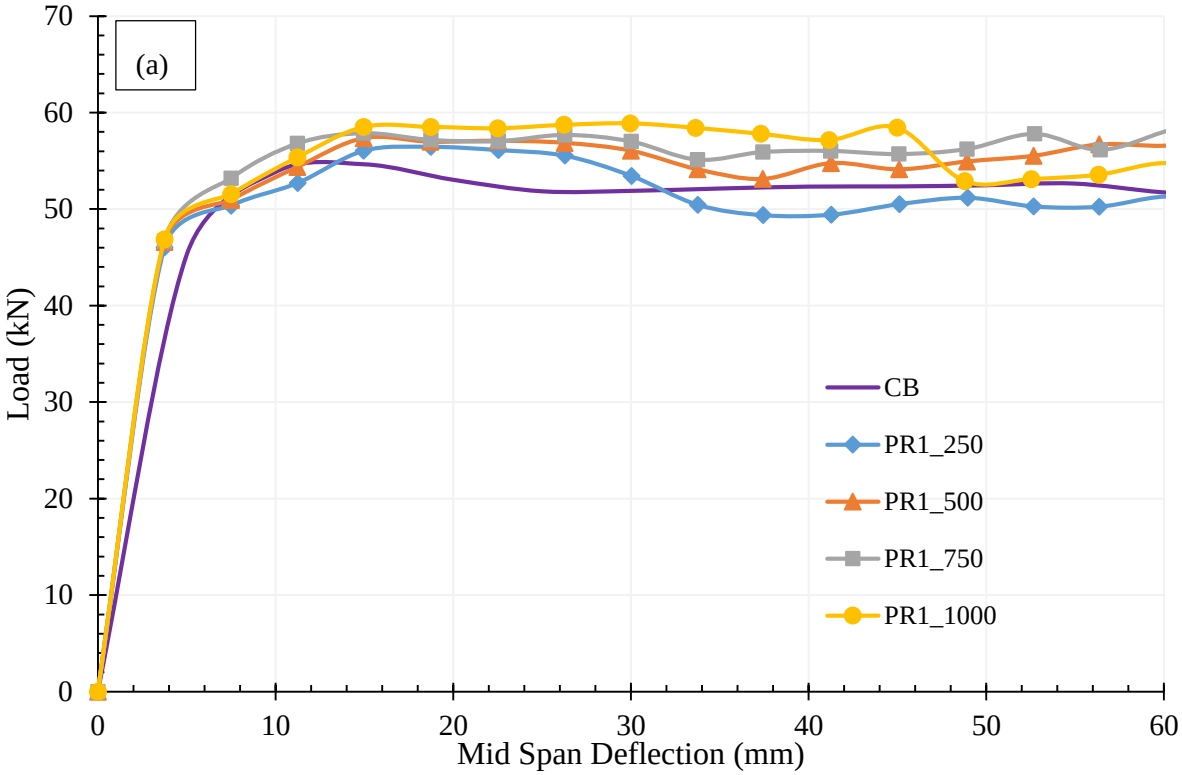
(a)
Load (kN)
Mid Span Deflection (mm)
CB
PR1_250
PR1_500
PR1_750
PR1_1000

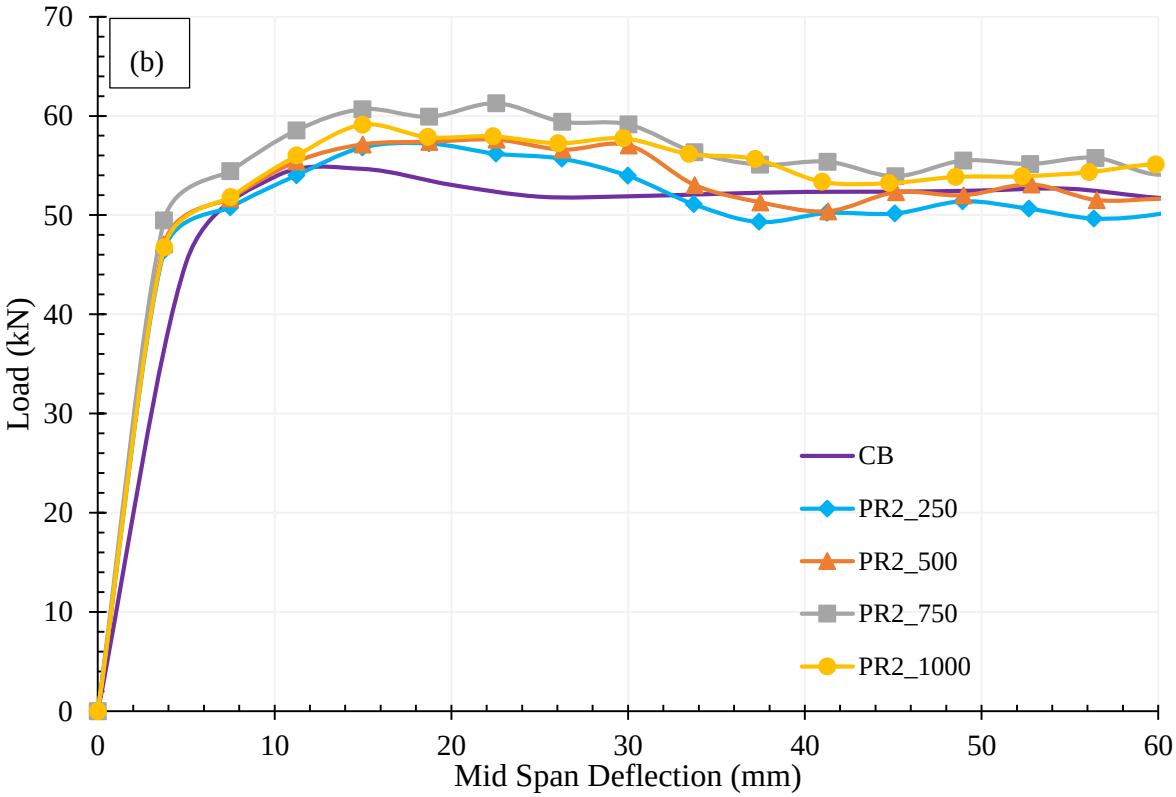
(b)
Load (kN)
Mid Span Deflection (mm)
CB
PR2_250
PR2_500
PR2_750
PR2_1000

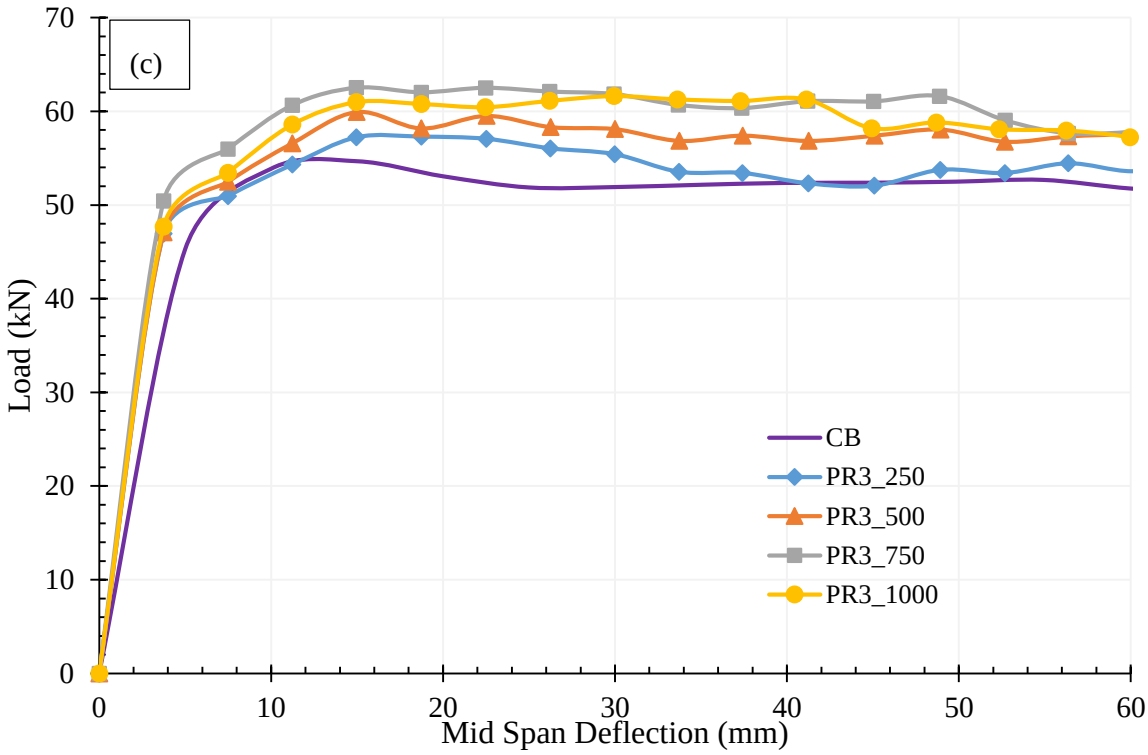

Figure 7.10 Load-deflection responses for I beams with 4000 mm radii strengthened with various CFRP configurations and CFRP lengths, (a) PR1, (b) PR2, and (c) PR3

Figure 7.10 shows the load-med span deflection responses for horizontally curved steel beams with 6000 mm radius strengthened with various CFRP profiles and CFRP lengths. As per Figure 7.10(a), the highest ultimate load was observed in beams with 1000 mm long CFRP when strengthened with PR1 CFRP application profile. This percentage increment was noted as 8%. The second, third and fourth highest strength gains were recorded in beams with 750 mm, 500 mm and 250 mm long CFRP respectively for this CFRP application profile. The highest strength gains were observed in beams strengthened with 750 mm long CFRP in beams strengthened with PR2 and PR3 CFRP application profiles and these percentage increments were 12% and 14% respectively. The highest to the lowest strength gains were recorded in beams with 1000 mm, 500 mm and 250 mm long CFRP for remaining beams respectively. It was also noted that the stiffness of all the beams were enhanced with the application

of CFRP irrespective of CFRP application profiles and CFRP application lengths. It was also observed that the deflection of the mid span at the ultimate loads were increased compared to control beams when strengthened with CFRP irrespective CFRP profile and length.

7.5.2 Elastic modulus of CFRP

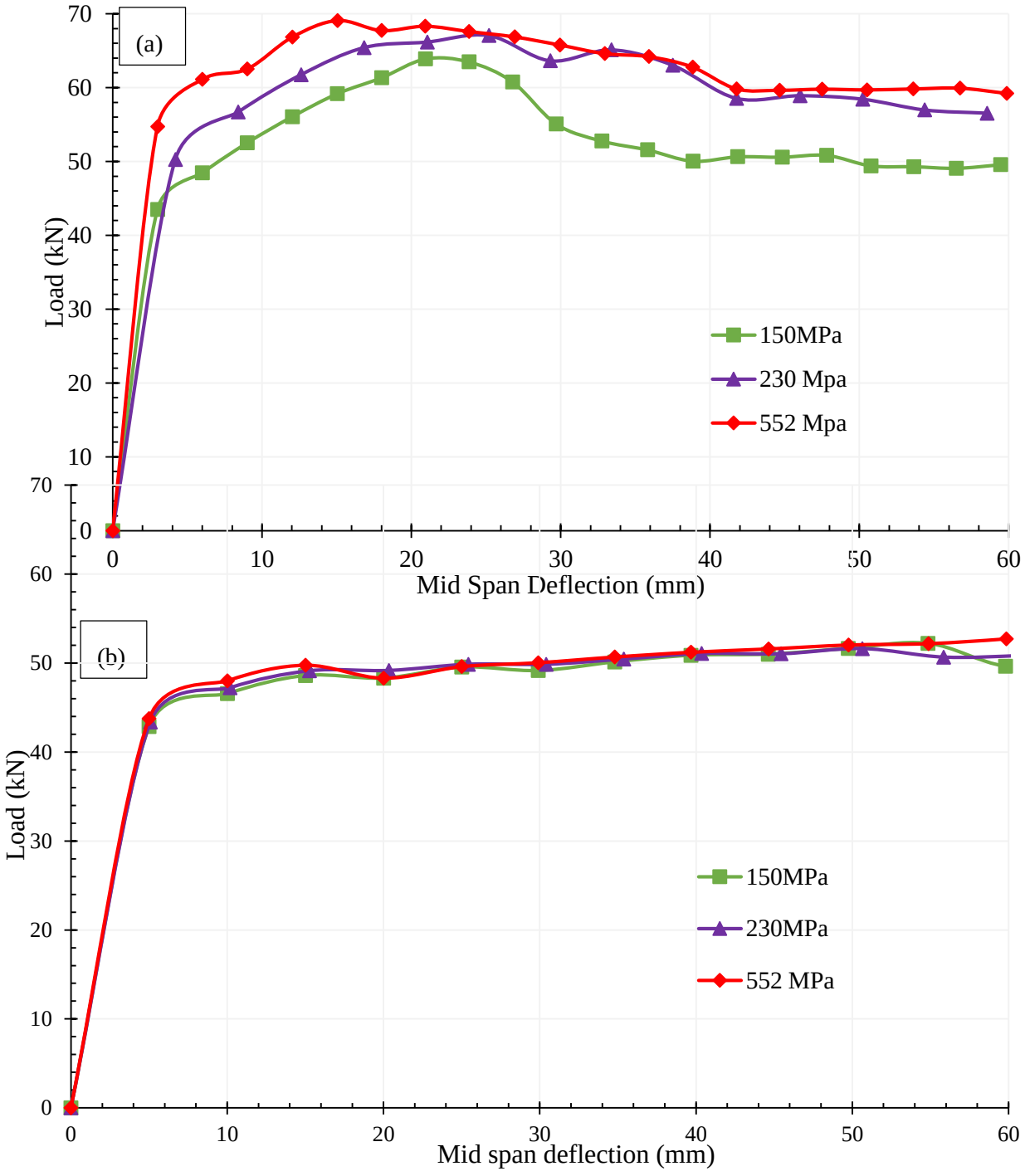

Figure 7.11. Load-deflection responses for steel I beams strengthened with PR3 CFRP profile having different elastic moduli (a) straight beams, and (b) beams with 4000 mm radii

With the development of material industry, manufactures tend to produce FRP materials with various elastic moduli for different applications. Figure 7.11 shows the load Vs mid span deflection curves for straight and beams with 4000 mm radii strengthened with PR3 CFRP application profile for different elastic moduli of CFRP. The elastic moduli, 150 MPa, 230 MPa and 552 MPa were considered. It can be clearly noted that the ultimate load for straight beams strengthened with CFRP increase with the increase in elastic modulus of CFRP. These increments for elastic moduli 235 MPa and 552 MPa are 5% and 8% respective when compared to the ultimate load obtained with CFRP having 150 MPa elastic modulus. As per Figure 7.11 (b), the ultimate strength gain in 4000 mm curved beams strengthened with CFRP having different elastic moduli does not show significant strength gain. This may be due to the failure of the beams due to lateral torsional buckling prior to fully load transfer to the CFRP patches.

7.5.3 Number of CFRP layers

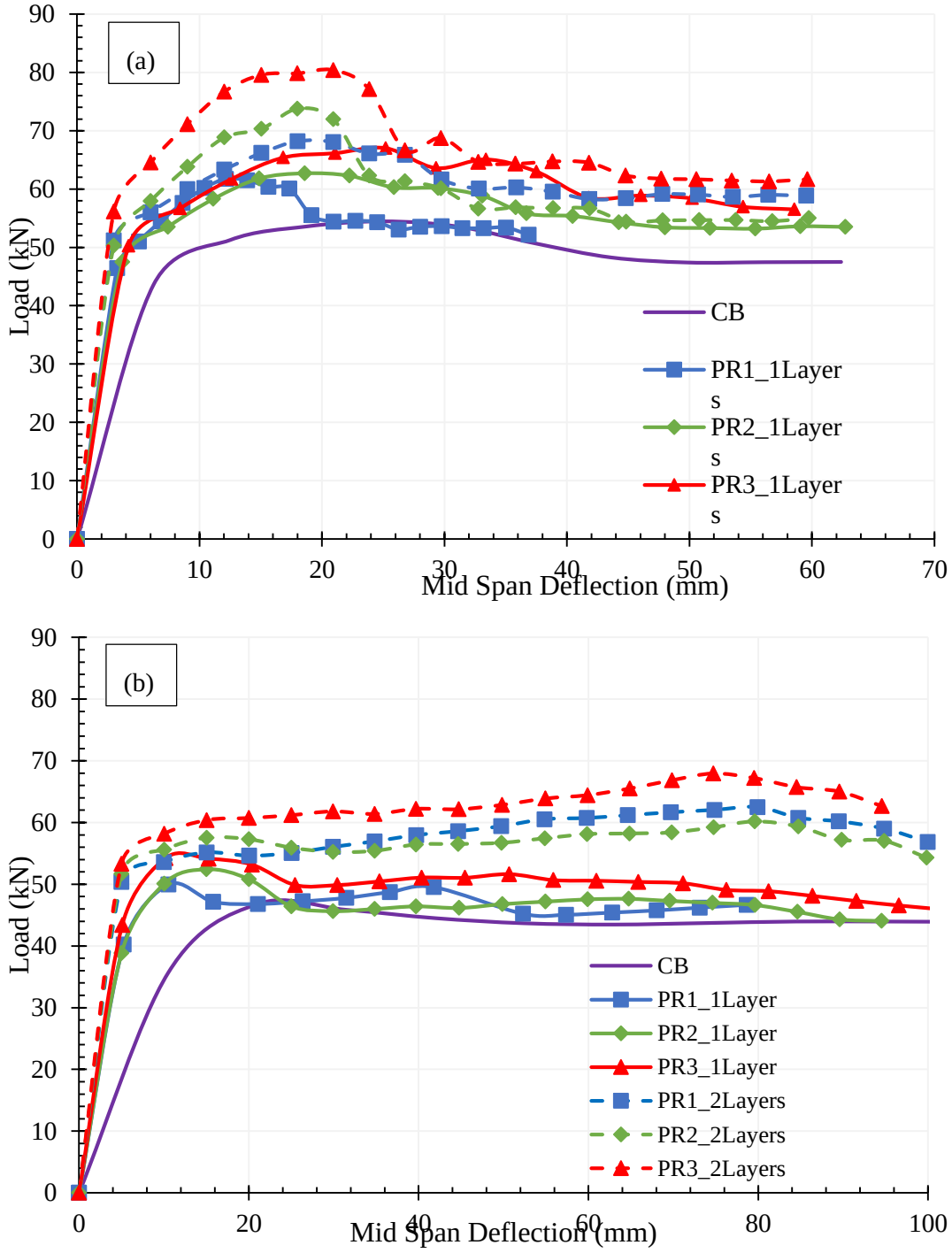

Figure 7.12. Load-deflection responses for straight and horizontally curved steel I beams strengthened with various CFRP configurations and CFRP layers (a) straight beams, and (b) beams curved with 4000 mm radius

The number of CFRP layers is a crucial factor in deciding the time and the cost of any retrofitting project using CFRP. Figure 7.12 shows the load-deflection responses for

straight and horizontally curved steel I beams strengthened with various CFRP configurations CFRP layers for straight beams and beams curved with 4000 mm curvature. For straight beams, the ultimate load increased compared to control beams when the number of CFRP layers increases, irrespective of CFRP application profile. This increase is comparatively large when compared with the beams curved to 4000 mm radius. The highest ultimate strength gain for straight beams strengthened with two CFRP layers obtained with the PR3 CFRP application profile and the value is 48% greater than the control beam and 20% greater than the beam with single CFRP layers. Second highest increment in ultimate load for straight beams was noted in beams strengthened with PR2 CFRP profile and it showed 35% and 18% increments compared to control beam and beam with single CFRP layer respectively. For the straight beams strengthened with PR1 CFRP profile with two CFRP layers showed percentage increment in ultimate loads by 25% and 15% compared to ultimate strength of control beam and beam strengthened with single CFRP layer respectively.

The highest ultimate load for beams curved with 4000 mm radius strengthened with two CFRP layers was observed in the beam with PR3 CFRP application profile. These percentages were 50% and 25%, compared to the control beams and beams with one CFRP layer of PR3 configuration. The beams strengthened with two layers of CFRP having PR2 CFRP application profile showed percentage increment in ultimate strengths 29% and 15% compared to control beam and beam with single CFRP layer respectively. The beam strengthened with two CFRP layers of PR1 profile showed higher ultimate strength compared to beams strengthened with PR2 CFRP application profile. With percentage compared to control beam is 34% while the percentage increment compared to beam with single CFRP layer is 25%. It was highlighted that the deflection at ultimate loads were greater in beams strengthened with two CFRP

layers compared to beams strengthened with single CFRP layer, irrespective of CFRP application profile. This may be due to the higher stiffness provided by the increased numbers of CFRP layers.

7.5.4. Elastic Modulus of Steel

As indicated in Figure 7.13 (c) and (d), the percentage increment in ultimate load reduces with the increase in elastic modulus of steel for beams curved with 4000 mm radius. It can be again noted that the deflections at the ultimate load increases with the increment in elastic modulus of curved steel I beams.

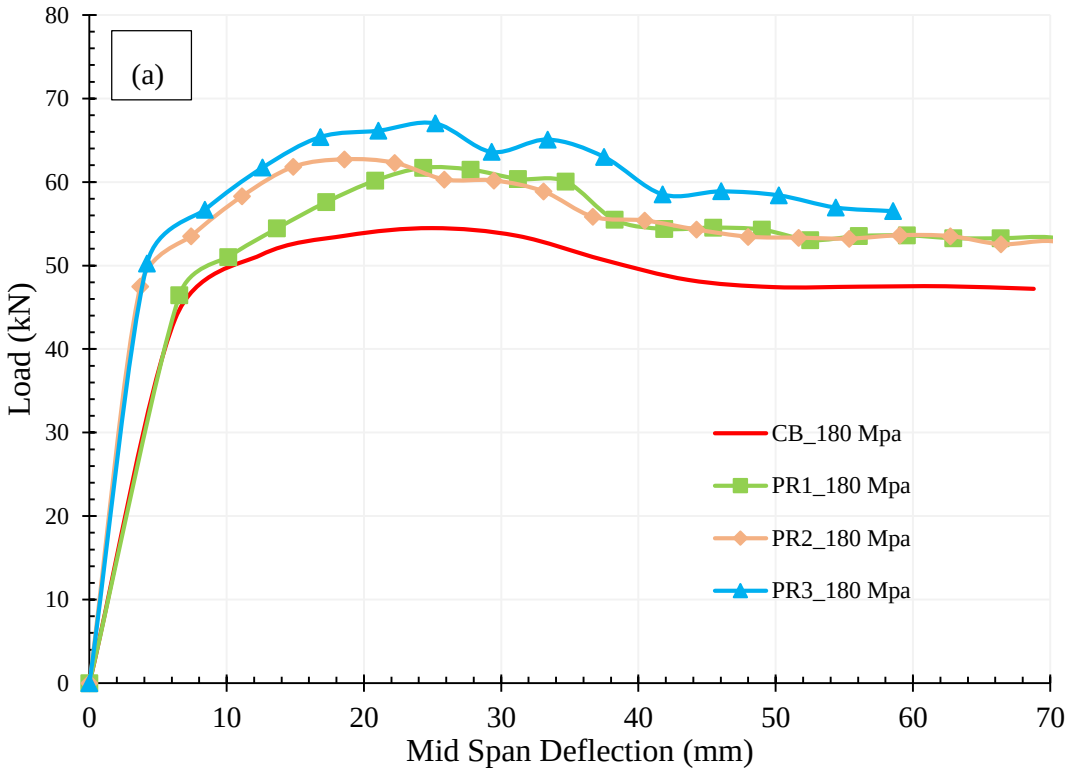

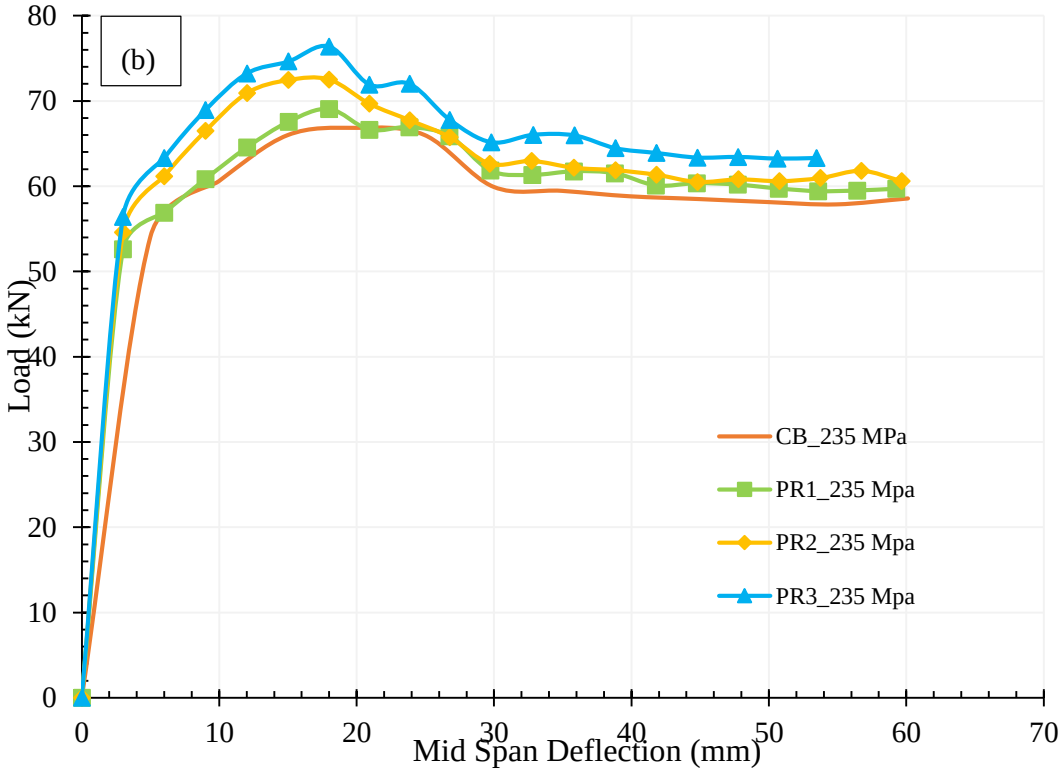
(b)
Load (kN)
Mid Span Deflection (mm)
CB_235 MPa
PR1_235 Mpa
PR2_235 Mpa
PR3_235 Mpa

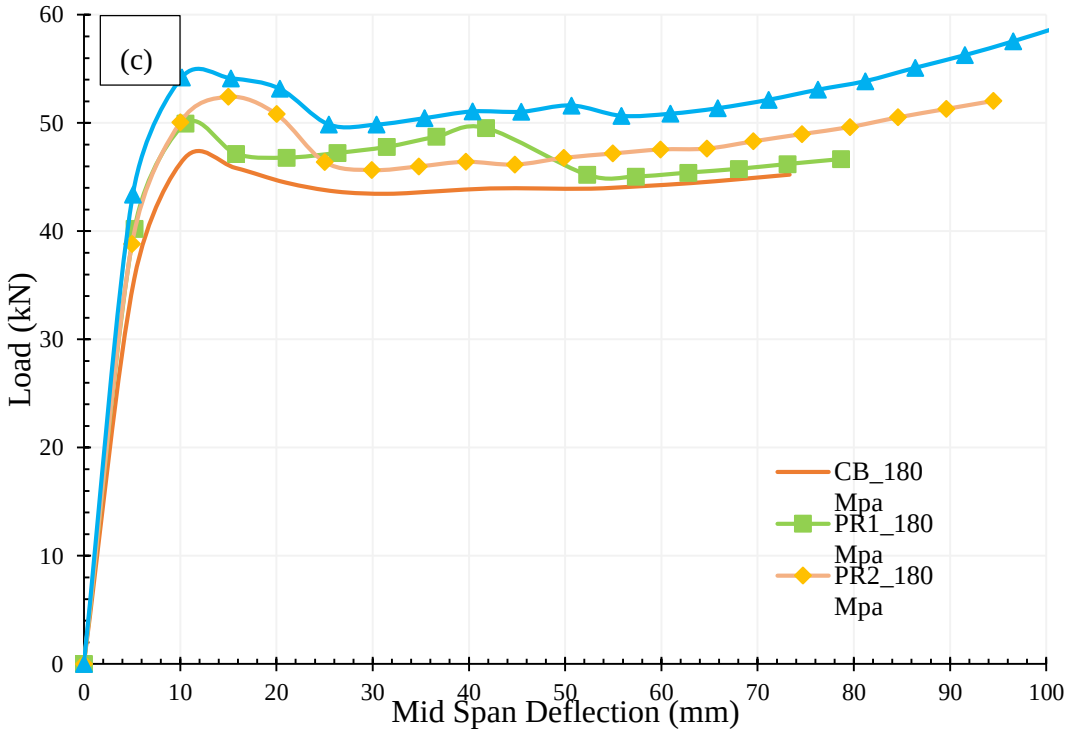
(c)
Load (kN)
Mid Span Deflection (mm)
CB_180 Mpa
PR1_180 Mpa
PR2_180 Mpa

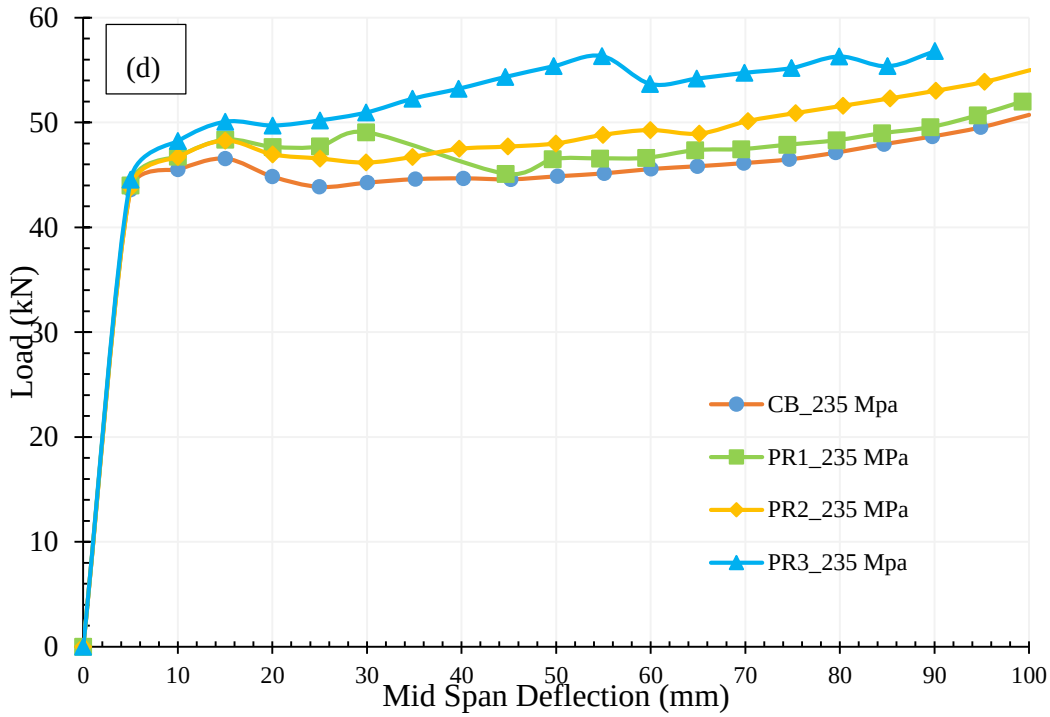

Figure 7.13. Load deflection responses for straight and curved beams with different elastic moduli (a) straight beam with 180 MPa elastic modulus, (b) straight beam with 235 MPa elastic modulus, (c) 4000 mm curved beam with 180 MPa elastic modulus, and (d) 4000 mm curved beam with 235 MPa elastic modulus

7.6 Conclusions

This study presents an experimental and numerical study on the flexural behaviour of CFRP strengthened straight and curved I beams. Experimental results revealed that CFRP is a promising technique to retrofit steel structures constructed with either straight or horizontally curved I beams. Full scale 3D models were developed to conduct parametric study to identify the effect of various sensitive bond parameters on the ultimate strength gain of CFRP strengthened straight and horizontally curved steel I beams. Finite element models were validated using experimental results. Following conclusions were drawn based on the results of both experimental and numerical studies.

- Several failure modes were observed for both straight and horizontally curved beams which include lateral torsional buckling of unstrengthened straight beam, lateral torsional buckling of strengthened straight beam, CFRP debonding at the tension face, lateral torsional buckling of curved beams, and CFRP debonding at the either side of the web in line with the load for CFRP profiles PR2 and PR3. The CFRP application profile and CFRP patch length drastically affect the failure modes observed in the beams. When CFRP length is lower, the CFRP debonding was observed due to the adhesive failure.
- Increase in number of CFRP layers increase the ultimate load irrespective of CFRP application profile. However, these increments for straight beams were comparatively greater than that of the horizontally curved beams. Increase in length of CFRP patches increase the ultimate load until the ratio between CFRP length to span become 0.75. However, the ultimate load decrease when this ratio greater than 0.75, which implies the economical CFRP length of CFRP is given when CFRP length to span of the beams ratio become 0.75. The increase in elastic modulus of CFRP drastically increase the ultimate load of straight beams while horizontally curved beams do not show a significant effect of elastic modulus of CFRP on the ultimate strength gain. For both straight and horizontally curved beams, the percentage increment of ultimate load was effected by the elastic modulus of the steel. It was noted that the percentage increment in ultimate load was reduced with the increase in elastic modulus.

- Further studies required for the proper verification of these sensitive bond parameters on the ultimate strength gain of straight and horizontally curved steel beams strengthened with CFRP.

7.7 Chapter Summery

This chapter discussed the experimental and numerical analysis of behaviour of horizontally curved steel I beams strengthened with CFRP. Results obtained for straight beams strengthened with CFRP were presented for comparison purposes. First part of the chapter discussed the experimental study done on twelve steel beams which included both straight and curved beams. 3D finite element models were developed to carry out parametric study to evaluate the effect of various bond parameters such as CFRP application profile, CFRP bond length, number of CFRP layers, elastic modulus of CFRP and Elastic modulus of steel on the ultimate strength gain of CFRP strengthened straight and cured beams. Numerical models were validated using experimental results prior to conduct the parametric study using ultimate loads, deflection at modes. Finally, the recommendations were given for industrial applications of outcomes of this study.

Chapter 8

Conclusions, Recommendation and Future Works

8.1 Introduction

This chapter presents the overall conclusions and recommendations of the conducted study. The conclusion part explains the main findings of the study while recommendations provide and insight on how the findings of the study are can be practically applied in construction industry. The related future works on this study are also presented in order to aware the future researchers on the presented study in order to obtain new findings.

8.2 Conclusions

The Following conclusions can be drawn as per the findings of the experimental, numerical and analytical studies conducted on the in plane curved steel circular hollow sectioned beams.

1. CFRP is a promising solution for strengthening of in plane curved circular hollow sections under the flexural loading.
2. The ultimate strengths of the CFRP retrofitted in plane curved SCHS were obtained when the ratio of CFRP length to the span of beam becomes 0.625. The ultimate strengths were observed to be lower for the values of this ratio less than or greater than 0.625.
3. The ultimate load carrying capacity of a in plane curved SCHS for a certain CFRP wrapping length decreases when radius of curvature of the beam increases
4. Strengthening of SCHS using CFRP reduces the amount of mid span deflection at the ultimate load and when the radius of curvature decreases the

mid span deflection also decreases. This is due to the increase in stiffness of the beam due to the effect of CFRP wrapping.

5. Four major failure types were observed in CFRP strengthened in plane curved curved SCHS beams which include debonding of CFRP due to adhesive failure, bearing of the steel tube near the loading point, crushing of CFRP near the loading point, CFRP rupture on the tension face of the beam and bearing of steel tube under the loading point.

6. It was noted that the developed numerical model is capable of conducting parametric studies related to CFRP strengthening of in plane curved steel CHS. The developed numerical models were validated using the experiment results on load-deflection beahaviour and failure modes.

7. According to the conducted parametric study the number of CFRP layers, CFRP layer orientation, aspect ratio of steel section, elastic modulus and adhesive thickness found to be drastically effect the ultimate strength gain.

8. Number of CFRP layers increases the ultimate load carrying capacity of CFRP strengthened curved CHSs, but this increment is proportional to the number of layers. The rate of percentage increase in the ultimate load between successive CFRP layers decreases with increased number of CFRP layers. Hence, it is important to identify the bond enhancing technique which can delay pre mature failure rather than increasing the number of CFRP layers for economical applications.

9. Layer orientation of CFRP patches is an important factor to be considered for better performance. Longitudinal layer orientation was found to be best for the flexural performance compared to hoop, spiral and reverse spiral orientations.

10. Aspect ratios of steel beams do not have significant effects on percentage increases in ultimate load carrying capacities of CFRP strengthened curved beams with CHS, if the section is sufficiently rigid.
11. A bond-slip model was developed for the CFRP strengthened curved steel tubular beams subjected to bending. It was observed that the bod-slip model has a trapezoidal shape and the fracture energy at the end debonding depends on the beam curvature. Moreover, yield slip, initial slip and final slip for steel-CFRP interface of curved beams depends on the curvature of the beam and the length of CFRP sheet.

The following conclusions were drawn based on the results of the experimental, analytical and numerical studies conducted on the CFRP strengthened out of plane curved steel I beams.

1. The CFRP application profile drastically affect the strength gain of CFRP strengthened straight and out of plane curved I beams. The most effective CFRP application profile found under this study was strengthening of beams with CFRP at both web and the tensile face of the beams
2. Several failure modes were identified in both straight and horizontally curved I beams which include lateral torsional buckling of un-strengthened beams, lateral torsional buckling of strengthened beams, debonding of CFRP either at the web or tensile flange, CFRP tearing etc.
3. Increase in number of CFRP layers increase the ultimate load irrespective of CFRP application profile.
4. The economical CFRP length of CFRP is given when CFRP length to span of the beams ratio become 0.75 for out of plane curved I beams

5. The increase in elastic modulus of CFRP and steel increases the ultimate load capacity of out of plane curved I beams
6. Increase in adhesive thickness reduces the ultimate load carrying capacity of the strengthened I beams
7. The developed analytical model is capable of predicting the ultimate loads and deflections of CFRP strengthened out of plane curved steel I beams.

8.3 Recommendations

The following recommendations can be suggested to the benefit of future researchers and the industry, based on the results of the studies conducted on in plane curved steel circular hollow sections and out of plane curved steel I beams.

1. The results of the studies presented in this thesis can be used by the industry professionals in retrofitting steel structures constructed with in plane curved tubular sections and out of plane curved I beams
2. The developed sound numerical models may use to conduct parametric studies necessary for the industry professionals for various applications
3. Results may be utilized in developing design guidelines for CFRP strengthening of steel beams curved in plane and curved out of plane with various section shapes
4. Theoretical analysis of the curved steel beams presented in this thesis may retrofitted with CFRP presented in this thesis may be used by industry professionals, and
5. The results presented in this thesis may introduce a method to retrofit curved structural elements with minimum time and minimum labour requirement

8.4. Future Works

The following future works on the same research area is suggested for future researchers based on the gaps identified during the current study presented in this

thesis. This future works included studies on both in plane curved steel circular hollow sections and out of plane curved steel I beams strengthened with CFRP.

- Extended parametric studies for CFRP strengthened curved CHS beams
- Development of Design guidelines for CFRP strengthened curved CHS beams
- Development of various analysis methods in order to predict ultimate loads and deflections of CFRP strengthened CHS beams
- Development and improve more reliable bon-slip models for CFRP strengthened CHS beams
- Extended parametric studies for CFRP strengthened horizontally curved steel I beams
- Development and improve more reliable bon-slip models for CFRP strengthened horizontally curved steel I beams
- Development of Design guidelines for CFRP strengthened horizontally curved I beams
- Development of various analysis methods in order to predict ultimate loads and deflections of CFRP strengthened horizontally curved I beams
- Experimental and numerical investigation for combined actions on the CFRP strengthened horizontally curved steel I beams

References

Abbas, M. A. 2010. *Durability of CFRP-Concrete Bond under Sustained Load in Harsh Environment.* PhD by Thesis, Department of Civil Engineering, Monash.

Abdollahi Chahkand, N. et al. 2013. "Experimental and Theoretical Investigation on Torsional Behaviour of CFRP Strengthened Square Hollow Steel Section." *Thin-Walled Structures* 68: 135–40. http://dx.doi.org/10.1016/j.tws.2013.03.008.

Al-ridha, Ahmed S D, Ali A Abbood, and Ali F Atshan. 2020. "Improving the Performance of Steel Beams by Using Carbon Fiber Reinforced Polymer : A Review ةعماجلا ةيرصنتسملا - ةيلك ةسدنهلا ةعماجلا ةيرصنتسملا - ةيلك ةسدنهلا." *Journal of Al Rafidain University College* (47): 199–213.

Al-Zubaidy, Haider, Xiao Ling Zhao, and Riadh Al-Mahaidi. 2013. "Mechanical Characterisation of the Dynamic Tensile Properties of CFRP Sheet and Adhesive at Medium Strain Rates." *Composite Structures* 96: 153–64. http://dx.doi.org/10.1016/j.compstruct.2012.09.032.

Alam, Md Iftekharul, Fawzia, Sabrina, Liu, Xuemei, Batuwitage, Chamila Rajeev Jayanath. 2014. "Dynamic Simulation of CFRP Strengthened Steel Column under Impact Loading." In *Proceedings of the 23rd Australasian Conference on the Mechanics of Structures and Materials (ACMSM23), Volume 1. Southern Cross University, Australia,* , 503–8.

Alam, Md Iftekharul., Fawzia, Sabrina. 2015. "Numerical Studies on CFRP Strengthened Steel Columns under Transverse Impact." *Composite Structures* 120: 428–41.

Alam, M I, and S Fawzia. 2017. "FE Modeling of FRP Strengthened CHS Members

Subjected to Lateral Impact." In *16th International Symposium on Tubular Structures, ,* 4–6.

Alam, Md Iftekharul et al. 2017. "Performance and Dynamic Behaviour of FRP Strengthened CFST Members Subjected to Lateral Impact." *Engineering Structures* 147: 160–76. http://dx.doi.org/10.1016/j.engstruct.2017.05.052.

Altaee, Mohammed, Lee S Cunningham, and Martin Gillie. 2019. "Practical Application of CFRP Strengthening to Steel Floor Beams with Web Openings : A Numerical Investigation." *Journal of Constructional Steel Research* 155: 395–408. https://doi.org/10.1016/j.jcsr.2019.01.006.

Altaee, Mohammed J, Lee S Cunningham, and Martin Gillie. 2017. "Experimental Investigation of CFRP-Strengthened Steel Beams with Web Openings." *Journal of Constructional Steel Research* 138: 750–60. http://dx.doi.org/10.1016/j.jcsr.2017.08.023.

Amir Hamzeh Keykha. 2018. "Investigation of the Effect of CFRP Strengthening on the Behavior of Deficient Steel Members under Combined Lateral and Torsional Loading." *Jordan Journal of Civil Engineering* 12(04): 590–602.

Ashcroft I.A., Mubashar A. 2011. *Numerical Approach: Finite Element Analysis. In: Da Silva L.F.M., Öchsner A., Adams R.D. (Eds) Handbook of Adhesion Technology.*

ASTM A 370-19ei. 2019. *Standard Testing Methods and Definitions for Mechanical Testing of Steel Products*. West Conshohocken.

ASTM A370 / ASME SA-370: Standard Test Methods and Definitions for Mechanical Testing of Steel Products 1. 2016. USA: ASTM Standard, American Society for Testing Materials.

ASTM D3030/D3039M: Standard Test Method for Tensile Properties of Polymer Matrix Composite Materials 1. 2002. 15 USA: ASTM Standard, American Society for Testing Materials.

ASTM D638 - 14: Standard Test Method for Tensile Properties of Plastics 1. 2015. USA: ASTM Standard, American Society for Testing Materials.

Austin, W.J. and Ross, T. J. 1976. "Elastic Buckling of Arches under Symmetric Loading." *Journal of the Structural Division, ASCE* 102(05): 1085–95.

Avgoulas, Evangelos I, and Michael P F Sutcliffe. 2016. "Biomimetic-Inspired CFRP to Perforated Steel Joints." *Composite Structures* 152: 929–38.

Babu, B Rajesh, and M C Sundarraja. "Strengthening of Square Hollow Structural Steel (Hss) Tubular Sections Using Cfrp Strips." : 25–34.

Badawy, Anwar et al. 2019. "Behavior of Hollow Steel Sections Strengthened with CFRP." *Construction and Building Materials* 205: 306–20. https://doi.org/10.1016/j.conbuildmat.2019.01.237.

Bagale, Bibek Regmi, S M Asce, and Azadeh Parvin. 2020. "Fiber-Reinforced Polymer Strengthening of Steel Beams under Static and Fatigue Loadings." *Practice Periodical on Struc- tural Design and Construction* 26(1): 1–9.

Baldan, A. 2004a. "Adhesively-Bonded Joints and Repairs in Mattalic Alloys, Polymers and Composite Materials: Adhesives, Adhesion Theories and Surface Pretreatments." *Journal of Materials Science* 39(1): 1–49.

———. 2004b. "Adhesively-Bonded Joints and Repairs in Metallic Alloys, Polymers and Composite Materials: Adhesives, Adhesion Theories and Surface Pretreatment." *Journal of Materials Science* 39(1): 1–49.

———. 2004c. “Adhesively-Bonded Joints and Repairs in Metallic Alloys, Polymers and Composite Materials: Adhesives, Adhesion Theories and Surface Pretreatment.” *Journal of Materials Science* 39(1): 1–49.

Banea, M. D. and Silva, L. F. M. da. 2009. “Adhesively Bonded Joints in Composite Materials: An Overview.” *Proceedings of the Institution of Mechanical Engineers* 223(L1): 1–18.

Bank, L.C. and Gentry, T.R. 1995. “Accelerated Test Methods to Determine the Long- Term Behavior of FRP Composite Structures: Environmental Effects.” *Journal of Reinforced Plastic and Composites* 14: 558–87.

Belytschko, T. and Glaum, L.W. 1979. “Applications of Higher Order Corotational Stretch Theories to Nonlinear Finite Element Analysis.” *Computers & Structures* 10: 175–82.

Bocciarelli, M., Colombi, P., Fava, G., and Poggi, C. 2007. “Interaction of Interface Delamination and Plasticity in Tensile Steel Members Reinforced by CFRP Plates.” *International Journal of Fracture* 146(1-2): 79–92.

———. 2009. “Prediction of Debonding Strength of Tensile Steel/CFRP Joints Using Fracture Mechanics and Stress Based Criteria.” *Engineering Fracture Mechanics* (76(2)): 299–313.

Bocciarelli, M. 2009. “Response of Statically Determined Steel Beams Reinforced by CFRP Plates in the Elastic-Plastic Regime.” *Engineering Structures* 31(4): 956–67.

Bocciarelli, Massimiliano, Pierluigi Colombi, Giulia Fava, and Lisa Sonzogni. 2016. “Energy-Based Analytical Formulation for the Prediction of End Debonding in Strengthened Steel Beams.” *Composite Structures*. doi: http://

dx.doi.org/10.1016/j.compstruct.2016.05.084%0AThis.

Boulton, N. S., and Boonsukha, B. 1959. “Plastic Collapse Loads for Circular-Arc Bow Girders.” *Proc., Institution of Civil Engineers* 13(6): 161–78.

Brown, ARG. 1974. “The Corrosion of CFRP-to-Metal Couples in Saline Environments.” In *Proceedings of the 2nd International Conference on Carbon Fibres, ,* 18–20.

Brown, David. 2007. “Design of Curved Steel.” *The Steel Construction Institute*.

Byars, E. A., Waldron, P., Dejke, V., Demis, S. and Heddadin, S. 2003. “Durability of FRP in Concrete - Deterioration Mechanisms.” *International Journal of Materials & Product Technology* 19(1-2): 28–39.

Calhoun, P.R. and DaDeppo, D. 1983. “Nonlinear Finite Element Analysis of Clamped Arches.” *Journal of Structural Engineering, ASCE* 109: 599–612.

Camanho PP, Davila CG, de Moura MF. 2003. “Numerical Simulation of Mixed Mode Progressive Delamination in Composite Materials.” *Journal of Composite Materials* 37(16): 1415–38.

Cazzani, Antonio, Marcello Malagù, and Emilio Turco. 2014. “Isogeometric Analysis of Plane-Curved Beams.” *Mathematics and Mechanics of Solids* 21(5): 562–77.

Chawla, K.K. 1998. *Composite Materials: Science and Engineering*. Springer Netherlands.

Che, Y., Q. L. Wang, and Y. B. Shao. 2012. “Compressive Performances of the Concrete Filled Circular CFRP-Steel Tube (C-CFRP-CFST).” *Advanced Steel Construction* 8(4): 331–58.

Chen, J.F., Teng, J.G. 2001. “Anchorage Strength Models for FRP and Steel Plates Bonded to Concrete.” *Journal of Structural Engineering* 127(7): 784–91.

Chen, Tao et al. 2018. “Experimental Study on Fatigue Behavior of Cracked Rectangular Hollow-Section Steel Beams Repaired with Prestressed CFRP Plates.” *Journal of Composites for Construction* 22(5): 1–11.

Chiew, S P, Y Yu, and C K Lee. 2011. “Bond Failure of Steel Beams Strengthened with FRP Laminates – Part 1 : Model Development.” *Composites : Part B* 42: 1114–21.

Chini, S.A. and Wolde-Tinsae, A. M. 1988. “Critical Load and Postbuckling of Arch Frameworks.” *Journal of Engineering Mechanics, ASCE* 114(09): 1435–53.

Colombi, P. and Poggi, C. 2006. “Strengthening of Tensile Steel Members and Bolted Joints Using Adhesively Bonded CFRP Plates.” *Construction and Building Materials* 20(1-2): 22–33.

Colombi, Pierluigi, and Carlo Poggi. 2006. “An Experimental , Analytical and Numerical Study of the Static Behavior of Steel Beams Reinforced by Pultruded CFRP Strips.” *Composites Part B: Engineering* 37: 64–73.

Conway, H.D. and Lo, C.F. 1967. “Further Studies on the Elastic Stability of Curved Beams.” *International Journal of Mechanical Sciences* 09: 707–18.

Crasto, A.S. and Kim, R.Y. 1996. “Environmental Durability of a Composite-to-Composite Adhesive Bond in Infrastructure Applications.” In *28th International SAMPE Technical Conference, ,* 837–49.

D3039/D3039M-17, ASTM. 2017. *Standard Test Methods for Tensile Properties of Polymer Matrix Composite Materials*.

DaDeppo, D.A. and Schmidt, R. 1969. “Nonlinear Analysis of Buckling and Postbuckling Behavior of Circular Arches.” *Journal of Applied Mathematics and Physics* 20: 847–57.

El Damatty, A.A., M. Abushagur, and M.A. Youssef. 2003. “Experimental and Analytical Investigation of Steel Beams Rehabilitated Using GFRP Sheets.” *Steel and Composite Structures* 3(6): 421–38.

Dawe, D.J. 1971. “A Finite-Deflection Analysis of Shallow Arches by the Discrete Element Method.” *International Journal for Numerical Methods in Engineering* 02: 529–52.

Dawood, M.M.R. 2008. *Bond Characteristics and Environmental Durability of CFRP Materials for Strengthening Steel Bridges and Structures*. PhD in Civil Engineering, Graduate Faculty, North Carolina State University.

Dawood, Mina. 2008. “Bond Charactersistics and Environmental Durability of CFRP Materials for Strengthening Steel Bridges and Structures.” *Materials science*.

Deng, J. and Lee, M.M.K. “Bwhaviour under Static Loading of Metalic Beams Reinforced with a Bonded CFRP Plate.” *Composite Structures* 78: 232–42.

Deng, J., Lee M.M.K. 2007. “Behaviour under Static Loading of Metallic Beams Reinforced with a Bonded CFRP Plate.” *Composite Structures* 78(2): 232–42.

Deng J, Lee MMK, Moy SSJ. 2004. “Stress Analysis of Steel Beams Reinforced with a Bonded CFRP Plate.” *Composite* (65): 205–15.

Deng, Jiangang. 2008. *Durability of Carbon Fiber Reinforced Polymer (CFRP) Repair/Strengthening Concrete Beams.* PhD in Civil Engineering, Department of Civil & Architectural Engineering and The Graduate School, The University

of Wyoming.

Devi, Urmi, and Khan Mahmud Amanat. 2015. “Non-Linear Finite Element Investigation on the Behavior of CFRP Strengthened Steel Square HSS Columns under Compression.” *International Journal of Steel Structures* 15(3): 671–80.

Dimitri, R., M. Trullo, L. De Lorenzis, and G. Zavarise. 2015. “Coupled Cohesive Zone Models for Mixed-Mode Fracture: A Comparative Study.” *Engineering Fracture Mechanics* 148: 145–79. http://dx.doi.org/10.1016/j.engfracmech.2015.09.029.

EI Damatty, A.A., and Abushagur, M. 2003. “Testing and Modelling of Shear and Peel Behaviour for Bonded Steel/FRP Connections.” *Thin Walled Structures* 41(11): 987–1003.

Elchalakani, Mohamed. 2014a. “CFRP Strengthening and Rehabilitation of Degraded Steel Welded RHS Beams under Combined Bending and Bearing.” *Thin-Walled Structures* 77: 86–108. http://dx.doi.org/10.1016/j.tws.2013.12.002.

———. 2014b. “Plastic Collapse Analysis of CFRP Strengthened and Rehabilitated Degraded Steel Welded RHS Beams Subjected to Combined Bending and Bearing.” *Thin-Walled Structures* 82: 278–95. http://dx.doi.org/10.1016/j.tws.2014.05.002.

Elchalakani, Mohamed, Xiao Ling Zhao, and Raphael Grzebieta. 2004. “Cyclic Bending Tests to Determine Fully Ductile Section Slenderness Limits for Cold-Formed Circular Hollow Sections.” *Journal of Structural Engineering* 130(7): 1001–10.

Elias, Z. and Chen, K.-L. 1988. “Nonlinear Shallow Curved-Beam Finite Element”, Journal of Engineering Mechanics.” *Journal of Engineering Mechanics, ASCE* 114: 1076–87.

Farmer N & Smith I. 2001. “King Street Railway Bridge}strengthening of Cast Iron Girders with FRP Composites.” In *Proceedings of the 9th International Conference on Structural Faults and Repairs, London,*.

Fawzia, S., Al-Mahaidi, R., Zhao, X. L. and Rizkalla, S. 2007. “Strengthening of Circular Hollow Steel Tubular Sections Using High Modulus CFRP Sheets.” *Construction and Building Materials* 21(4): 839–45.

Fawzia, S., R. Al-Mahaidi, X. L. Zhao, and S. Rizkalla. 2007. “Strengthening of Circular Hollow Steel Tubular Sections Using High Modulus CFRP Sheets.” *Construction and Building Materials* 21(4): 839–45.

Fawzia, Sabrina et al. 2015. “Effects of CFRP Layer Orientation on Strengthening of Hollow Steel Elements.” *Journal of the Croatian Association of Civil Engineers* 67(5): 441–51. http://casopis-gradjevinar.hr/archive/article/1127.

Fernado, D. 2010. *Bond Behaviour and Bonding Failures of CFRP Strengthened Steel Sructures*. PhD by Thesis, Department of Civil and Structural Engineering, The Hong Kong Polytechnic University, Hong Kong.

Fernando, D., T. Yu, J. G. Teng, and X. L. Zhao. 2008. “CFRP Strengthening of Rectangular Steel Tubes Subjected to End Bearing Loads: Effect of Adhesive Properties.” *Proceedings of the 4th International Conference on FRP Composites in Civil Engineering, CICE 2008* (Schnerch 2005): 22–24.

Fernando, D, T Yu, J G Teng, and X L Zhao. 2009. “Thin-Walled Structures CFRP Strengthening of Rectangular Steel Tubes Subjected to End Bearing Loads :

Effect of Adhesive Properties and Finite Element Modelling." *Thin Walled Structures* 47(10): 1020–28. http://dx.doi.org/10.1016/j.tws.2008.10.008.

Fernando, Dilum. 2010. *Bond Behaviour Nd Debonding Failures in CFRP Strengthened Steel Members*. PhD by Thesis, Department of Cvil and Structural Engineering, The Hong Kong Plytechnic University.

Fernando ND. 2010. "Bond Behaviour and Debonding Failures in CFRP-Strengthened Steel Members." The Hong Kong Polytechnic University, Hong Kong, China.

Flinn, R.A. and Trojan, P.K. 1995. *Engineering Materials and Their Applications*. John Wiley and Sons.

Francis, R. 2000. *Bimetallic Corrosion: Guides to Good Practice in Corrosion Control*. National Physical Laboratory, Teddington, Middlesex.

Fukumoto, Y., Nishida, S. 1981. "Ultimate Load Behavior of Curved I-Beams." *J. Engrg. Mech. Div., ASCE* 107(2): 367–85.

Gamage, J.C.P.H. 2009. *Cyclic Temperature and Humidity Effects on Bond between CFRP and Concrete*. PhD by Thesis, Department of Civil Engineering, Monash University, Australia.

Gao, X Y, T Balendra, and C G Koh. 2013. "Buckling Strength of Slender Circular Tubular Steel Braces Strengthened by CFRP." *Engineering Structures* 46: 547–56. http://dx.doi.org/10.1016/j.engstruct.2012.08.010.

Gendy, A. S., and A. F. Saleeb. 1992. "On the Finite Element Analysis of the Spatial Response of Curved Beams with Arbitrary Thin-Walled Sections." *Computers and Structures* 44(3): 639–52.

George C. Tsiatas, Nick G. Babouskos. 2017. “Linear and Geometrically Nonlinear Analysis of Nonuniform Shallow Arches under a Central Concentrated Force.” *International Journal of Non-Linear Mechanics* 92: 92–101.

Gjelsvik, A. and Bodner, S.R. 1962. “The Energy Criterion and Snap Buckling of Arches.” *Journal Engineering of the Mechanic Division, ASCE* 88(05): 87–134.

Haedir, J., M. R. Bambach, X. L. Zhao, and R. H. Grzebieta. 2009. “Strength of Circular Hollow Sections (CHS) Tubular Beams Externally Reinforced by Carbon FRP Sheets in Pure Bending.” *Thin-Walled Structures* 47(10): 1136–47. http://dx.doi.org/10.1016/j.tws.2008.10.017.

Haedir, Jimmy, and Xiao Ling Zhao. 2011. “Design of Short CFRP-Reinforced Steel Tubular Columns.” *Journal of Constructional Steel Research* 67(3): 497–509. http://dx.doi.org/10.1016/j.jcsr.2010.09.005.

“Hamburg Airport Roof.” https://www.shutterstock.com/image-photo/hamburg-airport-roof-26921713 (April 25, 2020).

Hamood, Mohammed J, Maha Ghalib Ghaddar, Zinah Asaad, and Abdul Husain. 2020. “STRENGTHENING OF STRUCTURAL STEEL CHANNELS BY DIFFERENT CFRP WRAPPING CONFIGURATIONS-FINITE ELEMENT ANALYSIS.” *Journal of Engineering Science and Technology* 15(2): 1079–91.

Hand, H. M., Arah, C. O., McNamara, D. K. and Mecklenburg, M. F. 1991. “Effects of Environmental Exposure on Adhesively Bonded Joints.” *International Journal of Adhesion and Adhesives* 11(1): 15–23.

Harries, K.A., Peck, A.J. and Abraham, E.J. 2009. “Enhancing Stability of Structural Steel Sections Using FRP.” *Thin Walled Structures* 47(10): 1092–1101.

Harries, Kent A., and Sherif El-Tawil. 2008. “Steel-FRP Composite Structural

Systems.” *International Conference on Composite Construction in Steel and Concrete* (May): 1–30.

Hashim, S. A. 1999. “Adhesive Bonding of Thick Steel Adherends for Marine Structures.” *Marine Structures* 12(6): 405–23.

He, Xiaocong. 2011. “A Review of Finite Element Analysis of Adhesively Bonded Joints.” *International Journal of Adhesion and Adhesives* 31(4): 248–64.

Heshmati, Mohsen, Reza Haghani, and Mohammad Al-emrani. 2015. “Environmental Durability of Adhesively Bonded FRP/Steel Joints in Civil Engineering Applications: State of the Art.” *Composites Part B*. http://dx.doi.org/10.1016/j.compositesb.2015.07.014.

Heshmati, Mohsen, Reza Haghani, Mohammad Al-Emrani, and Alann André. 2018. “On the Strength Prediction of Adhesively Bonded FRP-Steel Joints Using Cohesive Zone Modelling.” *Theoretical and Applied Fracture Mechanics* 93: 64–78. http://dx.doi.org/10.1016/j.tafmec.2017.06.022.

Hii, Adrian K. Y. and Al-Mahaidi, Riadh. 2006. “Experimental Investigation on Torsional Behavior of Solid and Box-Section RC Beams Strengthened with CFRP Using Photogrammetry.” *Journal of Composites for Construction* 10(4): 321–29.

Hollaway, L. C., Teng, J. G. and Institute of Materials, Minerals and Mining. 2008. *Strengthening and Rehabilitation of Civil Infrastructures Using Fibre-Reinforced Polymer (FRP) Composites.* Cambridge, UK: Woodhead Publishing/CRC Press.

Hollaway, LC and Cadei, J. 2002. “Progress in the Technique of Upgrading Metallic Structures with Advanced Polymer Composites.” *Progress in Structural*

Engineering and Materials 4(2): 131–48.

Horibe T. and Asano, N. 2000. “Boundary Integral Equation Method Analysis of Large Deflection of Shallow Arch.” *Transactions of the Japan Society of Mechanical Engineers* 66: 1091–95.

Horton, T., Spinks, G.M. and Isles, N.A. 1992. “Structural Adhesive Performance in Marine Environments.” *Polymer International* 28(1): 9–17.

Hu, Lili, Peng Feng, and Xiao Ling Zhao. 2017. “Fatigue Design of CFRP Strengthened Steel Members.” *Thin-Walled Structures* 119(January): 482–98. http://dx.doi.org/10.1016/j.tws.2017.06.029.

Huang, Cheng, Tao Chen, and Xian Wang. 2017. “Compressive Characteristics of Damaged Circular Hollow Section (CHS) Steel Columns Repaired by CFRP or Grout Jacketing.” *Thin-Walled Structures* 119(February): 635–45. http://dx.doi.org/10.1016/j.tws.2017.07.008.

Hui, C. Y., A. Ruina, R. Long, and A. Jagota. 2011. “Cohesive Zone Models and Fracture.” *Journal of Adhesion* 87(1): 1–52.

Hutchinson, A. R. 1987. “Surface Pretreatment-the Key to Durability.” *Proceedings of the International Conference on Structural Faults & Repair*: 235–44.

Ibrahim, Amer M. 2018. “The Ovalisation of Steel Circular Hollow Sections under Bending.” 11(1): 12–19.

Jackson, N. 1966. “Collapse Loads for Circular-Arc Beams.” *J. Struct. Div., ASCE* 92(5): 1–14.

Jana S and Zhong W H. 2007. “FTIR Study of Ageing Epoxy Resin Reinforced by Reactive Graphitic Nanofibers.” *J Appl Polym Sci* 106: 3555–63.

Jiao, H. and Zhao, X. L. 2004. “CFRP Strengthened Butt-Welded Very High Strength (VHS) Circular Steel Tubes.” *Thin-Walled Structures* 42(7): 963–78.

Kabir, M H., S. Fawzia . T. H. T. Chan . J. C. P. H. Gamage. 2015. “Comparative Durability Study of CFRP Strengthened Tubular Steel Members under Cold Weather.” *Materials and Structures* 10 April. http://dx.doi.org/10.1617/s11527-015-0610-x.

Kabir, M. H., S. Fawzia, T. H.T. Chan, J. C.P.H. Gamage, et al. 2016. “Experimental and Numerical Investigation of the Behaviour of CFRP Strengthened CHS Beams Subjected to Bending.” *Engineering Structures* 113: 160–73. http://dx.doi.org/10.1016/j.engstruct.2016.01.047.

Kabir, M. H., S. Fawzia, and T. H.T. Chan. 2016. “Durability of CFRP Strengthened Circular Hollow Steel Members under Cold Weather: Experimental and Numerical Investigation.” *Construction and Building Materials* 123: 372–83. http://dx.doi.org/10.1016/j.conbuildmat.2016.06.116.

Kabir, M. H., S. Fawzia, T. H.T. Chan, and M. Badawi. 2016a. “Durability of CFRP Strengthened Steel Circular Hollow Section Member Exposed to Sea Water.” *Construction and Building Materials* 118: 216–25. http://dx.doi.org/10.1016/j.conbuildmat.2016.04.087.

———. 2016b. “Numerical Studies on CFRP Strengthened Steel Circular Members under Marine Environment.” *Materials and Structures/Materiaux et Constructions* 49(10): 4201–16.

Kabir, Mohammad Humayun, Sabrina Fawzia, Tommy H T Chan, and Jeeva C P H Gamage. 2014. “Durability Performance of Carbon Fibre-Reinforced Polymer Strengthened Circular Hollow Steel Members under Cold Weather.” *Australian*

Journal of Structural Engineering 15(4): 377–92.

Kadhim, Majid M.A., Zhangjian Wu, and Lee S. Cunningham. 2018a. "Loading Rate Effects on CFRP Strengthened Steel Square Hollow Sections under Lateral Impact." *Engineering Structures* (xxxx): 0–1. http://dx.doi.org/10.1016/j.engstruct.2018.04.066.

Kadhim, Majid M A et al. 2019. "Experimental and Numerical Investigation of CFRP-Strengthened Steel Beams under Impact Load." *Journal of Structural Engineering, ASCE* 145(4).

———. "Experimental and Numerical Investigation of CFRP Strengthened Steel Beams under Impact Load." (1).

Kadhim, Majid M A, Zhangjian Wu, and Lee S Cunningham. 2018b. "Loading Rate e Ff Ects on CFRP Strengthened Steel Square Hollow Sections under Lateral Impact." *Engineering Structures* (xxxx): 0–1. http://dx.doi.org/10.1016/j.engstruct.2018.04.066.

Kang Young J. Yoo Chai H. 1994. "Thin Walled Curved Beams. Ⅰ: Formulation of Nonlinear Equations." *J Eng Mech, ASCE* 122(5): 2072–2101.

Karimian, Masoumeh, Kambiz Narmashiri, Mehdi Shahraki, and Omid Yousefi. 2017. "Structural Behaviors of Deficient Steel CHS Short Columns Strengthened Using CFRP." *Journal of Constructional Steel Research* 138: 555–64.

Karnovsky, I.A. 2012. *Theory of Arched Structures: Strength, Stability, Vibration*. Springer Netherlands.

Karnovsky, Igor A. 2012. 9781461404699 Theory of Arched Structures: Strength,

Stability, Vibration *Theory of Arched Structures: Strength, Stability, Vibration*.

Katrizadeh, Eshagh, and Kambiz Narmashiri. 2019. “Experimental Study on Failure Modes of MF-CFRP Strengthened Steel Beams.” *Journal of Constructional Steel Research* 158: 120–29. https://doi.org/10.1016/j.jcsr.2019.03.027.

Keesei Lee, James S. Davidson, Junho Choi, Youngjong Kang. 2017. “Ultimate Strength of Horizontally Curved Steel I-Girders with Equal End Moments.” *Engineering Structures* 153(2017): 17–31.

Kelly P. 1999. “Epoxy Vinyl Ester and Other Resins in Chemical Process Equipment.” *Reinforced Plastics Durability* Cambridge,: 282–93.

Keykha, Amir Hamzeh. 2017. “3D FINITE ELEMENT ANALYSIS OF DEFICIENT HOLLOW STEEL BEAMS STRENGTHENED USING CFRP COMPOSITE UNDER TORSIONAL LOAD.” *Composites: Mechanics, Computations, Applications: An International Journal* 8: 287–97.

———. 2018. “Investigation of the Behavior of Deficient Steel Members Strengthened Using Carbon Fiber Reinforced Polymer under Combined Compressive Load and Torsional Moment.” *Mechanics of Advanced Materials and Structures* 0(0): 1–9. https://doi.org/10.1080/15376494.2018.1501833.

———. 2019. “Assessment of Structural Behavior of Vertical Curved Hollow Steel Beams Strengthened Using CFRP Composite.” *Practice Periodical on Structural Design and Construction* 24(2009): 1–8.

Keykha, Amir Hamzeh, Masoud Nekooei, Reza Rahgozar, and Kambiz Narmashiri. 2015. “Investigation of Load Increment in Hollow Steel Short and Slender Columns Strengthened Using CFRP.” *WALIA journal* 31(S3): 163–69.

Kim, J.G. and Kim, Y.Y. 1998. “A NEW HIGHER-ORDER HYBRID-MIXED

CURVED BEAM ELEMENT.” 940(February): 925–40.

Kostovailis, D.K.S.G., Hussein, M.F.M. and Owen, J.S. 2013. “A Comparison between the Use of Straight and Curved Beam Elements for Modelling Curved Railway Tracks.” In *In: 11th Biennial International Conference on Vibration Problems (ICOVP-2013), 9th ? 12th September 2013*, Lisbon, Portugal.

Kotnarowska D. 1999. “Influence of Ultraviolet Radiation and Aggressive Media on Epoxy Coating Degradation.” *Prog Org Coa* 37: 149–59.

Kozák, Vladislav. 2008. “Cohesive Zone Modelling.” *AIP Conference Proceedings* 1048: 328–31.

L C Hollaway and J Cadei. 2002. “Progress in the Technique of Upgrading Metallic Structures with Advanced Polymer Composites.” *Prog. Struct. Engng Mater* 4: 131–48.

Lane IR & Ward JA. 2000. “Restoring Britains Bridge Heritage.” *Institution of Civil Engineers (South Wales Association) Transport Engineering Group Award,*.

Lee, P.-G. and Sin, H.C. 1994. “Locking-Free Curved Beam Element Based on Curvature.” *International Journal for Numerical Methods in Engineering* 317: 989–1007.

Lenwari, Akhrawat, Thaksin Thepchatri, Pedro Albrecht, and M Asce. 2005. “Flexural Response of Steel Beams Strengthened with Partial-Length CFRP Plates.” (August): 296–303.

———. 2006. “Debonding Strength of Steel Beams Strengthened with CFRP Plates.” *Journal of Composites for Construction* 10(1): 69–78.

Li, Chuanxi et al. 2018. “Effects of Mechanical Properties of Adhesive and CFRP

on the Bond Behavior in CFRP-Strengthened Steel Structures." *Composite Structures*. doi: https://doi.org/ 10.1016/j.compstruct.2018.12.020%0AThis.

———. 2019. "Effects of Mechanical Properties of Adhesive and CFRP on the Bond Behavior in CFRP-Strengthened Steel Structures." *Composite Structures* 211: 163–74.

Liew, J Y Richard, V Thevendran, N E Shanmugam, and L O Tan. 1995. "Behaviour and Design of Horizontally Curved Steel Beams." 32: 37–67.

Linghoff, D., Al-Emrani, M. 2010. "Performance of Steel Beams Strengthened with CFRP Laminate – Part 2 : FE Analyses." *Composites Part B* 41(7): 516–22. http://dx.doi.org/10.1016/j.compositesb.2009.07.002.

Liu F, Zhang Z, Xu L and Tang M. 2012. "'Study on the Resistance of Ultraviolet Radiation of Composite Materials Based on Epoxy Resin." *Adv Mater Res* (391–392): 812–16.

Lo, C.F. and Conway, H.D. 1967. "The Elastic Stability of Curved Beams." *International Journal of Mechanical Sciences* 09: 527–38.

Lu, X.Z., Teng, J.G., Ye, L.P. and Jiang, J.J. 2005. "Bond-Slip Model for FRP Sheets/Plates Bonded to Concrete." *Engineering Structures* 27(6): 920–37.

Luu, A.-T. and Lee, J. 2016. "Non-Linear Buckling of Elliptical Curved Beams." *International Journal of Non-Linear Mechanics* 82: 132–43.

Madhavan, M., V. Sanap, R. Verma, and S. Selvaraj. 2015. "Flexural Strengthening of Structural Steel Angle Sections Using CFRP : Experimental Investigation." *Journal of Composites for Construction*: 1–10.

Mahmoud, Karam, and Ehab El-Salakawy. 2012. "Behavior of Full-Scale Railway

Turnout Sleepers from Glue-Laminated Fiber Composite Sandwich Structures." *Journal of Composites for Construction* 16(December): 724–36.

Mamalis, A. G., D. E. Manolakos, M. B. Ioannidis, and P. K. Kostazos. 2006. "Bending of Cylindrical Steel Tubes: Numerical Modelling." *International Journal of Crashworthiness* 11(1): 37–47.

Mays, G.C. and Hacinson, A.R. 1992. *Adhesives in Civil Engineering*. Cambridge University Press, Cambridge, England.

Mays, Geoffrey and Hutchinson, A. R. 1992. *Adhesives in Civil Engineering*. Cambridge [England]: Cambridge University Press.

Md Humayun Kabir. 2015. *ENVIRONMENTAL DURABILITY STUDY OF CFRP STRENGTHENED STEEL TUBULAR STRUCTURES UNDER FOUR-POINT BENDING*. PhD Thesis, Queensland University of Technology.

Miller, T.C., Chajes, M.J., Mertz, D.R., and Hasting, J.N. 2001. "Strengthening of Steel Bridge Girders Using CFRP Plates." *Journal of Bridge Engineering* 6(6): 523–28.

Miller, By Trent C et al. 2001. "Strengthening of a Steel Bridge Girder Using CFRP Plates." *Journal of Bridge Engineering* 6(December): 514–22.

Mirmiran, A. and Wolde-Tinsae, A.M. 1993. "Buckling and Postbuckling of Prestressed Sandwich Arches." *Journal of Structural Engineering, ASCE* 119(01): 262–78.

Mitsui, Kazuya et al. 2017. "Experimental Analysis and FE Modeling of Square Hollow Sections under Combined Axial and Bending Loads." *Eurosteel* 1(2): 4732–39.

Miyake, S., Nonaka, M. and Tosaka, N. 1991. “An Integral Equation Method for Geometrically Nonlinear Bending Problem of Elastic Circular Arch.” *Boundary Integral Methods, Springer-Verlag*: 349–58.

Moy, S. S. J., Hill, P., Moriarty, J., Dier, A. F., Kenchington, A. and Iverson, B. 2001. “Strengthening of Tunnel Supports Using Carbon Fibre Composites.” *Proceedings of the I MECH E Part L Journal of Materials:Design and Applications* 215(4): 235–43.

Naghipour, P. et al. 2009. “Fracture Simulation of CFRP Laminates in Mixed Mode Bending.” *Engineering Fracture Mechanics* 76(18): 2821–33. http://dx.doi.org/10.1016/j.engfracmech.2009.05.009.

Nakai, H., and Yoo, C. H. 1988. *Analysis and Design of Curved Steel Bridges.* McGraw-Hill, New York.

Narmashiri, Kambiz, Mohd Zamin Jumaat, and N H Ramli Sulong. 2010. “Investigation on End Anchoring of CFRP Strengthened Steel I-Beams.” *International Journal of Physical Sciences* 5(9): 1360–71.

Narmashiri, Kambiz, N H Ramli Sulong, and Mohd Zamin Jumaat. 2011. “Flexural Strengthening of Steel I-Beams by Using CFRP Strips.” *International Journal of the Physical Sciences* 6(7): 1620–27.

Narmashiri, Kambiz, N H Ramli Sulong, and Mohd Zamin. 2012. “Failure Analysis and Structural Behaviour of CFRP Strengthened Steel I-Beams.” *Construction and Building Materials* 30: 1–9. http://dx.doi.org/10.1016/j.conbuildmat.2011.11.009.

De Nève, B. and Shanahan, M. E. R. 1992. “Effects of Humidity on an Epoxy Adhesive.” *International Journal of Adhesion and Adhesives* 12(3): 191–96.

Nguyen, T. C., Bai, Y., Zhao, X. L. and Al-Mahaidi, R. “Durability of Steel/CFRP Double Strap Joints Exposed to Sea Water, Cyclic Temperature and Humidity.” *Composite Structures* 94(5): 1834–45.

Nishida S, Yoshida H, Fukumoto Y. 1978. “Large Deflection Analysis of Curved Members with Thin-Walled Open Cross-Section.” In *24th Symposium of Structural Engineering*, , 77–84.

Noor, A.K., Greene W.H. and Hartley, S.J. 1977. “Nonlinear Finite Element Analysis of Curved Beams.” *Computer Methods in Applied Mechanics and Engineering* 12: 289–307.

Noor, A.K. and Peters, J.M. 1981. “Mixed Models and Reduced/Selective Integration Displacement Models for Nonlinear Analysis of Curved Beams.” *International Journal for Numerical Methods in Engineering* 17: 615–31.

Nozaka, K., Shield, C.K., and Hajjar, J.F. 2005. “Effective Bond Length of Carbon-Fibre-Reinforced Polymer Strips Bonded to Fatigued Steel Bridge I-Girders.” *Journal of Bridge Engineering* 10(2): 195–205.

Park, Kyoungsoo, Kyungsu Ha, Habeun Choi, and Changjoon Lee. 2015. 63 Cement and Concrete Composites *Prediction of Interfacial Fracture between Concrete and Fiber Reinforced Polymer (FRP) by Using Cohesive Zone Modeling*. Elsevier Ltd. http://dx.doi.org/10.1016/j.cemconcomp.2015.07.008.

Patodi, S.C. and Buragohain, D.N. 1979. “Geometric Nonlinear Analysis of Structures by Discrete Energy Method.” *IABSE Proceedings* P-20/70: 1–12.

Pi, Y.-L., Bradford, M.A., and Uy, B. 2002. “In-Plane Stability of Arches.” *International Journal of Solids and Structures* 39(02): 105–25.

Pi, Y.-L. and Trahair, N.S. 1996. “Three-Dimensional Nonlinear Analysis of Elastic

Arches.” *Engineering Structures* 18: 49–63.

Pi, Y.L. and Bradford, M.A. 2004. “In-Plane Strength and Design of Fixed Steel I-Section Arches.” *Engineering Structures* 26(03): 291–301.

Pi, Y.L. and Trahair, N.S. 1996. “In-Plane Inelastic Buckling and Strength of Steel Arches.” *Journal of Structural Engineering, ASCE* 122(07): 734–47.

———. 1999. “In-Plane Buckling and Design of Steel Arches.” *Journal of Structural Engineering, ASCE* 125(11): 1291–98.

Pi, By Yong-lin, Mark A Bradford, and Nicholas S Trahair. 2000a. “Inelastic Analysis and Behavior of Steel I-Beams Curved in Plan.” *Journal of Structural Engineer- ing* 126(July): 772–79.

———. 2000b. “INELASTIC ANALYSIS AND BEHAVIOR OF STEEL I-BEAMS CURVED IN PLAN.” *JOURNAL OF STRUCTURAL ENGINEERING* 126(July): 772–79.

Pi, Yong Lin, Mark Andrew Bradford, and Francis Tin-Loi. 2008. “In-Plane Strength of Steel Arches.” *Advanced Steel Construction* 4(4): 306–22.

Rabinovitch, O. and Frostig, Y. 2000. “Closed-for High-Order Analysis of RC Beams Strengthened with FRP Strips.” *Journal of Composites for Construction* (4(2)): 65–74.

Rathnaweera, Gayan, Yvonne Durandet, Dong Ruan, and Michael Hajj. 2012. “Performance of Advanced High Strength Steel and Aluminium Alloy Tubes in Three-Point Bending.” *Sustainable Automotive Technologies 2012* 61(03): 25–32.

Reddy, B.D. and Volpi, M.B. 1992. “Mixed Finite Element Methods for the Circular

Arch Problem." *Computer Methods in Applied Mechanics and Engineering* 97: 125–45.

Reddy, J.N. and Sing, I.R. 1981. "Large Deflections and Large-Amplitude Free Vibrations of Straight and Curved Beams." *nternational Journal for Numerical Methods in Engineering* 17: 829–52.

Ren, Qing-xin, Lin-hai Han, Chao Hou, and You-xing Hua. 2017. "Experimental Behaviour of Tapered CFST Columns under Combined Compression and Bending." *JCSR* 128: 39–52. http://dx.doi.org/10.1016/j.jcsr.2016.08.005.

S S J Moy, P Hill, J Moriarty, A F Dier, A Kenchington and B Iverson. 2001. "Strengthening of Tunnel Supports Using Carbon _bre Composites." In *Proc Instn Mech Engrs, Vol 215 Part L,* , 235–42.

Sabir, A.B. and Lock, A. C. 1973. "Large Deflexion, Geometrically Non-Linear Finite Element Analysis of Circular Arches." *International Journal of Mechanical Sciences* 15: 37–47.

Sallam, H.E.M., Ahmad, S.S.E., Badawy, A.A.M., And Mandouh, W. 2006. "Evaluation of Steel I Beams Strengthened by Various Plating Methods." *Advances in Structural Engineering* 9(4): 535–44.

Schenerch, D., Dawood, M., Rizkalla, S. and Sumner, E. 2007. "Proposed Design Guidelines for Strengthening of Steel Bridges with FRP Materials." *Construction and Building Materials* 21(5): 1001–10.

Schnerch, D. A. 2005a. *Strengthening of Steel Structures with High Modulus Carbon Fiber Reinforced Polymer (CFRP) Materials.* PhD by Thesis, Department of Civil, Construction and Environmental Engineeirng, Raleigh, North Carolina.

———. 2005b. *Strengthening of Steel Structures with High Modulus Carbon Fiber Reinforced Polymer (CFRP) Materials*. PhD by Thesis, Department of Civil, Construction and Environmental Engineeirng, Raleigh, North Carolina.

Schnerch, D et al. 2005. "BOND BEHAVIOR OF CFRP STRENGTHENED STEEL BRIDGES." In *Proceedings of International Symposium on Bond Behaviour of FRP in Structures (BBFS 2005)*, International Institute for FRP in Construction.

Schnerch, D, M Dawood, S Rizkalla, and E Sumner. 2007. "Proposed Design Guidelines for Strengthening of Steel Bridges with FRP Materials." *Construction and Building Materials* 21: 1001–10.

Schnerch, David, and Sami Rizkalla. 2008. "Flexural Strengthening of Steel Bridges with High Modulus CFRP Strips." *Journal of Bridge Engineering* 13(2): 192–201.

Schreyer, H.L. and Masur, E.F. 1966. "Buckling of Shallow Arches." *Journal of the Engineering Mechanic Division, ASCE* 92(04): 1–20.

Seica, Michael V., and Jeffrey A. Packer. 2007. "FRP Materials for the Rehabilitation of Tubular Steel Structures, for Underwater Applications." *Composite Structures* 80(3): 440–50.

Selvaraj, Sivaganesh et al. 2013. "Experimental Studies on Strength and Stiffness Enhancement in CFRP-Strengthened Structural Steel Channel Sections under Flexure." *Journal of Composites for Construction*: 1–12.

———. 2019. "Strengthening of Laterally Restrained Steel Beams Subjected to Flexural Loading Using Low-Modulus CFRP." *Journal of Performance of Constructed Facilities* 33(3): 1–15.

Selvaraj, Sivaganesh, A M Asce, Mahendrakumar Madhavan, and M Asce. 2020. "Design of Steel Beams Strengthened with Low-Modulus CFRP Laminates." 24(1): 1–14.

Selvaraj, Sivaganesh, and Mahendrakumar Madhavan. 2017. "CFRP Strengthened Steel Beams: Improvements in Failure Modes and Performance Analysis." *Structures*. http://dx.doi.org/10.1016/j.istruc.2017.08.008.

———. 2019. "Retro Fitting of Steel Beams Using Low-Modulus Carbon Fi Ber Reinforced Polymer Laminates." *Journal of Constructional Steel Research*. https://doi.org/10.1016/j.jcsr.2019.105825.

Sen, Rajan, Larry Liby, and Gray Mullins. 2001. "Strengthening Steel Bridge Sections Using CFRP Laminates." 32: 309–22.

Serror, Mohammed H, Essam G Soliman, and Ahmed F Hassan. 2017. "Numerical Study on the Rotation Capacity of CFRP Strengthened Cold Formed Steel Beams." *Steel and Composite Structures* 4: 385–97.

Shaat, Amr, and Amir Fam. 2006. "Axial Loading Tests on Short and Long Hollow Structural Steel Columns Retrofitted Using Carbon Fibre Reinforced Polymers." *Canadian Journal of Civil Engineering* 33(4): 458–70. http://www.nrcresearchpress.com/doi/abs/10.1139/l05-042.

Shabila, H. I. 2005. *Strength and Durability Assessment of Flexure and Axial RC Members Strengthened with Carbon Fiber Polymer.* PhD by Thesis, Civil Engineering, The Graduate College, University of Illinois.

Shanmugam, N. E., V. Thevendran, J. Y. Richard Liew, and L. O. Tan. 1995. "Experimental Study on Steel Beams Curved in Plan." *Journal of Structural Engineering* 121(2): 249–59.

http://ascelibrary.org/doi/10.1061/%28ASCE%290733-9445%281995%29121%3A2%28249%29.

Shen, H.S., Teng, J.G., and Yang, J. 2001. “Interfacial Stresses in Beams and Slabs Bonded with Thin Plate.” *Journal of Engineering Mechanics* 127(4): 399–406.

Sika adhesive group. 2009. *Product Data Sheet(Sika-31).*

Silvestre, N., Young, B., and Camotim, D. 2008. “Non-Linear Behaviour and Load Carrying Capacity of CFRP-Strengthend Lipped Channel Steel Columns.” *Engineering Structures* 30(10): 2613–30.

Singha K. 2012. “A Short Review on Basalt Fiber.” *Int. J. Text. Sci.* 1(4): 19–28.

Sitnikova, Elena et al. 2019. “On the Representativeness of the Cohesive Zone Model in the Simulation of the Delamination Problem.” *Journal of Composites Science* 3(1): 22.

Siwowski, Tomasz W, and Paulina Siwowska. 2018. “Experimental Study on CFRP-Strengthened Steel Beams.” *Composites Part B*. https://doi.org/10.1016/j.compositesb.2018.04.060.

Smith, S.T. and Teng, J.G. 2001. “Interfacial Stresses in Plated Beams.” *Engineering Structures* 23(7): 857–71.

SMRITI RAJ, V RAMESH KUMAR, B H BHARATH KUMAR and NAGESH R IYER. 2016. “Basalt: Structural Insight as a Construction Material.” *Indian Academy of Sciences*.

Soudki, Khaled, and Ann Schumacher. 2009. “FLEXURAL STRENGTHENING OF A STEEL BEAM WITH PRESTRESSED CFRP STRIPS – PRELIMINARY INVESTIGATION.” In *FRPRCS-9 Sydney, Austrailia,* , 13–

16.

Srpčič, S. and Saje, M. 1986. “Large Deformations of Thin Curved Plane Beam of Constant Initial Curvature.” *International Journal of Mechanical Sciences* 28: 275–87.

Stolarski, H. and Belytschko, T. 1982. “Membrane Locking and Reduced Integration for Curved Elements.” *Journal of Applied Mechanics, ASME* 49: 172–76.

Sun, C.T., and Z.-H. Jin. 2012. “Cohesive Zone Model.” *Fracture Mechanics*: 227–46.

Sundaramoorthy Rajasekaran and S. Padmanabhan. 1989. “EQUATIONS OF CURVED BEAMS.” *J. Eng. Mech.* 115(5): 1094–1111.

Sundarraja, M. C., and G. Ganesh Prabhu. 2012. “Experimental Study on CFST Members Strengthened by CFRP Composites under Compression.” *Journal of Constructional Steel Research* 72: 75–83. http://dx.doi.org/10.1016/j.jcsr.2011.10.014.

Sundarraja, M. C., P. Sriram, and G. Ganesh Prabhu. 2014. “Strengthening of Hollow Square Sections under Compression Using FRP Composites.” *Advances in Materials Science and Engineering* 2014.

Surana, K.S. and Sorem, R.M. 1989. “Geometrically Non-Linear Formulation for Three Dimensional Curved Beam Elements with Large Rotations.” *International Journal for Numerical Methods in Engineering* 28: 43–73.

Tao, Zhong, Lin-hai Han, and Jin-ping Zhuang. 2007. “Axial Loading Behavior of CFRP Strengthened Concrete-Filled Steel Tubular Stub Columns.” *Advances in Structural Engineering* 10(1): 37–46.

Tao, Zhong, and Lin Hai Han. 2007. “Behaviour of Fire-Exposed Concrete-Filled Steel Tubular Beam Columns Repaired with CFRP Wraps.” *Thin-Walled Structures* 45(1): 63–76.

Tao, Zhong, Lin Hai Han, and Ling Ling Wang. 2007. “Compressive and Flexural Behaviour of CFRP-Repaired Concrete-Filled Steel Tubes after Exposure to Fire.” *Journal of Constructional Steel Research* 63(8): 1116–26.

Tavakkolizadeh, M. and Saadatmanesh, H. 2001. “Galvanic Corrosion of Carbon and Steel in Aggressive Environments.” *Journal of Composites for Construction* 5(3): 200–210.

Teng, J. G., Fernando, D., Zhao, X. L. and Yu, T. 2013. “Preparation and Characterization of Steel Surfaces for Adhesive Bonding.” *of Composites for Construction* 17.

Teng, J. G., D. Fernando, and T. Yu. 2015a. “Finite Element Modelling of Debonding Failures in Steel Beams Flexurally Strengthened with CFRP Laminates.” *Engineering Structures* 86: 213–24.

Teng, J. G., and Y. M. Hu. 2007. “Behaviour of FRP-Jacketed Circular Steel Tubes and Cylindrical Shells under Axial Compression.” *Construction and Building Materials* 21(4): 827–38.

Teng, J. G., T. Yu, and D. Fernando. 2012a. “Strengthening of Steel Structures with Fiber-Reinforced Polymer Composites.” *Journal of Constructional Steel Research* 78: 131–43.

Teng, J G, D Fernando, and T Yu. 2015b. “Finite Element Modelling of Debonding Failures in Steel Beams Flexurally Strengthened with CFRP Laminates.” *Engineering Structures* 86: 213–24.

Teng, J G, T Yu, and D Fernando. 2012b. “Strengthening of Steel Structures with Fi Ber-Reinforced Polymer Composites.” *Journal of Constructional Steel Research* 78: 131–43.

Trethewey, Kenneth R. and Chamberlain, John. 1988. *Corrosion: For Students of Science and Engineering*. Harlow, England: Longman Scientific & Technical.

Tu, Haoyun. 2018. “The Cohesive Zone Model.” In *Numerical Simulation and Experimental Investigation of the Fracture Behaviour of an Electron Beam Welded Steel Joint*, Springer International Publishing, 97–117.

Viveka, V, B Shanmugavalli, and M C Sundarraja. 2014. “Analytical Investigation on the Compressive Behaviour of CHS Tubular Columns Strengthened Using FRP Composites.” *International Journal of Civil Engineering Research* 5(4): 2278–3652. http://www.ripublication.com/ijcer.htm.

Walker A.C. 1974. “A Non-Linear Finite Element Analysis of Shallow Circular Arches.” *Computers & Structures* 04: 559–80.

Wang, Q.-L., J. Li, Y.-B. Shao, and W.-J. Zhao. 2015. “Flexural Performances of Square Concrete Filled CFRP-Steel Tubes (S-CF-CFRP-ST).” *Advances in Structural Engineering* 18(8): 1319–44.

Wang, Zhi Bin, Qing Yu, and Zhong Tao. 2015. “Behaviour of CFRP Externally-Reinforced Circular CFST Members under Combined Tension and Bending.” *Journal of Constructional Steel Research* 106: 122–37. http://dx.doi.org/10.1016/j.jcsr.2014.12.007.

Wardenier, J. 2001. “HOLLOW SECTIONS Hollow Sections in Structural Applications.” *Technology*: 199.

West, T.D. 2001. “Enhancements to the Bond between Advanced Composite

Materials and Steel for Bridge Rehabilitation." *Materials science*.

Wong, Yee-Chit. 1970. "HORIZONTALLY CURVED BEAM ANALYSIS AND DESIGN." A thesisi submitted to Oregon State University.

Wu, Chao, Li He, Elyas Ghafoori, and Xiao-ling Zhao. 2018. "Torsional Strengthening of Steel Circular Hollow Sections (CHS) Using CFRP Composites." *Engineering Structures* 171: 806–16.

Xenidis, H., Morfidis, K. and Papadopoulos, P.G. 2013. "Nonlinear Analysis of Thin Shallow Arches Subject to Snap-through Using Truss Models." *Structural Engineering and Mechanics* 45: 521–42.

Xia, S.H., and Teng, J.G. 2005. "Behaviour of FRP-to-Steel Bonded Joints." In *Proceedings, International Symposium on Bond Behaviour of FRP in Structures*, Hong Kong, China.

Yang, j. and Ye, J.Q. 2010. "An Improved Closed-Form Solution to Interfacial Stresses in Plated Beams Using a Two-Stage Approach." *International journal of mechanical sciences* 52(1): 13–30.

Yang, Zhibo et al. 2014. "The Analysis of Curved Beam Using B-Spline Wavelet on Interval Finite Element Method." *Shock and Vibration* 2014.

Yao, J., Teng, J.G. and Chen, J.F. 2005. "Experimental Study on FRP-to Concrete Bonded Joints." *Composites Part B: Engineering* 36(2): 99–113.

Yoo, C. H., and Heins, C. P. 1972. "Plastic Collapse of Horizontally Curved Bridge Girders." *J. Struct. Div., ASCE* 98(4): 899–914.

Yoo Chai H, Davidson James S. 1997. "Yield Interaction Equations for Nominal Bending Strength of Curved I-Girders." *J Bridge Eng, ASCE* 2(2): 37–44.

Yoshida, By Hiroshi, and Kouji Maegawa. 1983. “Ultimate Strength Analysis of Curved I-Beams.” 109(1): 192–214.

Yu, Y, S P Chiew, and C K Lee. 2011. “Bond Failure of Steel Beams Strengthened with FRP Laminates – Part 2 : Verification.” *Composites : Part B* 42: 1122–34.

Yuan, H. and Wu, Z. 1999. “Theoratical Solutions on Interfacial Stress Transfer of Externally Bonded Steel/Composite Laminates.” In *Proceedings of the Symposium of China and Japan: Science and Technology of 21st Century*, Tokyo.

Zhang, L. and Teng, J.G. 2010. “Finite Element Prediction of Interfacial Stresses in Structural Members Bonded with s Thin Plate.” *Engineering Structures* 32: 459–71.

Zhang, Zhujing et al. 2018. “Cyclic Performance of Bonded Sleeve Beam-Column Connections for FRP Tubular Sections.” *Composites Part B: Engineering* 142: 171–82. https://doi.org/10.1016/j.compositesb.2018.01.024.

Zhang, Zong-xing, Shan-hua Xu, Lin Mu, and Sheng-yuan Peng. 2020. “Experimental and Theoretical Investigation on Flexural Behavior of Corroded Steel Beams Strengthened by CFRP Plate.” *KSCE Journal of Civil Engineering* 24(7): 2160–72.

Zhao, X. L., Fernando, D., and Al-Mahaidi, R. 2006. “CFRP Strengthened RHS Subjected to Transverse End Bearing Force.” *Engineering Structures* 28(11): 1555–65.

Zhao, Ou et al. 2015. “Experimental and Numerical Studies of Ferritic Stainless Steel Tubular Cross Sections under Combined Compression and Bending.” *Journal of Structural Engineering, ASCEng*.

Zhao, Xiao Ling, and Lei Zhang. 2007. “State-of-the-Art Review on FRP Strengthened Steel Structures.” *Engineering Structures* 29(8): 1808–23.

Zhou, Feng, and Ben Young. 2007. “Experimental and Numerical Investigations of Cold-Formed Stainless Steel Tubular Sections Subjected to Concentrated Bearing Load.” *Journal of Constructional Steel Research* 63(11): 1452–66.

Zojaji, A. R., and M. Z. Kabir. 2011. “Analytical Approach for Predicting Full Torsional Behavior of Reinforced Concrete Beams Strengthened with FRP Materials.” *Scientia Iranica* 19(1): 51–63. http://dx.doi.org/10.1016/j.scient.2011.12.004.